

A New Material Characterization Approach for Evaluating the Deformational Capacity of
Onshore Pipelines

by

Onyekachi Ndubuaku

A thesis submitted in partial fulfillment of the requirements for the degree of

Doctor of Philosophy

in

Structural Engineering

Department of Civil and Environmental Engineering
University of Alberta

© Onyekachi Ndubuaku, 2019

ABSTRACT

The buckling instability phenomenon in shell structures is inherently influenced by a variety of parameters which may exhibit direct nonlinear relationships with the resultant stress and consequent deformation in the structure, as well as complex interrelationships, under various loading combinations. Hence, a computerized simulation of complex nonlinear mechanics problems, such as shell buckling, is often required for predicting the deformational behavior of cylindrical shell structures by means of numerical optimization methods. Notwithstanding the numerous advantages of numerical simulation, semi-empirical derivation of constitutive mathematical models for predicting the deformational response of shell structures is usually fraught with inadequacies due to improper characterization of the material stress-strain relationship and consequent misrepresentation of the strain-hardening behavior. A simple and versatile stress-strain model was therefore developed as an essential component of this research for accurate parameterization of the stress-strain behavior of a wide range of metallic materials over the full range of strains, including materials with a well-defined yield point and extended yield plateau. The applicability of the developed stress-strain model was validated using experimental data from tensile coupon tests of various standard pipeline steels and other metallic materials. Preliminary studies, to show the adaptation of the material model to shell stability analysis, was also performed on uniformly-compressed simply-supported flat plated FE models and material curve shape variations were observed to play a pivotal role in the load-deformation response. The buckling behavior of thin-walled cylindrical shells subjected to various loading conditions was numerically evaluated using a computerized finite element (FE) simulation program, ABAQUS CAE. Extensive parametric analysis was conducted based on the main factors that influence the buckling response of cylindrical-shell structures, i.e. dimensional

properties, loading conditions, material grade, and strain-hardening properties. Nonlinear multiple regression techniques were employed, using a powerful general-purpose computational software package (Wolfram Mathematica), to derive the coefficients of several constitutive nonlinear mathematical expressions, developed as handy design tools for estimating the critical limit strain (CLS) in onshore steel pipelines. The strain-hardening properties of the material stress-strain curve were incorporated into the constitutive equations based on the shape constants of the newly-developed stress-strain model. The semi-empirical models were developed according to two material-type classifications (yield-plateau type and round-house type) of the stress-strain curves of pipeline steels. Excellent goodness-of-fit with the critical limit strains obtained from the numerical finite element simulation was obtained for all the developed semi-empirical models. Good alignment with the trends of data obtained from full-scale experiments of pipe segments was also illustrated using the developed semi-empirical equations.

PREFACE

All the research work presented for this thesis forms part of a research collaboration between the University of Alberta and TransCanada Pipelines Ltd., with Professor Samer Adeeb being the lead collaborator at the University of Alberta and Michael Martens being responsible for facilitation and acquisition of research funding at TransCanada Pipelines.

The three introductory chapters in this thesis, i.e., Chapter 1 (Introduction), Chapter 2 (Review of Literature), and Chapter 3 (Basic Theoretical Formulations), are all my original work, and include appropriate citation of references as required.

The subsequent chapters (Chapter 4 – Chapter 9) are derived from either conference proceedings, journal publication, or research articles intended for publication in selected journals. Chapter 4 is derived from the combination of two published conference proceedings: (1) O. Ndubuaku, M. Martens, J.J.R. Cheng, S. Adeeb, Expression of a Generic Full-Range True Stress-True Strain Model for Pipeline Steels Using the Product-Log (Omega) Function, in: Vol. 6B Mater. Fabr., ASME, 2017: p. V06BT06A050. doi:10.1115/PVP2017-65236, and (2) O. Ndubuaku, M. Martens, R. Cheng, A. Ahmed, S. Adeeb, A Novel Approach for True Stress-True Strain Material Characterization of Metallic Materials Using the Product-Log (Omega) Function, in: 6th Int. Conf. Eng. Mech. Mater., CSCE, May 31 - June 3, Vancouver, B.C., Canada, 2017. Chapter 5 is derived from a research article published in the Elsevier Construction and Building Materials journal: O. Ndubuaku, X. Liu, M. Martens, J.J. Roger Cheng, S. Adeeb, The effect of material stress-strain characteristics on the ultimate stress and critical buckling strain of flat plates subjected to uniform axial compression, Constr. Build. Mater. 182 (2018) 346–359. doi:10.1016/j.conbuildmat.2018.06.100. Chapter 6 is derived from a research article submitted for publication in the Elsevier Thin-walled Structures journal. Chapter 7 is derived from a research article submitted for publication in the Elsevier Engineering Structures journal. Chapter 8 is derived from a research article submitted for publication in the Elsevier International Journal of Solids and Structures. Chapter 9 is derived from a research article submitted for publication in the MDPI Applied Sciences journal.

I was the lead investigator for all the research conducted herein and, therefore, responsible for concept formation, data collection and analysis, and manuscript composition. Being the

supervisory author, S. Adeeb was involved in concept improvement and manuscript edits. All other authors, including S. Adeeb, provided extensive and resourceful technical input for methodology formulation and results validation.

O. Ndubuaku

Dedicated

with love

to my beautiful sunshine, my darling wife, Uzoma

to my cute shiny moon, my handsome little boy, Gosioha

and to my priceless shining stars, so far away yet always present.

ACKNOWLEDGEMENTS

First and foremost, I will like to give thanks to the Almighty God, the maker of heaven and earth, the one who gives me life. Thank you, my heavenly father. It is only by your grace, favor, and enablement that I am where I am today. I return all the glory to you. Now and forever.

My deepest gratitude goes to my supervisor, Professor Samer Adeeb, for his invaluable and consistent support, motivation, guidance, and availability. I am extremely grateful to you Sir, for your undiminishing positive energy, which has driven me to always strive to surpass expectations. You make even the most difficult tasks seem like a walk-over, with your perpetual indomitable disposition. Thank you for your excellent mentorship in my academic, professional and career endeavors. And thank you for always being so kind and patient and understanding.

My sincere appreciation also goes every member of my examination committee, Professor Roger Cheng, Professor Chong-Qing Ru, Dr. Ali Imanpour and Dr. Yong Li, for their astute oversight, and for consistently and graciously nudging me towards producing a better version of this research work. I am also grateful to my external examiner, Dr. Wenxing Zhou, for his investment of time and effort into making this research endeavor a success.

Further thanks go to all my professors in the Structures group, Professor Robert Driver, Dr. Carlos Cruz-Noguez, Dr. Mustafa Gul, and Dr. Douglas Tomlinson, whose masterly tutelage and invaluable academic insight have immensely contributed to my current academic achievements and, undoubtedly, to my future career accomplishments.

Many thanks also go to the amiable and highly-cooperative technicians at the I.F. Morrison Structural Engineering Laboratory, Greg Miller and Cameron West, for their constructive technical guidance and support. And for helping me learn how to break and deform specimens in the laboratory without breaking or deforming myself in the process.

This research will not have been possible without funding facilitated by my supervisor, Professor Samer Adeeb, and I am overly appreciative. Also, for the funds provided by the Faculty of Graduate Studies and Research (University of Alberta Doctoral Recruitment Scholarship), MITACS Accelerate, and TransCanada Pipelines Limited, I am utterly grateful. I will also like to thank the Niger Delta Development Commission in Nigeria for awarding me the Post-Graduate

Foreign Scholarship award. Many thanks also go to the two industrial partners that I have been opportune to work with in the course of my Ph.D. program, Dr. Ali Fathi of Alfa Upgrades Inc. and Mr. Michael Martens of TransCanada Pipelines Ltd., for mentorship, technical support, and fund facilitation.

What will the world be without good friends and fond memories? My heartfelt thanks go to all my friends at the University of Alberta: Chike Okoloekwe, Jonelle Jn Baptiste, Diana Abdulhameed, Meng Lin, Sylvester Agbo, Allan Okodi, Kairs Wong, Yueying Li, Ramón Rosales-Espinoza, Fatemeh Fallahi Arezodar, Maliheh Ghaneei, Bernado Garcia, Jeffrey Hung, Victoria Buffam, Riley Quintin and Xiaoben Liu. I am grateful for all the happy conversations and joyful celebrations, and for the academic support you were all ever-willing to lend.

I also like to express my sincere and utmost appreciation to my parents, Dr. and Prof. (Mrs) Theophilus Ndubuaku. You have invested your time, sweat and resources into providing me the opportunities that have inevitably made it possible for me to be sitting here right now and writing this. I can never thank you enough and God knows I will forever be grateful to both of you for your endless love and care and dedication.

I am also utterly thankful, from the bottommost parts of my heart, to my siblings, Chijioke Ndubuaku, Ekene Ebido, and Amaka Asuquo, for their emotional and spiritual support. For your unending prayers and countless words of encouragement, I am very grateful. And to my long-time friend, Nosa Ogbomo, I hope that we meet and become friends again and again in all our future lives, if any. You will always have a special place in my heart. Thank you for always being there, even when you have not found it convenient. Only God can truly reward you for your selfless support throughout the years and I pray He blesses you, more than you can ever imagine.

Last but not least, to my loving wife, Uzoma, words cannot describe the joy and happiness that you have given me every day of this endeavor. You have remained unwaveringly kind, extremely patient, infinitely loving and incredibly understanding. Thank you very much for all your care, selfless support, and prayers. You always spur me towards my greater potential. With every fiber of your bones, you have devoted your time and energy to help make this journey seamless for us and I will always love you. God bless you.

TABLE OF CONTENTS

TITLE PAGE	i
ABSTRACT	ii
PREFACE	iv
DEDICATION	vi
ACKNOWLEDGEMENTS	vii
TABLE OF CONTENTS.....	ix
LIST OF TABLES	xvi
LIST OF FIGURES	xvii
1. INTRODUCTION	1
1.1 Background	2
1.2 The Buckling Phenomenon: Overview	4
1.3 Problem Statement	7
1.4 Objectives and Scope	8
1.5 Research Methodology.....	9
1.6 Organization of Thesis	11
1.7 References	14
2. REVIEW OF LITERATURE	17
2.1 Introduction	18
2.2 Buckling of Cylindrical Shells	21
2.3 Critical Buckling Stress: Axial Compression vs. Bending	24
2.4 Influence of Slenderness Properties on Buckling	27
2.5 Measurement of Compressive Strain	29
2.6 References	31

3.	BASIC THEORETICAL FORMULATIONS.....	39
3.1	Introduction	40
3.2	Critical Buckling Stress for a Simply-supported Flat Plate	40
3.3	Critical Buckling Stress for a Perfect Cylindrical Shell.....	47
3.4	Considering Plasticity and Anisotropy in Axially-compressed Cylinders: A Brief Overview	52
3.5	Conclusions	54
3.6	References	54
4.	EXPRESSION OF A GENERIC FULL-RANGE MATERIAL MODEL FOR STRESS-STRAIN CHARACTERIZATION OF PIPELINE STEELS AND OTHER METALLIC MATERIALS USING THE PRODUCT-LOG (OMEGA) FUNCTION.....	57
4.1	Abstract	58
4.2	Introduction	60
4.3	Effect of Microstructural Properties on Mechanical Response.....	63
4.4	Stress-strain Material Characterization	65
4.5	Review of Existing Stress-strain Equations	67
4.6	Description of the Proposed Stress-strain Model.....	74
4.7	Methodology for Nonlinear Curve-fitting.....	76
4.8	Validation of Proposed Model (General Application to Metallic Materials).....	78
4.9	Validation of Proposed Model (Application to Pipeline Steels).....	82
4.10	Numerical Model Application.....	85
4.11	Conclusions	89
4.12	References	90

5. THE EFFECT OF MATERIAL STRESS-STRAIN CHARACTERISTICS ON THE BUCKLING CAPACITY OF FLAT PLATES SUBJECTED TO UNIFORM AXIAL COMPRESSION.....	95
5.1 Abstract	96
5.2 Introduction	97
5.3 Buckling Capacity of Flat Plates.....	102
5.4 Proposed Material Model.....	106
5.4.1 Model definition.....	107
5.4.2 Inverted form of the proposed model.....	109
5.4.3 Derivation of model constants	111
5.5 Numerical Simulation of Plate Buckling	112
5.5.1 Geometric properties/ support conditions.....	112
5.5.2 Material properties	114
5.5.3 Imperfection modeling.....	116
5.6 Results and Discussions	117
5.7 Conclusions	128
5.8 References	129
6. A SEMI-EMPIRICAL MODELLING APPROACH FOR PREDICTING THE DEFORMATIONAL CAPACITY OF AXIALLY-COMPRESSED CYLINDRICAL SHELLS BASED ON A NOVEL MATERIAL STRESS-STRAIN CHARACTERIZATION METHOD	135
6.1 Abstract	136
6.2 Introduction	138
6.3 Constitutive Model for Material Characterization	145
6.4 Theoretical Formulations	149

6.5	Methodology of Numerical Research	150
6.5.1	Test matrix	151
6.5.2	Geometry, mesh, and elements	156
6.5.3	Symmetry, boundary conditions, and loading	157
6.5.4	Post-processing	158
6.5.5	Imperfection sensitivity analysis.....	159
6.6	Validation of FE Models	160
6.7	Results of Numerical Analysis	162
6.7.1	Parametric study for YPT pipes	162
6.7.2	Parametric study for RHT pipes	165
6.8	Discussion	167
6.8.1	YPT pipes.....	169
6.8.2	RHT pipes	171
6.9	Semi-Empirical Models for CLS Prediction	173
6.10	Statistical Accuracy Analysis.....	177
6.11	Conclusions	180
6.12	References	182
7.	A PARAMETRIC STUDY ON THE EFFECT OF UNIFORMLY-INDUCED CURVATURE ON THE DEFORMATIONAL CAPACITY OF STEEL ONSHORE PIPELINES BASED ON A NOVEL MATERIAL CHARACTERIZATION PROCEDURE..	189
7.1	Abstract	190
7.2	Introduction	192
7.3	Materials and Methods	200
7.3.1	Stress-strain characterization model	200
7.3.2	Matrix of parameters.....	202

7.3.3	Numerical finite element (FE) simulation	205
7.4	Validation of FE Model.....	208
7.5	Results of Parametric FE Study	213
7.5.1	Influence of D/t ratio.....	213
7.5.2	Influence of internal pressure.....	214
7.5.3	Influence of material grade	215
7.5.4	Influence of material curve shape	216
7.6	Development of CLS Equations.....	217
7.7	Goodness-of-Fit.....	220
7.8	Discussion	223
7.9	Comparison of CLS Model with Existing Equations.....	227
7.10	Conclusions	232
7.11	References	233
8.	DEVELOPMENT OF NONLINEAR REGRESSION EQUATIONS FOR PREDICTING THE CRITICAL LIMIT STRAIN OF STEEL PIPELINES SUBJECTED TO COMBINED UNIFORM AXIAL COMPRESSION AND BENDING USING A NOVEL MATERIAL CURVE SHAPE PARAMETERIZATION APPROACH.....	241
8.1	Abstract	242
8.2	Introduction	244
8.3	Material Curve Shape Characterization	250
8.4	Test Matrix	251
8.5	FE Model.....	256
8.5.1	FE mesh & elements	257
8.5.2	Boundary conditions	258
8.5.3	Loading sequence.....	259

8.5.4	Output and post-processing.....	259
8.6	Results of FE Analysis.....	260
8.6.1	FE model validation.....	260
8.6.2	Influence of D/t ratio.....	261
8.6.3	Influence of internal pressure.....	262
8.6.4	Influence of material grade.....	263
8.6.5	Influence of material curve shape.....	264
8.6.6	Influence of compressive net-section axial force.....	265
8.7	Semi-empirical Modelling.....	266
8.7.1	CLS equations.....	266
8.7.2	Limit stress equations.....	270
8.7.3	Goodness-of-fit.....	272
8.8	Discussion.....	276
8.9	Comparison of CLS Model with Experimental Results.....	279
8.10	Conclusions.....	282
8.11	References.....	284
9.	INTEGRATING THE SHAPE CONSTANTS OF A NOVEL MATERIAL STRESS-STRAIN CHARACTERIZATION MODEL FOR PARAMETRIC NUMERICAL ANALYSIS OF THE DEFORMATIONAL CAPACITY OF HIGH-STRENGTH X80-GRADE STEEL PIPELINES.....	291
9.1	Abstract.....	292
9.2	Introduction.....	294
9.3	Characterization of Material Stress-Strain Behavior.....	299
9.4	Methodology of Numerical Analysis.....	302
9.5	Numerical Results.....	306

9.5.1	Validation of numerical model	306
9.5.2	Evolution of stress in pipes	307
9.5.3	Results of parametric analysis	311
9.6	Derivation of Semi-Empirical Models	317
9.6.1	CLS derivation	317
9.6.2	Limit stress derivation.....	320
9.7	Goodness-of-fit.....	321
9.8	Discussion of Results	321
9.9	Conclusions	325
9.10	References	326
10.	SUMMARY, CONCLUSIONS AND RECOMMENDATIONS.....	333
10.1	Summary	334
10.2	Conclusions	338
10.3	Recommendations	341
	BIBLIOGRAPHY.....	345
	APPENDIX: MATHEMATICA CODES FOR IMPLEMENTING NEW MATERIAL STRESS- STRAIN CHARACTERIZATION PROCEDURE.....	379

LIST OF TABLES

Table 4-1: Model parameters and R2 values for model-to-experiment curve-fit evaluations.....	80
Table 4-2: R-squared values for model parameters	83
Table 4-3: Model constants for stress-strain curves	86
Table 5-1: Constitutive model parameters for derivation of idealized stress-strain curves.....	124
Table 6-1: Model constants for derivation of stress-strain curves	155
Table 6-2: Nonlinear regression coefficients	175
Table 6-3: Applicable range for dimensionless parameters.....	176
Table 6-4: Values of linear model intercept for correction function and corresponding POUs .	179
Table 7-1: Shape constants for variation of material curve shape	205
Table 7-2: Constitutive equation coefficients	219
Table 7-3: Applicable range for dimensionless parameters.....	220
Table 7-4: Values of <i>Iorig</i> for correction function and corresponding POUs.....	222
Table 8-1: Model constants for derivation of stress-strain curves	256
Table 8-2: Nonlinear regression coefficients	268
Table 8-3: Applicable range for dimensionless parameters.....	269
Table 8-4: Values of <i>Iorig</i> for correction function and corresponding POUs.....	275
Table 8-5: Evaluation of test-to-predicted ratios	280
Table 9-1: Model shape constants for the derivation of stress-strain curves	302
Table 9-2: Nonlinear regression coefficients	319
Table 9-3: Applicable range for dimensionless parameters.....	320

LIST OF FIGURES

Figure 1-1: Upheaval buckling of a buried pipeline [6]	3
Figure 1-2: Shell-type buckling due to large ground movement [5]	3
Figure 3-1: Schematic of flat plate under uniform axial compression.....	44
Figure 3-2: Schematic of strain components for axially-compressed cylinder.....	48
Figure 4-1: Typical stress-strain curve.	66
Figure 4-2: Schematic of stress-strain curve showing proportionality limit and ultimate point ..	77
Figure 4-3: Model-to-experiment stress-strain plots for AA5083 at 110K	79
Figure 4-4 Model-to-experiment stress-strain plots for AA5083 at 0.00016/s.....	79
Figure 4-5: Model-to-experiment stress-strain plots for AISI 304L at 110K.....	79
Figure 4-6: Model-to-experiment stress-strain plots for AISI 304L at 0.00016/s	79
Figure 4-7: Model-to-experiment stress-strain plots for Invar Steel at 110K.....	80
Figure 4-8: Model-to-experiment stress-strain plots for Invar Steel at 0.00016/s.....	80
Figure 4-9: Model prediction for X-52 pipe steel (longitudinal).....	82
Figure 4-10: Model prediction for X-52 pipe steel (circumferential).....	82
Figure 4-11: Model prediction for X-60 & X-65 pipe steel.....	82
Figure 4-12: Model prediction for X-80 pipe steel.....	82
Figure 4-13: Model prediction for X-100 pipe steel.....	83
Figure 4-14: Illustration of yield plateau approximation.....	84
Figure 4-15: Picture of undeformed rectangular ABAQUS steel plate model; dimensions = 800 mm × 1600 mm × 9 mm	86
Figure 4-16: Stress-strain curves of steel plate models with varying strain-hardening characteristics.....	87
Figure 4-17: Load-deformation behavior of 9 mm-thick square plate	88
Figure 4-18: Load-deformation behavior of 15 mm-thick square plate	88
Figure 4-19: Load-deformation behavior of 9 mm-thick rectangular plate.....	88
Figure 4-20: Load-deformation behavior of 15 mm-thick rectangular plate.....	88
Figure 5-1: Schematic of flat plate under uniform axial compression.....	102
Figure 5-2: Plot of stress ratio to strain ratio ($H_{NM} = 1.3$; K_{NM} - varied).....	109
Figure 5-3: Plot of stress ratio to strain ratio ($K_{NM} = 1.3$; H_{NM} - varied)	109

Figure 5-4: Plate model geometric and edge support details	114
Figure 5-5: Comparison of equivalent stress approaches	115
Figure 5-6: Elastic buckling mode for initial imperfection	117
Figure 5-7: YPT curves.....	119
Figure 5-8: CHT curves - class 1	119
Figure 5-9: CHT curves - class 2	119
Figure 5-10: Ultimate strength and corresponding strain results for YPT curves with varying lengths of yield plateau and varying UTS.....	120
Figure 5-11: Ultimate strength and corresponding strain results for YPT curves with same lengths of yield plateau and varying UTS.....	120
Figure 5-12: Ultimate strength and corresponding strain results for YPT curves with varying lengths of yield plateau and same UTS.....	121
Figure 5-13: Ultimate strength and corresponding strain results for YPT curves with varying YPLs and intersecting strain-hardening.....	121
Figure 5-14: Ultimate strength and corresponding strain results for CHT curves with varying equivalent YS and varying UTS	122
Figure 5-15: Ultimate strength and corresponding strain results for CHT curves with varying equivalent YS and same UTS	122
Figure 5-16: Ultimate strength and corresponding strain results for CHT curves same equivalent YS and varying UTS.....	123
Figure 5-17: Ultimate strength and corresponding strain results for CHT curves with same equivalent YS and same UTS	123
Figure 5-18: Comparison of FEA and Winter curve	126
Figure 6-1: Flowchart of iterative procedure for derivation of inflection point knee factor	148
Figure 6-2: Schematic of strain components for axially-compressed cylinder.....	149
Figure 6-3: Idealized variations for stress-strain curves of X52-YPT and X52-RHT materials	153
Figure 6-4: Idealized variations for stress-strain curves of X60-YPT and X60-RHT materials	154
Figure 6-5: Idealized variations for stress-strain curves of X70-YPT and X70-RHT materials	154
Figure 6-6: Idealized variations for stress-strain curves of X80-YPT and X80-RHT materials	154
Figure 6-7: Linear superposition of eigenmodes	159

Figure 6-8: Plots of ϵ_{cr} for 50% scale (all imperfection types)	160
Figure 6-9: Plots of ϵ_{cr} for Type 2 imperfection	160
Figure 6-10: Comparison of FEA result with experimental result (UGA508) by Ref. [63].....	161
Figure 6-11: Plot of axial force vs. average strain for X60 pipe with D/t ratio = 104.62, $f_p = 0.8$, and YPL = 1.25.	162
Figure 6-12: Plot of ϵ_{cr} vs. D/t ratio for X70 pipe (YPL = 1.25)	163
Figure 6-13: Plot of ϵ_{cr} vs. D/t ratio for X70 pipe (YPL = 2.0)	163
Figure 6-14: Plot of ϵ_{cr} vs. f_p for X52 pipe (YPL = 1.0).....	164
Figure 6-15: Plot of ϵ_{cr} vs. f_p for X70 pipe (YPL = 1.5).....	164
Figure 6-16: Plot of ϵ_{cr} vs. YS for DT1 pipe ($f_p = 0.6$).....	164
Figure 6-17: Plot of ϵ_{cr} vs. YS for DT4 pipe ($f_p = 0.8$).....	164
Figure 6-18: Plot of ϵ_{cr} vs. D/t ratio for X70 pipe (PL/US = 0.73).....	165
Figure 6-19: Plot of ϵ_{cr} vs. D/t ratio for X70 pipe (PL/US = 0.58).....	165
Figure 6-20: Plot of ϵ_{cr} vs. f_p for X52 pipe (YPL = 1.0).....	166
Figure 6-21: Plot of ϵ_{cr} vs. YS for DT1 pipe ($f_p = 0.6$).....	167
Figure 6-22: Plot of ϵ_{cr} vs. PLUS ratio for DT4 pipe ($f_p = 0.8$).....	167
Figure 6-23: YPT model prediction vs. FEA.....	177
Figure 6-24: RHT model prediction vs. FEA	177
Figure 6-25: FTP distribution for YPT model	178
Figure 6-26: FTP distribution for RHT model.....	178
Figure 7-1: Idealized variations for stress-strain curves of X52-YPT and X52-RHT materials	203
Figure 7-2: Idealized variations for stress-strain curves of X60-YPT and X60-RHT materials	203
Figure 7-3: Idealized variations for stress-strain curves of X70-YPT and X70-RHT materials	204
Figure 7-4: Idealized variations for stress-strain curves of X80-YPT and X80-RHT materials	204
Figure 7-5: Pipe model geometry showing FE discretization.....	207
Figure 7-6: Comparison of FEA result with experimental result (UGA508) by Ref. [54].....	209
Figure 7-7: Comparison of moment-curvature responses for half-length and full-length pipe model.....	211
Figure 7-8: Evolution of wrinkle deformation for half-length pipe model.....	211
Figure 7-9: Evolution of wrinkle deformation for full-length pipe model	212

Figure 7-10: Plot of ϵ_{cr} vs. D/t ratio for YPT X70 pipe (YPL = 1.75).....	213
Figure 7-11: Plot of ϵ_{cr} vs. D/t ratio for RHT X52 pipe (PL/US = 0.81).....	213
Figure 7-12: Plot of ϵ_{cr} vs. f_p for YPT X60 pipe (YPL = 2.0)	214
Figure 7-13: Plot of ϵ_{cr} vs. f_p for RHT X52 pipe (PL/US = 0.81).....	214
Figure 7-14: Plot of ϵ_{cr} vs. σ_{ys} for YPT DT1 pipe (YPL = 1.25)	215
Figure 7-15: Plot of ϵ_{cr} vs. PL/US for RHT DT3 pipe ($f_p = 0.20$)	215
Figure 7-16: Plot of ϵ_{cr} vs. sh_f for YPT X70 pipe ($D/t = 41.152$).....	216
Figure 7-17: Plot of ϵ_{cr} vs. sh_f for YPT X52 pipe ($D/t = 82.156$).....	216
Figure 7-18: Model prediction vs. FEA for YPT.....	221
Figure 7-19: Model prediction vs. FEA for RHT	221
Figure 7-20: Comparison of CLS models with experimental test results for RHT X60 pipe: (a) $f_p = 0.0$, (b) $f_p = 0.4$, and (c) $f_p = 0.8$	230
Figure 7-21: Comparison of CLS models with experimental test results for RHT X70 pipe: (a) $f_p = 0.0$, (b) $f_p = 0.4$, and (c) $f_p = 0.8$	230
Figure 7-22: Comparison of CLS models with experimental test results for YPT X60 pipe: (a) $f_p = 0.0$, (b) $f_p = 0.4$, and (c) $f_p = 0.8$	230
Figure 7-23: Comparison of CLS models with experimental test results for YPT X70 pipe: (a) $f_p = 0.0$, (b) $f_p = 0.4$, and (c) $f_p = 0.8$	231
Figure 8-1: Idealized variations for stress-strain curves of X52-YPT and X52-RHT materials	254
Figure 8-2: Idealized variations for stress-strain curves of X60-YPT and X60-RHT materials	254
Figure 8-3: Idealized variations for stress-strain curves of X70-YPT and X70-RHT materials	254
Figure 8-4: Idealized variations for stress-strain curves of X80-YPT and X80-RHT materials	255
Figure 8-5: Pipe mid-length reduced-thickness sleeve (not drawn to scale)	257
Figure 8-6: Comparison of FEA result with experimental result (UGA508) by Ref. [55].....	260
Figure 8-7: Plot of ϵ_{cr} vs. D/t ratio for X52 pipe (YPL = 1.75%, $f_c = 0.2$)	261
Figure 8-8: Plot of ϵ_{cr} vs. D/t ratio for X52 pipe (PL/US = 0.811, $f_c = 0.2$)	261
Figure 8-9: Plot of ϵ_{cr} vs. f_p for X60 pipe (YPL = 1.50%, $f_c = 0.4$)	262
Figure 8-10: Plot of ϵ_{cr} vs. f_p for X60 pipe (PL/US = 0.674, $f_c = 0.4$)	262
Figure 8-11: Plot of ϵ_{cr} vs. yield stress for DT1 pipe (YPL=1.0%, $f_c = 0.8$)	263
Figure 8-12: Plot of ϵ_{cr} vs. PLUS ratio for DT2 pipe ($f_p = 0.2$, $f_c = 0.6$).....	263

Figure 8-13: Plot of ϵ_{cr} vs. sh_f for (a) X70 DT1 pipe and (b) X70 DT3 pipe ($f_c = 0.4$)	264
Figure 8-14: Plot of ϵ_{cr} vs. sh_f for (a) X52 DT1 pipe and (b) X52 DT3 pipe ($f_c = 0.4$)	264
Figure 8-15: Plot of ϵ_{cr} vs. f_c for X52 DT2 pipe (YPL=1.50%).....	265
Figure 8-16: Plot of ϵ_{cr} vs. f_c for X52 DT2 pipe (PL/US = 0.811).....	265
Figure 8-17: YPT X60 plots of σL vs. (a) D/t ratio (b) internal pressure, and (c) yield stress...	271
Figure 8-18: RHT X70 plots of σL vs. (a) D/t ratio (b) internal pressure, and (c) yield stress ..	271
Figure 8-19: Model prediction vs. FEA for CLS of (a) YPT pipe and (b) RHT pipe under combined axial compression and bending	273
Figure 8-20: Model prediction vs. FEA for limit stress of (a) YPT pipe and (b) RHT pipe under uniform axial compression.....	273
Figure 8-21: Resultant end moment vs. average compressive strain plot for X52-DT1 YPT pipe ($f_p=0.0$, $f_c = 0.2$)	278
Figure 8-22: Resultant end moment vs. average compressive strain plot for X52-DT1 YPT pipe (YPL = 1.0%, $f_c = 0.2$).....	278
Figure 8-23: Model prediction vs. experimental CLS (original)	281
Figure 8-24: Model prediction vs. experimental CLS (corrected).....	281
Figure 9-1: Idealized variations for stress-strain curves of (a) X80-YPT, and (b) X80-RHT materials	301
Figure 9-2: Meshed area for average strain measurement	305
Figure 9-3: Comparison of FEA result with experimental result (UGA508) by Ref. [60].....	306
Figure 9-4: Axial load-displacement response and stress evolution in YPT DT4 pipes under uniform axial compression (YPL = 1.0%, $f_p = 0.4$)	308
Figure 9-5: Axial load-displacement response and stress evolution in RHT DT4 pipes under uniform axial compression (PL/US = 0.691, $f_p = 0.4$)	309
Figure 9-6: Moment-curvature response and stress evolution in YPT DT4 pipes under uniform bending (YPL = 1.0%, $f_p = 0.4$)	309
Figure 9-7: Moment-curvature response and stress evolution in RHT DT4 pipes under uniform bending (PL/US = 0.691, $f_p = 0.4$)	310
Figure 9-8: Plots of CLS vs. D/t ratio of YPT pipes with YPL = 1.50% for (a) uniform axial compression, (b) uniform bending, and (c) combined loading ($f_c = 0.6$).....	312

Figure 9-9: Plots of CLS vs. D/t ratio of RHT pipes with PL/US = 0.634 for (a) uniform axial compression, (b) uniform bending, and (c) combined loading ($f_c = 0.6$).....	312
Figure 9-10: Plots of CLS vs. f_p of YPT pipes with YPL = 1.25% for (a) uniform axial compression, (b) uniform bending, and (c) combined loading ($f_c = 0.6$).....	313
Figure 9-11: Plots of CLS vs. f_p of RHT pipes with PL/US = 0.691 for (a) uniform axial compression, (b) uniform bending, and (c) combined loading ($f_c = 0.6$).....	313
Figure 9-12: Plots of CLS vs. YPL of YPT DT1 pipes for (a) uniform axial compression, (b) uniform bending, and (c) combined loading ($f_c = 0.2$).....	314
Figure 9-13: Plots of CLS vs. YPL of YPT DT3 pipes for (a) uniform axial compression, (b) uniform bending, and (c) combined loading ($f_c = 0.2$).....	314
Figure 9-14: Plots of CLS vs. PLUS ratio of RHT DT1 pipes for (a) uniform axial compression, (b) uniform bending, and (c) combined loading ($f_c = 0.2$).....	315
Figure 9-15: Plots of CLS vs. PLUS ratio of RHT DT3 pipes for (a) uniform axial compression, (b) uniform bending, and (c) combined loading ($f_c = 0.2$).....	315
Figure 9-16: Plots of CLS vs. f_c for YPT pipes with YPL = 1.25%.....	316
Figure 9-17: Plots of CLS vs. f_c for RHT pipes with PL/US = 0.577.....	316
Figure 9-18: Model prediction vs. FEA results for YPT pipes for (a) LC1, (b) LC2, and (c) LC3	321
Figure 9-19: Model prediction vs. FEA results for RHT pipes for (a) LC1, (b) LC2, and (c) LC3	321
Figure 10-1: Plot of Curve-fitted R-squared value vs. heel constant.....	342



1. INTRODUCTION

1.1 Background

Pipelines are used offshore and onshore as the preferred means for transportation of gases and liquids including; hydrocarbons, water, and sewage. In order to transmit fluids from remote sources or through remote areas to target locations, a significant number of pipelines are installed such that they traverse a wide variety of soil types, geological conditions, and regions of varying seismicity. As a result, such pipelines are exposed to geohazards which pose a significant risk to their structural and mechanical integrity; especially in mountainous areas prone to landslides, areas that are seismically active, or areas where the ground is prone to subsidence [1].

Pipelines are also commonly subject to thermally induced axial loads and hoop stresses due to the internal pressure exerted by the fluids they convey; especially in the hydrocarbon industry where most steel pipelines are used to transport crude oil and a variety of other hydrocarbons from natural reservoirs at significantly high pressures and temperatures, thereby inducing large axial forces along the length of the pipeline. Thermal loading due to the heat of the hydrocarbons flowing through the pipeline induces axial extension which is restrained by the pipe-soil frictional forces along the length of the pipeline resulting in a net compressive axial force along its length [2, 3]. Also, a tensile stress develops in the hoop direction when a pipeline is subjected to internal pressure which interacts with the induced compressive axial force along the length of the pipeline to cause a magnification of the von Mises stresses in the pipe, thus resulting in premature buckling of the pipeline before attainment of the theoretical critical buckling load.

Two main classifications of the buckling phenomena have been observed in buried pipelines [4]: a *beam-type buckling* phenomenon usually occurs in small diameter pipelines buried in relatively shallow trenches. This generally results when pressure-temperature effects and/or ground movement initiate a transverse buckling deflection due to the compressive axial force in the pipeline which exceeds the overburden pressure of the overlying soil, causing an entire section of the pipeline to break out through the soil surface (Figure 1-1). On the other hand, larger diameter pipelines buried in relatively deep trenches usually exhibit a *shell-type buckling* phenomenon which results due to the constraint against transverse deflection of the pipeline by the trench walls and soil cover. The compressive axial force in the pipe thus builds up to a magnitude which initiates a local buckling mode in the pipe wall; characterized by a number of circumferential waves. A collapse of this type occurred in a 16-inch gas pipeline during the San Fernando

earthquake of 1971 (Figure 1-2). The pipeline was buried along the Glenoaks Boulevard at an angle with an active fault and as the fault moved, the pipeline experienced axial compression, buckled and collapsed in a folding pattern characterized by two circumferential waves [5].



Figure 1-1: Upheaval buckling of a buried pipeline [6]

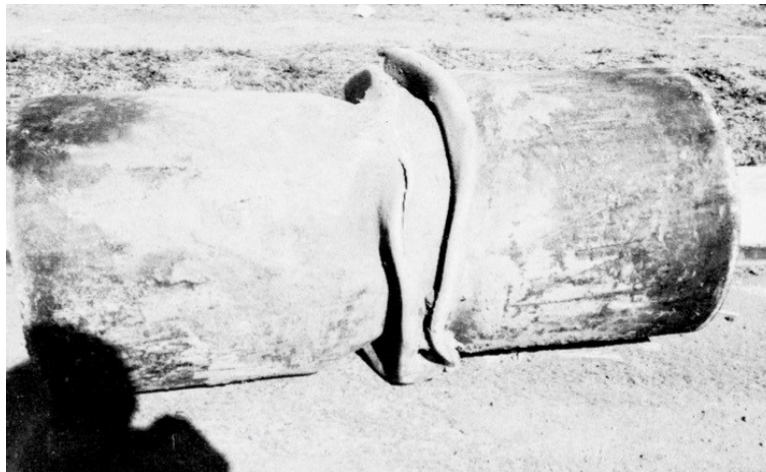


Figure 1-2: Shell-type buckling due to large ground movement [5]

Most existing modern design methods are able to account for diverse and often extreme ambient conditions such as in arctic cold or desert hot onshore environments and in deep, and sometimes turbulent, offshore environments. However, the loads imposed by large ground motion due to fault movements, landslides, permafrost melting, and soil liquefaction frequently exceeds all other types of loading that may be experienced over the entire lifecycle of a pipeline. In many

cases, ground movement loads develop plastic strains in the pipeline which are occasionally sufficient to cause tensile fracture or localized buckling, possibly leading to leakage or rupture of the pipeline [7].

In the event of large and drastic ground movement such as occurs during an earthquake, localized buckling/collapse and ruptures of pipelines conveying flammable liquids have been observed to result in catastrophic consequences such as fires and explosions [4,5]. Rupture of utility pipelines for water supply and sewage discharge has also been known to result in flooding, pollution, disease outbreaks, and extended periods of hardship [8–12].

1.2 The Buckling Phenomenon: Overview

The failure of a pipeline may either be caused by material failure or result due to structural instability. The yield stress and the ultimate tensile stress are usually considered for the evaluation of material failure whereas structural instability is evaluated based on the buckling behavior of the pipeline which constitutes a more complex structural/mechanical phenomenon involving a relatively significant number of influential and interrelating factors. When the buckling load of a component is reached, its stable equilibrium state suddenly becomes unstable and with or without an accompanying deflection or deformation, the previously stable configuration of the component changes to a different (buckled) stable configuration. Subsequent to its buckling, a pipe ceases to deform in its initial stable equilibrium state (axially) and begins to deform in its secondary stable equilibrium state; either in a global lateral mode or by localized cross-sectional deformation [13].

The buckling behavior of a pipe is a direct consequence of its stiffness, as well as the state of stress under which it is subjected due to its loading configuration. Buckling failure is typically characterized by a loss of structural stiffness and may or may not occur prior to the onset of plasticization in the material; thus the distinction between elastic or plastic buckling. In the elastic region, the axial stress typically increases simultaneously with the bending moment until the moment attains a magnitude whereby the stresses at the extreme fibers of the pipe wall reach the yield stress of the material. Generally, the axial stresses in the pipe wall are derived based on the cumulative effects of the internal pressure, axial force and bending moment. The ratio of the

maximum bending moment at buckling to the plastic bending moment of a pipe is essential for the classification and prediction of either elastic or plastic buckling. If the maximum bending moment at buckling is higher than the plastic bending moment, buckling will be governed by local plastic deformation of the pipe. In contrast, if the maximum bending moment is lower than the plastic bending moment at the onset of buckling, buckling will be governed by elastic instability of the cross section of the pipe under loading [14].

Bending of a pipe causes a loss of circularity in the cross-sectional profile of the cylinder: a phenomenon referred to as *ovalization* [15]. *Ovalization* leads to the development of bending stresses in the hoop direction of the cylinder and causes a modification of the local curvature at the compressive side of the cylinder wall. Hence, large lateral displacements may eventually lead to local buckling in form of wrinkling on the compression side of the buckled pipeline [16].

For pipelines that are installed above the ground and flexibly supported, compressive axial loading due to either fault movements or thermal/pressure induced forces can often be accommodated by the flexibility of the pipeline. On the other hand, when the pipeline is required to be buried in the ground for security, environmental, or other reasons, it is confined by the surrounding soil to a varying degree depending on the rigidity of the soil thereby developing a more uniform compressive axial force in the pipe cross-section; compared to unburied pipelines. Previous studies have shown that the firmer the surrounding soil the shorter the segment of the pipeline to absorb strain energy and, in the event of large ground movement, the higher the strains in the pipeline [17]. As the compressive stress in the pipe cross-section is increased, the strain in the pipe wall will simultaneously increase to a level at which a series of axisymmetric wrinkles may begin to form. Axisymmetric deformation typically occurs in steel cylinders of diameter-to-thickness (D/t) ratio in the range of 10 – 100 while non-axisymmetric wrinkling has been observed in past research studies to be a more common collapse response in thinner wall (higher D/t ratio) cylinders [18-20].

Local buckling involves gross deformation of the cross-section of pipelines and is commonly characterized by features such as collapse, localized wall wrinkling and kinking. Dama *et al.* [21] noted that local buckling significantly reduces the fatigue resistance and burst capacity of pipelines due to the likelihood of high strain concentrations in the buckled areas. However, pipelines are still capable of sustaining operational stresses provided the steel material still

possesses adequate residual ductility and cracks do not develop due to excessive wrinkling and fracture.

Mohareb et al. [22] explained that two types of local buckling can occur in a pipe: non-linear collapse buckling and bifurcation buckling. For the non-linear collapse buckling, the load-deformation curve corresponds to that of the elastic stiffness of the pipe's material at the initial stage of the pipe's mechanical response. Due to geometric and material nonlinearities, the slope of the curve becomes flatter as the pipe undergoes further deformation and eventually, the load-deformation curve reaches a point of zero slope; referred to as the "limit point". Upon further deformation, the slope of the load-deformation curve becomes negative due to zero or negative stiffness of the pipe. For the bifurcation buckling, they explained that such behavior is typically characteristic of idealistic perfect structures. At the beginning of the buckling response, the pipe response follows the initial equilibrium path (the primary path) until it reaches a point in the load-deformation curve where the pipe may possess two (or more) different possible equilibrium paths, and subsequently the pipe may follow a new deformation pattern (the secondary path). The point where the primary path intersects with a secondary path is referred to as a bifurcation point and the slope of the secondary path in the load-deformation curve is typically negative. In real structures, as in the cases of pipes with geometric imperfections and material nonuniformities, the load-deformation curve does not exhibit the sharp kink observed at the point of bifurcation of a perfect pipe. However, the load-deformation curve of a real pipe approaches that of a perfect pipe as the magnitude of imperfections in the real pipe decreases.

Onshore pipelines are typically subject to a combination of three main loading conditions. These include internal pressure caused by the action of the fluids they convey; axial forces due to ground movement and/or pressure-temperature effects/pipe-soil frictional interaction; and bending induced by differential settlements and/or p - Δ effects of the induced compressive axial forces [7]. Numerous research works have been conducted to understand the behavior of pipelines subjected to various loads and load combinations [22-30]. Several of these investigations are aimed at determining appropriate design values for the critical buckling strain (usually regarded as the compressive strain at which a wrinkle or local buckle initiates), while some others are focused on deriving realistic limit values for the wrinkle strain or the strain corresponding to the maximum axial load/bending moment capacity.

1.3 Problem Statement

The subjection of onshore pipelines (especially buried pipelines) to compressive forces may lead to beam-type buckling where the force exerted by the pipe due to lateral deformation surpasses the resistance of the surrounding material. On the other hand, due to the build-up of compressive stresses in the pipe wall, shell-type buckling may be initiated in a pipeline under significant axial compression if lateral deformation is restricted by the surrounding material. Shell-type buckling may also occur along the intrados of a pipeline under bending deformation due to escalation of compressive longitudinal strains. Shell-type buckling induces significant strains in pipelines and is, therefore, more detrimental to the integrity of pipelines compared to beam-type buckling.

Pipelines used for onshore applications are typically within the range of D/t ratios between 40 and 100 hence, the compressive strain capacity is strongly influenced by the shape of the stress-strain curve immediately past the proportionality limit point of the pipe material. Therefore, the influence of the material stress-strain response on the buckling behavior cannot be fully captured by simply incorporating the material yield strength or the yield-to-tensile ratio in the numerically-derived or experimentally-obtained regression equations for predicting the critical limit strain of pipelines. A more accurate approach has thus been adopted by a few researchers whereby the strain-hardening exponent of the Ramberg-Osgood material stress-strain model is applied as a constitutive parameter in developing the nonlinear regression equations for predicting the critical limit strain. However, the Ramberg-Osgood model is based on a simple power law expression and is only applicable for pipe materials with a round-house stress-strain relationship, and not suitable for characterization of pipe materials with a distinct yield point and an extended yield plateau in the stress-strain relationship. Several researchers have observed that the Ramberg-Osgood (R-O) stress-strain model tends to lose predictive accuracy beyond a limited strain range; especially for materials which exhibit non-gradual strain-hardening characteristics (e.g., high-strength steel) beyond the proportionality limit stress, and a number of modifications have thus been proposed to improve the predictive accuracy of the R-O stress-strain approximation over the full range of strains. However, some important limitations of the modified stress-strain models existing in literature have been observed, largely due to the inherent drawback of losing simplicity as the accuracy and versatility of the model is increased.

Additionally, the existing critical limit strain expressions are all specific to the reported testing conditions. Most of the existing expressions are based on results of experimental testing or numerical simulation of pipes subjected to bending while a few experimental tests and numerical studies have focused on the buckling response of pipelines to uniform axial compression. The influence of combined axial compression and bending has been reported in a few researches but no attempt has yet been made to properly characterize the deformational capacity of pipe segments under such loading conditions. There is, therefore, a need to evaluate the effect of varying the loading conditions on the buckling behavior and associated limit strain such that the response spectrum between uniform axial compression and uniform bending of pipelines is better understood. Consequently, the loading conditions evaluated herein include uniform axial compression (no bending), uniform bending (zero axial compression), and uniform axial compression with monotonically increasing curvature (combined axial compression and bending) of both unpressurized and pressurized pipe segments.

1.4 Objectives and Scope

The main purpose of this research is to develop a new material characterization model which is suitable for parameterization of the entire shape of the stress-strain curve for a diverse range of metallic materials, even materials with a well-defined yield point and yield plateau, and is thus better suited to account for the material-related attributes that govern the deformational capacity of pipelines. To assess the applicability of the developed material model to the buckling response of shell structures in general, a numerical modeling approach based on computerized finite element discretization will be employed to perform extensive parametric analyses.

The overarching objective of this research program is to develop a set of high-fidelity nonlinear regression equations for predicting the critical limit strain of unpressurized and pressurized pipelines subjected to three distinct loading conditions: uniform axial compression, uniform bending, and combined axial compression and bending.

Specific objectives are summarized as follows:

1. Performing extensive literature review on existing analytical stress-strain models to determine the limitations that exist, and developing a novel mathematical expression that is

capable of representing the stress-strain curve of metallic materials; including materials with a well-defined yield plateau.

2. Testing the applicability and accuracy of using the newly-developed stress-strain model for fitting experimentally-obtained stress-strain data to the mathematical expression, as well as the applicability of the developed stress-strain model for evaluating buckling in shell-type structures, using a representative numerical model.
3. Reviewing literature to determine the limitations that exist in existing analytical and semi-empirical expressions for predicting the deformational capacity of onshore pipelines under uniform axial compression and/or bending.
4. Conducting extensive parametric numerical analyses to examine the influence of varying material curve shape parameters and other essential parameters on the critical limit strain in pipelines subjected to uniform axial compression, uniform bending, and combined axial compression and bending.
5. Based on the material curve shape parameterization approach presented, developing unified expressions suitable for predicting the compressive strain capacity of pipelines under the three investigated loading scenarios.

1.5 Research Methodology

The formulation of the proposed stress-strain model is based on the normalization of the full stress and strain range of the stress-strain curve such that the exact magnitudes of the values of the stress and strain at any specified reference points are unchanged. The proposed model is expressed for two segments of the stress-strain curve:

- The first segment is the linear elastic portion of the curve and is defined by the initial modulus of elasticity of the material, E_o , up to the proportionality limit stress.
- The second segment of the stress-strain curve is characterized by a nonlinear stress-strain relationship up to the ultimate stress and strain values and is defined using the mathematical expression of the proposed model.

The applicability and efficiency of the proposed stress-strain model are evaluated by comparison of model-approximated stress-strain curves (derived using the proposed equation) to results of

various experimental tests on metallic materials where the stress-strain curves are elaborated. Nonlinear curve-fitting techniques are used to fit the obtained experimental data to the stress-strain expression, and to obtain the constitutive model parameters that give the best approximation of the model-to-experiment curve fit.

To validate the applicability of the proposed stress-strain model to shell-type buckling in pipelines, extensive parametric numerical analyses are conducted, using idealized material stress-strain properties, to investigate the load-end shortening behavior of simply-supported flat plates subjected to uniform edge compression in the longitudinal direction. The effects of aspect ratio, b/t ratio, and initial out-of-plane imperfection (based on the buckling mode shapes) are briefly examined while the main focus is on using the proposed material stress-strain model to determine the effect of the strain-hardening characteristics and overall shape of the material stress-strain curve on the ultimate compressive strength and strain capacity of the idealized metal plate models.

The influence of material properties and other essential parameters on the critical limit strain of pipelines subjected to uniform axial compression, pure bending, and a combination of uniform axial compression and bending is investigated by numerical modelling of a vast array of pipe models using the general-purpose finite element (FE) analysis software package (ABAQUS CAE). The parametric analysis is performed according to two material curve classifications: round-house type (RHT) curves and yield-plateau type (YPT) curves.

The main parameters to be considered for the parametric evaluation are the material-dependent stress-strain properties (i.e., proportionality limit stress, length of the yield plateau, nominal yield stress, ultimate tensile stress, and the constitutive model constants from the developed stress-strain model), the internal pressure, geometric properties (diameter-to-thickness ratio), initial imperfections, and magnitude of axial compression (for combined loading conditions).

For pipe models subjected to uniform axial compression, the load-axial shortening relationship will be plotted and the value of strain corresponding to the maximum value of the applied compressive stress will be determined as the strain capacity. The moment-curvature response curves for pipe models subjected to bending or a combination of axial compression and bending will also be plotted and the peak moment strain criterion [31,32] will be applied for determining the compressive strain capacity of the pipe models.

The proposed test matrix for each of the three loading scenarios (uniform axial compression, pure bending, and combined axial loading and bending) includes: four variations of the D/t ratio, five variations of the pressure factor, four variations of the material grade, four variations (for RHT curves) or five variations (for YPT curves) of the material curve shape factor, and four variations of the compression factor. A full-factorial design adopted for the parametric analyses such that every possible combination of the constituent parameters is investigated. Consequently, a total of 1920 simulations (for RHT pipes) plus 2400 FE simulations (for YPT pipes) are performed in this study.

Finally, advanced nonlinear multiple regression techniques are used to derive unified nonlinear expressions suitable for predicting the compressive strain capacity of pipes under the three investigated loading scenarios.

1.6 Organization of Thesis

This thesis consists of ten chapters wherein Chapter four to Chapter nine correspond to different peer-reviewed publications that are separately focused on various aspects of the research objectives of this research study. While the chapters are not arranged chronologically with respect to the date of publication of the different papers, the sequential arrangement is aimed to follow the systematic progression of the specific objectives of this research.

Chapter two performs an in-depth review of literature on aspects related to the fundamental concepts of the buckling phenomenon in shell structures, with specific focus on the design criteria applied by various codes and standards for assessing the deformational capacity of pipelines.

Chapter three covers relevant theoretical formulations referred to as the classical buckling theories, most of which are based on concepts developed in the early 20th century for estimating the critical buckling stress in shell structures. The analytical derivations are presented as an introductory precursor to the mathematical concepts that are emulated in the evaluation of relevant underlying criteria for shell buckling analyses.

In line with the first specific objective, Chapter four delves into the world of material stress-strain characterization models and unveils the evolution process, mathematical framework, scope

of application, and essential limitations of existing stress-strain models. A new stress-strain model is presented in this chapter and its applicability to diverse material curve shapes of common pipeline steels, as well as to a wider range of metallic materials, is depicted. A significant number of the experimental stress-strain curves of three characteristically different metallic materials: austenitic stainless steel (AISI 304L), aluminum alloy (AA5083), and nickel alloyed steel (Invar steel) are successfully approximated using Least-squares curve-fitting techniques. The effect of material curve shape variations on the load-deformation response of a simple shell structure (represented by a numerical model of a simply-supported flat plate) is also briefly investigated. This chapter is derived from the combination of two published conference proceedings: (1) the ASME 2017 Pressure Vessels and Piping Conference, and (2) the 2017 CSCE 6th International Conference on Engineering Mechanics and Materials.

In line with the second specific objective, Chapter five presents additional analytical relationships for estimating the constitutive constants of the proposed stress-strain model. The concept of defining the shape of the stress-strain curve using ‘control’ points is discussed. The ease of using the presented methodology for curve shape characterization is further illustrated by defining idealized stress-strain curves according to a YPT/RHT material curve classification approach. The idealized stress-strain curves are then used to define the material behavior of numerical FE models developed to simulate the mechanical response of simply-supported flat plates to uniform edge compression. The ultimate stress and corresponding end-shortening strain for each simulation are plotted against the slenderness ratio of the plates and the effect of material curve shape variation is illustrated. The contents of this chapter are obtained from a paper published in the Journal of Construction and Building Materials.

All of the last three specific objectives are captured in each of the four chapters following Chapter five. Chapter six, Chapter seven, and Chapter eight focus, respectively, on the deformational capacity of pipes subjected to uniform axial compression, uniform bending, and combined axial compression + bending while Chapter nine studies the effects of all three loading conditions on the deformational capacity of X80-grade pipelines.

Chapter six extends the methodology presented in Chapter five for deriving the model constants of the stress-strain model to include an iterative procedure for specifying the allowable length of the yield plateau based on an analytically-implemented control of the inflection point of the

stress-strain curve. The stress-strain model is then used to apply curve shape variations to four selected material grades typically used for onshore pipeline applications. The effect of material curve shape variations, as well as other essential parameters, on the critical limit strain of numerical FE pipe models under uniform axial compression is investigated, followed by the development of predictive nonlinear regression equations, derived based on the results of the parametric FE analyses. This chapter is based on a research paper submitted to the *Thin-walled Structures* journal.

Chapter seven follows the same procedure as Chapter six except that the numerical FE pipe models generated are subjected to monotonically-increasing uniform curvature and no axial compression is applied. The effect of material curve shape variation, as well as variation of other essential parameters, is also investigated. The developed nonlinear regression equations are compared to two of the most recent notable semi-empirical equations developed independently for predicting the critical limit strain in pipelines under bending. This chapter is culled from a research paper submitted to the *Engineering Structures* journal.

Chapter eight somewhat ‘bridges the gap’ between the results of Chapter six and Chapter seven. The research focuses on the buckling behavior of pipelines simultaneously subjected to constant uniform net-section compressive stress and monotonically-increasing uniform curvature. This chapter comprises the bulk of the numerical simulations performed in this thesis due to the inclusion of an additional parameter (the compression factor) and consequent dimensional expansion of the test matrix. The research is aimed at evaluating the spectral transition of the buckling response of pipelines under combined axial compression and bending from a pure compression status to a pure bending status. Parameterization of the material curve shape is also achieved in this paper using the presented stress-strain model and nonlinear regression equations are subsequently developed, from the parametric FE analyses, for predicting the critical limit strain in pipelines subjected to combined axial compression and bending. This chapter is based on a research paper submitted to the *International Journal of Solids and Structures*.

Chapter nine streamlines the focus of the numerical investigations to high-strength steel pipelines. This paper navigates a comparative evaluation of the buckling response of numerical FE pipe models under the three different loading scenarios investigated. The functional relationships between the critical limit strain and the essential parameters are graphically

illustrated. The paper finalizes the research endeavor with the development of six nonlinear regression equations for estimating the critical limit strain in a typical high-strength pipeline subjected to either of the three investigated loading conditions. This paper consists of research work submitted for publication in the MDPI Applied Sciences journal.

Chapter ten provides a general summary and conclusions of the undertakings of this research program, as well as highlights of recommended areas for further research work.

1.7 References

- [1] J.P. Lee, J.A. Bohinsky, Design of buried pipeline subjected to large fault movement, in: Proc. 11th World Conf. Earthq. Eng., Acapulco, Mexico, 1996: pp. 23–28.
- [2] R.E. Hobbs, In-Service Buckling of Heated Pipelines, *J. Transp. Eng.* 110 (1984) 175–189. doi:10.1061/(ASCE)0733-947X(1984)110:2(175).
- [3] O. Fyrileiv, L. Collberg, Influence of Pressure in Pipeline Design: Effective Axial Force, in: 24th Int. Conf. Offshore Mech. Arct. Eng. Vol. 3, ASME, 2005: pp. 629–636. doi:10.1115/OMAE2005-67502.
- [4] H. Yun, S. Kyriakides, On the beam and shell modes of buckling of buried pipelines, *Soil Dyn. Earthq. Eng.* 9 (1990) 179–193. doi:10.1016/S0267-7261(05)80009-0.
- [5] P.C. Jennings, Engineering features of the San Fernando earthquake of February 9, 1971, EERL 71-02, Pasadena, California, 1971.
- [6] Jee, Course Material for The Subsea Pipeline Design Course held for employees at IKM Ocean Design in Trondheim, Jee, Tonbridge, Kent, 2013.
- [7] A. Lockey, A. Young, Predicting Pipeline Performance in Geohazard Areas Using ILLI Mapping Techniques, in: Vol. 2 Pipeline Integr. Manag., ASME, 2012: p. 491. doi:10.1115/IPC2012-90496.
- [8] A.E. Eskel, D.C. Martin, Seismic Risks of California’s Water Lifeline, *J. Tech. Council. ASCE.* 103 (1977) 25–37.
- [9] J. Isenberg, C.E. Taylor, Performance of Water and Sewer Lifelines in the May 2, 1983 Coalinga, California Earthquake, in: Proc. ASCE Lifeline Earthq. Eng. Performance, Des. Constr., San Francisco, California, USA, 1984: pp. 176–189.

- [10] T. Iwasaki, Soil liquefaction studies in Japan: state-of-the-art, *Soil Dyn. Earthq. Eng.* 5 (1986) 2–68. doi:10.1016/0267-7261(86)90024-2.
- [11] G.M. Lee, S.M. Mejia, The Effects of the 1985 Mexico City Earthquake on Underground Water and Sewer Pipelines, in: *Proc. ASCE Lifeline Seism. Risk Anal. – Case Stud.*, Seattle, Washington, USA, 1986: pp. 131–136.
- [12] G.M. Lee, The 1985 Mexico Earthquakes: Effects on Water Supply Systems, in: *Mex. Earthquakes—1985 Factors Involv. Lessons Learn.*, ASCE, 1987: pp. 364–367.
- [13] J.E. Akin, FEA Buckling Analysis, *MECH* 403, (2009). https://www.clear.rice.edu/mech403/HelpFiles/FEA_Buckling_analysis.pdf (accessed August 28, 2016).
- [14] H. Karbasian, S. Zimmermann, U. Marewski, M. Steiner, Combined Loading Capacity of Pipelines: Approaches Towards the Compressive Strain Limit, in: *Vol. 4 Pipelining North. Offshore Environ. Strain-Based Des. Risk Reliab. Stand. Regul.*, ASME, 2012: p. 375. doi:10.1115/IPC2012-90615.
- [15] L.G. Brazier, On the Flexure of Thin Cylindrical Shells and Other “Thin” Sections, *Proc. R. Soc. A Math. Phys. Eng. Sci.* 116 (1927) 104–114. doi:10.1098/rspa.1927.0125.
- [16] A.M. Gresnigt, S.A. Karamanos, Local Buckling Strength and Deformation Capacity of Pipes, in: *Ninet. Int. Offshore Polar Eng. Conf.*, International Society of Offshore and Polar Engineers, Osaka, Japan, 2009: pp. 212–224.
- [17] M.A. Rahman, H. Taniyama, Analysis of a buried pipeline subjected to fault displacement: A DEM and FEM study, *Soil Dyn. Earthq. Eng.* 71 (2015) 49–62. doi:10.1016/J.SOILDYN.2015.01.011.
- [18] S.C. Batterman, Plastic buckling of axially compressed cylindrical shells, *AIAA J.* 3 (1965) 316–325. doi:10.2514/3.2848.
- [19] C.G. Schilling, Buckling Strength of Circular Tubes, *J. Struct. Div.* 91 (1965) 325–348.
- [20] N.W. Murray, P. Bilston, Local buckling of thin-walled pipes being bent in the plastic range, *Thin-Walled Struct.* 14 (1992) 411–434. doi:10.1016/0263-8231(92)90011-K.
- [21] E. Dama, S.A. Karamanos, A.M. Gresnigt, Failure of Locally Buckled Pipelines, *J. Press. Vessel Technol.* 129 (2007) 272. doi:10.1115/1.2716431.

- [22] M.E. Mohareb, A.E. Elwi, G.L. Kulak, D.W. Murray, Deformation Behavior of Line Pipe, Structural Engineering Report No. 202, Edmonton, Alberta, 1994.
- [23] D.R. Sherman, Test of Circular Steel Tubes in Bending, *J. Struct. Div.* 102 (1976) 2181–2195.
- [24] J.G. Bouwkamp, R.M. Stephen, Large diameter pipe under combined loading, *Transp. Eng. J. ASCE.* 99 (1973) 521–536.
- [25] N. Yoosef-Ghodsi, G.L. Kulak, D.W. Murray, Behavior of Girth-welded Line Pipe, Structural Engineering Report No. 203, Edmonton, Alberta, 1994.
- [26] S.P. Schneider, Flexural Capacity of Pressurized Steel Pipe, *J. Struct. Eng.* 124 (1998) 330–340. doi:10.1061/(ASCE)0733-9445(1998)124:3(330).
- [27] P.R. DelCol, G.Y. Grondin, J.J.R. Cheng, D.W. Murray, Behavior of Large Diameter Line Pipe Under Combined Loads, Structural Engineering Report No. 224, Edmonton, AB, Canada, 1998.
- [28] A.B. Dorey, J.J.R. Cheng, D.W. Murray, Critical Buckling Strains for Energy Pipelines, Structural Engineering Report No. 237, Edmonton, Alberta, 2001.
- [29] A.B. Dorey, D.W. Murray, J.J.R. Cheng, Critical Buckling Strain Equations for Energy Pipelines—A Parametric Study, *J. Offshore Mech. Arct. Eng.* 128 (2006) 248. doi:10.1115/1.2199561.
- [30] D. Row, G.H. Powell, M.W. Goodson, Finite Element Techniques for Pipelines Subjected to Extreme Loads, in: *Pipelines Advers. Environ. II*, ASCE, 1983: pp. 474–485.
- [31] M.J. Stephens, R.T. Petersen, Y.-Y. Wang, D. Horsley, An Experimental Basis for Improved Strain-based Design Models, in: *Ninet. Int. Offshore Polar Eng. Conf.*, International Society of Offshore and Polar Engineers (ISOPE), Osaka, Japan, 2009: pp. 29–35.
- [32] M. Stephens, R. Petersen, Y.-Y. Wang, R. Gordon, D. Horsley, Large Scale Experimental Data for Improved Strain-Based Design Models, in: *2010 8th Int. Pipeline Conf. Vol. 4*, ASME, 2010: pp. 195–203. doi:10.1115/IPC2010-31396.



2. REVIEW OF LITERATURE

2.1 Introduction

From as far back as the latter half of the 20th century, extensive effort has been made, and numerous approaches have been suggested, by various researchers to examine the resultant state of stress in continuous pipelines due to relative displacement of surrounding soils. One of the pioneering research endeavors to calculate the strains induced in a pipeline due to ground-induced actions was included in the work of Newmark and Hall [1] where a simplified analytical model for calculating the tensile strains in a pipeline subjected to tectonic fault movement was proposed. The model proposed by Ref. [1] assumed that the passive soil resistance was uniformly distributed around the perimeter of the pipe and assumed small deflection theory for estimating the strains along the pipe length. Kennedy et al. [2] proposed a slight improvement to the work of Ref. [1] by analyzing the unanchored length of the pipe as an arc thus considering large deflection theory, as well as non-uniform friction interface between the pipe and the soil. The model by Ref. [2] however assumed the deformation in the pipe to be analogous to the deformation of a flexible cable and thus, ignored the effect of the bending stiffness of the pipe, especially at the inflection point between the deformed and undeformed portions of the pipe. An extensive parametric study by Vougioukas et al. [3] was performed based on the numerical simulation of buried pipelines under horizontal and vertical fault movement, considering the pipes as elastic beams. To improve the results of previous studies and generalize the formulations for buried pipelines subjected to ground displacement, Wang and Yeh [4] proposed a refined approach, based on a semi-infinite beam on an elastic foundation concept, which included the effects of axial force and bending moment interaction, as well as large deformation. Whereas the earlier models considered pipes as either cables or beams, Takada et al. [5] proposed a simplified analytical method, taking the shell properties of the pipe into consideration, to find the maximum strain in buried pipes under ground motion. The model proposed by Ref. [5] was based on a beam-shell hybrid concept such that a simple relation between the pipe's longitudinal deformation and cross-sectional deformation was presented.

Liu et al. [6,7] pointed out that most of the currently existing analytical expressions for stress and strain prediction in pipelines subjected to ground-induced deformation are based on the beam theory and are therefore incapable of capturing sectional deformation behavior resulting from the development of tensile/compressive strains under relative axial displacement or bending due to

transversely-applied ground displacement. The rapid advancement of computational simulation tools over recent decades has however facilitated the employment of numerical optimization procedures, such as the finite element method (FEM), by numerous research studies for investigating the response of buried pipelines to large induced deformation [8]. Karamitros et al. [9] presented a refined analytical methodology for computing the axial forces and bending moment strains in buried pipelines using a combination of the beam-on-elastic-foundation and the beam theory. Their proposed analytical model was compared to a series of numerically analyzed three-dimensional finite element pipeline models which accounted for the pipe-soil interaction using axial and transverse nonlinear soil springs, and the analytical predictions were observed to have a fairly-good overall agreement with the results of the FE analyses. To model the pipe-soil interaction in buried subsea pipelines subjected to transient and permanent relative ground displacement, Arifin et al. [10] used beam finite elements and nonlinear soil springs and proposed several recommendations for better estimation of pipeline response under seismic wave actions. Odina and Tan [11] employed the use of discrete structural beam-type elements as pipe models while the surrounding soil was modeled using discrete nonlinear soil springs in the axial, lateral and vertical (up/down) directions. Using the finite element method, Yimsiri et al. [12] created two soil models (Mohr-Coloumb and Nor-Sand models) and studied the effect of the variations in the geo-mechanical properties of the surrounding soil, as well as embedment conditions of the pipe, on the soil-pipeline interactions in sand under lateral and upward movements.

Mainly for calibration of numerical models, and as a means to provide complementary validity to results of numerical studies, a number of notable experimental studies have been carried out by various researchers on the behavior of pipelines subjected to large differential movement of the supporting or surrounding soil. Due to feasibility restrictions associated with costs, loading rates and capacity of hydraulic loading facilities, a lot of the experimental studies have been limited to small-scale tests (rather than full-scale model tests) performed on low-to-medium-strength steels and high-density polyethylene (HDPE) pipes with a similar nonlinear stress-strain response as steels [13]. One of the most common approaches for experimental testing of buried pipelines subjected to permanent or quasi-static ground deformation is the centrifuge-based modeling of buried pipeline response using a split-box to test pipe specimens within a geotechnical

centrifuge. This method has been adopted by a number of researchers and proven to be adequate for examining the influence of various parameters such as the type of faulting, the alignment of the pipeline in relation to the direction of the relative ground movement, the moisture content and geomechanical properties of the soil, the burial depth of the pipeline, and the geometrical and material properties of the pipeline [14–17]. Jalali et al. [18] employed the use of three-dimensional finite element modeling to simulate the behavior of buried pipelines under reverse faulting using shell elements for the pipe models and solid continuum elements for the soil. Geometrical and material nonlinearities were considered as well as pipe-soil interaction contact properties, and Von Mises plasticity and Mohr-Coulomb yield criteria were applied to the pipe and soil models respectively. The FE models were validated based on results of a number of large spit-box experiments.

Results obtained from the above-detailed experimental tests and numerical evaluations indicated the occurrence of a combination of axial and bending strains that became larger with increasing fault offset and larger ground displacement. Double-curvature bending, accompanied with severe yielding and plastic deformation at locally-buckled regions of the pipe, was also observed. In addition to the longitudinal stresses and strains arising from combined bending and relative axial displacement due to ground displacements, additional hoop and axial stresses and strains may also result due to the interaction between the friction restraint by the surrounding soil and the temperature/pressure resultant displacement of the pipe; especially during the passage of high-temperature and/or high-pressure fluids. A common phenomenon referred to as “thermal buckling”, which is primarily caused by the temperature variation in transitory pipeline fluids, is generally known to cause global buckling deformation such as upheaval buckling (wherein the pipe segment upwards in the vertical plane) and snaking (wherein the pipe segment buckles laterally in the horizontal plane) in above-ground and shallowly-buried pipelines; both onshore and offshore [19–23]. Such global buckling failures may result in localization of strains at critical sections of the pipe segment and ultimately lead to gross deformation of the pipe cross-section characterized by local bulging or wrinkling [24,25]. Wijewickreme et al. [26] indicated that according to the longitudinal orientation of a buried pipeline with respect to the direction of the relative movement of the surrounding soil, the mode of deformation in the pipeline may be classified according to four main designations: vertical uplift, vertical bearing, transverse (this

may be horizontal-lateral as in strike-slip faults or vertical-lateral as in normal and reverse faults), and axial (or longitudinal). They further emphasized the importance of taking into consideration, during design, the effects of combinations of the different modes on the response of buried pipelines subjected to various forms of differential ground settlement.

2.2 Buckling of Cylindrical Shells

In the field of civil engineering, a metallic tube is structurally classified and typically designed as a circular-hollow section (C-H section), whereas it is modeled as a circular cylindrical shell structure. The application of metallic tubes is usually distinguished according to the diameter-to-thickness (D/t) ratio which is appropriate for its intended use. Typically, D/t ratios range from values as low as 10, for applications such as load-bearing columns for bridges and buildings or structural components of automotive vehicles, to values as high as 500 or even greater, for applications such as silos, liquid storage tanks, and nuclear reactors. Intermediate D/t ratios (between 10 and 500) are common for cylindrical shell structures such as pipelines and wind tube towers.

Unlike flat plates, cylindrical shells are able to withstand lateral loads by pure membrane action only (i.e., without bending), making them very efficient for use as structures required to withstand significant longitudinal and circumferential strains [27]. However, this property also makes cylindrical shell structures susceptible to “catastrophic” elastic instabilities, especially where such strains are compressive in nature, and thus makes it essential for the buckling and post-buckling behavior to be well understood for proper design and modeling of such structures [28]. Typical examples of metallic cylinders subjected to such axial compression are pipelines, which are generally used for long-range transportation and distribution of fluids and are usually installed such that they traverse large geographical areas. Consequently, pipelines are exposed to diverse geological conditions along the pipeline route which potentially impact on their structural and mechanical integrity. Such detrimental geological conditions typically arise from significant movement of the supporting soil medium due to scenarios such as landslides, fault movement, ground subsidence, slope failures, direct seismic wave activity, soil liquefaction, and permafrost melting [24,29,30]. If substantial, especially in the case of buried pipelines which are restricted

from lateral movement, ground movement will induce severe compressive strains in the pipeline and lead to a phenomenon known as shell-type buckling [31]. Compressive resultant stresses may also be induced in the pipeline as longitudinal expansion caused by the passage of hot fluids is restricted by the surrounding soil [32].

Buckling in cylindrical shells is broadly classified as either elastic buckling or inelastic (plastic) buckling. In the case of elastic buckling, the material of the structure is presumed to remain in the elastic region (i.e., the stress in the structure does not exceed the proportionality limit stress) before the incident of buckling. On the other hand, plastic buckling of cylindrical shell structures implies the exceedance of the elastic limit of the material before the inception of buckling thus the stiffness components of the analytical formulations need to be modified to account for the altered stiffness of the properties of the material associated with plastic deformation [33]. The type of buckling that a cylindrical shell experiences is mainly influenced by two factors: the slenderness properties and the material strain-hardening behavior.

Inelastic (plastic) buckling behavior has been a subject of extensive theoretical and experimental investigations for many decades [34,35]. Early analytical studies by Shanley [36] and Hill [37,38] on the plastic buckling phenomenon in uniaxially compressed structures revealed that bifurcation in the plastic range generally occurs under increasing load. Consequently, and in order to accurately predict the bifurcation and collapse mechanisms in the plastic range, it has become essential for analytical and numerical investigation of plastic buckling in cylindrical shells to develop and implement appropriate asymptotic post-buckling theories that are able to predict the nonlinear load-deflection path and account for bifurcation and mode changes. Such analytical and numerical methods must also consider the static and dynamic behavior of shell structures including large deflections, large strains and nonlinear material behavior [39]. The two plasticity theories, essentially based on the consideration of path-dependence, which are generally employed for analytical modeling of nonlinear material behavior are the deformation theory and the incremental (flow) theory. The deformation theory is considered as a special class of path-independent nonlinear elasticity theories and assumes that the state of stress is uniquely defined by the state of total strain and not dependent on the material stress history. It is only useful as a plasticity model in cases of continuous flow as it does not account for the recovery of initial elastic stiffness upon strain reversal. The flow theory, even though more rigorous than the

deformation theory, is more physically realistic as it considers the state of stress to be defined by both the actual strain value and its increment. The flow theory is, therefore, able to accommodate recovery of the initial elastic stiffness immediately after a strain reversal. Despite its inadequacies, the deformation theory has been consistently reported by various research studies on the buckling behavior of shell structures [40–45] to produce results that correspond better with experimental results than the flow theory. Murphy and Lee [46] however maintained that the discrepancy between the incremental theory of plasticity and experimental test results can be eliminated by introducing realistic pre-buckling deformations or implementing appropriate boundary conditions such that a realistic buckling process is implied.

Bardi and Kyriakides [47] explained that unlike elastic shell buckling, which is characterized by sudden and catastrophic collapse, plastic buckling failure of uniformly-compressed perfect isotropic cylindrical shells is preceded by a series of traceable events. As the stress applied uniformly to the cross-section of the shell structure is increased, the resultant strain in the wall of the cylindrical shell increases concurrently until a level is reached where an axisymmetric wrinkle is formed at some point along the length of the cylinder. This axisymmetric deformation is initially small and inconspicuous but grows gradually as the axial stress continues to increase, accompanied by a corresponding decrease in the axial rigidity of the shell. The progressive reduction of the shell's axial rigidity expedites the attainment of a limit load instability characterized by rapid growth and localization of the asymmetric deformation with decreasing axial stress. As the D/t ratio of a cylindrical shell increases, the deformation tends to a non-axisymmetric pattern characterized by two or more circumferential waves which develop in the zone of localization prior to attainment of the limit load. This non-axisymmetric mode of deformation is typically associated with thinner unpressurized cylindrical shells and induces additional softening of the load-deformation response compared to the axisymmetric mode of deformation. The mode of deformation that occurs in an axially-compressed cylindrical shell is mainly influenced by the D/t ratio and the material stress-strain relationship. The form and magnitude of the initial imperfections, as well as the presence and magnitude of internal pressure, also influence the mode of deformation at the point of limit load instability [48].

It is imperative to differentiate between the onset of wrinkling and the onset of collapse in cylindrical shells. While the onset of wrinkling is essentially associated with initial bifurcation of

the load-deformation response and characterized by the formation of axisymmetric wrinkles, the onset (or more precisely, the incidence) of collapse is associated with the maximum attainable load in the load-deformation response and is characterized by the localization of wrinkles (axisymmetric or non-axisymmetric). The path followed by the load-deformation response between the point of bifurcation and the limit load point involves the growth of the initial axisymmetric wrinkles. For cylindrical shells with certain combinations of dimensional and material properties, a second bifurcation may occur before the axisymmetric limit load, resulting in a transformation of the wrinkles from an axisymmetric mode to a non-axisymmetric mode and following a lower load-deformation path to localization and collapse. The limit strain is generally regarded as the value of strain which is coincident with the axisymmetric or non-axisymmetric collapse load [28–30].

Bardi and Kyriakides [47] noted that the bifurcation strain (ε_C) and the limit strain (ε_L) coincide for elastic buckling, but the former was significantly lower for pipes with lower D/t ratios due to the occurrence of inelastic buckling. The difference between the two strain values also increased progressively as the D/t ratio decreased. They pointed out that the bifurcation stress (σ_C) can serve as a conservative design criterion for stress-controlled applications whereas the limit strain (ε_L) is more appropriate than the bifurcation strain (ε_C) for deformation-controlled loading conditions, such as the case of buried pipelines subjected to surrounding ground displacement. While analytical formulations for deriving the bifurcation stress (σ_C) and corresponding strain (ε_C) are readily obtainable, estimation of the limit load (σ_L) and corresponding limit strain (ε_L) is hampered by numerous complexities related to material nonlinearity and the inherent unpredictability of wrinkle formation and metamorphosis.

2.3 Critical Buckling Stress: Axial Compression vs. Bending

Karamanos [49] explains that the main characteristic of a tubular shell under bending is ovalization of the cross-section which ideally triggers a limit-load type of instability due to progressive loss of the structure's bending rigidity. Ovalization also modifies the local curvature and facilitates the escalation of longitudinal stresses on the compression side of the structure such that a bifurcation instability, which is essentially a buckling type of instability characterized

by the development of longitudinal wrinkles in form of waves, may precede the ovalization instability point. The incidence of buckling creates a secondary path in the moment-curvature response of the structure resulting in eventual attainment of a lower limit moment. The point where the slope of the moment vs. curvature curve becomes zero is referred to as the limit point. Beyond the limit point, the structure experiences collapse characterized by a negative slope of the load-deformation response curve, implying a drop in the load-carrying capacity.

A study by Karman [50] on the mechanical response of pipe elbows subjected to in-plane bending led to the pioneering observation of ovalization (or in other words, “flattening of the cross-section”). The study by Ref. [50] adopted a Rayleigh-Ritz method, based on the representation of the cross-sectional displacements by doubly-symmetric trigonometric functions, to relate the ovalization to the bending-induced curvature. Brazier [51] extended the research by Ref. [50] towards investigating the nonlinear mechanical response of initially-straight infinitely-long cylindrical shells subjected to pure bending¹ and, assuming isotropic elastic material properties, a variational approach was employed to derive trigonometric and quadratic analytical formulations for the cross-sectional displacements and ovalization respectively, in terms of the bending-induced curvature. The ovalization instability moment derived by Brazier is given by:

$$M_{L,BR} = 0.987 \frac{Et^2r}{\sqrt{1-\mu^2}} \quad (2-1)$$

where E is Young’s modulus, t and r are the cylinder wall thickness and cross-sectional radius respectively, and μ is Poisson’s ratio. Subsequent experimental investigations [52–55] however observed that Brazier’s ovalization stability phenomenon only applies to sufficiently-long cylinders under bending as the boundary conditions of moderate-length cylinders prevents flattening of the cross-section under bending. The instability of small-to-medium-length cylinders, therefore, constitutes a buckling problem associated with a highly-nonlinear pre-

¹ Within the context of this study, “uniform bending” is used as a general term to refer to uniform inducement of curvature, with or without additional loading such as internal pressurization or axial compression, while “pure bending” refers to sole subjection to uniform bending without any additional loading. Likewise, “uniform compression” refers to subjection of a straight pipe to concentric axial stress (no bending), with or without internal pressurization, whereas “pure compression” is used to indicate the nonpresence of any additional loads.

buckling state, similar to the behavior of pipes under uniform axial compression, whereby the moment-curvature response is controlled by the formation and evolution of diamond-shaped buckles [34]. Further studies on the interaction between Brazier's ovalization instability and bifurcation instability have been performed [56–59] and the results obtained by Stephens and Starnes [56] indicate that the instance of ovalization instability tends to diminish at a length-to-radius ratio (l/r) < 3 .

Flügge [60] outlined an analytical formulation to assess the mechanical response as a bifurcation instability problem and concluded that the critical buckling stress on the compressive pipe under bending is approximately 30% more than the critical buckling stress in a pipe under uniform axial compression. Based on results obtained from an extensive series of experimental tests, Suer et al. [61] performed a statistical semi-empirical procedure to estimate the critical bending stress of unpressurized and pressurized cylindrical shells and determined that the critical buckling compressive stress in pipe segments is generally between 20% to 60% higher under bending than under uniform axial compression, depending on the pipe wall slenderness factor (measured as the width-to-thickness ratio: D/t ratio). Seide and Weingarten [62], however, faulted the empirical reduction coefficient postulated by Ref. [60] which presupposes that the theoretical critical buckling stress of a cylindrical shell under pure bending is 1.3 times the critical buckling stress under uniform axial compression. Ref. [62] employed Batdorf's modified Donnell's equation for buckling of cylindrical shells subjected to uniform axial compression and, assuming a wavy post-buckling shape characterized by trigonometric shape functions, they analytically obtained the critical maximum bending stresses for cylinders with various longitudinal buckle wavelengths. The formulation ignores the effect of ovalization in the pre-buckling state, and the results were inconclusive as to the differences in the post-buckling behavior between bending and axial compression. They, however, maintained that the nominal compressive stress which corresponds to the buckling moment of a pipe under bending is similar to the critical buckling compressive stress of a pipe, with a similar radius, under uniform axial compression. They further opined that the higher experimentally-recorded values of the critical stress under bending were likely due to the tendency for the buckling instability of a pipe under bending to be sensitive to only geometric imperfections on the compressive side of the pipe whereas the uniformity of the resultant stress in a pipe under axial compression implies sensitivity to geometric imperfections regardless of

cross-sectional location. Reddy and Calladine [63] extended the study by Ref. [62] to consider the classical buckling of isotropically elastic thin-walled cylindrical shells subjected simultaneously to uniform bending moment and internal pressure and analytically derived an approximate closed-form solution for the critical buckling compressive stress by assuming an appropriate eigenfunction. The results obtained by Ref. [63] showed reasonable agreement with the earlier conclusions of Ref. [62]. Following similar procedures as Ref. [62], Chen and Kemper [64,65] employed the linearized Donnell–Mushtari–Vlassov equations in an attempt to evaluate the buckling response of oval cylinders subjected to combined axial compression and bending in the elastic range of the material. The numerical computation considered the local curvature around the oval cross-section but the buckling stress was determined on the basis of an assumed linear pre-buckling state, and the effect of pre-buckling ovalization was ignored in the analyses. Axelrad [66,67] however presented a simple alternative to the above rigorous methods based on an “equivalent cylinder” concept whereby the critical buckling stress under bending is assumed to be equal to the critical buckling stress of an axially-compressed pipe with radius equal to the local radius of the curved arc on the compression side of ovalized pipe under bending. The classical Donnell shell buckling equation [68] for the elastic critical buckling stress of a pipe under uniform meridional compression can, therefore, be written for a bent pipe as:

$$\sigma_{x,b} = \frac{E}{\sqrt{3(1-\mu^2)}} \left(\frac{t}{r_{\theta 0}} \right) \quad (2-2)$$

where E is Young’s modulus, t is the cylinder wall thickness, μ is Poisson’s ratio, and $1/r_{\theta 0}$ is the center curvature of the compression side of the cylinder’s ovalized cross-section.

2.4 Influence of Slenderness Properties on Buckling

The above analytical and numerical works are based on elastic material behavior for the cylindrical shells considered and may therefore not be applicable for most onshore and offshore pipelines as the range of the D/t ratio for onshore pipelines is typically between 45 to 120 while that of offshore pipelines is usually between 15 and 40 [69]. Experimental studies by some

researchers [70,71] have indicated that at D/t ratio < 100 , cylindrical shells commonly experience inelastic (or plastic) buckling, implying that the deformation of the material exceeds the proportionality limit of the stress-strain curve before the initiation of buckling. The distinction between thin-walled and thick-walled cylinders is physically highlighted by the deformation reserve of the structure beyond initial wrinkling: while the moment vs. curvature relationship for thin-walled pipes experiences sudden and catastrophic collapse at the instance of buckling, thicker-walled pipes exhibit a more gradual loss of stability at the onset of wrinkling and are able to sustain significant deformation before eventual failure [72]. Some notable experimental investigations [73–76] have therefore focused on the buckling behavior of relatively thick-walled pipe specimens subjected to pure bending. Reddy [75] performed a series of tests on aluminum alloy and stainless-steel tubes subjected to pure bending; with sufficiently-thick walls to ensure buckling in the plastic range of the materials. The results confirmed that the formation of wave-like ripples on the compression side of the tubes, rather than flattening of the cross-section, was responsible for collapse. The extreme fiber compression strain was also adopted as the buckling criterion and comparison with the critical strains of aluminum tubes experimentally subjected to uniform axial compression by Batterman [40] showed a similar relationship with respect to the D/t ratio. Kyriakides and Ju [76] conducted experiments on long aluminum cylindrical specimens with different D/t ratios ranging from 60.5 to 19.5. The results obtained by Ref. [76] indicate that the prevalent mode of instability in ‘relatively thinner’ shells (D/t ratio > 40) is the development of short randomly-distributed wave-like ripples along the length of the specimens. The amplitudes of the wave-like ripples were observed to progressively become less uniform as additional curvature was induced to the specimens and the instance of collapse was immediately preceded by a second instability triggered in the pocket of one of the ripples. Ovalization of ‘relatively thinner’ shells was also observed to be uniform up to collapse. Longitudinal wave-like wrinkling was also observed to be primarily responsible for bifurcation instability of ‘moderately thick’ shells ($26 < D/t$ ratio < 40) but unlike ‘relatively thinner’ shells, ovalization of the cross-section became increasingly nonuniform with corresponding increase in applied curvature and eventual collapse was characterized by a sharp local kink on the compression side of the specimen. The instability of ‘relatively thick’ shells (D/t ratio < 26) under pure bending was markedly governed by the natural ovalization instability phenomenon

stipulated by Ref. [51] as bifurcation instability was observed to be initiated by uniform ovalization and nonappearance of wave-like ripples. Only as the applied curvature is further increased, and when the specimen is close to collapse, do ripples become amplified. Similar to ‘moderately thick’ shells, uniformity of ovalization diminishes for ‘relatively thick’ shells with increasing curvature until collapse is triggered in the region of localized nonuniform ovalization.

2.5 Measurement of Compressive Strain

It has been suggested by a few researchers [77–79] to use of the extreme fiber compressive strain as a measure upon which to establish local inelastic buckling criteria. Preference for a strain-based, rather than a stress-based, criteria is predicated on the viewpoint that strains are easier to measure or estimate in the field and, more importantly, the stress-strain curve is generally flat in the plastic range of deformation of the material so that a small variation in stresses corresponds to a large variation in strains. Stress is therefore regarded as a poor basis for the assessment of post-yield buckling criteria in pipelines. Strain-based design (SBD) affords the opportunity to evaluate the mechanical response under displacement-controlled loading conditions and assess the fitness-for-purpose of pipe segments based on real, rather than arbitrary, performance limits [29]. SBD also provides much better insight into the actual behavior and safety of pipelines and permits a safe amount of plastic deformation thereby paving the way for more economical designs [80].

Displacement-controlled loading conditions are generally idealized as a combination of constant internal pressure, constant axial force, and monotonically-increasing curvature [29]; an idealization which has somewhat inadvertently become the standardized procedure for experimental testing and numerical evaluation of the deformational capacity of pipes. Several phenomena of valuable interest in pipe segments subjected to various deformational loading conditions have been extensively studied, both experimentally and numerically, in recent decades, including; ovalization/bifurcation instability, initiation and evolution of wrinkles, and peak moment capacity and associated compressive strain [70,75–77,81–83]. Consequently, most of the current pipeline design standards (e.g., API RP 1111 [84], ABS 2006 [85], CSA Z-662 [86], DNV-OS-F101 [87]), adopt a strain-based limit state design (LSD) approach with specific

goals of maintaining the strain demand (applied strain from ground movement) below a characteristic strain limit (strain capacity). The strain (deformational) capacity of pipelines is evaluated based on the quantitative assessment of cumulative cross-sectional deformation, and resultant material strain, in the region of localized wrinkle formation [88].

Review of literature reveals three common limit state criteria; conceptualized by researchers for determining the limit of the longitudinal compressive strains induced in pipelines due to ground movement.

1. *Bifurcation instability criterion*: This approach attempts to set the limit for the compressive longitudinal strain at the initiation of buckling of the pipe wall which corresponds to the bifurcation point in the load-deformation response curve. Rigorous analytical formulations are required to achieve reasonable accuracy in determining the bifurcation stress and bifurcation strain values, and such formulations are only feasible where geometric perfectness and material elasticity are assumed. Bouwkamp and Stephen [70,77] attempted to experimentally determine the buckling initiation strain by visual observation, but the reported strains were marred by severe inadequacies and incorrectness.
2. *Rapid wrinkle growth criterion*: Lara [89] attempted to replicate the tests performed by Refs. [70] and [77] using elbow elements of the ABAQUS FE program. He suggested the average compressive strain associated with a rapid change in the curvature of the developed longitudinal wrinkle of the pipe wall as a more rational, and less conservative, strain limit. This approach, however, relies strongly on visual observation as the procedures for determining the acceleration of wrinkle growth are unstandardized.
3. *Peak load criterion*: This approach relies on the premise that buckling deformations grow rapidly once the maximum load on the load-deformation response curve is attained. Murphey and Langner [90] performed some of the pioneering work on the deformational capacity of pipe segments subjected to pure bending using the average strain corresponding to the maximum moment on the moment-curvature response curve as the strain limit. This approach is, however, better-suited for unpressurized pipelines, whose moment-curvature response are characterized by a distinct peak point followed by an abrupt drop in the load. For pressurized pipelines, which typically feature an extended

plateau, the average strain corresponding to the point of significant softening in the moment-curvature response curve is regarded as the appropriate strain limit [75,91]. The limit load criterion offers the relative advantage of being easily determinable, both visually and arithmetically, from the load-deformation response data of a pipe segment subjected to various loading conditions. This approach is therefore adopted for obtaining the strain limit throughout this research.

2.6 References

- [1] N.M. Newmark, W.J. Hall, Pipeline design to resist large fault displacement, in: Proc. US Natl. Conf. Earthq. Eng., Earthquake Engineering Research Institute, June 18-20, 1975. Ann Arbor, Michigan, 1975: pp. 416–425.
- [2] R.P. Kennedy, A.M. Chow, R.A. Williamson, Fault movement effects on buried oil pipeline, *Transp. Eng. J. Am. Soc. Civ. Eng.* 103 (1977) 617–633.
- [3] E.A. Vougioukas, C. Theodossis, P.G. Carydis, Seismic Analysis of Buried Pipelines Subjected to Vertical Fault Movement, *Lifeline Earthq. Eng.* (1991) 432–441.
- [4] L.R.-L. Wang, Y.-H. Yeh, A refined seismic analysis and design of buried pipeline for fault movement, *Earthq. Eng. Struct. Dyn.* 13 (1985) 75–96. doi:10.1002/eqe.4290130109.
- [5] S. Takada, N. Hassani, K. Fukuda, A new proposal for simplified design of buried steel pipes crossing active faults, *Earthq. Eng. Struct. Dyn.* 30 (2001) 1243–1257. doi:10.1002/eqe.62.
- [6] X. Liu, H. Zhang, B. Wang, M. Xia, K. Wu, Q. Zheng, Y. Han, X. Liu, H. Zhang, B. Wang, M. Xia, K. Wu, Q. Zheng, Y. Han, Local Buckling Behavior and Plastic Deformation Capacity of High-Strength Pipe at Strike-Slip Fault Crossing, *Metals (Basel)*. 8 (2017) 22. doi:10.3390/met8010022.
- [7] X. Liu, H. Zhang, K. Wu, M. Xia, Y. Chen, M. Li, Buckling failure mode analysis of buried X80 steel gas pipeline under reverse fault displacement, *Eng. Fail. Anal.* 77 (2017) 50–64. doi:10.1016/J.ENGFAILANAL.2017.02.019.
- [8] X. Liu, H. Zhang, O. Ndubuaku, M. Xia, J.J.R. Cheng, Y. Li, S. Adeeb, Effects of stress-strain characteristics on local buckling of X80 pipe subjected to strike-slip fault movement, *J. Press. Vessel Technol.* (2018).

- [9] D.K. Karamitros, G.D. Bouckovalas, G.P. Kouretzis, Stress analysis of buried steel pipelines at strike-slip fault crossings, *Soil Dyn. Earthq. Eng.* 27 (2007) 200–211. doi:10.1016/J.SOILDYN.2006.08.001.
- [10] R.B. Arifin, W.M.S.B. Wan M. Yusof, P. Zhao, Y. Bai, Seismic Analysis for the Subsea Pipeline System, in: 29th Int. Conf. Ocean. Offshore Arct. Eng. Vol. 5, Parts A B, ASME, 2010: pp. 659–667. doi:10.1115/OMAE2010-20671.
- [11] L. Odina, R. Tan, Seismic Fault Displacement of Buried Pipelines Using Continuum Finite Element Methods, in: Vol. 3 Pipeline Riser Technol., ASME, 2009: pp. 617–625. doi:10.1115/OMAE2009-79739.
- [12] S. Yimsiri, K. Soga, K. Yoshizaki, G.R. Dasari, T.D. O’Rourke, Lateral and Upward Soil-Pipeline Interactions in Sand for Deep Embedment Conditions, *J. Geotech. Geoenvironmental Eng.* 130 (2004) 830–842. doi:10.1061/(ASCE)1090-0241(2004)130:8(830).
- [13] X. Xie, Numerical analysis and evaluation of buried pipeline response to earthquake-induced ground fault rupture. Doctoral dissertation., Department of Civil and Environmental Engineering, Rensselaer Polytechnic Institute, 2008.
- [14] M. O’Rourke, V. Gadicherla, T. Abdoun, Centrifuge Modeling of Buried Pipelines, in: *Adv. Mitig. Technol. Disaster Response Lifeline Syst.*, American Society of Civil Engineers, Reston, VA, 2003: pp. 757–768. doi:10.1061/40687(2003)77.
- [15] D. Ha, T.H. Abdoun, M.J. O’Rourke, M.D. Symans, T.D. O’Rourke, M.C. Palmer, H.E. Stewart, Buried high-density polyethylene pipelines subjected to normal and strike-slip faulting — a centrifuge investigation, *Can. Geotech. J.* 45 (2008) 1733–1742. doi:10.1139/T08-089.
- [16] T.H. Abdoun, D. Ha, M.J. O’Rourke, M.D. Symans, T.D. O’Rourke, M.C. Palmer, H.E. Stewart, Factors influencing the behavior of buried pipelines subjected to earthquake faulting, *Soil Dyn. Earthq. Eng.* 29 (2009) 415–427. doi:10.1016/J.SOILDYN.2008.04.006.
- [17] M. Rojhani, M. Moradi, A. Galandarezadeh, S. Takada, Centrifuge modeling of buried pipelines response due to reverse faulting, in: *Proc. 5th Int. Conf. Earthq. Geotech. Eng.* January 10-13, 2011, Santiago, Chile, 2011: p. CMBRO.

- [18] H.H. Jalali, F.R. Rofooei, N.K.A. Attari, M. Samadian, Experimental and finite element study of the reverse faulting effects on buried continuous steel gas pipelines, *Soil Dyn. Earthq. Eng.* 86 (2016) 1–14. doi:10.1016/J.SOILDYN.2016.04.006.
- [19] R.E. Hobbs, Pipeline buckling caused by axial loads, *J. Constr. Steel Res.* 1 (1981) 2–10. doi:10.1016/0143-974X(81)90027-4.
- [20] R.E. Hobbs, In-Service Buckling of Heated Pipelines, *J. Transp. Eng.* 110 (1984) 175–189. doi:10.1061/(ASCE)0733-947X(1984)110:2(175).
- [21] N.-J.R. Nielsen, B. Lyngberg, P.T. Pedersen, Upheaval Buckling Failures of Insulated Buried Pipelines: A Case Story, in: *Offshore Technol. Conf., Offshore Technology Conference*, 1990. doi:10.4043/6488-MS.
- [22] R. Liu, S. Yan, Brief History of Upheaval Buckling Studies for Subsea Buried Pipeline, *J. Pipeline Syst. Eng. Pract.* 4 (2013) 170–183. doi:10.1061/(ASCE)PS.1949-1204.0000127.
- [23] R. Liu, P. Basu, H. Xiong, Laboratory tests and thermal buckling analysis for pipes buried in Bohai soft clay, *Mar. Struct.* 43 (2015) 44–60. doi:10.1016/J.MARSTRUC.2015.05.001.
- [24] M. Mohareb, G.L. Kulak, A. Elwi, D.W. Murray, Testing and Analysis of Steel Pipe Segments, *J. Transp. Eng.* 127 (2001) 408–417. doi:10.1061/(ASCE)0733-947X(2001)127:5(408).
- [25] N. Nazemi, S. Das, Behavior of X60 Line Pipe Subjected to Axial and Lateral Deformations, *J. Press. Vessel Technol.* 132 (2010) 031701. doi:10.1115/1.4001426.
- [26] D. Wijewickreme, H. Karimian, D. Honegger, Response of buried steel pipelines subjected to relative axial soil movement, *Can. Geotech. J.* 46 (2009) 735–752. doi:10.1139/T09-019.
- [27] Yong Bai, Wei-Liang Jin, Ultimate Strength of Cylindrical Shells, in: *Mar. Struct. Des.*, 2nd ed., Elsevier, Oxford, United Kingdom, 2016: pp. 353–365. doi:https://doi.org/10.1016/B978-0-08-099997-5.00018-6.
- [28] J. Singer, J. Arbocz, T. Weller, *Buckling Experiments, Volume 1: Basic Concepts, Columns, Beams and Plates*, John Wiley & Sons, New York, 1998.
- [29] D.W. Murray, Local buckling, strain localization, wrinkling and postbuckling response of line pipe, *Eng. Struct.* 19 (1997) 360–371. doi:10.1016/S0141-0296(96)00096-X.

- [30] R. Peek, Axisymmetric Wrinkling of Cylinders with Finite Strain, *J. Eng. Mech.* 126 (2000) 455–461. doi:10.1061/(ASCE)0733-9399(2000)126:5(455).
- [31] G.T. Ju, S. Kyriakides, Thermal Buckling of Offshore Pipelines, *J. Offshore Mech. Arct. Eng.* 110 (1988) 355. doi:10.1115/1.3257073.
- [32] F.J. Klever, A.C. Palmer, S. Kyriakides, Limit-state design of high-temperature pipelines, in: 13th Int. Conf. Offshore Mech. Arct. Eng., Houston, Texas, 1994: p. Vol. 5, pp. 77–92.
- [33] E. Jaberzadeh, M. Azhari, Elastic and inelastic local buckling of stiffened plates subjected to non-uniform compression using the Galerkin method, *Appl. Math. Model.* 33 (2009) 1874–1885. doi:10.1016/j.apm.2008.03.020.
- [34] J. Singer, J. Arbocz, T. Weller, Wiley InterScience (Online service), Buckling experiments: experimental methods in buckling of thin-walled structures. Shells, built-up structures, composites and additional topics, Volume 2, John Wiley & Sons, 2002.
- [35] R. Shamass, G. Alfano, F. Guarracino, A numerical investigation into the plastic buckling paradox for circular cylindrical shells under axial compression, *Eng. Struct.* 75 (2014) 429–447. doi:10.1016/J.ENGSTRUCT.2014.05.050.
- [36] F.R. Shanley, Inelastic Column Theory, *J. Aeronaut. Sci.* 14 (1947) 261–268. doi:10.2514/8.1346.
- [37] R. Hill, A general theory of uniqueness and stability in elastic-plastic solids, *J. Mech. Phys. Solids.* 6 (1958) 236–249. doi:10.1016/0022-5096(58)90029-2.
- [38] R. Hill, Bifurcation and uniqueness in non-linear mechanics of continua, in: *Probl. Contin. Mech.*, Society of Industrial and Applied Mathematics, Philadelphia, PA, 1961: pp. 155–164.
- [39] D. Bushnell, Plastic Buckling of Various Shells, *J. Press. Vessel Technol. Trans. ASME.* 104 (1982) 51–72. doi:10.1115/1.3264190.
- [40] S.C. Batterman, Plastic buckling of axially compressed cylindrical shells, *AIAA J.* 3 (1965) 316–325. doi:10.2514/3.2848.
- [41] E.T. Onat, Inelastic Instability and Incremental Theories of Plasticity, *J. Aeronaut. Sci.* 20 (1953) 181–186. doi:10.2514/8.2585.
- [42] L.H.N. Lee, Inelastic Buckling of Initially Imperfect Cylindrical Shells Subject to Axial Compression, *J. Aerosp. Sci.* 29 (1962) 87–95. doi:10.2514/8.9306.

- [43] M.J. Sewell, A general theory of elastic and inelastic plate failure—I, *J. Mech. Phys. Solids*. 11 (1963) 377–393. doi:10.1016/0022-5096(63)90016-4.
- [44] E. Ore, D. Durban, Elastoplastic buckling of axially compressed circular cylindrical shells, *Int. J. Mech. Sci.* 34 (1992) 727–742. doi:10.1016/0020-7403(92)90005-2.
- [45] J. Blachut, G.D. Galletly, S. James, On the Plastic Buckling Paradox for Cylindrical Shells, *Proc. Inst. Mech. Eng. Part C J. Mech. Eng. Sci.* 210 (1996) 477–488. doi:10.1243/PIME_PROC_1996_210_221_02.
- [46] L.M. Murphy, L.H.N. Lee, Inelastic buckling process of axially compressed cylindrical shells subject to edge constraints, *Int. J. Solids Struct.* 7 (1971) 1153–1170. doi:10.1016/0020-7683(71)90059-X.
- [47] F.C. Bardi, S. Kyriakides, Plastic buckling of circular tubes under axial compression—part I: Experiments, *Int. J. Mech. Sci.* 48 (2006) 830–841. doi:10.1016/J.IJMECSCI.2006.03.005.
- [48] H. Yun, S. Kyriakides, On the beam and shell modes of buckling of buried pipelines, *Soil Dyn. Earthq. Eng.* 9 (1990) 179–193. doi:10.1016/S0267-7261(05)80009-0.
- [49] S.A. Karamanos, Bending instabilities of elastic tubes, *Int. J. Solids Struct.* 39 (2002) 2059–2085. doi:10.1016/S0020-7683(02)00085-9.
- [50] T.H. Karman, Über die Formänderung dünnwandiger Rohre, *Z. VDI.* (1911) 1889–1895.
- [51] L.G. Brazier, On the Flexure of Thin Cylindrical Shells and Other “Thin” Sections, *Proc. R. Soc. A Math. Phys. Eng. Sci.* 116 (1927) 104–114. doi:10.1098/rspa.1927.0125.
- [52] R.W. Mossman, R.G. Robinson, Bending tests of metal monocoque fuselage construction. NACA Technical Note 357., Washington DC, United States, 1930.
- [53] Imperial F.F., The criterion of elastic instability of thin duralumin tubes subjected to bending. MS Thesis, Dept. of Mechanical Engineering, University of California., 1932.
- [54] E.E. Lundquist, Strength Tests of Thin-walled Duralumin Cylinders in Pure Bending. NACA Technical Note, No 479, Langley Field, VA, United States, 1933.
- [55] L.H. Donnell, A new theory for the buckling of thin cylinders under axial compression and bending, *Trans. A.S.M.E.* 56 (1934) 795–806.

- [56] W.B. Stephens, J.H. Starnes, B.O. Almroth, Collapse of Long Cylindrical Shells under Combined Bending and Pressure Loads, *AIAA J.* 13 (1975) 20–25. doi:10.2514/3.49624.
- [57] O. Fabian, Collapse of cylindrical, elastic tubes under combined bending, pressure and axial loads, *Int. J. Solids Struct.* 13 (1977) 1257–1270. doi:10.1016/0020-7683(77)90099-3.
- [58] A. Libai, C.W. Bert, A mixed variational principle and its application to the nonlinear bending problem of orthotropic tubes—II. application to nonlinear bending of circular cylindrical tubes, *Int. J. Solids Struct.* 31 (1994) 1019–1033. doi:10.1016/0020-7683(94)90009-4.
- [59] B.F. Tatting, Z. Gürdal, V.V. Vasiliev, The brazier effect for finite length composite cylinders under bending, *Int. J. Solids Struct.* 34 (1997) 1419–1440. doi:10.1016/S0020-7683(96)00094-7.
- [60] W. Flügge, Die Stabilität der Kreiszylinderschale, *Ing Arch.* 3 (1932) 463–506.
- [61] H.S. Suer, L.A. Harris, W.T. Skene, R.J. Benjamin, The Bending Stability of Thin-Walled Unstiffened Circular Cylinders Including the Effects of Internal Pressure, *J. Aerosp. Sci.* 25 (1958) 281–287. doi:10.2514/8.7639.
- [62] P. Seide, V.I. Weingarten, On the Buckling of Circular Cylindrical Shells Under Pure Bending, *J. Appl. Mech.* 28 (1961) 112. doi:10.1115/1.3640420.
- [63] B.D. Reddy, C.R. Calladine, Classical buckling of a thin-walled tube subjected to bending moment and internal pressure, *Int. J. Mech. Sci.* 20 (1978) 641–650. doi:10.1016/0020-7403(78)90022-X.
- [64] J. Kempner, Y.-N. Chen, Buckling and initial postbuckling of oval cylindrical shells under combined axial compression and bending, *Trans. N. Y. Acad. Sci.* 36 (1974) 171–191. doi:10.1111/j.2164-0947.1974.tb01564.x.
- [65] Y.N. Chen, J. Kempner, Buckling of oval cylindrical shells under compression and asymmetric bending, *AIAA J.* 14 (1976) 1235–1240. doi:10.2514/3.7215.
- [66] E.L. Axelrad, Refinement of buckling-load analysis for tube flexure by way of considering precritical deformation, *Izv. Akad. Nauk SSSR, Otd. Tekhnicheskikh Nauk. Mekhanika i Mashinostr.* 4 (1965) 133–139.
- [67] E.L. Axelrad, *Theory of Flexible Shells*, 28th ed., Elsevier Science Publishers B.V., Amsterdam, The Netherlands, 1987.

- [68] D.O. Brush, B.O. Almroth, *Buckling of Bars, Plates, and Shells*, McGraw-Hill, New York, 1975.
- [69] N. Yoosef-Ghodsi, I. Ozkan, Q. Chen, Comparison of Compressive Strain Limit Equations, in: Vol. 4 Prod. Pipelines Flowlines; Proj. Manag. Facil. Integr. Manag. Oper. Maintenance; Pipelining North. Offshore Environ. Strain-Based Des. Stand. Regul., ASME, 2014: p. V004T11A001. doi:10.1115/IPC2014-33182.
- [70] J.G. Bouwkamp, R.M. Stephen, Full-scale studies on the structural behavior of large diameter pipes under combined loading. Report No. UCSESM 74-1, Berkeley, California, 1974.
- [71] D.R. Sherman, Test of Circular Steel Tubes in Bending, *J. Struct. Div.* 102 (1976) 2181–2195.
- [72] C.I. Papadaki, G. Chatzopoulou, G.C. Sarvanis, S.A. Karamanos, Buckling of internally-pressurized spiral-welded steel pipes under bending, *Int. J. Press. Vessel. Pip.* 165 (2018) 270–285. doi:10.1016/J.IJPVP.2018.07.006.
- [73] J.C. Wilhoit, J.E. Merwin, Critical Plastic Bucking Parameter for Tubing in Bending Under Axial Tension, in: *Offshore Technol. Conf., Offshore Technology Conference*, 1973. doi:10.4043/1874-MS.
- [74] P. Tugcu, J. Schroeder, Plastic deformation and stability of pipes exposed to external couples, *Int. J. Solids Struct.* 15 (1979) 643–658. doi:10.1016/0020-7683(79)90077-5.
- [75] B.D. Reddy, An experimental study of the plastic buckling of circular cylinders in pure bending, *Int. J. Solids Struct.* 15 (1979) 669–683. doi:10.1016/0020-7683(79)90066-0.
- [76] S. Kyriakides, G.T. Ju, Bifurcation and localization instabilities in cylindrical shells under bending—I. Experiments, *Int. J. Solids Struct.* 29 (1992) 1117–1142. doi:10.1016/0020-7683(92)90139-K.
- [77] J.G. Bouwkamp, R.M. Stephen, Large diameter pipe under combined loading, *Transp. Eng. J. ASCE.* 99 (1973) 521–536.
- [78] G.H. Workman, Pipe wall stability analysis of 12.75 in OD* 0.25 in WT grade 52 pipe, 1981.
- [79] H.O. Kim, Velasco P., Review of Pipe Buckling for Arctic Pipeline Design, in: *Proc. 7th Int. Conf. Offshore Mech. Arct. Eng.*, Houston, Texas, 1988.

- [80] A.M. Gresnigt, R.J. van Foeken, S.L. Chen, Effect of Local Buckling On Burst Pressure, in: Sixth Int. Offshore Polar Eng. Conf., International Society of Offshore and Polar Engineers, Los Angeles, California, USA, 1996: pp. 80–88.
- [81] J.O. Jirsa, F.H. Lee, J.C. Wilhoit, J.E. Merwin, Ovaling Of Pipelines Under Pure Bending, in: Offshore Technol. Conf., Offshore Technology Conference, 1972. doi:10.4043/1569-MS.
- [82] R.. Korol, Critical buckling strains of round tubes in flexure, *Int. J. Mech. Sci.* 21 (1979) 719–730. doi:10.1016/0020-7403(79)90052-3.
- [83] D.R. Sherman, Inelastic flexural buckling of cylinders, in: M.N. Pavlovic (Ed.), *Steel Struct. Recent Res. Adv. Their Appl. to Des.*, Elsevier Applied Science Publishers, 1986: pp. 339–357.
- [84] API 1111, Design, construction, operation, and maintenance of offshore hydrocarbon pipelines, (1999).
- [85] American Bureau of Shipping, ABS Guide for Building and Classing Subsea Pipeline Systems, (2006).
- [86] Canadian Standards Association, Oil and gas pipeline systems. CSA-Z662-2007, (2007).
- [87] Det Norske Veritas, Submarine pipeline systems - DNV-OS-F101, DNV, Oslo, Norway, 2010.
- [88] Y. Zhang, S. Das, Failure of X52 Wrinkled Pipelines Subjected to Monotonic Axial Deformation, *J. Press. Vessel Technol.* 130 (2008) 021702. doi:10.1115/1.2894294.
- [89] P.F. Lara, Revisiting the failure criteria of buried pipelines, in: ASME Pipeline Eng. Symp., Dallas, Texas, 1987: pp. 143–145.
- [90] C.E. Murphey, C.G. Langner, Ultimate pipe strength under bending, collapse and fatigue, in: Proc. 4th Int. Conf. Offshore Mech. Arct. Eng., 1985: pp. 467–477.
- [91] Z. Zhou, D.W. Murray, Towards rational deformation limit states for buried pipelines, in: Third Int. Offshore Polar Eng. Conf., Singapore, 1993: pp. 18–24.



3. BASIC THEORETICAL FORMULATIONS

3.1 Introduction

This chapter is based on a review of relevant classical theories which are fundamental to the development of analytical formulations for predicting the critical buckling stress in two widely-applied shell structures, flat plates and cylindrical shells, both subjected to pure axial compression. Derivations of the bifurcation instability load are outlined separately for each structure and are primarily intended to present an introductory analytical examination of the stability phenomenon in such structures. However, the following derivations are essentially based on assumptions of isotropic elastic material behavior and initially-perfect geometrical conditions hence, the applicability of such derivations is severely limited for stability analysis of real structures. The imperativeness of computerized applications for shell stability analysis, as adopted for this research, is therefore implied.

3.2 Critical Buckling Stress for a Simply-supported Flat Plate

The postulations of the classical plate theory are somewhat similar to those of the Euler theory for columns. Ideally, if a thin, flat, and perfect elastic plate is subjected to uniaxial in-plane compressive stress, acting directly in the middle plane of the plate thickness, the initial configuration of the plate is such that the out-of-plane deflection, w , is zero. In this initial configuration, the applied loading and the resultant stresses are in equilibrium and the relationship between the applied loading and the edge strain is dependent on the restraint provided against in-plane displacement by the edges parallel to the applied loading. As the applied external loading attains a critical value, the work done by the resultant stresses in the flat configuration will supersede the potential energy due to out-of-plane bending of the plate, resulting in an unstable equilibrium and the formation of corrugations or dimples on the plate surface. By transforming into a non-flat or undulated configuration, some of the compression energy is relieved and the plate achieves a new mode of equilibrium stability such that the potential energy of the system remains the same [1].

The classical theory for describing the governing constitutive equations for a buckled thin plate or, more generally, for a thin shell is generally defined based on the Kirchoff-Love two-

dimensional thin shell concept [2] developed over a hundred years ago. According to the Kirchoff-Love assumption, plane sections remain plane and perpendicular to the middle surface after deformation hence, the effects of transverse shear strains are neglected and the angle of rotation of the cross-section is taken as the first derivative of the vertical displacement.

If a small element is cut out from the plate and, the curvature, κ , of the deformed element due to bending action is given by [3]:

$$\kappa = \frac{\partial}{\partial s} \left(\frac{\partial w}{\partial s} - \gamma_{sz} \right) \quad (3-1)$$

where s represents the direction tangential to the middle surface in either the x - or y -direction and z represents the direction along the thickness of the plate.

Since the transverse shear deformations are neglected, the components of curvature are defined as:

$$\kappa_x = \frac{\partial^2 w}{\partial x^2} \quad ; \quad \kappa_y = \frac{\partial^2 w}{\partial y^2} \quad \text{and} \quad \kappa_{xy} = \frac{\partial^2 w}{\partial x \partial y} \quad (3-2)$$

Once a plate buckles, the out-of-plane deflection ceases to be negligible and small deformation assumptions are no longer applicable to describe the load-end shortening relationship of the plate. The following set of nonlinear partial differential equations, proposed by von Kármán, are therefore required to describe the large deflections in the plate [4]:

$$\nabla^4 \Phi = E \left[\left(\frac{\partial^2 w}{\partial x \partial y} \right)^2 - \frac{\partial^2 w}{\partial x^2} \frac{\partial^2 w}{\partial y^2} \right] \quad (3-3)$$

$$\nabla^4 w = \frac{t}{D} \left(\frac{\partial^2 \Phi}{\partial y^2} \frac{\partial^2 w}{\partial x^2} - \frac{2 \partial^2 \Phi}{\partial x \partial y} \frac{\partial^2 w}{\partial x \partial y} + \frac{\partial^2 \Phi}{\partial x^2} \frac{\partial^2 w}{\partial y^2} \right) \quad (3-4)$$

where t represents the thickness of the plate, Φ represents Airy's stress function, and D is the flexural rigidity of the plate given by:

$$D = \frac{Et^3}{12(1-\nu^2)} \quad (3-5)$$

where E is Young's modulus and ν is the Poisson's ratio.

The in-plane resultant stresses may be expressed in terms of the Airy stress function as:

$$N_x = t \frac{\partial^2 \Phi}{\partial y^2} ; N_y = t \frac{\partial^2 \Phi}{\partial x^2} ; N_{xy} = t \frac{\partial^2 \Phi}{\partial x \partial y} \quad (3-6)$$

where N_x and N_y are the normal membrane forces per unit width and N_{xy} is the shearing membrane force per unit width.

Assuming non-existence of body forces acting in the plate, a projection of the normal membrane forces in the x - and y -directions yields the following equations of equilibrium:

$$\frac{\partial N_x}{\partial x} + \frac{\partial N_{yx}}{\partial y} = 0 \quad (3-7)$$

$$\frac{\partial N_y}{\partial y} + \frac{\partial N_{xy}}{\partial x} = 0 \quad (3-8)$$

The bending moment resultants (M_x and M_y) and the twisting moment resultant (M_{xy}) are obtained by integrating the stresses over the thickness of the plate (neglecting the effect of shearing forces on the curvature of the plate) to obtain:

$$M_x = \int_{-t/2}^{t/2} \sigma_x z dz = -D \left(\frac{\partial^2 w}{\partial x^2} + \nu \frac{\partial^2 w}{\partial y^2} \right) \quad (3-9)$$

$$M_y = \int_{-t/2}^{t/2} \sigma_y z dz = -D \left(\frac{\partial^2 w}{\partial y^2} + \nu \frac{\partial^2 w}{\partial x^2} \right) \quad (3-10)$$

$$M_{xy} = M_{yx} = \int_{-t/2}^{t/2} \tau_{xy} z dz = \int_{-t/2}^{t/2} \tau_{yx} z dz \quad (3-11)$$

Assuming a distributed lateral load, q , to be acting perpendicular to the middle plane of the plate, and taking the moment of all the forces acting on the plate with respect to the x - and y -axis, as well as the projections of all the forces on the z -axis, the following equation of equilibrium is obtained:

$$\frac{\partial^2 M_x}{\partial x^2} - \frac{2\partial^2 M_{xy}}{\partial x \partial y} + \frac{\partial^2 M_y}{\partial y^2} + q = 0 \quad (3-12)$$

Substituting Eqs. (3-9) - (3-11) in Eq. (3-12) and adding the normal membrane forces to the equilibrium equation (neglecting higher order quantities) yields:

$$\frac{\partial^4 w}{\partial x^4} + 2 \frac{\partial^4 w}{\partial x^2 \partial y^2} + \frac{\partial^4 w}{\partial y^4} = \frac{1}{D} \left(q + N_x \frac{\partial^2 w}{\partial x^2} + 2N_{xy} \frac{\partial^2 w}{\partial x \partial y} + N_y \frac{\partial^2 w}{\partial y^2} \right) \quad (3-13)$$

The inherent difficulty in obtaining the exact solution to the above equation makes it imperative for approximate solutions to be formulated by assuming functions for the displacements. The functions contain arbitrary parameters and the approximate solution is determined by deriving the values of the parameters.

To obtain a realistic or reasonably approximate representation of the stress distribution experienced in actual plates used for engineering applications, it is important that the boundary conditions applied for obtaining the solution to the theoretical expression in Eq. (3-13) must agree with the typical edge conditions of the respective application. A commonly used model for assessment of the critical buckling stress of flat rectangular plates, especially in offshore and marine structures, is a perfectly flat plate (as shown in Figure 3-1) which is simply supported on all four sides and subjected to a uniform compressive axial force per unit length in the x -direction, N_x [5].

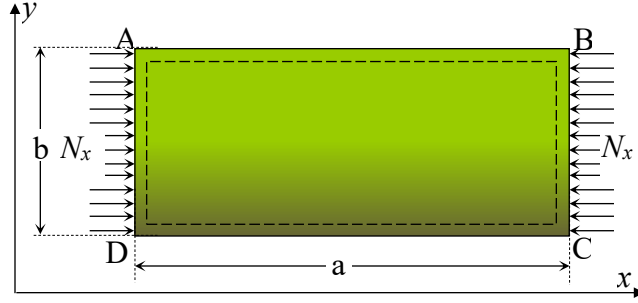


Figure 3-1: Schematic of flat plate under uniform axial compression

For the general case of simply supported flat plates, the boundary conditions are such that the out-of-plane deflections and normal bending moments are zero at all the edges (AB, BC, CD, and AD). Also, the distributed lateral load, q , and the normal membrane forces, N_y and N_{xy} are zero hence, the theoretical expression reduces to:

$$\frac{\partial^4 w}{\partial x^4} + 2 \frac{\partial^4 w}{\partial x^2 \partial y^2} + \frac{\partial^4 w}{\partial y^4} = \frac{1}{D} \left(-N_x \frac{\partial^2 w}{\partial x^2} \right) \quad (3-14)$$

The function, $w(x,y)$ for the out-of-plane deflection across the surface area of the plate, which satisfies the simply-supported boundary conditions, can be assumed as a product of two harmonic functions:

$$w(x,y) = \sum_{m=1}^{\infty} \sum_{n=1}^{\infty} w_{mn} \sin \frac{m\pi x}{a} \sin \frac{n\pi y}{b} \quad (3-15)$$

where m and n are the number of half-sine waves in the x - and y -directions respectively. a and b represent the dimensions of the plate in the x - and y -directions respectively. The amplitude of the out-of-plane deflection is represented by w_{mn} .

By applying the respective boundary conditions at all the edges of the plate, the expression in Eq. (3-14) gives:

$$\left[\left(\frac{m\pi}{a} \right)^4 + 2 \left(\frac{m\pi}{a} \right)^2 \left(\frac{n\pi}{b} \right)^2 + \left(\frac{n\pi}{b} \right)^4 - \frac{N_x}{D} \left(\frac{m\pi}{a} \right)^2 \right] w_{mn} \sin \frac{m\pi x}{a} \sin \frac{n\pi y}{b} = 0 \quad (3-16)$$

The smallest value of the critical membrane buckling load is obtained for $n = 1$ such that only one half-sine wave is formed in the y -direction, and Eq. (3-16) is therefore simplified as:

$$(N_x)_{cr} = \frac{\pi^2 D}{b^2} \left(\frac{mb}{a} + \frac{a}{mb} \right)^2 \quad (3-17)$$

The simplified expression is however only valid for cases where the restraint against in-plane displacement of the longitudinal edges (AB and CD) is zero and thus the longitudinal edges are allowed free expansion because of the Poisson effect. Also, due to the interaction between adjoining panels or adjacent plate elements in typical engineering applications, all the edges are assumed to remain straight so that the in-plane displacement does not vary with respect to the length or width of the plate.

Alternatively, the longitudinal edges may be assumed to be restrained against in-plane displacement and as a result, the normal membrane force in the y -direction, N_y , develops in the transverse direction as follows:

$$N_y = \nu N_x \quad (3-18)$$

where ν represents the Poisson's ratio. The longitudinal edge restraint introduces a modification to the expression in Eq. (3-17) as follows [6]:

$$(N_x)_{cr} = \frac{\pi^2 D}{b^2} \frac{\left[\left(\frac{mb}{a} \right)^2 + n^2 \right]^2}{\left(\frac{mb}{a} \right)^2 + \nu n^2} \quad (3-19)$$

The inclusion of the longitudinal edge restraint has been observed to have a negligible effect on the buckled shape, the post-buckling behavior, and the ultimate strength of simply supported plates as only the elastic buckling load tends to be primarily affected. The compressive reaction

force that develops in the y -direction tends to cause the plate to buckle more easily and hence, reduces the elastic buckling load by a factor of $\frac{3}{4}$ [7].

The expressions in Eqs. (3-17) and (3-19) can be written in a more compact form as:

$$(N_x)_{cr} = \frac{\pi^2 D}{b^2} k_c \quad (3-20)$$

where k_c represents the buckling coefficient and is a function of the plate aspect ratio, the wavelength parameter, and the Poisson's ratio.

The critical buckling load obtained in Eqs. (3-17) and (3-19), is a product of the critical buckling stress, σ_{cr} , and the thickness of the plate hence, the critical buckling stress can be expressed as:

$$\sigma_{cr} = \frac{\pi^2 E}{12(1 - \nu^2) \left(\frac{b}{t}\right)^2} k_c \quad (3-21)$$

The b/t ratio in Eq. (3-21) indicates the inversely proportional effect and the directly proportional effect of the plate width, b , and the plate thickness, t , respectively on the buckling resistance of the plate. As the applied compressive axial load is increased and reaches the critical buckling stress of the plate, tensile membrane stresses are generated along the y -direction due to the consequent curvature and stretching of the plate upon buckling.

If the plate is idealized as a continuum of longitudinal (x -direction) strips and transverse (y -direction) ties with finite width, and each of the longitudinal strips is assumed to behave like an individual column on an elastic foundation, the tensile membrane stresses which are developed in the transverse ties will induce a resistance effect against the mid-length out-of-plane deflection of the longitudinal strips depending on the width and thickness of the plate. Thus, a shorter width and/or a larger thickness will increase the buckling resistance of the plate, and vice versa.

Besides, the effect of edge restraint against in-plane displacement on the foregoing formulations, the fixity of the longitudinal and transverse edges, as well as the loading conditions (such as shear loading), also have a significant effect on the buckling resistance of steel plates. A number of studies have indicated that the establishment of a closed form solution for the buckling

coefficient of plates under various loading and support conditions may be complex hence, approximate analytical solutions or empirically-derived expressions become imperative [7,8].

For practical considerations, it is usually desirable that a plate or plated structural element subjected to compressive loading should experience yielding prior to buckling hence, given the relevant loading and support conditions, the limiting value of the width-to-thickness ratio is:

$$\left(\frac{b}{t}\right)_{lim} \leq \left[\frac{\pi^2 E}{12(1-\nu^2)} \left(\frac{k_c}{\sigma_y}\right) \right]^{0.5} \quad (3-22)$$

where σ_y represents the yield strength of the plate material.

3.3 Critical Buckling Stress for a Perfect Cylindrical Shell

The best-suited procedure for developing the analytical formulations for cylindrical shell stability analysis is based on the well-established Donnell-type shell equations [9 -12]. Consider the long cylindrical shell shown in Figure 3-2 which has a radius, R , and thickness, h . The Donnell equations are formulated based on the following median-surface kinematic relations which define the strain components at any point in the deformed configuration:

$$\begin{aligned} \varepsilon_x &= \frac{\partial u}{\partial x} + \frac{1}{2} \left(\frac{\partial w}{\partial x}\right)^2 & \varepsilon_y &= \frac{\partial v}{\partial y} + \frac{1}{2} \left(\frac{\partial w}{\partial y}\right)^2 + \frac{w}{R} & \gamma_{xy} &= \frac{\partial u}{\partial y} + \frac{\partial v}{\partial x} + \frac{\partial w}{\partial x} \frac{\partial w}{\partial y} \\ \kappa_x &= -\frac{\partial^2 w}{\partial x^2} & \kappa_y &= -\frac{\partial^2 w}{\partial y^2} & \kappa_{xy} &= -\frac{1}{2} \left(\frac{\partial^2 w}{\partial x \partial y} + \frac{\partial^2 w}{\partial y \partial x} \right) \end{aligned} \quad (3-23)$$

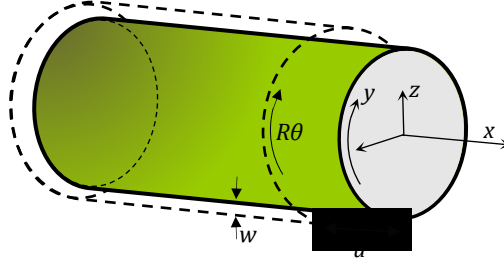


Figure 3-2: Schematic of strain components for axially-compressed cylinder

where x , y and z are the longitudinal, circumferential and radial axes respectively in the mid-thickness layer of the undeformed cylindrical shell while u , $v (= R\theta)$, and w represent the warping, circumferential and flexural displacement components corresponding to the x , y and z axes respectively, as illustrated in Figure 3-2. The terms, ε_x , ε_y and γ_{xy} represent the axial, circumferential and x - y shear strains respectively while κ_x , κ_y and κ_{xy} represent the middle surface curvatures along the x , y and x - y axes respectively.

The expressions in Eq. (3-23) are essentially the same as the postulations for the extensional and flexural strains in the middle surface of a flat plate, except for the addition of the w/R term to ε_y which is due to the relative change in the circumferential dimension with respect to radial deformation. The additional term to the circumferential strain is derived as:

$$\varepsilon_y^+ = \frac{2\pi(R + w) - 2\pi R}{2\pi R} = \frac{w}{R} \quad (3-24)$$

Taking the second derivative of the strain components in Eq. (3-23) and eliminating the torsional and circumferential displacement components, a combination of the resulting expressions yields the following compatibility equation:

$$\frac{\partial^2 \varepsilon_x}{\partial y^2} + \frac{\partial^2 \varepsilon_y}{\partial x^2} + \frac{\partial^2 \gamma_{xy}}{\partial x \partial y} = \left(\frac{\partial^2 w}{\partial x \partial y} \right)^2 - \frac{\partial^2 w}{\partial x^2} \frac{\partial^2 w}{\partial y^2} - \frac{1}{R} \frac{\partial^2 w}{\partial x^2} \quad (3-25)$$

The stationary potential energy criterion is employed to represent the following nonlinear differential equations as the governing equations for equilibrium in the post-buckling stage of the cylindrical shell:

$$\begin{aligned}
\frac{\partial \sigma_x}{\partial x} + \frac{\partial \tau_{xy}}{\partial y} &= 0 \\
\frac{\partial \sigma_y}{\partial y} + \frac{\partial \tau_{xy}}{\partial x} &= 0 \\
\frac{\partial^2 M_x}{\partial x^2} + 2 \frac{\partial^2 M_{xy}}{\partial x \partial y} + \frac{\partial^2 M_y}{\partial y^2} + h \left(\sigma_x \frac{\partial^2 w}{\partial x^2} + 2 \tau_{xy} \frac{\partial^2 w}{\partial x \partial y} + \sigma_y \frac{\partial^2 w}{\partial y^2} - \frac{\sigma_y}{R} \right) + p &= 0
\end{aligned} \tag{3-26}$$

where M_x , M_{xy} and M_y are the in-plane bending moments, the terms, σ_x , τ_{xy} and σ_y represent the membrane stresses initiated in the median surface of the cylindrical shell as a result of the combined action of extensional and flexural strains, and p represents the applied external pressure.

The resultant membrane stresses and in-plane bending moments are mathematically derived according to Kirchoff-Love's thin shell theory by summing up the stresses over the thickness of the cylindrical shell. The resultant stresses and moments are related to the strains and curvature changes based on the following isotropic constitutive equations.

$$\begin{aligned}
\sigma_x &= \frac{C}{h} (\varepsilon_x + \mu \varepsilon_y) & M_x &= D (\kappa_x + \mu \kappa_y) \\
\sigma_y &= \frac{C}{h} (\varepsilon_y + \mu \varepsilon_x) & M_y &= D (\kappa_y + \mu \kappa_x) \\
\tau_{xy} &= C \frac{(1 - \mu)}{2h} \gamma_{xy} & \frac{M_{xy} + M_{yx}}{2} &= D (1 - \mu) \kappa_{xy}
\end{aligned} \tag{3-27}$$

where C and D represent the extensional stiffness and flexural rigidity parameters respectively and are derived as:

$$C = \frac{Eh}{(1 - \mu^2)} \quad ; \quad D = \frac{Eh^3}{12(1 - \mu^2)}$$

The terms, E and μ represent Young's modulus of elasticity and the Poisson's ratio respectively. The in-plane equilibrium equations in Eq. (3-26) can be simultaneously satisfied such that a simpler set of equations are obtained by introducing an Airy stress function (Φ) as follows:

$$\sigma_x = \frac{\partial^2 \Phi}{\partial x^2} \quad \sigma_y = \frac{\partial^2 \Phi}{\partial y^2} \quad \tau_{xy} = \frac{\partial^2 \Phi}{\partial x \partial y} \quad (3-28)$$

By substituting the moment constitutive expressions in Eq. (3-27) into the out-of-plane equilibrium equation in Eq. (3-26), and regrouping the compatibility equations in Eq. (3-26) and the stress constitutive equations in Eq. (3-27) according to the stress functions in Eq. (3-28), the governing equations for a circular cylindrical shell are realized thus:

$$\begin{aligned} \frac{D}{h} \nabla^2 \nabla^2 w - \frac{\partial^2 w}{\partial x^2} \frac{\partial^2 \Phi}{\partial y^2} + 2 \frac{\partial^2 w}{\partial x \partial y} \frac{\partial^2 \Phi}{\partial x \partial y} - \frac{\partial^2 \Phi}{\partial x^2} \left(\frac{\partial^2 w}{\partial y^2} - \frac{1}{R} \right) - \frac{p}{h} &= 0 \\ \frac{1}{E} \nabla^2 \nabla^2 \Phi - \left(\frac{\partial^2 w}{\partial x \partial y} \right)^2 + \frac{\partial^2 w}{\partial x^2} \frac{\partial^2 w}{\partial y^2} - \frac{1}{R} \frac{\partial^2 w}{\partial x^2} &= 0 \end{aligned} \quad (3-29)$$

where,

$$\nabla^2 = \frac{\partial^2}{\partial x^2} + \frac{\partial^2}{\partial y^2} \quad ; \quad \nabla^2 \nabla^2 = \frac{\partial^4}{\partial x^4} + 2 \frac{\partial^4}{\partial x^2 \partial y^2} + \frac{\partial^4}{\partial y^4}$$

The derived form of the governing equations makes it possible for the exact solutions of the flexural displacement, w , and the stress function, Φ , to be obtained by simply solving the two equations in Eq. (3-29) simultaneously. Xue [13] however pointed out that, in practice, such mathematical derivations prove to be complicated and sometimes infeasible hence approximate methods are often employed to obtain required solutions.

Applying the governing equations outlined in Eq. (3-29), the analytical solutions for the special case of a cylindrical shell subjected to a uniform compressive axial load, P , and zero internal or external pressure can be obtained by neglecting end effects and applying the following assumptions for the initial stresses and initial deformation in the pre-buckling state [9,14]:

$$N_{x0} = \sigma_{x0} h = \frac{P}{2\pi R}, \quad N_{y0} = \sigma_{y0} h = 0, \quad N_{xy0} = \tau_{xy0} h = 0, \quad w_0 = \text{constant}$$

yielding,

$$D\nabla^8 w + \frac{Eh}{R^2} \frac{\partial^4 w}{\partial x^4} + \frac{P}{2\pi R} \nabla^4 \left(\frac{\partial^2 w}{\partial x^2} \right) = 0 \quad (3-30)$$

The unknown deflection is represented by a set of functions, each of which satisfies the boundary conditions. Thus, for simply-supported conditions, the solution to the differential equation in Eq. (3-30) assumes the form:

$$w = \delta_{mn} \cdot \sin\left(\frac{m\pi x}{L}\right) \cdot \sin\left(\frac{ny}{R}\right) \quad (3-31)$$

where δ_{mn} is the buckling amplitude, and the number of axial and circumferential half-waves are represented by m and n respectively. Substituting the deflection function in Eq. (3-31) into the governing equation in Eq. (3-30) yields:

$$\left[\frac{D}{R^2} (\bar{m}^2 + n^2)^4 + \bar{m}^4 (1 - \mu^2) C - \frac{P}{2\pi R} \bar{m}^2 (\bar{m}^2 + n^2)^2 \right] \frac{\delta_{mn}}{R^6} \sin\left(\frac{\bar{m}x}{R}\right) \sin\left(\frac{ny}{R}\right) = 0 \quad (3-32)$$

where the dimensionless buckling number, $\bar{m} = \frac{m\pi R}{L}$. The critical buckling membrane force can be obtained by rearranging Eq. (3-32) thus:

$$N_{cr} = \frac{P_{cr}}{2\pi R} = \frac{D}{R^2} \frac{(\bar{m}^2 + n^2)^2}{\bar{m}^2} + (1 - \mu^2) C \frac{\bar{m}^2}{(\bar{m}^2 + n^2)^2} \quad (3-33)$$

By introducing the dimensionless parameter χ where,

$$\chi_{mn} = \frac{(\bar{m}^2 + n^2)^2}{\bar{m}^2},$$

and treating \bar{m} and n as continuous variables an optimum value of the dimensionless parameter, χ_{opt} , can be obtained directly by analytical minimization of the critical buckling membrane force in Eq. (3-33) as:

$$\frac{dN_{cr}}{d\chi_{mn}} = \frac{D}{R^2} - (1 - \mu^2) C \frac{1}{\chi_{mn}^2} = 0 \quad (3-34)$$

Hence:

$$\chi_{opt} = \sqrt{\frac{(1 - \mu^2)CR^2}{D}} = \frac{R}{h}\sqrt{12(1 - \mu^2)} \quad (3-35)$$

By introducing χ_{opt} into the equation of for the critical buckling membrane force in Eq. (3-33), the classical solution for the critical buckling stress of a simply-supported cylindrical shell subjected to uniform axial compression is derived as:

$$\sigma_{cr} = \frac{E}{\sqrt{3(1 - \mu^2)}} \frac{h}{R} \quad (3-36)$$

3.4 Considering Plasticity and Anisotropy in Axially-compressed Cylinders: A Brief Overview

For a series of systematic experiments conducted to study the axial buckling and collapse of steel tubes, Kyriakides et al. [15] considered the effect of plastic anisotropy on the critical buckling stress (σ_c), the associated bifurcation strain (ε_c), and associated half-wavelength of the buckling mode (λ_c). To derive the analytical formulations for the critical states, they adopted Sanders' [16] shell kinematics based on the assumptions of small strains and moderately small rotations and represented the anisotropy of the material using Hill's [17] anisotropic yield function which, for a plane stress, is given as:

$$\sigma_e = \left[\sigma_x^2 - \left(1 + \frac{1}{S_\theta^2} - \frac{1}{S_r^2} \right) \sigma_x \sigma_\theta + \frac{1}{S_\theta^2} \sigma_\theta^2 + \frac{1}{S_{x\theta}^2} \sigma_{x\theta}^2 \right]^{\frac{1}{2}} \quad (3-37)$$

where σ_x is the applied axial stress and σ_θ represents the resultant circumferential stress due to applied internal pressure, derived as: $\sigma_\theta = pR/h$. The yield stress ratios ($S_\theta, S_r, S_{x\theta}$) are derived as:

$$S_\theta = \sigma_{0\theta}/\sigma_0 \quad ; \quad S_r = \sigma_{0r}/\sigma_0 \quad ; \quad S_{x\theta} = \sigma_{0x\theta}/\sigma_0$$

The yield stress parameters $(\sigma_0, \sigma_{0r}, \sigma_{0\theta})$ represent, respectively, the yield stresses of the material according to the axial, radial and circumferential orientations of the cylindrical shell structure while $\sigma_{0x\theta}$ is the yield stress under pure shear.

The anisotropic yield function yields the following work compatible measure of the equivalent strain increment:

$$d\varepsilon_e^p = \sqrt{2} \left[\frac{\frac{1}{S_\theta^2} (d\varepsilon_x^p)^2 + (d\varepsilon_\theta^p)^2 + \left(1 + \frac{1}{S_\theta^2} - \frac{1}{S_r^2}\right) d\varepsilon_x^p d\varepsilon_\theta^p}{\frac{1}{S_\theta^2} + \frac{1}{S_r^2} - \frac{1}{2} - \frac{1}{2} \left(\frac{1}{S_\theta^2} - \frac{1}{S_r^2}\right)^2} \right]^2 \quad (3-38)$$

where $d\varepsilon_x^p$ and $d\varepsilon_\theta^p$ represent the resultant axial and circumferential strain increments respectively.

The bifurcation stress of a cylindrical shell subjected to uniform axial compression in the plastic range is associated with an axisymmetric mode of deformation hence, depending on the plasticity model adopted, the critical buckling stress (σ_c) and the associated half-wavelength of the buckling mode (λ_c) can be obtained as [18 - 20]:

$$\sigma_c = \frac{h}{R} \left(\frac{C_{11}C_{22} - C_{12}^2}{3} \right)^{\frac{1}{2}} \quad \lambda_c = (\pi^2 R h)^{\frac{1}{2}} \left(\frac{C_{11}^2}{12(C_{11}C_{22} - C_{12}^2)} \right)^{\frac{1}{4}} \quad (3-39)$$

where $C_{\alpha\beta}$ are the instantaneous material moduli at bifurcation, derived as the respective components of the inverse of the generalized matrix of constitutive equations for the incremental strain-stress relationships. Naturally, with applicable modifications of the constitutive matrix according to the flow and deformation theories of plasticity, the traditional form of the constitutive equations for isotropic J_2 flow and deformation theory are obtained when the yield stress ratios $S_\theta = S_r = 1$ [15]. The bifurcation strain (ε_c) is calculated incrementally with respect to the critical buckling stress (σ_c) and the internal pressure (p), following the stress history [21].

3.5 Conclusions

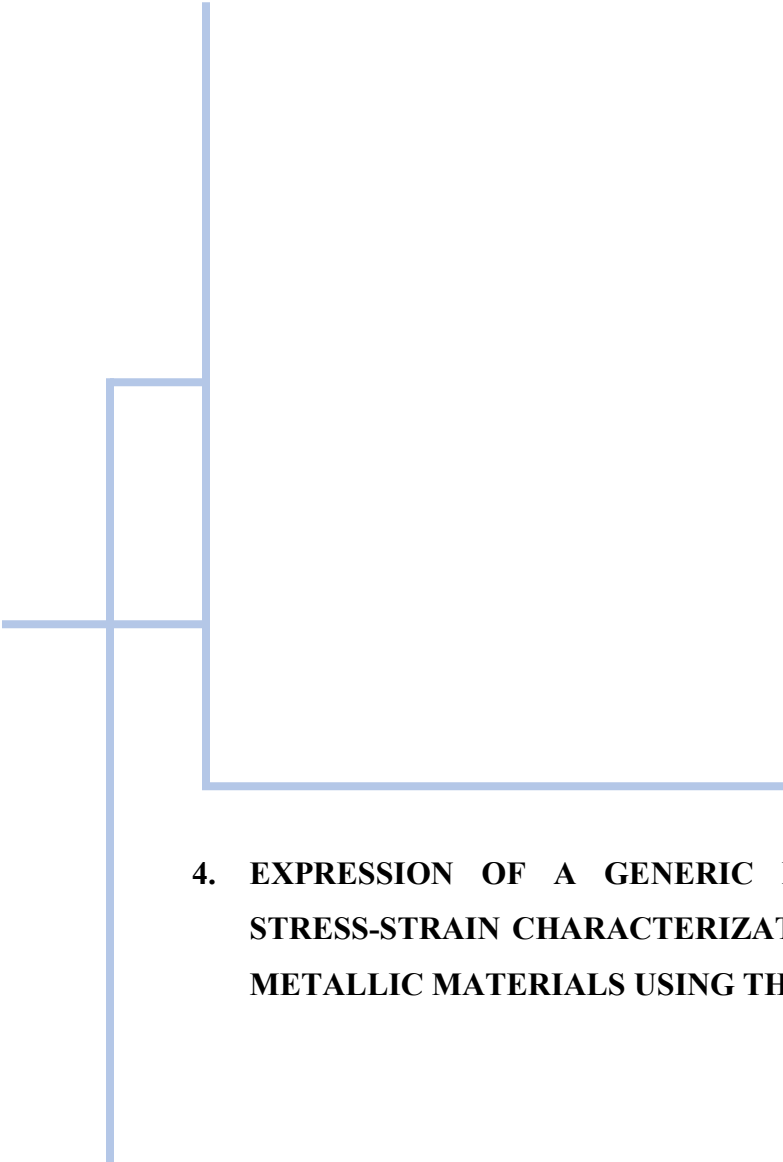
Derivations of the simplest theoretical formulas have been presented for the critical buckling stress of flat plates and cylinders under pure axial compression. The analytical formulations are derived from first principles, based on the fundamental laws of mechanics, and thus are unable to predict the buckling response beyond the elastic limit of the material. Such classical theories are also not able to account for anisotropic material behavior and geometric imperfections. A brief overview of research efforts which have successfully tackled the material-related limitations of the classical theories for axially-compressed cylinders is presented in [Section 2.4](#). However, the evaluation procedure is inherently complex and requires numerical computation, and is also constrained in application to other loading conditions. Computerized numerical evaluation, based on finite element discretization methodology, is therefore adopted for shell buckling analysis in this study

3.6 References

- [1] G.H. Bryan, On the Stability of a Plane Plate under Thrusts in its own Plane, with Applications to the “Buckling” of the Sides of a Ship, Proc. London Math. Soc. s1-22 (1890) 54–67. doi:10.1112/plms/s1-22.1.54.
- [2] A.E.H. Love, The Small Free Vibrations and Deformation of a Thin Elastic Shell, Philos. Trans. R. Soc. London, A Math. Phys. Eng. Sci. 179 (1888) 491–546. doi:10.1098/rsta.1888.0016.
- [3] G.Z. Voyiadjis, P. Woelke, Elasto-Plastic and Damage Analysis of Plates and Shells, Springer Science & Business Media, Berlin, Heidelberg, 2008. doi:10.1007/978-3-540-79351-9.
- [4] T. Von Kármán, Festigkeitsprobleme im Maschinenbau, in: Encycl. Der Math. Wissenschaften IV, Teubner, 1910: pp. 348–352.
- [5] J.K. Paik, A.K. Thayamballi, Ultimate limit state design of steel plated structures, John Wiley & Sons, Inc., Chichester, England, 2003.
- [6] J.R. Vinson, The Behavior of Thin-Walled Structures: Beams, Plates, and Shells, Springer Netherlands, Dordrecht, 1988. doi:10.1007/978-94-009-2774-2.

- [7] S.P. Timoshenko, J.M. Gere, *Theory of Elastic Stability*, McGraw-Hill Book Company, New York, 1961.
- [8] P.S. Bulson, *Theory of flat plates*, Chatto and Windus, London, 1970.
- [9] J. Singer, J. Arbocz, T. Weller, *Buckling Experiments, Volume 1: Basic Concepts, Columns, Beams and Plates*, John Wiley & Sons, New York, 1998.
- [10] L.H. Donnell, *Stability of thin-walled tubes under torsion*, NACA Report No. 479, Washington D.C., 1933.
- [11] L.A. Harris, *The Stability of Thin-Walled Unstiffened Circular Cylinders Under Axial Compression Including the Effects of Internal Pressure*, *J. Aeronaut. Sci.* 24 (1957) 587–596. doi:10.2514/8.3911.
- [12] L.S.D. Morley, *An improvement on Donnell's approximation for thin-walled circular cylinders*, *Q. J. Mech. Appl. Math.* 12 (1959) 89–99. doi:10.1093/qjmam/12.1.89.
- [13] J. Xue, *Local buckling in infinitely, long cylindrical shells subjected uniform external pressure*, *Thin-Walled Struct.* 53 (2012) 211–216. doi:10.1016/J.TWS.2012.01.008.
- [14] Yong Bai, Wei-Liang Jin, *Ultimate Strength of Cylindrical Shells*, in: *Mar. Struct. Des.*, 2nd ed., Elsevier, Oxford, United Kingdom, 2016: pp. 353–365. doi:https://doi.org/10.1016/B978-0-08-099997-5.00018-6.
- [15] S. Kyriakides, F.C. Bardi, J.A. Paquette, *Wrinkling of Circular Tubes Under Axial Compression: Effect of Anisotropy*, *J. Appl. Mech.* 72 (2005) 301–305. doi:10.1115/1.1839590.
- [16] J.L. Sanders, *Nonlinear theories for thin shells*, *Q. Appl. Math.* 21 (1963) 21–36. doi:10.1090/qam/147023.
- [17] R. Hill, *A general theory of uniqueness and stability in elastic-plastic solids*, *J. Mech. Phys. Solids.* 6 (1958) 236–249. doi:10.1016/0022-5096(58)90029-2.
- [18] P.P. Bijlaard, *Theory and Tests on the Plastic Stability of Plates and Shells*, *J. Aeronaut. Sci.* 16 (1949) 529–541. doi:10.2514/8.11851.
- [19] S.C. Batterman, *Plastic buckling of axially compressed cylindrical shells*, *AIAA J.* 3 (1965) 316–325. doi:10.2514/3.2848.
- [20] S.C. Batterman, L.H.N. Lee, *Effect of modes on plastic buckling of compressed cylindrical shells.*, *AIAA J.* 4 (1966) 2255–2257. doi:10.2514/3.3900.

[21] J.A. Paquette, S. Kyriakides, Plastic buckling of tubes under axial compression and internal pressure, *Int. J. Mech. Sci.* 48 (2006) 855–867. doi:10.1016/J.IJMECSCI.2006.03.003.



4. EXPRESSION OF A GENERIC FULL-RANGE MATERIAL MODEL FOR STRESS-STRAIN CHARACTERIZATION OF PIPELINE STEELS AND OTHER METALLIC MATERIALS USING THE PRODUCT-LOG (OMEGA) FUNCTION

This chapter is derived from the combination of two published conference proceedings:

- (1) O. Ndubuaku, M. Martens, J.J.R. Cheng, S. Adeeb, Expression of a Generic Full-Range True Stress-True Strain Model for Pipeline Steels Using the Product-Log (Omega) Function, in: Vol. 6B Mater. Fabr., ASME, 2017: p. V06BT06A050. doi:10.1115/PVP2017-65236.
- (2) O. Ndubuaku, M. Martens, R. Cheng, A. Ahmed, S. Adeeb, A Novel Approach for True Stress-True Strain Material Characterization of Metallic Materials Using the Product-Log (Omega) Function, in: 6th Int. Conf. Eng. Mech. Mater., CSCE, May 31 - June 3, Vancouver, B.C., Canada, 2017.

4.1 Abstract

Steel pipelines are subjected to a variety of complex, and sometimes difficult to predict, loading schemes during the fabrication, installation and operation phases of their lifecycles. Consequently, the mechanical behavior of steel pipelines is not only influenced by the steel grade but also by the loading history of the pipe segments. Due to the resultant intricacies of the nonlinear load-deformation behavior of pipelines, adequate numerical analysis techniques are usually required for simulation of pipelines under different loading schemes. The validity of such numerical simulations is largely influenced by the accuracy of the true stress-true strain characterization of the pipeline steels. However, existing stress-strain mathematical expressions, developed for the characterization of metallic materials over the full range of the stress-strain relationship, have been observed to either lose predictive accuracy beyond a limited strain range or, for the more accurate full-range models, are cumbersome due to their requirement of a large number of constituent parameters. This paper presents a relatively accurate and simple true stress-true strain model which is capable of accurately predicting the stress-strain behavior of pipeline steels over the full range of strains. The proposed stress-strain model is characteristically unlike existing stress-strain models as it is essentially defined by a Product-Log function using two proposed parameters, and is capable of capturing a reasonable approximation of the yield plateau in the stress-strain curve. To validate the proposed model, curve-fitting techniques are employed for comparison to experimental stress-strain data obtained from cryogenic tensile tests of three different metallic materials; 300 series austenitic stainless steel (AISI 304L), 5000 (Al-Mg) series aluminum alloy (AA5083), and nickel steel alloy (Invar steel-FeNi36). Curve-fitting techniques are also employed for comparison to experimental data of the stress-strain behavior of different pipeline steel grades (X52 – X100). Using the proposed model, excellent approximations of the nonlinear load-deformation behavior of the tested specimens are observed over the full range of the true stress-true strain relationship. Furthermore, the applicability of the proposed model is validated by means of a proposed parametric procedure for predicting the ultimate compressive strength of shell elements using representative numerical plate models subjected to uniform axial compression.

Nomenclature

$\varepsilon_{0.2}$	plastic strain corresponding to the offset yield strength
ε	true strain
ε_p	strain at the intersection of a yielding platform and initial strain-hardening portion
ε_{pl}	corresponding strain at proportionality limit of Ndubuaku model
$\varepsilon_{p,u}$	ultimate plastic strain
ε_R	Ndubuaku model strain ratio
ε_u	ultimate total strain
E	Young's modulus
E_o	initial elastic modulus
$E_{o,T}$	initial elastic modulus of temperature-altered stress-strain curve at the 0.2% proof stress
$E_{y,T}$	tangent modulus of temperature-altered stress-strain curve at the 0.2% proof stress
f_T	applied stress of temperature-altered stress-strain curve
f_{UT}	ultimate tensile stress of temperature-altered stress-strain curve
f_{YT}	0.2% proof stress of temperature-altered stress-strain curve
H_{NM}	Ndubuaku model heel constant
H_{RO}	Ramberg-Osgood model constant
K_{NM}	Ndubuaku model knee constant
m	second-stage strain-hardening exponent
m_T	second-stage strain-hardening exponent of temperature-altered stress-strain curve
n	strain-hardening exponent
n_T	strain-hardening exponent of temperature-altered stress-strain curve
n_{RO}	Ramberg-Osgood strain-hardening exponent
$\sigma_{0.01}$	0.01% proof stress
$\sigma_{0.2}$	0.2% proof stress
σ	true stress
σ_e	proportionality limit of Zhang and Alam model
σ_{pl}	proportionality limit of Ndubuaku model
σ_R	Ndubuaku model stress ratio
σ_u	ultimate tensile strength

σ_y	yield strength
ARB	Accumulative roll bonding
IA	Intercritical annealing
LNG	Liquefied natural gas
Q&P	Quenching and partitioning treatment
ROE	Ramberg-Osgood equation
SPD	Severe plastic deformation
TRIP	Transformation-Induced Plasticity

4.2 Introduction

Pipelines have become the most preferred means for transportation of hydrocarbons from natural reservoirs to processing plants, as well as for transportation of processed hydrocarbon fluids from processing plants to energy markets. Due to their excellent chemical and mechanical properties, metallic materials are commonly used for the construction of hydrocarbon pipelines. However, among the extensive variety of metallic materials that exist, steel provides a relative advantage of adequate mechanical reliability and economic feasibility.

Steel is a metallic alloy composed mainly of iron. Although various other elements such as manganese (Mn), silicon (Si), chromium (Cr), niobium (Nb) [formerly columbium (Cb)], molybdenum (Mo), vanadium (V), nickel (Ni), aluminum (Al), and copper (Cu) may also be included in, and affect the properties of, steel the carbon (C) content has the most significant effect on the properties of steel. The strength and hardness of steel increases as the carbon content increases but at the expense of the strength and ductility, which both decrease with an increase in the carbon content.

Steel materials used for the manufacture of pipelines are generally classified as different grades according to their mechanical properties. One of the most commonly used specifications which provides the standards for determination of the suitability of pipe for conveying gas, water, and oil in both the oil and natural gas industries is the API 5L Specification [1]. The specification covers seamless and welded steel pipelines and includes specifications for various pipe-end

configurations: plain-ends, threaded-ends, belled-ends, and pipe-ends prepared for special couplings.

Recent technological advancement and the ever-increasing world energy demand has resulted in the venture of the hydrocarbon industry into more remote oil fields thereby increasing the requirement for pipelines to traverse much longer distances and sustain significantly higher operating temperatures and pressures. The development of higher strength pipeline steel grades over the years has been necessitated and driven by the desire of the hydrocarbon industry for better installation feasibility (based on higher strength-to-weight considerations) and ultimately, lower overall cost of pipeline projects [2].

The capacity of pipelines to withstand the various modes and magnitudes of loading that are experienced during their operational lifecycle is typically assessed either by a stress-based criterion or a strain-based criterion. In considering the burst pressure capacity of pipelines, a stress-based criterion is typically employed as most pipeline design standards are essentially focused on limiting the pipe wall circumferential stress, caused by the operational internal pressure in the pipeline, to the specified minimum yield stress (SMYS) of the pipe material. On the other hand, pipelines may experience external overpressures when installed in ultra-deep subsea environments; in which case, the shell buckling characteristics of the pipe need to be considered in the design of such pipelines. Besides circumferentially-exerted compressive loads due to external overpressure in pipelines, shell-type buckling in pipelines may also be induced by longitudinally-exerted compressive loads; caused by large ground motion due to fault movements, landslides, permafrost melting and soil liquefaction [3–6]. Strain-based design criteria are typically employed in the design of pipelines against shell-type buckling and a number of research endeavors have resulted in various design equations for predicting the compressive strain capacity (CSC) of pipelines [7–13].

The mechanical behavior of metallic materials is generally characterized by a nonlinear stress-strain relationship typically obtained from the results of an axial tension coupon test carried out in a laboratory-controlled environment. Due to the nonlinearity associated with the load-deformation characteristics of metallic materials, an appropriate mathematical expression, comprising a number of defining constituent parameters, is usually employed for describing a reasonable approximation of the stress-strain relationship. With the modern-day existence of fast

and efficient computational capability, simulation of the mechanical behavior of materials used in the design and construction of civil engineering structures, and under subjection to several loading configurations, is easily achieved using a variety of numerical evaluation tools. To ensure the accuracy of computational simulations, it is however imperative that the constitutive equation used to describe the mechanical behavior of materials is robust and precise.

Stress-strain material characterization of pipe materials, as well as almost every other industrially-applied metallic material, is typically achieved using a mathematical expression which is able to capture the nonlinear relationship between the stress and strain values obtained from a typical uniaxial tensile coupon test. The Ramberg-Osgood equation (ROE), developed in 1943 [14], employs a simple power law approach which expresses the strain as a function of the stress and is governed by two material constants (the 0.2% proof stress $\sigma_{0.2}$ and the initial elastic modulus E_0) and one model constant (the strain-hardening exponent, n). The ROE has been widely-adopted for many civil engineering applications, however, several researchers have observed the ROE to lose predictive accuracy beyond a limited strain range; especially for materials which exhibit significant or non-gradual strain-hardening characteristics (e.g., high-strength steel) beyond the proportionality limit stress. In a bid to improve the predictive accuracy of the ROE, a number of modified stress-strain expressions have been subsequently put forward by several researchers. Most of the modified expressions are however designed to capture the tensile stress-strain behavior of metallic materials at room temperature [14–19].

It is generally desirable that the mathematical expressions used to describe the stress-strain behavior of metallic materials are versatile enough such that the model parameters can be easily adjusted to define the changes in the stress-strain curve due to temperature- and strain rate-induced microstructural alterations. However, there are some important limitations associated with existing stress-strain models: the simpler models lack the desired robustness and accuracy for defining a wide range of stress-strain behaviors, and the applicability of more advanced models is hampered by the large number of constituent parameters required for improved accuracy.

This research is therefore focused on presenting a newly-developed mathematical expression which possesses the much-desired simplicity similar to the ROE, and additionally offers a significant improvement of the predictive accuracy of the stress-strain approximation over the

full-range of strains; even in materials which exhibit a well-defined yield plateau. The novel stress-strain curve model is also capable of providing an accurate approximation of the stress-strain behavior of metallic materials at different temperatures and strain rates, as demonstrated in this paper.

4.3 Effect of Microstructural Properties on Mechanical Response

With the development and application of various microstructure-transformation techniques, attempts have been made over the years to improve the ductility, strength properties, and strength-to-weight ratio characteristics of metallic materials. The chemical composition and thermo-mechanical processing route, which are the most influential factors of the resulting microstructure of metals, are invariably considered in the material selection process; which involves the determination of the appropriate combination of desired mechanical properties (strength, hardness, toughness, ductility, fatigue resistance, etc.) and non-mechanical properties (formability, wear resistance, corrosion resistance, machinability, weldability, etc.) for each specific civil engineering application [20].

Steels and cast irons are the most commonly used materials for the design and construction of civil engineering structures and their microstructural constituents (austenite, bainite, cementite, ferrite, martensite, and pearlite), as well as the multiphase character of their microstructure can be systematically manipulated or altered to yield desired performances for various structural applications [21]. According to Zhao et al. [22], the Transformation Induced Plasticity (TRIP) concept has been used in automotive applications for many years and has recently begun to receive much attention due to excellent improvements obtained in the outstanding combination of ductility and strength of steels. TRIP techniques include processes such as intercritical annealing (IA), severe plastic deformation (SPD), quenching and partitioning treatment (Q&P), accumulative roll bonding (ARB), bimodal grain size distribution, etc. [23–28].

A good illustration of the effect of thermo-mechanical processes on the mechanical behavior of metallic materials is given by Curtze et al. [29] in their study on the dependence of the mechanical behavior of Dual Phase (DP) steels and TRIP steels on temperature and strain rate: while both DP and TRIP steels comprise multiphase microstructures, DP steels are obtained by

intercritical annealing followed by quenching to room temperature in order to transform the ferrite/austenitic microstructure to martensite, while TRIP steels are obtained by inducing an isothermal hold below the bainite start temperature during cooling from the intercritical annealing temperature. Consequently, DP steels typically possess a two-phase ferritic-martensitic microstructure whereas the microstructure of TRIP steels is characterized by an embedment of bainite, martensite, and retained austenite in a continuous ferrite matrix. They explain that the soft ferritic phase associated with DP and TRIP steels is the main factor responsible for their characteristic low yield strengths whereas the hard martensite and bainite constituents dispersed in the ferrite matrix are responsible for high ultimate strength and strain-hardenability.

Thermo-mechanical loading in the operational phase of a material's lifecycle also affects the deformability of polycrystalline materials, such as metals and metallic alloys, and is a direct consequence of microstructural gliding dislocation and grain boundary characteristics. Therefore, under subsection to loading, the mechanical behavior of metallic materials is significantly affected by temperature and strain rate: the effect of thermal energy makes it easier for gliding dislocations to occur thereby decreasing the strength with increasing temperature and, on the other hand, development of various interfacial slip-resisting mechanisms causes an increase of the strength with increasing strain rate [21,30].

After exposure to either cryogenic or elevated temperatures, significant alterations occur to the mechanical behavior of metallic materials and past research has indicated that the behavior of structures is usually very complex either when using precooled or preheated materials or when using materials in environments with temperatures significantly above or below ambient temperature. The load-deformation characteristics of structural elements and components have been determined to be highly sensitive to the stress-condition relative to the affected mechanical properties. A few researches have been carried out to study the effects of high and low temperatures on the stress-strain behavior of various metallic materials and a number of constitutive stress-strain equations have been developed for structural analysis and design purposes [31–35].

4.4 Stress-strain Material Characterization

The mechanical behavior of steel is generally represented by a stress-strain curve; which is typically characterized by a nonlinear relationship between the so-called “nominal” (or engineering) stress and strain values obtained from the results of a standard uniaxial tension coupon test of a material specimen.

The nominal stress values are established using the original cross-section area of the specimen while the nominal strain values are determined as the average strain over the originally specified gauge length. The nominal (or so-called “engineering”) stress and strain values obtained directly from the coupon test experiments do not portray a realistic representation of the load-deformation process, especially at high levels of axial deformation, due to non-consideration of the simultaneous changes in geometric dimensions alongside axial deformation and development of non-uniform stress-strain distributions [36]. For practical applications, it is therefore preferable to determine the true stress-true strain relationship from the tensile test based on instantaneous values of the geometric dimensions of the material specimen and gauge length [37,38].

Stress-strain curves are not only indicative of the grade and mechanical behavior of the steel used in the manufacture of the tested specimen but they are also significantly influenced by the method of manufacture or fabrication of the parent structure from which the specimen is obtained. The metal grade generally determines the yield strength and the ultimate tensile strength of the material, while the shape of the stress-strain curve is more significantly affected by the method of manufacture and/or fabrication conditions. The stress-strain curve of some materials, such as mild or low-strength carbon steel, is characterised by a linear elastic portion, a well-defined yield plateau, and a subsequent strain-hardening region, while some other materials, such as stainless steels and high-strength steels, generally exhibit a “round-house” stress-strain curve shape without any distinct yield plateau [11].

Besides the strength properties (yield strength and ultimate tensile strength), stress-strain curves are also commonly used as a basis for the determination of other properties, such the elastic deformation properties (Young’s modulus), ductility properties (elongation and reduction of area) and other characteristics (strain-hardening and necking) [39].

A sketch of the typical engineering stress-strain curve of a metallic material, superimposed with a true stress-true strain curve, is presented in Figure 4-1. A comparison of the engineering stress-strain curve (bold line) and the true stress-true strain curve indicates that they both coincide up to the point of yielding, and become substantially divergent beyond the point of yielding. Also, there exists a characteristic decrease in the slope of the engineering stress-strain curve once the ultimate tensile strength of the material is attained whereas the slope of the true stress-true strain curve continues to increase up to the point of fracture. Since the engineering stress and engineering strain data is directly obtained from experimental force and deformation data, the engineering stress-strain data bears a close resemblance to the force-deformation curve; the only difference being the range and magnitude of the axis dimensions [40].

The validity of the true stress-true strain material characterization of pipeline steel only exists prior to the onset of necking (when deformation is isochoric). At the onset of necking, a complex tri-axial stress state develops in the specimen and the resultant radial stresses and hoop stresses increase the longitudinal stress required to cause the plastic flow. Hence the true stress values, which are calculated based on the minimum cross-sectional area at the neck, become invalid [36].

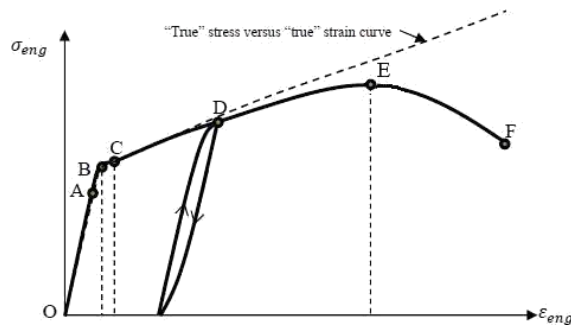


Figure 4-1: Typical stress-strain curve.

As previously stated, accurate numerical modeling of the mechanical behavior of various metallic materials requires the implementation of a suitable analytical model for true stress-true strain material characterization. The proposed true stress-true strain model in this paper offers the advantage of a more simplified, and yet accurate, stress-strain formulation compared to existing

models. However, due to analytical complications and practical uncertainties, the proposed model does not consider the stress-strain behavior beyond the strain-hardening region.

4.5 Review of Existing Stress-strain Equations

The power-law approach provides a feasible option for mathematical representation of the nonlinearity associated with the stress-strain behavior of metallic materials hence many of the earliest stress-strain curve equations, as well as the subsequent modifications, are essentially based on an expression of the stress as a power function of the strain or vice versa [14,41,42].

The Ramberg-Osgood equation was originally formulated for approximation of the stress-strain behavior of aluminum alloys and was subsequently extended for other materials such as stainless-steel alloys [43]. Most of the subsequent stress-strain model developments and modifications are similarly based on the power law form of the ROE, which is essentially described by the expression:

$$\varepsilon = \frac{\sigma}{E_o} + K \left(\frac{\sigma}{E_o} \right)^n \quad (4-1)$$

where the true stress (σ) and true strain (ε) relationship is described based on the initial elastic modulus, E_o , and two model constants, K and n .

Hill [44] proposed the earliest modification of the ROE by describing the stress-strain relationship using three material parameters (E_o , $\sigma_{0.2}$, and $\varepsilon_{0.2}$) and only one model constant, n_{RO} :

$$\varepsilon = \frac{\sigma}{E_o} + \varepsilon_{0.2} \left(\frac{\sigma}{\sigma_{0.2}} \right)^{n_{RO}} \quad (4-2)$$

The model constant, n_{RO} , represents the strain-hardening exponent, which is sometimes referred to as the Ramberg-Osgood ‘knee’ parameter; as its value controls the sharpness or convexity of the stress-strain curve. The parameter, $\sigma_{0.2}$, represents the 0.2% proof stress. $\varepsilon_{0.2}$, is generally

determined as the value of the plastic strain corresponding to the *offset yield strength*, $\sigma_{0.2}$ (taken as 0.002), and E_o is the initial Young's modulus.

The strain-hardening exponent may be derived from the 0.2% and 0.01% proof stresses ($\sigma_{0.2}$ and $\sigma_{0.01}$ respectively) as follows:

$$n_{RO} = \frac{\ln(20)}{\ln(\sigma_{0.2}/\sigma_{0.01})} \quad (4-3)$$

As previously indicated, a considerable amount of research studies over the years have observed that the ROE tends to lose accuracy and overestimate the stress corresponding to values of strain higher than approximately 0.002. A series of notable attempts to overcome the setback in the ROE are briefly presented.

A slightly modified version of the ROE is expressed by API 579-1/ASME FFS-1 [45] as follows:

$$\varepsilon = \frac{\sigma}{E_o} + \left(\frac{\sigma}{H_{RO}}\right)^{\frac{1}{n_{RO}}} \quad (4-4)$$

Where multiple data points for a stress-strain curve are provided, the constants (H_{RO} and n_{RO}) are derived using curve-fitting regression techniques otherwise, where only the yield strength (σ_y) and ultimate tensile strength (σ_u) are known, the constants are obtained (for the range $0.02 \leq \sigma_y/\sigma_u \leq 1.0$) as follows:

$$n_{RO} = \frac{1 + 1.3495 \left(\frac{\sigma_y}{\sigma_u}\right) - 5.3117 \left(\frac{\sigma_y}{\sigma_u}\right)^2 + 2.9643 \left(\frac{\sigma_y}{\sigma_u}\right)^3}{1.1249 + 11.0097 \left(\frac{\sigma_y}{\sigma_u}\right) - 11.7464 \left(\frac{\sigma_y}{\sigma_u}\right)^2} \quad (4-5)$$

$$H_{RO} = \frac{\sigma_u \exp[n_{RO}]}{n_{RO}^{n_{RO}}} \quad (4-6)$$

Macdonald *et al.* [16] carried out extensive tensile testing of stainless-steel specimens and proposed a modification of the ROE such that the strain-hardening exponent is described as a

function of the stress; in which case, the value of the strain-hardening exponent is increased for higher values of strain.

Olsson [46] opined that the stresses beyond the 2% proof stress, $\sigma_{0.2}$, can be approximated as a straight line on the stress-strain curve hence, the ROE can be applied for estimation of stresses corresponding to the range of strains less than the 2% total strain, $\varepsilon_{t,2.0}$.

Mirambell and Real [17] determined that the accuracy of the original form of the ROE is only applicable up to the 0.2% proof stress, beyond which a modified form of the ROE can be applied by linear transformation of the stress-strain reference point. The modified expression for the portion of the stress-strain curve beyond the 0.2% proof stress, was further simplified by Rasmussen [43] such that a lesser number of parameters are required to define the stress-strain curve as follows:

$$\varepsilon = \frac{\sigma - \sigma_{0.2}}{E_{0.2}} + \varepsilon_u \left(\frac{\sigma - \sigma_{0.2}}{\sigma_u - \sigma_{0.2}} \right)^m + \varepsilon_{0.2} \quad \text{for } \sigma_{0.2} < \sigma \leq \sigma_u \quad (4-7)$$

where $E_{0.2}$ represents the tangent modulus of the stress-strain curve at $\sigma_{0.2}$.

Furthermore, equations for the second-stage strain-hardening exponent, m , the ultimate strain, ε_u , and the ultimate strength, σ_u , were developed using the three basic ROE parameters:

$$m = 1 + 3.5 \frac{\sigma_{0.2}}{\sigma_u} \quad (4-8)$$

$$\varepsilon_u = 1 - \frac{\sigma_{0.2}}{\sigma_u} \quad (4-9)$$

$$\frac{\sigma_{0.2}}{\sigma_u} = \begin{cases} 0.2 + 185 \frac{\sigma_{0.2}}{E_o} & \left(\begin{array}{l} \text{for austenitic and} \\ \text{duplex alloys} \end{array} \right) \\ \frac{0.2 + 185 \frac{\sigma_{0.2}}{E_o}}{1 - 0.0375(n_{RO} - 5)} & \left(\begin{array}{l} \text{for all stainless} \\ \text{steel alloys} \end{array} \right) \end{cases} \quad (4-10)$$

In an attempt to further improve the accuracy of the ROE and extend its applicability to the compressive stress-strain behavior of cold-formed stainless steel sections, Gardner and Nethercot [19] proposed a modification to the Mirambell-Real and Rasmussen models such that the

ultimate stress, σ_u , and the ultimate strain, ε_u , are both replaced by the proof stress corresponding to a 1% plastic strain, $\sigma_{1.0}$ and the total strain at the 1% proof stress, $\varepsilon_{t,1.0}$ respectively.

More complex multi-stage extensions of the ROE have also been proposed by a number of researchers. Quach [47] proposed a three-stage stress-strain model which was essentially derived as a combination of: (1) the original form of the ROE (for stresses and strains below the 0.2% proof stress), (2) a modified form of Gardner and Nethercot's formulation (for stresses and strains between the 0.2% proof stress and the 2.0% proof stress) and, (3) the Olsson's straight-line approximation (for stresses and strains between the 2.0% proof stress and the ultimate stress). Mirambell and Real's concept was employed by Hradil *et al.* [48] to formulate a multistage stress-strain model, whereby the stress-strain curve is divided into a desired number of segments and the approximation of the stress-strain behavior for each segment is determined using the initial tangent modulus of elasticity (E_i), stress (σ_i), plastic strain ($\varepsilon_{p,i}$), and the nonlinearity coefficient (n_i) for each segment.

One of the most recent and versatile stress-strain models, developed by Zhang and Alam [49], was specifically proposed to describe the stress-strain behavior of steel sheet materials that exhibit a relatively long yield plateau. The Zhang-Alam model is an expanded Ramberg-Osgood model expressed as:

$$\varepsilon = \begin{cases} \frac{\sigma}{E} & 0 \leq \sigma \leq \sigma_e \\ \frac{\sigma}{E} + k_1 \left(\frac{\sigma}{E}\right)^{n_1} & \sigma_e < \sigma \leq f_y \\ \varepsilon_y + \frac{(\sigma - f_y)}{\alpha E} & f_y < \sigma \leq \sigma_p \\ \frac{\sigma}{E} + k_2 \left(\frac{\sigma}{E}\right)^{n_2} & \sigma > \sigma_p \end{cases} \quad (4-11)$$

where σ , ε , and E represent the true stress, true strain, and Young's modulus respectively. f_y represents the lower yield strength and ε_y represents the strain at f_y . σ_e is the proportional limit; described by the point where the relative difference between the R-O stress and the linear stress is larger than 0% but less than or equal to 0.5%. α is a coefficient multiplied with E which

represents the slope of the yielding platform. ε_p represents the strain at the intersection of a yielding platform and initial strain-hardening portion. n_1 , n_2 , k_1 , and k_2 are the model constants derived by equations described in Zhang and Alam [49].

The two-stage approach proposed by Mirambell and Real [17] and Rasmussen [43] was extended by Chen and Young [32] to the stress-strain characterization of stainless-steel types EN 1.4462 (Duplex) and EN 1.4301 (AISI 304) at temperatures ranging from 20⁰C to 1000⁰C:

$$\varepsilon_T = \begin{cases} \frac{f_T}{E_{0,T}} + 0.002 \left(\frac{f_T}{f_{y,T}} \right)^{n_T} & \text{for } f_T \leq f_{y,T} \\ \frac{f_T - f_{y,T}}{E_{y,T}} + \varepsilon_{u,T} \left(\frac{f_T - f_{y,T}}{f_{u,T} - f_{y,T}} \right)^{m_T} + \varepsilon_{y,T} & \text{for } f_T > f_{y,T} \end{cases} \quad (4-12)$$

where f_T , $f_{u,T}$, and $f_{y,T}$ represent the stress, the ultimate stress, and the 0.2% proof stress at the temperature T (in ⁰ C) respectively. ε_T , $\varepsilon_{u,T}$, and $\varepsilon_{y,T}$ represent the strain, the strain corresponding to ultimate stress, and the strain corresponding to proof stress at the temperature T (in ⁰ C) respectively. $E_{0,T}$ is the initial elastic modulus at the respective temperature T (in ⁰ C) and the tangent modulus of the temperature-altered stress-strain curve at the 0.2% proof stress, $E_{y,T}$ is derived as:

$$E_{y,T} = \frac{E_{0,T}}{1 + 0.002 n_T \frac{E_{0,T}}{f_{y,T}}} \quad (4-13)$$

and the first-stage strain-hardening exponent, n_T and the second-stage strain-hardening exponent, m_T are both derived as:

$$n_T = 6 + 0.2\sqrt{T} \quad (4-14)$$

$$m_T = \begin{cases} 5.6 - \frac{T}{200} & (\text{for stainless steel type EN 1.4462}) \\ 2.3 - \frac{T}{200} & (\text{for stainless steel type EN 1.4462}) \end{cases} \quad (4-15)$$

Chen and Young [32] determined that the temperature-altered material properties (the 0.2% proof stress, $f_{y,T}$; the initial elastic modulus, $E_{0,T}$; the ultimate stress, $f_{u,T}$; and the ultimate strain, $\varepsilon_{u,T}$) can be expressed as the following function of the temperature:

$$\frac{P_T}{P_N} = A_T - \frac{(T - B_T)^{D_T}}{C_T} \quad (4-16)$$

where P_N and P_T represent the value of any of the four above-listed material properties at the normal room temperature and the temperature-altered value respectively, and the coefficients A_T , B_T , C_T , and D_T are empirically obtained from the results of the experiment.

Based on the constitutive model (BP model) developed by Bodner and Partom [50] for representing time-dependent phenomena such as viscoplasticity and inelastic creep behavior, Park et al. [33] studied the effect of temperature and strain rate on - and proposed a unified constitutive equation for - the nonlinear material behavior of AISI 300 series ASS, aluminum alloy, and nickel steel alloys. To account for the effect of microstructural phase transformation on the plastic deformation characteristics of the material, the strain-hardening rate and the strain-rate sensitivity are directly used as the material parameters. The BP model does not explicitly incorporate the yield function but is observed to be capable of expressing the yield phenomenon of materials [34].

The BP model expresses the total strain rate, $\dot{\varepsilon}_{ij}$, as a sum of the elastic strain rate, $\dot{\varepsilon}_{ij}^e$, and the inelastic strain rate, $\dot{\varepsilon}_{ij}^p$:

$$\dot{\varepsilon}_{ij}^p = D_o \exp \left\{ -\frac{1}{2} \left(\frac{Z}{\sigma_{eff}} \right)^{2N} \right\} \frac{\sqrt{3} S_{ij}}{\sigma_{eff}} \quad (4-17)$$

where σ_{eff} and S_{ij} represent the effective stress and deviatoric stress respectively. D_o , N and Z are the internal parameters: D_o sets the maximum limit for the strain rate predicted by the model and N controls the strain rate sensitivity. The strain-hardening behavior of the material is controlled by Z which is derived, for the case of isotropic hardening, as:

$$Z = Z_1 + (Z_0 - Z_1). \exp(-mW_p) \quad (4-18)$$

Z_0 , Z_1 , and m control the yield stress, saturation of stress, and the slope of the hardening curve respectively. The plastic work, W_p is derived as:

$$W_p = \int dW_p = \int \sigma_{ij} d\varepsilon_{ij}^p \quad (4-19)$$

The Mirambell-Real and Rasmussen models adopted by Chen and Young for material characterization at elevated temperatures and the modifications applied to the BP model by Park et al. exhibit advanced capabilities for stress-strain curve approximation over the full range of strains for a wide range of applications. Zhang and Alam's expanded R-O model was also observed to perform well in approximating the stress-strain curve of steel sheet materials with well-defined yield plateau; with errors beyond the proportional limit < 5%. However, as is observable from the above-presented expressions, the applicability of the proposed models is limited by the associated complexity and numerous constituent parameters.

As detailed above, review of existing stress-strain models reveals the existence of the following limitations:

- (1) The prediction of corresponding stresses for strains beyond 0.2% total strain may sometimes be underestimated, especially for compression coupon tests.
- (2) None of the existing models is capable of providing a reasonable approximation of the yield plateau in materials that exhibit a well-defined yield point.
- (3) Every attempt to improve the predictive accuracy of the existing stress-strain model is observed to be accompanied with a corresponding decrease in the simplicity of the stress-strain formulation.

The proposed true stress-true strain model, herein referred to as the 'Ndubuaku model', has been formulated as a mathematical expression which can provide an exact approximation of the yield-to-tensile ratio for various metallic materials and hence, address the problem of loss of correspondence between the model-approximated stress values and the experimentally-obtained stresses, especially at the ultimate strain, as commonly observed in existing stress-strain models.

The proposed model also has the additional advantage of providing a realistic estimation of the stress-strain behavior of yield-plateau-type (YPT) materials. The motivation for the proposed model in this study is the development of a stress-strain curve model which is capable of providing a reasonable approximation of both continuous hardening-type stress-strain curves and yield plateau-type stress-strain curves.

4.6 Description of the Proposed Stress-strain Model

The concept behind the formulation of the ‘Ndubuaku model’ is the normalization of the full stress range and the full strain range of the stress-strain curve such that the exact magnitudes of the values of the stress and strain at any specified reference points are preserved. For simplicity, the proposed model is herein presented to estimate the corresponding stresses over the full range of strains for two segments of the stress-strain curve:

- (1) The first segment is the linear elastic portion of the curve and is defined by the initial modulus of elasticity of the material, E_o , up to the proportionality limit stress.
- (2) The second segment of the stress-strain curve is characterized by a nonlinear stress-strain relationship from the proportionality limit stress and strain up to the ultimate stress and strain, and is defined using the mathematical expression of the proposed model.

The definition of the first segment implies that for YPT materials, the proportionality limit stress coincides with the actual yield plateau stress, unlike the case of continuous-hardening type (CHT) materials whereby the yield stress is nominally defined as a 0.2% plastic strain or 0.5% total strain offset.

A total of four material parameters and two model constants are required to describe the proposed model, based on the following mathematical expression:

$$\sigma_R = \varepsilon_R \frac{\varepsilon_R^{-\left(\frac{1}{H_{NM}}\right)}}{K_{NM}} \quad (4-20)$$

where,

σ_R is the stress ratio; which is defined as the ratio of the incremental stress beyond the proportionality limit to the full stress range (the difference between the ultimate stress, σ_u , and the proportionality limit stress, σ_{pl}), and is expressed as:

$$\sigma_R = \frac{\sigma - \sigma_{pl}}{\sigma_u - \sigma_{pl}} \quad (4-21)$$

ε_R is the strain ratio; which is defined as the ratio of the incremental strain beyond the proportionality limit to the full strain range (the difference between the ultimate strain, ε_u , and the corresponding total strain at the proportionality limit stress, ε_{pl}), and is expressed as:

$$\varepsilon_R = \frac{\varepsilon - \varepsilon_{pl}}{\varepsilon_u - \varepsilon_{pl}} \quad (4-22)$$

K_{NM} and H_{NM} are the model constants; herein referred to as the “knee” parameter and the “heel” parameter respectively.

Due to the nonlinear form of most stress-strain expressions, numerical iterations are sometimes required for inversion of the mathematical formulation. Although the expression of stress as a function of strain may be preferred for certain applications, it may be required, for alternative significance, to present an explicit inverted form of the mathematical expression such that the strain is defined as a function of stress. The inverted form of the proposed expression is formulated using the Product log function (also referred to as the *Omega* function).

The *Product log* function is expressed in the following form:

$$y = xe^x \Leftrightarrow W(y) = x$$

Hence, the closed form inversion of the proposed model is obtained as follows:

$$\begin{aligned}
\sigma_R &= \varepsilon_R \frac{\varepsilon_R^{-\left(\frac{1}{H_{NM}}\right)}}{K_{NM}} \\
\ln(\sigma_R) &= \ln\left(\varepsilon_R \frac{\varepsilon_R^{-\left(\frac{1}{H_{NM}}\right)}}{K_{NM}}\right) \\
\ln(\sigma_R) &= \frac{1}{K_{NM}} \cdot e^{-\frac{1}{H_{NM}} \cdot \ln(\varepsilon_R)} \cdot \ln(\varepsilon_R) \\
-\frac{1}{H_{NM}} \cdot \ln(\sigma_R) &= \frac{1}{K_{NM}} \cdot e^{-\frac{1}{H_{NM}} \cdot \ln(\varepsilon_R)} \cdot \ln(\varepsilon_R) \cdot -\frac{1}{H_{NM}} \\
-\frac{1}{H_{NM}} \cdot \ln(\varepsilon_R) &= W\left[-\frac{K_{NM}}{H_{NM}} \cdot \ln(\sigma_R)\right] \\
\varepsilon_R &= e^{-H_{NM} \cdot W\left[-\frac{K_{NM}}{H_{NM}} \cdot \ln(\sigma_R)\right]}
\end{aligned} \tag{4-23}$$

The applicability of the proposed expression for describing the typical stress-strain behavior of pipe steel specimens is presented in the following section.

4.7 Methodology for Nonlinear Curve-fitting

Curve-fitting techniques are required to derive the model constants of the proposed stress-strain equation for approximating the shape of the stress-strain curve, given true stress and true strain data experimentally-obtained from a standard axial tension coupon test. The proposed model relies on the determination of the proportionality limit point and the ultimate point, indicated respectively by Point A and Point B in Figure 4-2.

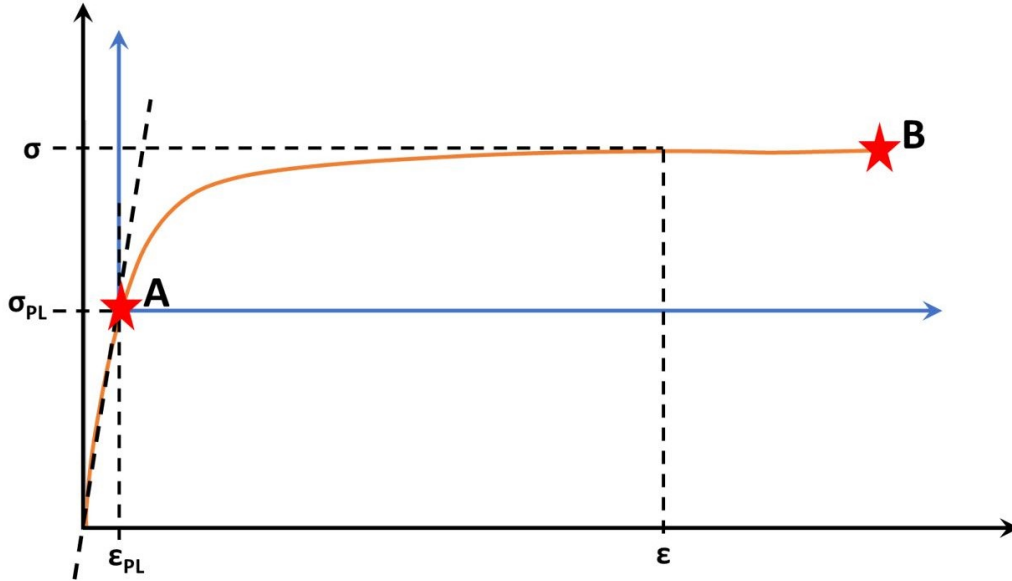


Figure 4-2: Schematic of stress-strain curve showing proportionality limit and ultimate point

The following procedure should, therefore, be followed for applying a curve-fitting technique to approximate the shape of the stress-strain curve:

1. Obtain the proportionality limit stress and strain values at point A by applying a linearity deviation principle as follows:

$$\Delta_l(\%) = 100 \times \frac{\varepsilon - \frac{\sigma}{E}}{\frac{\sigma}{E}} \quad (4-24)$$

where σ and ε represent the incremental stress and incremental strain respectively, and E is Young's modulus of elasticity.

2. Determine the ultimate stress and strain values at point B based on the maximum values of the experimental stress and strain data, or at a nominal proof stress and proof strain value.
3. Apply the proportionality limit values and ultimate values to the stress-strain equation.
4. Derive the model parameters using curve-fitting techniques (the "NonlinearModelFit" command in Mathematica is used throughout this research).

The linearity deviation technique makes it easy to handle proportionality limit ambiguities caused by irregularities associated with experimental stress-strain data by specifying an

allowable (and reasonably small) eccentricity between the proportionality limit point and the linear elastic line of the stress-strain curve.

4.8 Validation of Proposed Model (General Application to Metallic Materials)

Park et al. [33,51] explained that the 300 series of austenitic stainless steel (ASS), aluminum alloys, and nickel steel provide high strength and excellent ductility over a wide range of low temperatures hence, they are generally preferred over other metallic materials for cryogenic applications in many industrial fields. In an effort to introduce a robust design scheme for structures used for storing and shipping liquefied natural gas (LNG), they conducted a series of cryogenic tensile tests under various temperatures (110 - 293 K) and strain rates (0.00016 - 0.01 s⁻¹). The material specimens for the tests were obtained from the three representative types of low-temperature application materials; AISI 304L, AA5083, and Invar steel.

To properly portray the robustness and versatility of the proposed model, the results of the cryogenic tensile tests conducted by Park et al. have been selected for model evaluation. The test matrix for the experiments was designed such that five graduations of temperature (293K, 223K, 153K, 133K, and 110K) were selected, and three strain rates (0.00016s⁻¹, 0.001s⁻¹, 0.01s⁻¹) were determined as the test variables at each temperature; however, only two arrays of results from the test matrix was utilized for the model evaluation.

The stress-strain data obtained from the results of the experimental studies conducted by Park et al. were converted to the respective true stress and true strain values. However, the portion of the stress-strain curve beyond the ultimate stress (after the onset of necking) was excluded from the model evaluation as it is considered to be practically irrelevant to the applicability of the proposed model. The ultimate stresses (σ_u) used for the model evaluation were taken as the highest values of true stress reported from the experiments, while the ultimate strains (ϵ_u) were taken as the corresponding values of true strain at the respective ultimate stresses.

The proposed model is applied to the stress-strain curve in two segments: the linear elastic portion of the curve is defined by the initial modulus of elasticity of the material, E_o , up to the proportionality limit stress and from the proportionality limit, the nonlinear stress-strain relationship is defined using the proposed expression up to the ultimate limit. Least-squares

curve fitting was used to obtain the best fit between the experimental data points and the model-predicted stress-strain curve by minimizing the sum of the squares of the errors between the model-predicted values and the experimentally-obtained values for each data point. The plots of the model-to-experiment curve-fit evaluations are presented in Figure 4-3 - Figure 4-8.

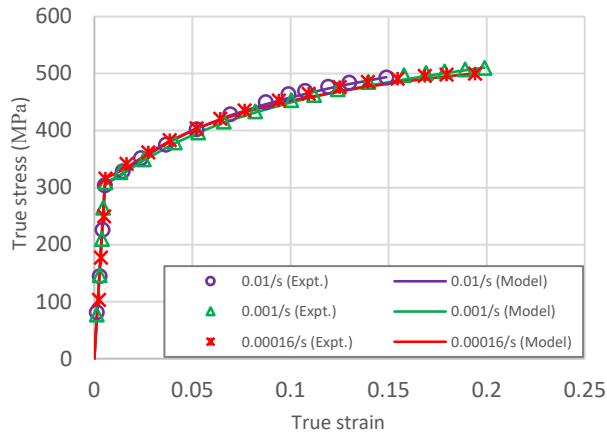


Figure 4-3: Model-to-experiment stress-strain plots for AA5083 at 110K (strain rate - varied)

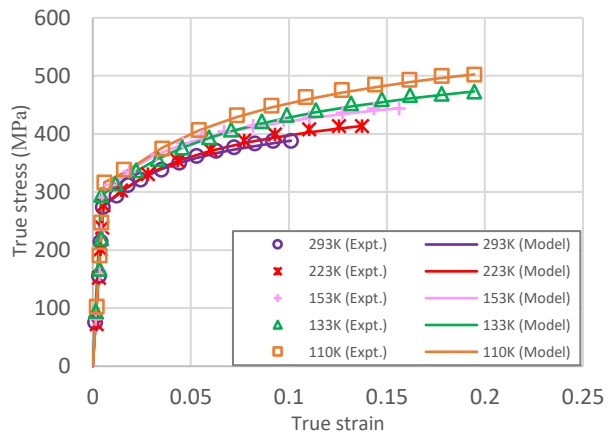


Figure 4-4: Model-to-experiment stress-strain plots for AA5083 at 0.00016/s (temperature - varied)

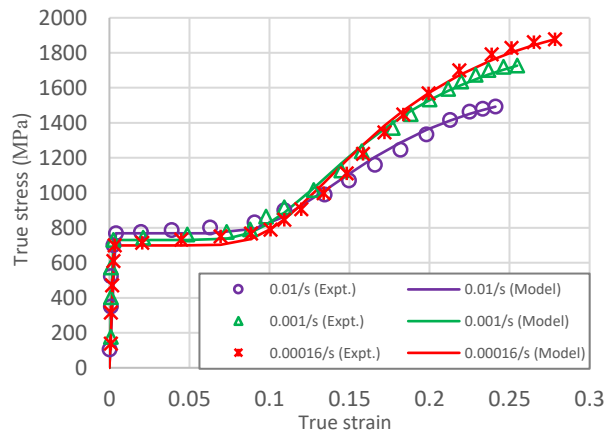


Figure 4-5: Model-to-experiment stress-strain plots for AISI 304L at 110K (strain rate - varied)

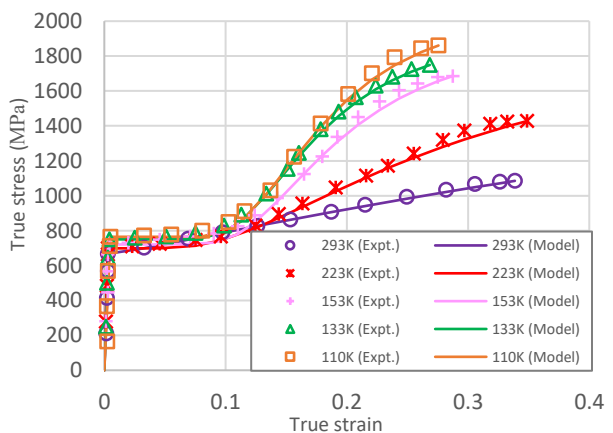


Figure 4-6: Model-to-experiment stress-strain plots for AISI 304L at 0.00016/s (temperature - varied)

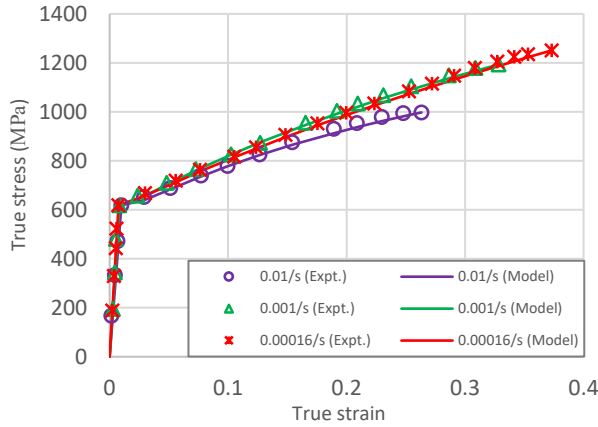


Figure 4-7: Model-to-experiment stress-strain plots for Invar Steel at 110K (strain rate - varied)

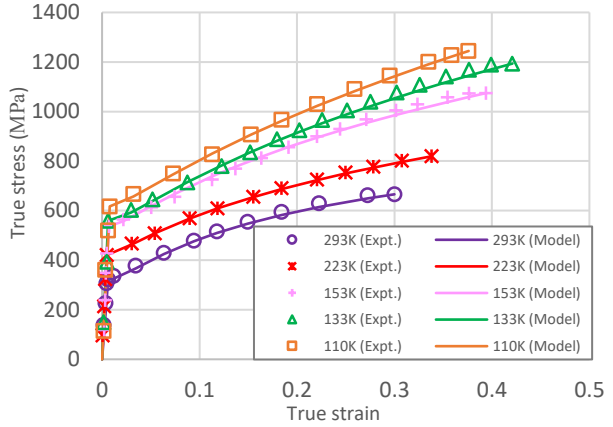


Figure 4-8: Model-to-experiment stress-strain plots for Invar Steel at 0.00016/s (temperature - varied)

The R-squared values and values of the model parameters are presented for the strain rate-effect tensile tests and the temperature-effect tensile tests in Table 4-1.

Table 4-1: Model parameters and R2 values for model-to-experiment curve-fit evaluations

Material	Model parameters	Strain rate			Temperature				
		(sec ⁻¹)			(K)				
		0.01	0.001	0.00016	293	223	153	133	110
AA 5083	K _{NM}	2.17	2.31	2.79	2.71	2.89	3.25	2.78	2.71
	H _{NM}	4.92	4.49	3.55	4.26	4.09	4.91	4.24	3.64
	R ²	0.9986	0.9988	0.9981	0.9976	0.9984	0.9986	0.9987	0.9989
AISI 304L	K _{NM}	1.32	1.56	1.74	1.12	1.52	1.53	1.66	1.71
	H _{NM}	0.68	0.71	0.73	13.53	0.98	0.67	0.62	0.59
	R ²	0.9924	0.9962	0.9939	0.9989	0.9961	0.9973	0.9989	0.9985
Invar Steel	K _{NM}	1.46	1.38	1.25	2.03	1.68	1.58	1.46	1.34
	H _{NM}	5.12	8.69	12.52	4.02	6.73	7.06	7.17	8.95
	R ²	0.9981	0.9993	0.9994	0.9982	0.9998	0.9979	0.9988	0.9996

The high R-squared values presented in Table 4-1, as obtained from the curve-fit evaluations in Figure 4-3 - Figure 4-8, indicate that the proposed model provides a highly accurate approximation of the stress-strain curves for all the experimental results considered.

From the observed consistency in the variation of the obtained results, it is evident that the range of the values of the model parameters is reflective of the shape of the stress-strain curve. An explanation is given of the mean value and standard deviation of the model parameters, for a combination of the temperature- and strain rate-effect tensile tests of the three studied materials, as follows:

AA5083- The mean value and standard deviation of K_{NM} are 2.701 and 0.335 respectively, while the mean value and standard deviation of H_{NM} are 4.263 and 0.511 respectively. The mean value of H_{NM} is higher than the mean value of K_{NM} , indicating that the convexity of the ‘knee’ of the curve is favored relative to the concavity of the ‘heel’.

AISI304L- Considering the values obtained at 0.00016/s and 293K as outliers, the mean value and standard deviation of K_{NM} are 1.577 and 0.143 respectively, while the mean value and standard deviation of H_{NM} are 0.711 and 0.128 respectively. The mean value of H_{NM} is lower than the mean value of K_{NM} , indicating that the concavity of the ‘heel’ of the curve is favored relative to the convexity of the ‘knee’.

Invar Steel- The mean value and standard deviation of K_{NM} are 1.523 and 0.245 respectively, while the mean value and standard deviation of H_{NM} are 7.533 and 2.602 respectively. The mean value of H_{NM} is higher than the mean value of K_{NM} , indicating that the convexity of the ‘knee’ of the curve is favored compared to the concavity of the ‘heel’.

A comparison between the obtained results for AA5083 and Invar Steel indicates that when the value of K_{NM} is significantly reduced (approximately below a value of 2), the positive effect of a higher value of H_{NM} on the convexity of the knee begins to diminish infinitely. Also, a low value of H_{NM} (approximately below a value of 3) typically indicates the presence of a yield plateau in the stress-strain curve. However, the yield plateau diminishes as the ratio of K_{NM} to H_{NM} exceeds a value of 6. The knee-to-heel parameter ratio that causes the yield plateau to vanish reduces as the value of H_{NM} increases.

4.9 Validation of Proposed Model (Application to Pipeline Steels)

The proposed model has been evaluated based on a set of experimental stress-strain curves obtained from the uniaxial tensile test of specimens sampled from different pipeline steels, with grades ranging from API 5L X52 to X100 [1]. All the experimental data were obtained from previous tests conducted at the University of Alberta where strip specimens were machined in the longitudinal direction from X52, X60, X65, X80, and X100 steel pipes, and round specimens were machined in the circumferential direction from X52, X80 and X100 steel pipes [52].

Least-squares curve fitting was used to obtain the best fit between the experimental data points and the model-predicted stress-strain curve and the plots of the model-to-experiment curve fit are presented in Figure 4-9 – Figure 4-13.

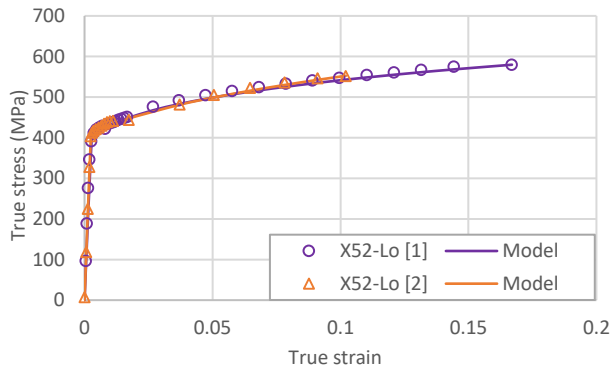


Figure 4-9: Model prediction for X-52 pipe steel (longitudinal)

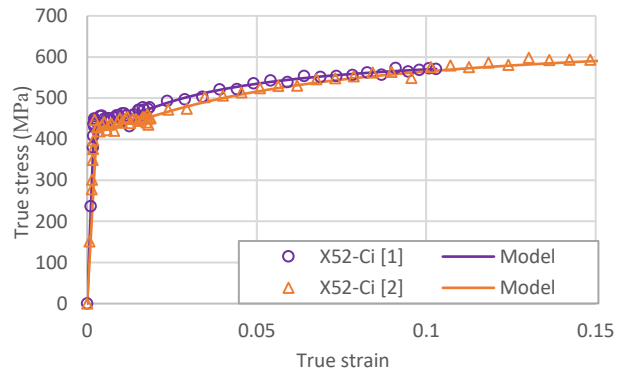


Figure 4-10: Model prediction for X-52 pipe steel (circumferential)

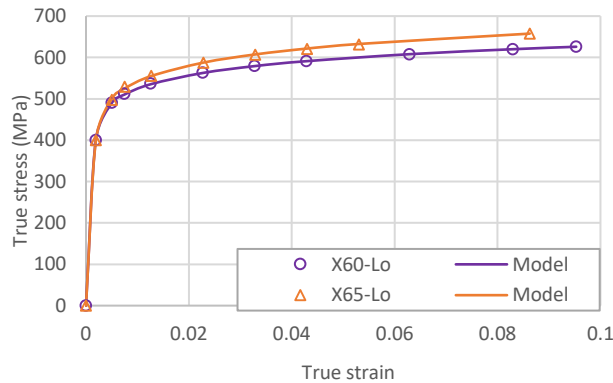


Figure 4-11: Model prediction for X-60 & X-65 pipe steel

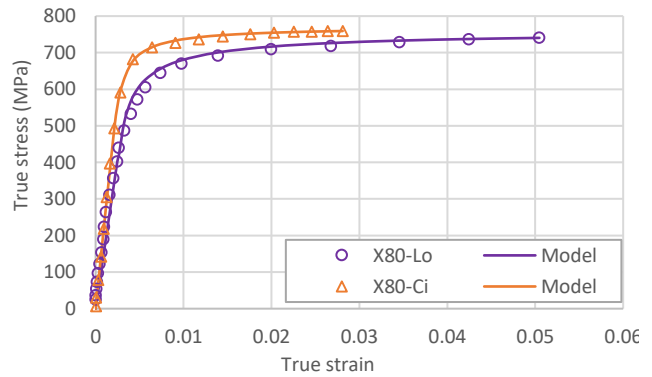


Figure 4-12: Model prediction for X-80 pipe steel

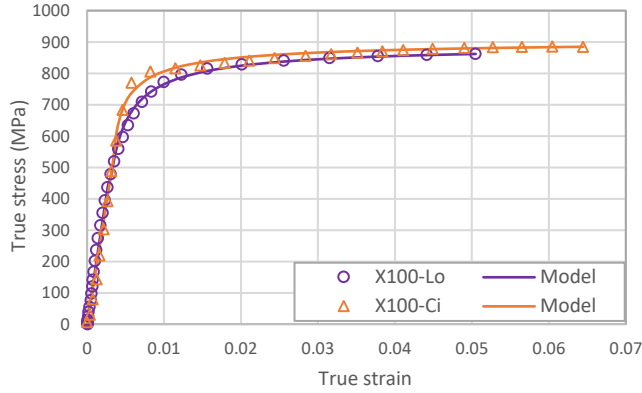


Figure 4-13: Model prediction for X-100 pipe steel

The stress-strain curves for longitudinal specimens are indicated using the designation, “-Lo” against the respective pipe steel grade. For the circumferential specimens, the designation, “-Ci” is used.

The R-squared values and values of the model constants, obtained from the curve-fitting procedures, are presented in Table 4-2 [Error! Reference source not found.](#).

Table 4-2: R-squared values for model parameters

Pipe steel	K_{NM}	H_{NM}	R^2
<i>X52-Lo [1]</i>	2.4	17.3	0.9965
<i>X52-Lo [2]</i>	1.7	25.1	0.9941
<i>X52-Ci [1]</i>	3.4	2.1	0.9708
<i>X52-Ci [2]</i>	3.1	2.6	0.9854
<i>X60-Lo</i>	5.4	8.9	0.9998
<i>X65-Lo</i>	5.2	8.3	0.9995
<i>X80-Lo</i>	21.4	2.3	0.9985
<i>X80-Ci</i>	25.6	1.9	0.9986
<i>X100-Lo</i>	17.8	2.1	0.9941
<i>X100-Ci</i>	24.1	2.5	0.9888

It is noteworthy that, for some of the collected data, the measurement of strains was not conclusive up to the nominal ultimate strength of the material hence, the ultimate stresses (σ_u) and ultimate strains (ϵ_u) used for the model evaluation were taken as the highest values of stresses and strains reported from the experiments.

From the plots in Figure 4-9 – Figure 4-13, and with the high R^2 values presented in Table 4-2, it is evident that the proposed model provides a highly accurate approximation of the stress-strain curves for all the experimental results considered.

A clearer illustration of the approximation of the stress-strain of the circumferential X-52 pipe steel material (with a well-defined yield plateau) is presented using a magnified image of the yield plateau region in Figure 4-14.

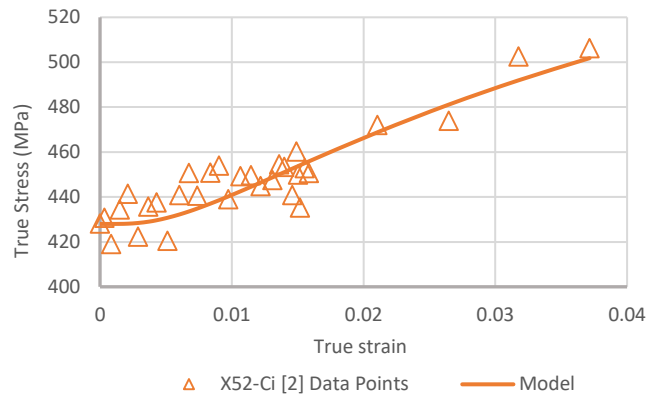


Figure 4-14: Illustration of yield plateau approximation

As evident in Figure 4-14, there exists a large amount of scatter in the data points around the yield plateau region; which is a common feature in axial tensile tests of mild strength steel materials. However, the least-squares optimization procedure, when applied to the proposed model, provides a remarkably reasonable double-curvature nonlinear curve that passes through the experimental data points at the yield plateau region and the strain-hardening region. In addition, the applicability of the proposed model may be extended for the approximation of much higher magnitudes of yield point elongation (YPE).

4.10 Numerical Model Application

The buckling behavior of a pipe is a direct consequence of its stiffness, as well as the state of stress under which it is subjected due to its loading configuration. Buckling failure is typically characterized by a loss of structural stiffness and may or may not occur prior to the onset of plasticization in the material (elastic or plastic buckling). In the elastic region, the axial stress typically increases simultaneously with the applied force or bending moment until a magnitude is attained whereby the stresses at the extreme fibers of the pipe wall reach the yield stress of the material. Generally, the axial stresses in the pipe wall are derived based on the cumulative effects of the internal pressure, axial force and bending moment [53].

Parks *et al.* [54] points out that accurate analytical prediction of the buckling behavior of curved and cylindrical shell elements, especially in the post-buckling range, is usually difficult due to factors such as dependency on complex and nonlinear large deflection theories, sensitivity to imperfections and/or edge restraints, and unpredictability of residual stress effects. It is therefore inevitable, in most cases, that the approximation of the compressive strain capacity of such elements is achieved using empirical or semi-empirical procedures.

In consideration of the post-buckling behavior of flat plates and cylinders due to large deformation, Gerard and Becker [55] explain that, under compressive deformation, a cylinder and a flat plate follow a similar load-deformation path prior to buckling. However, at the onset of buckling a flat plate develops significant transverse tensile membrane stresses due to edge restraint conditions whereas a cylinder develops transverse compressive membrane stresses due to inward buckling. Consequently, buckling of an axially compressed cylinder is typically coincident with failure and a subsequent drop in load whereas a flat plate is able to sustain higher loads in the post-buckling range than the theoretical buckling load. For simplicity, FE-modeled flat steel plates are used as a representative model, in this study, for analyzing the buckling response of shell elements subjected to uniform compressive axial loading for various material stress-strain curves.

In the present study, two thickness variations and five material (stress-strain curve) variations are applied to a flat square and a flat rectangular steel plate numerical model, each subjected to a uniform compressive axial load (applied at the shorter edge for the rectangular plate model); using the commercial finite element analysis package, ABAQUS CAE. A 3D model was

generated using linear 4-node reduced-integration (S4R) shell elements with hourglass control and a convergence study was undertaken to determine the optimum number of shell elements required to achieve an accurate approximation of the buckling behavior of the steel plates. The undeformed picture of the rectangular steel plate model is shown in Figure 4-15 below.

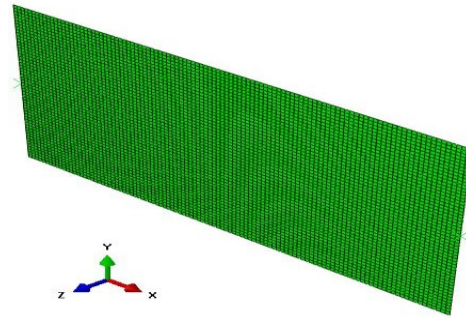


Figure 4-15: Picture of undeformed rectangular ABAQUS steel plate model; dimensions = 800 mm × 1600 mm × 9 mm

To account for the strain-hardening characteristics, the model constants used to generate the five variations of the stress-strain curves are presented in Table 4-3.

Table 4-3: Model constants for stress-strain curves

Type	K_{NM}	H_{NM}
<i>A</i>	Perfectly plastic	
<i>B</i>	3.5	2.0
<i>C</i>	2.5	17.0
<i>D</i>	5.5	9.0
<i>E</i>	24.5	3.0

The dimensions of the rectangular plate model are 800 mm × 1600 mm while those of the square plate model are 800 mm × 800 mm. Two thickness variations (9 mm and 15 mm) are applied to each of the plate models and the strain-hardening characteristics are incorporated in the material model such that the proportionality limit stress (352.8 MPa) and the ultimate stress (666.8 MPa)

are kept constant while the offset yield strength is allowed to vary. The stress-strain curves generated using the proposed model are plotted as shown in Figure 4-16.

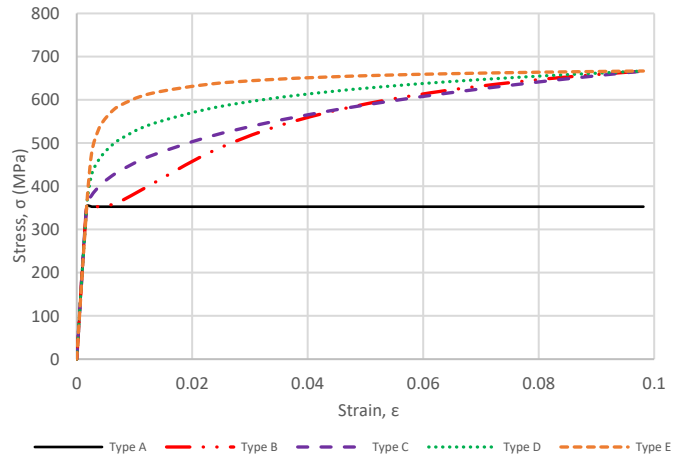


Figure 4-16: Stress-strain curves of steel plate models with varying strain-hardening characteristics

A value of 205800 MPa and 0.3 is applied for Young’s modulus and Poisson’s ratio respectively. Simply supported boundary conditions are applied to the plate models on all four edges to restrain both in-plane and out-of-plane deformations at the edges, and to prevent the development of edge moments due to lateral deformation of the plate. Paik and Thayamballi [56] posit that the simply supported edges, as adopted for this study, are representative of the boundary conditions generally applied for the modeling and design of the ultimate strength of steel plates in offshore structures and marine vessels.

The load-deformation behavior of the flat plate models is represented using plots of the average compressive stress (applied on the loaded edge of the plates) versus the average longitudinal strain along the length of the plate (adjacent to the loaded edge) in Figure 4-17 – Figure 4-20.

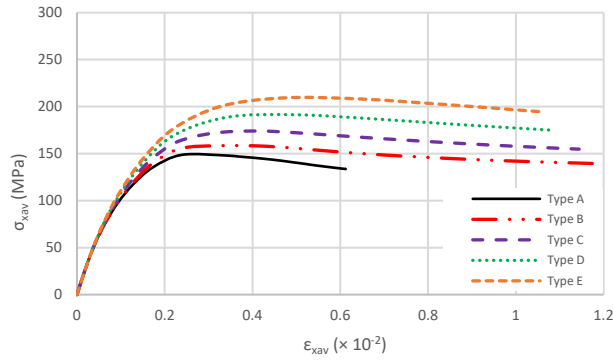


Figure 4-17: Load-deformation behavior of 9 mm-thick square plate

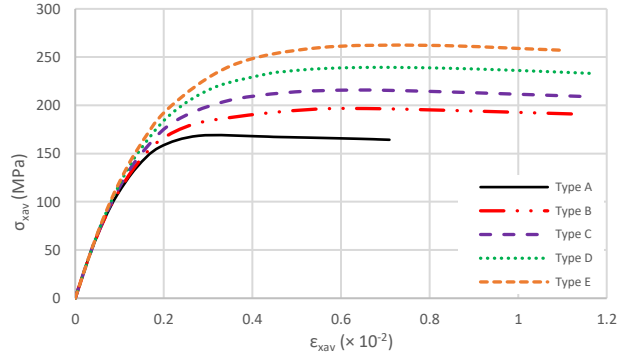


Figure 4-18: Load-deformation behavior of 15 mm-thick square plate

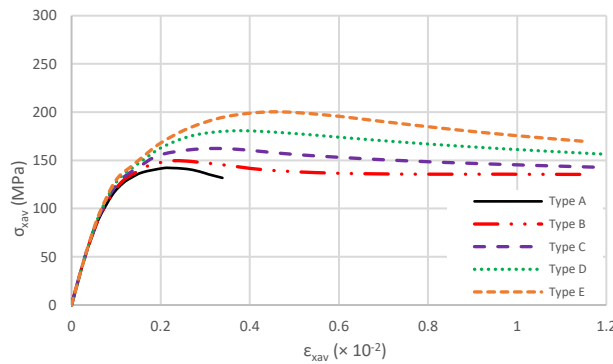


Figure 4-19: Load-deformation behavior of 9 mm-thick rectangular plate

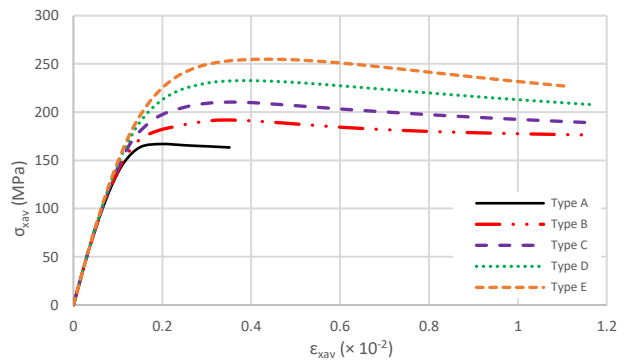


Figure 4-20: Load-deformation behavior of 15 mm-thick rectangular plate

The plots of the load-deformation relationship for the plate models indicate that the strain-hardening characteristics of the steel material have a significant influence on the buckling response of the plate to compressive axial loading. As observed from the plots, increased strain-hardening is accompanied with an increase in the load-carrying capacity of the plates. Additionally, the thickness of the plates has a considerable effect on the ultimate compressive strength whereas the effect of the dimensional aspect ratio (length vs. width) has a much less significant effect.

The proposed stress-strain model, which is this focus of this present study, therefore proves to be an easily applicable tool which can be employed for parameterization of the relationship between the stress-strain relationship and the ultimate compressive strength of plate elements and, invariably, other shell elements such as pipes.

4.11 Conclusions

Complex nonlinearities and plasticization problems are frequently encountered in the design and analysis of civil engineering structures and structural elements. Past research studies indicate that the phase transformations that occur within the microstructure are the most important factors that cause significant changes in the mechanical behavior of metallic materials; especially at varying temperatures and strain rates.

Proper characterization of the stress-strain behavior of materials is therefore important for practical considerations, especially where parametric numerical simulations are required for structural design and analysis. Unfortunately, the widely-applied Ramberg-Osgood stress-strain expression is known to lose accuracy in stress-strain curve approximation beyond a limited strain range. Moreover, subsequent modifications of the Ramberg-Osgood equation seem to either have the disadvantage of complexity or, in some cases, limited applicability.

A novel stress-strain curve model has been developed and presented in this paper to provide a simple, highly-versatile and accurate tool for stress-strain material characterization and parameterization of the strength and strain-hardening characteristics of different structural materials, over a wide range of processing and operational conditions. Characteristically unlike existing equations, which are mostly based on a power law relationship, the proposed stress-strain equation expresses the strain as a function of stress based on a Product Log function. The proposed model is established based on the true stress-true strain relationship and only requires empirical derivation of two model parameters for the approximation of the stress-strain curve over the full range of strains; even for materials with a well-defined yield plateau. The most important characteristic of the proposed model is the ability to describe a continuous transition from yield plateau-type stress-strain curves to continuous hardening-type stress-strain curves; even so that curves that may be regarded as bilinear (as in Figure 4-7 and Figure 4-8) can also be approximated. The robustness and precision provided by the proposed model are illustrated by the model-to-experiment curve-fit evaluations presented in this paper.

As indicated by the simple plate buckling analysis used for testing its applicability to numerical modeling, the proposed model is expected to be widely useful for design and analysis of structures and structural elements, especially for cases where consideration of the effects of

material stress-strain characteristics on large deformation and complex nonlinear problems are imperative.

4.12 References

- [1] American Petroleum Institute, API 5L: Specification for Line Pipe, 44th ed., American Petroleum Institute, USA, 2007.
- [2] K.T. Corbett, R.R. Bowen, C.W. Petersen, High Strength Steel Pipeline Economics, in: Proc. Thirteen. Int. Offshore Polar Eng. Conf., International Society of Offshore and Polar Engineers, Honolulu, Hawaii, USA, 2003: pp. 105–112.
- [3] H.D. Yun, S. Kyriakides, Buckling of pipelines in seismic environments, in: Proc. 3rd U.S. Natl. Conf. Earthq. Eng., Charleston, South Carolina, USA, 1986: pp. 2179–2189.
- [4] G.T. Ju, S. Kyriakides, Thermal Buckling of Offshore Pipelines, *J. Offshore Mech. Arct. Eng.* 110 (1988) 355. doi:10.1115/1.3257073.
- [5] H. Yun, S. Kyriakides, On the beam and shell modes of buckling of buried pipelines, *Soil Dyn. Earthq. Eng.* 9 (1990) 179–193. doi:10.1016/S0267-7261(05)80009-0.
- [6] C.C. Chen, T. Ariman, L.H.N. Lee, Elastic buckling analysis of buried pipelines under seismic loads, in: ASME Century 2 Press. Vessel Pip. Conf., San Francisco, California, 1980.
- [7] A.B. Dorey, J.J.R. Cheng, D.W. Murray, Critical Buckling Strains for Energy Pipelines, Structural Engineering Report No. 237, Edmonton, Alberta, 2001.
- [8] C.E. Murphey, C.G. Langner, Ultimate pipe strength under bending, collapse and fatigue, in: Proc. 4th Int. Conf. Offshore Mech. Arct. Eng., 1985: pp. 467–477.
- [9] N. Yoosef-Ghodsii, I. Ozkan, Q. Chen, Comparison of Compressive Strain Limit Equations, in: Vol. 4 Prod. Pipelines Flowlines; Proj. Manag. Facil. Integr. Manag. Oper. Maintenance; Pipelining North. Offshore Environ. Strain-Based Des. Stand. Regul., ASME, 2014: p. V004T11A001. doi:10.1115/IPC2014-33182.
- [10] T.J.E. Zimmerman, M.J. Stephens, D.D. DeGeer, Q. Chen, Compressive strain limits for buried pipelines, in: Proc. 14th Int. Conf. Offshore Mech. Arct. Eng. Vol. 5, ASME, Copenhagen, Denmark, 1995.
- [11] Canadian Standards Association, Oil and gas pipeline systems. CSA-Z662-2007, (2007).

- [12] A.M. Gresnigt, Plastic Design of Buried Steel Pipelines in Settlement Areas, Heron. 31 (1986).
- [13] Det Norske Veritas, Submarine pipeline systems - DNV-OS-F101, DNV, Oslo, Norway, 2010.
- [14] W. Ramberg, W.R. Osgood, Description of stress-strain curves by three parameters, NACA Technical Note No. 902, Washinton, D.C., 1943.
- [15] R.P. Skelton, H.J. Maier, H.-J. Christ, The Bauschinger effect, Masing model and the Ramberg–Osgood relation for cyclic deformation in metals, Mater. Sci. Eng. A. 238 (1997) 377–390. doi:10.1016/S0921-5093(97)00465-6.
- [16] M. Macdonald, J. Rhodes, G.T. Taylor, Mechanical properties of stainless metal lipped channels, in: 15th Int. Spec. Conf. Cold-Formed Met. Struct., University of Missouri-Rolla, Mo., 2000: pp. 673–686.
- [17] E. Mirambell, E. Real, On the calculation of deflections in structural stainless steel beams: an experimental and numerical investigation, J. Constr. Steel Res. 54 (2000) 109–133. doi:10.1016/S0143-974X(99)00051-6.
- [18] M.K. Chryssanthopoulos, Y.M. Low, A method for predicting the flexural response of tubular members with non-linear stress-strain characteristics, J. Constr. Steel Res. 57 (2001) 1197–1216. doi:10.1016/S0143-974X(01)00033-5.
- [19] L. Gardner, D.A. Nethercot, Experiments on stainless steel hollow sections—Part 1: Material and cross-sectional behavior, J. Constr. Steel Res. 60 (2004) 1291–1318. doi:10.1016/J.JCSR.2003.11.006.
- [20] K.J. Kurzydłowski, Structure and properties of metals, Acta Phys. Pol. A. 96 (1999) 69–79.
- [21] J.R. Davis, Metals Handbook: Desk Edition, 2nd ed., American Society for Metals (ASM International), Materials Park, Ohio, 1998.
- [22] X. Zhao, Y. Shen, L. Qiu, Y. Liu, X. Sun, L. Zuo, X. Zhao, Y. Shen, L. Qiu, Y. Liu, X. Sun, L. Zuo, Effects of Intercritical Annealing Temperature on Mechanical Properties of Fe-7.9Mn-0.14Si-0.05Al-0.07C Steel, Materials (Basel). 7 (2014) 7891–7906. doi:10.3390/ma7127891.

- [23] R.Z. Valiev, A.V. Korznikov, R.R. Mulyukov, Structure and properties of ultrafine-grained materials produced by severe plastic deformation, *Mater. Sci. Eng. A.* 168 (1993) 141–148. doi:10.1016/0921-5093(93)90717-S.
- [24] P.J. Jacques, Transformation-induced plasticity for high strength formable steels, *Curr. Opin. Solid State Mater. Sci.* 8 (2004) 259–265. doi:10.1016/J.COSSMS.2004.09.006.
- [25] J. Bouquerel, K. Verbeken, B.C. De Cooman, Microstructure-based model for the static mechanical behavior of multiphase steels, *Acta Mater.* 54 (2006) 1443–1456. doi:10.1016/J.ACTAMAT.2005.10.059.
- [26] D. Terada, S. Inoue, N. Tsuji, Microstructure and mechanical properties of commercial purity titanium severely deformed by ARB process, *J. Mater. Sci.* 42 (2007) 1673–1681. doi:10.1007/s10853-006-0909-7.
- [27] Y.F. Shen, C.M. Wang, X. Sun, A micro-alloyed ferritic steel strengthened by nanoscale precipitates, *Mater. Sci. Eng. A.* 528 (2011) 8150–8156. doi:10.1016/J.MSEA.2011.07.065.
- [28] E. Paravicini Bagliani, M.J. Santofimia, L. Zhao, J. Sietsma, E. Anelli, Microstructure, tensile and toughness properties after quenching and partitioning treatments of a medium-carbon steel, *Mater. Sci. Eng. A.* 559 (2013) 486–495. doi:10.1016/J.MSEA.2012.08.130.
- [29] S. Curtze, V.-T. Kuokkala, M. Hokka, P. Peura, Deformation behavior of TRIP and DP steels in tension at different temperatures over a wide range of strain rates, *Mater. Sci. Eng. A.* 507 (2009) 124–131. doi:10.1016/J.MSEA.2008.11.050.
- [30] D. Slavik, H. Sehitoglu, Constitutive Models Suitable for Thermal Loading, *J. Eng. Mater. Technol.* 108 (1986) 303. doi:10.1115/1.3225887.
- [31] A. Buchanan, P. Moss, J. Seputro, R. Welsh, The effect of stress-strain relationships on the fire performance of steel beams, *Eng. Struct.* 26 (2004) 1505–1515. doi:10.1016/J.ENGSTRUCT.2004.05.003.
- [32] J. Chen, B. Young, Stress-strain curves for stainless steel at elevated temperatures, *Eng. Struct.* 28 (2006) 229–239. doi:10.1016/J.ENGSTRUCT.2005.07.005.
- [33] W.S. Park, M.S. Chun, M.S. Han, M.H. Kim, J.M. Lee, Comparative study on the mechanical behavior of low-temperature application materials for ships and offshore structures: Part I—Experimental investigations, *Mater. Sci. Eng. A.* 528 (2011) 5790–5803. doi:10.1016/J.MSEA.2011.04.032.

- [34] S.-W. Yoo, C.-S. Lee, W.-S. Park, M.-H. Kim, J.-M. Lee, Temperature and strain rate dependent constitutive model of TRIP steels for low-temperature applications, *Comput. Mater. Sci.* 50 (2011) 2014–2027. doi:10.1016/J.COMMATSCI.2011.02.002.
- [35] X.-Q. Wang, Z. Tao, T.-Y. Song, L.-H. Han, Stress-strain model of austenitic stainless steel after exposure to elevated temperatures, *J. Constr. Steel Res.* 99 (2014) 129–139. doi:10.1016/J.JCSR.2014.04.020.
- [36] S.M. Adeb, Introduction to solid mechanics and finite element analysis using Mathematica, Kendall Hunt Publishing Company, Dubuque, IA, 2011.
- [37] A.C. Mackenzie, J.W. Hancock, D.K. Brown, On the influence of state of stress on ductile failure initiation in high strength steels, *Eng. Fract. Mech.* 9 (1977) 167–188. doi:10.1016/0013-7944(77)90062-5.
- [38] P. Arasaratnam, K.S. Sivakumaran, M.J. Tait, True stress-true strain models for structural steel elements, *ISRN Civ. Eng.* (2011).
- [39] J.M. Holt, Uniaxial tension testing, in: H. Kuhn, D. Medlin (Eds.), *ASM Handbook, Vol. 8 Mech. Test. Eval.*, American Society for Metals (ASM International), Materials Park, Ohio, 2000: pp. 124–142.
- [40] C. Moosbrugger, Representation of stress-strain behavior, in: Y. Tamarin (Ed.), *Atlas Stress. Curves*, 2nd ed., American Society for Metals (ASM International), Materials Park, Ohio, 2002: pp. 1–19.
- [41] P. Ludwik, *Elemente der Technologischen Mechanik*, Verl. v. Julius Springer, Berlin, 1909.
- [42] J.H. Hollomon, Tensile Deformation, *Trans. Metall. Soc. AIME.* 162 (1945) 268–290.
- [43] K.J.R. Rasmussen, Full-range stress-strain curves for stainless steel alloys, *J. Constr. Steel Res.* 59 (2003) 47–61. doi:10.1016/S0143-974X(02)00018-4.
- [44] H.N. Hill, Determination of stress-strain relations from the offset yield strength values. NACA Technical Note No. 927, Washington, D.C., 1944.
- [45] API 579-1/ASME FFS-1, Fitness-for-service, The American Society of Mechanical Engineers., Houston, Texas, 2007.

- [46] A. Olsson, Stainless steel plasticity – Material modelling and structural applications. Ph.D. thesis, Department of Civil and Mining Engineering, Lulea University of Technology, Sweden, 2001.
- [47] W.M. Quach, Residual stresses in cold-formed steel sections and their effect on column behaviour, The Hong Kong Polytechnic University, Hong Kong, 2005.
- [48] P. Hradil, A. Talja, E. Real, E. Mirambell, B. Rossi, Generalized multistage mechanical model for nonlinear metallic materials, *Thin-Walled Struct.* 63 (2013) 63–69. doi:10.1016/J.TWS.2012.10.006.
- [49] P. Zhang, M.S. Alam, Experimental investigation and numerical simulation of pallet-rack stub columns under compression load, *J. Constr. Steel Res.* 133 (2017) 282–299. doi:10.1016/J.JCSR.2017.02.023.
- [50] S.R. Bodner, Y. Partom, Constitutive Equations for Elastic-Viscoplastic Strain-Hardening Materials, *J. Appl. Mech.* 42 (1975) 385. doi:10.1115/1.3423586.
- [51] W.-S. Park, C.-S. Lee, M.-S. Chun, M.-H. Kim, J.-M. Lee, Comparative study on the mechanical behavior of low-temperature application materials for ships and offshore structures: Part II – Constitutive model, *Mater. Sci. Eng. A.* 528 (2011) 7560–7569. doi:10.1016/J.MSEA.2011.06.040.
- [52] M. Lin, Characterization of Tensile and Fracture Properties of X52 Steel Pipes and Their Girth Welds (MSc. Thesis), Department of Civil and Environmental Engineering, University of Alberta, Canada., 2015.
- [53] H. Karbasian, S. Zimmermann, U. Marewski, M. Steiner, Combined Loading Capacity of Pipelines: Approaches Towards the Compressive Strain Limit, in: *Vol. 4 Pipelining North. Offshore Environ. Strain-Based Des. Risk Reliab. Stand. Regul.*, ASME, 2012: p. 375. doi:10.1115/IPC2012-90615.
- [54] M.B. Parks, C. Santaputra, W.W. Yu, Local buckling of curved elements, in: *Proc. Eighth Int. Spec. Conf. Cold-Formed Steel Struct.*, University of Missouri-Rolla, 1986: p. 277.
- [55] G. Gerard, H. Becker, Handbook of structural stability part III : buckling of curved plates and shells. NACA Technical Note 3783, Washington, DC, United States, 1957.
- [56] J.K. Paik, A.K. Thayamballi, Ultimate limit state design of steel plated structures, John Wiley & Sons, Inc., Chichester, England, 2003.



5. THE EFFECT OF MATERIAL STRESS-STRAIN CHARACTERISTICS ON THE BUCKLING CAPACITY OF FLAT PLATES SUBJECTED TO UNIFORM AXIAL COMPRESSION

This chapter is derived from the following journal publication:

O. Ndubuaku, X. Liu, M. Martens, J.J. Roger Cheng, S. Adeeb, The effect of material stress-strain characteristics on the ultimate stress and critical buckling strain of flat plates subjected to uniform axial compression, *Constr. Build. Mater.* 182 (2018) 346–359. doi:10.1016/j.conbuildmat.2018.06.100.

5.1 Abstract

The buckling capacity of uniformly compressed flat plates has been investigated in this study. Material properties were characterized based on parameterization of the stress-strain curves using a simple and novel mathematical expression. Idealized stress-strain relationships were developed using the proposed material model and extensive parametric numerical analyses were conducted to investigate the effect of the material stress-strain properties on the buckling capacity of flat plates. For stress-strain curves with a yield plateau, the results of the parametric study showed a minimal influence of the material properties on the buckling capacity of the plates whereas a significant effect of the strain-hardening properties was observed in plates with round-house curves. Ultimately, the proposed stress-strain model was shown to be remarkably useful for capturing the relevant intricacies associated with material nonlinearity when predicting the buckling capacity and post-buckling behavior of uniformly-compressed flat plates.

Keywords: flat plate, buckling, post-buckling, uniaxial compression, load-axial shortening, ultimate strength, critical buckling strain, deformation capacity, stress-strain model, strain-hardening.

Abbreviations and Symbols:

b	plate width
b_e	effective plate width
CHT	continuously-hardening type
CSM	continuous strength method
DSM	direct strength method
E	elastic modulus
E_o	Young's modulus
$E-PP$	elastic-perfectly plastic
H_{NM}	Ndubuaku model 'heel' parameter
K_{NM}	Ndubuaku model 'knee' parameter
N_u	longitudinally-applied uniform compressive force

t	plate thickness
UTS	ultimate tensile strength
YPT	yield-plateau type
YS	yield strength
β	slenderness ratio coefficient
ε_{pl}	proportionality limit strain
ε_R	constitutive model strain ratio
ε_u	ultimate strain
ε_{ult}	plate deformation capacity
ν	Poisson's ratio
σ_{cr}	elastic critical buckling stress
σ_{pl}	proportionality limit stress
$\sigma_{p,0.2}$	equivalent yield stress (corresponding to 0.2% plastic strain)
σ_R	constitutive model stress ratio
σ_u	ultimate tensile stress
σ_{ult}	plate load-carrying capacity (ultimate strength)
σ_y	plate material yield stress
$\sigma_{0.5}$	equivalent yield stress (corresponding to 0.5% total strain)
ω_{mn}	amplitude of out-of-plane deflection

5.2 Introduction

In many of the industrial or engineering applications where plates or plate elements are used, they are required to withstand diverse types of in-plane (compressive, tensile, shear, etc.) and/or out-of-plane (flexural, torsional, etc.) loading conditions.

Under operational conditions, one of the most common loading phenomena, which is of widespread concern, is the application of in-plane loads to two parallel edges of metal plates (uniaxial/longitudinal compressive or biaxial compressive and/or tensile loading). Where the expected compressive loads on a stiffened plate or plated structural member is significant, the

compressive buckling resistance becomes of primary concern to the designer. Some of the main parameters which are generally considered in the design of axially loaded metal plates include the material properties, geometric properties (width/thickness ratio and aspect ratio) edge boundary conditions, and initial out-of-plane imperfections [1–3].

In various industrial applications and fields of engineering, there is extensive use of moderately thick to thick plates thus introducing complexity in the approximation of the buckling capacity². Besides the inclusion of shear deformation effects, increase in the thickness of compressive axially loaded plates increases the likelihood of inelastic buckling, especially in cases of plates whose uniaxial stress-strain behavior exhibits a relatively low proportionality limit stress compared to the nominal yield stress [4–12].

For almost two centuries, several researchers have investigated the elastic and inelastic buckling phenomenon in metal plates using various analytical, experimental, and numerical approaches, hence a considerable amount of information on the buckling capacity of metal plates is available. Specifically, various numerical and experimental investigations have been recently carried out to determine the buckling and post-buckling behavior of flat, simply-supported metal plates subjected to uniform compression. Rasmussen *et al.* [13] conducted two experimental tests on single plates cut from a 3 mm-thick UNS31803 stainless steel plate: the nominal widths were chosen as 125 mm and 250 mm, while the nominal length for the two plates was chosen as 750 mm. To simulate the post-buckling behavior of typical mild and higher strength steels used in marine structures, Mateus and Witz [1] developed numerical models for Grade B and API X52 steels respectively: the width of the plate models was fixed at 500 mm while they varied the slenderness ratio of the plate models between 0.5 and 6 and the aspect ratio was varied between 0.5 and 4. Bezkorovainy *et al.* [14] investigated the effect of material properties on the compressive strength of metal plates using an FE model similar to that used in Rasmussen *et al.* [13]: however, only square plates, with a width of 100 mm, were modeled in their study and the slenderness ratios were varied between 0.5 and 3. Paik *et al.* [15] studied the effects of shape, size (depth and diameter), and location of dents on the compressive capacity of dented simply-supported flat plates using the FE modelling approach: the width of the plate models was fixed at

² While in literature, the term “buckling behavior” is generally used in relation to the elastic critical buckling stress, the term “buckling capacity” is used, specifically within the context of this study, to refer to the methodological approximations of the ultimate compressive strength and corresponding uniform axial strain of flat plates subjected to uniform axial compression.

800 mm, and five variations of the aspect ratio (1, 2, 3, 4 and 5) and three variations of the plate thickness (10mm, 15 mm, and 20 mm) were applied. El-Sawy *et al.* [16] considered the problem of elastic and inelastic buckling of simply-supported perforated rectangular plates subjected to uniform compression using three grades of steel (A36, A572 Grade 50, and A572 Grade 60): two variations of the aspect ratio (1 and 2) were applied to the plate models while the b/t ratios were varied between 30 and 100.

Curve-fitting techniques are generally used to develop strength curve equations that correspond to experimentally and numerically obtained ultimate strengths. To determine the structural design resistance of metallic sections, a distinctive method of cross-section classification is generally used in most structural design codes. The cross-section classification approach is based on a *direct strength method* (DSM) [17, 18] which relates the ultimate strength of a section to the overall cross-section slenderness. It is, however, based on the assumption of an elastic, perfectly-plastic material model which has been observed to be generalizable for structural sections made of carbon steel or any material with a yield plateau in its stress-strain response. For materials such as aluminum and stainless steel, which have a gradual yielding behavior and an absence of a distinct yield point, the direct strength cross-section classification approach tends to yield unduly conservative results hence, a deformation (strain) based design approach referred to as the *continuous strength method* (CSM) [19–21] is typically applied to relate the cross-section resistance to the cross-section deformation capacity such that the benefits of strain-hardening in the stress-strain response are accounted for. The measure of the cross-section deformation capacity is derived from the end-shortening corresponding to the ultimate applied load in the compressive axial load-deformation response plot. The accuracy of the CSM has been observed to rely heavily on the correctness of the representation of the stress-strain behavior of the material using an analytical model that can accurately evaluate the stress as a function of the strain [22, 23].

The most notable attempt to examine the effect of material properties on the buckling response of flat plates was by Bezkorovainy *et al.* [14]; which resulted in the development of a generalized formula for predicting the ultimate strength of uniformly compressed plates using material-dependent parameters based on the Ramberg-Osgood expression (ROE) [24]. Even though the use of the strain-based continuous strength method has been observed to yield a high level of

accuracy of resistance predictions for stainless steel cross-sections subjected to various loading conditions [25], significant work has not been done to investigate the effect of an extensive range of material properties on the deformation capacity of flat plates. Additionally, research by Neupane *et al.* [26, 27] on the buckling capacity of pipelines indicated that the presence of a yield plateau in the material stress-strain curve has a significant effect on the critical local buckling strain in pipelines hence, it is important to extend such an investigation of material property effects to flat plates, using an applicable and reasonably accurate model. Previous studies by Liu *et al.* [28–30] have also highlighted the importance of taking the material stress-strain properties into account in the buckling failure analysis of high-strength pipelines.

Characterization of the strain-hardening behavior of metallic materials typically requires the application of analytical expressions, such as the widely-used ROE, which are useful for mathematically representing the nonlinear aspects of the stress-strain relationship. The ROE, as well as most of the existing stress-strain models, is essentially in the form of a power-law relationship which expresses the strain as a function of the stress. The power-law material characterization approach was originally designed for aluminum and stainless-steel alloys, as well as carbon steels with very small plastic strains, hence it is considered to be generally suitable for so-called ‘round-house’ stress-strain curves with an undefined yield stress, or which exhibit a gradual yielding behavior (CHT materials). However, approximation of the true stress-true strain relationship of metallic materials using the simple power-law expressions has been observed to be inadequate for accurately predicting the stress-strain behavior beyond a limited strain range hence, a number of researchers have proposed various modifications and piecewise extensions of the simple power-law expressions to improve the accuracy of prediction over the full range of strains [31–35]. Nevertheless, a major setback of the more advanced stress-strain models is characteristic increased complexity due to the requirement of a large number of constituent parameters.

A simple true stress-true strain model is presented in this study; which is capable of accurately approximating the stress-strain relationship of metallic materials over the full range of strains. The proposed stress-strain model is characteristically unlike existing stress-strain models as it is essentially defined by a Product-Log function using two constitutive model parameters, and can capture a reasonable approximation of the yield plateau in the stress-strain curve. With

knowledge of the proportionality limit stress and the ultimate stress, a continuum of nonlinear stress-strain curves can be derived within the natural stress-strain space of any continuously strain-hardening material. Previous studies by Ndubuaku *et al.* [36, 37] on the applicability of the proposed stress-strain expression, using a highly-advanced computational nonlinear model-fitting algorithm in the Mathematica software package, showed that the model is highly versatile and capable of providing a good approximation of the entire stress-strain curve for a diverse range of material types. They also showed that the proposed model is able to derive a reasonably accurate approximation of the stress-strain curve for different pipeline steels (even with the presence of a yield plateau) using one single equation and without the need for discretization.

Results of extensive parametric numerical analyses conducted to investigate the load-end shortening behavior of simply-supported flat plates subjected to uniform edge compression in the longitudinal direction are presented. The effects of aspect ratio, b/t ratio, and initial out-of-plane imperfection (based on the buckling mode shapes) are briefly examined while the main focus is on using the proposed material stress-strain model to determine the effect of the strain-hardening characteristics and overall shape of the material stress-strain curve on the ultimate compressive strength and strain capacity of the idealized metal plate models.

The analyses in this study were performed using ABAQUS CAE 6.14, a general-purpose finite element analysis (FEA) application, developed by Hibbitt *et al.* [38]. The application of the FEM for analysis of the behavior of perfect, dented, and perforated metal plates under compressive loading has been extensively validated by past researches [13–16] and is therefore considered by the authors to be suitable for simulating the mechanical response of metal plates subjected to uniform edge compression.

A review of the relevant theoretical postulations on the buckling capacity of simply-supported flat plates subjected to uniform axial compression is presented in [Section 5.3](#) followed by a detailed outline of the proposed material stress-strain model employed for this study in [Section 5.4](#). Parameters and methodology adopted for the creation and analysis of numerical models are outlined in [Section 5.5](#), and the results obtained from the extensive parametric numerical analyses performed in this study are expatiated in [Section 5.6](#).

5.3 Buckling Capacity of Flat Plates

For the general case of simply supported flat plates subjected to uniform axial compression (as illustrated in Figure 5-1), the following fourth order differential equation is required to describe the large deflections in the plate [39, 40]:

$$\frac{\partial^4 \omega}{\partial x^4} + 2 \frac{\partial^4 \omega}{\partial x^2 \partial y^2} + \frac{\partial^4 \omega}{\partial y^4} = \frac{1}{D} \left(-N_u \frac{\partial^2 \omega}{\partial x^2} \right) \quad (5-1)$$

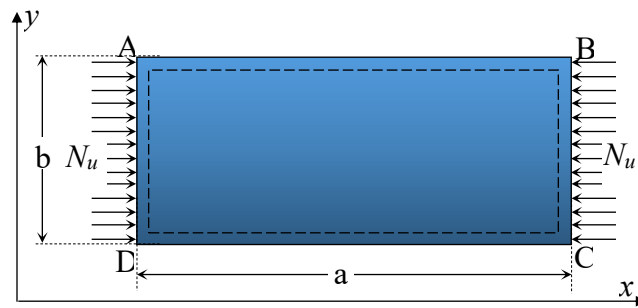


Figure 5-1: Schematic of flat plate under uniform axial compression

where N_u is the longitudinally-applied uniform compressive force.

The function, $\omega(x,y)$ for the out-of-plane deflection across the surface area of the plate, which satisfies the simply-supported boundary conditions, can be assumed as a product of two harmonic functions:

$$\omega(x,y) = \sum_{m=1}^{\infty} \sum_{n=1}^{\infty} \omega_{mn} \sin \frac{m\pi x}{a} \sin \frac{n\pi y}{b} \quad (5-2)$$

where m and n are the number of half-sine waves in the x - and y -directions respectively. a and b represent the dimensions of the plate in the x - and y -directions respectively. The amplitude of the out-of-plane deflection is represented by ω_{mn} [41].

Flat plates and plated elements are usually idealized as a continuum of longitudinal (x -direction) strips and transverse (y -direction) ties with a finite width, and each longitudinal strip is assumed

to behave like an individual column on an elastic foundation. Tensile membrane stresses are developed in the transverse ties which induce a resistance effect against the mid-length out-of-plane deflection of the longitudinal strips depending on the width and thickness of the plate. Thus, a shorter width and/or a larger thickness will increase the buckling resistance of the plate, and vice versa.

The mode of out-of-plane deflection that occurs in the plate due to buckling indicates that the lateral restraint provided by the transverse ties reduces from the longitudinal edges towards the center of the plate. Thus, once the critical buckling stress is reached, the stress distribution across the width of the plate becomes nonuniform and most of the post-buckling strength is derived from the longitudinal strips closer to the edges of the plate.

There are typically two approaches that are employed in the evaluation of the buckling capacity of uniformly compressed simply-supported plates: the *effective width* concept and the *ultimate stress* concept. Based on the effective width concept, as the load applied to a uniformly compressed and simply-supported flat plate is increased beyond the critical buckling stress, the nonuniformity of the stress distribution across the width of the plate continues to increase, and more of the load in the middle longitudinal strips is transferred to the edges. The plate is, therefore, able to resist the applied loads in the stable post-buckling range until failure occurs at the load at which the yield stress of the plate material is reached in the two edge strips of equal width. This approach, therefore, assumes that the load at failure is entirely carried by the edge strips where the applied stress has attained the yield stress of the material while the rest of the plate remains unloaded. The effective width, b_e , is given by the widths of the load-carrying edge strips and may be derived as [1]:

$$\frac{b_e}{b} = \frac{N_u}{bt\sigma_y} \quad (5-3)$$

where N_u is the uniform compressive axial force, σ_y is the yield stress of the material, b is the actual (unreduced) width of the plate, and t is the thickness of the plate.

Since the effective width is directly related to the stress distribution across the width of the buckled plate, the effective width ratio, b_e/b , can be expressed in terms of the elastic critical buckling stress, σ_{cr} , and the yield strength, σ_y , of the plate material as:

$$\frac{b_e}{b} = \sqrt{\frac{\sigma_{cr}}{\sigma_y}} \quad (5-4)$$

By introducing an arbitrary slenderness ratio coefficient, β , which is related to the width-to-thickness (b/t) ratio, material yield strength, σ_y , and elastic modulus, E , as follows:

$$\beta = \frac{b}{t} \sqrt{\frac{\sigma_y}{E}} \quad (5-5)$$

The critical buckling stress-to-yield stress ratio (σ_{cr}/σ_y) can be expressed in terms of the slenderness parameter:

$$\frac{\sigma_{cr}}{\sigma_y} = \frac{4\pi^2}{12(1-\nu^2)} \frac{E}{\sigma_y} \left(\frac{t}{b}\right)^2 = \frac{\pi^2}{3(1-\nu^2)\beta^2} \quad (5-6)$$

To determine the load-carrying capacity of a flat plate, semi-empirical methods typically employ the *ultimate strength* concept whereby the plate is measured based on the average stress at failure and the actual (unreduced) width of the plate. The ultimate stress is defined by the average direct stress supported by the plate at failure and is identified as the peak point (or maximum stress reached) on the load-end shortening curve. The average strains (defined as the plate end-shortening distance) which are coincident with the ultimate strength of the plate may be regarded as the *local buckling strain* or *deformation capacity* of the plate [19].

Based on the results obtained from a series of experiments on cold-formed lipped channel steel sections, Winter [42] derived the following empirical formula for the effective width of plated structural steel elements subjected to uniform compression:

$$\frac{b_e}{t} = 1.9 \sqrt{\frac{E}{\sigma_y}} \left(1 - \frac{0.475 t}{b} \sqrt{\frac{E}{\sigma_y}} \right) \quad (5-7)$$

A general approach for assessment of the buckling capacity is to derive median bound analytical models, representing the average curve that fits the envelope of all experimental data points considered, using nonlinear regression techniques. A generalized expression which represents the curve-fitted model of Winter's empirical derivation for the effective width ratio can be written as [43–45]:

$$\frac{b_e}{b} = \frac{\sigma_{ult}}{\sigma_y} = \frac{k_1}{\beta} - \frac{k_2}{\beta^2}, \text{ for } \beta \geq 1 \quad (5-8)$$

where σ_{ult} is the value of the peak stress on the load-end shortening curve and the constants, k_1 and k_2 depend on the plate support and loading conditions (derived by Faulkner [44] as $k_1 = 2.0$ and $k_2 = 1.0$ for simply-supported plates and $k_1 = 2.25$ and $k_2 = 1.25$ for fixedly-supported plates).

Guedes Soares [46] suggested that an improvement of the approximation of the ultimate strength curves can be achieved by applying an uncertainty quantification factor, B_b , and a reduction factor, R_δ , to the generalized model in Eq. (5-8):

$$\frac{b_e}{b} = \left(\frac{k_1}{\beta} - \frac{k_2}{\beta^2} \right) B_b R_\delta \quad (5-9)$$

For practical applications, a realistic estimation of the buckling capacity of actual plates requires a consideration of a myriad of factors including the resultant shear stresses and appropriate shear deformation theory to be applied; the constitutive relationship for the material stress-strain behavior and the applicable hardening law; the existence and extent, as well as distribution, of residual stresses and strains; the yield criterion to be employed; the magnitude and distribution of initial geometric imperfections; and various configurations of loading and support conditions. The numerous factors entail a high level of complex analyses which invariably necessitate the

adoption of parametric semi-empirical approaches for evaluating the buckling response of flat plates; achieved either through extensive experimental testing or, as adopted for the purpose of this study, highly-advanced nonlinear numerical collapse analysis techniques [3, 47–49].

5.4 Proposed Material Model

Bezkorovainy *et al.* [14] observed that the strength curves obtained using Winter's empirical formula generally lie below the strength curves based on an extrapolated approximation of the material stress-strain approximation over the full range of strains using the ROE. They, therefore, affirmed that the ultimate strength of uniformly-compressed flat plates may be significantly overestimated if the material model is defined by extrapolating the ROE beyond the 0.2% plastic strain and corresponding equivalent yield stress. For their study on metallic alloys with nonlinear stress-strain curves (such as aluminum and stainless steel), Bezkorovainy *et al.* [14] adopted the Rasmussen stress-strain model [33] for the formulation of a generalized Winter-curve based on two material-dependent parameters: e and n : where $e = \sigma_{0.2}/E_0$ and n is the ROE sharpness parameter. They also applied Rasmussen's empirically-derived expressions for deriving the second-stage strain-hardening exponent, m , the ultimate total strain, ε_u , and the ultimate tensile strength, σ_u , using the ROE parameters, and opined that, even though the empirical expressions were derived based on the measurement of the stress-strain curves of stainless-steel alloys, the generalized Winter curve expressions developed using the Rasmussen stress-strain model can provide a reasonable approximation of the strength curves of other types of nonlinear materials. Based on the proposed stress-strain model in this paper two model parameters, which are associated with the strain-hardening characteristics and the shape of the material stress-strain curve, are defined and a parametric study is conducted to investigate the effect of variation of material properties on the buckling capacity and post-buckling behavior of flat uniformly-compressed simply-supported plates.

5.4.1 Model definition

The proposed material stress-strain model, herein referred to as the ‘*Ndubuaku model*’ is defined based on the true stress-true strain space of a metallic material. The basic form of the proposed equation is defined using a 2D orthogonal x - and y -coordinate system such that:

$$y = f(x) = x^{\left(\frac{1}{x}\right)} \quad (5-10)$$

The function, $f(x)$, has a real and imaginary part, and the real domain for $f(x)$ can only be obtained for $x \in \mathbb{X}$ where \mathbb{X} is the set of all positive real numbers:

$$\mathbb{X} = \{x | x \in \mathbb{R} : x > 0\} \quad (5-11)$$

The range, \mathbb{Y} , is the set $f(\mathbb{X})$, which satisfies:

$$\mathbb{Y} = \left\{ y \mid y \in \mathbb{R} : 0 < y \leq e^{\left(\frac{1}{e}\right)} \right\} \quad (5-12)$$

To define the stress-strain relationship within the possible range for \mathbb{Y} , the full range of stresses and strains is normalized over the entire nonlinear portion of the stress-strain curve, i.e. between the proportionality limit stress and ultimate total stress (on the y -axis) and the proportionality limit strain and ultimate total strain (on the x -axis).

The stress ratio, σ_R , is therefore defined as the ratio of the true plastic stress magnitude (stresses beyond the proportionality limit stress) and the full plastic stress range (the difference between the ultimate stress, σ_u , and the proportionality limit stress, σ_{pl}):

$$\sigma_R = \frac{(\sigma - \sigma_{pl})}{(\sigma_u - \sigma_{pl})} \quad (5-13)$$

Likewise, the strain ratio, ε_R , is defined as the ratio of the true plastic strain magnitude (strains beyond the proportionality limit strain) and the full plastic strain range (the difference between the ultimate strain, ε_u , and the proportionality limit strain, ε_{pl}):

$$\varepsilon_R = \frac{(\varepsilon - \varepsilon_{pl})}{(\varepsilon_u - \varepsilon_{pl})} \quad (5-14)$$

Based on the above-defined expression in Eq. (5-10), the basic form of the proposed stress-strain model can therefore be written as:

$$\sigma_R = \varepsilon_R^{\frac{1}{\varepsilon_R}} \quad (5-15)$$

To control the shape of the stress-strain curve, two constitutive model constants are applied to the stress-strain expression. The first constant (herein referred to as the ‘*Ndubuaku knee parameter*’) is applied directly as an exponent of the strain ratio. The second constant (herein referred to as the ‘*Ndubuaku heel parameter*’) is applied as an index to the strain-ratio inverse. The final form of the proposed stress-strain model thus defines the stress ratio as a function of the strain ratio based on the following mathematical expression:

$$\sigma_R = \varepsilon_R^{K_{NM}} \cdot \left(\frac{1}{\varepsilon_R}\right)^{H_{NM}} \quad (5-16)$$

An illustration of the effect of variation of the constitutive model constants on the proposed model is shown by the nominal plots of the stress ratio, σ_R (on the y-axis) versus the strain ratio, ε_R (on the x-axis) in Figure 5-2 and Figure 5-3.

The transition between a fully concave curve and a fully convex curve (such as the lowest curve and the highest curve respectively in Figure 5-2) is defined by a straight line which may be derived by Eq. (5-16) such that: $K_{NM} = 1$ and $H_{NM} \rightarrow 0$. For a convex curve, $K_{NM} < 1$ whereas, $K_{NM} > 1$ for a concave curve.

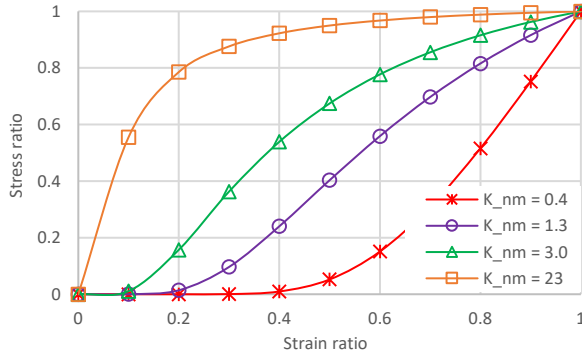


Figure 5-2: Plot of stress ratio to strain ratio
($H_{NM} = 1.3$; K_{NM} - varied)

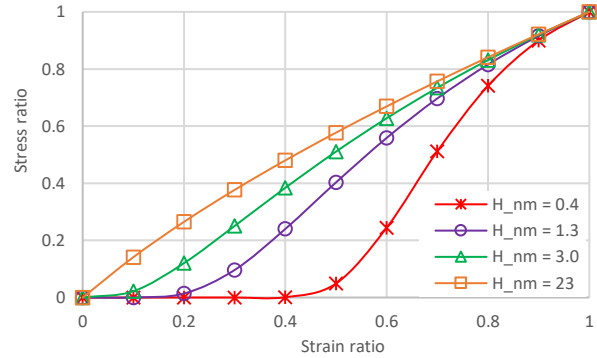


Figure 5-3: Plot of stress ratio to strain ratio
($K_{NM} = 1.3$; H_{NM} - varied)

However, the stress-strain curve is idealized as a combination of a ‘heel’ (representing the lower concave region or yield plateau) and a ‘knee’ (representing the upper convex region). From an observation of the interaction between the model parameters in plots in Figure 5-2 and Figure 5-3, increasing the magnitude of the “knee” parameter, K_{NM} , increases the convexity of the upper convex portion of the stress-strain curve and vice versa, while an increase in the “heel” parameter, H_{NM} , reduces the concavity of the lower concave portion of the stress-strain curve. The two parameters are also observed to be somewhat interrelated as a reduction of K_{NM} contributes to the effect of a reduction of H_{NM} and vice versa. Also, an increase in the value of K_{NM} contributes to the effect of an increase in the value of H_{NM} and vice versa.

5.4.2 Inverted form of the proposed model

For most of the existing stress-strain models, the strain is expressed as a function of the stress hence, graphical or iterative numerical procedures are typically employed for inversion of nonlinear expressions such that the stress is expressed as a function of the strain; especially in the case of the advanced models. However, due to associated computational demands and occasional numerical convergence problems, iterative procedures are generally considered to be undesirable. It is therefore advantageous to present a closed-form inversion of the proposed model.

In the proposed equation, the true stress is originally expressed as a function of the true strain using a power equation in which the exponent of the strain is also a linear function of the strain.

The inverted form of the proposed model is formulated using the *Product log* function (also referred to as the *Omega* function).

As in the case of the *Natural log* function, which provides a solution to an exponential relationship as follows:

$$y = e^x \Leftrightarrow \ln(y) = x \quad (5-17)$$

The *Product log* function is similarly expressed in the following form:

$$y = xe^x \Leftrightarrow W(y) = x \quad (5-18)$$

The closed form inversion of the proposed model can therefore be derived from the original expression as follows:

$$\begin{aligned}
\sigma_R &= \varepsilon_R^{K_{NM}} \cdot \varepsilon_R^{-(H_{NM})} \\
\ln(\sigma_R) &= \ln\left(\varepsilon_R^{K_{NM}} \cdot \varepsilon_R^{-(H_{NM})}\right) \\
\ln(\sigma_R) &= K_{NM} \cdot \varepsilon_R^{-(H_{NM})} \cdot \ln(\varepsilon_R) \\
\ln(\sigma_R) &= K_{NM} \cdot e^{-(H_{NM})} \cdot \ln(\varepsilon_R) \cdot \ln(\varepsilon_R) \\
-(H_{NM}) \cdot \ln(\sigma_R) &= -(H_{NM}) \cdot K_{NM} \cdot e^{-(H_{NM})} \cdot \ln(\varepsilon_R) \cdot \ln(\varepsilon_R) \\
-\left(\frac{H_{NM}}{K_{NM}}\right) \cdot \ln(\sigma_R) &= -(H_{NM}) \cdot \ln(\varepsilon_R) \cdot e^{-(H_{NM})} \cdot \ln(\varepsilon_R) \\
-(H_{NM}) \cdot \ln(\varepsilon_R) &= W\left[-\left(\frac{H_{NM}}{K_{NM}}\right) \cdot \ln(\sigma_R)\right] \\
\ln(\varepsilon_R) &= -\left(\frac{1}{H_{NM}}\right) \cdot W\left[-\left(\frac{H_{NM}}{K_{NM}}\right) \cdot \ln(\sigma_R)\right] \\
\varepsilon_R &= e^{-\left(\frac{1}{H_{NM}}\right) \cdot W\left[-\left(\frac{H_{NM}}{K_{NM}}\right) \cdot \ln(\sigma_R)\right]} \quad (5-19)
\end{aligned}$$

5.4.3 Derivation of model constants

To achieve a reasonably accurate representation of the stress-strain relationship of a material over the full range of strains, it may necessary to define “*control points*” along the stress-strain curve. The control points are stress and corresponding strain values which, if known, can be used to determine the specific values of the constitutive model constants that characterize a stress-strain curve that passes exactly through the predefined points.

Firstly, the *knee* parameter is expressed as a function of the stress ratio, the strain ratio, and the *heel* parameter as follows:

$$\begin{aligned}
 \sigma_R &= \varepsilon_R^{K_{NM}} \cdot \varepsilon_R^{-(H_{NM})} \\
 \ln(\sigma_R) &= K_{NM} \cdot \varepsilon_R^{-(H_{NM})} \cdot \ln(\varepsilon_R) \\
 K_{NM} &= \frac{\ln(\sigma_R)}{\ln(\varepsilon_R)} \cdot \left(\frac{1}{\varepsilon_R^{-(H_{NM})}} \right) \\
 K_{NM} &= \frac{\varepsilon_R^{(H_{NM})} \cdot \ln(\sigma_R)}{\ln(\varepsilon_R)}
 \end{aligned} \tag{5-20}$$

Next, two stress control points (σ_1 and σ_2) and two strain control points (ε_1 and ε_2) are defined.

The corresponding stress ratio expressions for the stress control points are thus defined as:

$$\sigma_{R1} = \frac{\sigma_1 - \sigma_{pl}}{\sigma_u - \sigma_{pl}} \quad \text{and} \quad \sigma_{R2} = \frac{\sigma_2 - \sigma_{pl}}{\sigma_u - \sigma_{pl}} \tag{5-21}$$

Likewise, the corresponding strain ratio expressions for the strain control points are defined as:

$$\varepsilon_{R1} = \frac{\varepsilon_1 - \varepsilon_{pl}}{\varepsilon_u - \varepsilon_{pl}} \quad \text{and} \quad \varepsilon_{R2} = \frac{\varepsilon_2 - \varepsilon_{pl}}{\varepsilon_u - \varepsilon_{pl}} \tag{5-22}$$

By equating the *knee* parameter for the two defined control points, an elimination procedure is used to express the *heel* parameter as a function of the stress and strain ratio expressions in Eqs. (5-21) and (5-22):

$$\begin{aligned}
\frac{\varepsilon_{R1}^{(H_{NM})} \cdot \ln(\sigma_{R1})}{\ln(\varepsilon_{R1})} &= \frac{\varepsilon_{R2}^{(H_{NM})} \cdot \ln(\sigma_{R2})}{\ln(\varepsilon_{R2})} \\
\frac{\varepsilon_{R1}^{(H_{NM})}}{\varepsilon_{R2}^{(H_{NM})}} &= \frac{\ln(\varepsilon_{R1}) \cdot \ln(\sigma_{R2})}{\ln(\sigma_{R1}) \cdot \ln(\varepsilon_{R2})} \\
\left(\frac{\varepsilon_{R1}}{\varepsilon_{R2}}\right)^{H_{NM}} &= \frac{\ln(\varepsilon_{R1}) \cdot \ln(\sigma_{R2})}{\ln(\sigma_{R1}) \cdot \ln(\varepsilon_{R2})} \\
\ln \left[\left(\frac{\varepsilon_{R1}}{\varepsilon_{R2}}\right)^{H_{NM}} \right] &= \ln \left[\frac{\ln(\varepsilon_{R1}) \cdot \ln(\sigma_{R2})}{\ln(\sigma_{R1}) \cdot \ln(\varepsilon_{R2})} \right] \\
H_{NM} \cdot [\ln(\varepsilon_{R1}) - \ln(\varepsilon_{R2})] &= \ln \left[\frac{\ln(\varepsilon_{R1}) \cdot \ln(\sigma_{R2})}{\ln(\sigma_{R1}) \cdot \ln(\varepsilon_{R2})} \right] \\
H_{NM} &= \frac{\ln \left[\frac{\ln(\varepsilon_{R1}) \cdot \ln(\sigma_{R2})}{\ln(\sigma_{R1}) \cdot \ln(\varepsilon_{R2})} \right]}{[\ln(\varepsilon_{R1}) - \ln(\varepsilon_{R2})]} \tag{5-23}
\end{aligned}$$

Based on the above-detailed derivations, a straightforward process for determining the specific values of the constitutive model constants for respective stress-strain curves involves firstly using the expression in Eq. (5-23) to determine the value of the *heel* parameter and then applying the result to obtain the *knee* parameter in Eq. (5-20).

5.5 Numerical Simulation of Plate Buckling

5.5.1 Geometric properties/ support conditions

The plates were modeled as unstiffened plates with simply-supported boundary conditions on all the edges. There are essentially two alternatives for simply-supported boundary conditions that may be applied to flat plate numerical models: one case restricts in-plane displacement of the unloaded longitudinal edges while the second alternative allows in-plane displacement of the unloaded edges. Results of previous studies however indicate that, for real applications, the ultimate compressive strength of the plate is similar for the two cases; provided the longitudinal edge is kept straight throughout the load application [48, 50, 51].

For the purpose of this study, the longitudinal edges of the plate models were prevented from in-plane displacement while rotation about the two axes perpendicular to each edge was also prevented at all the four edges; thereby ensuring straightness of all the plate edges during load application.

For computational efficiency, only half of the plate models was modeled and to obtain the buckling modes of the plate models, an elastic buckling (linear perturbation) analysis was implemented by applying a unit edge load to the plate in the longitudinal direction. Thereafter, a controlled edge displacement approach was used to obtain the mechanical response of the plate models in the subsequent nonlinear analysis steps.

Based on the results of the elastic buckling analysis, the undulations resulting from the lower buckling modes of the plate models were observed to be symmetric about the centerline of the plate in the longitudinal direction hence only half of the width, but the full length of the plates, was modeled (Figure 5-4).

The full width of the plate models was fixed at 800 mm while three variations of the aspect ratio (1, 2, and 3) were applied. Also, four thickness variations (6 mm, 9 mm, 15 mm, and 27 mm) were used for the plates. However, consistent with the theoretical postulations for the elastic critical buckling stress of a flat simply-supported uniformly-compressed plate, the ultimate compressive strengths of the plate models were observed to be similar for the three different aspect ratios, provided the ratio of the number of buckling waves in the longitudinal direction (m) to the number of buckling waves in the transverse direction (n) is equal to the aspect ratio of the plate. Hence, only results obtained for the plates with an aspect ratio of 3 are presented in this paper as these were observed to provide the best consistency in results.

The four-node reduced integration shell elements (S4R) with hourglass control in the ABAQUS element library were used for all the analyses; enabling up to five integration points through the thickness of the plate models. A mesh convergence study was conducted to establish the optimum number of elements required for the study and a mesh size of 16 was accordingly applied to all the plate models; implying approximately 25 elements in the transverse direction and 150 elements in the longitudinal direction.

A pictorial representation of the meshed plate model implemented in ABAQUS, illustrating the geometric and edge support details, is shown in Figure 5-4.

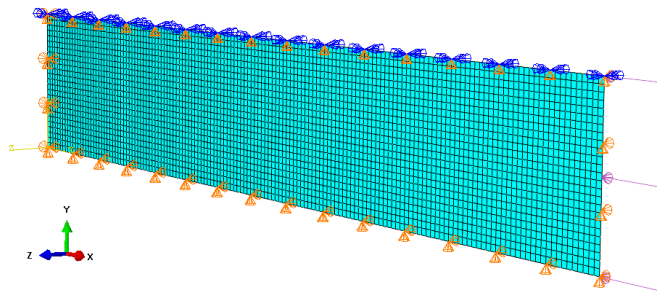


Figure 5-4: Plate model geometric and edge support details

As indicated in Figure 5-4, the two transverse edges and the bottom longitudinal edge of the plate are simply supported. However, translation in the x -direction is only allowed at one of the edges (where the load or displacement is applied) and at the two longitudinal edges (top and bottom). At the top longitudinal edge, the centerline symmetry condition was achieved by restricting translation in the y -direction and rotations about the x - and z -directions.

5.5.2 Material properties

For CHT materials, it is usually common in practice to determine the yield strength from the stress-strain curve based on an equivalent yield stress corresponding to either the 0.2% plastic strain ($\sigma_{p,0.2}$) as prescribed by the EN 1993-1-4 stainless steels standard [52] or the 0.5% total strain ($\sigma_{0.5}$) as prescribed by the API 5L pipeline steels standard [53]. Comparison of the differences in the values obtained using the two equivalent stress approaches for three different possible material curves is depicted in Figure 5-5.

The two equivalent stress approaches predict the values of the yield stress such that,

If :

$$\sigma_y = 0.003 \times E_0 \quad ; \quad \sigma_{p,0.2} = \sigma_{0.5}$$

$$\sigma_y < 0.003 \times E_0 \quad ; \quad \sigma_{p,0.2} < \sigma_{0.5}$$

$$\sigma_y > 0.003 \times E_0 \quad ; \quad \sigma_{p,0.2} > \sigma_{0.5}$$

where E_0 is Young's Modulus and σ_y is the value of the yield stress. $\sigma_{p,0.2}$ predicts a lesser value for the equivalent yield stress than $\sigma_{0.5}$ when the yield stress is less than $0.003 \times E_0$, and predicts a greater value for the equivalent yield stress than $\sigma_{0.5}$ when the yield stress is greater than $0.003 \times E_0$.

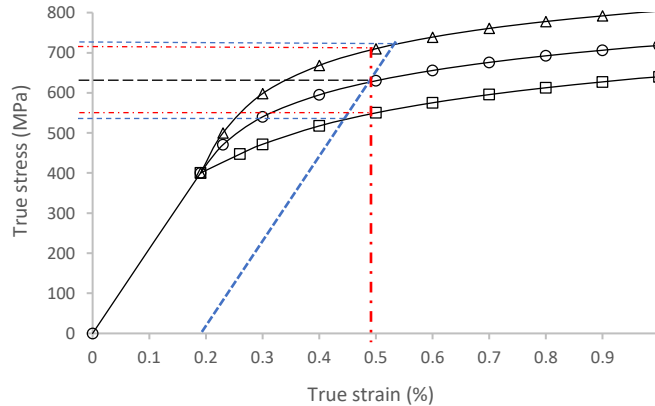


Figure 5-5: Comparison of equivalent stress approaches

The plot presented in Figure 5-5 comprises the idealized true stress vs true strain plots for three different materials with the same elastic modulus (205800 MPa) and proportionality limit stress (400 MPa). The stress-strain curves for the three materials are indicated by the black solid lines with hollow square, hollow circular, and hollow triangular markers. The equivalent yield stresses corresponding to the 0.5% total strain ($\sigma_{0.5}$) are indicated using the dotted red lines while the equivalent yield stresses corresponding to the 0.2% plastic strain ($\sigma_{p,0.2}$) are indicated using the dotted blue lines. The horizontal dotted black line indicates the yield stress at which the values approximated based on both equivalent yield stress approaches coincide (equals $0.003 \times E_0 = 617.4$ MPa).

The magnitude of the difference between the equivalent stress values obtained using the two approaches is dependent on the slope of the portion of the stress-strain curve between the two points. A steeper slope will yield a greater magnitude and vice versa.

The concept on which the proposed material stress-strain model is based is the selection of “control points” which are essentially defined by the total strains and corresponding stress values. Hence, the 0.5% total strain method was selected for this study to maintain

correspondence with the “control point” concept of the presented material model. Also, the analogy of the equivalent stress methods presented in Figure 5-5 indicates that the degree of conservativeness of the buckling capacity results obtained using either method is dependent on the strain-hardening properties of the portion of the stress-strain curve between the approximated yield stress values obtained using the two methods. Recognizing this limitation of irregularity in the implementation of the equivalent stress methods, this study aims to present a methodology for representing the material stress-strain relationship which is less dependent on the equivalent yield stress but more focused on an overall characterization of the nonlinear portion of the stress-strain curve, starting at the proportionality limit stress.

To investigate the effect of material stress-strain characteristics on the buckling performance of the modeled plates, it was necessary to generate a significant number of idealized stress-strain curves hence, nine different families of stress-strain curves were created: one family comprised five different bilinear curves with the same proportionality limit stress but varying ultimate tensile strengths (including one elastic-perfectly plastic material), four other families comprised yield plateau type (YPT) materials with different variations in the length of the yield plateau and magnitude of ultimate stress, and the last four families comprised CHT materials with different variations in the proportionality limit stress, yield stress, and ultimate stress. A total of 37 stress-strain curves were thus created using the proposed stress-strain expressions in Eqs. (5-16) and (5-19), and applying the control-point expressions in Eqs. (5-20) – (5-23).

Based on the good agreement observed in Rasmussen *et al.* [13] between experimental tests and FE analyses of uniformly-compressed simply-supported flat plates, the standard multilinear material definition facility in ABAQUS was used to specify the material stress-strain relationship for each plate model; assuming isotropic hardening plasticity. The Poisson’s ratio and Young’s modulus were fixed as 0.3 and 205800 MPa respectively for all the analyses.

5.5.3 Imperfection modeling

For this study, the initial imperfection was modeled such that the number of half-sine waves in the transverse and longitudinal directions of the half-width plate models was assumed to be 1 and 3 respectively (Figure 5-6). The average model of Smith *et al.* [54] was used to determine the

maximum amplitude of the initial imperfection and the plates were assumed to be free of residual stresses.

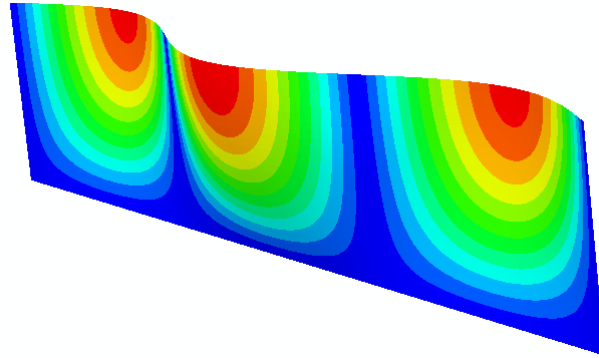


Figure 5-6: Elastic buckling mode for initial imperfection

5.6 Results and Discussions

To determine the maximum load-carrying capacity of the plates, load vs. axial shortening curves were plotted using a spreadsheet application based on the values of the average stress applied on the transverse surface of the plate vs. the values of the ratio between in-plane longitudinal shortening due to applied loading and the original length of the plate.

The load vs. axial shortening relationship between the models in each family of stress-strain curves was observed to be influenced by the relationship between the proportionality limit stress, the 0.5% equivalent yield stress, and the ultimate stress of the material. Each family of curves was observed to exhibit one of three distinct characteristics: a similar response was observed between the bilinear stress-strain curves and the YPT curves while the CHT curves were observed to exhibit either of the other two characteristics. An illustration of the buckling and post-buckling behavior of the plate models for each family of stress-strain curves is presented for three cases of 9 mm-thick plates in Figure 5-7 – Figure 5-9.

The results presented for the YPT and bilinear families in Figure 5-7 indicate that the strain-hardening characteristics play a significant role in the ultimate strength and post-buckling performance of plates. For both cases, the existence of a distinct yield point introduces a sharp deviation in the load-axial deformation path at the end of the elastic limit such that significantly

more deformation is experienced in the yielded portions of the plate for a relatively slight increase in applied stress. The implication is that if the critical buckling stress is reached before the yield stress of the material as is typically the case of slender plates, the ultimate compressive strength of the plate is governed by the yield stress and plastic flow of the edge longitudinal strips and since the effective width of the plate in the post-buckling range is directly proportional to the thickness of the plates (as previously indicated in Eq. (5-6), a sharp drop is experienced in the load-axial shortening curve immediately the maximum applied average stress is reached. In the case of thicker plates where the yield stress of the material is reached before the critical buckling stress, the post-buckling reserve strength of the plate is higher due to a larger effective width and thus, a more gradual loss of strength is experienced after the maximum stress is reached.

Unlike the load-axial deformation relationship for YPT and bilinear materials, a distinct yield point does not exist in CHT materials hence, the load-axial shortening behavior is influenced by the proportionality limit and strain-hardening characteristics. The load-axial shortening curve for an elastic-perfectly plastic (E-PP) material is included in all the plots to indicate the shared load-deformation path for all the curves and the points of diversion. As shown in Figure 5-8 and Figure 5-9, the point of diversion of the load-axial shortening curves for different materials is observed to be related to the proportionality limit of the material: while the curves in Figure 5-8 have the same proportionality limit and are observed to share a somewhat similar point of diversion analogous to that of the E-PP material, the curves in Figure 5-9 have different proportionality limits and disparate points of diversion in the load-axial shortening curves.

The strain-hardening behavior and equivalent yield stress of the stress-strain curve also impact on the ultimate strength of the plates under uniform axial compression. The curves in Figure 5-8 show a clear difference between the maximum stresses obtained for the different materials indicating that the 0.5% equivalent yield stress has a more significant effect on the ultimate compressive strength of the plates than the proportionality limit stress. For all the materials in Figure 5-9, the proportionality limits are different and the transition of the stress-strain curve from the proportionality limit to the ultimate tensile stress (UTS) alternates at the same equivalent yield stress thus, a smaller disparity is observed between the ultimate strength of the different plates.

The effect of the width-to-thickness ratio and the material stress-strain characteristics on the ultimate strength, σ_{ult} , and strain capacity, ϵ_{ult} , of the plates is illustrated in Figure 5-10 – Figure 5-17.

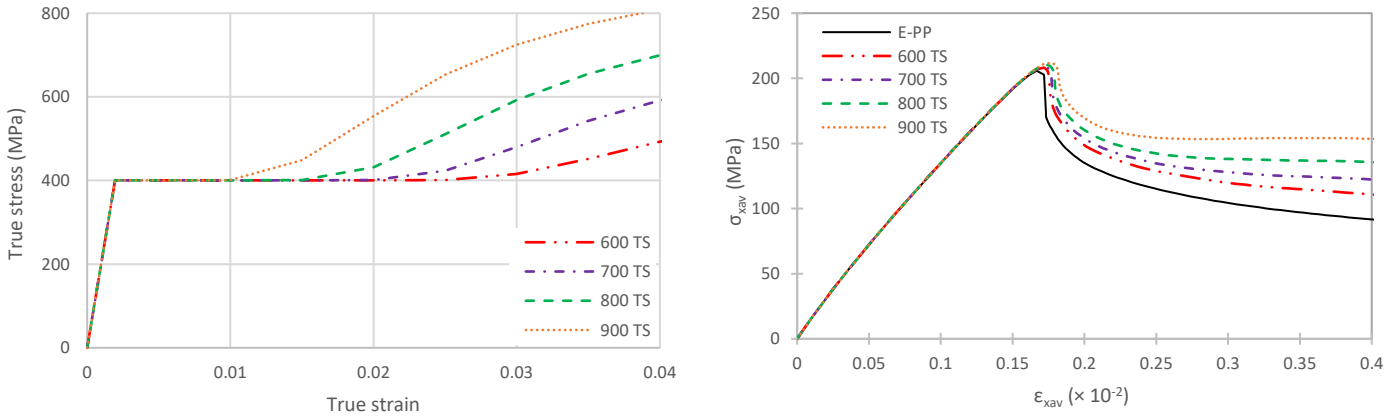


Figure 5-7: YPT curves

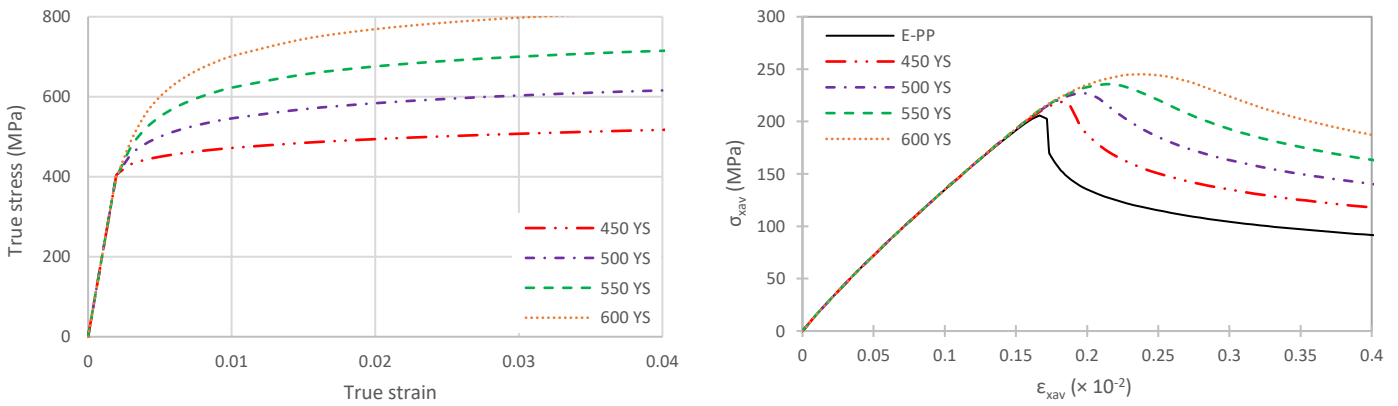


Figure 5-8: CHT curves - class 1

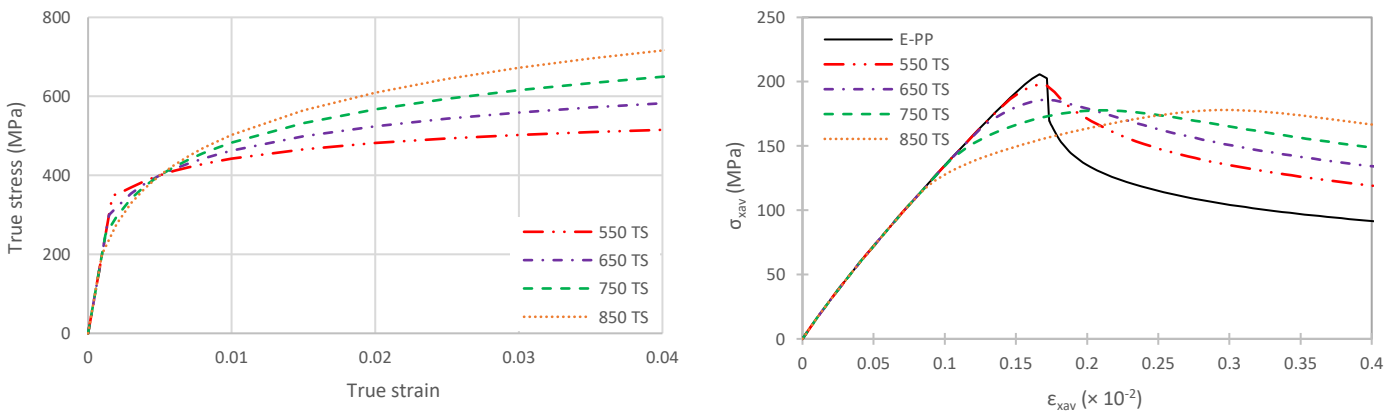
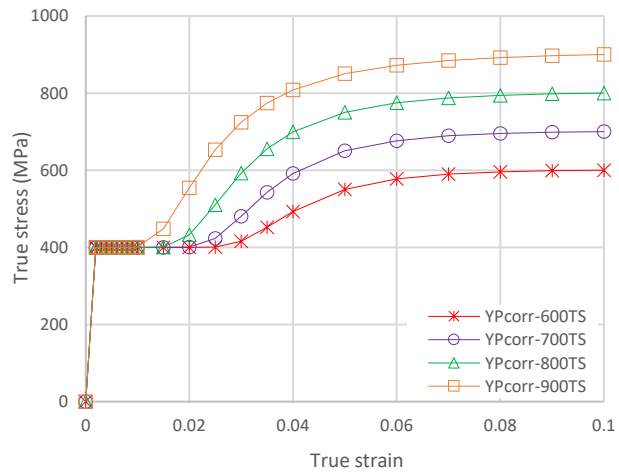
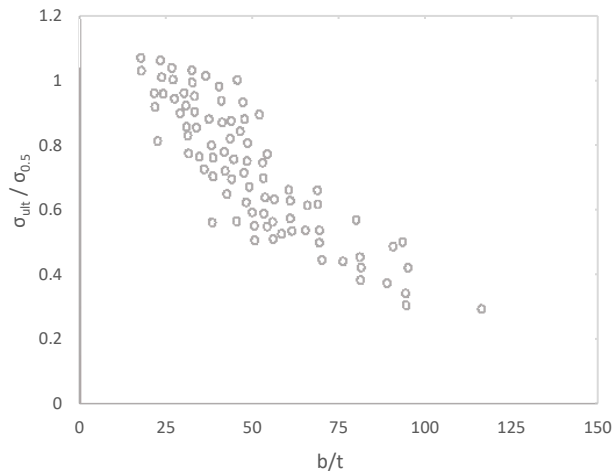


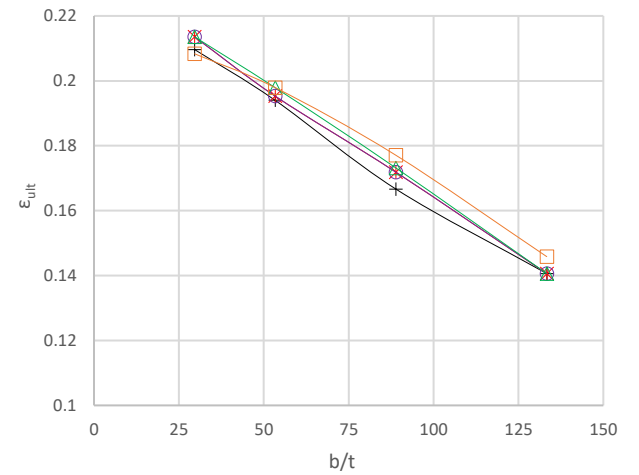
Figure 5-9: CHT curves - class 2



(a) Stress-strain curves

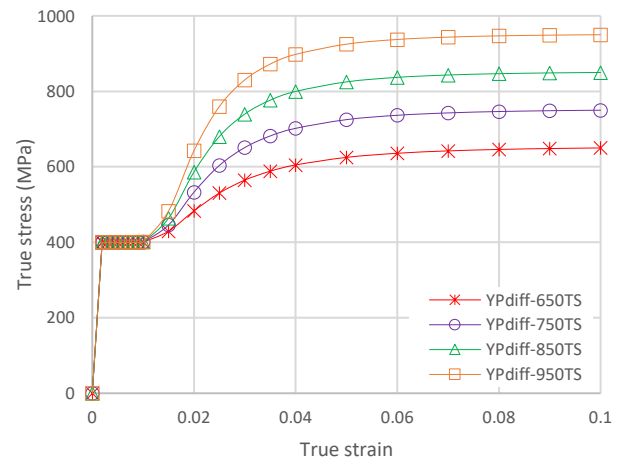


(b) Ultimate strength vs. Slenderness

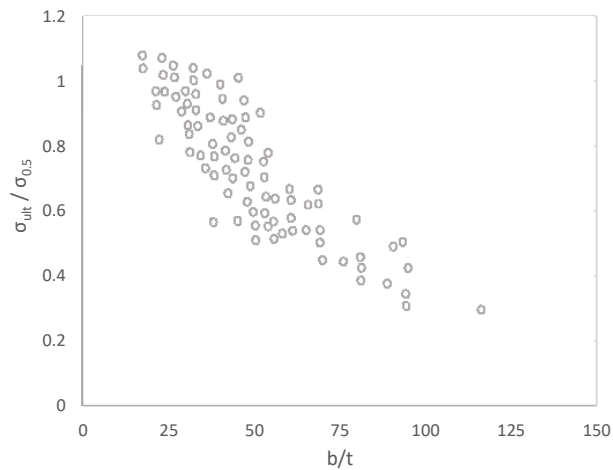


(c) Deformation capacity vs. Slenderness

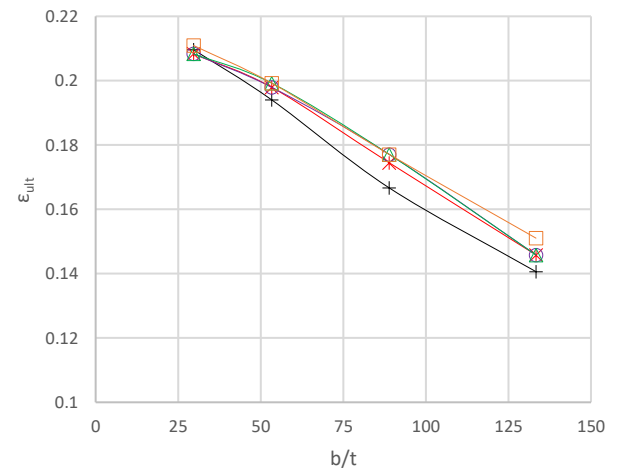
Figure 5-10: Ultimate strength and corresponding strain results for YPT curves with varying lengths of yield plateau and varying UTS



(a) Stress-strain curves

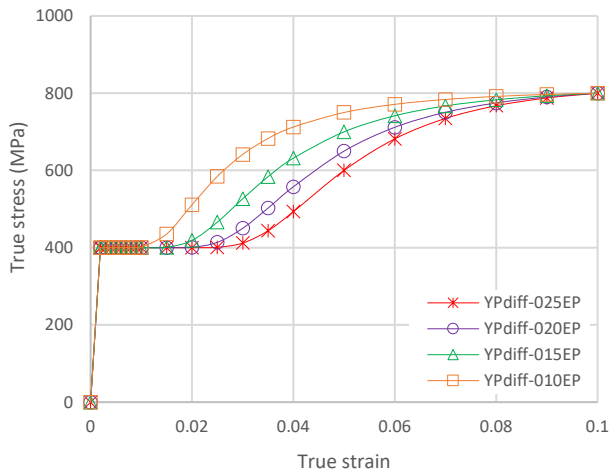


(b) Ultimate strength vs. Slenderness

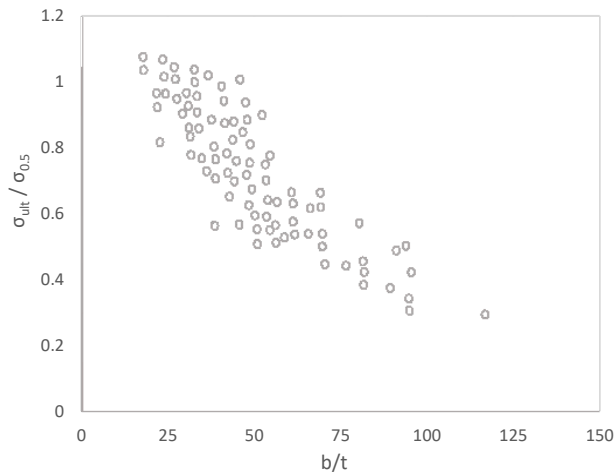


(c) Deformation capacity vs. Slenderness

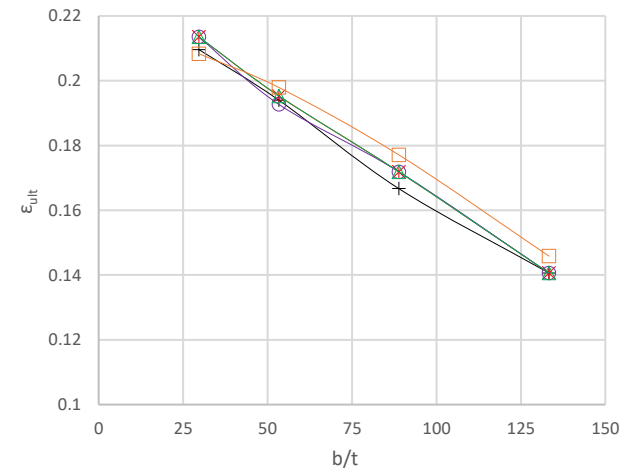
Figure 5-11: Ultimate strength and corresponding strain results for YPT curves with same lengths of yield plateau and varying UTS



(a) Stress-strain curves

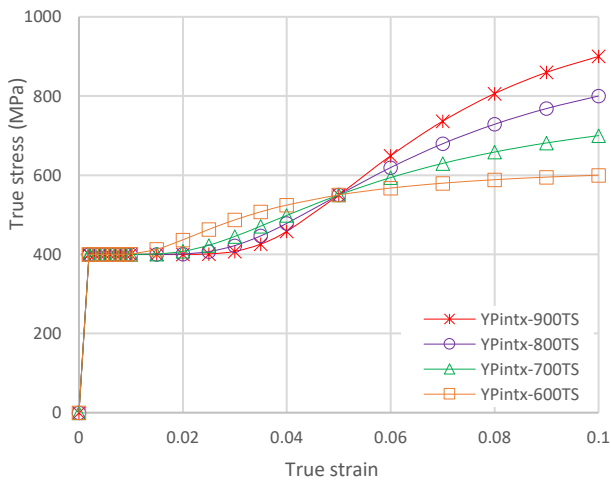


(b) Ultimate strength vs. Slenderness

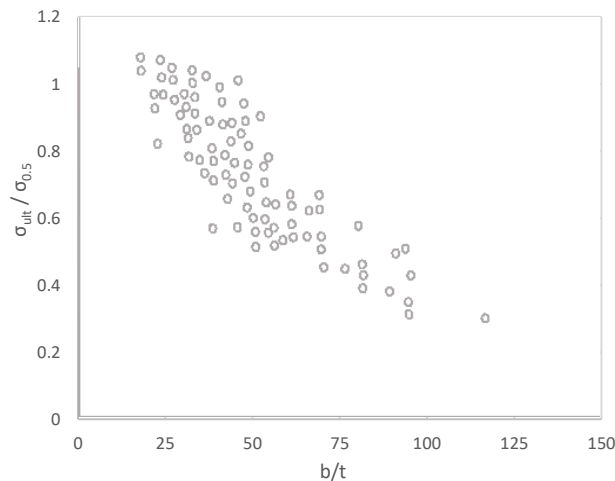


(c) Deformation capacity vs. Slenderness

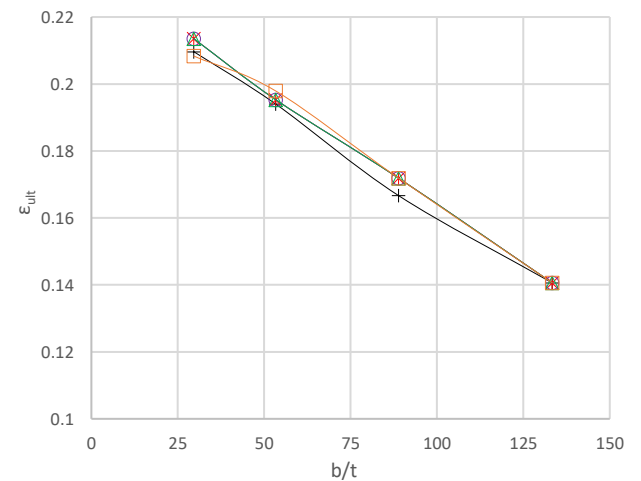
Figure 5-12: Ultimate strength and corresponding strain results for YPT curves with varying lengths of yield plateau and same UTS



(a) Stress-strain curves

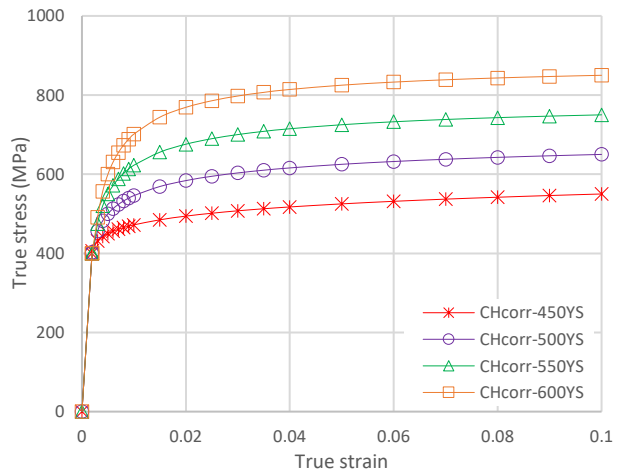


(b) Ultimate strength vs. Slenderness

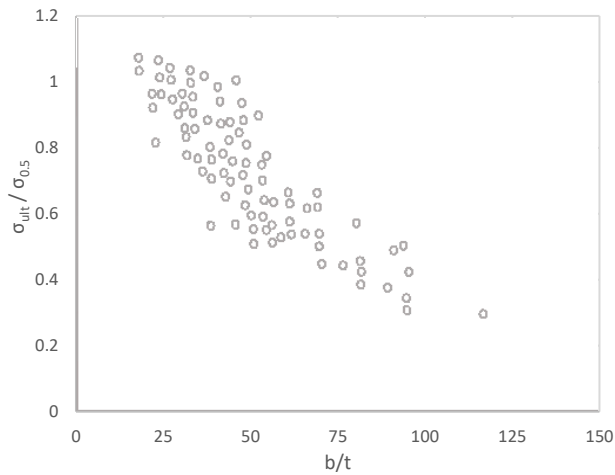


(c) Deformation capacity vs. Slenderness

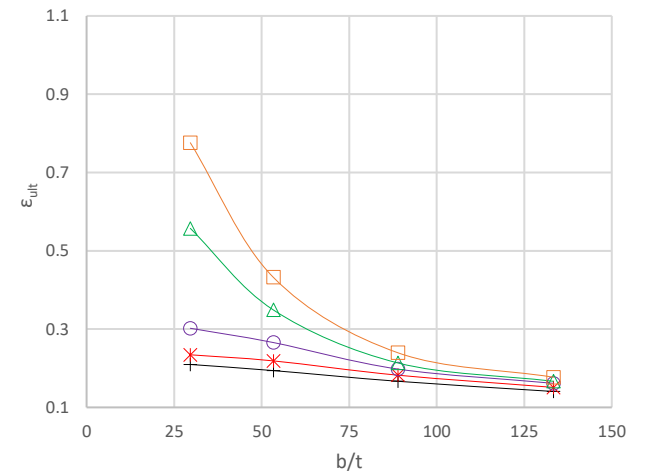
Figure 5-13: Ultimate strength and corresponding strain results for YPT curves with varying YPLs and intersecting strain-hardening



(a) Stress-strain curves

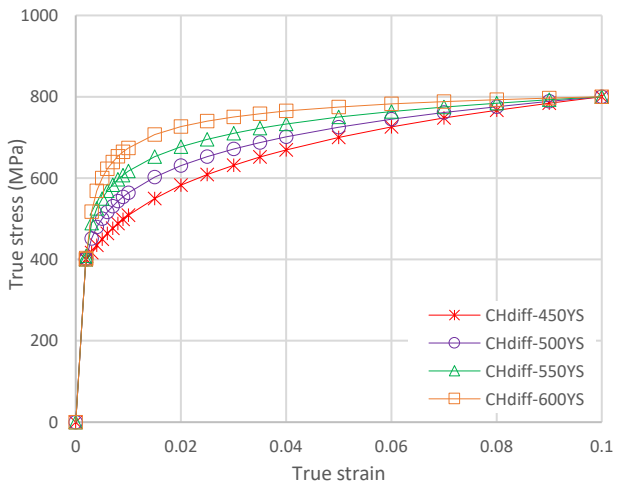


(b) Ultimate strength vs. Slenderness

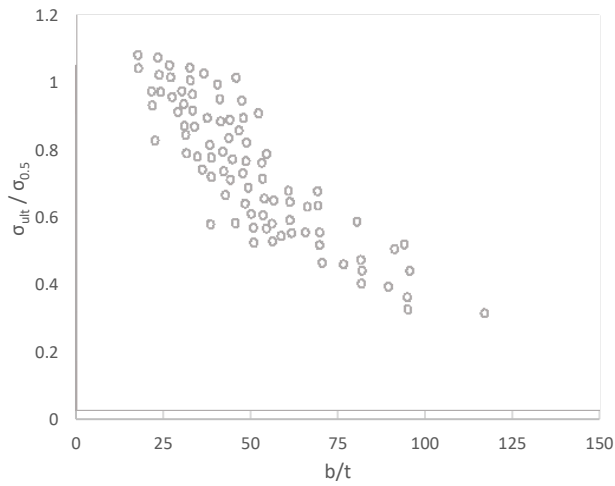


(c) Deformation capacity vs. Slenderness

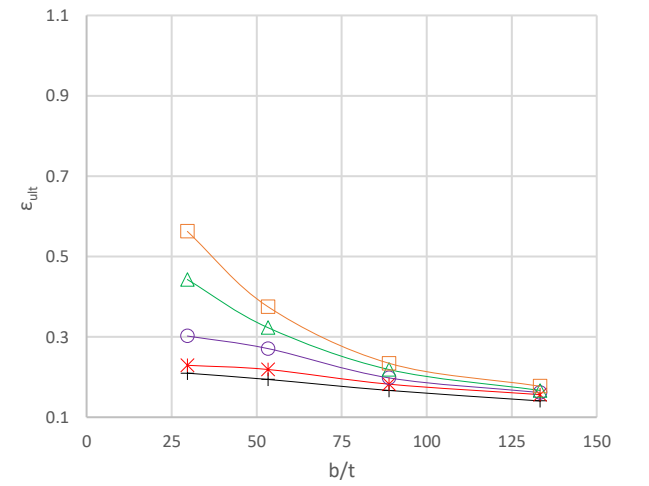
Figure 5-14: Ultimate strength and corresponding strain results for CHT curves with varying equivalent YS and varying UTS



(a) Stress-strain curves

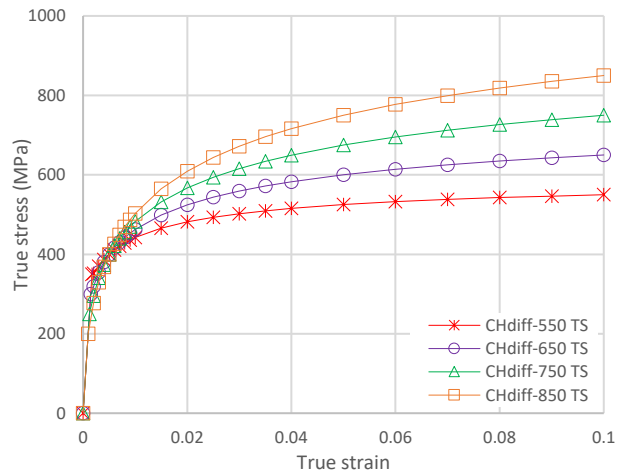


(b) Ultimate strength vs. Slenderness

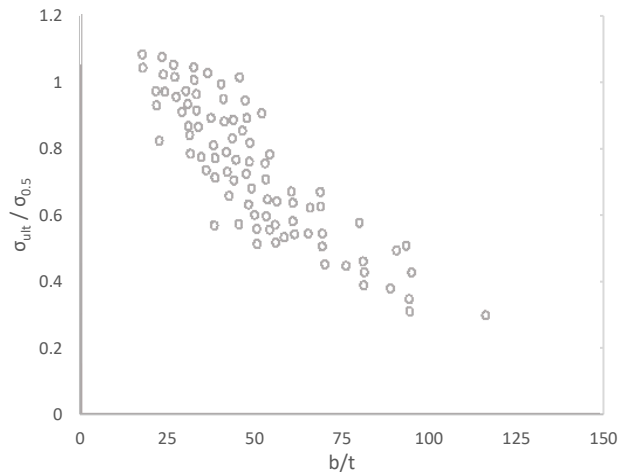


(c) Deformation capacity vs. Slenderness

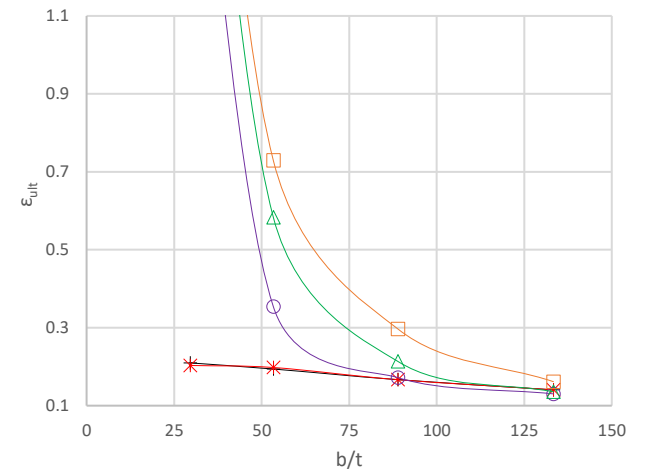
Figure 5-15: Ultimate strength and corresponding strain results for CHT curves with varying equivalent YS and same UTS



(a) Stress-strain curves

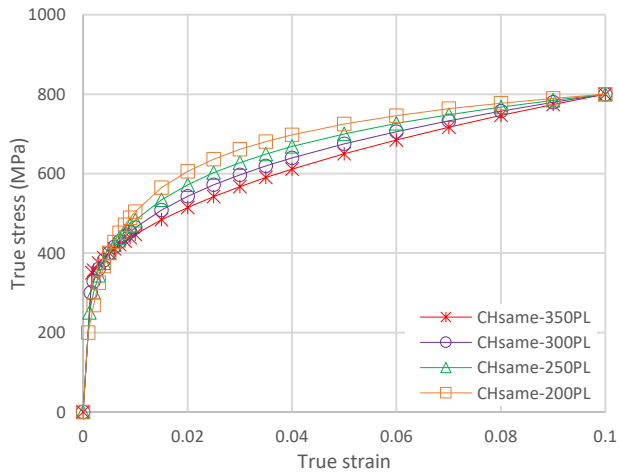


(b) Ultimate strength vs. Slenderness

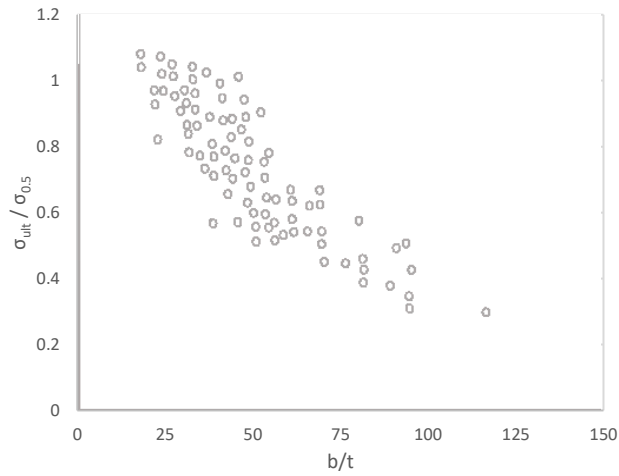


(c) Deformation capacity vs. Slenderness

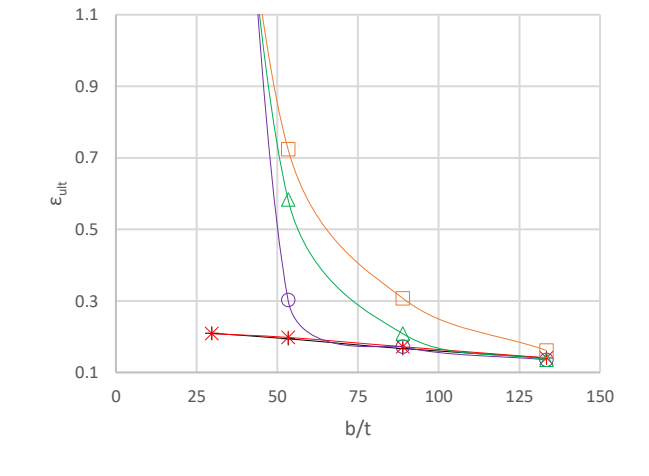
Figure 5-16: Ultimate strength and corresponding strain results for CHT curves same equivalent YS and varying UTS



(a) Stress-strain curves



(b) Ultimate strength vs. Slenderness



(c) Deformation capacity vs. Slenderness

Figure 5-17: Ultimate strength and corresponding strain results for CHT curves with same equivalent YS and same UTS

...

Details of the ‘knee’ and ‘heel’ parameters used to obtain the stress-strain curves in Figure 5-10 - Figure 5-17 are presented in Table 5-1.

Table 5-1: Constitutive model parameters for derivation of idealized stress-strain curves

YPT CURVES				CHT CURVES			
<i>Designated name</i>	K_{NM}	H_{NM}	H/K ratio	<i>Designated name</i>	K_{NM}	H_{NM}	H/K ratio
<i>YPcorr-600TS</i>	21.102	0.333	0.0158	<i>CHcorr-450YS</i>	4.135	12.855	3.1091
<i>YPcorr-700TS</i>	25.610	0.440	0.0172	<i>CHcorr-500YS</i>	7.868	4.740	0.6025
<i>YPcorr-800TS</i>	24.248	0.471	0.0194	<i>CHcorr-550YS</i>	12.007	3.223	0.2684
<i>YPcorr-900TS</i>	20.900	0.633	0.0303	<i>CHcorr-600YS</i>	16.462	2.573	0.1563
<i>YPdiff-650TS</i>	19.936	0.660	0.0331	<i>CHdiff-450YS</i>	2.747	6.952	2.5311
<i>YPdiff-750TS</i>	33.399	0.573	0.0172	<i>CHdiff-500YS</i>	3.728	8.695	2.3321
<i>YPdiff-850TS</i>	48.848	0.523	0.0107	<i>CHdiff-550YS</i>	5.942	6.682	1.1244
<i>YPdiff-950TS</i>	66.009	0.488	0.0074	<i>CHdiff-600YS</i>	13.566	3.478	0.2563
<i>YPdiff-025EP</i>	4.201	0.507	0.1206	<i>CHdiff-550TS</i>	6.536	3.457	0.5289
<i>YPdiff-020EP</i>	5.165	0.582	0.1127	<i>CHdiff-650TS</i>	5.327	4.775	0.8962
<i>YPdiff-015EP</i>	7.395	0.653	0.0882	<i>CHdiff-750TS</i>	4.944	5.422	1.0966
<i>YPdiff-010EP</i>	14.785	0.700	0.0474	<i>CHdiff-850TS</i>	4.760	5.711	1.1998
<i>YPintx-900TS</i>	1.206	0.997	0.8265	<i>CHsame-350PL</i>	1.812	21.270	11.7379
<i>YPintx-800TS</i>	1.448	1.035	0.7147	<i>CHsame-300PL</i>	2.580	14.970	5.8014
<i>YPintx-700TS</i>	1.846	1.220	0.6606	<i>CHsame-250PL</i>	3.858	7.590	1.9673
<i>YPintx-600TS</i>	4.809	1.076	0.2238	<i>CHsame-200PL</i>	6.217	4.227	0.6798

The plots in Figure 5-7, Figure 5-8, and Figure 5-9 are zoomed-in versions of Figure 5-10, Figure 5-14, and Figure 5-16 respectively and thus have the same corresponding parameters as presented in Table 5-1.

Three sets of plots are presented in Figure 5-10 - Figure 5-17: the first set (on the left) comprises the plots for the different families of stress-strain curves, the second set of plots (in the middle) comprises the plots of the non-dimensional relative ultimate compressive strength ($\sigma_{ult}/\sigma_{0.5}$) vs. the b/t ratio for each respective family of stress-strain curves, and the third set of plots (on the right) comprises the plots of the strain corresponding to the ultimate compressive strength for each model vs. the b/t ratio.

Since experimental test data for the ultimate strain capacity of simply-supported flat metal plates subjected to uniform axial compression is not available in literature, only the plots for the ultimate compressive strength are validated against experimental data. The experimental results data used for validation are represented by the light grey hollow circles graphically superimposed on the ultimate strength plots and were obtained from the results of an extensive study by Ellinas *et al.* [55] on structural plating in marine structures.

Even though it is hardly feasible to obtain an exact representation of the real behavior of structural systems using numerical simulation techniques, the results of the FE analyses presented in the ultimate strength plots indicate a close agreement with the trend of the experimental results data. Variations in key conditions such as anisotropic material properties, geometric imperfections, residual stresses, edge support conditions, and loading mechanisms may be considered to be responsible for the large scatter in the experimental data. However, the effect of material stress-strain properties was not explicitly considered in the experiments conducted.

To verify the consistency of the results of this study, the ultimate compressive strengths obtained from the results of the numerical analyses performed in this study (presented in Figure 5-10 - Figure 5-17) were further compared against a graphical plot of the classical Winter curve equation presented in Eq. (5-8).

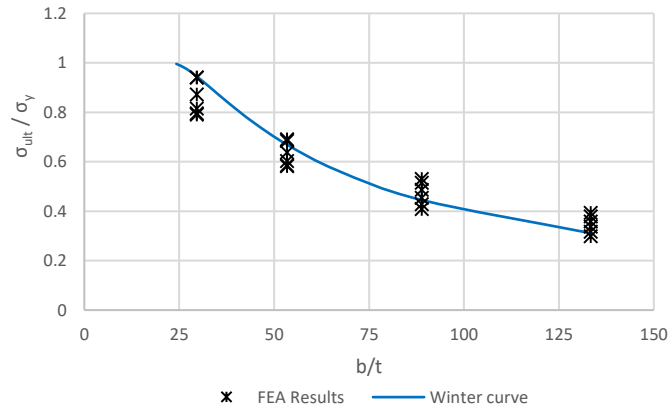


Figure 5-18: Comparison of FEA and Winter curve

As indicated in Figure 5-18, overlooking the effect of material property variation in the approximation of the ultimate strength of simply-supported flat plates subjected to uniform compression, and using a single curve such as the Winter curve, may lead to inaccurate results. Comparative observation of the results presented in Figure 5-18 shows that the Winter curve is likely to overestimate the ultimate strength prediction for thick plates, while the ultimate strength of thinner plates may be underpredicted.

The results obtained indicate that for plates made of YPT materials, the ultimate compressive strength is not significantly affected by any variation in either the length of the yield plateau or the magnitude of the UTS, and are observed to be very similar to the results obtained for plates made of E-PP material.

For CHT materials that share the same proportionality limit, the ultimate compressive strength of the plate is governed by the equivalent yield stress of the material hence, the ultimate strength of the plate generally increases as the equivalent yield stress of the material is increased. However, due to elastic and inelastic buckling effects, the magnitude of the maximum average applied stress relative to the equivalent yield stress of the material ($\sigma_{ult}/\sigma_{0.5}$) generally reduces as the strain-hardening improves. This may be attributed to the acceleration towards collapse of the plate once the proportionality limit of the material is exceeded: acceleration towards collapse is slower in materials with superior strain-hardening hence, such materials tend to fail at a magnitude of applied stress which is farther from the equivalent yield stress of the material compared to materials with inferior strain-hardening.

Typically, the proportionality limit and the strain-hardening properties of CHT materials are somewhat inversely related: CHT materials with a relatively lower proportionality limit stress tend to exhibit superior strain-hardening, and vice versa (as indicated in as indicated in Figure 5-16(a) and Figure 5-17(a)). The correlative effect of the proportionality limit stress on the ultimate strength is, therefore, more pronounced in slender plates. This may be attributed to the earlier incidence of the critical buckling stress in slender plates compared to stockier plates. In slender plates, buckling typically occurs within the elastic limit hence, for materials with a lower proportionality limit, the plate is unable to take advantage of the superior strain-hardening before reaching collapse at the maximum average applied stress. However, buckling typically occurs beyond the proportionality limit in thick plates so the superior strain-hardening of the material has a positive effect on the ultimate compressive strength of the plate. For CHT materials with different proportionality limits, since all the stress-strain curves share the same equivalent yield stress, the relative ultimate strengths ($\sigma_{ult}/\sigma_{0.5}$) are observed to exhibit a comparative improvement for lower proportionality limits as the thickness of the plate increases.

In thick plates, the presence of a yield plateau is observed to have a detrimental effect on the strain capacity for YPT materials with superior strain-hardening. This may be attributed to the reduced ductility associated with the sharp change in the slope of the stress-strain curve at the onset of strain-hardening. Hence, the characteristic occurrence of inelastic buckling causes the effect of the reduced ductility to reflect as a lower strain capacity in thick YPT material plates. Contrarily, slender plates experience elastic buckling and since the onset of strain-hardening in the material occurs in the post-buckling range of the plate, superior strain-hardening contributes to the post-buckling reserve strength which translates to a slight improvement in the strain capacity of the plate.

In addition to the magnitude of the UTS, the convexity of the ‘knee’ of the stress-strain curve is also observed to influence the strain capacity of CHT material plates: a greater ‘knee’ convexity tends to favor the strain capacity of thicker plates whereas slender plates seem to exhibit better strain capacity when the change in slope of the stress-strain curve up to the UTS is more gradual. A smaller ‘knee’ convexity leads to increased ductility of slender plates in the post-buckling range whereas thicker plates lose strength due to inelastic buckling, which may result in loss of strain capacity. In comparison, the ductility of slender plates in the post-buckling range reduces

while the loss of strength due to inelastic buckling in thicker plates also reduces as the convexity of the ‘knee’ increases. This phenomenon is more prominent in the families of stress-strain curves with different proportionality limits due to the existence of a larger transition zone between the proportionality limit and the UTS, compared with the families of stress-strain curves with the same proportionality limit.

5.7 Conclusions

A review of relevant theoretical postulations on the buckling and post-buckling behavior of plates was carried out in this study and it was concluded that analytical formulations are only suitable for predicting the mechanical behavior of uniformly compressed plates in the elastic range of the material while advanced computational techniques are generally required for achieving a reasonable estimation of the inevitable and complex nonlinearities associated with real engineering applications.

The finite element method was therefore adopted in this study to investigate the effect of parametric variation of material stress-strain properties on the ultimate strength and strain capacity of simply-supported flat plates subjected to uniform axial compression.

The geometric dimensions, edge support conditions and initial imperfection assumptions applied to the numerical models in this study are consistent with numerical and experimental applications from previous research studies and the results obtained from the FE analyses showed reasonable agreement with results from past studies.

Based on review and consideration of the limitations associated with currently-existing mathematical models in characterizing the true stress-true strain relationship of metallic materials, a novel analytical expression was developed and applied for generating the vast array of stress-strain curves used for parametric variation on this study. The proposed stress-strain model proves to be very versatile in approximating the shape of the stress-strain curve over the entire range of strains, even for materials with a distinct yield point and yield plateau.

Plates with yield plateau type (YPT) materials were all observed to have similar ultimate compressive strengths comparable to that of plates with an elastic-perfectly plastic (E-PP)

material. The strain capacities were however slightly affected by the strain-hardening properties of the stress-strain curve according to the thickness of the plates.

Unlike plates with YPT materials, the mechanical behavior of plates with continuously-hardening type (CHT) materials was observed to be more significantly affected by most of the stress-strain shape parameters including the proportionality limit, equivalent yield stress, strain-hardening behavior, ‘knee’ convexity of the stress-strain curve, and ultimate tensile stress. Summarily, the results show that superior strain-hardening has a positive effect on the ultimate compressive strength and strain capacity of a plate, and this effect becomes more prominent as the plate becomes thicker.

One of the most valuable advantages of the proposed stress-strain model in this study is providing a reasonable approximation of the shape of the stress-strain curve using only two constitutive model parameters, thus easing the process of parameterizing the material stress-strain properties for an extensive array of metallic material variations.

Acknowledgments

The authors wish to express their appreciation to TransCanada Pipelines Ltd. for providing the financial support and technical input necessary for conducting this research study.

5.8 References

- [1] A.F. Mateus, J.A. Witz, Parametric study of the post-buckling behaviour of steel plates, *Eng. Struct.* 23 (2001) 172–185. doi:10.1016/S0141-0296(00)00005-5.
- [2] M. Maarefdoust, M. Kadkhodayan, Elastoplastic buckling analysis of rectangular thick plates by incremental and deformation theories of plasticity, *Proc. Inst. Mech. Eng. Part G J. Aerosp. Eng.* 229 (2015) 1280–1299. doi:10.1177/0954410014550047.
- [3] G.Z. Voyiadjis, P. Woelke, *Elasto-Plastic and Damage Analysis of Plates and Shells*, Springer Science & Business Media, Berlin, Heidelberg, 2008. doi:10.1007/978-3-540-79351-9.
- [4] J. Betten, C.H. Shin, Elastic-plastic buckling analysis of rectangular plates subjected to biaxial loads, *Forsch. Im Ingenieurwes.* 65 (2000) 273–278. doi:10.1007/s100109900023.

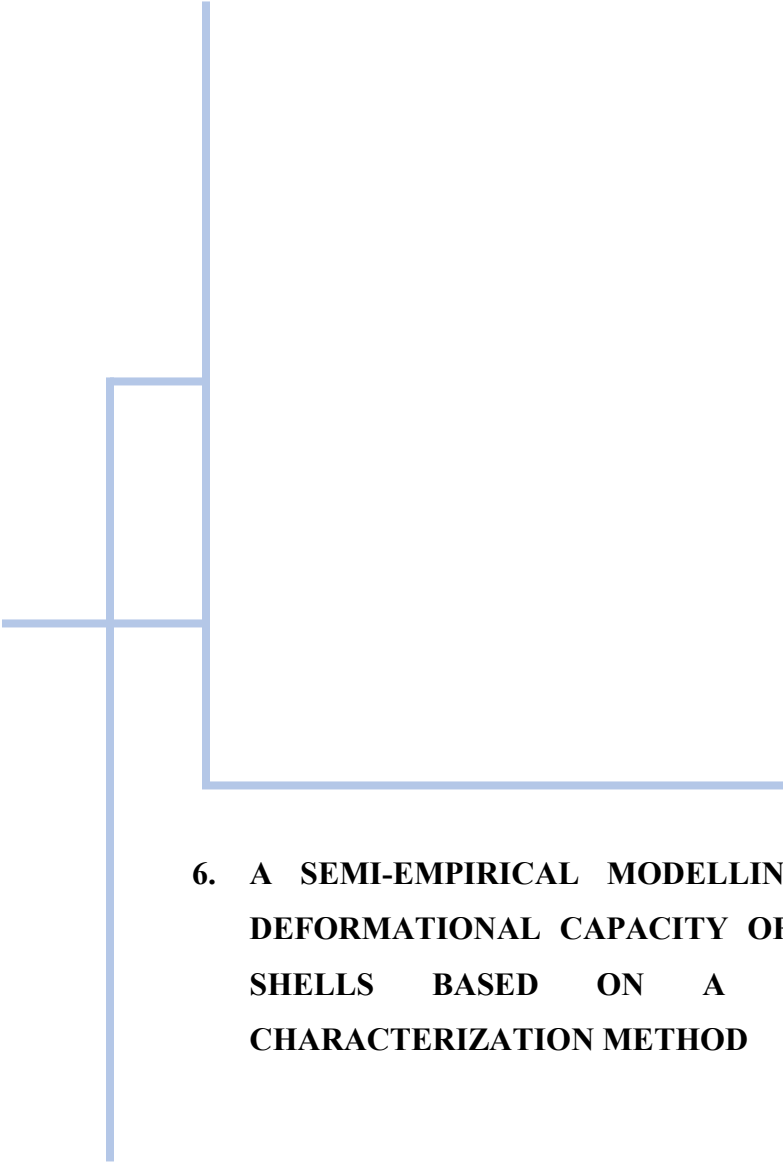
- [5] M. Kadkhodayan, M. Maarefdoust, Elastic/plastic buckling of isotropic thin plates subjected to uniform and linearly varying in-plane loading using incremental and deformation theories, *Aerosp. Sci. Technol.* 32 (2014) 66–83. doi:10.1016/J.AST.2013.12.003.
- [6] A.A. Ilyushin, *The Elasto-Plastic Stability of Plates*, NACA Technical Memorandum, No. 1188, Washington, D.C., 1947.
- [7] G.H. Handelman, W. Prager, Plastic buckling of rectangular plates under edge thrusts, NACA Technical Note, No. 1530, Washington, D.C., 1948.
- [8] E.Z. Stowell, *A Unified Theory of Plastic Buckling of Columns and Plates*, NACA Technical Note, No. 1556, Washington, D.C., 1948. doi:10.1016/j.engstruct.2010.06.012.
- [9] R.A. Pride, G.J. Heimerl, Plastic buckling of simply supported compressed plates, NACA Technical Note, No. 1817, Washington, D.C., 1949.
- [10] P.P. Bijlaard, Theory and Tests on the Plastic Stability of Plates and Shells, *J. Aeronaut. Sci.* 16 (1949) 529–541. doi:10.2514/8.11851.
- [11] S.C. Shrivastava, Inelastic buckling of plates including shear effects, *Int. J. Solids Struct.* 15 (1979) 567–575. doi:10.1016/0020-7683(79)90084-2.
- [12] C.M. Wang, Y. Xiang, J. Chakrabarty, Elastic/plastic buckling of thick plates, *Int. J. Solids Struct.* 38 (2001) 8617–8640. doi:10.1016/S0020-7683(01)00144-5.
- [13] K.J.R. Rasmussen, T. Burns, P. Bezkorovainy, M.R. Bambach, Numerical modelling of stainless steel plates in compression, *J. Constr. Steel Res.* 59 (2003) 1345–1362. doi:10.1016/S0143-974X(03)00086-5.
- [14] P. Bezkorovainy, T. Burns, K.J.R. Rasmussen, Strength Curves for Metal Plates in Compression, *J. Struct. Eng.* 129 (2003) 1433–1440. doi:10.1061/(ASCE)0733-9445(2003)129:11(1433).
- [15] J.K. Paik, J.M. Lee, D.H. Lee, Ultimate strength of dented steel plates under axial compressive loads, *Int. J. Mech. Sci.* 45 (2003) 433–448. doi:10.1016/S0020-7403(03)00062-6.
- [16] K.M. El-Sawy, A.S. Nazmy, M.I. Martini, Elasto-plastic buckling of perforated plates under uniaxial compression, *Thin-Walled Struct.* 42 (2004) 1083–1101. doi:10.1016/J.TWS.2004.03.002.

- [17] J. Becque, M. Lecce, K.J.R. Rasmussen, The direct strength method for stainless steel compression members, *J. Constr. Steel Res.* 64 (2008) 1231–1238. doi:10.1016/J.JCSR.2008.07.007.
- [18] B.W. Schafer, Review: The Direct Strength Method of cold-formed steel member design, *J. Constr. Steel Res.* 64 (2008) 766–778. doi:10.1016/J.JCSR.2008.01.022.
- [19] M. Ashraf, L. Gardner, D.A. Nethercot, Structural Stainless Steel Design: Resistance Based on Deformation Capacity, *J. Struct. Eng.* 134 (2008) 402–411. doi:10.1061/(ASCE)0733-9445(2008)134:3(402).
- [20] S. Afshan, L. Gardner, The continuous strength method for structural stainless steel design, *Thin-Walled Struct.* 68 (2013) 42–49. doi:10.1016/J.TWS.2013.02.011.
- [21] L. Gardner, F. Wang, A. Liew, Influence of strain-hardening on the behavior and design of steel structures, *Int. J. Struct. Stab. Dyn.* 11 (2011) 855–875. doi:10.1142/S0219455411004373.
- [22] S. Ahmed, M. Ashraf, M. Anwar-Us-Saadat, The Continuous Strength Method for slender stainless steel cross-sections, *Thin-Walled Struct.* 107 (2016) 362–376. doi:10.1016/J.TWS.2016.06.023.
- [23] A. Liew, L. Gardner, Ultimate capacity of structural steel cross-sections under compression, bending and combined loading, *Structures.* 1 (2015) 2–11. doi:10.1016/J.ISTRUC.2014.07.001.
- [24] W. Ramberg, W.R. Osgood, Description of stress-strain curves by three parameters, NACA Technical Note No. 902, Washinton, D.C., 1943.
- [25] O. Zhao, S. Afshan, L. Gardner, Structural response and continuous strength method design of slender stainless steel cross-sections, *Eng. Struct.* 140 (2017) 14–25. doi:10.1016/J.ENGSTRUCT.2017.02.044.
- [26] S. Neupane, S. Adeeb, R. Cheng, J. Ferguson, M. Martens, Modeling the Deformation Response of High Strength Steel Pipelines—Part II: Effects of Material Characterization on the Deformation Response of Pipes, *J. Appl. Mech.* 79 (2012) 051003. doi:10.1115/1.4006381.
- [27] S. Neupane, S. Adeeb, R. Cheng, J. Ferguson, M. Martens, Modeling the Deformation Response of High Strength Steel Pipelines—Part I: Material Characterization to Model the Plastic Anisotropy, *J. Appl. Mech.* 79 (2012) 051002. doi:10.1115/1.4006380.

- [28] X. Liu, H. Zhang, M. Li, M. Xia, W. Zheng, K. Wu, Y. Han, Effects of steel properties on the local buckling response of high strength pipelines subjected to reverse faulting, *J. Nat. Gas Sci. Eng.* 33 (2016) 378–387. doi:10.1016/J.JNGSE.2016.05.036.
- [29] X. Liu, H. Zhang, O. Ndubuaku, M. Xia, J.J.R. Cheng, Y. Li, S. Adeeb, Effects of stress-strain characteristics on local buckling of X80 pipe subjected to strike-slip fault movement, *J. Press. Vessel Technol.* (2018).
- [30] X. Liu, H. Zhang, K. Wu, M. Xia, Y. Chen, M. Li, Buckling failure mode analysis of buried X80 steel gas pipeline under reverse fault displacement, *Eng. Fail. Anal.* 77 (2017) 50–64. doi:10.1016/J.ENGFAILANAL.2017.02.019.
- [31] M. Macdonald, J. Rhodes, G.T. Taylor, Mechanical properties of stainless metal lipped channels, in: 15th Int. Spec. Conf. Cold-Formed Met. Struct., University of Missouri-Rolla, Mo., 2000: pp. 673–686.
- [32] E. Mirambell, E. Real, On the calculation of deflections in structural stainless steel beams: an experimental and numerical investigation, *J. Constr. Steel Res.* 54 (2000) 109–133. doi:10.1016/S0143-974X(99)00051-6.
- [33] K.J.R. Rasmussen, Full-range stress-strain curves for stainless steel alloys, *J. Constr. Steel Res.* 59 (2003) 47–61. doi:10.1016/S0143-974X(02)00018-4.
- [34] L. Gardner, D.A. Nethercot, Experiments on stainless steel hollow sections—Part 1: Material and cross-sectional behaviour, *J. Constr. Steel Res.* 60 (2004) 1291–1318. doi:10.1016/J.JCSR.2003.11.006.
- [35] W.M. Quach, Residual stresses in cold-formed steel sections and their effect on column behaviour, The Hong Kong Polytechnic University, Hong Kong, 2005.
- [36] O. Ndubuaku, M. Martens, J.J.R. Cheng, S. Adeeb, Expression of a Generic Full-Range True Stress-True Strain Model for Pipeline Steels Using the Product-Log (Omega) Function, in: Vol. 6B Mater. Fabr., ASME, 2017: p. V06BT06A050. doi:10.1115/PVP2017-65236.
- [37] O. Ndubuaku, M. Martens, R. Cheng, A. Ahmed, S. Adeeb, A Novel Approach for True Stress-True Strain Material Characterization of Metallic Materials Using the Product-Log (Omega) Function, in: 6th Int. Conf. Eng. Mech. Mater., CSCE, May 31 - June 3, Vancouver, B.C., Canada, 2017.

- [38] D. Hibbitt, B. Karlsson, P. Sorensen, ABAQUS Standard User's and Reference Manuals, Version 6.14, (2014).
- [39] A.E.H. Love, The Small Free Vibrations and Deformation of a Thin Elastic Shell, *Philos. Trans. R. Soc. London, A Math. Phys. Eng. Sci.* 179 (1888) 491–546. doi:10.1098/rsta.1888.0016.
- [40] T. Von Kármán, Festigkeitsprobleme im Maschinenbau, in: *Encycl. Der Math. Wissenschaften IV*, Teubner, 1910: pp. 348–352.
- [41] T. Von Kármán, E.. Sechler, L.. Donnell, The strength of Thin Plates in Compression, *Trans. Appl. Mech. Div. ASME.* 54 (1932) 53. doi:1.
- [42] G. Winter, Strength of thin steel compression flanges, *Trans. Am. Soc. Civ. Eng.* 112 (1947) 527. doi:1.
- [43] F. Bleich, H.H. Bleich, L.B. Ramsey, Buckling strength of metal structures, 1st ed., McGraw-Hill, New York, 1952.
- [44] D. Faulkner, A Review of Effective Plating to be Used in the Analysis of Stiffened Plating in Bending and Compression, *J. Sh. Res.* 19 (1975) 1–17.
- [45] T. Peköz, Development of a Unified Approach to the Design of Cold-Formed Steel Members (Report SG 86-4): AISI Specifications for the Design of Cold-Formed Steel Structural Members, Washington, D.C., 1987.
- [46] C. Guedes Soares, Design equation for the compressive strength of unstiffened plate elements with initial imperfections, *J. Constr. Steel Res.* 9 (1988) 287–310. doi:10.1016/0143-974X(88)90065-X.
- [47] D.R. Ziemian, Guide to Stability Design Criteria for Metal Structures, John Wiley & Sons, Inc., Hoboken, NJ, USA, 2010. doi:10.1002/9780470549087.
- [48] J.R. Vinson, The Behavior of Thin-Walled Structures: Beams, Plates, and Shells, Springer Netherlands, Dordrecht, 1988. doi:10.1007/978-94-009-2774-2.
- [49] J.K. Paik, A.K. Thayamballi, Ultimate limit state design of steel plated structures, John Wiley & Sons, Inc., Chichester, England, 2003.
- [50] S.P. Timoshenko, J.M. Gere, Theory of Elastic Stability, McGraw-Hill Book Company, New York, 1961.
- [51] P.S. Bulson, Theory of flat plates, Chatto and Windus, London, 1970.

- [52] EN 1993-1-4 2006, Eurocode 3: Design of steel structures - Part 1-4: General rules - Supplementary rules for stainless steels, CEN, Brussels, 2006.
- [53] American Petroleum Institute, API 5L: Specification for Line Pipe, 44th ed., American Petroleum Institute, USA, 2007.
- [54] C.S. Smith, P.C. Davidson, J.C. Chapman, Strength and stiffness of ships plating under in-plane compression and tension, R. Inst. Nav. Archit. Trans. 130 (1988) 227–96.
- [55] C.P. Ellinas, W.J. Supple, A.C. Walker, Buckling of offshore structures: a state-of-the-art review, Gulf Publishing Company, Houston, 1984.



6. A SEMI-EMPIRICAL MODELLING APPROACH FOR PREDICTING THE DEFORMATIONAL CAPACITY OF AXIALLY-COMPRESSED CYLINDRICAL SHELLS BASED ON A NOVEL MATERIAL STRESS-STRAIN CHARACTERIZATION METHOD

This chapter is derived from a research article submitted for publication in the Elsevier Thin-walled Structures journal.

6.1 Abstract

Adoption of cylindrical shell structures for various load-resistance applications has enjoyed wide-spread acceptance in the field of civil, mechanical and aerospace engineering, mainly due to the exceptional structural efficiency of cylindrical shells to withstand significant longitudinal and circumferential in-plane loading without bending. However, where such in-plane loading conditions are compressive, cylindrical shells are likely to exhibit an unstable response characterized by localized out-of-plane deformation. Computerized numerical simulation is often required for accurate and efficient estimation of the strains and resultant stresses in cylindrical shells under loading, especially where the thickness of the shell is sufficient to evoke an inelastic buckling response in the structure. The buckling behavior of thin-walled cylindrical shells subjected to uniform axial compression has been studied in this paper using the finite element (FE) simulation method to assign respective material, geometric, loading and boundary properties to computer-generated cylindrical shell specimens. Extensive parametric analysis, consisting of approximately 720 FE runs, was then conducted based on a full-factorial empirical design, applying ample variations of the relevant parameters that influence the buckling response of axially-compressed cylindrical-shell structures. Nonlinear multiple regression techniques were then employed to derive the coefficients of nonlinear mathematical expressions, each developed as an arithmetic product of appropriate variable functions related to the respective functional sensitivities of the investigated parameters. Strain-hardening properties were incorporated into the mathematical expressions based on the shape constants of the Ndubuaku stress-strain model; which has proven to be remarkably useful for accurate parameterization of the stress-strain behavior over the full range of strains for a wide range of metallic materials, including materials with a well-defined yield plateau. Excellent predictions of FEA-derived values for the critical limit strain limit were obtained and a simple statistical approach was presented to increase the conservativeness of the semi-empirical model as required.

Nomenclature

D	pipe's outer diameter
ε	true strain
ε_{cr}	critical limit strain
ε_{pl}	corresponding strain at proportionality limit stress of Ndubuaku model
ε_R	Ndubuaku model strain ratio
ε_{up}	corresponding strain at ultimate proof stress of Ndubuaku stress-strain model
E	Young's modulus of elasticity
f_p	pressure factor (ratio of applied pressure to pipe yield pressure)
h	Ndubuaku model heel constant
k	Ndubuaku model knee constant
μ	Poisson's ratio
n	Ramberg-Osgood strain-hardening exponent
p	applied internal pressure
p_y	pipe's circumferential yield pressure
R	pipe's cross-sectional radius
$\sigma_{0.5}$	0.5% total strain proof stress
σ	true stress
σ_c	elastic critical buckling stress
$\sigma_{p,0.2}$	0.2% plastic strain proof stress ('offset' stress)
σ_{pl}	proportionality limit stress of Ndubuaku stress-strain model
σ_R	Ndubuaku model stress ratio
σ_{up}	ultimate proof stress of Ndubuaku stress-strain model
σ_{us}	ultimate tensile stress of pipe material
σ_y	yield stress of pipe material
sh_f	material curve shape factor
t	pipe's wall thickness
CLS	Critical limit strain

<i>D/t ratio</i>	Ratio of pipe's outer diameter to pipe's wall thickness
<i>PLUS ratio</i>	Ratio of proportionality limit stress to ultimate tensile stress
<i>RHT</i>	Round-house type
<i>UTS</i>	Ultimate tensile stress
<i>YPL</i>	Yield plateau length
<i>YPT</i>	Yield-plateau type
<i>YS</i>	Nominal yield stress
<i>Y/T ratio</i>	Ratio of yield stress to ultimate tensile stress

6.2 Introduction

Cylindrical shells comprise some of the most widely-used thin-walled structures for civil and aerospace engineering applications, as well as various industrial applications including pipelines, water reservoirs, submarines, silos, oil storage tanks, nuclear reactors, aircraft fuselages, steel tube towers for mounting of wind turbines, etc. [1–3]. The wide acceptance of cylindrical shells is mainly attributable to their considerable longitudinal strength and ample torsional resistance, as well as their remarkable capacity to withstand high circumferential stresses.

The buckling phenomenon in cylindrical shell structures has remained a matter of research interest and active analytical, experimental and numerical investigation for over a century [4]. The earliest attempts to address the issue of shell buckling comprise the independent works of Lorenz [5], Timoshenko [6] and Southwell [7] which culminated in the derivation of what is regarded as the classical analytical expression for the critical buckling stress of a perfect, isotropic cylindrical shell. However, the analytical expression was derived based on the assumption of simply-supported conditions and a purely-membrane stress state in the pre-buckling range and did not account for the effect of the length-diameter interaction of the structure on the bifurcation stress. The shortcomings of the classical bifurcation load equation became apparent as subsequent results of experimental research studies by a number of researchers [8–10] indicated significant discrepancies between the analytical predictions and experimentally-derived buckling loads of real cylindrical shell structures. A myriad of factors such as boundary conditions, loading eccentricities, and pre-buckling deformations are

considered to be responsible for the inconsistencies in the theoretical predictions and experimental results [11]. However, later theoretical investigations by von Kármán and Tsien [12] and Koiter [13] also observed additional inadequacies of the classical theory in approximating the initiation and growth of wrinkle deformation, and they concluded that the buckling phenomenon in cylindrical shells can only be adequately captured by means of a non-linear large deflection theory. Based on the premises of the advanced theoretical postulations by Ref. [12] and Ref. [13], the form and amplitude of initial geometric imperfections were identified as being chiefly responsible for the discrepancies between analytically-derived estimates of the buckling load and experimental results. Wagner et al. [14] however maintained that the deviation of analytical predictions from experimental buckling loads was not only caused by traditional imperfections or irregularities in the geometric profile but also by non-traditional imperfections like boundary condition imperfections (caused by loading eccentricities) and stiffness imperfections (due to thickness variations). They opined that the leading cause of such deviations in buckling load prediction results from the existence of a generally-overlooked bending moment in experimental investigations which are presumably regarded as pure compression tests.

Geometric defects inevitably result from manufacturing/welding processes and, regrettably, the imperfection profiles of cylindrical shell structures are generally characterized by a high degree of randomness and unpredictability. In practice, geometric irregularities are induced by an exhaustive list of factors, e.g., material memory, sheet metal forming and curing process flaws, residual stresses, thickness variations, shape deviations, ovalization, etc. [15,16]. Owing to the randomness of imperfections, classically-simplified assumptions of pre-buckling deformations and inherent geometric defects are usually adopted for analytical and numerical analyses but are hardly representative of real existing defects. As a means to obtain realistic buckling loads, Arbocz [17] suggested the use of imperfection data generated from measurements of geometric irregularities in a real cylindrical shell structure as the direct input for the imperfection profile of numerical models. The approach suggested by Ref. [17] however has the drawback of being unfeasible, especially at the early design stage where imperfection data is not available. Another concept which has been explored is the implementation of a mathematically-derived “worst possible” imperfection pattern in the governing equations for the critical buckling stress [18]. The method typically involves an analytically rigorous finite element formulation which employs

a standard isoparametric interpolation scheme with bilinear and biquadratic shape functions, and functions by an algorithm which treats the nodal positions as extra degrees-of-freedom (DOFs) and minimizes the buckling load by changing the imperfection shape. There are three main approaches for implementation of geometric imperfections in numerically-based buckling designs of imperfect cylinders which are based on the single dimple perturbation concept: (1) the “Single-Perturbation Load Approach (SPLA)” induces a single dimple in the side of a cylinder (usually the middle cross-section) by means of a concentrated normal perturbation load [19], (2) the “Single-Perturbation Displacement Approach (SPLA)” involves a displacement-controlled introduction of a constant single buckle imperfection to the side of the cylinder [20], and (3) the “Single Boundary Perturbation Approach (SBPA)” induces a single dimple at the top edge of the shell by boundary perturbation such that a small bending moment is generated in the shell structure under axial compression [21]. Other common methods for FE-based imperfection modeling include [22]: (1) Geometric Dimple-shaped Imperfection (GDI) - which is commonly referred to as a “cosine dimple” and is defined by a cosine function for two (one longitudinal and one circumferential) wavelengths [23], and (2) Axi-symmetric Imperfection- (ASI) – which is a simplified form of the GDI and only requires specification of the cosine function for the longitudinal wavelength [24]. The GDI and ASI methods are similarly implemented by translating the nodes of the FE mesh according to the prescribed cosine function. Castro et al. [22] performed a comparative study of different imperfection methods and reported that the Linear Buckling Mode-shaped Imperfection (LBMI) approach is a widely-preferred method for prescription of the initial nodal displacement field of an FE mesh, especially because the imperfection profile can be easily generated from a linear buckling analysis, and most of the general-purpose FE codes provide an automatic means to prescribe the initial imperfections as an initial state in the nonlinear numerical simulation. They, however, stated that the LBMI approach is highly sensitive to the chosen eigenmode and tends to produce a high degree of variability in obtained results.

There exists an enormous collection of empirical data for axially-loaded cylindrical shells [25] and the generally-adopted procedure for the stress-based design of axially-compressed cylindrical structures based on the critical buckling stress is achieved by means of an empirical knock-down factor (KDF), e.g., NASA SP-8007 [26]. NASA SP-8007 attempts to circumvent

the observed discrepancies in experimentally-obtained results for the critical buckling stress of cylinders under uniform axial compression by defining a design curve based on the statistical lower-bound of a collection of experimental results. Results of comparative studies by a number of researchers have however indicated that the application of empirical KDFs often leads to very conservative and acutely uneconomical designs in the modeling of cylindrical shell structures [14,27,28].

Gellin [29] performed analytical studies on the imperfection sensitivity of axially-compressed cylindrical shells which undergo buckling in the plastic range and he concluded that the collapse loads of such cylinders are less sensitive to imperfections compared to the collapse loads of elastically-buckled cylinders. Ravn-Jensen and Tvergaard [30] applied a computational procedure for incremental finite element analysis of longitudinally-welded cylindrical shells. They affirmed that residual stresses are commonly induced in cylindrical shells during fabrication processes such as welding and cold bending of the parent metal sheets and explained that such residual stresses significantly reduce the bifurcation loads of geometrically perfect shells or may even result in buckling without external loading; as in the case of nonuniformly-heated shells which experience thermal buckling. Results of the analyses by Ref. [30] indicated that residual stresses tend to reduce the sensitivity of cylindrical shell structures to initial geometric imperfections; however, the observed sensitivity-reducing effect gradually disappears as the amplitude of geometric imperfections increases. Results of experimental tests and numerical analyses on longitudinally-welded axially-compressed stub C-H sections by Guo et al. [31] showed that the effect of residual stresses on the load-carrying capacity of cylindrical shells reduces as the D/t ratio is reduced and vice versa. Analytical evaluations by Hutchinson [32] and experimental/numerical investigations by Limam et al. [33] have also indicated that internal pressurization tends to diminish initial geometric imperfections and thus mitigate the imperfection sensitivity of axially-compressed cylindrical shells.

Based on results of a three-part research series of experimental and analytical investigations involving displacement-controlled axial compression of stainless steel specimens with D/t ratios ranging between 23 and 52, Bardi et al. [34] presented a method for estimating the limit load and associated limit strains by tracking the evolution of the axisymmetric wrinkling using the principle of virtual work. They noticed that careful appropriation of the wavelength of induced

initial axisymmetric imperfections and the consideration of non-axisymmetric imperfections is necessary for proper qualitative and quantitative reproduction of experimental results. Hence, their method allowed the assignment of initial imperfections with a combination of axisymmetric and non-axisymmetric components and involved a special algorithm for testing the compressed cylinder for possible bifurcation of initial axisymmetric wrinkles into a non-axisymmetric mode. The shell formulation used in the analytical procedure presented by Ref. [34] did not account for through-thickness shear effects; hence, it was suggested by the authors that the effects of shear deformations on the obtained results should be further explored. However, they established that the limit strain resulting from either axisymmetric or non-axisymmetric wrinkling is significantly influenced by the hardening of the material, and even though the limit strain is influenced by the material yield stress, the effect is relatively secondary. Notwithstanding the reasonable agreement between their analytically-derived results and experimental results by Ref. [34], the existence of fundamental uncertainties in the functional dependence of the obtained results on the uniqueness of the parameters used for the analyses was noted and a more extensive investigation was recommended to ascertain the generalizability of their findings.

Paquette and Kyriakides [35] extended the analytical procedure presented by Ref. [34] to consider the plastic buckling and collapse of cylindrical shells subjected to combined axial compression and internal pressure. The method employed by Ref. [35] estimated the critical buckling stress (σ_c) and the associated half-wavelength of the buckling mode (λ_c) based on the deformation theory of plasticity whereas, to account for the non-proportionality of the stress history, the corresponding bifurcation strain (ε_c) was calculated based on the incremental (flow) theory of plasticity. The results of their study showed that increasing the pressure and the hardening of the material increased both the bifurcation strain and the limit strain, however, the effect was significant on the limit strain but marginal on the bifurcation strain. In the same manner, increasing the material hardening and the internal pressure resulted in a corresponding increase of λ_c but contrarily, σ_c was observed to increase with increased material hardening while increased pressure caused an opposite effect of lowering the material response and resulting in a corresponding decrease of σ_c . Internal pressure was observed to have a stabilizing effect on the initial axisymmetric deformation, making a transformation into a non-axisymmetric mode less feasible. Assumption of anisotropic material yielding was found to produce better

agreement between the analytically-derived results and experimental results, compared to isotropic yielding. However, Neupane et al. [36,37] investigated the deformation response of numerical pipe models using a combined kinematic hardening material model and concluded that an isotropic material model may be suitable for modeling pipes subjected to low internal pressure by using the material data of the pipe's longitudinal direction and by using the material data of the pipe's circumferential direction for modeling pipes subjected to high internal pressure. Despite satisfactory ability to predict the limit state values, the analytically-derived results obtained by Ref. [35] portrayed some discrepancies which are attributable to sensitivity of the analytical procedure to initial assumptions of imperfection.

Dundu [38] recently conducted a detailed review of the evolution of stress-strain models of stainless steel. He concluded that the non-linear stress-strain model, proposed by Ramberg and Osgood [39], and modified by Hill [40] is still the best model for stresses up to the 0.2% proof stress. He went further to discuss various modifications and extensions of the Ramberg-Osgood model which have been proposed by various researchers over time in an attempt to improve the accuracy of stress-strain characterization over the full range of the stress-strain relationship. He, however, pointed out the somewhat inevitable requirement for discretization and, in most cases, a large number of model parameters to improve the description of the stress-strain behavior beyond the 0.2% proof stress. To tackle the limitations of existing stress-strain models, Ndubuaku et al. [41–43] recently developed a novel mathematical expression (referred to as the “Ndubuaku model”) which features a combination of moderate complexity and remarkable accuracy in approximating the true stress-true strain relationship of a diverse range of metallic materials over the full range of strains; including materials with a distinct yield point and yield plateau. The model precludes the need for discretization and, with two constitutive model constants, completely defines any continuously-hardening nonlinear curve extending from the proportionality limit point to a predefined ultimate stress point within the normalized natural stress-strain space.

The applicability of the material model to simply-supported flat plates under uniform axial compression was recently investigated by Ndubuaku et al. [43]. A total of 37 idealized variations of the material stress-strain curve and a four-level variation of the slenderness ratio was used to generate a significant number of FE-simulated flat plate models. The results of the study

indicated that the ultimate stress of the flat plate models is strongly dependent on the yield stress of the plate material but not so much on the material hardening. On the other hand, the strain-hardening behavior and overall shape of the nonlinear portion of the stress-strain curve has a relatively tremendous influence on the deformational capacity of the plate models, compared to the yield stress.

In line with the review on the broad subject of axially-compressed cylindrical shells, the methods employed in this study are focused on the analysis of pipelines or other metallic tubes subjected to axial compression, with or without internal pressurization. A finite element (FE) numerical procedure was developed for this study to evaluate the limit loads and corresponding limit strains of axially-compressed cylindrical shells. An extensive parametric study was subsequently conducted based on the results of the FE analyses and a semi-empirical modeling approach, by means of advanced nonlinear regression techniques, was used to develop mathematical expressions for predicting the limit strain. The four constituent parameters of the derived mathematical expressions, considered to have the most influential impact on the limit strain, are D/t ratio, internal pressure, material strain-hardening, and the proportionality-limit stress. The distinction between yield-plateau type (YPT) stress-strain curves and round-house type (RHT) stress-strain curves for metallic materials was considered in this study; hence, a total of 144 specimens were numerically analyzed (80 YPT specimens and 64 RHT specimens). A five-level variation of the internal pressure was also performed in this study, and a full-factorial design approach was adopted such that all possible combinations of the parametric variations were applied across all the factors considered for the FE analyses. Consequently, a total of 400 runs were performed for the YPT pipes while 320 runs were performed for the RHT pipes bringing the total number of separate numerical simulations conducted to 720.

It is common practice, in the formulation of mathematical models for the prediction of the deformational capacity of pipelines, for the strain hardening properties to be accounted for either by the Ramberg-Osgood hardening exponent, n [44] or the yield-to-tensile stress (Y/T) ratio [45,46]. The approach adopted for material characterization in this study is based on full-range parameterization of the stress-strain relationship and is considered to be more appropriate for incorporation into the mathematical prediction models. The constitutive constants of the Ndubuaku material model are remarkably useful for accurately estimating the stress-strain

relationship with minimal simplification and are therefore used instead of the Ramberg-Osgood hardening exponent for parameterization of the strain-hardening behavior of all the materials investigated in this study.

6.3 Constitutive Model for Material Characterization

The Ndubuaku stress-strain model, Eq. (6-1), mathematically expresses the true stress (σ) as a function of the true strain (ε) using two constitutive model constants, the “knee” parameter (k_{nm}) and the “heel” parameter (h_{nm}), thus:

$$\sigma = \begin{cases} E\varepsilon & \sigma \leq \sigma_{pl} \\ \sigma_{pl} + (\sigma_{up} - \sigma_{pl}) \left(\frac{\varepsilon - \varepsilon_{pl}}{\varepsilon_{up} - \varepsilon_{pl}} \right)^{k_{nm} \left(\frac{\varepsilon - \varepsilon_{pl}}{\varepsilon_{up} - \varepsilon_{pl}} \right)^{h_{nm}}} & \sigma > \sigma_{pl} \end{cases} \quad (6-1)$$

where E is Young’s modulus of elasticity, σ_{pl} and ε_{pl} represent the proportionality limit stress and the proportionality limit strain respectively, and σ_{up} and ε_{up} represent the ultimate proof stress and the corresponding ultimate proof strain respectively. The proportionality limit values and the ultimate proof values are obtained at the lowest point and the highest point, respectively, in the natural stress-strain space under consideration.

A major advantage of the Ndubuaku stress-strain model is the ability to prescribe specific control points which the nonlinear portion of the stress-strain curve is required to pass through. By applying the procedure outlined by Ndubuaku et al. [43], the two model constants can be derived by specifying two stress control points (σ_{c1} and σ_{c2}) and two strain control points (ε_{c1} and ε_{c2}), using the following expressions:

$$k_{nm} = \frac{\varepsilon_{R1}^{(h_{nm})} \ln(\sigma_{R1})}{\ln(\varepsilon_{R1})} \text{ or } \frac{\varepsilon_{R2}^{(h_{nm})} \ln(\sigma_{R2})}{\ln(\varepsilon_{R2})} \quad (6-2)$$

$$h_{nm} = \frac{\ln \left[\frac{\ln(\varepsilon_{R1}) \cdot \ln(\sigma_{R2})}{\ln(\sigma_{R1}) \cdot \ln(\varepsilon_{R2})} \right]}{[\ln(\varepsilon_{R1}) - \ln(\varepsilon_{R2})]} \quad (6-3)$$

where,

$$\sigma_{R1} = \frac{\sigma_{c1} - \sigma_{pl}}{\sigma_{up} - \sigma_{pl}}, \quad \sigma_{R2} = \frac{\sigma_{c2} - \sigma_{pl}}{\sigma_{up} - \sigma_{pl}}, \quad \varepsilon_{R1} = \frac{\varepsilon_{c1} - \varepsilon_{pl}}{\varepsilon_{up} - \varepsilon_{pl}}, \quad \text{and} \quad \varepsilon_{R2} = \frac{\varepsilon_{c2} - \varepsilon_{pl}}{\varepsilon_{up} - \varepsilon_{pl}}$$

The model features a transition between a fully concave curve and a fully convex curve which is defined by the straight diagonal line that transcends from the proportionality limit point to the ultimate proof point. The straight diagonal line is only achievable if k_{nm} equals 1 and h_{nm} equals 0. If h_{nm} equals 0, then a purely convex curve is obtained for $k_{nm} < 1$ otherwise, a purely concave curve is obtained for $k_{nm} > 1$. However, the mathematical inference of a zero-value heel factor is a simple power law expression that lacks the essence of the model. The implication of such non-zero constraint on the heel factor is the inevitable existence of a yield plateau for every classification of stress-strain curves. While this attribute poses no challenge for YPT curves, it becomes imperative in the case of RHT curves to employ applicable control measures to specify any desired yield plateau length within acceptable tolerance limits.

The implementation of a YPL-control procedure takes advantage of the double-curvature of the derived stress-strain relationship by specifying the location of the curve inflection point with respect to the strain. The inflection point is derived by equating the second derivative of the stress, evaluated against the strain, to zero as follows:

$$\frac{d^2 \sigma_{Ri}}{d\varepsilon_{Ri}^2} = \varepsilon_{Ri}^k \cdot \left(\frac{1}{\varepsilon_{Ri}} \right)^h \cdot \left[\begin{array}{l} \left(\left(\frac{1}{\varepsilon_{Ri}} \right)^{1+h} (k - k \cdot h \cdot \ln[\varepsilon_{Ri}]) \right)^2 \\ - \left(\left(\frac{1}{\varepsilon_{Ri}} \right)^{2+h} \cdot (k \cdot h + k \cdot (1 + h) - k \cdot h \cdot (1 + h) \cdot \ln[\varepsilon_{Ri}]) \right) \end{array} \right] = 0 \quad (6-4)$$

where,

$$\sigma_{Ri} = \frac{\sigma_{ci} - \sigma_{pl}}{\sigma_{up} - \sigma_{pl}} \quad \varepsilon_{Ri} = \frac{\varepsilon_{ci} - \varepsilon_{pl}}{\varepsilon_{up} - \varepsilon_{pl}}$$

σ_{Ri} and ε_{Ri} represent the stress ratio and strain ratio, respectively, derived from the stress control value, σ_{ci} and the corresponding strain control value, ε_{ci} at the inflection point.

Rearranging Eq. (6-4) to express the inflection point knee factor, k_i in terms of the remaining parameters yields:

$$k_i = - \frac{\left(\frac{1}{\varepsilon_{Ri}}\right)^{-h_i} \cdot (-1 - 2h_i + h_i \cdot \ln[\varepsilon_{Ri}] + h_i^2 \cdot \ln[\varepsilon_{Ri}])}{(-1 + h_i \cdot \ln[\varepsilon_{Ri}])^2} \quad (6-5)$$

The flowchart in Figure 6-1 illustrates the iterative procedure which is implemented to minimize the error between the original knee factor, k_{nm} and the inflection point knee factor, k_i .

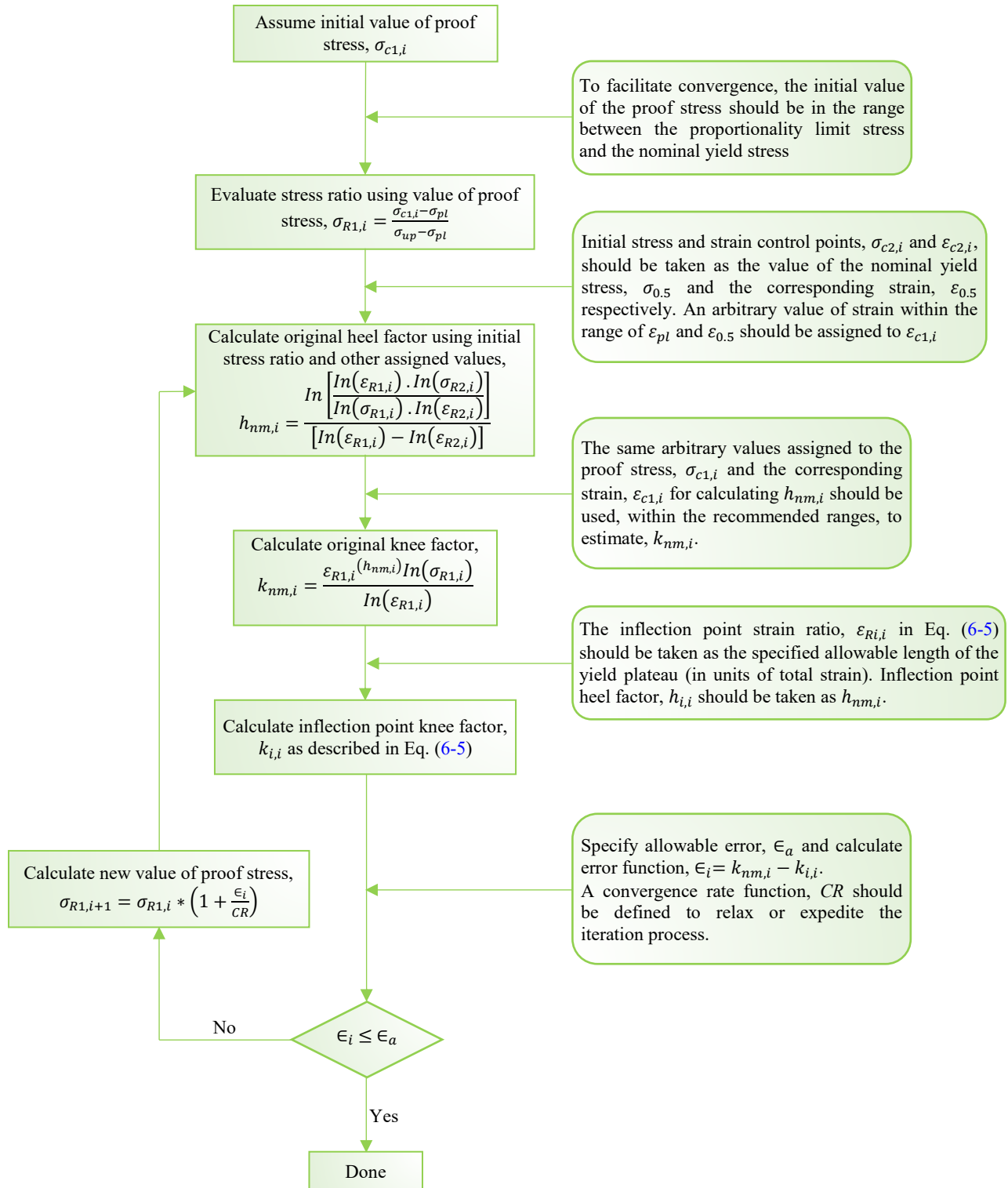


Figure 6-1: Flowchart of iterative procedure for derivation of inflection point knee factor

6.4 Theoretical Formulations

Consider the long cylindrical shell shown in Figure 6-2 which has a radius, R , and wall thickness, t .

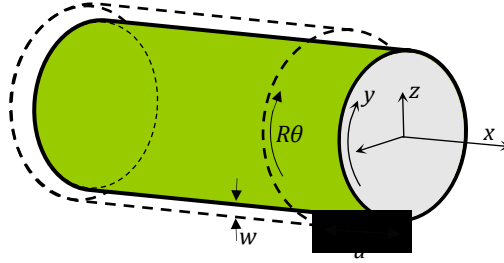


Figure 6-2: Schematic of strain components for axially-compressed cylinder

where x , y , and z are the longitudinal, circumferential, and radial axes respectively in the mid-thickness layer of the undeformed cylindrical shell while u , $v (= R\theta)$, and w represent the warping, circumferential and flexural displacement components corresponding to the x -, y - and z -axes respectively.

The governing equations for the circular cylindrical shell are expressed thus [47–50]:

$$\frac{D}{h} \nabla^2 \nabla^2 w - \frac{\partial^2 w}{\partial x^2} \frac{\partial^2 \Phi}{\partial y^2} + 2 \frac{\partial^2 w}{\partial x \partial y} \frac{\partial^2 \Phi}{\partial x \partial y} - \frac{\partial^2 \Phi}{\partial x^2} \left(\frac{\partial^2 w}{\partial y^2} - \frac{1}{R} \right) - \frac{p}{t} = 0 \quad (6-6)$$

$$\frac{1}{E} \nabla^2 \nabla^2 \Phi - \left(\frac{\partial^2 w}{\partial x \partial y} \right)^2 + \frac{\partial^2 w}{\partial x^2} \frac{\partial^2 w}{\partial y^2} - \frac{1}{R} \frac{\partial^2 w}{\partial x^2} = 0$$

where,

$$\nabla^2 = \frac{\partial^2}{\partial x^2} + \frac{\partial^2}{\partial y^2}, \quad \nabla^2 \nabla^2 = \frac{\partial^4}{\partial x^4} + 2 \frac{\partial^4}{\partial x^2 \partial y^2} + \frac{\partial^4}{\partial y^4}$$

The derived form of the governing equations makes it possible for the exact solutions of the flexural displacement, w , and the stress function, Φ , to be obtained by simply solving the two equations in Eq. (6-6) simultaneously.

Applying the governing equations outlined in Eq. (6-6), the analytical solutions for the special case of a cylindrical shell subjected to a uniform compressive axial load, P , and zero internal or external pressure can be obtained by neglecting end effects and applying the following assumptions for the initial stresses and initial deformation in the pre-buckling state [47,51]:

$$N_{x0} = \sigma_{x0}h = \frac{P}{2\pi R}, \quad N_{y0} = \sigma_{y0}h = 0, \quad N_{xy0} = \tau_{xy0}h = 0, \quad w_0 = \text{constant}$$

yielding,

$$D\nabla^8 w + \frac{Eh}{R^2} \frac{\partial^4 w}{\partial x^4} + \frac{P}{2\pi R} \nabla^4 \left(\frac{\partial^2 w}{\partial x^2} \right) = 0 \quad (6-7)$$

By representing the unknown deflection by a set of functions, each of which satisfies the boundary conditions, the classical solution for the critical buckling stress of a simply-supported cylindrical shell subjected to uniform axial compression is derived as:

$$\sigma_c = \frac{E}{\sqrt{3(1-\mu^2)}} \frac{t}{R} \quad (6-8)$$

Xue [52] pointed out that, in practice, such mathematical derivations prove to be complicated and sometimes infeasible hence approximate methods are often employed to obtain required solutions.

6.5 Methodology of Numerical Research

Nonlinear finite element analysis of uniform axial compression of cylindrical shells was performed in this study using the general-purpose finite element program, ABAQUS CAE [53]. As previously indicated, shell buckling typically involves large deflections and large rotations [12,13,54]; hence, it is essential that the displacement- and rotation-induced strains be evaluated using membrane finite strain formulations analogous to the approximations of the Koiter-Sanders shell theory [55].

6.5.1 Test matrix

The FE pipe models analyzed in this study were generated based on parametric variation of four factors considered to be most influential to the deformational capacity of pipelines: the dimensional factor (D/t ratio), the load factor (internal pressure), the material grade factor (proportionality limit stress), and the strain-hardening factor (constitutive material model shape constants). In order to properly capture the nonlinearities in the relationships between the deformational response of the pipe and various associated parameters, a minimum of four variations was applied to each of the parameters evaluated. To maintain correspondence with the non-dimensionality of the critical buckling strain, the parameters were also normalized.

6.5.1.1 Dimensional properties

The diameter, D , is normalized with the nominal pipe wall thickness, t , to yield the D/t ratio. The range of evaluation for the dimensional parameter (D/t ratio) was between 41 and 105 with a four-level variation thus: 41.152 (DT1), 64.078 (DT2), 82.156 (DT3) and 104.622 (DT4). For simplicity of numerical analyses, the same pipe size (i.e., nominal pipe size (NPS) = 36 in) was maintained for all the FE pipe models while the pipe wall thickness was varied according to the prescribed D/t ratios thus: $t_1 = 22.22$ mm (for DT1), $t_2 = 14.27$ mm (for DT2), $t_3 = 11.13$ mm (for DT3), and $t_4 = 8.74$ mm (for DT4).

6.5.1.2 Loading conditions

The internal pressure, p , is normalized with the pipe yield pressure ($p_y = \frac{2\sigma_y t}{D}$). The ratio of the applied pressure to pipe yield pressure (i.e., $\frac{p}{p_y}$) is herein referred to as “pressure factor (f_p)”. Values of the internal pressure applied to the FE pipe models were determined based on the pressure-resultant hoop stress corresponding to percentages of the nominal yield stress³ (YS).

³ The API 5L standard prescribes specific values of the specified minimum yield stress (SMYS) for different grades of pipeline steel which are essentially intended as a quality control guideline for steel pipeline manufactures and provide guidance to pipeline designers and operators on the required material grades for intended operating pressures. However, the yield stress (YS) values specified for this research are intended to more closely reflect practical values obtained from standard tensile tests of pipeline steels and are, therefore, nominally selected at values that are slightly higher than the API 5L SMYS specifications.

Four variations of the YS values were derived according to the material grade specifications of the API 5L standard [56] for pipeline steels thus: X52 grade = 379 MPa, X60 grade = 441 MPa, X70 grade = 503 MPa, and X80 grade = 586 MPa. A five-level variation of the pressure factor (0%, 20%, 40%, 60% and 80%) was then applied to the FE models for each material grade.

6.5.1.3 Material grade

The proportionality limit stress, σ_{pl} , for RHT materials is normalized with the ultimate tensile stress, σ_{us} to yield $\frac{\sigma_{pl}}{\sigma_{us}}$. The ratio of the proportionality limit stress (PLS) to the ultimate tensile stress (UTS) is herein referred to as the “PLUS” ratio. It is acknowledged that the description of the material grade of RHT metals is customarily based on the nominal yield stress corresponding to either the 0.2% plastic strain ($\sigma_{p,0.2}$) prescribed by the EN 1993-1-4 stainless steels standard [57] or the 0.5% total strain ($\sigma_{0.5}$) prescribed by the API 5L pipeline steels standard [56]. However, it will be shown in a later section that the PLUS ratio has a direct influence on the critical buckling strain of RHT structures while the influence of the yield stress is more or less indirect, i.e., the material characteristics that tend to indicate better deformational capacities in higher grade pipes made of RHT materials are fundamentally more as a result of the superior hardening properties of the material than the higher value of the nominal yield stress.

On the other hand, YPT materials are characteristically defined by a distinct yield point which is coincident for materials of the same grade; hence, the yield stress and the proportionality limit stress are always equal. Nondimensionalization of the material grade factor for YPT materials was therefore achieved by applying the ratio of the yield stress, σ_y to the elastic modulus, E . The elastic modulus of the steel materials (205800 MPa) was carefully chosen to correspond with results of experimental observations by Kong et al. [58] based on tensile tests performed on pipeline steels with comparable properties, using a state-of-the-art three-dimensional digital image correlation (3D-DIC) technique.

Similar to the YS values, the values for the ultimate tensile stress, σ_{us} selected for each material grade were selected according to the API 5L specifications thus: X52 grade = 455 MPa, X60 grade = 565 MPa, X70 grade = 593 MPa and X80 grade = 703 MPa.

6.5.1.4 Constitutive material model constants (k_{nm} & h_{nm})

The nonlinear portions of the plots generated to characterize the various stress-strain relationships for the four different material grades analyzed in this study were parameterized using the novel stress-strain model developed by Ndubuaku et al. [43]. For the four selected material grades (X52, X60, X70, and X80), different curves (5 curves each for YPT materials and 4 curves each for RHT materials) were generated, as shown in Figure 6-3 - Figure 6-6, with the same prescribed YS and the same ultimate proof stress (UPS) but different hardening properties. To ensure uniformity in the strain range, the ultimate proof stress was maintained at the stress corresponding to a total strain of 10% (i.e., σ_{10}), and the nominal yield stress was maintained at the stress corresponding to a total strain of 0.5% (i.e., $\sigma_{0.5}$) for respective material grades of various strain-hardening. The selection of a constant magnitude of total strain = 10% as the elongation for all the material grades studied herein is intended to tackle the inevitable issue of variability in the elongation of stress-strain curves due to factors such as testing conditions and ductility differences. A 10% elongation is therefore defined to effectively capture a reasonable range of the stress-strain curve beyond which the shape of the stress-strain curve has no significant effect on the deformational capacity of pipe segments.

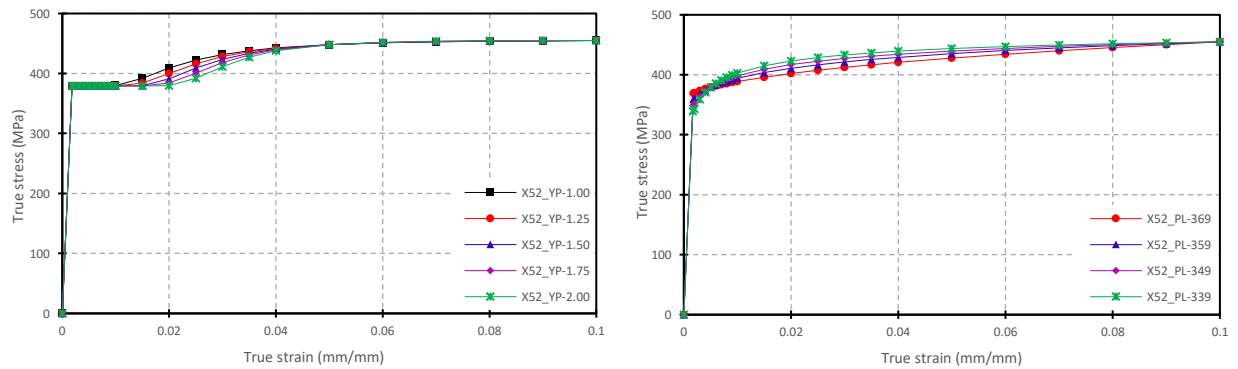


Figure 6-3: Idealized variations for stress-strain curves of X52-YPT and X52-RHT materials

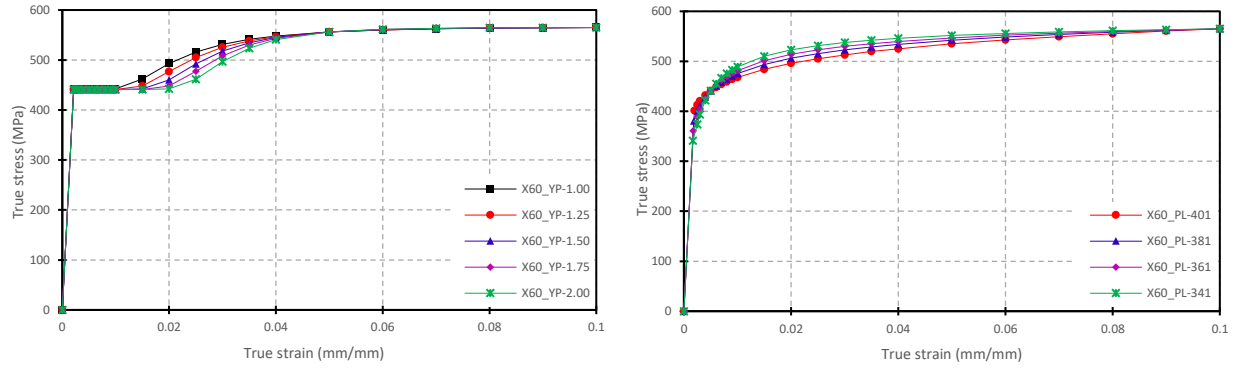


Figure 6-4: Idealized variations for stress-strain curves of X60-YPT and X60-RHT materials

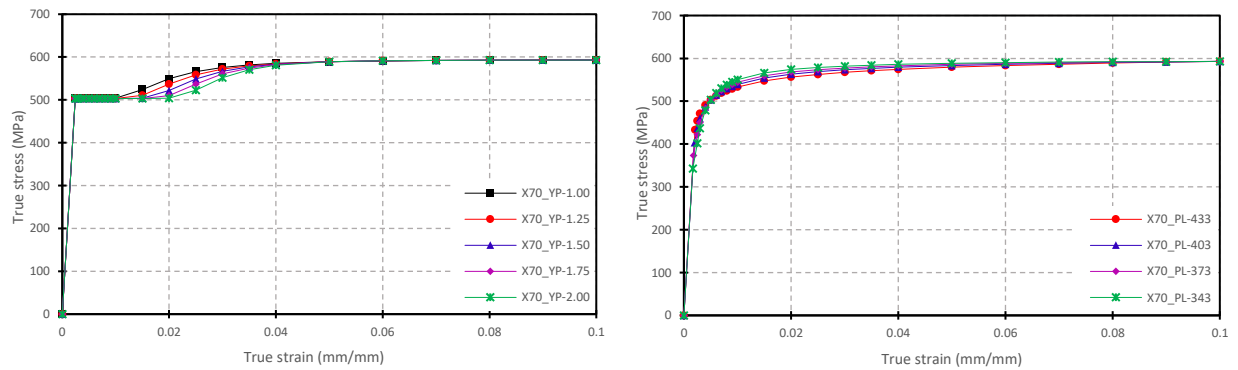


Figure 6-5: Idealized variations for stress-strain curves of X70-YPT and X70-RHT materials

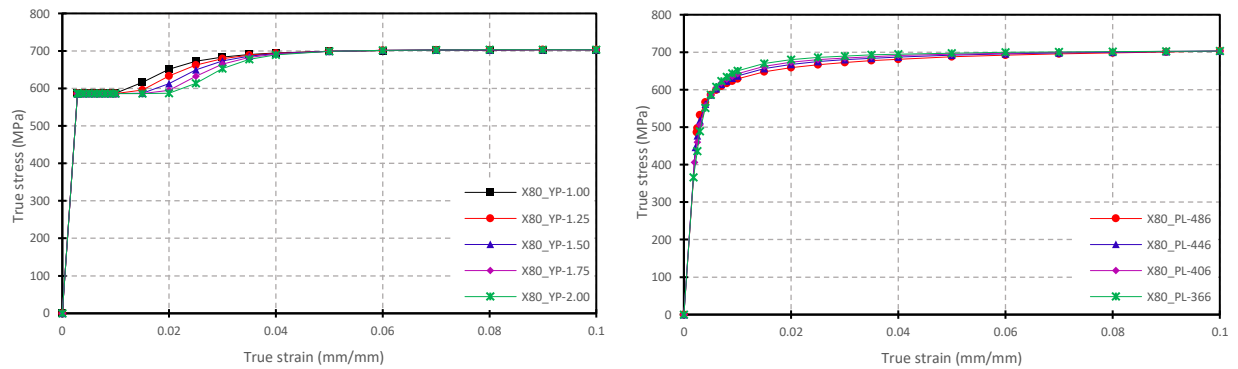


Figure 6-6: Idealized variations for stress-strain curves of X80-YPT and X80-RHT materials

As indicated by the plots in Figure 6-3 - Figure 6-6, the stress-strain relationships for the different material grades exhibit slight differences in the hardening behavior. Each curve is labeled to reflect the peculiarities of its hardening property; hence, the numeric designations for the YPT curve labels are in percentage (%) units and indicate the length of the yield plateau in

terms of the total strain whereas the numeric designations for the RHT curve labels are in megapascal (MPa) units and indicate the proportionality limit stress for the respective curves. The values of the model constants used to generate the stress-strain curves presented in Figure 6-3 - Figure 6-6 are outlined in Table 6-1.

Table 6-1: Model constants for derivation of stress-strain curves

Material Grade	YPT			RHT		
	<i>Curve label</i>	$K_f = 1/K_{nm}$	$H_f = 1/H_{nm}$	<i>Curve label</i>	$K_f = 1/K_{nm}$	$H_f = 1/H_{nm}$
X52	<i>YP-1.00</i>	20.5077	0.6958	<i>PL-369</i>	1.9578	16.4530
	<i>YP-1.25</i>	25.9422	0.5658	<i>PL-359</i>	3.3881	7.6640
	<i>YP-1.50</i>	33.6157	0.4692	<i>PL-349</i>	5.2603	5.0535
	<i>YP-1.75</i>	45.0310	0.3934	<i>PL-339</i>	8.5164	3.4226
	<i>YP-2.00</i>	63.0332	0.3318			
X60	<i>YP-1.00</i>	29.9027	0.6234	<i>PL-401</i>	3.8457	7.7602
	<i>YP-1.25</i>	38.8327	0.5078	<i>PL-381</i>	6.1646	4.9322
	<i>YP-1.50</i>	51.7336	0.4219	<i>PL-361</i>	9.3150	3.6322
	<i>YP-1.75</i>	71.4369	0.3544	<i>PL-341</i>	15.359	2.6046
	<i>YP-2.00</i>	103.465	0.2994			
X70	<i>YP-1.00</i>	57.9192	0.5532	<i>PL-433</i>	9.5412	4.3644
	<i>YP-1.25</i>	77.6927	0.4512	<i>PL-403</i>	17.4955	2.9594
	<i>YP-1.50</i>	107.0977	0.3755	<i>PL-373</i>	29.5817	2.2654
	<i>YP-1.75</i>	153.5094	0.3160	<i>PL-343</i>	58.0424	1.6629
	<i>YP-2.00</i>	231.8488	0.2675			
X80	<i>YP-1.00</i>	83.7395	0.5187	<i>PL-486</i>	11.5448	3.9814
	<i>YP-1.25</i>	115.2048	0.4221	<i>PL-446</i>	21.1099	2.7531
	<i>YP-1.50</i>	162.9859	0.3510	<i>PL-406</i>	35.3391	2.1374
	<i>YP-1.75</i>	240.2443	0.2953	<i>PL-366</i>	69.2445	1.5847
	<i>YP-2.00</i>	374.3178	0.2501			

As may be inferred from Table 6-1, the model constants generally tend to yield values less than 1 hence the values are inverted as listed for convenience of representation and clarity.

An isotropic material model was adopted for this study and was assigned to all the generated pipe models using the piecewise linear isotropic hardening stress-strain model definition facility in ABAQUS. The material model was also assumed to obey the von Mises yield criterion and the associative flow rule.

6.5.2 Geometry, mesh, and elements

The mesh of the FE pipe models was created with 4-node quadrilateral finite-membrane-strain shell elements with reduced integration (S4R). The S4R element has been used extensively in previous numerical investigations [59–63] and has proven to be remarkably effective for finite membrane strain shell analyses involving large displacements and rotations. Each node of the doubly-curved S4R element has six degrees of freedom: three translations (u_1, u_2, u_3) in the directions of the global axes and three rotations ($\theta_1, \theta_2, \theta_3$) about the directions of the three global axes.

The S4R element is able to account for changes in the thickness of the shell under load or displacement increments through its characteristic finite membrane strain formulation by evaluating the derivatives of the position vector at points in the deformed configuration of a reference shell surface with respect to respective points in the undeformed configuration. The strain in the direction of the normal to any point on the reference surface of the shell is assumed to remain constant throughout the shell thickness. Bending strains are derived by computing the derivatives of the normal to the mid-thickness surface of the shell and are derived based on small strain assumptions [53].

The S4R is a shear-flexible element which is suitable for modeling the deformational behavior of both thick and thin shells. Default values of the shear stiffness are prescribed in ABAQUS based on the area-to-thickness ratio of the element and are automatically adjusted to prevent transverse shear locking. Transverse shear deformation is generally considered to be negligible in thin shells thus, the S4R element tends to satisfy the assumptions of the classical Kirchhoff shell theory for thin shells by imposing a constraint to the vector normal to a reference surface of the undeformed shell such that the vector remains normal to the respective reference surface in the

deformed configuration. To prevent the occurrence of “hourglass” modes of deformation, the transverse shear strain components are evaluated at the mid-edge points of the shell elements [53].

The element has an isoparametric formulation, i.e., each nodal coordinate has the dual function of defining the element’s geometry and describing the element’s nodal displacements hence, the same functions are used to interpolate both displacements and position vectors. Being a reduced-integration element, the S4R has only one integration point on its mid-surface, and ABAQUS forms the element stiffness matrix using a lower-order integration unlike for full-integration elements, where the number of integration points sufficient to integrate the virtual work expression exactly must be generated. Reduced integration potentially optimizes the accuracy of shell load and displacement predictions with reasonable efficiency of computational resources. A mesh sensitivity analysis was performed, and an optimum mesh size of 30 mm was selected. The default number of 5 points was selected for through-thickness integration throughout this study, and the Simpson’s rule was employed to perform the integration.

A value equal to six times the pipe diameter ($6*D$) was specified as the length of all the pipe models generated in this study, and the average compressive strain in the wrinkle area of all pipe models analyzed in this study was measured using a gauge length of two times the pipe diameter ($2*D$).

6.5.3 Symmetry, boundary conditions, and loading

To optimize computational effort, longitudinal (i.e., symmetry across the x - y plane) symmetry and horizontal-transverse (i.e., symmetry across the y - z plane) symmetry boundary conditions were applied to the pipe so that only a quarter of each pipe specimen (half-length and half-circumference) was modeled. Hence, to simulate the specified length of $6*D$, the ABAQUS pipe models were extruded to a length of $3*D$. With the reference point of orthogonal coordinate axes being coincident with the center of the pipe cross-section at the longitudinal symmetry plane, a new reference point was created along the z -axis at the extruded pipe end. The new reference point was fixed in all principal axis directions except to allow longitudinal translation along the z -axis. To allow a uniform stress field along the pipe length under internal pressurization, a kinematic coupling constraint was defined to constrain the motion of the nodes on the pipe-end

cross-section to the rigid body motion of the reference point. The kinematic coupling constraint was defined with respect to the cylindrical coordinate system such that all the degrees of freedom, except translational hoop strain, were restricted. Allowing translational hoop strain under the kinematic constraint specification was observed to be relatively most effective for mitigating the stresses generated at the pipe ends under internal pressurization.

Following, the default “Initial” step in ABAQUS CAE, two loading steps were defined using the built-in “Step” module. In the first loading step, internal pressure corresponding to a hoop stress equivalent of respective ratios (or percentages) of the pipe’s YS was applied to the inner surface of the pipe and maintained constant in the subsequent loading step. Since the second loading step was displacement-controlled, the “Static General” step which is performed based on the default “Newton’s method” iterative solution technique in ABAQUS would have been sufficient for evaluating the load-deformation response. However, the displacement-controlled deformation in the second loading step was simulated by incrementally imposing an axial displacement onto the pipe-end reference point using the linearized arc-length Riks algorithm in ABAQUS. Similar results are generally obtained using either the “Static General” method or the “Static Riks” method.

6.5.4 Post-processing

After the completion of the numerical analysis for each pipe model, the incremental values of the axial reaction force (RF3) at the predefined pipe-end reference point were directly obtained from the “ODB field output” in the ABAQUS post-processing module. On the other hand, the incremental values of the average strain had to be derived using the “Operate on XY Data” tool in ABAQUS to calculate the mean of the combined values of axial logarithmic strain (LE11; defined with respect to the cylindrical coordinate system) in all the elements within the prescribed gauge length and area. The incremental values were then exported into a Microsoft Excel spreadsheet, where the average strain corresponding to the peak value of force in the axial force vs. average strain plot was selected as the critical limit strain (CLS).

6.5.5 Imperfection sensitivity analysis

Three different linear combinations of the eigenmodes (Type 1 = mode 1 + mode 7, Type 2 = mode 2 + mode 7, Type 3 = mode 3 + mode 7) were used to create imperfection shapes considered to bear approximate resemblance with the imperfection profiles obtained by Kainat et al. [64–66] and Chen et al. [67]. For each combination, mode 1, mode 2 and mode 3 were five times the scale of mode 7 so that the designation of scale factors was assigned with respect to the primary modes (1, 2 and 3) while mode 7 was considered to be the secondary imperfection. The three imperfection shapes were superposed to perfect models in the nonlinear analysis and a parametric variation of the scale of the imperfections as well as the ASTR was performed (see Figure 6-7 - Figure 6-9).

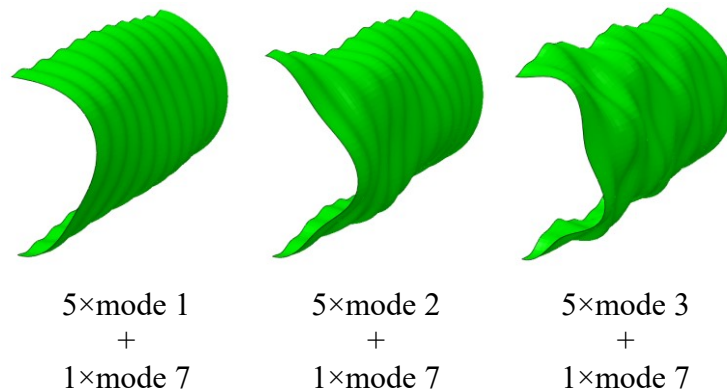


Figure 6-7: Linear superposition of eigenmodes

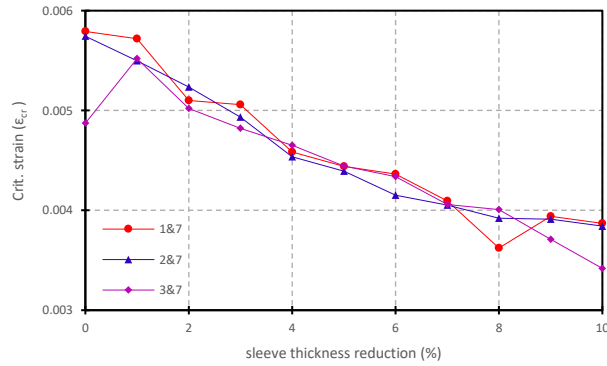


Figure 6-8: Plots of ϵ_{cr} for 50% scale (all imperfection types)

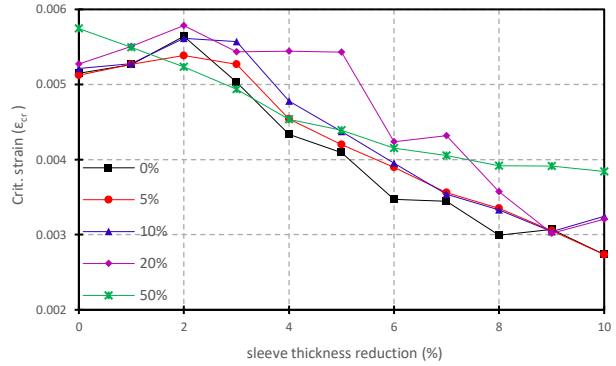


Figure 6-9: Plots of ϵ_{cr} for Type 2 imperfection

The plots in Figure 6-7 – Figure 6-9 were obtained for an FE-simulated unpressurized pipe with a D/t ratio of 78. The plots of the CLS against percentage reduction of the mid-length sleeve, presented in Figure 6-8, indicate that difference in the imperfection types has a negligible effect on the deformation response of the pipe, even with a scale factor as high as 50% of the wall thickness, and the results become more similar as the scale factor is reduced. A cumulative plot of all the results obtained for the Type 2 imperfection are presented in Figure 6-9, and the results corroborate the findings of Ref. [31] and Ref. [66] from two aspects: (1) thickness variations have a more significant effect on the deformational capacity than diametric variations, and (2) below a D/t ratio of 100, the effect of geometric imperfections on the load-deformation response becomes negligible.

6.6 Validation of FE Models

For the purpose of this study, geometric imperfections are assumed to have a negligible effect on the deformational capacity of the pipe models within the range of D/t ratios covered herein; hence, a reduced-thickness “buckling trigger” sleeve (3% less than the nominal pipe wall thickness) was introduced at the pipe’s mid-span for analysis of all the FE models. An unpressurized pipe segment of D/t ratio = 64 was modeled using ABAQUS and subjected to pure bending. The FEA result was then compared to experimental test results by Mohareb et al. [63]

and satisfactory correspondence with the results of Ref. [63] was obtained for the moment-curvature response as well as the wrinkling deformation mode at failure (Figure 6-10).

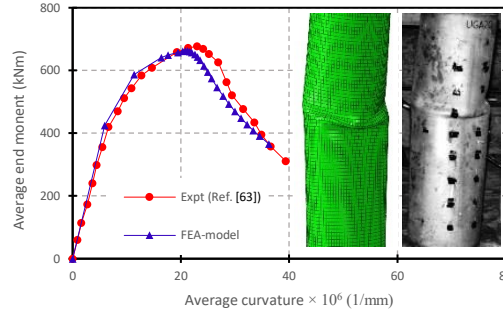


Figure 6-10: Comparison of FEA result with experimental result (UGA508) by Ref. [63]

Figure 6-10 indicates the ability of the FE model to reproduce the diamond-shape buckling mode obtained from the experimental test of the pipe segment. The Ndubuaku model was used to derive the appropriate shape constants for approximation of the material stress-strain relationship obtained from the ancillary tension coupon test by Ref. [63]. The geometrical and material properties of the experimental test specimen, designated as “UGA508” by Ref. [63], are as follows:

- Outer diameter	508 mm
- D/t ratio	64
- Length of pipe	1690 mm
- Material grade	API X56
- Elastic modulus	203704 MPa
- Yield stress ($\sigma_{0.5}$)	391 MPa
- Proportionality limit stress	329 MPa
- Knee constant ($1/K_{nm}$)	3.53
- Heel constant ($1/H_{nm}$)	29.61
- Net-section compressive axial force	1303 kN

6.7 Results of Numerical Analysis

6.7.1 Parametric study for YPT pipes

Generally, the deformational capacity and post-buckling response of YPT pipes are both inferior compared to RHT pipes, and this is attributable to the abrupt change in the stress-strain curve at the elastic limit of the material. Results of this study, however, indicate the possibility of recovery of the load-deformation response (as shown in Figure 6-11) of YPT pipes at elevated levels of internal pressure and/or for low D/t ratios.

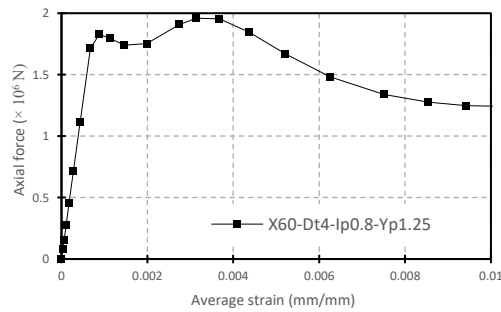


Figure 6-11: Plot of axial force vs. average strain for X60 pipe with D/t ratio = 104.62, $f_p = 0.8$, and $YPL = 1.25$.

The plot in Figure 6-11 is obtained for an X60 pipe with a D/t ratio of 104.6 and yield plateau length of 1.25% total strain subjected to an internal pressure equal to 80% Y_S . The plot shows an initial drop in the peak load which is somewhat catastrophic (as indicated by the sharp drop in the load at approximately 0.1% average axial strain) but as loading continues, the pipe material quickly reaches the strain-hardening portion of the stress-strain curve beyond the yield plateau and the load resistance recovers resulting in a higher CLS ($\approx 0.3\%$). This phenomenon contrasts with the general notion that the material stress-strain behavior of YPT structures can be represented by a bilinear curve. While such bilinear representation may be sufficient for stress-based design, as the difference between the lower and higher loads is not significant, a strain-based design that relies on such bilinear simplification is prone to considerable conservativeness.

6.7.1.1 Influence of D/t ratio

The trend of the FE-predicted CLS with respect to the D/t ratio is presented in Figure 6-12 and Figure 6-13. The plots in Figure 6-12 are obtained for an X70 pipe with a YPL of 1.25% total strain subjected to internal pressures ranging from 0% to 80% YS while the plots in Figure 6-13 are obtained for the same parameters as in Figure 6-12 except with a YPL of 2.0% total strain. The D/t ratio is generally observed to be negatively correlated with the CLS as a decrease in the D/t ratio tends to increase the CLS. However, the influence of the D/t ratio on the CLS is also observed to be affected by the magnitude of internal pressure and, even though slightly, by the YPL.

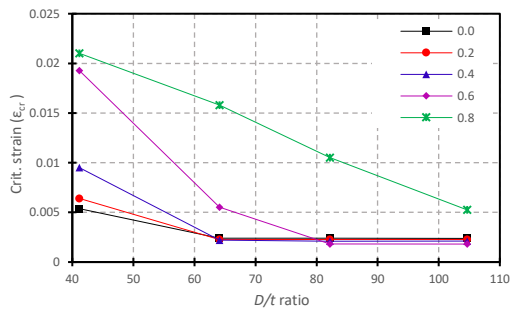


Figure 6-12: Plot of ϵ_{cr} vs. D/t ratio for X70 pipe (YPL = 1.25)

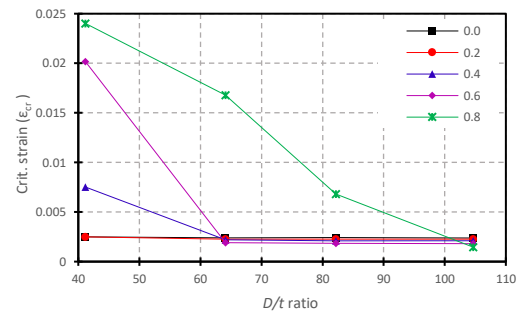


Figure 6-13: Plot of ϵ_{cr} vs. D/t ratio for X70 pipe (YPL = 2.0)

6.7.1.2 Influence of internal pressure

The four D/t ratios covered in this study are plotted in Figure 6-14 and Figure 6-15 to show the influence of the internal pressure on the CLS for YPT pipes. The plots in Figure 6-14 are obtained for an X52 pipe with a YPL of 1.0% total strain while the plots in Figure 6-15 are for an X70 pipe with a YPL of 1.5% total strain. The results indicate that for high D/t ratios (DT3 and DT4), increase in internal pressure generally has no effect on the CLS until f_p reaches a value of 0.6 whereas, depending on the YPL, the effect of internal pressure on the CLS becomes apparent at $0.4 \leq f_p \leq 0.6$ for intermediate D/t ratios (DT2), and typically takes effect in low D/t -ratio (DT1) pipes at $0 \leq f_p \leq 0.2$.

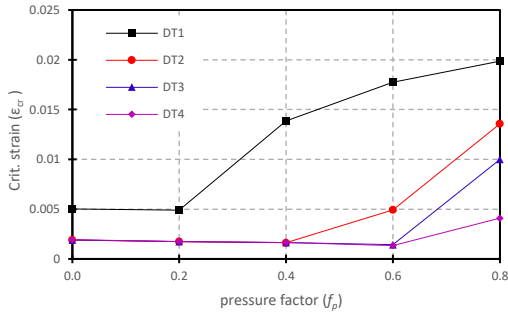


Figure 6-14: Plot of ϵ_{cr} vs. f_p for X52 pipe
(YPL = 1.0)

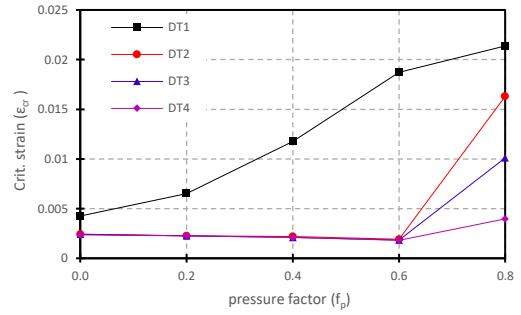


Figure 6-15: Plot of ϵ_{cr} vs. f_p for X70 pipe
(YPL = 1.5)

6.7.1.3 Influence of material grade and YPL

The material grade designation of YPT pipes is simply implied by the yield stress of the pipe material. The trends of the CLS with respect to the yield stress of the pipe material are shown in Figure 6-16 and Figure 6-17. The plots in Figure 6-16 are obtained for a pipe with a D/t ratio of 41.15 and $f_p = 0.6$ while the plots in Figure 6-17 are obtained for a pipe with a D/t ratio of 104.62 and $f_p = 0.8$. The numeric designations in the graph legends for Figure 6-16 and Figure 6-17 refer to the YPL.

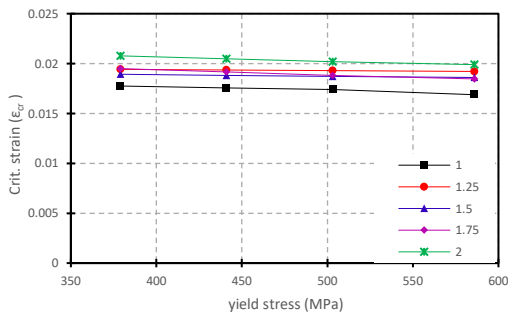


Figure 6-16: Plot of ϵ_{cr} vs. YS for DT1 pipe
($f_p = 0.6$)

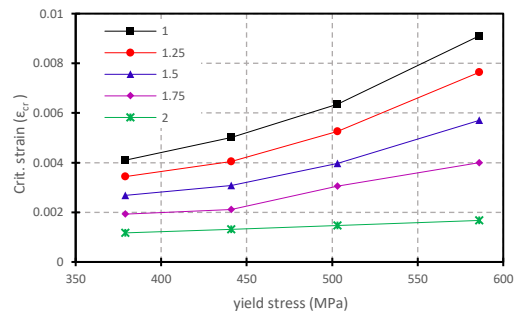


Figure 6-17: Plot of ϵ_{cr} vs. YS for DT4 pipe
($f_p = 0.8$)

6.7.2 Parametric study for RHT pipes

The absence of a distinct yield point at the elastic limit, and invariably the nonoccurrence of an abrupt change in the material stress-strain curve, generally affords RHT pipes with superior deformational capacity compared to YPT pipes.

6.7.2.1 Influence of D/t ratio

The trend of the CLS of RHT pipes with respect to the D/t ratio is presented in Figure 6-18 and Figure 6-19. The plots in Figure 6-18 are obtained for an X70 pipe with a PLUS ratio of 0.73 subjected to f_p values ranging from 0.0 to 0.8 while the plots in Figure 6-19 are obtained for an X70 pipe with a PLUS ratio of 0.58 and subjected the same range of f_p values as in Figure 6-18. As in the case of YPT pipes increase in the D/t ratio also is also observed to be detrimental to the CLS of RHT pipes, and the internal pressure effects are also usually negligible except at extreme f_p values. However, the influence of internal pressure on the CLS vs. D/t -ratio trends for RHT pipes indicates more gradual variation. Lower values of the PLUS ratio (as in Figure 6-19) indicate superior hardening and are observed to reduce the divergence of the CLS vs. D/t -ratio plots.

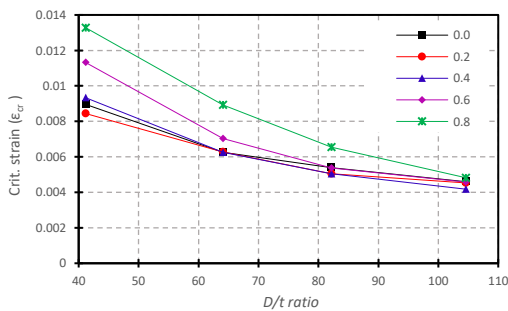


Figure 6-18: Plot of ϵ_{cr} vs. D/t ratio for X70 pipe (PL/US = 0.73)

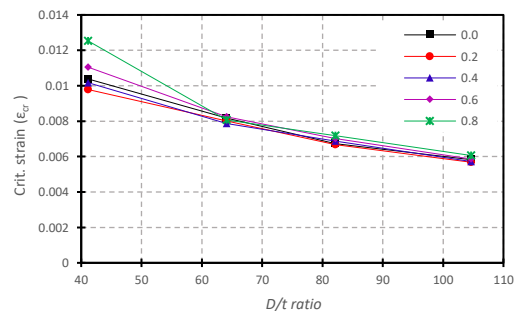


Figure 6-19: Plot of ϵ_{cr} vs. D/t ratio for X70 pipe (PL/US = 0.58)

6.7.2.2 Influence of internal pressure

The influence of the pressure factor on the CLS of RHT pipes is shown by the plots in Figure 6-20, which are obtained for an X80 pipe with a PLUS ratio of 0.69. Compared to YPT pipes, the

results indicate a better variation in the influence of the D/t ratio on the CLS vs. f_p trends as a tangible difference is recorded in the changes in CLS with respect to the D/t ratio regardless of the magnitude of internal pressure. The trends of the individual CLS vs. f_p plots for RHT pipes are however somewhat similar to those obtained for YPT pipes as the influence of pressure on the CLS of high and intermediate D/t -ratio pipes (DT2, DT3, and DT4) is observed to be negligible at low f_p values with a slight increase at $f_p = 0.8$. Internal pressure effects however begin at lower f_p values ($0.0 \leq f_p \leq 0.2$) for low D/t -ratio (DT1) pipes.

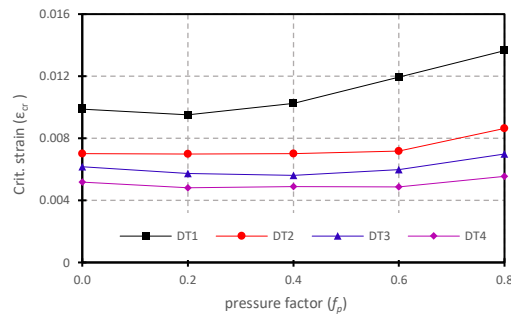


Figure 6-20: Plot of ϵ_{cr} vs. f_p for X52 pipe (YPL = 1.0)

6.7.2.3 Influence of material grade and strain-hardening

The plots in Figure 6-21 and Figure 6-22 are both obtained for a pipe with D/t ratio = 64.08 and $f_p = 0.0$. While Figure 6-21 comprises plots of the CLS against yield stress, Figure 6-22 comprises plots of the CLS against the PLUS ratio. The plots in Figure 6-21 indicate the nonexistence of a smooth relationship between the CLS and the yield stress of the material. Even though nonlinear, the plots in Figure 6-22 portray an inverse relationship between the PLUS ratio and the CLS. The numeric designations in the graph legend for Figure 6-21 refer to the ‘shape factors’ (discussed in [Section 6.9](#)).

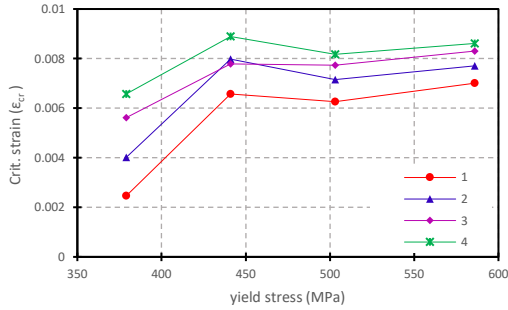


Figure 6-21: Plot of ϵ_{cr} vs. YS for DT1 pipe ($f_p = 0.6$)

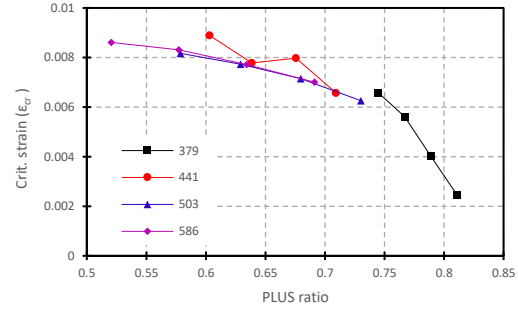


Figure 6-22: Plot of ϵ_{cr} vs. PLUS ratio for DT4 pipe ($f_p = 0.8$)

6.8 Discussion

Pipelines are generally manufactured by two conventional processes: cold-forming and seamless fabrication. Pipes made of the seamless procedure tend to have superior mechanical properties compared to cold-formed pipes as the heat treatment involved in the manufacturing process produces pipes with relatively minimal residual stresses and reduced out-of-roundness. On the other hand, cold-formed pipes are usually less expensive than seamless pipes but are manufactured by a process of circumferential expansion and longitudinal seam welding which introduces directional or spatial mechanical property variations in the pipe material such that they often exhibit higher strength but lower strain hardening capacity in their circumferential direction compared to their longitudinal direction [62,68,69]. Plastic anisotropy in pipe materials may be theoretically accounted for either by treating the material as intrinsically anisotropic [70] or by assuming the anisotropy of the pipe to be due solely to the forming process [36,37]. Liu et al. [45] reported that the findings of previous research studies on the effect of the material's anisotropy on the deformational capacity of pipes are somewhat inconclusive; especially due to inability to simultaneously represent the longitudinal vs. circumferential differences in the tensile strength and strain hardening properties of the pipe. They maintained that the response of a pipe to local buckling deformation is mainly determined by the compressive stress-strain curve of the pipe's longitudinal direction and thus recommended the use of isotropic material modeling for buckling analyses of pipes by using the compressive stress-strain curve of the pipe's longitudinal direction. Results of numerical investigations by Neupane et al. [36,37] however indicate that

assumption of isotropic yielding based on the longitudinal stress-strain curve will produce results similar to anisotropic yielding at zero or low internal pressures while isotropic yielding based on the circumferential stress-strain curve will produce results similar to anisotropic yielding at high internal pressures. Isotropic yielding assumptions were adopted for this study and are considered to adequately represent the material behavior, especially since dynamic and cyclic loading conditions are not considered in this study.

Detailed FE study by Liu et al. [45] on numerical pipe models subjected to local buckling deformation showed that the deformational capacity of pipes tends to increase as the length of the pipe specimen increases, but the length effect diminishes once the length of the pipe reaches a value equal to approximately six times the pipe diameter (i.e., $6*D$). Also, a consensus by researchers on the measurement criteria for the CLS of locally buckled pipelines, especially with regards to gauge length measurement, does not exist. Various researchers adopt different gauge lengths for measuring the average strain, ranging from a length of $1*D$ up to the full length of the pipe. However, to maintain consistency with the calculation of the strain demand, Liu et al. [45] recommend a gauge length of $2*D$ for pipes subjected to local buckling deformation. According to the recommendations of Ref. [45], the length of the FE pipe models and the gauge length over which the average strain was measured were specified as $6*D$ and $2*D$ respectively, throughout this study.

In the absence of statistical representation of the geometric imperfection profile of a cylinder based on actual measurements of test specimens, it is common practice to apply alternative imperfection modeling schemes for calibrating the load/deformation responses of analytically/numerically analyzed cylindrical shells in order to achieve conformity with results of experimental tests on real cylinders. Two commonly-adopted schemes are the “single dimple” approach [45,60], and the linear eigenmode superposition approach; wherein the latter approach tends to be more desirable for shell buckling analysis due to its relative simplicity of application. With the linear eigenmode superposition approach, an elastic buckling analysis is first carried out to determine the eigenmodes of the cylindrical shell after which one or more eigenmodes are selected and scaled by a prescribed amplitude. A linear combination of the scaled eigenmodes (if more than one) is adopted as the imperfection shape and subsequently superposed to the perfect geometry to produce an approximate representation of a geometrically imperfect cylinder.

With the use of a 3D surface scanner to obtain the geometric imperfection profile of a number of pipe specimens Kainat et al. [64–66] performed a series of rigorous experimental studies on the effect of diametric and thickness deviations from nominal values on the buckling behavior of UOE manufactured steel pipes. By individually taking measurements of the two types of imperfections along the perimeter of the pipe cross-section and plotting the imperfections against the circumferential distance of the pipe wall (with the origin at the longitudinal seam weld), they observed the pattern of the diametric deviation to be in a continuous sinusoidal form while the thickness deviation pattern resembled a bell-curved shape. They pointed out that diametric and thickness variations in the longitudinal direction were insignificant, so their study only focused on circumferential variations. They further performed parametric numerical analyses by incorporating mathematically-derived approximations (an ellipse equation for diametric deviation and a Gaussian function for thickness deviation) of the observed imperfections in their FE models. From the results of their study, they concluded that geometric imperfections in the form of circumferential diametric variation have a negligible effect on the buckling behavior of pipes while thickness variations have a considerable effect. The imperfection profiles obtained by Kainat et al. [64,66] showed strong similarities to the measurements by Chen et al. [67] of the circumferential thickness and diametric variation in a pipe specimen using an ultrasonic thickness gauge and a laser tracking system respectively. Experimental and numerical studies by Guo et al. [31] also indicated that the load-deformation response of axially-compressed steel cylinders is largely unaffected by initial geometric imperfections at D/t ratios below 100. The corrugated modes of diametric imperfection which are commonly observed in pipelines were briefly investigated in this study and were observed to have a negligible effect on the deformational capacity.

6.8.1 YPT pipes

The results obtained for *YPT* pipes suggest that at high D/t ratios, there is negligible change in the CLS with respect to changes in the pipe slenderness for low pressures and high YPL values. However, as the D/t ratio reduces, the influence of pressure and YPL becomes more significant. This is attributable to the tendency of the pipe to experience inelastic buckling for low D/t ratios and high internal pressures hence, buckling occurs in the strain-hardening range of the pipe

material beyond the yield plateau resulting in a higher capacity of the pipe to sustain higher deformation. Also, the influence of the YPL indicates that the pipe is less capable of taking advantage of material strain-hardening before the limit load is reached as the YPL is increased.

The influence of pipe slenderness on the occurrence of inelastic buckling is also considered to be responsible for the observed trends in the CLS- f_p plots. High and intermediate D/t -ratio pipes are less likely to experience inelastic buckling and are thus susceptible to catastrophic collapse once the yield point of the material is reached. Since the yield strain (i.e., the strain corresponding to the yield stress) is coincident for all YPT materials of the same grade, the CLS remains unchanged for all cases of buckling in the elastic region or at the elastic limit. However, a deviation from the similarity in the CLS of high and intermediate D/t -ratio pipes occurs at a high f_p value of 0.8. At $f_p = 0.8$, the CLS increases progressively as the D/t ratio of the pipe decreases, and this trend is considered to be caused by the resultant stress state in the pipe under internal pressurization, as well as increased stiffness of the pipe wall against catastrophic collapse, which facilitates the recovery of the load-deformation response as pointed out in Figure 6-11. The same phenomenon holds for relatively thick-walled pipes (DT1).

The overall trends indicate a slightly positive influence of the yield stress on the CLS, especially for the occurrence of elastic buckling such as in high and intermediate D/t -ratio pipes subjected to low internal pressure. The observed favorable influence is consistent with the assertion that the buckling of high and intermediate D/t -ratio pipes is typically within the elastic range hence the CLS is directly related to the yield strain of the pipe material. For high D/t -ratio pipes, the influence of the yield stress on the CLS becomes more evident under high pressure (as in Figure 6-17) due to a higher incidence of buckling beyond the elastic range of the material. The YPL also has a more significant influence on the CLS of high D/t -ratio pipes at high pressure as a shorter YPL allows the material to recover faster from initial catastrophic collapse and vice versa.

Contrastingly, the influence of the YPL on the CLS of low D/t -ratio pipes is somewhat reversed compared to high D/t -ratio pipes as the deformational capacity tends to improve with longer YPLs. This trend is attributed to the fact that, unlike high D/t -ratio pipes, low D/t -ratio pipes do not depend solely on internal pressure to recover from initial catastrophic collapse but are able to utilize the inherent deformational capacity associated with their superior wall thickness to

facilitate their load-deformation response. This, therefore, implies that low D/t -ratio pipes have the ability and advantage of deforming gradually over the range of the YPL before eventual collapse. Also, for low D/t -ratio pipes (DT1), the influence of the yield stress on the CLS is observed to be negligible (as in Figure 6-16) due to the fact that the buckling of low D/t -ratio pipes (DT1) naturally occurs beyond the elastic range of the material; hence, the catastrophic collapse recovery phenomenon, which is essentially afforded by the YPL, implies that materials of different yield stress will buckle at similar strains if they have the same YPL.

6.8.2 RHT pipes

For *RHT* pipes, a gradual change in the slope of the stress-strain curve commences at the proportionality limit, but metallic materials are known to behave elastically beyond the proportionality limit up to a point referred to as the “elastic limit”, which is considered to characteristically define the yield stress of the material. The portion of the stress-strain curve between the proportionality limit and the elastic limit is commonly overlooked in the stress-based design of RHT structures as reference to the elastic limit has proven to be generally adequate for evaluating the strength capacity. Contrarily, a strain-based design which overlooks the proportionality-to-elastic limit range is prone to erroneous estimation of the strain capacity as the characterization of the strain-hardening properties and overall shape of the stress-strain curve, and invariably calculation of the mechanical behavior, may be inadequate. The material model employed for the parametric FE analysis in this study is based on a complete characterization of the mechanical behavior of the pipe materials such that the entire nonlinear essence of the stress-strain relationship is incorporated into the prediction of the deformation response.

The results obtained for *RHT* pipes indicate that even though internal pressure tends to improve the deformational capacity of RHT pipes, the resultant gain in the CLS diminishes as the strain-hardening of the material becomes more superior. This is attributable to the increased steepness of the tangent modulus of the stress-strain curve immediately beyond the proportionality limit for low PLUS ratios which causes less change in corresponding strain by alteration of the stress state due to internal pressurization.

Increase in internal pressure systematically facilitates the occurrence of buckling further away from the proportionality limit. However, gain in deformational capacity is only substantial if buckling occurs in the region of the stress-strain curve beyond the elastic limit of the material which is characterized by a more progressive drop in the gradient of the tangent modulus compared to the pre-elastic-limit region. Consequently, due to inherent superior strain resistance capacity of low D/t -ratio pipes (DT1), CLS gain is generally significant at all levels of pressure. CLS gain is however observed to be insignificant in high and intermediate D/t -ratio pipes (DT2, DT3, and DT4) except at a very high magnitude of pressure ($f_p = 0.8$), which induces a resultant stress state in the pipe material that delays the initiation of buckling beyond the elastic limit.

The material grade of RHT pipes is generally described using an equivalent yield stress approach which is essentially based on statistical estimation of the elastic limit of the material. However, sensitivity studies through FEA by Liu et al. [45] have shown that sole consideration of the yield strength without the variation of the strain-hardening capacity has a secondary effect on the CLS. The plots in Figure 6-21 and Figure 6-22 indicate that the normalization of the proportionality limit stress over the ultimate proof stress (i.e., PLUS ratio) is more useful for predicting the trend of the CLS of RHT pipes with respect to the material grade factor than directly considering the yield stress of the material. The results obtained elucidate that solely considering the yield stress of the material will likely result in a misleading perception of the trends in the CLS with respect to the material grade. Compared to the CLS vs. yield stress plots in Figure 6-21, the CLS vs. PLUS ratio plots in Figure 6-22 provide a more generalizable illustration of the CLS trend with respect to the material grade. Generally, increase in the PLUS ratio is observed to be detrimental to the CLS of RHT pipes.

The numeric designations of the plots in Figure 6-21 are based on a superiority classification of the hardening properties across the four different material grades. While the same numeric designation for different material grades does not imply similarity in the *knee* and *heel* constants that describe the shape of the stress-strain curve, the numeric designations stipulate a calibration of the shape constants over a linear scale; with “1” having the lowest hardening capacity (and invariably the highest proportionality limit) and “4” having the highest hardening capacity (and invariably the lowest proportionality limit) for respective material grades. The numeric

designations of the plots in Figure 6-22 refer to the yield stresses (in MPa) according to different material grades.

6.9 Semi-Empirical Models for CLS Prediction

Based on systematic sensitivity examination of the four influential factors considered in this study, an appropriate variable function representative of the trend of the CLS with respect to each individual parameter was developed, taking all relevant functional interrelationships into consideration. A multiplicative approach, which has proven to be effective for the formulation of semi-empirical models for pipelines [45,71,72], was employed such that the separate variable functions were multiplied together to form a nonlinear expression having the following basic form:

$$\varepsilon_{cr} = f_{cr}[\pi_1, \pi_2, \pi_3, \pi_4, \pi_5] = f_1 \cdot f_2 \cdot f_3 \cdot f_4 \cdot f_5 \quad (6-9)$$

In order to ensure that the individual trends and interrelationships of all the parameters considered are suitably integrated into the final form of the nonlinear expression, the basic mathematical form for each variable function is expressed as:

$$f_i = f[\pi] = a + b \cdot (f[\pi_i])^c = f[\pi_{j,k,\dots}] + f[\pi_{j,k,\dots}] \cdot (f[\pi_i])^{f[\pi_{j,k,\dots}]} \quad (6-10)$$

where a, b, and c may be functions of other parameters according to observed interrelationships. Respective parameters for each variable function are represented by “i” while other parameters are represented by “j,k,..”.

The derived forms of the individual variable functions for YPT pipes are given by:

$$\begin{aligned}
f_1 = f_{dt} &= a_1 \cdot (\pi_1)^{b_1} \\
f_2 = f_{fp} &= (a_2 + b_2 \pi_3) + (c_2 + d_2 \pi_1) \cdot \text{Exp}(\pi_2)^{(e_2 + f_2 \pi_3)} \\
f_3 = f_{sh} &= a_3 \pi_4 + (b_3 \pi_2 + c_3 \pi_1) \cdot (\pi_3)^{d_3} \\
f_4 = f_{hf} &= a_4 + (b_4 \pi_1) \cdot (\pi_4)^{c_4} \\
f_5 = f_{kh} &= a_5 + (b_5 \pi_3) \cdot (\pi_5)^{c_5}
\end{aligned} \tag{6-11}$$

while the derived forms of the individual variable functions for RHT pipes are given by:

$$\begin{aligned}
f_1 = f_{dt} &= a_1 \cdot (\pi_1)^{b_1} \\
f_2 = f_{fp} &= (a_2 + b_2 \cdot \pi_2) \cdot [c_2 + (d_2 + e_2 \pi_1) \cdot \text{Exp}(\pi_2)^{(f_2)}] \\
f_3 = f_{sh} &= a_3 + (b_3 \pi_2 + c_3) \cdot (\pi_3)^{d_3} \\
f_4 = f_{hf} &= a_4 + b_4 \cdot (\pi_4)^{c_4} \\
f_5 = f_{kh} &= a_5 + b_5 \cdot (\pi_5)^{c_5}
\end{aligned} \tag{6-12}$$

where f_1, f_2, f_3, f_4 , and f_5 represent the D/t ratio function (f_{dt}), the pressure factor function (f_{fp}), the proportionality limit function (f_{pl}), the heel factor function (f_{hf}), and the knee-to-heel ratio function (f_{kh}) respectively. π_1 represents the D/t ratio ($\frac{D}{t}$), π_2 represents the pressure factor ($\frac{p}{p_y}$), π_3 represents the ratio of the yield stress to the elastic modulus ($\frac{\sigma_y}{E}$) or the PLUS ratio ($\frac{\sigma_{pl}}{\sigma_{us}}$) for YPT pipes and RHT pipes respectively, π_4 represents the heel factor (h_f), and π_5 represents the “knee-to-heel” ratio ($\frac{k_f}{h_f}$).

Due to the complex nonlinear interactions between the variables and the CLS, as well as the intricate interrelationships between the individual parameters, development of each form of the variable functions was by a rigorous examination and iterative process. The main rationale for settling on the final form of the overall expression for the CLS was driven by ensuring that the highest possible R^2 value was achieved hence, modifications to the f_i terms for each model was continued until each function provided a satisfactory representation of the observed trends and a desired value of ≥ 0.95 was attained for the overall function, f_{cr} . The “NonlinearModelFit” command in the powerful computational package, Wolfram Mathematica [73], was used to

perform the nonlinear regression analysis and obtain the values of the nonlinear regression coefficients (presented in Table 6-2).

Table 6-2: Nonlinear regression coefficients

<i>Reg. Coeff.</i>	<i>YPT</i>	<i>RHT</i>
a_1	4.652	1.227
b_1	-4.227	-0.7632
a_2	430.7	0.2493
b_2	25840	-0.1831
c_2	-2.738	99.6
d_2	6.748×10^{-2}	19.15
e_2	7.311	-6.49×10^{-2}
f_2	555.9	3.281
a_3	4.486	-0.158
b_3	1.178×10^{-4}	-0.266
c_3	1.439×10^{-7}	0.454
d_3	-2.044	6.417
a_4	101.7	-1.52×10^{-3}
b_4	1.445	-0.3372
c_4	1.277	-0.8974
a_5	-4.44×10^{-3}	6.418×10^{-2}
b_5	5.937	0.5704
c_5	0.1017	-0.4785
R^2	0.951074	0.991057

The applicable range for the dimensionless parameters that constitute the developed semi-empirical models is determined by the range of the parameters used in the FE analyses, given in Table 6-3 as follows:

Table 6-3: Applicable range for dimensionless parameters

<i>Par.</i>	YPT		RHT	
	\geq	\leq	\geq	\leq
<i>D/t</i>	41	105	41	105
<i>f_p</i>	0.0	0.8	0.0	0.8
σ_y/E	0.0018	0.0029		-
σ_p/σ_{us}		-	0.52	0.85
<i>sh_f</i>	1	5	1	4

The parameter, sh_f , in Table 6-3 represents what is hereafter referred to as the “*shape factor*” and was formerly introduced as the numeric designations of the plots in Figure 6-21. The shape factor serves to translate the combined effects of the shape constants (k_{nm} and h_{nm}) and their respective yield stresses onto a linear scale for easier representation.

Within the range of yield stresses covered in this study (i.e., 379 MPa – 586 MPa), the following regression equations can be used to ensure that the shape factor is within the specified ranges in Table 6-3.

For YPT pipes,

$$sh_{f,YP} = 0.0507483 \times (0.0293137 - 9.86288 * 10^{-5} \cdot \sigma_y \cdot h_f^{1.12036}) \times \left(4154.41 + 0.351787 \cdot \sigma_y \cdot \ln \left(\frac{k_f}{h_f} \right) \right) \quad (6-13)$$

For RHT pipes,

$$sh_{f,RH} = 8.85104 * 10^{-6} \times (307.19 - 0.312884 \cdot \sigma_y \cdot h_f^{0.303706}) \times \left(2863.64 + 0.615032 \cdot \sigma_y \cdot \ln \left(\frac{k_f}{h_f} \right) \right) \quad (6-14)$$

6.10 Statistical Accuracy Analysis

To measure the accuracy of the developed semi-empirical models with respect to the FEA, the model-predicted CLS values were plotted against the FEA-derived CLS values as shown in Figure 6-23 and Figure 6-24.

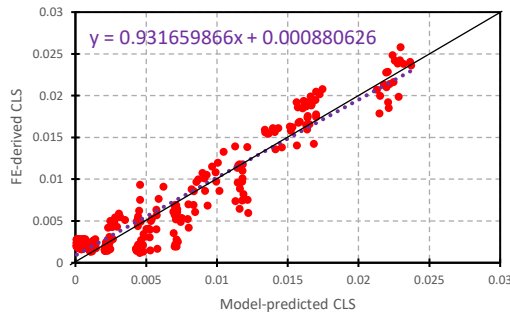


Figure 6-23: YPT model prediction vs. FEA

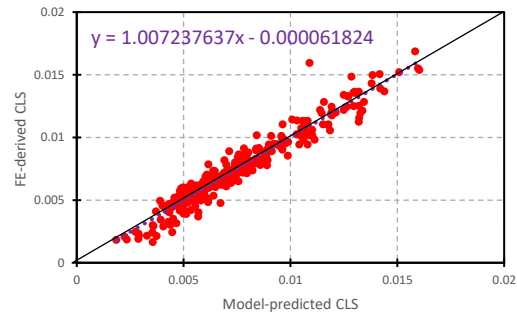


Figure 6-24: RHT model prediction vs. FEA

For the semi-empirical model to be considered an unbiased model, the gradient and intercept of the linear equation (represented by the dotted purple line) displayed on each of the charts should have a value of one and zero, respectively. If the value of the gradient is below 1 (as in the YPT model), it implies that higher CLS values are likely to be underpredicted while lower CLS values are likely to be overpredicted. Otherwise, if the value of the gradient is above 1 (as in the RHT model), it implies that higher CLS values are likely to be overpredicted while lower CLS values are likely to be underpredicted. A positive value of intercept (as in the YPT model) implies that all the predicted results are likely to be overpredicted while a negative value of intercept (as in the RHT model) implies that all the predicted results are likely to be underpredicted.

A simple way to correct the bias in the model is to apply specific values to the semi-empirical model such that the gradient and intercept of the linear equation in the chart are set to one and zero, respectively, thus ensuring that the linear model of the FE vs. model prediction scatter plot is perfectly aligned with the diagonal of the chart (represented by the solid black line).

Applying the following correction function to each of the models effectively corrects the bias:

$$\varepsilon_{cr,corr} = G_{orig} \times \varepsilon_{cr,orig} + I_{orig} \quad (6-15)$$

where G_{orig} and I_{orig} are the original gradient and intercept values, respectively, for the linear equation of the FEA vs. model prediction scatter plot. $\varepsilon_{cr,orig}$ and $\varepsilon_{cr,corr}$ are the original and corrected versions, respectively, of the semi-empirical model.

A procedure is also presented herein which can be easily implemented to control the overpredicted region of the model (i.e., the portion of the FE vs. model prediction plot that lies below the diagonal) and apply knock-down factors as required with respect to various factors, such as initial geometric imperfections, weld defects, induced mechanical defects, etc., which are detrimental to the CLS of pipes.

The procedure is based on manipulation of the distribution of FE-to-predicted (FTP) ratios for the corrected model, $\varepsilon_{cr,corr}$. FTP ratios are obtained by dividing the FEA-predicted CLS values with the corrected model-predicted CLS values. FTP distributions for the corrected YPT model and the corrected RHT model are presented in Figure 6-25 and Figure 6-26.

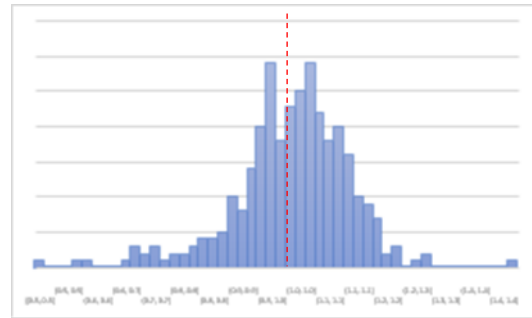
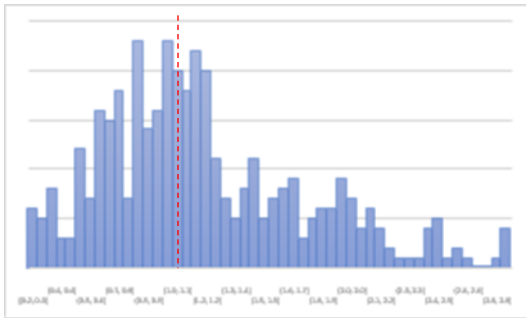


Figure 6-25: FTP distribution for YPT model Figure 6-26: FTP distribution for RHT model

The histogram charts in Figure 6-25 and Figure 6-26 indicate that the FTP ratios of the corrected model are approximately normally distributed, even though the YPT model is more skewed than the RHT model. The dotted red vertical line in both charts represents the FTP ratio with a mean value of one (i.e., the number of values that are perfectly predicted by the model). The bars on the left and right side of the dotted red line represent the model-overpredicted and model-underpredicted values respectively.

By resetting value of the mean of the FTP-ratio distribution to values higher than one, a more conservative corrected model can be obtained by simply adjusting the linear model intercept, I_{orig} accordingly. The “Goal Seek” function in Microsoft Excel was used to determine the value of the linear model intercept, I_{orig} that must be applied to the correction function in Eq. (6-15) to obtain various probabilities of underprediction (POU). POU was calculated by simply dividing the number of model predictions with an FTP ratio greater than 1 by the respective total number of FE runs. The results are presented in Table 6-4.

Table 6-4: Values of linear model intercept for correction function and corresponding POU

Mean	I_{orig}	POU
YPT		
1.00	0.001259522	0.4875
1.25	0.00079234	0.6025
1.50	0.000529142	0.655
2.00	0.000258156	0.7075
2.50	0.000128825	0.7275
RHT		
1.00	-8.21956E-05	0.5344
1.05	-0.000390117	0.6813
1.10	-0.000664754	0.8125
1.15	-0.000909808	0.8813
1.20	-0.001127937	0.9219

The stipulated procedure is effective at making the semi-empirical model more conservative as desired. Due to the spread of YPT model, and consequent heavy distribution of model-predicted values at the tail of the distribution, it was impossible to increase the conservativeness of the model beyond a POU of 0.7275 without obtaining negative model-predicted CLS values. Conversely, the RHT model is better distributed and a high level of conservativeness could be achieved.

For the original (uncorrected) CLS models, the mean and standard deviation of the FTP ratios for YPT pipes are 3.5007 and 5.0635 respectively while the mean and standard deviation of the FTP ratios for RHT pipes are 0.99304 and 0.12099 respectively. Both models follow a normal distribution. The bias-correction procedure presented herein has the potential to reduce the spread of distribution of the CLS model predictions, especially the YPT model, e.g., achieving a mean value of 1.0 for the YPT FTP ratios (as shown in [Table 6-4](#)) reduces the standard deviation of the original (uncorrected) YPT CLS model from 5.0635 to 0.38455.

6.11 Conclusions

An FE simulation procedure was implemented in this study to investigate the deformational response of cylindrical shells to axial compression, with and without internal pressurization. Focusing on four main factors that typically influence the deformational capacity of steel cylinders, i.e., dimensional properties, material grade, internal pressure, and the overall shape of the stress-strain curve, a parametric sensitivity analysis consisting of over 700 runs was conducted using the ABAQUS CAE package. Nondimensionalization was performed to convert each of the considered factors to dimensionless parameters required for the development of a constitutive mathematical prediction model. The scope of the dimensional properties comprised D/t ratios ranging between 41.15 and 104.62 while the internal pressure comprised ratios of the equivalent pressure-resultant hoop stress to the yield stress of the steel material ranging between 0.0 and 0.8. The designated yield stress values for four material grades ranging from X52 to X80 were derived based on the API 5L specification for pipeline steels and, keeping the ratio of the yield stress to the ultimate proof stress constant, four and five variations of the stress-strain relationship for each material grade were developed for RHT and YPT materials respectively.

The development of the stress-strain curves was achieved using the novel Ndubuaku material model which is easily capable of accurately parameterizing the stress-strain curve of metallic materials (including YPT materials) over the full range of strains. Material characterization using the adopted material model yields two shape constants (k_{nm} and h_{nm}) which completely define the stress-strain relationship. Derivation of the shape constants through an iterative procedure which allows prescription of the allowable length of the yield plateau based on an inflection

point control algorithm was presented. The incorporation of the hardening factor in the prediction model therefore required the inclusion of the two shape constants as separate parameters, bringing the total number of constitutive dimensionless parameters for the developed prediction model to five. While the trends of the CLS were not directly compared to the shape constants, factors such as the YPL (for YPT pipes) and the PLUS ratio (for RHT pipes) implicitly represent the curve shape properties of material stress-strain curve and were used to highlight the influence of the material stress-strain properties on the CLS of pipes.

For both YPT pipes and RHT pipes, increase in slenderness (D/t ratio) was observed to reduce the deformational capacity of the pipes while increase in internal pressure improved the deformational capacity. Increasing the yield stress, and invariably the material grade, increased the CLS of YPT pipes but the effect was observed to diminish as slenderness of the pipe reduced. For YPT pipes, long YPLs were observed to be detrimental to the CLS of high and intermediate D/t -ratio pipes whereas the CLS of low D/t -ratio pipes tends to improve as the YPL is increased. The CLS of RHT pipes generally reduces as the PLUS ratio increases, however, increased PLUS ratio was observed to improve the CLS gain due to increased internal pressure and reduced D/t ratio. The yield stress showed an untraceable influence on the trend of the CLS of RHT pipes.

Two nonlinear mathematical expressions (one for YPT pipes and another for RHT pipes) were subsequently developed using a variable function multiplication approach whereby individual functions for each parameter were derived, based on their respective functional influence on the trend of the CLS, and multiplied together to form a constitutive equation. The final form of both equations includes a number of unknown constants whose values were determined by nonlinear regression analysis using the highly advanced computational tool, Wolfram Mathematica.

The nonlinear regression analysis yielded high R^2 values (> 0.95), indicating excellent goodness of fit between the model prediction and the FE-derived results of the CLS. Furthermore, a simple statistical procedure was presented to improve the conservativeness of the developed semi-empirical models by manipulating the linear model intercept derived from the FEA vs. model prediction plot.

It is envisaged that the model equations derived in this study will be useful for predicting the deformational capacity of pressurized and unpressurized pipelines, as well as other

dimensionally and materially similar cylindrical shells, which are predominantly subjected to uniform axial compression under external loads and operational conditions.

6.12 References

- [1] J.G. Teng, Y. Zhao, L. Lam, Techniques for buckling experiments on steel silo transition junctions, *Thin-Walled Struct.* 39 (2001) 685–707. doi:10.1016/S0263-8231(01)00030-1.
- [2] C.T.F. Ross, A.P.F. Little, K.A. Adeniyi, Plastic buckling of ring-stiffened conical shells under external hydrostatic pressure, *Ocean Eng.* 32 (2005) 21–36. doi:10.1016/j.oceaneng.2004.05.007.
- [3] T.A. Winterstetter, H. Schmidt, Stability of circular cylindrical steel shells under combined loading, *Thin-Walled Struct.* 40 (2002) 893–909. doi:10.1016/S0263-8231(02)00006-X.
- [4] C.R. Calladine, The theory of thin shell structures 1888–1988, *Proc. Inst. Mech. Eng. Part A J. Power Energy.* 202 (1988) 141–149. doi:10.1243/PIME_PROC_1988_202_020_02.
- [5] R. Lorenz, Achsensymmetrische Verzerrungen in dünnwandigen Hohlzylindern, *Zeitschrift Des Vereines Dtsch. Ingenieure.* 52 (1908) 1706–1713.
- [6] S.P. Timoshenko, Einige stabilitäts probleme der elastizitäts theorie, *Zeitschrift Für Math. Und Phys.* 58 (1910) 337–385.
- [7] R. V. Southwell, On the General Theory of Elastic Stability, *Philos. Trans. R. Soc. A Math. Phys. Eng. Sci.* 213 (1914) 187–244. doi:10.1098/rsta.1914.0005.
- [8] A. Robertson, The Strength of Tubular Struts. Report and Memorandum No. 1185, 1929.
- [9] W.M. Wilson, N.M. Newmark, The strength of thin cylindrical shells as columns, in: *Sel. Pap. By Nathan M. Newmark Civ. Eng. Class.*, 1933: pp. 1–42.
- [10] E.E. Lundquist, Strength tests of thin-walled duralumin cylinders in compression. NACA Technical Note, No 473, Washington, D.C., 1934.
- [11] J.G. Teng, Buckling of Thin Shells: Recent Advances and Trends, *Appl. Mech. Rev.* 49 (1996) 263. doi:10.1115/1.3101927.

- [12] T. Von Kármán, H.S. Tsien, The Buckling of Thin Cylindrical Shells under Axial Compression, in: Collect. Work. Hsue-Shen Tsien, 2012: pp. 165–181. doi:10.1016/B978-0-12-398277-3.50009-9.
- [13] W.T. Koiter, The Stability of Elastic Equilibrium, Dep. Mech. Shipbuilding, Airpl. Build. Ph.D. (1945).
- [14] H.N.R. Wagner, C. Hühne, S. Niemann, R. Khakimova, Robust design criterion for axially loaded cylindrical shells - Simulation and Validation, *Thin-Walled Struct.* 115 (2017) 154–162. doi:10.1016/j.tws.2016.12.017.
- [15] C.D. Babcock, Experiments in shell buckling, in: Y.C. Fung, E.E. Sechler (Eds.), *Thin-Shell Struct. Theory, Exp. Des.*, Prentice-Hall, Englewood Cliffs, NJ, 1974: pp. 345–369.
- [16] S.M. Fatemi, H. Showkati, M. Maali, Experiments on imperfect cylindrical shells under uniform external pressure, *Thin-Walled Struct.* 65 (2013) 14–25. doi:10.1016/j.tws.2013.01.004.
- [17] J. Arbocz, The Imperfection Data Bank, a Mean to Obtain Realistic Buckling Loads, in: *Buckling of Shells*, Springer Berlin Heidelberg, Berlin, Heidelberg, 1982: pp. 535–567. doi:10.1007/978-3-642-49334-8_19.
- [18] M. Deml, W. Wunderlich, Direct evaluation of the “worst” imperfection shape in shell buckling, *Comput. Methods Appl. Mech. Eng.* 149 (1997) 201–222. doi:10.1016/S0045-7825(97)00055-8.
- [19] C. Hühne, R. Rolfes, J. Tessler, A new approach for robust design of composite cylindrical shells under axial compression, in: Karen Fletcher (Ed.), *Proc. Eur. Conf. Spacecr. Struct. Mater. Mech. Test. (ESA SP-581)*, Noordwijk, The Netherlands, 2005: p. 141.1-141.8.
- [20] H.N.R. Wagner, C. Hühne, S. Niemann, Constant single-buckle imperfection principle to determine a lower bound for the buckling load of unstiffened composite cylinders under axial compression, *Compos. Struct.* 139 (2016) 120–129. doi:10.1016/j.compstruct.2015.11.047.
- [21] H.N.R. Wagner, C. Hühne, K. Rohwer, S. Niemann, M. Wiedemann, Stimulating the realistic worst case buckling scenario of axially compressed unstiffened cylindrical composite shells, *Compos. Struct.* 160 (2017) 1095–1104. doi:10.1016/j.compstruct.2016.10.108.
- [22] S.G.P. Castro, R. Zimmermann, M.A. Arbelo, R. Khakimova, M.W. Hilburger, R. Degenhardt, Geometric imperfections and lower-bound methods used to calculate knock-down

factors for axially compressed composite cylindrical shells, *Thin-Walled Struct.* 74 (2014) 118–132. doi:10.1016/j.tws.2013.08.011.

[23] L. Wullschleger, H.R. Meyer-Piening, Buckling of geometrically imperfect cylindrical shells - Definition of a buckling load, *Int. J. Non. Linear. Mech.* 37 (2002) 645–657. doi:10.1016/S0020-7462(01)00089-0.

[24] D.B. Muggeridge, R.C. Tennyson, Buckling of axisymmetric imperfect circular cylindrical shells under axial compression, *AIAA J.* 7 (1969) 2127–2131. doi:10.2514/3.5568.

[25] E.J. Morgan, P. Seide, V.I. Weingarten, Elastic stability of thin-walled cylindrical and conical shells under axial compression, *AIAA J.* 3 (1965) 500–505. doi:10.2514/3.2893.

[26] I. Weingarten, V. P. Seide, P. Peterson, J. Buckling of thin-walled circular cylinders, NASA SP-8007. (1968) 1–60. doi:19690013955.

[27] M.W. Hilburger, M.P. Nemeth, J.H. Starnes, Shell Buckling Design Criteria Based on Manufacturing Imperfection Signatures, *AIAA J.* 44 (2006) 654–663. doi:10.2514/1.5429.

[28] C. Hühne, R. Rolfes, E. Breitbach, J. Teßmer, Robust design of composite cylindrical shells under axial compression - Simulation and validation, *Thin-Walled Struct.* 46 (2008) 947–962. doi:10.1016/j.tws.2008.01.043.

[29] S. Gellin, Effect of an Axisymmetric Imperfection on the Plastic Buckling of an Axially Compressed Cylindrical Shell, *J. Appl. Mech.* 46 (1979) 125. doi:10.1115/1.3424483.

[30] K. Ravn-Jensen, V. Tvergaard, Effect of residual stresses on plastic buckling of cylindrical shell structures, *Int. J. Solids Struct.* 26 (1990) 993–1004. doi:10.1016/0020-7683(90)90013-L.

[31] L. Guo, Y. Liu, H. Jiao, S. An, Behavior of thin-walled circular hollow section stub columns under axial compression, *Int. J. Steel Struct.* 16 (2016) 777–787. doi:10.1007/s13296-015-0159-0.

[32] J. Hutchinson, Axial buckling of pressurized imperfect cylindrical shells, *AIAA J.* 3 (1965) 1461–1466. doi:10.2514/3.3169.

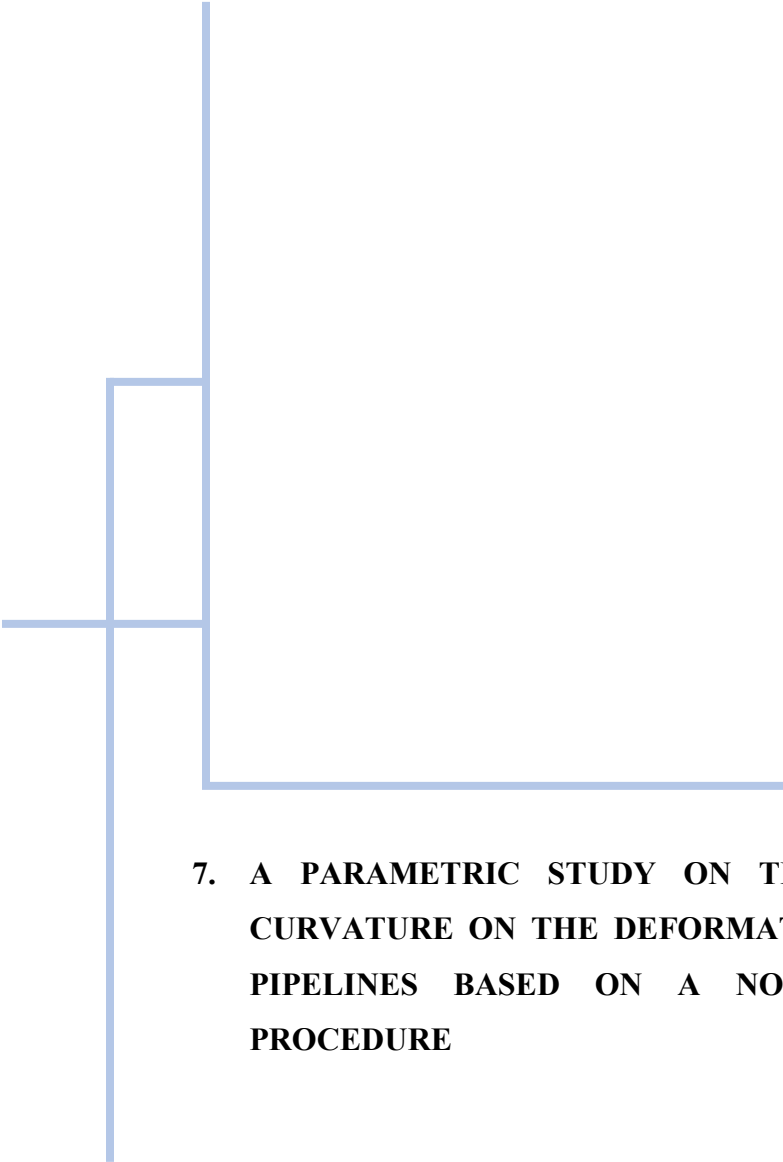
[33] A. Limam, J.F. Jullien, E. Greco, D. Lestrat, Buckling of Thin-Walled Cylinder Under Axial Compression and Internal Pressure, in: J.F. Jullien (Ed.), *Buckling Shell Struct. Land, Sea Air*, Elsevier, Essex, England, 1991: pp. 359–369.

- [34] F.C. Bardi, S. Kyriakides, H.D. Yun, Plastic buckling of circular tubes under axial compression—part II: Analysis, *Int. J. Mech. Sci.* 48 (2006) 842–854. doi:10.1016/J.IJMECSCI.2006.03.002.
- [35] J.A. Paquette, S. Kyriakides, Plastic buckling of tubes under axial compression and internal pressure, *Int. J. Mech. Sci.* 48 (2006) 855–867. doi:10.1016/J.IJMECSCI.2006.03.003.
- [36] S. Neupane, S. Adeeb, R. Cheng, J. Ferguson, M. Martens, Modeling the Deformation Response of High Strength Steel Pipelines—Part II: Effects of Material Characterization on the Deformation Response of Pipes, *J. Appl. Mech.* 79 (2012) 051003. doi:10.1115/1.4006381.
- [37] S. Neupane, S. Adeeb, R. Cheng, J. Ferguson, M. Martens, Modeling the Deformation Response of High Strength Steel Pipelines—Part I: Material Characterization to Model the Plastic Anisotropy, *J. Appl. Mech.* 79 (2012) 051002. doi:10.1115/1.4006380.
- [38] M. Dundu, Evolution of stress-strain models of stainless steel in structural engineering applications, *Constr. Build. Mater.* 165 (2018) 413–423. doi:10.1016/J.CONBUILDMAT.2018.01.008.
- [39] W. Ramberg, W.R. Osgood, Description of stress-strain curves by three parameters, NACA Technical Note No. 902, Washinton, D.C., 1943.
- [40] H.N. Hill, Determination of stress-strain relations from the offset yield strength values. NACA Technical Note No. 927, Washington, D.C., 1944.
- [41] O. Ndubuaku, M. Martens, R. Cheng, A. Ahmed, S. Adeeb, A Novel Approach for True Stress-True Strain Material Characterization of Metallic Materials Using the Product-Log (Omega) Function, in: 6th Int. Conf. Eng. Mech. Mater., CSCE, May 31 - June 3, Vancouver, B.C., Canada, 2017.
- [42] O. Ndubuaku, M. Martens, J.J.R. Cheng, S. Adeeb, Expression of a Generic Full-Range True Stress-True Strain Model for Pipeline Steels Using the Product-Log (Omega) Function, in: Vol. 6B Mater. Fabr., ASME, 2017: p. V06BT06A050. doi:10.1115/PVP2017-65236.
- [43] O. Ndubuaku, X. Liu, M. Martens, J.J. Roger Cheng, S. Adeeb, The effect of material stress-strain characteristics on the ultimate stress and critical buckling strain of flat plates subjected to uniform axial compression, *Constr. Build. Mater.* 182 (2018) 346–359. doi:10.1016/j.conbuildmat.2018.06.100.

- [44] C.M.J. Timms, D.D. DeGeer, M.R. Chebaro, Y. Tsuru, Compressive Strain Limits of Large Diameter X80 UOE Linepipe, in: Ninet. Int. Offshore Polar Eng. Conf., International Society of Offshore and Polar Engineers, Osaka, Japan, 2009.
- [45] M. Liu, Y.-Y. Wang, F. Zhang, K. Kotian, Realistic strain capacity models for pipeline construction and maintenance. Prepared for the US Department of Transportation. Pipeline and Hazardous Materials Safety Administration, Office of Pipeline Safety. Contract No. DTPH56-10-T-000016, Dublin, OH, USA, 2013.
- [46] Det Norske Veritas, Submarine pipeline systems - DNV-OS-F101, DNV, Oslo, Norway, 2010.
- [47] J. Singer, J. Arbocz, T. Weller, Buckling Experiments, Volume 1: Basic Concepts, Columns, Beams and Plates, John Wiley & Sons, New York, 1998.
- [48] L.H. Donnell, Stability of thin-walled tubes under torsion, NACA Report No. 479, Washington D.C., 1933.
- [49] L.A. Harris, The Stability of Thin-Walled Unstiffened Circular Cylinders Under Axial Compression Including the Effects of Internal Pressure, *J. Aeronaut. Sci.* 24 (1957) 587–596. doi:10.2514/8.3911.
- [50] L.S.D. Morley, An improvement on donnell's approximation for thin-walled circular cylinders, *Q. J. Mech. Appl. Math.* 12 (1959) 89–99. doi:10.1093/qjmam/12.1.89.
- [51] Yong Bai, Wei-Liang Jin, Ultimate Strength of Cylindrical Shells, in: *Mar. Struct. Des.*, 2nd ed., Elsevier, Oxford, United Kingdom, 2016: pp. 353–365. doi:https://doi.org/10.1016/B978-0-08-099997-5.00018-6.
- [52] J. Xue, Local buckling in infinitely, long cylindrical shells subjected uniform external pressure, *Thin-Walled Struct.* 53 (2012) 211–216. doi:10.1016/J.TWS.2012.01.008.
- [53] Hibbit, Karlsson, Sorensen Inc., ABAQUS/STANDARD - Theory Manual, Version 6.14, (2003).
- [54] D. Bushnell, Plastic Buckling of Various Shells, *J. Press. Vessel Technol. Trans. ASME.* 104 (1982) 51–72. doi:10.1115/1.3264190.
- [55] K.J. Bathe, H. Saunders, Finite Element Procedures in Engineering Analysis, *J. Press. Vessel Technol.* 106 (1984) 421. doi:10.1115/1.3264375.

- [56] American Petroleum Institute, API 5L: Specification for Line Pipe, 44th ed., American Petroleum Institute, USA, 2007.
- [57] EN 1993-1-4 2006, Eurocode 3: Design of steel structures - Part 1-4: General rules - Supplementary rules for stainless steels, CEN, Brussels, 2006.
- [58] L.Z. Kong, X.Y. Zhou, L.Q. Chen, J. Shuai, K. Huang, G.J. Yu, True Stress-Strain Curves Test and Material Property Analysis of API X65 and API X90 Gas Pipeline Steels, *J. Pipeline Syst. Eng. Pract.* 9 (2018) 04017030. doi:10.1061/(ASCE)PS.1949-1204.0000300.
- [59] P.R. DelCol, G.Y. Grondin, J.J.R. Cheng, D.W. Murray, Behavior of Large Diameter Line Pipe Under Combined Loads, Structural Engineering Report No. 224, Edmonton, AB, Canada, 1998.
- [60] A.B. Dorey, J.J.R. Cheng, D.W. Murray, Critical Buckling Strains for Energy Pipelines, Structural Engineering Report No. 237, Edmonton, Alberta, 2001.
- [61] S. Das, J.J.R. Cheng, D.W. Murray, Fracture of Wrinkled Energy Pipelines. Structural Engineering Report No. 247, Edmonton, AB, Canada, 2002.
- [62] S. Adeeb, J. Zhou, D. Horsley, Investigating the Effect of UOE Forming Process on the Buckling of Line Pipes Using Finite Element Modeling, in: Vol. 1 Proj. Manag. Des. Constr. Environ. Issues; GIS/Database Dev. Innov. Proj. Emerg. Issues; Oper. Maintenance; Pipelining North. Environ. Stand. Regul., ASME, 2006: pp. 169–174. doi:10.1115/IPC2006-10175.
- [63] M. Mohareb, G.L. Kulak, A. Elwi, D.W. Murray, Testing and Analysis of Steel Pipe Segments, *J. Transp. Eng.* 127 (2001) 408–417. doi:10.1061/(ASCE)0733-947X(2001)127:5(408).
- [64] M. Kainat, S. Adeeb, J.J.R. Cheng, J. Ferguson, M. Martens, Measurement of Initial Imperfection of Energy Pipelines Using 3D Laser Scanner, in: 3rd Int. Struct. Spec. Conf., CSCE, Edmonton, AB, Canada., 2012.
- [65] M. Kainat, S. Adeeb, J.J.R. Cheng, J. Ferguson, M. Martens, Identifying Initial Imperfection Patterns of Energy Pipes Using a 3D Laser Scanner, in: 2012 9th Int. Pipeline Conf., ASME, 2012: pp. 57–63. doi:10.1115/IPC2012-90201.
- [66] M. Kainat, M. Lin, J.J.R. Cheng, M. Martens, S. Adeeb, Effects of the Initial Geometric Imperfections on the Buckling Behavior of High-Strength UOE Manufactured Steel Pipes, *J. Press. Vessel Technol. Trans. ASME.* 138 (2016) 051206. doi:10.1115/1.4032990.

- [67] H. Chen, H. Wang, S. Gong, H. Li, C. Huang, W. Xie, L. Ji, D. Qu, Test Evaluation of High Strain Line Pipe Material, in: Twenty-First Int. Offshore Polar Eng. Conf., International Society of Offshore and Polar Engineers, Maui, Hawaii, USA, 2011.
- [68] G.H. Workman, Manufacturing residual stress effects on buried pipeline structural response, in: Seventh Int. Conf. Offshore Mech. Arct. Eng., Houston, Texas, 1988: pp. 7–12.
- [69] M. Paredes, J. Lian, T. Wierzbicki, M.E. Cristea, S. Münstermann, P. Darcis, Modeling of plasticity and fracture behavior of X65 steels: seam weld and seamless pipes, *Int. J. Fract.* 213 (2018) 17–36. doi:10.1007/s10704-018-0303-x.
- [70] R. Hill, A Theory of the Yielding and Plastic Flow of Anisotropic Metals, *Proc. R. Soc. A Math. Phys. Eng. Sci.* 193 (1948) 281–297. doi:10.1098/rspa.1948.0045.
- [71] A.B. Dorey, D.W. Murray, J.J.R. Cheng, Critical Buckling Strain Equations for Energy Pipelines—A Parametric Study, *J. Offshore Mech. Arct. Eng.* 128 (2006) 248. doi:10.1115/1.2199561.
- [72] X. Liu, H. Zhang, Y. Han, M. Xia, W. Zheng, A semi-empirical model for peak strain prediction of buried X80 steel pipelines under compression and bending at strike-slip fault crossings, *J. Nat. Gas Sci. Eng.* 32 (2016) 465–475. doi:10.1016/J.JNGSE.2016.04.054.
- [73] Wolfram Research Inc., Mathematica, Version 11.3, Champaign, IL, 2018.



7. A PARAMETRIC STUDY ON THE EFFECT OF UNIFORMLY-INDUCED CURVATURE ON THE DEFORMATIONAL CAPACITY OF STEEL ONSHORE PIPELINES BASED ON A NOVEL MATERIAL CHARACTERIZATION PROCEDURE

This chapter is derived from a research article submitted for publication in the Elsevier Engineering Structures journal.

7.1 Abstract

Onshore pipelines are generally required to transport various hydrocarbon fluids and other liquid consumables over considerably long distances and. In many cases, pipe segments are unavoidably installed across geotechnically unstable environments, making them prone to significant ground deformation-induced stresses and strains which may lead to local buckling or pipe wrinkling, and possible rupture of the pipe wall. Current practice idealizes the typical deformation induced in a pipeline by movement of the surrounding or supporting soil medium as a displacement-controlled loading phenomenon characterized by monotonically-increasing uniform curvature, with or without internal pressurization and/or net-section axial stress. The above idealization is adopted in this study to investigate the moment vs. curvature response of unpressurized and pressurized pipelines, with no axial stress, subjected to uniform bending deformation; with a view to develop a set of constitutive design equations for predicting the critical values of the average strain, measured over a 2D (two times pipe diameter) gauge length, that coincides with the maximum attainable bending moment. The shortcoming of existing equations, which is related to inadequate characterization of the shape of the material stress-strain curve, is effectively tackled by employing a novel stress-strain model, referred to as the ‘Ndubuaku model’, for accurately parametrizing the shape of stress-strain curves, including curves with a distinct yield point and extended yield plateau. Other relevant parameters investigated include the D/t ratio, the internal pressure, and the material grade. A parametric study, comprising about 720 numerical simulations, is implemented herein using finite element methodology. Two semi-empirical equations are developed based on a material curve classification approach that distinguishes between ‘yield-plateau’ stress-strain curve materials and ‘round-house’ stress-strain curve materials. The predictions of the developed models are compared to results of previous experiments on pipe segments subjected to uniform bending, and a good agreement is obtained.

Nomenclature

ε	true strain
ε_{cr}	critical limit strain
ε_{pl}	corresponding strain at proportionality limit stress of Ndubuaku model
ε_R	Ndubuaku model strain ratio
ε_{up}	corresponding strain at ultimate proof stress of Ndubuaku stress-strain model
E	Young's modulus of elasticity
f_p	pressure factor (ratio of applied pressure to pipe yield pressure)
h	Ndubuaku model heel constant
k	Ndubuaku model knee constant
n	Ramberg-Osgood strain-hardening exponent
OD	pipe's outer diameter
p	applied internal pressure
p_y	pipe's circumferential yield pressure
$\sigma_{0.5}$	0.5% total strain proof stress
σ	true stress
σ_{pl}	proportionality limit stress of Ndubuaku stress-strain model
σ_R	Ndubuaku model stress ratio
σ_{up}	ultimate proof stress of Ndubuaku stress-strain model
σ_{us}	ultimate tensile stress of pipe material
σ_{ys}	yield stress of pipe material
sh_f	material curve shape factor
t	pipe's wall thickness
CLS	Critical limit strain
D/t ratio	Ratio of pipe's outer diameter to pipe's wall thickness
$PLUS$ ratio	Ratio of proportionality limit stress to ultimate tensile stress
RHT	Round-house type
SBD	Strain-based design

<i>UTS</i>	Ultimate tensile stress
<i>YPL</i>	Yield plateau length
<i>YPT</i>	Yield-plateau type
<i>YS</i>	Nominal yield stress
<i>Y/T ratio</i>	Ratio of yield stress to ultimate tensile stress

7.2 Introduction

Research on the buckling behavior of pipelines has experienced a spike in recent decades. It is, however, not unfounded to attribute this trend to the gradually-unfolding realization, in the energy and public utilities industry, of the inability of traditional pipeline design procedures to sufficiently forestall the incidence of pipeline failures. Field observations have highlighted the harmful consequences that geotechnical movement of the surrounding (for buried pipes) or supporting (for above-grade pipes) soil medium can have on the mechanical and structural integrity of onshore pipelines. Geotechnical movement is typically associated with unfavorable geoenvironmental actions such as landslides, slope failures, ground subsidence, discontinuous permafrost (frost heave and thaw settlement), tectonic shifting, etc. [1–4]. Such displacements tend to induce large deformations and localized curvature of the pipe such that a local buckling phenomenon, characterized by concentrated wrinkling of the pipe wall, is triggered [5–7]. It is quite common for the imposed deformation caused by geotechnical movement to induce longitudinal strains that are significantly greater than the yield strain of the pipe material; hence, the pipeline designer is naturally saddled with the imperative encumbrance of accounting for large nonlinear geometric deformations and simultaneously considering the intrinsic nonlinear material peculiarities of the pipe under various loading [8–10]. There is unquestionably an increasing need for the overall framework of pipeline design, both during installation (especially for offshore pipelines) and during operation, to incorporate strain-based methodologies, especially as more pipelines are inevitably installed in harsher and more geotechnically unstable environments [11–14].

Current industry practice defines the local buckling capacity of pipes as the critical limit strain (CLS), which is derived as the average compressive strain over a prescribed gauge length that

corresponds to the highest possible bending moment experienced in the immediate vicinity of the localized buckle (referred to as the ‘peak moment’ criterion [15–17]). The gauge length spans longitudinally over a typically-acceptable range of one to two times the pipe’s outer diameter. Earlier versions of equations for predicting the CLS in pipes were either formulated analytically, based on classical shell buckling theory, or developed empirically, based on results of small-scale tests and a few large-scale tests. More recently, since the late 1980s and early 1990s, the desire to increase the accuracy and range of applicability of the developed CLS equations, as well as the need to surmount the limitations of the classical theories in accounting for the nonlinear geometric/material intricacies of the shell buckling phenomenon, has led to greater reliance on computerized FEM-based numerical simulation. More comprehensive large-scale experiments have also been conducted by various research organizations in recent years, mainly with an aim to validate the numerical models [18].

Bouwkamp and Stephen [19] observed that the magnitudes of the longitudinal compressive strains due to buckling do not depend on the gauge length in the pre-buckling range of deformation. However, after the strains become non-uniform, in the post-buckling range of the load-deformation response, measurement of the strains becomes dependent on the gauge length. The longitudinal compressive strain averaged over the length of a buckled pipe segment, therefore, decreases as the length of the measured section increases. The observations of Ref [19] significantly highlight the importance of specifying the gauge length used for the evaluation of the strain measurements of a deformed pipe segment, especially in the post-buckling range of deformation, in order to correctly describe its state of deformation.

Murphey and Langner [16] proposed two empirical equations for the CLS of unpressurized pipes, with zero axial loads, subjected to pure bending. Both equations were expressed solely as functions of the pipe D/t ratio; the first equation represents the bending strain corresponding to the maximum bending moment of the pipe’s moment-curvature response while the second equation represents the lower bound of the critical bending strain. Effects of factors such as material plasticity and girth welds were not considered, and the gauge length was not specified. The empirical derivations were based on 40 full-scale laboratory tests, 18 of which were conducted by Sherman [20] on pipes with D/t ratios ranging from 18 to 102. It has been observed

that the predictions by Murphy and Langner's equations are only consistent with the results of experiments on unpressurized pipes for $D/t > 50$ [18].

Gresnigt [21] conducted 13 full-scale tests on pressurized pipes, with D/t ratios of 80 and 100, under uniform bending and net-section axial stress. A set of semi-analytical equations which are able to account for ovalization of the pipe cross-section under bending were developed for predicting the CLS and validated with the results of the laboratory tests. The proposed expressions for the CLS were derived from the compressive strains corresponding to the maximum bending moment but are based on an idealized elastic-perfectly plastic stress-strain representation and do not account for the yield strength and strain-hardening characteristics of the pipe material. Also, no gauge length was specified and, similar to Murphey and Langner's equations, Ref [18] pointed out that Gresnigt's equations also indicate a relatively good agreement with the results of laboratory tests for unpressurized pipes with $D/t > 50$ but result in a few unconservative predictions for $D/t < 50$. In the case of pressurized pipes, the predictions for lower-grade pipes were observed to be overly conservative in some cases and unconservative in other cases while unconservative predictions were generally obtained for pressurized higher-grade pipes.

Lara [22] conducted a series of nonlinear FE analyses to investigate the post-buckling behavior of pressurized pipes under bending and established that local buckling of pipes with low internal pressure is typically characterized by an inward diamond-shaped wrinkle whereas pipes subjected to high internal pressure form an outward bulge-type wrinkle. It was also observed that the compressive axial strain in the pipe model at which a rapid change in the curvature of the wrinkle is observed on the compression side of the model was significantly higher than the compressive axial strain at local buckle initiation; especially at higher values of internal pressure. Ref [22] maintains that, even though less conservative than the buckle initiation criterion, the rapid wrinkle growth criterion represents a more rational critical limit for local buckling strain.

Zimmerman et al. [11] conducted five full-scale laboratory tests on pipe specimens under combined axial loading and uniform bending. A parametric study was subsequently performed using a number of numerical (FE) models, calibrated using the test data from the full-scale experimental work, based on a 2D gauge length. Ref [11] argued that for buried pipelines, where the pipe is laterally and longitudinally restrained by the surrounding soil, the CLS should be

derived based on the compressive strains associated with the hoop tensile strains that develop on the crest of the localized wrinkle. The so-called '*tensile hoop strain*' criterion was considered to be more rational and less conservative compared to the commonly-employed peak moment criterion and was followed for developing semi-empirical regression equations for the critical limit strain, based on results of the parametric FE analyses.

To study the post-buckling behavior of pipelines, Zhou and Murray [10,23,24] performed sophisticated nonlinear numerical analyses on FE pipe models made of three-dimensional shell elements using an arc-length iterative algorithm. Three classifications of so-called '*cross-sectional distortion limit states*' were defined based on the modes of deformation associated with the localized wrinkles. Results obtained for the local buckling modes of deformation were observed to be similar to Ref [22]. To improve design practices and relax the conservativeness of design limits, Ref [23] proposed a discretionary approach to limit states design of pipelines based on three criteria: (1) limiting the magnitude of pipe's cross-sectional distortion according to operational and pigging requirements, (2) avoiding significant softening of the pipe material by limiting the induced pipeline curvature based on quantitative evaluation of critical soil settlement or geotechnical movement, and (3) limiting the growth of wrinkles to avoid rapid localization of non-uniform plastic deformation according to the load-deformation response of pipes. Both internal pressure and axial load were observed to have a significant influence on the post-buckling behavior [25]. Ref [23] posits that the '*tensile hoop strain*' criterion can be implemented by limiting the diametric expansion at the location of outward-bulge type local buckles such that the magnitude of the circumferential stress at the crest of the buckle is reduced to prevent possible rupture under high internal pressure.

According to Gresnigt and Karamanos [26], the buckling response of a pipe can be considered to be stable as long as the bending moment continues to increase. However, as the bending moment begins to decrease, the curvature becomes concentrated at the deepening imperfection or local buckle, and the response is no longer stable. They proposed the corresponding curvature at the maximum moment as the limit state for local buckling. Ref [9], Ref [27] and Ref [28] studied the pre-buckling and post-buckling behavior of pipes by numerically simulating the response of plain and girth-welded pipe models subjected to various monotonic load combinations. The models were calibrated by full-scale test data, and parametric FE analysis was conducted to

derive equations for the CLS. To examine the influence of initial imperfections on the buckling behavior of pipelines, Dorey et al. [28–30] conducted a series of experimental tests to investigate the buckling response of pipe segments to various load combinations. They further performed an extensive parametric study on the CLS of pipelines, resulting in the development of four generalized equations for critical wrinkle strain; based on variables such as initial imperfection, D/t ratio, girth weld misalignment, internal pressure, and material behavior. Each equation applies to one of four possible combinations: a plain or girth-welded pipe in combination with a round-house type (RHT) stress-strain curve or a yield-plateau type (YPT) stress-strain curve. The Dorey et al. equations were determined using a global versus local curvature plot that describes the bilinear relationships between the local and global strains in the pre-buckling region and post-buckling region. The slope change indicates strain localization and the onset of wrinkle formation, and the critical buckling strain is defined based on the local strain over a $1D$ gauge length at the intersection point of the pre-buckling and post-buckling lines. The equations explicitly account for the magnitude of geometric imperfections and the distinction between plain and girth-welded pipes. The shape of the linear elastic portion of the stress-strain curve is considered but the strain-hardening characteristics of the pipe material are neglected, and the effect of applied net-section axial stress is not accounted for. A comparative evaluation of the CLS predictions by the Dorey et al. equations indicates a close correlation with experimental results as the predicted strains were generally either marginally below or above the test values [18].

A modification of Gresnigt's equations [21] for the CLS of pressurized pipes was indicated in Annex C of the Canadian pipeline design standard, CSA Z662-15 [31]. The CSA equation does not consider the ovalization effects in Gresnigt's equation and introduces a cut-off on the strain limit at $\sigma_\theta/\sigma_y = 0.4$. Also, the CSA equations are based on the outside diameter of the pipe whereas Gresnigt's equations are based on the average (mid-wall) diameter of the pipe. Additionally, the CSA equations do not explicitly account for the yield strength and strain-hardening characteristics of the pipe material, and the gauge length is not specified. For near-zero pressure levels, the CSA equations yield results that are analogous to the results of Gresnigt's equations whereas for, pressurized pipes, the CSA equations are significantly conservative for both lower and higher-grade pipes except in the case of the X100 pipe grade

which indicates some degree of non-conservatism. The degree of non-conservativeness observed for the CSA equations for pressurized pipes is generally lower than Gresnigt's equations [18].

On behalf of C-FER Technologies, Stephens et al. [32,33] obtained results of large-scale experimental data as part of a joint industry program and subsequently performed parametric FE analyses for the sake of extending the empirical investigations beyond the range of the limited experimental parameters. Nonlinear FE pipe models were developed and calibrated according to the obtained experimental data, and a number of curve-fitting and multiple regression techniques were employed to develop a semi-empirical equation for the CLS of pipes based on the peak moment strain criterion. The material characteristics of the pipe were incorporated into the equation by including the “knee-factor” of the Ramberg-Osgood stress-strain relation [34], thereby accounting for the strain-hardening characteristics of the pipe material, while the geometric and loading characteristics of the pipe were described by the D/t ratio and the hoop stress due to internal pressure respectively. The C-FER equation was derived based on a $1D$ gauge length, and the effects of girth-weld defects and geometric imperfections are not accounted for. A comparison, by Ref [18], of the C-FER equation to experimental data indicates a high degree of non-conservatism for combinations of high D/t and low n values.

DNV-OS-F101 [35] also derived an equation to predict the CLS of pipelines subjected to combined loading conditions. The equation accounts for geometric properties based on the D/t ratio and the hoop stress based on the ratio of the internal overpressure to the circumferential yield pressure. A girth weld reduction factor is also incorporated in the equation, but initial geometric imperfections and the effects of net-section axial stress are overlooked. The DNV equation incorporates the influence of the strain-hardening properties of the pipe material as the ratio of the yield stress to the ultimate tensile strength (Y/T ratio). However, the DNV equation is only valid for $D/t \leq 45$ and internal overpressure cases, and no particular gauge length is specified for the predicted CLS. A comparison of predictions with the DNV equation and experimental results by Ref [18] indicates a high degree of non-conservativeness for unpressurized pipes with $D/t \leq 30$, as well as for pressurized pipes with $D/t > 40$, except a safety factor is applied to the equation.

On behalf of Center for Reliable Engineering Systems (CRES), Liu et al. [36] developed a set of equations for predicting the CLS in pipes under displacement-controlled loading by conducting

extensive parametric analyses using experimentally-validated FE pipe models constructed with three-dimensional solid elements. The refined CLS models developed by Ref [36] considered a wide range of parameters including: pipe D/t ratio, internal pressure, Y/T ratio, geometric imperfection (in terms of the peak-to-valley height of initial pipe surface undulation, pipe uniform strain, length of the yield plateau (for YPT materials), and net-section tensile stress. It was opined that using a gauge length of two times the pipe's outer diameter (i.e., $2*OD$) for obtaining the CLS ensures adequate consistency with the definition of the strain demand since LSD is essentially based on a comparison of the CLS and the strain demand. It was also observed that the maximum bending moment and corresponding compressive strain generally increase as the length of the pipe specimen (or FE pipe model) increases. However, the observed positive effect on the maximum bending moment and the CLS diminishes at a specimen-length greater than six times the pipe's outer diameter (i.e., $L \geq 6*OD$). The effect of material anisotropy on the CLS was also investigated, and it was observed that the material-related deformational response of pipes is governed by the pipe's longitudinal compressive properties hence, the longitudinal compressive stress-strain curves are more appropriate, if available, for evaluating the CLS. The conclusions by Ref [36], however, contrast with the findings of Neupane et al. [37,38] who investigated the deformational response of numerical pipe models using a combined kinematic hardening material model and observed that the longitudinal tensile stress-strain curve produces results similar to the response based on anisotropic yielding assumptions at zero to low internal pressures while the circumferential tensile stress-strain curve produces results similar to the response based on anisotropic yielding assumptions at high internal pressures.

The prediction accuracy of currently existing CLS models has been observed to be hampered by two main factors: (1) inadequate characterization of shape peculiarities of the material stress-strain curve and (2) inaccurate representation of geometric imperfections and manufacturing-induced flaws [9,28,39]. Depending on the type of imperfection, accurate representation can be dicey as geometric undulations are extremely case-specific due to heavy dependence on an exhaustive list of factors, e.g., material memory, sheet metal forming and curing process flaws, residual stresses, thickness variations, shape deviations, ovalization, etc [40,41]. Owing to the randomness of imperfections, systematically-simplified assumptions of pre-buckling deformations and inherent geometric defects are usually adopted for analytical and numerical

analyses but are hardly representative of real existing defects. Compared to geometric imperfections, material stress-strain properties are relatively easier to characterize, and the two commonly-used parameters for incorporating the effects of strain hardening in the CLS equations are the Ramberg-Osgood exponent, “ n ” [32,33,42,43] or the yield-to-tensile stress (Y/T) ratio [35,36]. However, drawbacks remain inherent in either of these two approaches because: (1) the Ramberg-Osgood model has been observed to lose accuracy in approximating the stress-strain relationship beyond the 0.2% proof stress [44–48], and (2) the Y/T ratio does not accurately reflect the stress-strain behavior in the plastic range as it is possible for bilinear, YPT, and RHT curves to have entirely different shapes but the same Y/T ratios [18].

The overarching objective of this study is to tackle the material-related shortcomings of existing CLS equations by employing a moderately complex, yet reasonably simple, material model for parameterizing the entire shape of the stress-strain curve. A new set of CLS equations are developed herein based on the relevant influencing parameters, and the shape constants of a novel material characterization model, recently developed by Ndubuaku et al. [49–51], are used to represent the strain-hardening properties of the material stress-strain response. The ‘Ndubuaku’ stress-strain model provides the advantage of excellent approximation of any continuously-hardening material curve (i.e., any curve without a zero or negative slope; as is generally the case for the true stress-true strain response of metallic materials); even curves with a distinct yield point and an extended yield plateau. The response of unpressurized and pressurized pipe segments to uniform bending is studied herein by systematically implementing a comprehensive FE-based numerical parametric investigation using the general-purpose finite element analysis (FEA) software package, ABAQUS CAE [52]. Four variations of the pipe’s D/t ratio, five variations of the internal pressure, four variations of the material grade, and four (for RHT curves) or five (for YPT curves) variations of the material curve shape are implemented for the parametric analysis. Hence, adopting a full-factorial design of experiments (DOE) approach, the test matrix for this study consists of 320 and 400 FE simulations for RHT and YPT pipes respectively. The critical values of the average compressive strain are collated for all the simulations, and advanced nonlinear multiple regression techniques are employed for deriving semi-empirical equations for predicting the CLS of pipes under uniform bending.

7.3 Materials and Methods

7.3.1 Stress-strain characterization model

The ‘Ndubuaku’ model [49,50] mathematically defines the material stress-strain response using two expressions; one expression represents the linear elastic portion of the stress-strain curve while the second expression represents the remaining, characteristically nonlinear, portion of the stress-strain curve. The description of the nonlinear portion of the curve is based on normalization of the full stress range and the full strain range of the stress-strain curve such that the exact magnitudes of the values of the stress and strain at any specified reference points are preserved. The constitutive equation comprises two model constants (herein referred to as “shape” constants), the “knee” constant (k_{nm}) and the “heel” constant (h_{nm}) as follows:

$$\sigma = \begin{cases} E\varepsilon & \sigma \leq \sigma_{pl} \\ \sigma_{pl} + (\sigma_{up} - \sigma_{pl}) \left(\frac{\varepsilon - \varepsilon_{pl}}{\varepsilon_{up} - \varepsilon_{pl}} \right)^{k_{nm} \left(\frac{\varepsilon - \varepsilon_{pl}}{\varepsilon_{up} - \varepsilon_{pl}} \right)^{h_{nm}}} & \sigma > \sigma_{pl} \end{cases} \quad (7-1)$$

where E is Young’s modulus of elasticity, σ_{pl} and ε_{pl} represent the proportionality limit stress (PL-stress) and the corresponding proportionality limit strain (PL-strain) respectively, and the ultimate proof stress (UP-stress) and corresponding ultimate proof strain (UP-strain) are represented by σ_{up} and ε_{up} respectively.

The standard approach for determining the shape constants of a given curve is by least-squares curve-fitting, however, in the absence of engineering stress-strain data from a uniaxial coupon test, the following expressions can be used to derive the shape constants [51]:

$$k_{nm} = \frac{\varepsilon_{R1}^{(h_{nm})} \ln(\sigma_{R1})}{\ln(\varepsilon_{R1})} \text{ or } \frac{\varepsilon_{R2}^{(h_{nm})} \ln(\sigma_{R2})}{\ln(\varepsilon_{R2})} \quad (7-2)$$

$$h_{nm} = \frac{\ln \left[\frac{\ln(\varepsilon_{R1}) \cdot \ln(\sigma_{R2})}{\ln(\sigma_{R1}) \cdot \ln(\varepsilon_{R2})} \right]}{[\ln(\varepsilon_{R1}) - \ln(\varepsilon_{R2})]} \quad (7-3)$$

where,

$$\sigma_{R1} = \frac{\sigma_{c1} - \sigma_{pl}}{\sigma_{up} - \sigma_{pl}}, \quad \sigma_{R2} = \frac{\sigma_{c2} - \sigma_{pl}}{\sigma_{up} - \sigma_{pl}}, \quad \varepsilon_{R1} = \frac{\varepsilon_{c1} - \varepsilon_{pl}}{\varepsilon_{up} - \varepsilon_{pl}}, \quad \text{and} \quad \varepsilon_{R2} = \frac{\varepsilon_{c2} - \varepsilon_{pl}}{\varepsilon_{up} - \varepsilon_{pl}}$$

As indicated by the above expressions, the shape constants can be easily obtained by describing four ‘control points’, and since prescribed or standardized values of the yield stress and yield strain, as well as the ultimate stress and ultimate strain (uniform elongation), are usually available, the designer only has to define four additional control points to describe the shape of the stress-strain curve. For RHT materials, the first strain control point, ε_{c1} , corresponds to the yield strain while the first stress control point, σ_{c1} , represents the corresponding ‘offset’ proof stress. Hence the PL-strain and corresponding PL-stress need to be determined, as well as the second strain control point, ε_{c2} , and the corresponding stress control point, σ_{c2} , which can be discretionarily selected as any point on the curve between the offset proof point and the ultimate point. For YPT materials, however, the PL-stress corresponds to the designated yield stress according to the material grade while the PL-strain is analogous to the corresponding yield strain; hence, the first strain control point, ε_{c1} , is selected at the end of the Lüders plateau and the corresponding stress control point, σ_{c1} , is selected as a nominal value that is marginally higher than the yield stress. The second strain control point, ε_{c2} , and the corresponding stress control point, σ_{c2} , can then be selected as any point on the curve between the Lüders control point (σ_{c1} and ε_{c1}) and the ultimate point (σ_{up} and ε_{up}).

7.3.2 Matrix of parameters

A minimum of four variations is applied to each parameter to ensure that nonlinear trends in the relationship between the CLS and individual parameters are adequately captured. Also, to maintain consistency with the dimensionless form of the CLS, each of the investigated parameters is appropriately nondimensionalized.

The geometric properties of the pipe models are represented by ratio of the pipe's outer diameter to pipe's wall thickness (D/t ratio). Four variations of the D/t ratio are applied as follows: DT1 = 41.152, DT2 = 64.078, DT3 = 82.156, and DT4 = 104.622. The pipe size (invariably, the diameter) is kept constant at NPS (nominal pipe size) = 36 inches while the pipe's wall thickness is varied according to the D/t ratios as: $t_1 = 22.22$ mm (for DT1), $t_2 = 14.27$ mm (for DT2), $t_3 = 11.13$ mm (for DT3), and $t_4 = 8.74$ mm (for DT4).

The hoop stress is defined based on the ratio of internal pressure (p) to the circumferential yield pressure ($p_y = \frac{2\sigma_{ys}t}{D}$), and is herein referred to as the 'pressure factor' ($f_p = p/p_y$). Five variations of the pressure factor are applied to the test matrix as follows: $f_{p00} = 0.0$, $f_{p20} = 0.2$, $f_{p40} = 0.4$, $f_{p60} = 0.6$, and $f_{p80} = 0.8$.

The dimensionless form of the material grade is defined as either of two forms, depending on the material curve shape: for YPT materials, the material grade is represented by the ratio of the nominal yield stress (YS) to the elastic modulus of the material while for RHT materials, the material grade is represented by the ratio of the PL-stress to the UP-stress (herein referred to as the 'PLUS' ratio). For this study, the proportionality limit is selected as the material-grade parameter for RHT pipes as it is considered to provide a more precise indication of the material nonlinearity characteristics of pipeline steels, which is more relevant to the deformational capacity. Four variations of the material grades are applied to the matrix, as prescribed by the API 5L pipeline steels standard [53]: API X52 (YS = 379 MPa), API X60 (YS = 441 MPa), API X70 (YS = 503 MPa), and API X80 (YS = 586 MPa). The corresponding ultimate strengths for each material grade are also specified to closely align with API 5L specifications as follows: API X52 = 455 MPa, API X60 = 565 MPa, API X70 = 593 MPa, API X80 = 703 MPa. The elastic modulus of steel is chosen as 205800 MPa for this study.

The strain-hardening properties of the material curves are represented in the test matrix by the shape constants of the ‘Ndubuaku’ material model. The material curve shapes are varied differently for YPT curves and RHT curves: YPT curves are varied by changing the length of the yield plateau while RHT curves are varied by changing the proportionality limit stress (naturally, a lower proportionality limit is accompanied by a higher value of the second stress control point, σ_{c2}). The standard designations for each material grade are maintained by maintaining constant values for the yield stress and the ultimate stress. A uniform elongation equal to a total strain of 10% is assumed to be constant for all materials and the 0.5% total strain ($\sigma_{0.5}$) ‘offset’ proof stress approach specified by the API 5L standard [53] is adopted for defining the nominal yield stress (YS) for each material grade. The variations of the curve shape for each material grade are graphically presented in Figure 7-1 - Figure 7-4.

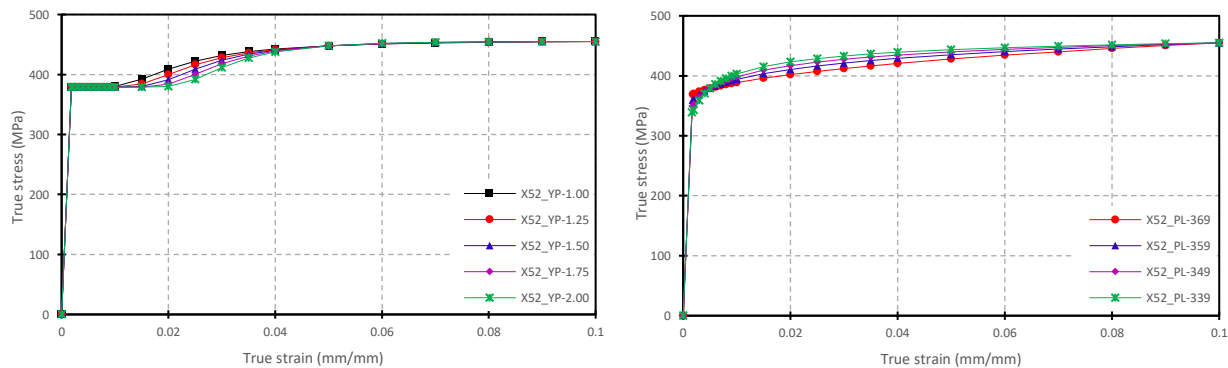


Figure 7-1: Idealized variations for stress-strain curves of X52-YPT and X52-RHT materials

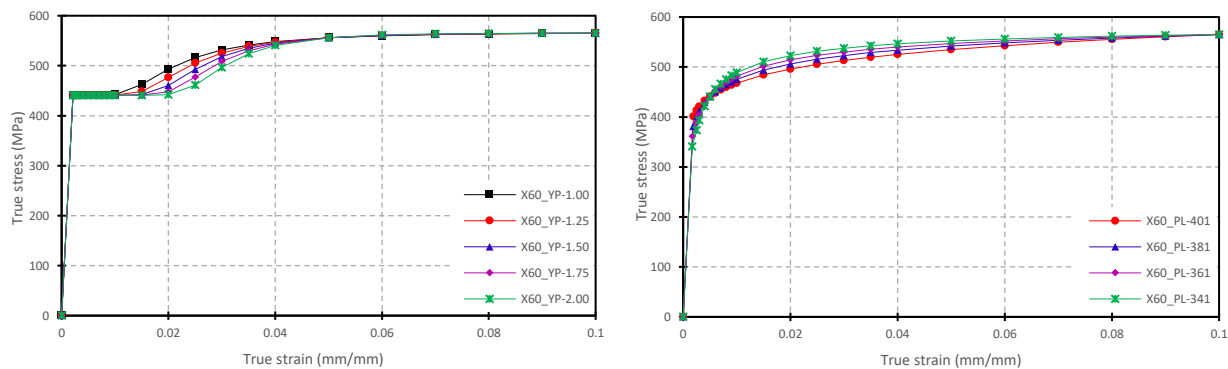


Figure 7-2: Idealized variations for stress-strain curves of X60-YPT and X60-RHT materials

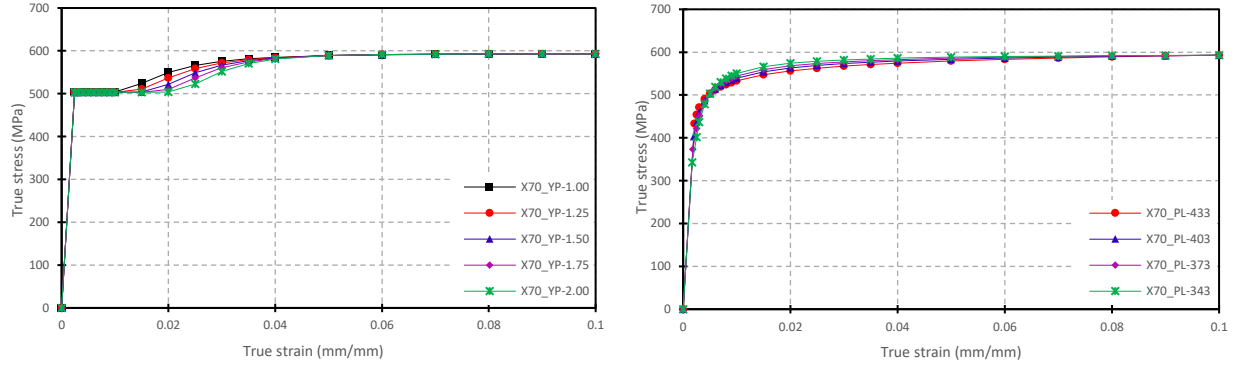


Figure 7-3: Idealized variations for stress-strain curves of X70-YPT and X70-RHT materials

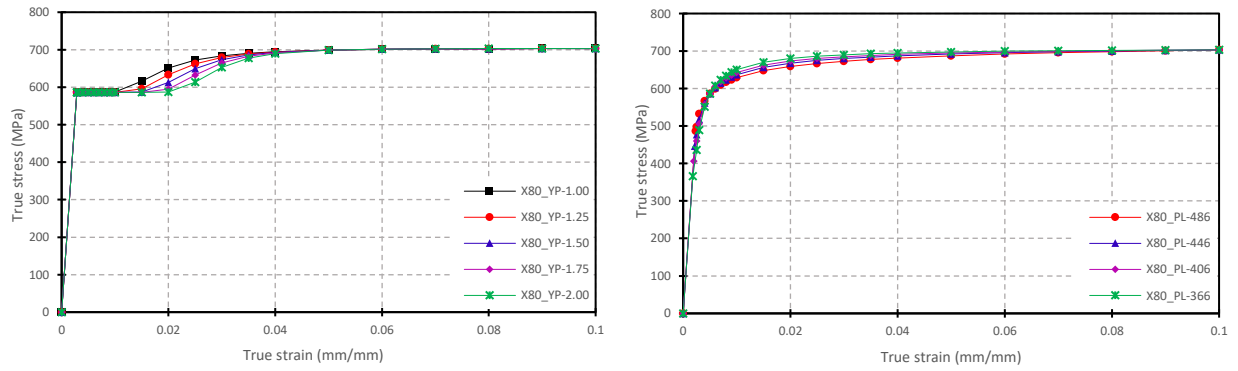


Figure 7-4: Idealized variations for stress-strain curves of X80-YPT and X80-RHT materials

In Figure 7-1 – Figure 7-4 above, the numeric designations for the YPT curve labels are specified in percentage (%) units to indicate the length of the yield plateau in terms of the total strain while the numeric designations for the RHT curve labels are specified in megapascal (MPa) units to indicate the proportionality limit stress of each curve shape variation. The shape constants corresponding to each curve shape variation are presented in Table 7-1.

Table 7-1: Shape constants for variation of material curve shape

Material Grade	YPT			RHT		
	<i>Curve label</i>	$K_f = 1/K_{nm}$	$H_f = 1/H_{nm}$	<i>Curve label</i>	$K_f = 1/K_{nm}$	$H_f = 1/H_{nm}$
X52	<i>YP-1.00</i>	20.5077	0.6958	<i>PL-369</i>	1.9578	16.4530
	<i>YP-1.25</i>	25.9422	0.5658	<i>PL-359</i>	3.3881	7.6640
	<i>YP-1.50</i>	33.6157	0.4692	<i>PL-349</i>	5.2603	5.0535
	<i>YP-1.75</i>	45.0310	0.3934	<i>PL-339</i>	8.5164	3.4226
	<i>YP-2.00</i>	63.0332	0.3318			
X60	<i>YP-1.00</i>	29.9027	0.6234	<i>PL-401</i>	3.8457	7.7602
	<i>YP-1.25</i>	38.8327	0.5078	<i>PL-381</i>	6.1646	4.9322
	<i>YP-1.50</i>	51.7336	0.4219	<i>PL-361</i>	9.3150	3.6322
	<i>YP-1.75</i>	71.4369	0.3544	<i>PL-341</i>	15.359	2.6046
	<i>YP-2.00</i>	103.465	0.2994			
X70	<i>YP-1.00</i>	57.9192	0.5532	<i>PL-433</i>	9.5412	4.3644
	<i>YP-1.25</i>	77.6927	0.4512	<i>PL-403</i>	17.4955	2.9594
	<i>YP-1.50</i>	107.0977	0.3755	<i>PL-373</i>	29.5817	2.2654
	<i>YP-1.75</i>	153.5094	0.3160	<i>PL-343</i>	58.0424	1.6629
	<i>YP-2.00</i>	231.8488	0.2675			
X80	<i>YP-1.00</i>	83.7395	0.5187	<i>PL-486</i>	11.5448	3.9814
	<i>YP-1.25</i>	115.2048	0.4221	<i>PL-446</i>	21.1099	2.7531
	<i>YP-1.50</i>	162.9859	0.3510	<i>PL-406</i>	35.3391	2.1374
	<i>YP-1.75</i>	240.2443	0.2953	<i>PL-366</i>	69.2445	1.5847
	<i>YP-2.00</i>	374.3178	0.2501			

7.3.3 Numerical finite element (FE) simulation

The FE pipe models for this study are constructed using three-dimensional shell elements and are subjected to monotonically-increasing curvature, such as to mimic the induced deformation caused by surrounding or supporting ground settlement. Geometric imperfections in form of

diametric undulations are not explicitly considered herein. However, a 3% reduction in the pipe's thickness, spanning longitudinally over 5% of the pipe's length, is applied as a sleeve at the pipe's mid-length cross-section to trigger the formation and growth of the localized wrinkle at the middle of the pipe's length without significantly impacting the overall moment vs. curvature response.

To optimize the allocation of computational resources and reduce computational time, symmetry conditions are applied longitudinally (horizontal-transverse symmetry; aligned with the bending plane) and transversely (longitudinal symmetry; aligned with the pipe's mid-length cross-section) to the pipe models such that only a quarter of the actual pipe segments are modeled and numerically evaluated. The specimen length ($6 \cdot OD$) recommended by Liu et al. [36] is adopted for the pipe models (i.e., $3 \cdot OD$ after applying the symmetry conditions) to forestall interference between the end boundary conditions and the pipe's mid-length cross-section, where the localized wrinkle is formed. A typical geometry of the full-length FE pipe model is presented in Figure 7-5. The horizontal-transverse symmetry for the quarter pipe model is achieved by restraining the displacements, u_x , and the rotations, ϑ_y and ϑ_z , at all the nodes along the longitudinal plane of the symmetry while the longitudinal symmetry is achieved by restraining the displacements, u_z , and the rotations, ϑ_x and ϑ_y , at all the nodes on the transverse plane of symmetry (i.e., at the mid-length cross-section of the pipe). A reference point (RP) is created at the loading end of the pipe and the displacements, u_x and u_y , as well as the rotations, ϑ_y and ϑ_z , are restrained such that the RP is only allowed to move in the longitudinal direction (i.e., along the z -axis; u_z) and free to rotate about the axis of bending (i.e., about the x -axis; ϑ_x). The pipe loading end is connected to the nodes at the end cross-section by applying a kinematic coupling constraint in the cylindrical coordinate system which restrains all degrees of freedom at the end cross-section of the pipe except circumferential extension, thereby allowing a uniform stress field under internal pressurization.

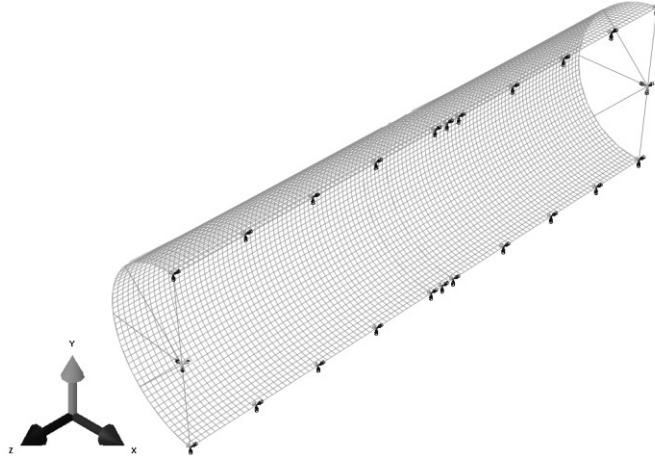


Figure 7-5: Pipe model geometry showing FE discretization

The geometry of the pipe models is three-dimensionally assembled using four-node isoparametric quadrilateral shell elements with reduced integration (S4R), which are immune to unconstrained hourglass modes and transverse shear locking. The S4R element has six degrees of freedom, three translations (u_1, u_2, u_3) in the directions of the global axes and three rotations ($\theta_1, \theta_2, \theta_3$) about the directions of the three global axes, at each of the four nodes. The S4R element is also shear-flexible and is, thus, suitable for modelling the behavior of both thin (Kirchhoff) shell and thick (Mindlin) shell. The element has an isoparametric formulation and accounts for finite membrane strains hence it is equipped for handling significant thickness change, large displacements and/or rotations, and transverse shear constraints. The element is also effective for modelling wrinkle formation and evolution in pipes under various loading and imposed deformation conditions and has excellent ability to account for material and geometric nonlinearities. The pipelines modeled in this study are assumed to be made of carbon steel and are therefore considered to have isotropic material properties. Hence, the yield criterion used for modelling is based on the classical large-strain von Mises plasticity model with nonlinear isotropic hardening and is assumed to follow the associated plastic flow rule. Since the simulated deformation is quasi-statically imposed, the isotropic model is assumed to be rate-independent and no cyclic strain responses or dynamic loading effects are considered. Based on the results of a preliminary mesh sensitivity analysis, an approximate global mesh size equal to 3% of the pipe diameter is applied to the FE pipe models.

The boundary/symmetry conditions are applied to the pipe models in the default “Initial” step of the ABAQUS software program followed by definition of a two-step loading scheme to simulate the response of the pipe models to uniform bending. The first step is defined using the “Static General” designation in ABAQUS, which performs the numerical analysis based on the classical Newton’s iterative numerical method. The internal pressure is calculated according to the respective pressure factors for each parametric combination ($p = f_p \times p_y$) and applied as a distributed load to the inner surface of the pipe geometry. The second step of the loading scheme is defined as a “Static Riks” step, which employs a linearized arc-length control technique performed based on the default equilibrium iterative incremental scheme in ABAQUS and is remarkably effective for simulating the load-deformation response of structural systems under various loading conditions. Monotonically-increasing curvature is imposed on the pipe model in the second step of the loading scheme by specifying a finite rotational displacement rotation about the global x -axes at the RP created at the end cross-section.

Incremental values of the average logarithmic axial strain (LE11) and the reaction bending moment (“RM1”) are extracted as X-data and Y-data respectively. The average logarithmic axial strain is obtained in the cylindrical coordinate system of the pipe geometry and calculated as the average value of the recorded longitudinal strains of all the nodal points in the ‘gauge area’. The ‘gauge area’ is defined according to the recommendations of Ref. [36] by a longitudinal span of two times the pipe’s outer diameter ($2*OD$) and a circumferential distance of approximately one quarter of the pipe diameter ($0.25*D$), centrally located with respect to the bending plane and the compressive side of the pipe’s mid-length cross-section. The reaction bending moment is simply obtained at the RP created at the pipe’s end cross-section. The CLS is defined by the ‘peak moment criterion’ [8,28] as the value of average strain corresponding to the maximum bending moment for each simulation.

7.4 Validation of FE Model

Mohareb et al. [54] carried out a series of full-scale laboratory experiments to observe the buckling behavior of pipe segments under combined loading and reported the moment-curvature response and wrinkle deformation pattern for different loading conditions. The results of one of

the specimens tested by Ref. [54] is used to validate the FE pipe models and numerical analysis procedures implemented herein. Least-squares curve-fitting was used to determine the Ndubuaku model shape constants corresponding to the stress-strain relationship of the material for the pipe segment tested by Ref. [54]. The geometric and material properties of the experimental test specimen, designated as “UGA508” by Ref. [54], are as follows:

- Outer diameter 508 mm
- D/t ratio 64
- Length of pipe 1690 mm
- Material grade API X56
- Elastic modulus 203704 MPa
- Yield stress ($\sigma_{0.5}$) 391 MPa
- Proportionality limit stress 329 MPa
- Knee constant ($1/K_{nm}$) 3.53
- Heel constant ($1/H_{nm}$) 29.61
- Internal pressure 0 MPa
- Net-section compressive axial force 1303 kN

A good correlation between the experimentally-observed behavior and the FE prediction is obtained for both the moment-curvature response and the localized buckling mode, as shown in Figure 7-6.

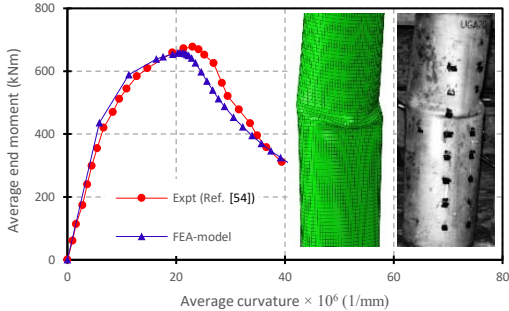


Figure 7-6: Comparison of FEA result with experimental result (UGA508) by Ref. [54]

The snapshots of the wrinkle deformation pattern in Figure 7-6 indicate, as expected for unpressurized or low-pressure conditions, that the deformation of a pipe segment after collapse is characterized by a diamond-shaped wrinkle which is evidently nonsymmetric about the pipe's mid-length cross-section. Hence, an imperative aspect of the FE pipe model validation involved comparison of the full-length and half-length pipe models to determine the existence of any significant discrepancies in the moment-curvature response. The geometric, material and loading properties of the two FE pipe models are as follows:

- Outer diameter	914 mm
- D/t ratio	76.8
- Length of pipe	5486.4 mm
- Material grade	API X65
- Elastic modulus	200000 MPa
- Yield stress ($\sigma_{0.5}$)	482 MPa
- Proportionality limit stress	409.7 MPa
- Knee constant ($1/K_{nm}$)	7.41
- Heel constant ($1/H_{nm}$)	7.28
- Internal pressure	0 MPa
- Net-section compressive axial force	0 kN

The plot in Figure 7-7 shows the superimposed moment-curvature responses of the half-length model and the full-length model under zero pressure and induced uniform curvature.

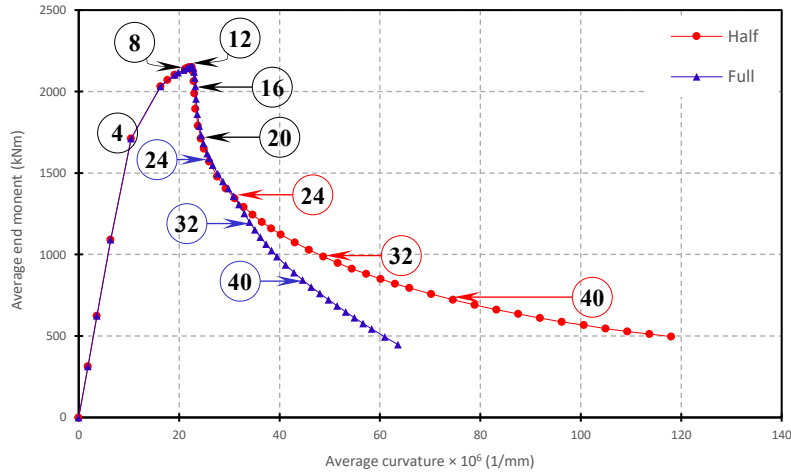


Figure 7-7: Comparison of moment-curvature responses for half-length and full-length pipe model

The evolution of the wrinkle deformation is also graphically presented using the stacked plots in Figure 7-8 and Figure 7-9, for the half-length model and the full-length model respectively.

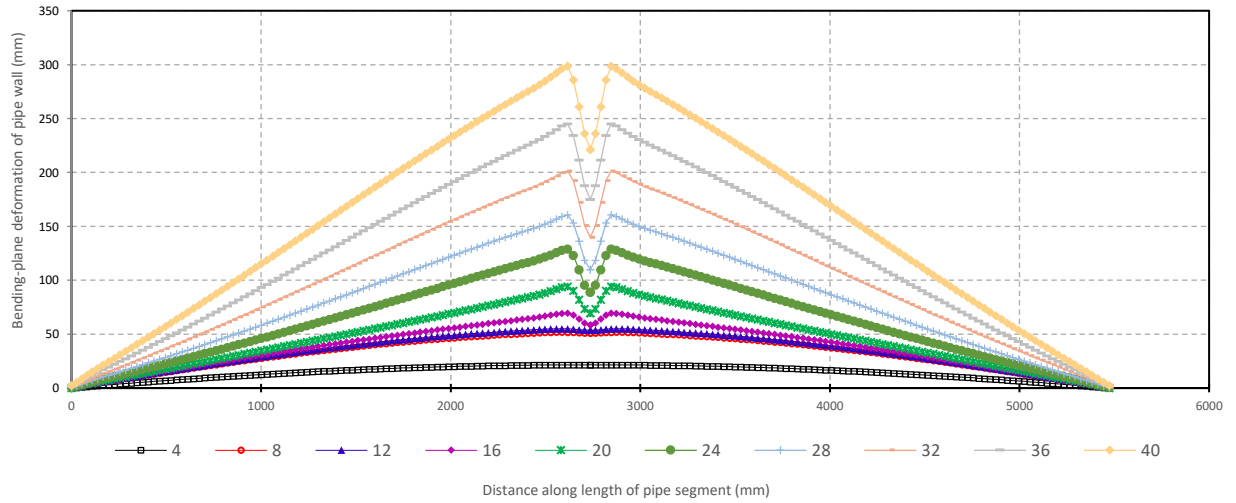


Figure 7-8: Evolution of wrinkle deformation for half-length pipe model

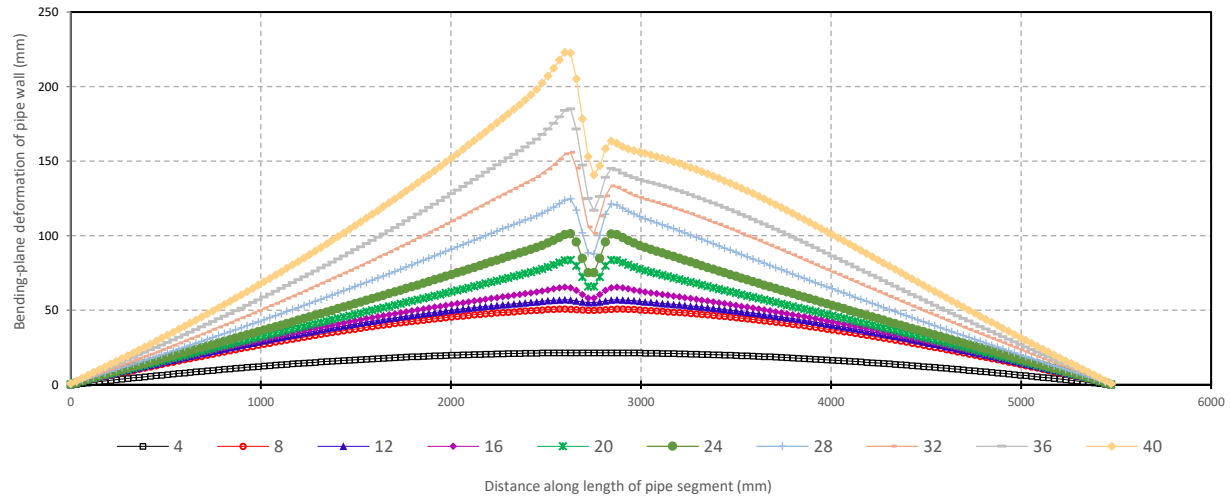


Figure 7-9: Evolution of wrinkle deformation for full-length pipe model

The numeric designations in the plot legends of Figure 7-8 and Figure 7-9 are traced along the moment-curvature plot in Figure 7-7 and correspond to the iteration steps of the numerical analysis for the respective models. The black markers (4, 8, 12, 16 and 20) show exact or approximate locations of respective iteration steps along the moment-curvature response curve while the purple markers (left; 24,32 and 40) and red markers (right; 24,32 and 40) show exact locations of respective iteration steps along the moment-curvature for the full-length and half-length pipe models respectively.

It can be inferred from the plot in Figure 7-7 that both models have similar moment-curvature responses up to the peak moment and even up to a tangible extent afterward. The symmetrical buckling mode imposed on the half-length model is observed to induce additional deformational capacity in the pipe, compared to the full-length model, after a certain level of deformation. Upon close observation of the evolution of the wrinkle deformation for both models in Figure 7-8 and Figure 7-9 it is realized that, for both pipe models, the wrinkle remains symmetric about the pipe's mid-length cross-section until around the 24th iteration. Likewise, divergence of the superimposed plots in Figure 7-7 begins at the 24th iteration, which coincides with the transformation of the wrinkle of the full-length model from a symmetric mode to a nonsymmetrical diamond-shaped mode. The superior deformational capacity of the half-length can, therefore, be attributed to the symmetrical mode of the wrinkle deformation. Essentially, the above observations indicate that the half-length model is suitable for obtaining the CLS since the

peak moment and corresponding average curvature are not affected by the application of longitudinal symmetry at the pipe's mid-length cross-section.

7.5 Results of Parametric FE Study

7.5.1 Influence of D/t ratio

The influence of the D/t ratio on the CLS of YPT pipes and RHT pipes is graphically illustrated by the plots in Figure 7-10 and Figure 7-11 respectively. The plots in Figure 7-10 are obtained for a YPT X70 pipe with yield plateau length (YPL) = 1.75 while the plots in Figure 7-11 are obtained for an RHT X52 pipe with PLUS ratio = 0.81. The plots in each figure are for pipes subjected to f_p values ranging from 0.0 to 0.8.

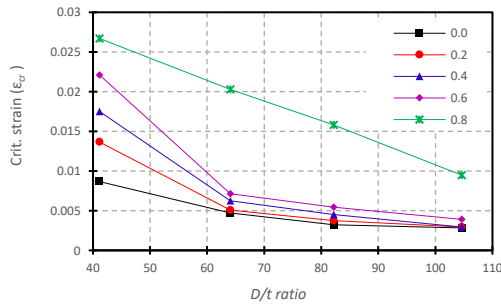


Figure 7-10: Plot of ϵ_{cr} vs. D/t ratio for YPT X70 pipe (YPL = 1.75)

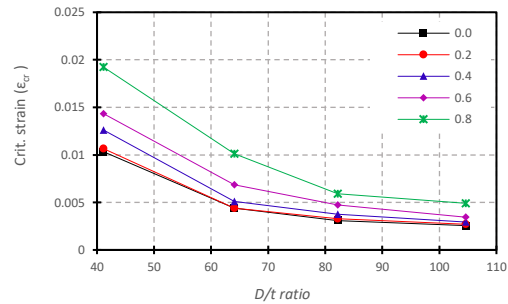


Figure 7-11: Plot of ϵ_{cr} vs. D/t ratio for RHT X52 pipe (PL/US = 0.81)

The plots in Figure 7-10 and Figure 7-11 indicate the D/t ratio generally has a negative correlation with the CLS of both YPT pipes and RHT pipes. The effect of the D/t ratio on the CLS is also observed to be significantly influenced by internal pressure as the steepness of the CLS vs. D/t ratio trends is observed to increase as the pressure factor is increased. The observed parametric interrelationship between the D/t ratio and the internal pressure is more evident in YPT pipes, compared to RHT pipes, especially at high internal pressure ($f_p = 0.8$) and low D/t ratio (DT1). The effect of the internal pressure on the CLS vs. D/t ratio trends of RHT pipes is observed to be relatively moderate, compared to YPT pipes.

7.5.2 Influence of internal pressure

The relationship between the internal pressure and the CLS of YPT pipes and RHT pipes is represented by the plots in Figure 7-12 and Figure 7-13: Plot of ϵ_{cr} vs. f_p for respectively. The plots in Figure 7-12: Plot of ϵ_{cr} vs. f_p for are obtained for a YPT X60 pipe with YPL = 2.0 while the plots in Figure 7-13: Plot of ϵ_{cr} vs. f_p for are obtained for an RHT X52 pipe with PLUS ratio = 0.81. Each plot in Figure 7-12: Plot of ϵ_{cr} vs. f_p for and Figure 7-13: Plot of ϵ_{cr} vs. f_p for corresponds to one of the four D/t ratios investigated.

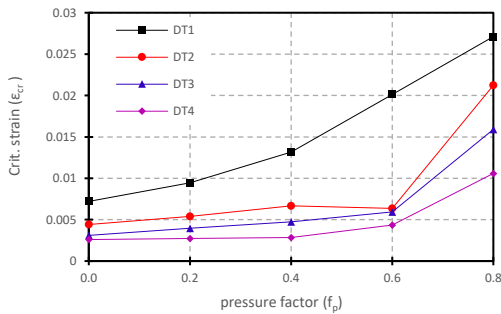


Figure 7-12: Plot of ϵ_{cr} vs. f_p for YPT X60 pipe (YPL = 2.0)

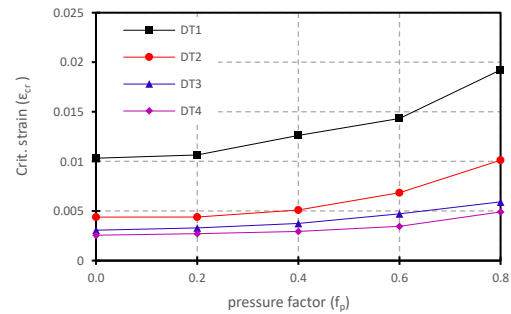


Figure 7-13: Plot of ϵ_{cr} vs. f_p for RHT X52 pipe (PL/US = 0.81)

The CLS vs. f_p plots clearly indicate a positive correlation between the CLS and internal pressure for both YPT pipes and RHT pipes. At pressure-resultant hoop stress levels less than or equal to 60% YS (i.e., $f_p \leq 0.6$) there is no significant effect of internal pressure variation on the CLS of YPT pipes and RHT pipes with intermediate D/t ratios (DT2 and DT3) and high D/t ratio (DT4). Contrastingly, the effect of internal pressure variation on the CLS of low- D/t ratio (DT1) pipes is observed to significant at all hoop stress levels. Strong similarities are observed between the CLS vs. f_p trends of YPT pipes and RHT pipes except at a low D/t ratio (DT1) or under high internal pressure ($f_p = 0.8$) where the internal pressure is observed to have a greater effect on YPT pipes compared to RHT pipes.

7.5.3 Influence of material grade

The material grades for YPT pipes are represented in the matrix of parameters by the ratio of the 0.5% total strain ‘offset’ proof stress ($\sigma_{0.5}$) to the elastic modulus while for RHT pipes, the material grades are represented by the ‘PLUS’ ratio. The plots in Figure 7-14 and Figure 7-15 provide a graphical illustration of the relationship between the respective dimensionless material grade parameters and the CLS. The plots in Figure 7-14 show the relationship between the yield stress ($\sigma_{0.5}$) and the CLS for a YPT DT1 pipe with YPL = 1.25 while the plots in Figure 7-15 show the relationship between the PLUS ratio and the CLS for an RHT DT3 pipe under hoop stress = 20% YS (i.e., $f_p = 0.2$). The numeric designations in the plot legend of Figure 7-14 correspond to the pressure factor, f_p while the numeric designations in the plot legend of Figure 7-15 represent the yield stress (in MPa) according to respective material grades.

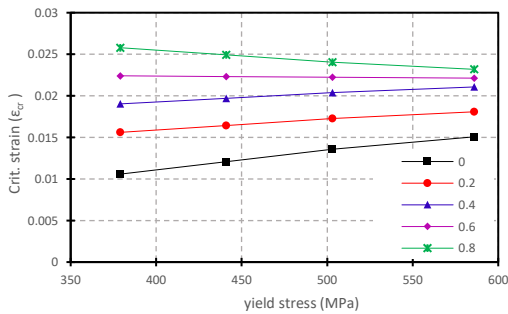


Figure 7-14: Plot of ϵ_{cr} vs. σ_{ys} for YPT DT1 pipe (YPL = 1.25)

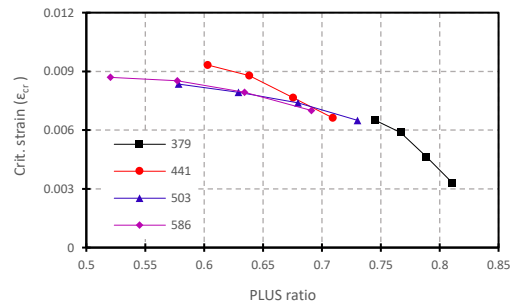


Figure 7-15: Plot of ϵ_{cr} vs. PL/US for RHT DT3 pipe ($f_p = 0.20$)

The plots in Figure 7-14 indicate that the relationship between the material grade and the CLS of YPT pipes is generally linear and positive except at high internal pressure ($f_p = 0.8$), where the CLS vs. $\sigma_{0.5}$ trend may exhibit a slightly negative linear slope. The slope of the CLS vs. $\sigma_{0.5}$ trend is also observed to progressively reduce as the internal pressure is increased. However, this is peculiar to the D/t ratio presented (i.e., DT1) as, even though not shown here, no significant change in slope is observed, due to internal pressure, at higher D/t ratios. On the other hand, a generally nonlinear negative relationship exists between the PLUS ratio and the CLS of RHT pipes, irrespective of the material grade.

7.5.4 Influence of material curve shape

Pipe segments with the range of D/t ratios covered in this study are prone to inelastic buckling. Hence, their deformational response is significantly influenced by the shape of the nonlinear portion of the material stress-strain curve beyond the proportional limit [19,20]. The material curve shapes are represented in Figure 7-16 and Figure 7-17 by numeric designations, referred to as “shape factors” (sh_f). The shape factors are arbitrarily defined to combine the two shape constants that describe the nonlinear portion of the stress-strain curve of respective material grades. The shape factors are calibrated onto a linear scale of one to four for RHT pipes and one to five for YPT pipes. For both YPT pipes and RHT pipes, $sh_f = 1$ represents a curve with the highest value of the heel constant (H_f) and lowest value of the knee constant (K_f) while $sh_f = 4$ and $sh_f = 5$ represent, respectively, RHT curves and YPT curves with the lowest values of the heel constant (H_f) and highest values of the knee constant (K_f). Invariably, a lower sh_f indicates a shorter YPL of YPT curves or a higher proportionality limit stress (inferior strain-hardening) in RHT curves, and vice versa.

Figure 7-16 comprises the plots of the CLS against sh_f , obtained at all five levels of internal pressurization investigated, for a YPT X70 DT1 pipe while Figure 7-17 comprises plots of the CLS against sh_f , also obtained at all five levels of internal pressurization investigated, for a YPT X52 DT3 pipe. Pressure factors are indicated by 0.0 – 0.8 in the plot legends.

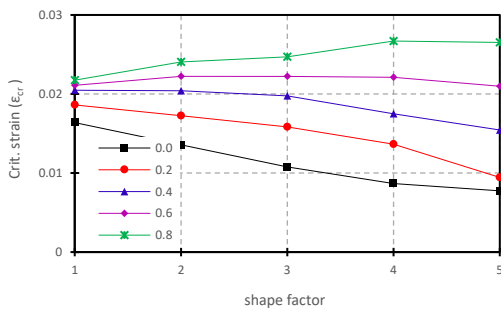


Figure 7-16: Plot of ϵ_{cr} vs. sh_f for YPT X70 pipe ($D/t = 41.152$)

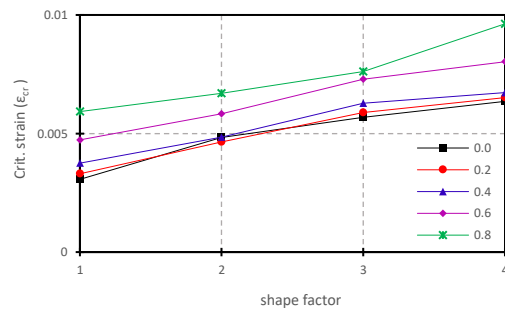


Figure 7-17: Plot of ϵ_{cr} vs. sh_f for YPT X52 pipe ($D/t = 82.156$)

It can be inferred from Figure 7-16 that, at a low D/t ratio, the slope of the CLS vs. sh_f trends of YPT pipes increases progressively as the internal pressure is increased such that the relationship between the CLS and the shape factor tends from a negative correlation, at zero-to-moderate pressure factors ($0.0 < f_p < 0.6$), to a slightly-positive correlation, at high internal pressure ($f_p > 0.6$). However, for RHT pipes, the relationship between the CLS and sh_f is generally positive and somewhat linear.

7.6 Development of CLS Equations

Derivations of the nonlinear constitutive equations for predicting the CLS follow a semi-empirical modeling approach and are presented in this section. Considering the significant distinctions observed in the trends of the CLS of YPT pipes and RHT pipes, with respect to the various investigated parameters, a feasible approach requires the development of two separate equations for each material curve shape classification. The functional relationships between each parameter and the CLS are deciphered visually from combined graphical plots, as presented above, and representative mathematical expressions (individual variable functions) are assigned to respective parameters accordingly. Graphical illustrations also highlight any significant interrelationships between the individual parameters, which can then be incorporated in the individual variable functions that make up each of the constitutive equations. Each constitutive equation is formed based on a direct combinative multiplication concept [29,36,55], whereby all the individual variable functions are simply multiplied together, as follows:

$$\varepsilon_{cr} = f_{cr}[\pi_1, \pi_2, \pi_3, \pi_4, \pi_5, \pi_6] = f_1 \cdot f_2 \cdot f_3 \cdot f_4 \cdot f_5 \quad (7-4)$$

where f_1, f_2, f_3, f_4 , and f_5 represent the D/t ratio function (f_{dt}), the pressure factor function (f_{fp}), the strain-hardening function (f_{sh}), the heel factor function (f_{hf}), and the knee-to-heel ratio function (f_{kh}). π_1 represents the D/t ratio ($\frac{D}{t}$), π_2 represents the pressure factor ($\frac{p}{p_y}$), π_3 represents the ratio of the yield stress to the elastic modulus ($\frac{\sigma_{ys}}{E}$) for YPT pipes or the PLUS

ratio $\left(\frac{\sigma_{pl}}{\sigma_{us}}\right)$ for RHT pipes, π_4 represents the heel factor (h_f), and π_5 represents the “*knee-to-heel*” ratio $\left(\frac{k_f}{h_f}\right)$.

Achieving good correspondence between the prediction of the developed constitutive equations and the results of the parametric FE analysis requires a thoroughly-implemented iterative process whereby the functional forms of the individual variable functions are changed repeatedly and the coefficient of multiple determination (R-squared) is evaluated. The guiding principle followed herein ensures that the highest possible R-squared value, not less than 0.95, is achieved.

The individual variable functions for YPT pipes are:

$$\begin{aligned}
 f_1 = f_{dt} &= a_1 \cdot (\pi_1)^{b_1} \\
 f_2 = f_{fp} &= a_2 + (b_2 + c_2 \pi_1) \cdot \text{Exp}(\pi_2)^{(d_2 + e_2 \pi_4)} \\
 f_3 = f_{sh} &= a_3 \pi_4 + (b_3 \pi_2 + c_3 \pi_1) \cdot (\pi_3)^{d_3} \\
 f_4 = f_{hf} &= a_4 + (b_4 \pi_1) \cdot (\pi_4)^{c_4} \\
 f_5 = f_{kh} &= a_5 + (b_5 \pi_3) \cdot (\pi_5)^{c_5}
 \end{aligned} \tag{7-5}$$

The individual variable functions for RHT pipes are:

$$\begin{aligned}
 f_1 = f_{dt} &= a_1 \cdot (\pi_1)^{b_1} \\
 f_2 = f_{fp} &= (a_2 + b_2 \cdot \pi_2) \cdot [c_2 + (d_2 + e_2 \pi_1) \cdot \text{Exp}(\pi_2)^{(f_2)}] \\
 f_3 = f_{sh} &= a_3 + (b_3 \pi_2 + c_3) \cdot (\pi_3)^{d_3} \\
 f_4 = f_{hf} &= a_4 + b_4 \cdot (\pi_4)^{c_4} \\
 f_5 = f_{kh} &= a_5 + b_5 \cdot (\pi_5)^{c_5}
 \end{aligned} \tag{7-6}$$

To obtain the regression coefficients for each constitutive equation, nonlinear multiple regression techniques are implemented using the highly-versatile general-purpose computational software program, Wolfram Mathematica [56]. The obtained coefficients and the final R-squared value for each equation are presented in Table 7-2.

Table 7-2: Constitutive equation coefficients

<i>Reg. Coeff.</i>	<i>YPT</i>	<i>RHT</i>
a_1	6.815	0.903
b_1	-3.099	-1.001
a_2	-686.6	0.5172
b_2	-166.2	0.6262
c_2	-0.2087	104.4
d_2	5.725	113.8
e_2	-3.05	-0.09382
f_2	-	-2.862
a_3	0.0133	0.1651
b_3	-420.1	0.2068
c_3	9.243	-0.4652
d_3	1.546	6.797
a_4	155.4	0.003259
b_4	-0.0902	0.1204
c_4	-1.297	-0.985
a_5	-0.07135	0.2484
b_5	8.452	1.921
c_5	0.07316	-0.5125
R^2	0.977358	0.993308

The applicable range for the dimensionless parameters that constitute the developed nonlinear regression equations is limited to the scope of investigation for each parameter in the test matrix as presented in Table 7-3:

Table 7-3: Applicable range for dimensionless parameters

<i>Par.</i>	YPT		RHT	
	\geq	\leq	\geq	\leq
<i>D/t</i>	41	105	41	105
<i>f_p</i>	0.0	0.8	0.0	0.8
<i>σ_y/E</i>	0.0018	0.0029		-
<i>σ_p/σ_{us}</i>		-	0.52	0.85
<i>sh_f</i>	1	5	1	4

The peculiarities that exist with respect to the values of the shape constants for each material grade must be considered in defining the shape factor. Essentially, the implication is that different material grades with the same shape factor will be defined by unsimilar combinations of shape constants. The same techniques implemented for developing the CLS equations are therefore employed to derive two nonlinear regression equations for calculating the shape factor as follows:

For YPT pipes,

$$sh_{f,YP} = 0.0507483 \times (0.0293137 - 9.86288 * 10^{-5} \cdot \sigma_y \cdot h_f^{1.12036}) \times \left(4154.41 + 0.351787 \cdot \sigma_y \cdot \ln \left(\frac{k_f}{h_f} \right) \right) \quad (7-7)$$

For RHT pipes,

$$sh_{f,RH} = 8.85104 * 10^{-6} \times (307.19 - 0.312884 \cdot \sigma_y \cdot h_f^{0.303706}) \times \left(2863.64 + 0.615032 \cdot \sigma_y \cdot \ln \left(\frac{k_f}{h_f} \right) \right) \quad (7-8)$$

7.7 Goodness-of-Fit

Besides simply obtaining a high R-squared value, the predictive accuracy of the developed constitutive equations is further examined by plotting the model-predicted CLS values against the FEA-derived CLS values for using the scatter plots in Figure 7-18 and Figure 7-19.

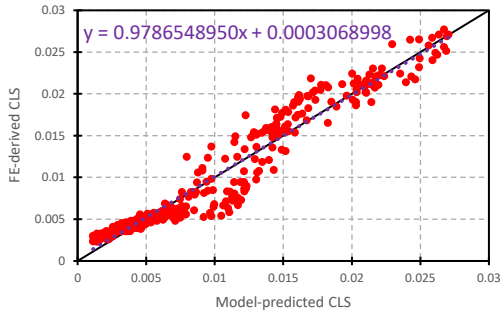


Figure 7-18: Model prediction vs. FEA for
YPT

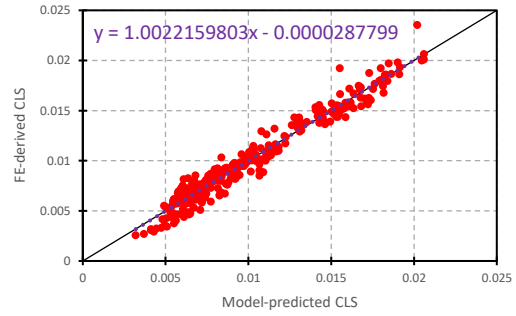


Figure 7-19: Model prediction vs. FEA for
RHT

As evident in Figure 7-18 and Figure 7-19, the nonlinear regression technique is formulated to obey laws of central tendency and therefore produces a median model that is centrally aligned with the diagonal of the scatter plot. A simple two-step statistical procedure is presented to introduce a desired level of conservativeness in the semi-empirical model by shifting the data points above the diagonal line of the scatter plot.

The first step in the procedure attempts to correct any bias in the linear equation of the scatter plot using the following expression:

$$\varepsilon_{cr,corr} = G_{orig} \times \varepsilon_{cr,orig} + I_{orig} \quad (7-9)$$

where G_{orig} and I_{orig} are the original gradient and intercept values, respectively, for the linear equation of the FEA vs. model prediction scatter plot. $\varepsilon_{cr,orig}$ and $\varepsilon_{cr,corr}$ are the original and corrected versions, respectively, of the semi-empirical model.

By applying the above expression to the CLS equation, the gradient and intercept of the linear scatter-plot equation are effectively changed from the original values to approximately one and zero respectively, implying a more perfect alignment with the diagonal of the scatter plot.

In the second step of the procedure, the FTP ratios (i.e., ratios of the FEA-predicted CLS values to the model-predicted CLS values of the corrected model, $\varepsilon_{cr,corr}$) are calculated and the mean FTP ratio, derived as the average value of all the individual FTP ratios, is set to a value above one according to the desired conservativeness.

The “Goal Seek” function in Microsoft Excel is used to iteratively compute the value of the linear model intercept, I_{orig} that is required to achieve various mean FTP ratios and corresponding probabilities of underprediction (POU). The POU is a measure of the conservativeness of the corrected model and is calculated by simply dividing the number of simulations with FTP ratio > 1 by the total number of simulations. The results are presented in Table 7-4.

Table 7-4: Values of I_{orig} for correction function and corresponding POUs

Mean	I_{orig}	POU	Max. FTP Ratio	Min. FTP Ratio
YPT				
1.00	0.000560356	0.515	1.7983	0.5028
1.10	0.000122098	0.6225	2.4404	0.5240
1.20	-0.000201315	0.6775	3.3133	0.5409
1.30	-0.000441248	0.7375	4.5102	0.5541
1.40	-0.00061954	0.7675	6.1650	0.5644
1.50	-0.000751753	0.78	8.4696	0.5722
RHT				
1.00	-4.40626E-05	0.546875	1.3441	0.6816
1.10	-0.000816296	0.80625	1.5402	0.7974
1.20	-0.001439957	0.928125	1.7459	0.9008
1.30	-0.001948625	0.990625	2.0403	0.9733
1.40	-0.002364886	1.0	3.0525	1.0219
1.50	-0.002701604	1.0	5.0990	1.0650

The max. FTP ratio and min. FTP ratios in Table 7-4 are included to indicate the boundary consequences of adjusting the conservativeness of the CLS model. The results presented also allude to the higher accuracy of the RHT CLS model as high POU values are achieved without significantly compromising the boundaries of the model. Unlike the RHT model, the YPT CLS

model has a larger spread of prediction and, thus, requires a significantly greater shift of the upper boundary of the model to achieve tangible change in the conservativeness of the model.

For the original (uncorrected) models, the mean and standard deviation of the FTP ratios for YPT pipes are 1.1095 and 0.31942 respectively while the mean and standard deviation of the FTP ratios for RHT pipes are 0.99595 and 0.11172 respectively.

7.8 Discussion

The ambiguity surrounding the representation of geometric imperfections in literature is considered to be quite significant hence it is opined that more substantial imperfection data, preferably analyzed using more rigorous statistical techniques such as probabilistic assessment methodologies, are required to derive adequate safety factors for incorporating the effects of geometric imperfections in the CLS equations. The commonly-adopted geometric dimple-shaped imperfection (GDI) approach, which is commonly referred to as a “cosine dimple” and is defined by a cosine function of two (one longitudinal and one circumferential) wavelengths, is considered to be simplistic and limited in applicability and representativeness. Moreover, results of an experimental/numerical study by Kainat et al. [57–59] on the effect of circumferential deviations of the pipe diameter and thickness from nominal values on the buckling behavior of UOE-manufactured steel pipes indicate that that geometric imperfections in form of circumferential diametric variation have a negligible effect on the buckling behavior of pipes while thickness variations have a relatively considerable effect. Consequently, geometric imperfections in form of diametric undulations are not explicitly considered in this study.

The relationships observed between the various investigated parameters and the CLS, as illustrated in Figure 7-10 - Figure 7-17, lead to a cumulative inference that the material stress-strain behavior plays a pivotal role in the deformational response of pipe segments under uniform bending. The deformational response can be said to mechanically trace the stress-strain curve of the pipe material and is therefore significantly affected by even slight variations in the material curve shape. The geometric slenderness of the pipe segment (represented by the D/t ratio), as well as the internal pressure, impact directly on the bending rigidity of the pipe segment. A higher D/t ratio implies higher slenderness and lower bending rigidity whereas a lower D/t ratio

implies lower slenderness and higher bending rigidity. Also, higher internal pressure directly increases the bending stiffness of the pipe segment thereby improving the deformational response. Besides the direct ‘global’ impact of internal pressure on the bending stiffness of pipes, a less noticeable, but crucial, effect of increased internal pressure is the resultant increase in the wavelength, as well as extension the evolution process, of the longitudinal wrinkles such that localization is delayed, and the structure is more stable to resist bending deformation [60].

The direct consequence of the increased stiffness associated with lower D/t ratios of the pipe segment during bending deformation is a shift of the location where local wrinkle formation is triggered at a point farther along the material stress-strain curve. In other words, for lower D/t ratios, significant plastification of the pipe wall occurs before local buckling. At intermediate-to-high D/t ratios (DT2 to DT4) and zero-to-moderate internal pressures (f_{p20} to f_{p60}), for YPT pipes, the herein-called ‘trigger point’ is coincident with the yield plateau of the material as the pipe is unable to mobilize any additional strength to withstand the yielding of the wrinkle, which is triggered by the abrupt zeroing of the slope of the stress-strain curve at the instance of the yield point. Contrastingly, at a low D/t ratio (DT1) and high internal pressure ($f_p = 0.8$), the YPT pipe has sufficient stiffness to withstand the initial yielding of the at the yield plateau of the material stress-strain curve, and subsequently mobilizes additional strength and corresponding increase in deformational capacity such that wrinkle formation is delayed until the strain-hardening portion beyond the yield plateau of the material stress-strain curve is reached.

The plots in Figure 7-10 and Figure 7-11 indicate that an increase in a pipe’s D/t ratio negatively affects the deformational capacity of the pipe under bending. The relationship between the D/t ratio and the CLS is also significantly nonlinear for both YPT pipes and RHT pipes and the CLS vs. D/t ratio trends exhibit a progressive increase in slope, from negative to zero, as the D/t ratio increases. This implies that the detrimental effect of a higher pipe wall slenderness on the CLS diminishes at higher D/t ratios. The nonlinearity of the slope of the CLS vs. D/t ratio trends is also observed to increase progressively as the internal pressure is increased; the only exemption being the CLS vs. D/t ratio relationship of YPT pipes under high internal pressure ($f_p = 0.8$) which is characterized by an almost-linear trend.

The plots of the CLS vs. f_p relationship in Figure 7-12 and Figure 7-13 are somewhat interrelated with the CLS vs. D/t trend plots in Figure 7-10 and Figure 7-11. However, contrary to the CLS

vs. D/t trend, the CLS vs. f_p trends indicate a positive nonlinear relationship and a progressive increase in slope, from negative to zero, as the internal pressure decreases. This implies that, at lower pressures, there is no significant gain in CLS due to increase in internal pressure. In RHT pipes, the change in slope of the CLS vs. f_p trends is observed to be gradual over the entire range of internal pressure variation while the slope of the CLS vs. f_p trends for YPT pipes is characterized by an abrupt change between $f_p = 0.6$ and $f_p = 0.8$. In both YPT pipes and RHT pipes, the nonlinear trend in the slope of the CLS vs. f_p relationship diminishes at a low D/t ratio (DT1).

Plots of the influence of the material grade of YPT pipes on the CLS, presented in Figure 7-14, indicate a direct linear relationship between the CLS and the yield stress (σ_{ys}), which is distinctively derived as the value of the stress that coincides with the yield plateau of the pipe material. The slopes of the individual CLS vs. σ_{ys} trends are observed to progressively decrease, from positive to negative, as the internal pressure is increased even though, as earlier mentioned, the observed change in slopes is virtually nonexistent in pipes with higher D/t ratios (DT2, DT3, and DT4). The near-perfect alignment of the various CLS vs. PLUS ratio plots along a similar trend path, as shown in Figure 7-15, suggests that the yield stress has no relevance to the deformational capacity of RHT pipes as the stress-strain curve can be entirely characterized by the PLUS ratio and the strain-hardening transition (represented by the material model's shape constants) from the proportionality limit point to the ultimate point. The combination of the PLUS ratio and the shape constants better represents the pipe material's nonlinear properties compared to the Y/T ratio adopted by some of the existing CLS prediction models [35,36]. Increase in the PLUS ratio is observed to be detrimental to the deformational capacity of RHT pipes, as indicated by the negative nonlinear trend in Figure 7-15. The CLS vs. PLUS ratio trend also exhibits a progressive decrease in slope, from positive to zero, as the PLUS ratio decreases implying that the positive effect of a lower PL-stress (which implies 'superior strain-hardening') on the CLS diminishes at lower PLUS ratios.

The trends observed in Figure 7-16 and Figure 7-17 indicate an almost-linear relationship between the CLS and the shape factor, for both YPT pipes and RHT pipes. The shape factor has different implications for either of the material curve shapes: it is directly related to the YPL of YPT pipes and indicates the strain-hardening properties of RHT pipes. The observed variation in

the CLS vs. sh_f trends due to internal pressure, as shown in Figure 7-16, is somewhat peculiar to YPT DT1 pipes as, even though not shown here, the effect of internal pressure on the CLS vs. sh_f trends of YPT pipes diminishes at higher D/t ratios (DT2, DT3, and DT4) except at a high internal pressure ($f_p = 0.8$) wherein the slope of the CLS vs. sh_f trend at higher D/t ratios (DT2, DT3, and DT4) shows a similar trend with the slope for $f_p = 0.8$ in DT1. The positive slope indicated by the CLS vs. sh_f plots for RHT pipes in Figure 7-17 is generally unaffected by changes in the D/t ratio. However, there is a slight tendency for the slope of the CLS vs. sh_f trends to become smaller as the D/t ratio decreases and as the nominal ‘offset’ yield stress ($\sigma_{0.5}$) increases.

The more gradual trends in the CLS vs. D/t ratio plots and the CLS vs. f_p plots for RHT pipes allude to the presupposition about the cardinal role of the material curve shape on the deformational response of pipe segments under bending, as RHT pipes are characterized by a continuous stress-strain relationship void of abrupt changes in slope. The same principle of shifting the ‘trigger point’ in the stress-strain curve as the bending stiffness is increased also applies to RHT pipes; however, since the response is continuous, the deformational capacity is primarily affected by the tangential modulus of the stress-strain curve. Generally, a smaller tangential modulus tends to improve the deformational capacity of pipes; a lower PLUS ratio implies that the deformational response of a pipe proceeds earlier along a smaller tangential modulus, compared to a higher PLUS ratio, and may consequently attain higher strains before wrinkle formation and resultant collapse of the bending moment. The diminishing benefit of superior strain hardening (implying a lower PL-stress) as the ‘offset’ yield stress is increased can also be attributed to the above phenomenon, as the deformational response of the pipe has to progress farther along a higher tangential modulus of the stress-strain curve before buckling, compared to a lower yield stress. The advantageous effect of a superior strain-hardening on the CLS also tends to decline as the D/t ratio decreases and this is due to the fact that the ‘trigger points’ for different material curve shapes are likely to converge close to the ‘offset’ yield stress point along the stress-strain curve at low D/t ratios.

Except for the combination of a stiff pipe (at the lowest D/t ratio) and higher internal pressures ($f_p > 0.6$), a higher yield stress translates to a higher deformational capacity in YPT pipes. The CLS vs. σ_{ys} plots in Figure 7-14 indicate that at a low D/t ratio and highest internal pressure ($f_p =$

0.8), increase in the yield stress is associated with a slight decrease in the CLS of YPT pipes. This may be attributed to the higher tendency for buckling to be initiated before the strain-hardening portion beyond the yield plateau of the stress-strain response is reached when internal pressures are low and D/t ratios are moderate-to-high, thereby causing the deformational capacity to be mainly influenced by the yield strain of the material. The yield strain marginally increases as the material grade becomes higher hence the positive trends of the CLS vs. σ_{ys} slopes at higher D/t ratios and lower internal pressures. Conversely, a combination of significantly high internal pressure and significantly low pipe wall slenderness causes buckling to be initiated further beyond the yield plateau of the pipe material's stress-strain response. As a result, lower material grades are more likely to take advantage of the strain-hardening of the stress-strain response before the limit load is reached, compared to higher material grades which may experience a drawback in the deformational response due to the longer path of the linear elastic portion of the stress-strain curve that precedes the yield plateau and strain-hardening response. Also, Figure 7-16 indicates that at lower internal pressures, for a low- D/t ratio (DT1) YPT pipe, a longer YPL makes it less feasible for the pipe material to mobilize additional strength and deformational capacity at the strain hardening portion beyond the yield plateau of the material curve. However, as the internal pressure is increased, mobilization of additional strength becomes more feasible and a longer YPL implies that the mobilization of additional strength is farther along the stress-strain curve thereby allowing the pipe to sustain higher deformation.

7.9 Comparison of CLS Model with Existing Equations

The developed CLS models are benchmarked against two of the most-recently developed CLS prediction models; the Dorey model [28,29] and the PRCI-CRES model [36,39]. These models, outlined below, are chosen for comparison mainly because, like the equations developed in this study, the RHT vs. YPT material curve classification is considered in both models.

(1) The Dorey model (for plain pipes)

$$\varepsilon_{cr,YPT}(\%) = 40.4 * \left(\frac{1}{D/t}\right)^2 * (1 - 0.906f_p)^{-1} * \left(\frac{E}{\sigma_{ys}}\right)^{0.8} * \left[1.12 - \left(\frac{h_g}{t}\right)^{0.15}\right] \quad \text{for YPT pipes}$$

$$(7-10)$$

$$\varepsilon_{cr,RHT}(\%) = 1.0 * \left(\frac{2.9398}{D/t}\right)^{1.5921} * (1 - 0.8679f_p)^{-1} * \left(\frac{E}{\sigma_{ys}}\right)^{0.8542} * \left[1.2719 - \left(\frac{h_g}{t}\right)^{0.1501}\right] \quad \text{for RHT pipes}$$

(2) The PRCI-CRES model

$$\varepsilon_{cr,PRCI}(\%) = \min(\varepsilon_w, F_{LD} * \varepsilon_r)$$

$$F_{LD} = \begin{cases} 1 - 0.5 * (1 - 0.75\varepsilon_r^{-0.23}) * \left[1 + \tanh\left(8\frac{\varepsilon_e}{\varepsilon_r} - 8.2\right)\right] & \text{for YPT pipes} \\ 1 & \text{for RHT pipes} \end{cases}$$

$$\varepsilon_r(\%) = F_{DP} * F_{YT} * F_{GI} * F_{NF}$$

$$F_{DP} = \begin{cases} 980 * \left[0.5\left(\frac{D}{t}\right)^{-1.6} + 1.9 \times 10^{-4}\right] & \text{for } f_p < f_{pc} \\ 980 * (1.06f_p + 0.5)\left(\frac{D}{t}\right)^{-1.6} & \text{for } f_p \geq f_{pc} \end{cases} \quad (7-11)$$

$$f_{pc} = 1.8 \times 10^{-4} * \left(\frac{D}{t}\right)^{1.6}$$

$$F_{YT} = 2.7 - 2.0\xi$$

$$F_{GI} = 1.84 - 1.6\left(\frac{h_g}{t}\right)^{0.2}$$

$$F_{NF} = \begin{cases} 1.2f_n^2 + 1 & \text{for } f_p \geq 0 \\ 1 & \text{for } f_p < 0 \end{cases}$$

where h_g represents the peak-to-valley height of the initial geometric imperfection, ε_e is the value of total strain at the end of the Lüder's extension (analogous to the YPL parameter in the current model), ξ is the Y/T ratio, and f_n is the net-section stress factor (i.e., the ratio between the

longitudinal stress induced by the net-section force and pipe's yield strength). Other parameters are according to the specifications applied to the current model.

The plots in Figure 7-20(a), Figure 7-20(b) and Figure 7-20(c) show the predictions of the CLS with respect to the D/t ratio, at $f_p = 0.0, 0.4$ and 0.8 respectively, for an RHT X60 pipe while the plots in Figure 7-21(a), Figure 7-21(b) and Figure 7-21(c) show the predictions of the CLS with respect to the D/t ratio, at $f_p = 0.0, 0.4$ and 0.8 respectively, for an RHT X70 pipe. The plots in Figure 7-22(a), Figure 7-22(b) and Figure 7-22(c) show the predictions of the CLS with respect to the D/t ratio, at $f_p = 0.0, 0.4$ and 0.8 respectively, for a YPT X60 pipe while the plots in Figure 7-23(a), Figure 7-23(b) and Figure 7-23(c) show the predictions of the CLS with respect to the D/t ratio, at $f_p = 0.0, 0.4$ and 0.8 respectively, for a YPT X70 pipe.

Data points from various test results collated by Ref. [18] are superimposed onto each of the plots to illustrate the agreement between the prediction of the CLS by the different models and the experimental test results. The exact values of the material and geometric parameters are not reported but agreement between the model and the test results can be inferred from the alignment of the model-predicted values with the trends of the experimental data points. The data points in Figure 7-20(a), Figure 7-21(a), Figure 7-22(a) and Figure 7-23(a) are obtained from results of tests on unpressurized plain pipes while the data points in the remaining plots are obtained from results of tests on plain pipes subjected to various values of pressure factor, ranging from 0.69 to 0.83. Since geometric imperfections are not considered in this study, the imperfection parameters in the two existing equations are set to zero to ensure unbiased comparison of the different models. The net-section axial tensile force parameter in the PRCI-CRES model is also set to zero since the effect of axial stress is not covered in this study. Values of 441 MPa and 503 MPa are assigned to the yield stress parameter (σ_{ys} ; in the Dorey model) for the X60 pipes and the X70 pipes respectively. The Y/T parameter (ξ ; in the PRCI-CRES model) is given as 0.78 and 0.85 for the for the X60 pipes and the X70 pipes respectively, similar to the values assigned for the parametric analysis in this study. A value of 1.5 is assigned to the Lüder's strain parameter in the PRCI-CRES model (ε_e).

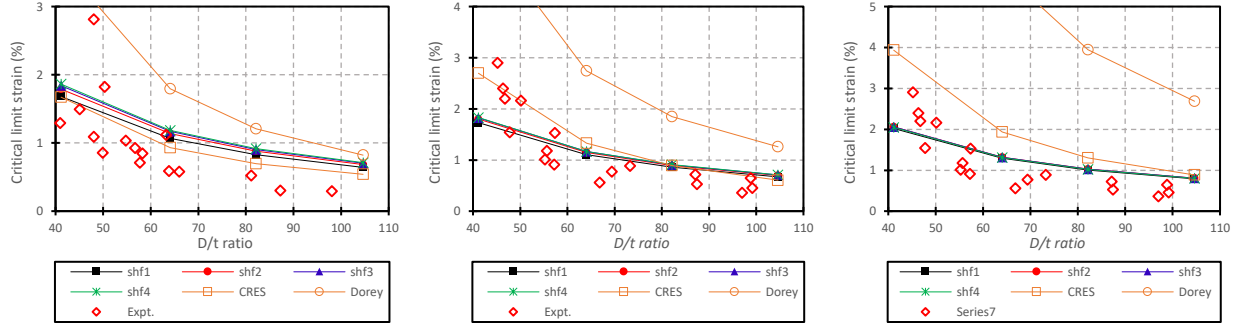


Figure 7-20: Comparison of CLS models with experimental test results for RHT X60 pipe:

(a) $f_p = 0.0$, (b) $f_p = 0.4$, and (c) $f_p = 0.8$

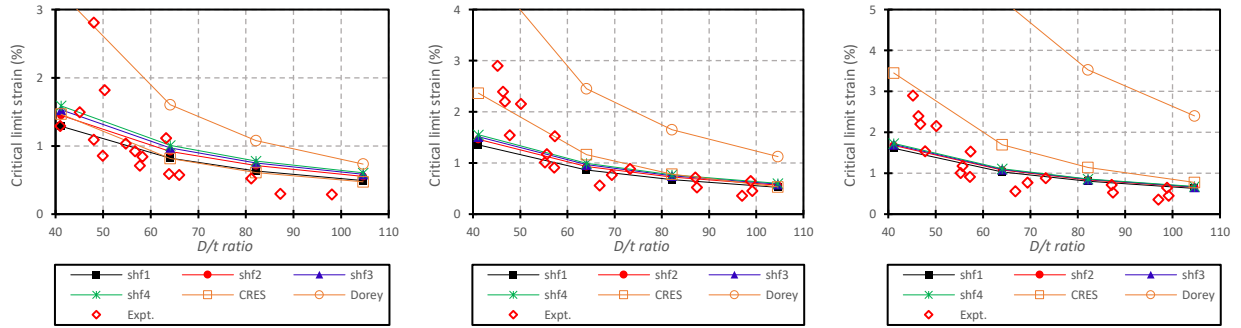


Figure 7-21: Comparison of CLS models with experimental test results for RHT X70 pipe:

(a) $f_p = 0.0$, (b) $f_p = 0.4$, and (c) $f_p = 0.8$

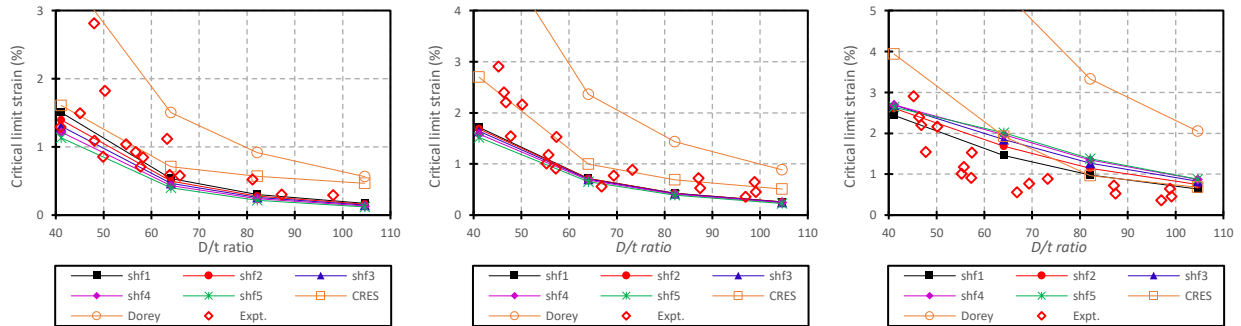


Figure 7-22: Comparison of CLS models with experimental test results for YPT X60 pipe:

(a) $f_p = 0.0$, (b) $f_p = 0.4$, and (c) $f_p = 0.8$

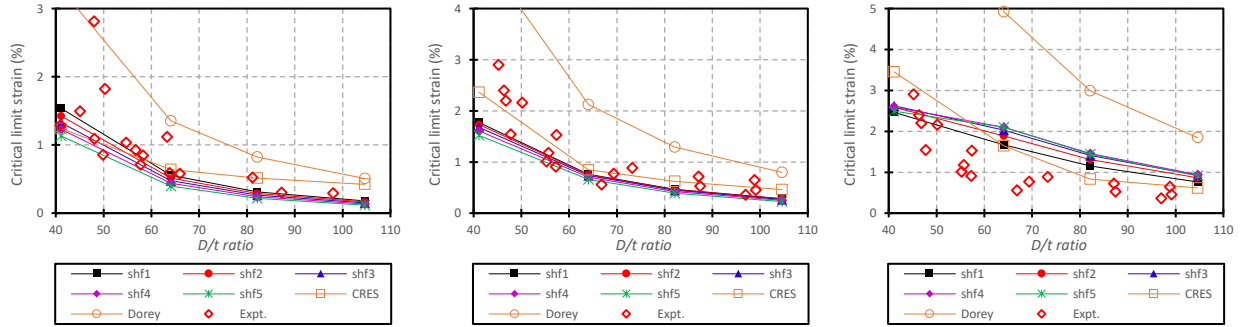


Figure 7-23: Comparison of CLS models with experimental test results for YPT X70 pipe:

(a) $f_p = 0.0$, (b) $f_p = 0.4$, and (c) $f_p = 0.8$

The plots presented in Figure 7-20 – Figure 7-23 indicate a good agreement between the current CLS model and the test results for most of the cases observed. The predictions of the current model also show considerable correspondence with the predictions of the PRCI-CRES model whereas the Dorey model is observed to overpredict the CLS in virtually all the cases. The highest value on the vertical axis of each plot is strategically truncated to improve legibility; hence, some of the high-value predictions of the Dorey model are excluded from the graphs. For RHT pipes, the current model and the PRCI-CRES model exhibit significant divergence in prediction as the D/t ratio decreases, and the divergence progresses even further as the internal pressure is increased. The assumptions made based on the RHT X70 material grade (Figure 7-21) are observed to produce a slightly better correlation with the trends of the experimental results compared with the RHT X60 material grade (Figure 7-20). Both RHT material grade assumptions, however, seem to produce lower predictions than the experimental results at median and high internal pressures ($f_p = 0.4$ and $f_p = 0.8$) and low pipe wall slenderness (D/t ratio < 55). Underprediction of experimental results at low D/t ratios is observed to be less prominent where YPT X60 and YPT X70 material grade assumptions are applied for unpressurized conditions ($f_p = 0.0$) and high internal pressure ($f_p = 0.8$). However, there exists a tendency to overpredict the experimental results at D/t ratios greater than 50 where YPT material grade assumptions are applied at high internal pressure ($f_p = 0.8$).

The observed discrepancies may be attributed to lack of fundamental information about the parametric framework of the presented experimental results; hence, consequent inaccuracy in assumptions regarding test loading conditions and material strain-hardening behavior. It has been

established in previous figures that the deformational capacity of pipes is highly sensitive to material properties, especially as the D/t decreases or the internal pressure increases; hence, more accurate deformation capacity values may be realized if the actual material properties are known and applied to the current model.

7.10 Conclusions

Extensive parametric analysis has been performed in this study, based on a significant number of numerical simulations of FE pipe models subjected to monotonically-increasing curvature. The FE pipe model used for this study were generated using the general-purpose FEA software package, ABAQUS CAE, and the pilot model was validated with reference to the results of a full-scale experiment. Excellent agreement was obtained between the moment-curvature response of the pilot pipe model and the experimental results.

The matrix of parameters was derived based on a full-factorial design of experiments concept such that each possible combination of the investigated parameters was included as a singular simulation in the analyses. Two matrices of parameters, one for each material curve shape classification (YPT and RHT), were developed to accommodate the observed material-related distinctions in the buckling response and deformational capacities. Four variations of the pipe's D/t ratio, five variations of the internal pressure, four variations of the material grade, and four (for RHT curves) or five (for YPT curves) variations of the material curve shape were specified as the test matrix for the FE simulations; hence, the adopted full-factorial design approach yielded a total of 400 simulations for YPT pipes and 320 simulations for RHT pipes.

The 'peak moment criterion' was used to derive the CLS for each simulation as the average 2D-gauge-length compressive strain corresponding to the maximum attained bending moment of the moment vs. curvature response plots extracted from the ABAQUS software program. Graphical presentations of the typical trends between each investigated parameter and the CLS were employed to visually decipher the functional relationships between the CLS and various parameters, as well as to detect any interrelationships between the individual parameters.

A semi-empirical modeling approach was subsequently adopted to develop two constitutive equations for predicting the CLS of pipe segments under uniform bending. The functional

relationships between the CLS and each parameter, determined by visual inspection of the graphical plots of CLS trends, provided needed guidance for specifying a representative mathematical expression for each individual parameter. A multiplicative approach was then applied to arithmetically combine all individual variable functions to form the constitutive equation for each material curve shape classification. Subsequently, advanced nonlinear multiple regression techniques were utilized for deriving the unknown constants for each constitutive equation, and high R^2 values (> 0.95) were obtained for each model, indicating an excellent goodness-of-fit between the model-predicted CLS and the FE-derived CLS. A statistical procedure to apply a desired level of conservativeness to the developed equations was presented afterward.

The developed equations were benchmarked against two of the most recent and most advanced existing CLS equations (the Dorey model and the PRCI-CRES model), and the current model was observed to align reasonably well with the PRCI-CRES model. A number of data points for the CLS of pipelines, obtained from previous full-scale experiments on unpressurized and pressurized pipe segments subjected to uniform bending and combined loading conditions, were superimposed onto the benchmarking plots. The current model and PRCI-CRES model were observed to give good predictions of the CLS whereas the Dorey model seemed to overpredict the CLS in virtually all the cases considered. Also, the agreement of the current model's predictions with experimental data alludes to the somewhat negligible effect of initial geometric imperfections on the CLS of pipelines within the range of D/t ratios covered in this study.

The constitutive equations developed in this study are useful for preliminary design purposes, in predicting the deformational capacity of pressurized and unpressurized onshore pipelines which are predominantly subjected to uniform bending due to significant deformation of the surrounding or supporting soil medium.

7.11 References

- [1] P.C. Jennings, Engineering features of the San Fernando earthquake of February 9, 1971, EERL 71-02, Pasadena, California, 1971. <http://resolver.caltech.edu/CaltechEERL:1971.EERL-71-02> (accessed November 13, 2018).

- [2] J. Isenberg, C.E. Taylor, Performance of Water and Sewer Lifelines in the May 2, 1983 Coalinga, California Earthquake, in: Proc. ASCE Lifeline Earthq. Eng. Performance, Des. Constr., San Francisco, California, USA, 1984: pp. 176–189.
- [3] T. Iwasaki, Soil liquefaction studies in Japan: state-of-the-art, Soil Dyn. Earthq. Eng. 5 (1986) 2–68. doi:10.1016/0267-7261(86)90024-2.
- [4] G.M. Lee, S.M. Mejia, The Effects of the 1985 Mexico City Earthquake on Underground Water and Sewer Pipelines, in: Proc. ASCE Lifeline Seism. Risk Anal. – Case Stud., Seattle, Washington, USA, 1986: pp. 131–136.
- [5] N. Yoosef-Ghodsi, G.L. Kulak, D.W. Murray, Some test results for wrinkling of girth-welded line pipe, in: Proc. 14th Int. Conf. Offshore Mech. Arct. Eng. Vol. 5, ASME, Copenhagen, Denmark, 1995: pp. 379–387.
- [6] K.R. Jayadevan, E. Ostby, C. Thaulow, Strain-based fracture mechanics analysis of pipelines, in: Proc. Int. Conf. Adv. Struct. Integr., 2004: pp. 04–0198.
- [7] Y. Zhang, S. Das, Failure of X52 Wrinkled Pipelines Subjected to Monotonic Axial Deformation, J. Press. Vessel Technol. 130 (2008) 021702. doi:10.1115/1.2894294.
- [8] M.E. Mohareb, A.E. Elwi, G.L. Kulak, D.W. Murray, Deformation Behavior of Line Pipe, Structural Engineering Report No. 202, Edmonton, Alberta, 1994.
- [9] N. Yoosef-Ghodsi, G.L. Kulak, D.W. Murray, Behavior of Girth-welded Line Pipe, Structural Engineering Report No. 203, Edmonton, Alberta, 1994.
- [10] Z. Zhou, D.W. Murray, Analysis of postbuckling behavior of line pipe subjected to combined loads, Int. J. Solids Struct. 32 (1995) 3015–3036. doi:10.1016/0020-7683(94)00261-T.
- [11] T.J.E. Zimmerman, M.J. Stephens, D.D. DeGeer, Q. Chen, Compressive strain limits for buried pipelines, in: Proc. 14th Int. Conf. Offshore Mech. Arct. Eng. Vol. 5, ASME, Copenhagen, Denmark, 1995.
- [12] J.P. Lee, J.A. Bohinsky, Design of buried pipeline subjected to large fault movement, in: Proc. 11th World Conf. Earthq. Eng., Acapulco, Mexico, 1996: pp. 23–28.
- [13] D.W. Murray, Local buckling, strain localization, wrinkling and postbuckling response of line pipe, Eng. Struct. 19 (1997) 360–371. doi:10.1016/S0141-0296(96)00096-X.
- [14] L. Vitali, R. Bruschi, K.J. Mork, E. Levold, R. Verley, Hotpipe Project: Capacity of Pipes Subject to Internal Pressure, Axial Force And Bending Moment, in: Ninth Int. Offshore Polar

- Eng. Conf., International Society of Offshore and Polar Engineers, Brest, France , 1999: pp. 22–33. <https://www.onepetro.org/conference-paper/ISOPE-I-99-123> (accessed October 29, 2018).
- [15] B.D. Reddy, An experimental study of the plastic buckling of circular cylinders in pure bending, *Int. J. Solids Struct.* 15 (1979) 669–683. doi:10.1016/0020-7683(79)90066-0.
- [16] C.E. Murphey, C.G. Langner, Ultimate pipe strength under bending, collapse and fatigue, in: *Proc. 4th Int. Conf. Offshore Mech. Arct. Eng.*, 1985: pp. 467–477.
- [17] H.G.L. Prion, P.C. Birkemoe, Beam-Column Behavior of Fabricated Steel Tubular Members, *J. Struct. Eng.* 118 (1992) 1213–1232. doi:10.1061/(ASCE)0733-9445(1992)118:5(1213).
- [18] N. Yoosef-Ghodsi, I. Ozkan, Q. Chen, Comparison of Compressive Strain Limit Equations, in: *Vol. 4 Prod. Pipelines Flowlines; Proj. Manag. Facil. Integr. Manag. Oper. Maintenance; Pipelining North. Offshore Environ. Strain-Based Des. Stand. Regul.*, ASME, 2014: p. V004T11A001. doi:10.1115/IPC2014-33182.
- [19] J.G. Bouwkamp, R.M. Stephen, Full-scale studies on the structural behavior of large diameter pipes under combined loading. Report No. UCSESM 74-1, Berkeley, California, 1974.
- [20] D.R. Sherman, Test of Circular Steel Tubes in Bending, *J. Struct. Div.* 102 (1976) 2181–2195. <http://cedb.asce.org/CEDBsearch/record.jsp?dockey=0007059> (accessed October 29, 2018).
- [21] A.M. Gresnigt, Plastic Design of Buried Steel Pipelines in Settlement Areas, *Heron*. 31 (1986).
- [22] P.F. Lara, Revisiting the failure criteria of buried pipelines, in: *ASME Pipeline Eng. Symp.*, Dallas, Texas, 1987: pp. 143–145.
- [23] Zhou Z., Murray D. W., Numeric Structural Analysis of Buried Pipelines, *Structural Engineering Report No. 181*, Edmonton, Alberta, Canada, 1993.
- [24] Z. Zhou, D.W. Murray, Towards rational deformation limit states for buried pipelines, in: *Third Int. Offshore Polar Eng. Conf.*, Singapore, 1993: pp. 18–24.
- [25] N. Nazemi, Behavior of X60 Line Pipe under Combined Axial and Transverse Loads with Internal Pressure, University of Windsor, 2009.
- [26] A.M. Gresnigt, S.A. Karamanos, Local Buckling Strength And Deformation Capacity of Pipes, in: *Ninet. Int. Offshore Polar Eng. Conf.*, International Society of Offshore and Polar

Engineers, Osaka, Japan, 2009: pp. 212–224. <https://www.onepetro.org/conference-paper/ISOPE-I-09-002> (accessed October 29, 2018).

[27] P.R. DelCol, G.Y. Grondin, J.J.R. Cheng, D.W. Murray, Behavior of Large Diameter Line Pipe Under Combined Loads, Structural Engineering Report No. 224, Edmonton, AB, Canada, 1998.

[28] A.B. Dorey, J.J.R. Cheng, D.W. Murray, Critical Buckling Strains for Energy Pipelines, Structural Engineering Report No. 237, Edmonton, Alberta, 2001.

[29] A.B. Dorey, D.W. Murray, J.J.R. Cheng, Critical Buckling Strain Equations for Energy Pipelines—A Parametric Study, *J. Offshore Mech. Arct. Eng.* 128 (2006) 248. doi:10.1115/1.2199561.

[30] A.B. Dorey, D.W. Murray, J.J.R. Cheng, G.Y. Grondin, Z.J. Zhou, Testing and experimental results for NPS30 line pipe under combined loads, in: Proc. 18th Int. Conf. Offshore Mech. Arct. Eng., ASME, St. Johns, Newfoundland, 1999: p. OMAE PL 99-5022.

[31] Canadian Standards Association, Oil and gas pipeline systems. CSA-Z662-2007, (2007).

[32] M.J. Stephens, R.T. Petersen, Y.-Y. Wang, D. Horsley, An Experimental Basis For Improved Strain-based Design Models, in: Ninet. Int. Offshore Polar Eng. Conf., International Society of Offshore and Polar Engineers (ISOPE), Osaka, Japan, 2009: pp. 29–35. <https://www.onepetro.org/conference-paper/ISOPE-I-09-493> (accessed November 13, 2018).

[33] M. Stephens, R. Petersen, Y.-Y. Wang, R. Gordon, D. Horsley, Large Scale Experimental Data for Improved Strain-Based Design Models, in: 2010 8th Int. Pipeline Conf. Vol. 4, ASME, 2010: pp. 195–203. doi:10.1115/IPC2010-31396.

[34] W. Ramberg, W.R. Osgood, Description of stress-strain curves by three parameters, NACA Technical Note No. 902, Washinton, D.C., 1943. <https://ntrs.nasa.gov/search.jsp?R=19930081614> (accessed May 7, 2018).

[35] Det Norske Veritas, Submarine pipeline systems - DNV-OS-F101, DNV, Oslo, Norway, 2010.

[36] M. Liu, Y.-Y. Wang, F. Zhang, K. Kotian, Realistic strain capacity models for pipeline construction and maintenance. prepared for US department of transportation. Pipeline and Hazardous Materials Safety Administration, Office of Pipeline Safety. Contract No. DTPH56-

10-T-000016, Dublin, OH, USA, 2013. <https://trid.trb.org/view/1471401> (accessed September 4, 2018).

[37] S. Neupane, S. Adeeb, R. Cheng, J. Ferguson, M. Martens, Modeling the Deformation Response of High Strength Steel Pipelines—Part I: Material Characterization to Model the Plastic Anisotropy, *J. Appl. Mech.* 79 (2012) 051002. doi:10.1115/1.4006380.

[38] S. Neupane, S. Adeeb, R. Cheng, J. Ferguson, M. Martens, Modeling the Deformation Response of High Strength Steel Pipelines—Part II: Effects of Material Characterization on the Deformation Response of Pipes, *J. Appl. Mech.* 79 (2012) 051003. doi:10.1115/1.4006381.

[39] M. Liu, F. Zhang, K. Kotian, S. Nanney, Refined Modeling Processes and Compressive Strain Capacity Models, in: Vol. 4 Prod. Pipelines Flowlines; Proj. Manag. Facil. Integr. Manag. Oper. Maintenance; Pipelining North. Offshore Environ. Strain-Based Des. Stand. Regul., ASME, 2014: p. V004T11A002. doi:10.1115/IPC2014-33202.

[40] C.D. Babcock, Experiments in shell buckling, in: Y.C. Fung, E.E. Sechler (Eds.), *Thin-Shell Struct. Theory, Exp. Des.*, Prentice-Hall, Englewood Cliffs, NJ, 1974: pp. 345–369.

[41] S.M. Fatemi, H. Showkati, M. Maali, Experiments on imperfect cylindrical shells under uniform external pressure, *Thin-Walled Struct.* 65 (2013) 14–25. doi:10.1016/j.tws.2013.01.004.

[42] C.M.J. Timms, D.D. DeGeer, M.R. Chebaro, Y. Tsuru, Compressive Strain Limits of Large Diameter X80 UOE Linepipe, in: *Ninet. Int. Offshore Polar Eng. Conf.*, International Society of Offshore and Polar Engineers, Osaka, Japan, 2009. <https://www.onepetro.org/conference-paper/ISOPE-I-09-332> (accessed September 4, 2018).

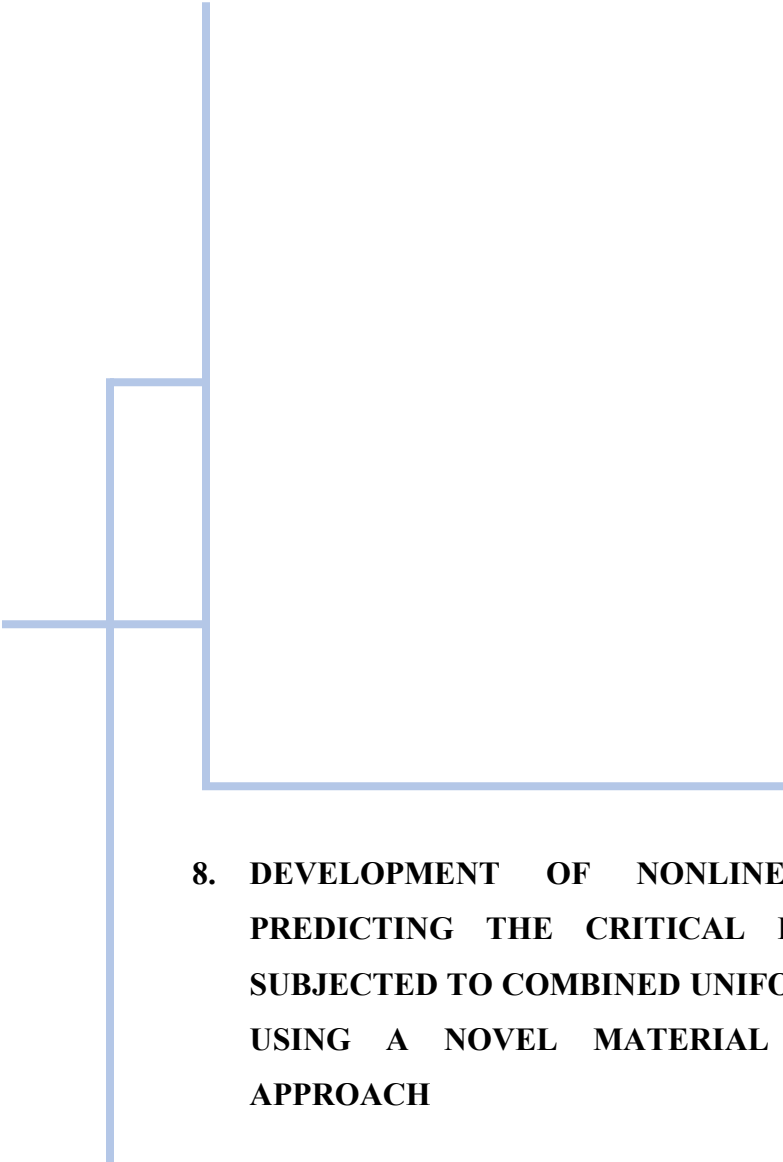
[43] D. DeGeer, C. Timms, J. Wolodko, M. Yarmuch, R. Preston, D. MacKinnon, Local Buckling Assessments for the Medgaz Pipeline, in: Vol. 3 Pipeline Riser Technol. CFD VIV, ASME, 2007: pp. 453–463. doi:10.1115/OMAE2007-29493.

[44] M. Dundu, Evolution of stress-strain models of stainless steel in structural engineering applications, *Constr. Build. Mater.* 165 (2018) 413–423. doi:10.1016/J.CONBUILDMAT.2018.01.008.

[45] E. Mirambell, E. Real, On the calculation of deflections in structural stainless steel beams: an experimental and numerical investigation, *J. Constr. Steel Res.* 54 (2000) 109–133. doi:10.1016/S0143-974X(99)00051-6.

- [46] K.J.R. Rasmussen, Full-range stress-strain curves for stainless steel alloys, *J. Constr. Steel Res.* 59 (2003) 47–61. doi:10.1016/S0143-974X(02)00018-4.
- [47] L. Gardner, D.A. Nethercot, Experiments on stainless steel hollow sections—Part 1: Material and cross-sectional behaviour, *J. Constr. Steel Res.* 60 (2004) 1291–1318. doi:10.1016/J.JCSR.2003.11.006.
- [48] L. Gardner, M. Ashraf, Structural design for non-linear metallic materials, *Eng. Struct.* 28 (2006) 926–934. doi:10.1016/J.ENGSTRUCT.2005.11.001.
- [49] O. Ndubuaku, M. Martens, R. Cheng, A. Ahmed, S. Adeeb, A Novel Approach for True Stress-True Strain Material Characterization of Metallic Materials Using the Product-Log (Omega) Function, in: 6th Int. Conf. Eng. Mech. Mater., CSCE, May 31 - June 3, Vancouver, B.C., Canada, 2017.
- [50] O. Ndubuaku, M. Martens, J.J.R. Cheng, S. Adeeb, Expression of a Generic Full-Range True Stress-True Strain Model for Pipeline Steels Using the Product-Log (Omega) Function, in: Vol. 6B Mater. Fabr., ASME, 2017: p. V06BT06A050. doi:10.1115/PVP2017-65236.
- [51] O. Ndubuaku, X. Liu, M. Martens, J.J. Roger Cheng, S. Adeeb, The effect of material stress-strain characteristics on the ultimate stress and critical buckling strain of flat plates subjected to uniform axial compression, *Constr. Build. Mater.* 182 (2018) 346–359. doi:10.1016/j.conbuildmat.2018.06.100.
- [52] D. Hibbitt, B. Karlsson, P. Sorensen, ABAQUS Standard User's and Reference Manuals, Version 6.14, (2014).
- [53] American Petroleum Institute, API 5L: Specification for Line Pipe, 44th ed., American Petroleum Institute, USA, 2007.
- [54] M. Mohareb, G.L. Kulak, A. Elwi, D.W. Murray, Testing and Analysis of Steel Pipe Segments, *J. Transp. Eng.* 127 (2001) 408–417. doi:10.1061/(ASCE)0733-947X(2001)127:5(408).
- [55] X. Liu, H. Zhang, Y. Han, M. Xia, W. Zheng, A semi-empirical model for peak strain prediction of buried X80 steel pipelines under compression and bending at strike-slip fault crossings, *J. Nat. Gas Sci. Eng.* 32 (2016) 465–475. doi:10.1016/J.JNGSE.2016.04.054.
- [56] Wolfram Research Inc., Mathematica, Version 11.3, Champaign, IL, 2018.

- [57] M. Kainat, S. Adeeb, J.J.R. Cheng, J. Ferguson, M. Martens, Measurement of Initial Imperfection of Energy Pipelines Using 3D Laser Scanner, in: 3rd Int. Struct. Spec. Conf., CSCE, Edmonton, AB, Canada., 2012.
- [58] M. Kainat, S. Adeeb, J.J.R. Cheng, J. Ferguson, M. Martens, Identifying Initial Imperfection Patterns of Energy Pipes Using a 3D Laser Scanner, in: 2012 9th Int. Pipeline Conf., ASME, 2012: pp. 57–63. doi:10.1115/IPC2012-90201.
- [59] M. Kainat, M. Lin, J.J.R. Cheng, M. Martens, S. Adeeb, Effects of the Initial Geometric Imperfections on the Buckling Behavior of High-Strength UOE Manufactured Steel Pipes, J. Press. Vessel Technol. Trans. ASME. 138 (2016) 051206. doi:10.1115/1.4032990.
- [60] A. Limam, L.-H. Lee, E. Corona, S. Kyriakides, Inelastic wrinkling and collapse of tubes under combined bending and internal pressure, Int. J. Mech. Sci. 52 (2010) 637–647. doi:10.1016/J.IJMECSCI.2009.06.008.



8. DEVELOPMENT OF NONLINEAR REGRESSION EQUATIONS FOR PREDICTING THE CRITICAL LIMIT STRAIN OF STEEL PIPELINES SUBJECTED TO COMBINED UNIFORM AXIAL COMPRESSION AND BENDING USING A NOVEL MATERIAL CURVE SHAPE PARAMETERIZATION APPROACH

This chapter is derived from a research article submitted for publication in the Elsevier International Journal of Solids and Structures.

8.1 Abstract

The pipe wall slenderness properties of onshore pipelines typically fall within the range of D/t ratios wherein the pipe segment is likely to undergo inelastic (or plastic) buckling on the side of the cross-section that experiences the highest compressive longitudinal strain. Accurate prediction of the bifurcation instabilities and collapse mechanisms in the plastic range, therefore, requires the implementation of appropriate asymptotic post-buckling theories that are able to predict the nonlinear load-deflection path associated with the material stress-strain relationship. The mechanical behavior of unpressurized and pressurized steel pipes is analyzed in this study using finite-element simulation methodology, with the purpose of estimating their deformational capacity against local buckling. Numerical pipe models are developed and subjected to a net-section compressive axial force followed by induced curvature, and the incremental average strains over a 2D gauge length are reported. The average value of strain corresponding to the highest attained resultant bending moment is taken as the critical limit strain for each simulation. Pipe models with D/t ratios ranging from 41 to 105, as commonly used for onshore pipeline applications, are subjected to internal pressures ranging from zero to 80% of the nominal yield pressure as well as uniform compressive stresses ranging from 20 to 80% of the maximum attainable compressive axial limit stress. Four material grades are defined and classified according to material curve shapes, which are varied for each material grade and parameterized using the shape constants of the 'Ndubuaku' material model. A full-factorial design is adopted to perform extensive parametric analyses yielding a total of 1280 and 1600 simulations for each of the two material curve shape classifications. Two nonlinear equations are defined based on the observed functional relationships between individual parameters and the critical limit strain, and advanced regression techniques are used to obtain the regression coefficients for each of the developed equations. Excellent predictive accuracy is obtained for the developed nonlinear regression equations.

Nomenclature

ε	true strain
ε_{cr}	critical limit strain
ε_{pl}	corresponding strain at proportionality limit stress of Ndubuaku model
ε_R	Ndubuaku model strain ratio
ε_{up}	corresponding strain at ultimate proof stress of Ndubuaku stress-strain model
E	Young's modulus of elasticity
f_c	compression factor (ratio of applied compressive stress to pipe's limit stress)
f_p	pressure factor (ratio of applied pressure to pipe yield pressure)
h	Ndubuaku model heel constant
k	Ndubuaku model knee constant
μ	Poisson's ratio
n	Ramberg-Osgood strain-hardening exponent
OD	pipe's outer diameter
p	applied internal pressure
p_y	pipe's circumferential yield pressure
r	pipe's cross-sectional radius
$\sigma_{0.5}$	0.5% total strain proof stress
σ	true stress
σ_c	applied compressive stress
σ_l	pipe's maximum compressive stress capacity (limit stress)
σ_{pl}	proportionality limit stress of Ndubuaku stress-strain model
σ_R	Ndubuaku model stress ratio
σ_{up}	ultimate proof stress of Ndubuaku stress-strain model
σ_{us}	ultimate tensile stress of pipe material
σ_{ys}	yield stress of pipe material
sh_f	material curve shape factor

t	pipe's wall thickness
CLS	Critical limit strain
D/t ratio	Ratio of pipe's outer diameter to pipe's wall thickness
$PLUS$ ratio	Ratio of proportionality limit stress to ultimate tensile stress
RHT	Round-house type
SBD	Strain-based design
UTS	Ultimate tensile stress
YPL	Yield plateau length
YPT	Yield-plateau type
YS	Nominal yield stress
Y/T ratio	Ratio of yield stress to ultimate tensile stress

8.2 Introduction

Pipelines are generally regarded as an efficient means for transporting water, hydrocarbons, and several other fluids over considerable distances, and across various onshore or offshore environments. The main considerations for the design of onshore pipelines typically focus on (1) limiting the internal pressure below a recommended fraction of the circumferential yield pressure to prevent loss of containment, and (2) limiting the axial stress caused by temperature differentials of the fluids being transported by the pipeline below the yield stress of the pipe material [1]. On the other hand, offshore pipelines are susceptible to propagating collapse caused by ambient hydrostatic pressure. Propagating collapse, which is essentially a buckling instability phenomenon, is triggered in the pipeline once the 'collapse pressure' is reached, followed by flattening of the pipe cross-section that extends progressively in the longitudinal direction of the pipeline at a pressure (referred to as 'propagation pressure') which is usually about 15-20% of the 'collapse pressure' [2]. Results of parametric studies indicate that the 'collapse pressure' is highly sensitive to initial geometric imperfections, particularly initial ovality, and is more likely to occur during periods of significant external overpressure such as during installation or shutdowns for maintenance [3–5].

Inevitably, limit states design of onshore and offshore pipelines must complement the traditional allowable stress design approach, which focuses on resultant or applied stresses, with adequate considerations of the deformational capacity of pipelines, especially in regions susceptible to significant deformation of the supporting medium or soil. Ground deformation tends to be more prevalent in onshore pipelines but may also present as seabed instabilities in offshore pipelines, and is typically caused by disastrous environmental scenarios such as landslides, slope failures, ground subsidence, soil liquefaction, seismic-related fault movements, frost heave, and thaw settlements, etc. [6,7]. Excessive deformation of pipelines due to surrounding (or supporting) ground movement may have serviceability limit state and ultimate limit state implications — excessive bending results in constriction of the cross-section of the pipe which hinders the passage of pigging devices used for monitoring of the pipeline. Flow assurance is also compromised due to constriction of flow caused by reduction of the area of the pipe's cross-section. Ultimate limits may also be exceeded resulting in rupture of the pipe wall due to excessive tensile strains in the locally buckled regions of the pipe where wrinkles or bulges have developed.

Below a D/t ratio of 100, the bifurcation instability characteristics and overall buckling response of cylindrical shells under pure bending are primarily governed by interaction between the induced ovalization and the nonlinear strain-hardening properties of the material stress-strain relationship [8]. Ades [9] assumed that the cross-section of a thick-walled cylinder under bending undergoes uniform ovalization and transforms into an elliptical shape, and applied the J_2 deformation theory of plasticity to account for the effect of the nonlinear material behavior on the moment-curvature response. Tugcu and Schroeder [10] assumed a linear strain-hardening material model using the J_2 deformation theory of plasticity and adopted the elliptical cross-sectional deformation concept put forward by Ref [9]. The results obtained by Ref [10] for the moment-curvature response were observed to be consistently higher than experimental values. Gellin [11] sought to improve the accuracy of the numerical solutions by Ref [9] using a set of improved kinematic relations originated from thin shell theory presented by Sanders [12]. The results obtained for bifurcation instability were generally observed to differ from the results obtained for the limit load instability, and the disparity was more pronounced in the case of the critical curvature than for the critical moment. Kyriakides and Shaw [13] performed

experimental and analytical investigation of the response and stability of circular cylindrical shells under combined bending and external pressure. A refinement of the analytical formulation and numerical solution procedure presented by Ref [11] was obtained using the deformation theory of plasticity with the Ramberg–Osgood nonlinear material model to characterize the inelastic material behavior. Ju and Kyriakides [8] analyzed the bifurcation instability of long initially-straight aluminum cylinders bent into the plastic range. Analytical formulations were derived using Sander’s shell kinematics and following the principle of virtual work while the discretization and numerical solution of the instability problem were achieved using a Rayleigh-Ritz procedure and Newton’s iteration method respectively. The inelastic material behavior was characterized through the J_2 flow theory of plasticity with isotropic hardening based on the Ramberg-Osgood nonlinear material model while bifurcation buckling calculations were carried out using the J_2 deformation theory of plasticity. Corona et al. [14] examined the results obtained by Ref [8] and observed that the predicted bifurcation curvature was consistent with experimental values whereas the predicted wrinkle wavelengths were generally longer than the experimental measurements. To correct the observed discrepancies, the anisotropy material properties of the cylinder specimens were measured and incorporated in the flow theory of plasticity for the pre-buckling calculations. Anisotropy was then accounted for in the bifurcation buckling evaluation by deformation theory of plasticity compatible with Hill’s quadratic anisotropic yield function, and better correspondence with the experimental results was achieved for the bifurcation curvature and the wrinkle wavelength.

Weingarten [15] employed an analytical procedure to determine the moment at which significant deformations begin to appear in a pressurized cylinder and revealed that the critical bending stress is slightly higher, depending on the D/t ratio, than the values obtained for unpressurized cylinders. A few experimental campaigns have extended the research on the inelastic buckling response of cylinders beyond the domain of cylindrical shells under pure bending towards investigating and characterizing the buckling response of pipe segments under combined pressure and flexure. Based on results of a series of experimental tests Suer et al. [16] concluded that, provided the pretension stress due to internal pressure is balanced by a compressive axial stress, the critical bending stress for pressurized metal cylinders under bending is equal to the classical critical buckling stress (independently identified by Lorenz [17], Timoshenko [18], and

Southwell [19]) under uniform axial compression. Gresnigt et al. [20] performed a series of tests on X42 steel pipe specimens with D/t ratio of 100 and demonstrated that internal pressurization significantly increases the deformational capacity of pipelines. Suzuki et al. [21] conducted large-scale experimental tests, as well as numerical simulations, on internally-pressurized NPS-30 pipes made of API-X80 grade line pipe steel with D/t ratio of 49 and observed that the ratio of the limit moment curvature of the pipes to the curvature at the onset of wrinkling is increased due to internal pressure. Limam et al. [5,22] systematically conducted a combination of small-scale experimental tests and numerical analyses to investigate the inelastic mechanical response of 1¹/₂-inch-diameter stainless-steel seamless pipes with D/t ratio of 52 subjected to internal pressures ranging between 0% and 75% of the yield pressure and bent until failure. A finite element (FE) shell model was developed for the numerical analysis to track the development and evolution of longitudinal wrinkles up to collapse, and a custom bifurcation buckling analysis was initially performed such that the bifurcation solution wavelength was introduced as initial geometric imperfections in the FE shell models. An inward kink was reported as the mode of deformation at collapse for unpressurized pipelines whereas the mode of deformation at collapse was characterized by an outward bulge for pressurized pipelines. In correspondence with the findings of Ref [21], the ability of the pipe specimens to sustain the induced bending curvature before collapse was observed to progressively increase as the internal pressure levels were increased. Ref [5] explained that internal pressure tends to counteract the resultant ovalization due to the induced curvature, thereby increasing the wavelength of the longitudinal wrinkles and stabilizing the structure so that the bending response is characterized by a significantly higher pipe curvature compared to unpressurized pipes. It was also pointed out that the ‘higher-deformability’ advantage that is derived from internal pressurization is only realizable if the pipe’s material exhibits considerable ductility and initial geometric imperfections are sufficiently small.

Numerous large-scale experiments [23–26] have been conducted at the University of Alberta, Canada (UofA) on steel pipelines of various sizes and material properties. Dorey et al. [27] developed a 3D FE pipe model, validated using the experimental data for the specimens in the UofA database, and performed extensive parametric analyses to produce a set of nonlinear semi-empirical equations for predicting the critical limit strain (CLS) of pressurized and unpressurized

pipe segments subjected to uniformly-induced curvature. Liu et al. [28] conducted extensive parametric numerical analyses using experimentally-validated FE pipe models constructed with three-dimensional solid elements, and employed nonlinear multiple regression techniques to develop a set of equations for predicting the CLS in pipe segments subjected to combined internal pressure, net-section tensile stress and displacement-controlled bending moment.

The buckling instability phenomenon in cylindrical shells essentially presents as a multivariate problem in which diverse constitutive parameters are sometimes nonlinearly related to the buckling response, and also tend to exhibit complex nonlinear interrelationships. It is therefore largely infeasible for purely-theoretical design expressions to be derived from first principles based on the laws of fundamental mechanics [27]. The development and steady expansion of the capabilities of computerized applications, however, make it feasible for experimentally-validated numerical simulations to be extensively conducted in order to empirically derive suitable equations for predicting the mechanical behavior of cylindrical shells subjected to various loading conditions and load combinations. Several numerical studies [6,28–34], performed using various FE-based codes embedded in standard structural computer programs, have established that finite element analysis (FEA) can be relied upon for robust and accurate representation and simulation of the buckling response of real cylinders under various loading.

Agreement between FEA-derived CLS values and experimental data has been observed to be strongly dependent on very accurate representation of the material inelastic properties defined by the shape of the material stress-strain curve [5,35,36]. Dorey et al. [35] examined the sensitivity of the deformational response to the material grade and the general shape of the material stress-strain curve of numerically-simulated pipes. Experimental data indicated a bilateral distinction between the material stress-strain curves according to the material curve shape hence two material curve shape classifications were presented; one classification (herein referred to as “round-house type” or “RHT” curves) for specimens with a “smooth” strain-hardening transition from the proportionality limit stress to the ultimate stress and the second classification (herein referred to as “yield-plateau type” or “YPT” curves) for specimens with a distinct yield point and an extended yield plateau. Material curve shape classification showed a minimal effect on the global moment capacity whereas the deformational performance was strongly influenced by the

material curve shape. Interestingly, increase in the proportionality limit stress was observed to decrease the deformational capacity of the pipe models and vice versa.

The Ramberg-Osgood expression [37], the most widely-adopted material stress-strain characterization model till date, has been observed to lose accuracy beyond a limited range of strains [38]. Various modifications of the Ramberg-Osgood model have been proposed by numerous researchers [39–47] to improve the accuracy of stress-strain characterization over a larger range of strains. However, the improved models are characterized by a common drawback; they are conceptually derived as multi-stage or piecewise partitions of the stress-strain curve thereby undermining the inherent simplicity of the original Ramberg-Osgood model. A unique mathematical formulation has been developed by Ndubuaku et al. [48–50] which has proven to be a simple and robust tool for accurate approximation of the stress-strain relationship for various metallic materials, regardless of the material curves shape classification. The ‘Ndubuaku’ stress-strain model makes it easy for the overall shape of the stress-strain curve to be parameterized using two constitutive model constants, referred to as ‘shape constants’.

Review of literature reveals that none of the existing CLS prediction models explicitly considers the effect of net-section compressive axial stress on the deformational capacity of pipe segments under uniform bending. Hence, the buckling behavior, particularly the deformational capacity, of pipe segments subjected to combined axial compression and induced curvature is investigated in this study. Representation of geometric and material properties, as well as simulation of loading/boundary conditions and resultant stresses/deformations, is achieved using a series of 3D FE shell models created using the general-purpose finite element software package, ABAQUS CAE [51]. Extensive parametric analysis is performed based on a full-factorial design of simulations such that every possible combination of the relevant parameters is modeled and reported. Five parameters are investigated, including: (1) the diameter-to-thickness ratio (D/t ratio), (2) the level of internal pressurization, (3) the material grade, (4) the level of uniform axial compression prior to bending, and (5) the material curve shape factor. To adequately capture any nonlinearities in the relationship between the CLS and respective parameters, a minimum of four variations are applied to each parameter thus: four variations of the D/t ratio, five variations of the pressure factor, four variations of the material grade, four variations (for RHT curves) or five variations (for YPT curves) of the material curve shape factor, and four variations of the

compression factor. Consequently, based on the full-factorial design adopted for the analyses, a total of 1280 simulations (for RHT pipes) plus 1600 simulations (for YPT pipes) are performed in this study. Finally, nonlinear multiple regression is performed to derive the regression coefficients of two expressions, one for each material curve shape classification, for predicting the critical limit strain of pipes subjected to combined axial compression and bending.

8.3 Material Curve Shape Characterization

The ‘Ndubuaku’ material model establishes the characteristic nonlinear relationship between the true stress (σ) and the true strain (ε) using the following special power law expression consisting of two model constants, the “knee” constant (k_{nm}) and the “heel” constant (h_{nm}):

$$\sigma = \begin{cases} E\varepsilon & \sigma \leq \sigma_{pl} \\ \sigma_{pl} + (\sigma_{up} - \sigma_{pl}) \left(\frac{\varepsilon - \varepsilon_{pl}}{\varepsilon_{up} - \varepsilon_{pl}} \right)^{k_{nm}} \left(\frac{\varepsilon - \varepsilon_{pl}}{\varepsilon_{up} - \varepsilon_{pl}} \right)^{h_{nm}} & \sigma > \sigma_{pl} \end{cases} \quad (8-1)$$

where E is Young’s modulus of elasticity, σ_{pl} and ε_{pl} represent the proportionality limit stress (PL-stress) and the corresponding proportionality limit strain (PL-strain) respectively, and the ultimate proof stress (UP-stress) and corresponding ultimate proof strain (UP-strain) are represented by σ_{up} and ε_{up} respectively. The relationship between the stress and the strain is linear up to the PL point and is simply defined by E as indicated in the first part of Eq. (8-1). The second part of Eq. (8-1) defines the curve shape over the entire nonlinear portion of the stress strain relationship, up to the UP-stress and corresponding UP-strain.

Where experimental data is available, regression techniques can be used for curve-fitting and derivation of the model constants. However, where only the manufacturer’s specifications are known, the material model stipulates a procedure for estimating the model constants based on the designation of two ‘stress-control points’ (σ_{c1} and σ_{c2}) and two corresponding ‘strain-control points’ (ε_{c1} and ε_{c2}) according to the following expressions [50]:

$$k_{nm} = \frac{\varepsilon_{R1}^{(h_{nm})} \ln(\sigma_{R1})}{\ln(\varepsilon_{R1})} \text{ or } \frac{\varepsilon_{R2}^{(h_{nm})} \ln(\sigma_{R2})}{\ln(\varepsilon_{R2})} \quad (8-2)$$

$$h_{nm} = \frac{\ln \left[\frac{\ln(\varepsilon_{R1}) \cdot \ln(\sigma_{R2})}{\ln(\sigma_{R1}) \cdot \ln(\varepsilon_{R2})} \right]}{[\ln(\varepsilon_{R1}) - \ln(\varepsilon_{R2})]} \quad (8-3)$$

where,

$$\sigma_{R1} = \frac{\sigma_{c1} - \sigma_{pl}}{\sigma_{up} - \sigma_{pl}}, \quad \sigma_{R2} = \frac{\sigma_{c2} - \sigma_{pl}}{\sigma_{up} - \sigma_{pl}}, \quad \varepsilon_{R1} = \frac{\varepsilon_{c1} - \varepsilon_{pl}}{\varepsilon_{up} - \varepsilon_{pl}}, \quad \text{and} \quad \varepsilon_{R2} = \frac{\varepsilon_{c2} - \varepsilon_{pl}}{\varepsilon_{up} - \varepsilon_{pl}}$$

Feasibility of the above procedure is somewhat contingent upon prior knowledge of at least two points on the stress-strain curve, typically corresponding to the yield stress and ultimate stress values as well as respective corresponding strains. The two stress-control and corresponding strain-control points can then be selected at any other locations along the stress-strain curve. For YPT curves, the proportionality limit stress is equal to the yield stress of the material hence the curve is defined based on the required length of the yield plateau such that the first stress-control point is located at the end of the yield plateau and the second stress-control point is located at any other point between the end of the yield plateau and the ultimate stress. The height of the second control point can be adjusted to reflect various strain-hardening properties. For RHT curves, values of the yield stress and ultimate stress are selected for each material grade according to API 5L specifications for line pipe steel [52] and to achieve better control of the curve shape, the first stress-control point is selected as the API-specified yield stress while the second point is located at any other point between the yield stress and the ultimate stress. A higher value of stress for the second control point indicates superior strain-hardening and is accompanied by a lower proportionality limit stress and vice versa.

8.4 Test Matrix

The non-dimensionality of the derived equations has been preserved in this study by appropriate normalization of the constitutive parameters.

(1) The geometric parameter is represented by a dimensionless ratio of the outer diameter of the pipe's cross-section to the pipe's wall thickness (i.e., D/t ratio). Four variations of the D/t ratio are adopted and assigned respective nominal designations as follows: DT1 = 41.152, DT2 = 64.078, DT3 = 82.156, and DT4 = 104.622. The D/t ratios are achieved by keeping the pipe size constant at NPS (nominal pipe size) = 36 inches while varying the pipe's wall thickness according to the D/t ratios as: $t_1 = 22.22$ mm (for DT1), $t_2 = 14.27$ mm (for DT2), $t_3 = 11.13$ mm (for DT3), and $t_4 = 8.74$ mm (for DT4).

(2) The internal pressure (p) is normalized against the circumferential yield pressure ($p_y = \frac{2\sigma_{ys}t}{D}$), and herein referred to as the 'pressure factor' ($f_p = p/p_y$). The circumferential yield pressure relates to the internal pressure corresponding to the nominal yield stress (YS) in the hoop direction of the pipe cross-section. Five variations of the pressure factor are adopted to determine the required amount of internal pressure to be applied to the pipe models: 0 (corresponding to an unpressurized pipe model), 0.2, 0.4, 0.6, and 0.8.

(3) The standard designation of material grades for YPT pipes is simply the yield stress whereas an equivalent approach has been established for specifying the material grade of RHT pipes based on the value of the 'proof stress' corresponding to either the 0.2% plastic strain ($\sigma_{p,0.2}$), as prescribed by the EN 1993-1-4 stainless steels standard [53], or the 0.5% total strain ($\sigma_{0.5}$), as prescribed by the API 5L pipeline steels standard [52]. Hence, the material grade is made dimensionless depending on the curve shape classification: nondimensionalization is achieved directly for YPT curves by rationing the nominal yield stress (σ_{ys}) with respect to the modulus of elasticity of the steel material (E) whereas, due to non-significance of the yield stress to the CLS, a subparameter is defined for RHT pipes based on the ratio of the proportionality limit stress (σ_{pl}) to the ultimate stress (σ_{us}) and herein referred to as the 'PLUS' ratio (σ_{pl}/σ_{us}). Basically, however, four standard material grades are selected for this study: API X52 (YS = 379 MPa), API X60 (YS = 441 MPa), API X70 (YS = 503 MPa), and API X80 (YS = 586 MPa). The corresponding ultimate strengths for each material grade are: X52 = 455 MPa, X60 = 565 MPa,

X70 = 593 MPa, X80 = 703 MPa. A value of 205800 MPa is applied as the elastic modulus for the pipe materials.

(4) The compressive stress applied uniformly in the longitudinal direction of the pipe prior to inducement of curvature (σ_c) is normalized against the maximum axial stress capacity (σ_L) and herein referred to as the ‘compression factor’ ($f_c = \sigma_c / \sigma_L$). The maximum axial stress capacity is obtained directly from the numerical evaluation of a similar pipe model (i.e., with the same combination of all other parameters) under uniform axial compression as the peak load on the axial load vs. longitudinal end-shortening curve. Four variations of the compression factor are adopted to determine the required amount of compressive axial stress to be applied to the pipe models prior to bending: 0.2, 0.4, 0.6, and 0.8.

(5) The two dimensionless shape constants derived from the Ndubuaku material model are automatically applied as subparameters for the material curve shape factor. For the four selected material grades (X52, X60, X70, and X80), different curve shapes (five each for YPT materials and four each for RHT materials) are defined, as shown in Figure 8-1 - Figure 8-4. The curves for each material grade share the same YS and the same ultimate strength but exhibit different strain-hardening properties. The curve shapes for YPT materials are defined by varying the length of the yield plateau while the curve shapes for RHT materials are defined by varying the proportionality limit stress. To maintain uniformity in the range of the stress-strain relationship for all selected material grades, the uniform elongation is assumed to be constant for all materials, and equal to a total strain of 10%. The 0.5% total strain ($\sigma_{0.5}$) equivalent yield stress approach specified by the API 5L standard is adopted for defining the YS of each material grade.

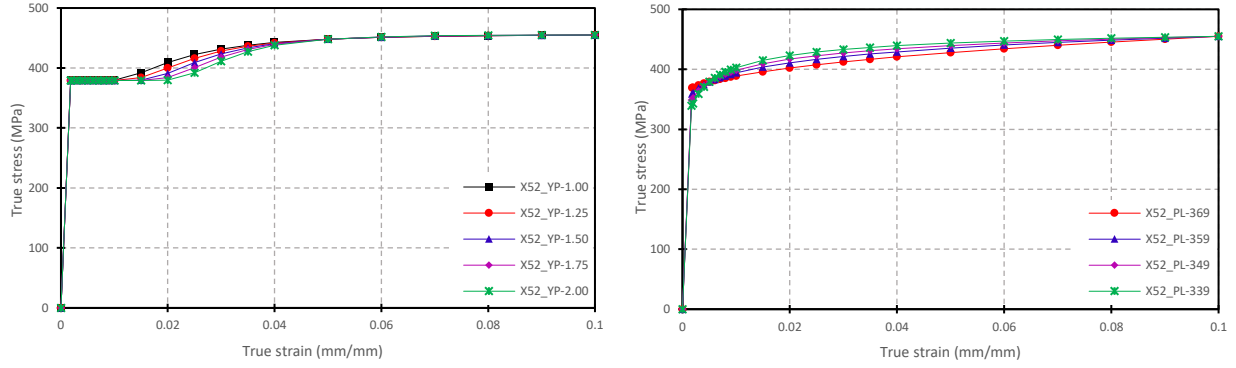


Figure 8-1: Idealized variations for stress-strain curves of X52-YPT and X52-RHT materials

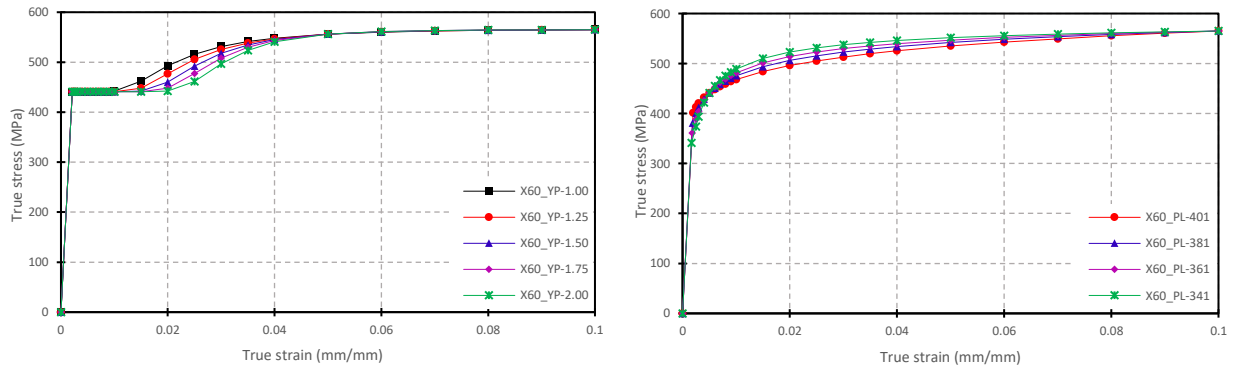


Figure 8-2: Idealized variations for stress-strain curves of X60-YPT and X60-RHT materials

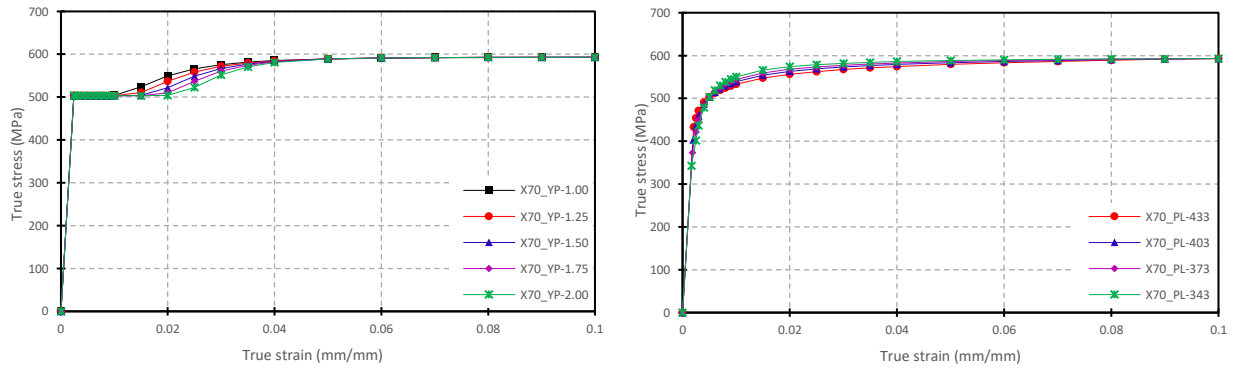


Figure 8-3: Idealized variations for stress-strain curves of X70-YPT and X70-RHT materials

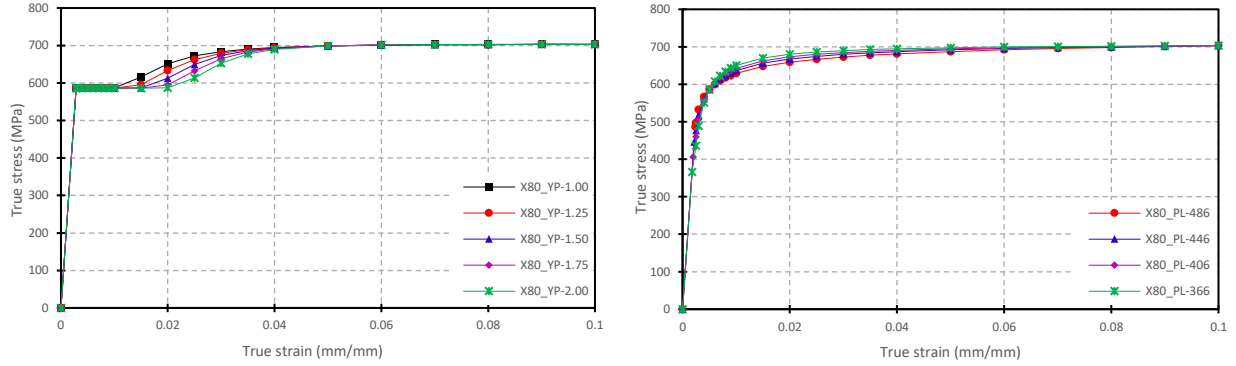


Figure 8-4: Idealized variations for stress-strain curves of X80-YPT and X80-RHT materials

Variations of the strain-hardening properties for each material grade are illustrated in the above figures. Each curve is labeled to reflect the peculiarities of its hardening property: the numeric designations for the YPT curve labels are in percentage (%) units and indicate the length of the yield plateau in terms of the total strain whereas the numeric designations for the RHT curve labels are in megapascal (MPa) units and indicate the proportionality limit stress for the respective curves.

The values of the model constants used to generate the stress-strain curves in the above figures are presented in Table 8-1.

Table 8-1: Model constants for derivation of stress-strain curves

Material	YPT			RHT		
	<i>Curve label</i>	$K_f = 1/K_{nm}$	$H_f = 1/H_{nm}$	<i>Curve label</i>	$K_f = 1/K_{nm}$	$H_f = 1/H_{nm}$
X52	<i>YP-1.00</i>	20.5077	0.6958	<i>PL-369</i>	1.9578	16.4530
	<i>YP-1.25</i>	25.9422	0.5658	<i>PL-359</i>	3.3881	7.6640
	<i>YP-1.50</i>	33.6157	0.4692	<i>PL-349</i>	5.2603	5.0535
	<i>YP-1.75</i>	45.0310	0.3934	<i>PL-339</i>	8.5164	3.4226
	<i>YP-2.00</i>	63.0332	0.3318			
X60	<i>YP-1.00</i>	29.9027	0.6234	<i>PL-401</i>	3.8457	7.7602
	<i>YP-1.25</i>	38.8327	0.5078	<i>PL-381</i>	6.1646	4.9322
	<i>YP-1.50</i>	51.7336	0.4219	<i>PL-361</i>	9.3150	3.6322
	<i>YP-1.75</i>	71.4369	0.3544	<i>PL-341</i>	15.359	2.6046
	<i>YP-2.00</i>	103.465	0.2994			
X70	<i>YP-1.00</i>	57.9192	0.5532	<i>PL-433</i>	9.5412	4.3644
	<i>YP-1.25</i>	77.6927	0.4512	<i>PL-403</i>	17.4955	2.9594
	<i>YP-1.50</i>	107.0977	0.3755	<i>PL-373</i>	29.5817	2.2654
	<i>YP-1.75</i>	153.5094	0.3160	<i>PL-343</i>	58.0424	1.6629
	<i>YP-2.00</i>	231.8488	0.2675			
X80	<i>YP-1.00</i>	83.7395	0.5187	<i>PL-486</i>	11.5448	3.9814
	<i>YP-1.25</i>	115.2048	0.4221	<i>PL-446</i>	21.1099	2.7531
	<i>YP-1.50</i>	162.9859	0.3510	<i>PL-406</i>	35.3391	2.1374
	<i>YP-1.75</i>	240.2443	0.2953	<i>PL-366</i>	69.2445	1.5847
	<i>YP-2.00</i>	374.3178	0.2501			

8.5 FE Model

The FE pipe model developed for this study is intended for simulation of the mechanical response of an actual pipe segment, both pressurized and unpressurized, subjected to a combination of constant uniform compressive net-section axial stress and monotonically-

increasing curvature. Initial imperfections, either in form of geometric irregularities, residual stress, corrosion or girth-weld misalignment, are not explicitly considered in the developed model. However, a reduced-thickness sleeve (Figure 8-5) is introduced as a trigger zone immediately adjacent to the mid-length cross-section of the pipe to facilitate initiation of buckling at the middle of the pipe's length. A 3% reduction in thickness spanning longitudinally over 5% of the pipe's length, applied to the mid-length sleeve as shown in Figure 8-5, is considered to be sufficient for triggering buckling at the middle of the pipe's length without significantly impacting the overall moment-curvature response.

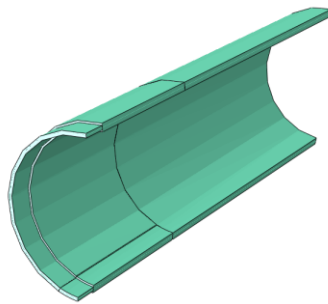


Figure 8-5: Pipe mid-length reduced-thickness sleeve (not drawn to scale)

To optimize computational resources, double symmetry is applied to the model with respect to both the bending plane and the mid-length cross-section such that only a quarter of the actual pipe segment is modeled for the numerical simulation. In line with the recommendations of Liu et al. [54] for avoiding interference between end boundary conditions and the buckling mechanism at the pipe's mid-span, the quarter pipe models are extruded to 3 times the pipe's outer diameter ($3 \cdot OD$), implying an actual length equal to 6 times the pipe's outer diameter for the full pipe segment.

8.5.1 FE mesh & elements

A preliminary mesh sensitivity assessment was performed, and an approximate global size equal to 3% of the pipe diameter was determined as the optimum size of mesh partitions to apply to the pipe models. A large-strain von Mises plasticity model with isotropic hardening, assumed to follow the associative flow rule, is applied to the pipe material. The four-node doubly curved,

reduced integration S4R shell element, with in-plane and rotational hourglass control, is used to assemble the pipe models. The S4R element has six degrees of freedom per nodal point: three translations (u_1, u_2, u_3) in the directions of the global axes and three rotations ($\theta_1, \theta_2, \theta_3$) about the directions of the three global axes. The S4R element is shear-flexible and suitable for modelling the mechanical behavior of thin to moderately thick shell structures with material and geometric nonlinearities. The element has a finite membrane strain formulation effective for modelling shell deformation mechanisms where significant thickness change, large displacements and rotations, and transverse shear constraints need to be considered.

8.5.2 Boundary conditions

The longitudinal alignment of the pipe model is in the direction of the global z -axis while the bending plane is aligned with the global y - z plane (i.e., curvature is induced at the pipe's end cross-section about the global x -axis). Horizontal-transverse symmetry boundary conditions are applied to the top and bottom longitudinal edges of the pipe such that displacement in global x -direction and rotation about the global y - and z -axes are fixed (i.e., $u_x = \vartheta_y = \vartheta_z = 0$). Longitudinal symmetry boundary conditions are applied to the mid-length cross-section of the pipe such that displacement in global z -direction and rotation about the global x - and y -axes are fixed (i.e., $u_z = \vartheta_x = \vartheta_y = 0$). A reference point (RP) is created at the geometric centroid of the end cross-section to relate the nodal displacements and rotations at the end cross section of the specimen to the displacements and rotation of the reference point. The RP is allowed to move in the longitudinal direction (i.e., along the z -axis) and free to rotate about the axis of bending (i.e., about the x -axis) while the other components of displacement and rotation are restrained (i.e., $u_x = u_y = \vartheta_y = \vartheta_z = 0$). A kinematic coupling constraint is defined in the cylindrical coordinate system to restrain all degrees of freedom except circumferential extension, thereby inducing in a uniform stress field at the end cross-section of the pipe under internal pressurization.

8.5.3 Loading sequence

Two loading steps are created: an initial load-controlled step followed by a displacement-controlled step. In the load-controlled step, a constant internal pressure is applied to the inner surface of the pipe while a constant compressive axial force is applied to the RP at the end cross-section of the pipe. The load-controlled step is defined as a “Static General” step which is performed based on the default “Newton’s method” iterative solution technique in ABAQUS. In the displacement-controlled step, a finite rotational displacement is specified about the x -axis at the end cross-section RP such that the pipe is subjected to monotonically-increasing curvature. The displacement-controlled step is defined as a “Static Riks” step which is performed based on the default equilibrium iterative incremental scheme in ABAQUS. The ABAQUS Riks method employs a linearized arc-length control technique which is able to provide a solution corresponding to an increase in displacements even when the reactive forces decrease. The applied bending moment is directly obtained at the end of each simulation as the reaction moment at the end cross-section RP.

8.5.4 Output and post-processing

To obtain appropriate results for the longitudinal strain, a cylindrical coordinate system is defined for the pipe model assembly whereas the reaction moment is derived in the default standard coordinate system. The recommendation by Ref. [54] for obtaining an average value of the longitudinal strains is adopted herein by calculating the average of the individual elemental compressive axial strains over a gauge length equal to 2 times the pipe diameter ($2*OD$). The incremental values of the average strain are evaluated by using the “Operate on XY Data” tool in ABAQUS to calculate the mean of the combined values of axial logarithmic strain (LE11; defined with respect to the cylindrical coordinate system) in all the elements within the prescribed gauge length and area. On the other hand, the incremental values of the reaction moment (RM1) at the RP are obtained directly from the “ODB field output” module in ABAQUS. The calculated incremental values of compressive axial strain, as well as the directly-obtained incremental values of the reaction moment, are exported to a Microsoft Excel spreadsheet using the “Report XY data” tool in ABAQUS. The ‘peak moment criterion’

[6,26,27] is applied for deriving the CLS for each simulation as the average strain that corresponds to the onset of “softening” in the moment-curvature response.

8.6 Results of FE Analysis

As indicated above, the buckling response of pipe segments is strongly influenced by the overall shape of the stress-strain curve. Effort is therefore made to highlight the notable distinctions in the deformational capacity of pipelines that are largely attributable to the material curve shape classification.

8.6.1 FE model validation

The FE models developed in this study are validated by thorough comparison with results of experimental tests by Mohareb et al. [6,55] on a real pipe segment. Satisfactory correspondence between the FEA results and the experimental results of Ref. [55] was obtained for both the moment-curvature response and the wrinkling deformation mode at failure (Figure 8-6).

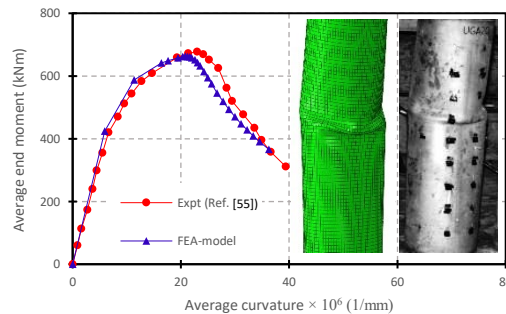


Figure 8-6: Comparison of FEA result with experimental result (UGA508) by Ref. [55]

Figure 8-6 shows a reasonably accurate prediction of the experimentally-obtained diamond-shape buckling mode by the FE model. The Ndubuaku model was used to derive the appropriate material curve shape constants for approximation of the stress-strain behavior obtained from the

ancillary tension coupon test by Ref. [55]. The geometrical and material properties of the experimental test specimen, designated as “UGA508” by Ref. [55], are as follows:

- Outer diameter 508 mm
- D/t ratio 64
- Length of pipe 1690 mm
- Material grade API X56
- Elastic modulus 203704 MPa
- Yield stress ($\sigma_{0.5}$) 391 MPa
- Proportionality limit stress 329 MPa
- Knee constant ($1/K_{nm}$) 3.53
- Heel constant ($1/H_{nm}$) 29.61
- Net-section compressive axial force 1303 kN

8.6.2 Influence of D/t ratio

The deformational capacities are plotted against the D/t ratio for YPT pipes and RHT pipes in Figure 8-7 and Figure 8-8 respectively. The plots in Figure 8-7 are obtained YPT pipes wit YPL = 1.75% while the plots in Figure 8-8 are obtained for RHT pipes with PLUS ratio = 0.811. The plots in both figures are all obtained for X52 pipes subjected to compression factor, $f_c = 0.2$, and f_p values ranging from 0.0 to 0.8.

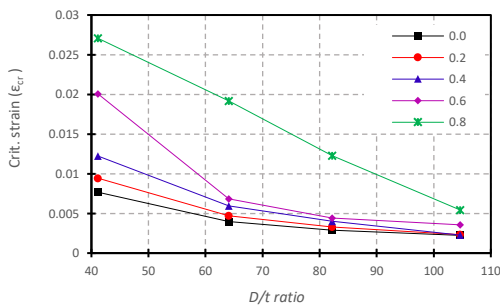


Figure 8-7: Plot of ϵ_{cr} vs. D/t ratio for X52 pipe (YPL = 1.75%, $f_c = 0.2$)

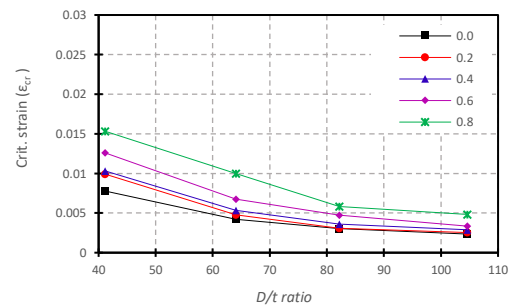


Figure 8-8: Plot of ϵ_{cr} vs. D/t ratio for X52 pipe (PL/US = 0.811, $f_c = 0.2$)

The CLS trends for both YPT and RHT pipes generally indicate a negative nonlinear correlation, as well as secondary effects of the internal pressure. For pressure levels below 80% YS ($f_p < 0.8$), the effect of internal pressure is less for RHT pipes compared to YPT pipes at a low D/t ratio (DT1) while the effect of internal pressure at intermediate D/t ratios (DT2 and DT3) and at a high D/t ratio (DT4) is largely unaffected by the material curve shape. At a high pressure level ($f_p = 0.8$), the deformational capacity of YPT pipes becomes significantly larger than RHT pipes for low D/t ratio (DT1) and intermediate D/t ratios (DT2 and DT3).

8.6.3 Influence of internal pressure

Plots illustrating the effect of internal pressure on the CLS are presented in Figure 8-9 and Figure 8-10 for YPT and RHT pipes respectively. The plots in Figure 8-9 are obtained YPT pipes with YPL = 1.50% while the plots in Figure 8-10 are obtained for RHT pipes with PLUS ratio = 0.674. The plots in both figures are all obtained for X60 pipes subjected to compression factor, $f_c = 0.4$, and presented for all four D/t ratios (DT1, DT2, DT3, and DT4) investigated herein.

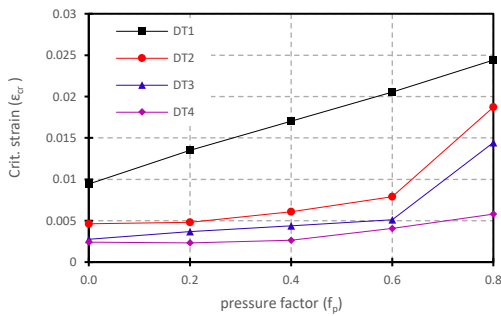


Figure 8-9: Plot of ϵ_{cr} vs. f_p for X60 pipe (YPL = 1.50%, $f_c = 0.4$)

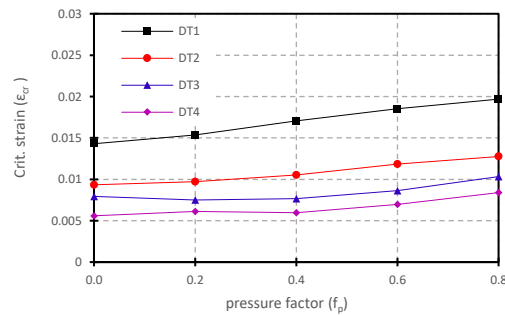


Figure 8-10: Plot of ϵ_{cr} vs. f_p for X60 pipe (PL/US = 0.674, $f_c = 0.4$)

The CLS trends shown in Figure 8-9 and Figure 8-10 indicate strong implication of the trends in Figure 8-7 and Figure 8-8 regardless of the difference in material curve and material grade properties. The CLS vs. internal pressure relationship is nonlinear and positive. The nonlinearity is however more evident in YPT pipes unlike the CLS trends of RHT pipes which indicate are

more gradual over the entire range of pressure levels. The nonlinearity of the CLS vs. f_p trends for both YPT and RHT pipes is observed to diminish at a low D/t ratio (DT1).

8.6.4 Influence of material grade

The effect of the material grade on the CLS is depicted by the plots in Figure 8-11 and Figure 8-12 for YPT pipes and RHT pipes respectively. The plots in Figure 8-11 show the relationship between the CLS and the yield stress for the five pressure levels investigated herein, obtained for YPT pipes subjected to compression factor, $f_c = 0.8$ with YPL = 1.0% and D/t ratio = 82.16. The CLS values are plotted against the PLUS ratio in Figure 8-12 for all four material grades of RHT pipes with D/t ratio = 64.08 subjected to compression factor, $f_c = 0.6$ and pressure factor, $f_p = 0.2$.

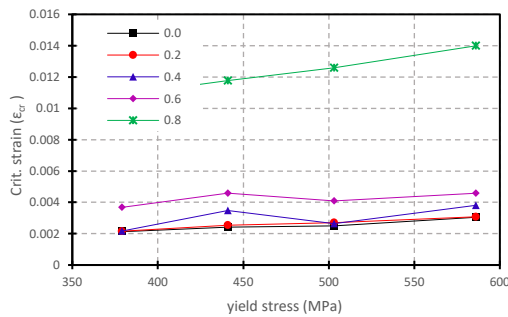


Figure 8-11: Plot of ϵ_{cr} vs. yield stress for DT1 pipe (YPL=1.0%, $f_c = 0.8$)

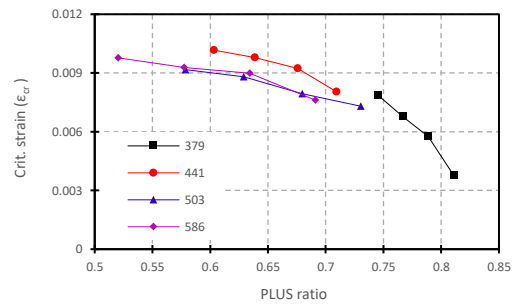


Figure 8-12: Plot of ϵ_{cr} vs. PLUS ratio for DT2 pipe ($f_p = 0.2$, $f_c = 0.6$)

The results presented in Figure 8-11 indicate a positive correlation between the CLS of YPT pipes and the yield stress. The secondary effect of the internal pressure on the CLS vs. yield stress relationship is also observed to be negligible except at a high level of pressure ($f_p < 0.8$). The plots in Figure 8-12 indicate a negative and highly nonlinear correlation between the CLS and the PLUS ratio: the plots show a gradual loss of deformational capacity for PLUS ratio approximately below 0.75. For PLUS ratio approximately greater than 0.75, the change in slope increase indicating a progressively greater loss of deformational capacity.

8.6.5 Influence of material curve shape

The plots in Figure 8-13 and Figure 8-14 illustrate the effect of the overall shape of the material stress-strain curve on the CLS for YPT pipes and RHT pipes respectively. The material curve shapes are assigned numeric designations (herein referred to as the “shape factor”, sh_f) which represent the calibration of parametric combinations for each curve over a linear scale such that “1” represents an RHT pipe with the highest PL-stress (or a YPT pipe with the shortest YPL) and “4” represents an RHT pipe with the lowest PL-stress (or “5” represents a YPT pipe with the longest YPL) for respective material grades. A lower PL-stress implies ‘superior’ strain-hardening while a higher PL-stress implies ‘inferior’ strain hardening.

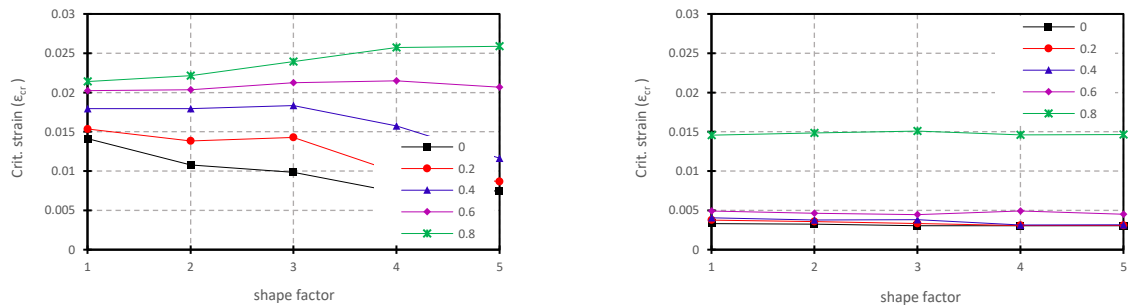


Figure 8-13: Plot of ϵ_{cr} vs. sh_f for (a) X70 DT1 pipe and (b) X70 DT3 pipe ($f_c = 0.4$)

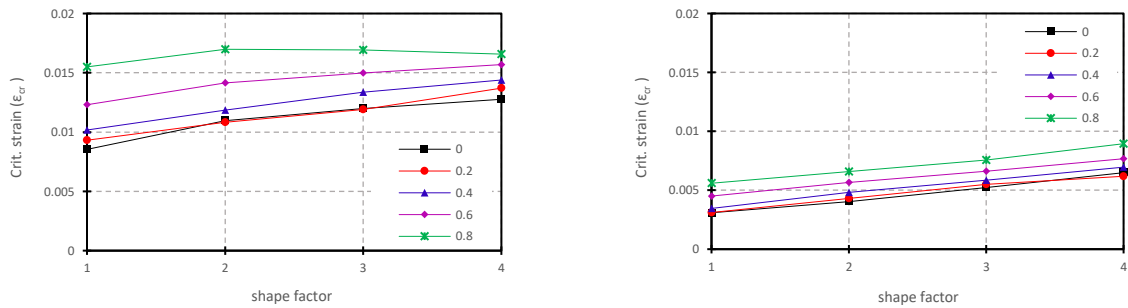


Figure 8-14: Plot of ϵ_{cr} vs. sh_f for (a) X52 DT1 pipe and (b) X52 DT3 pipe ($f_c = 0.4$)

Figure 8-13(a) and Figure 8-13(b) comprise plots of the CLS against the sh_f for all five pressure levels, obtained for YPT X70 pipes with D/t ratio = 41.15 and D/t ratio = 82.16 respectively, and subjected to compression factor, $f_c = 0.4$. The CLS values are plotted against the sh_f in Figure

8-14(a) and Figure 8-14(b) for all five pressure levels for RHT X52 pipes with D/t ratio = 41.15 and D/t ratio = 82.16 respectively, and subjected to compression factor, $f_c = 0.4$.

Figure 8-13(a) indicates a change in the slope of the CLS vs. sh_f plots from a negative trend to a positive trend as the pressure is increased. However, the observed effect of pressure on the CLS vs. sh_f trends diminishes as the D/t ratio increases, as indicated by Figure 8-13(b). The correlation between the CLS and sh_f is observed to be generally positive for the various D/t ratios considered, however, in contrast to the observed trends in YPT pipes, the effect of pressure on the CLS vs. sh_f trends diminishes as the D/t ratio decreases.

8.6.6 Influence of compressive net-section axial force

The effect of compressive net-section axial force on the CLS of pipes under various levels of internal pressure, and subjected to monotonically-increasing curvature is depicted in Figure 8-15 and Figure 8-16. The relationship between the CLS and the compression factor, f_c , is represented by the plots in Figure 8-15 for YPT X52 pipes with D/t ratio = 64.08 and YPL = 1.50%. Figure 8-16 comprises CLS vs. f_c plots for RHT X52 pipes with D/t ratio = 64.08 and PLUS ratio = 0.811. Each plot corresponds to a respective level of internal pressure as indicated by the elements of the graph legends.

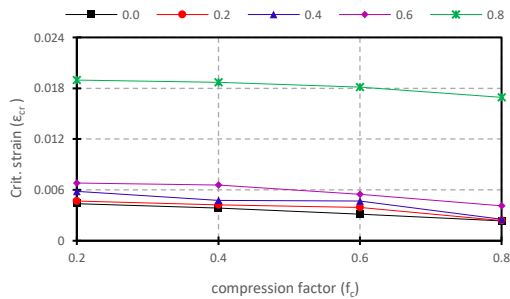


Figure 8-15: Plot of ϵ_{cr} vs. f_c for X52 DT2 pipe (YPL=1.50%)

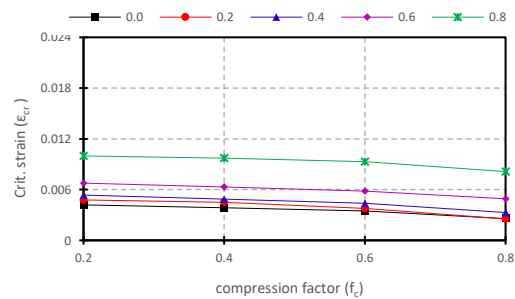


Figure 8-16: Plot of ϵ_{cr} vs. f_c for X52 DT2 pipe (PL/US = 0.811)

The plots in Figure 8-15 and Figure 8-16 indicate that, for all combinations of all parameters besides the compression factor, the CLS of both YPT and RHT pipes reduces

progressively and somewhat nonlinearly as the compressive net-section axial force is increased from 0% to 100% of the limit stress obtained under uniform axial compression.

8.7 Semi-empirical Modelling

8.7.1 CLS equations

The FEA-predicted CLS values corresponding to 1600 and 1280 different parametric combinations for YPT pipes and RHT pipes, respectively, have been collated into large global matrices of independent variables (6 parameters) and a dependent variable (the CLS). The phenomenological association between the CLS and respective parameters are visually observed and translated into individual variable functions which provide a reasonable mathematical description of the respective relationships. Physical interrelationships between parameters are strategically incorporated into individual variable functions to account for underlying secondary effects in each association. A constitutive nonlinear equation is formed as an arithmetic product of all individual variable functions, based on an established multiplicative concept [27,54,56] as follows:

$$\varepsilon_{cr} = f_{cr}[\pi_1, \pi_2, \pi_3, \pi_4, \pi_5, \pi_6] = f_1 \cdot f_2 \cdot f_3 \cdot f_4 \cdot f_5 \cdot f_6 \quad (8-4)$$

where f_1, f_2, f_3, f_4, f_5 and f_6 represent the D/t ratio function (f_{dt}), the pressure factor function (f_{fp}), the strain-hardening function (f_{sh}), the heel factor function (f_{hf}), the knee-to-heel ratio function (f_{kh}), and the compression factor function (f_{fc}) respectively. π_1 represents the D/t ratio ($\frac{D}{t}$), π_2 represents the pressure factor ($\frac{p}{p_y}$), π_3 represents the ratio of the yield stress to the elastic modulus ($\frac{\sigma_{ys}}{E}$) for YPT pipes or the PLUS ratio ($\frac{\sigma_{pl}}{\sigma_{us}}$) for RHT pipes, π_4 represents the heel factor (h_f), π_5 represents the “knee-to-heel” ratio ($\frac{k_f}{h_f}$), and π_6 represents the compression factor (f_c).

The final form of the constitutive equation is determined by an iterative refinement process involving several adjustments of the individual variable functions and recomputation of the overall goodness-of-fit between the FEA-derived CLS and the semi-empirical derivations until the highest possible value of the coefficient of multiple determination (R^2) is achieved. An R^2 value greater than 0.95 was considered to be a satisfactory goodness-of-fit between the FEA-derived CLS values and the predictions of the derived nonlinear expressions.

The individual variable functions for YPT pipes are:

$$\begin{aligned}
 f_1 = f_{dt} &= a_1 \cdot (\pi_1)^{b_1} \\
 f_2 = f_{fp} &= a_2 + (b_2 + c_2 \pi_1) \cdot \text{Exp}(\pi_2)^{(d_2 + e_2 \pi_4)} \\
 f_3 = f_{sh} &= a_3 \pi_4 + (b_3 \pi_2 + c_3 \pi_1) \cdot (\pi_3)^{d_3} \\
 f_4 = f_{hf} &= a_4 + (b_4 \pi_1) \cdot (\pi_4)^{c_4} \\
 f_5 = f_{kh} &= a_5 + (b_5 \pi_3) \cdot (\pi_5)^{c_5} \\
 f_6 = f_{fc} &= a_6 + (b_6 \pi_2 + c_6 \pi_1) \cdot (\pi_6)^{d_6}
 \end{aligned} \tag{8-5}$$

The individual variable functions for RHT pipes are:

$$\begin{aligned}
 f_1 = f_{dt} &= a_1 \cdot (\pi_1)^{b_1} \\
 f_2 = f_{fp} &= (a_2 + b_2 \cdot \pi_2) \cdot [c_2 + (d_2 + e_2 \pi_1) \cdot \text{Exp}(\pi_2)^{(f_2)}] \\
 f_3 = f_{sh} &= a_3 + (b_3 \pi_2 + c_3) \cdot (\pi_3)^{d_3} \\
 f_4 = f_{hf} &= a_4 + b_4 \cdot (\pi_4)^{c_4} \\
 f_5 = f_{kh} &= a_5 + b_5 \cdot (\pi_5)^{c_5} \\
 f_6 = f_{fc} &= a_6 + (b_6 \pi_1) \cdot (\pi_6)^{c_6}
 \end{aligned} \tag{8-6}$$

Advanced nonlinear regression analysis is performed, using the “NonlinearModelFit” command in the powerful computational package (Wolfram Mathematica [57]), to derive the nonlinear regression coefficients for the individual variable functions, as well as respective coefficients of multiple determination (R^2) for YPT pipes and RHT pipes. Results are presented in Table 8-2.

Table 8-2: Nonlinear regression coefficients

REG.		
COEF	YPT	RHT
F.		
a_1	0.9828	0.01271
b_1	-2.924	-0.8317
a_2	394.2	0.9942
b_2	95.79	-0.5198
c_2	-0.2963	283.5
d_2	6.121	52.44
e_2	-2.775	-0.06258
f_2	-	2.458
a_3	0.003257	0.01682
b_3	-167.4	0.01475
c_3	3.658	-0.03324
d_3	1.569	4.991
a_4	103.3	-0.0009634
b_4	-0.1003	0.3471
c_4	-1.295	-0.9193
a_5	-0.0286	0.1134
b_5	4.982	1.1132
c_5	0.02787	-0.5012
a_6	-79.15	74.71
b_6	-45.71	-0.2031
c_6	0.9977	2.331
d_6	3.211	-
R^2	0.974349	0.992728

The applicable range for the dimensionless parameters that constitute the developed semi-empirical models corresponds to the range of values for each variable in the parametric analysis, given in Table 8-3 as follows:

Table 8-3: Applicable range for dimensionless parameters

<i>Par.</i>	YPT		RHT	
	\geq	\leq	\geq	\leq
<i>D/t</i>	41	105	41	105
<i>f_p</i>	0.0	0.8	0.0	0.8
<i>σ_y/E</i>	0.0018	0.0029		-
<i>σ_p/σ_{us}</i>		-	0.52	0.85
<i>sh_f</i>	1	5	1	4
<i>f_c</i>	0.2	0.8	0.2	0.8

The applicable range of the shape constants is peculiar to the various material grades investigated in this study. Hence the shape factor (*sh_f*), reported in Figure 8-13 and Figure 8-14, is represented by the following regression equations to translate the respective combinations of shape constants (*k_{nm}* and *h_{nm}*) and material grade onto a linear scale ranging from 1 to 5 for YPT pipes and ranging from 1 to 4 for RHT pipes:

For YPT pipes,

$$sh_{f,YP} = 0.0507483 \times (0.0293137 - 9.86288 * 10^{-5} \cdot \sigma_y \cdot h_f^{1.12036}) \times \left(4154.41 + 0.351787 \cdot \sigma_y \cdot \ln \left(\frac{k_f}{h_f} \right) \right) \quad (8-7)$$

For RHT pipes,

$$sh_{f,RH} = 8.85104 * 10^{-6} \times (307.19 - 0.312884 \cdot \sigma_y \cdot h_f^{0.303706}) \times \left(2863.64 + 0.615032 \cdot \sigma_y \cdot \ln \left(\frac{k_f}{h_f} \right) \right) \quad (8-8)$$

Ideally, the regression equations in Eq. (8-7) and Eq. (8-8) are only valid within the range of yield stresses investigated in this study. However, the yield stress is observed to be largely irrelevant to the CLS of RHT pipes and the interaction between the ‘*knee-to-heel*’ ratio (k_f/h_f) and the yield stress (σ_{ys}) is incorporated in the CLS equation for YPT pipes hence, the shape factor essentially serves as a material modelling guide to ensure that approximated stress-strain relationships portray substantial similarity with the material curve parameters used in this study.

8.7.2 Limit stress equations

Additional parametric analyses were performed to determine the functional relationships between the parameters investigated in this study and the limit stress of YPT pipes and RHT pipes under uniform axial compression. The plots of the limit stress (σ_L) vs. the D/t ratio, internal pressure and yield stress are presented in Figure 8-17 and Figure 8-18 for YPT pipes and RHT pipes respectively. The plots in Figure 8-17(a) show the influence of the D/t ratio on σ_L at various internal pressure levels for a YPT X60 pipe with YPL = 1.75% while the plots in Figure 8-17(b) show the influence of the pressure factor on σ_L for a YPT DT4 pipe of various material grades with YPL = 1.25% and the plots in Figure 8-17(c) show the influence of the material grade (yield stress) on σ_L for a YPT DT1 pipe of various material curve shapes at internal pressure = 20% YS. The plots in Figure 8-18(a) show the influence of the D/t ratio on σ_L at various internal pressure levels for an RHT X70 pipe with PL/US = 0.629 while the plots in Figure 8-18(b) show the influence of the pressure factor on σ_L for an RHT DT1 pipe of various material grades with $sh_f = 2$ and the plots in Figure 8-18(c) show the influence of the material grade (yield stress) on σ_L for an RHT DT3 pipe of various material curve shapes at internal pressure = 40% YS.

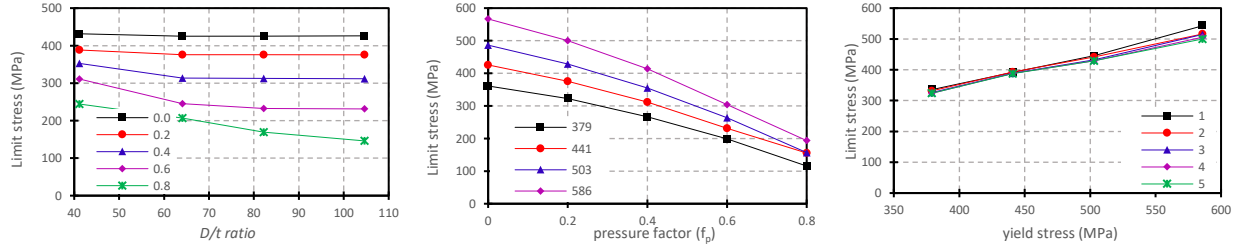


Figure 8-17: YPT X60 plots of σ_L vs. (a) D/t ratio (b) internal pressure, and (c) yield stress

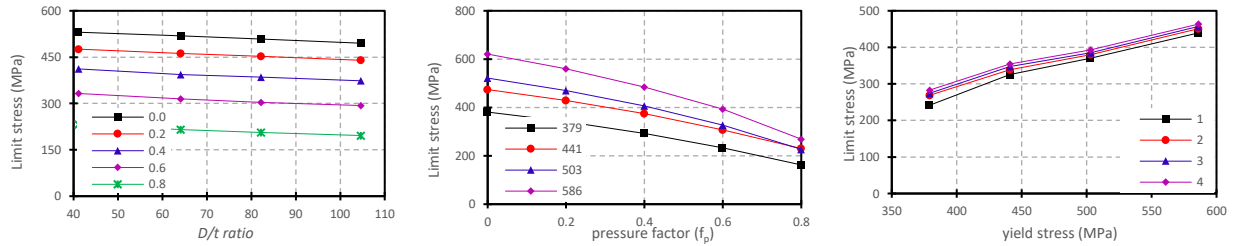


Figure 8-18: RHT X70 plots of σ_L vs. (a) D/t ratio (b) internal pressure, and (c) yield stress

The results for YPT pipes in Figure 8-17 indicate a negative and slightly nonlinear relationship between the D/t ratio and the limit stress. The effect of the D/t ratio on the limit stress however diminishes as the internal pressure reduces. The relationship between the pressure factor and the limit stress is also observed to be nonlinear and negative, and the effect of internal pressure on the limit stress is much more significant compared to the D/t ratio. There is a positive correlation, but no significant nonlinearity, between the yield stress and the limit stress and the effect of the shape factor on the limit stress is negligible. There is strong similarity between the trends of the RHT plots and the trends of the YPT plots, indicating significant correspondence of the functional relationships for both material curve classifications. However, the internal pressure is observed to have a relatively negligible effect on the relationship between the D/t ratio and the limit stress for RHT pipes compared to YPT pipes. On the other hand, the effect of the shape factor on the limit stress is observed to be relatively more significant for RHT pipes compared to YPT pipes.

Nonlinear regression procedures were also employed to derive suitable regression equations for predicting the limit stress for both YPT pipes and RHT pipes. The developed equations are necessary prerequisites for determining the maximum allowable uniform axial stress on a pipe, given the respective parameters considered herein. To reduce computational requirements while also being conservative, variation of the shape factor was considered to have a negligible

influence on the limit stress and only one set of values, corresponding to $sh_f = 5$ for YPT pipes and $sh_f = 1$ for RHT pipes, were included in the regression analyses. Hence, only 80 FE simulations each were implemented for derivation of the limit stress expressions for YPT pipes and RHT pipes. With the following regression equations, the appropriate fractions of the limit stress that feed into the semi-empirical equations for evaluating the CLS of pipes subjected to combined axial compression and bending can be evaluated:

For YPT pipes,

$$\begin{aligned} \sigma_{lim,YP} = & 6.163(\sigma_{ys}) * [(8.496 - 7.192.\pi_2) * (\pi_1^{-0.3075})] \\ & * [(-8.36548) + 8.36562 * (Exp(\pi_2)^{5.598*10^{-6}})] \\ & * [(1.523.\pi_1) + 350.3 * (\pi_3^{-0.03885})] \end{aligned} \quad (8-9)$$

For RHT pipes,

$$\begin{aligned} \sigma_{lim,RH} = & 5.451(\sigma_{ys}) * [(7.321 - 6.485.\pi_2) * (\pi_1^{-0.107})] \\ & * [(8.416) + 6.906 * (Exp(\pi_2)^{0.8432})] \\ & * [(5.232) + 7.782 * (\pi_4^{-0.4513})] \\ & * [(-5.67028) + 5.67057 * (\pi_5^{-2.72*10^{-6}})] \end{aligned} \quad (8-10)$$

where π_1 , π_2 , π_4 , and π_5 correspond to the respective parameter designations specified in Eq. (8-4).

8.7.3 Goodness-of-fit

The CLS values predicted using the developed nonlinear regression equations in Eq. (8-4), Eq. (8-5) and Eq. (8-6) are compared to the FEA-derived values and graphically represented as shown in Figure 8-19.

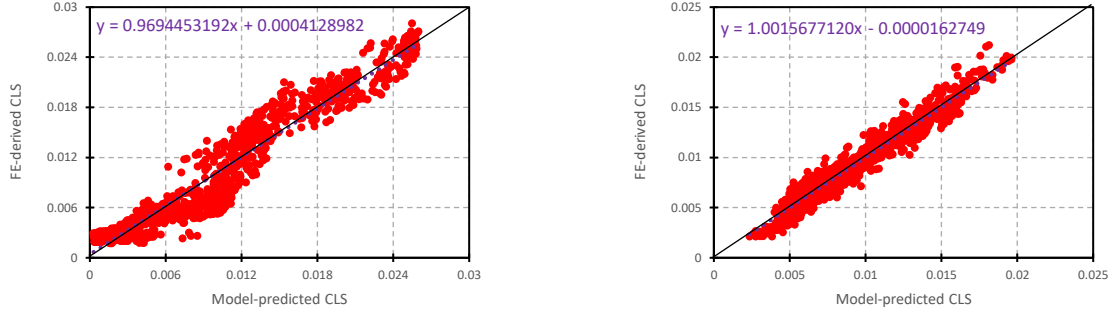


Figure 8-19: Model prediction vs. FEA for CLS of (a) YPT pipe and (b) RHT pipe under combined axial compression and bending

For the original (uncorrected) CLS models, the mean and standard deviation of the FTP ratios for YPT pipes are 1.2601 and 0.77815 respectively while the mean and standard deviation of the FTP ratios for RHT pipes are 0.99801 and 0.11207 respectively. Both models follow a normal distribution.

The predictions of the limit stress using the regression equations in Eq. (8-9) and Eq. (8-10) are also compared with the FEA-derived values, and graphically presented in Figure 8-20.

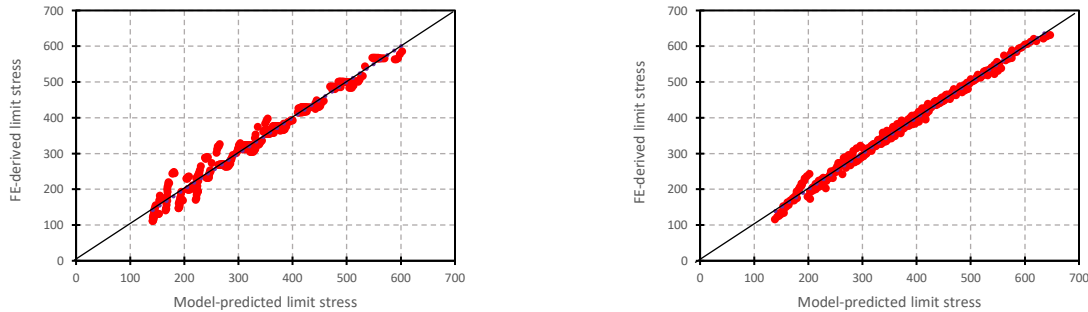


Figure 8-20: Model prediction vs. FEA for limit stress of (a) YPT pipe and (b) RHT pipe under uniform axial compression

For the limit stress models, the mean and standard deviation of the FTP ratios for YPT pipes are 1.0568 and 0.08855 respectively while the mean and standard deviation of the FTP ratios for RHT pipes are 0.99648 and 0.04592 respectively. Like the CLS models, both limit stress models also follow a normal distribution.

A statistical procedure is implemented to introduce a desired level of conservativeness in the regression equations. The procedure consists of two simple steps:

(1) Correct any bias in the semi-empirical model by applying the following correction functions such that the gradient and intercept of the linear equation obtained from the scatter plot of the model-predicted CLS values vs. the FEA-derived CLS values (shown in Figure 8-19) are set to one and zero respectively:

$$\varepsilon_{cr,corr} = G_{orig} \times \varepsilon_{cr,orig} + I_{orig} \quad (8-11)$$

where G_{orig} and I_{orig} are the original gradient and intercept values, respectively, for the linear equation of the FEA vs. model prediction scatter plot. $\varepsilon_{cr,orig}$ and $\varepsilon_{cr,corr}$ are the original and corrected versions, respectively, of the semi-empirical model.

(2) Manipulate the distribution of FE-to-predicted (FTP) ratios for the corrected model, $\varepsilon_{cr,corr}$ by resetting the value of the mean to values higher than one. FTP values are obtained by dividing the FEA-predicted CLS values with the corrected model-predicted CLS values.

The results presented in Table 8-4 are obtained using the “Goal Seek” function in Microsoft Excel to determine the value of the linear model intercept, I_{orig} that is required to achieve various mean values for the FTP-ratio distribution and respective probabilities of underprediction (POU). The POU is a measure of the conservativeness of the corrected (unbiased) model and is calculated by simply dividing the number of model predictions with FTP ratio > 1 with the total number of FE runs for each model.

Table 8-4: Values of I_{orig} for correction function and corresponding POUs

Mean	I_{orig}	POU	Max. FTP Ratio	Min. FTP Ratio
YPT				
1.00	0.000727887	0.4475	2.9253	0.2904
1.10	0.000400072	0.5600	4.3491	0.3014
1.20	0.000165768	0.6263	6.6690	0.3098
1.30	-2.46573E-07	0.6725	10.7212	0.3161
1.40	-0.000114999	0.6956	18.4845	0.3206
1.50	-0.000190134	0.7094	35.1491	0.3235
RHT				
1.00	-2.81919E-05	0.5125	1.4374	0.5549
1.10	-0.000735982	0.8039	1.6627	0.6607
1.20	-0.001305543	0.9484	1.9803	0.7765
1.30	-0.001765174	0.9852	3.4843	0.8971
1.40	-0.002126621	0.9969	8.6519	0.9399
1.50	-0.002329618	0.9984	51.7887	0.9657

The results presented in Table 8-4 indicate the gains in the conservativeness of the semi-empirical model that are achievable by adjusting the linear model intercept, I_{orig} . The last two columns (“Max. FTP ratio” and “Min. FTP ratio”) are useful for guiding the designer to implement the outlined procedure within desired tolerance limits of the maximum and/or minimum allowable FTP ratios. One of the benefits of the bias-correction procedure presented herein is the potential to reduce the spread of distribution of the CLS model predictions, especially the YPT model, e.g., achieving a mean value of 1.0 for the YPT FTP ratios (as shown in Table 4) reduces the standard deviation of the original (uncorrected) YPT CLS model from 0.77815 to 0.28765.

8.8 Discussion

Plasticity theories have highlighted the fundamental significance of the overall shape of the material stress-strain curve to the load-deformation response of pipe segments under various loading conditions [58–63]. Depending on the initial state of stress (such as residual stresses), as well as the initial state of deformation (such as dimensional irregularities), the mechanical response of a pipe segment under progressively-increasing applied loading or induced deformation is essentially governed by a combination of the nonlinearity of the change in stiffness of the overall structure and, if applicable; as with plastic buckling, the nonlinear evolution of the material stress-strain response path. Inferences can, therefore, be made about the CLS trends with respect to the various investigated parameters based on either or both of the above fundamental factors: structural rigidity and material behavior.

The CLS- D/t ratio trends generally exhibit a negative nonlinear slope. The nonlinearity is however less evident in RHT pipes compared to YPT pipes. Also, the spread of the CLS- D/t ratio trends with respect to the internal pressure is smaller for RHT pipes compared to YPT pipes. The plots in Figure 8-7 and Figure 8-8, both obtained for X52 pipes, indicate a negligible difference in the CLS of YPT pipes and RHT pipes of the same material grade at zero ($f_p = 0.0$), low ($f_p = 0.2$) and intermediate ($f_p = 0.4$ and $f_p = 0.6$) pressure levels for intermediate D/t ratios (DT2 and DT3) and high D/t ratios (DT4). The difference in the CLS of the YPT pipe and the RHT pipe, however, becomes significant for a low D/t ratio (DT1). The effect of internal pressure on the CLS- D/t ratio trends of YPT pipes is more significant at a high pressure level ($f_p = 0.8$) compared to RHT pipes. It can, therefore, be inferred that the increase in bending rigidity which results from a higher internal pressure or a lower D/t ratio only has a significant effect on the deformational capacity if the internal pressure is sufficiently high or the D/t ratio is sufficiently low, especially for YPT pipes. The above assertion is less beneficial to RHT pipes due to the gradual strain-hardening transition of the material curve beyond the proportionality limit. Higher internal pressure and lower D/t ratio tend to shift the initiation of buckling farther along the material curve, away from the proportionality limit such that more plastification occurs in the pipe wall before local buckling. The farther the point along the material curve where buckling is initiated, the lesser the ratio of the tangential modulus to the elastic modulus and the higher the deformational capacity. However, the tangential modulus of the RHT curve is

generally only slightly less than the elastic modulus at the instance of buckling hence there is a small gain in the deformational capacity of RHT pipes compared to YPT pipes at zero, low and intermediate pressure levels, as well as for intermediate and high D/t ratios. Interestingly, the buckling responses of both material curve types exhibit a reversal in trends at high internal pressure or low D/t ratio. The sudden change in the slope of the YPT curve tends to cause a herein-called ‘flash’ initiation of buckling, however, high internal pressure or low D/t ratio introduces sufficient bending rigidity in the pipe causing a somewhat ‘snap-through’ buckling response characterized by recovery of the initial softening of the load-deformation response such that eventual collapse occurs at a much higher value of average longitudinal strain.

The assertions made in the above paragraph are further corroborated by the plots in Figure 8-9 and Figure 8-10. The $CLS-f_p$ trends in Figure 8-9 and Figure 8-10 are both obtained for X60 pipes with various D/t ratios. For YPT pipes of intermediate D/t ratios (DT2 and DT3) and high D/t ratios (DT4), there is no significant change in the CLS, except at pressure levels with $f_p > 0.6$. However, YPT pipes of low D/t ratio (DT1) exhibit a constant and significant increase in the CLS at all pressure levels. Unlike YPT pipes the $CLS-f_p$ trends of RHT pipes are characterized by a positive nonlinear, but gradual, slope indicating a small effect of internal pressure on the deformational capacity of RHT pipes at all pressure levels. Also, the $CLS-f_p$ trend for a low- D/t ratio (DT1) RHT pipe does not show any marked difference from the $CLS-f_p$ trends at higher D/t ratios (DT2, DT3, and DT4) indicating a small effect of D/t ratio on the deformational capacity of RHT pipes.

The ‘flash’ buckling phenomenon associated with YPT pipes makes it possible for smooth trends of the CLS to be plotted against the yield stress since buckling is primarily initiated at the same value of yield stress and corresponding strain for materials of the same grade. Variations in the CLS of same-grade YPT pipes may, however, be obtained at low D/t ratios as the initiation of buckling is likely to extend beyond the yield plateau of the material curve. The plots in Figure 8-13 show significant effects of the YPL and the internal pressure on the CLS of YPT pipes at a low D/t ratio (DT1). From Figure 8-13(a) it can be deduced that the benefit of a longer YPL on the CLS of YPT pipes continues to increase as the internal pressure increases, due to the combinational effect of the internal pressure and the D/t ratio on the bending rigidity of the pipe

segment. The effects of the YPL and internal pressures are depicted by the plots of the resultant moment vs. the average strain in Figure 8-21 and Figure 8-22 respectively.

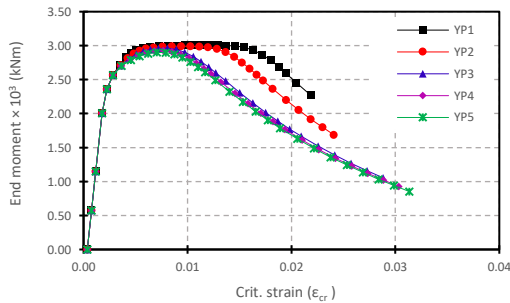


Figure 8-21: Resultant end moment vs. average compressive strain plot for X52-DT1 YPT pipe ($f_p=0.0$, $f_c=0.2$)

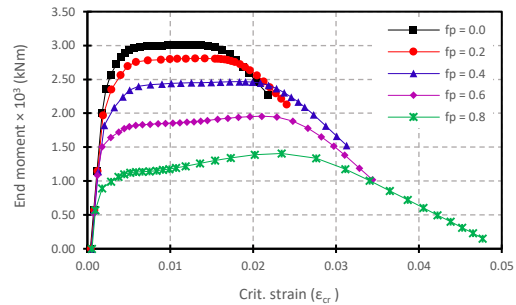


Figure 8-22: Resultant end moment vs. average compressive strain plot for X52-DT1 YPT pipe (YPL = 1.0%, $f_c=0.2$)

Figure 8-21 and Figure 8-22 indicate that at low internal pressure ($f_p = 0.0$), a shorter YPL facilitates initiation of buckling at the end of the yield plateau such that the pipe response can take advantage of the strain-hardening portion of the material curve. However, as the YPL gets longer, large plastic deformations are induced throughout the pipe's length without any increase in the stresses which might cause instabilities leading to a decrease in the CLS. The increase in the internal pressure reduces the moment capacity of the pipe segment but increases the pipe's deformational capacity such that initiation of buckling is more likely to be delayed until the strain-hardening portion of the material curve is attained, even with a considerable YPL. This implies that compressed regions along the pipe's length are able to sustain higher deformation before local buckling.

A lower PLUS ratio is generally observed to have a positive effect on the CLS of RHT pipes, and vice versa. A lower proportionality limit stress implies an earlier diversion from the linear elastic path of the material response such that the transition from the stiff elastic response to the slightly-less stiff plastic response translates to higher deformability. However, as indicated in Figure 8-14(a), the effect of the PLUS ratio on the CLS of various RHT pipes of the same material grade may diminish at high internal pressure ($f_p = 0.8$) and low D/t ratio (DT1). This is

attributed to the initiation of buckling closer to the yield stress which is characterized by the convergence of the various material curves with different PLUS ratios.

It can be inferred from the plots in Figure 8-15 and Figure 8-16 that increase in the magnitude of an applied net-section compressive force prior to inducement of curvature in a pipe speeds up the incidence of bifurcation instability, thus reducing the moment capacity and the corresponding compressive axial strain. The CLS values at $f_c = 0.0$ and $f_c = 1.0$ are expected to coincide with the CLS values obtained under uniform bending and uniform axial compression respectively; hence, the CLS- f_c trends in Figure 8-15 and Figure 8-16 can be inferred to correspond to the transition of the loading conditions from zero-compression bending state to a zero-bending compression state. The obtained results indicate that the ratio of the CLS under a zero-compression bending state to the CLS under a zero-bending compression state (herein referred to as the ‘bending-to-compression’, or BTC, ratio) ranges from about 1.1 to as high as 4.5, depending on the D/t ratio and internal pressure. For YPT pipes, lower BTC ratios are typically obtained under zero to moderate internal pressures ($0.0 \leq f_p \leq 0.6$) than at high internal pressures ($f_p = 0.8$). RHT pipes generally tend to have lower BTC ratios than YPT pipes and are not significantly affected by internal pressure variation. BTC ratios generally tend to be higher at lower D/t ratios.

8.9 Comparison of CLS Model with Experimental Results

The performance of the developed CLS models is evaluated using results of experiments, reported by Liu et al. [54], conducted independently by eight different researchers on the CLS of RHT pipes subjected to monotonically-increasing curvature under the additional influence of a net-section compressive axial stress. Details of the geometric properties, loading conditions, and material-specific input parameters are outlined in Table 8-5. Experimentally-obtained CLS values and model-predicted CLS values are also presented, indicating the respective test-to-predicted (TTP) ratio for each test. The CLS and TTP predictions of the original model are respectively indicated in Table 8-5 by CLS (Orig) and TTP (Orig). The bias-correction procedure presented above was subsequently applied to the original model to produce better alignment of the linear equation of the scatter plot of the experimental vs. model-predicted CLS with the

diagonal of the graph. The CLS and TTP predictions of the corrected model are respectively indicated in Table 8-5 by CLS (Corr) and TTP (Corr).

Table 8-5: Evaluation of test-to-predicted ratios

1	2	3	4	5	6	7	8	9	10	11	12	13	14	15	16		
No.	Ref.	Grade	D/t	σ_{ys} (MPa)	Y/T	f_p	H_f	K/H	σ_a (MPa)	f_c	CLS (Expt.)	CLS (Orig)	TTP (Orig)	CLS (Corr)	TTP (Corr)		
1	[64]	X60	53.0	441	0.80	0.00	8.90	0.607	0.00	0.000	0.79	1.007	0.784	1.218	0.648		
2	[65]	X60	103.9	441	0.78	0.76	8.90	0.607	-89.14	0.493	0.57	0.659	0.865	0.550	1.037		
3		X60	103.9	441	0.78	0.75	8.90	0.607	-93.63	0.499	0.47	0.653	0.720	0.537	0.875		
4		X60	103.9	441	0.78	0.02	8.90	0.607	-187.36	0.478	0.27	0.564	0.479	0.366	0.737		
5		X60	103.9	441	0.78	0.77	8.90	0.607	-21.68	0.122	0.82	0.699	1.174	0.625	1.312		
6		X60	103.9	441	0.78	0.12	8.90	0.607	-110.32	0.297	0.26	0.583	0.446	0.404	0.644		
7		X60	103.9	441	0.78	0.77	8.90	0.607	-21.68	0.122	0.41	0.699	0.587	0.625	0.656		
8		X65	85.4	503	0.83	0.09	8.30	0.627	-112.12	0.251	0.57	0.654	0.871	0.540	1.055		
9		X60	103.9	476	0.84	0.11	8.90	0.607	-105.22	0.261	0.23	0.512	0.450	0.266	0.863		
10	[66]	X70	91.7	503	0.84	0.00	4.30	2.209	-105.18	0.216	0.52	0.625	0.832	0.484	1.075		
11		X70	91.7	503	0.84	0.19	4.30	2.209	-74.64	0.171	0.51	0.638	0.799	0.510	1.000		
12		X70	91.7	503	0.84	0.39	4.30	2.209	-44.11	0.117	0.71	0.667	1.064	0.565	1.256		
13	[67]	X70	95.2	503	0.90	0.00	4.30	2.209	-99.75	0.205	0.4	0.480	0.834	0.206	1.946		
14	[68]	X65	44.2	483	0.84	0.00	8.30	0.627	0.00	0.000	1.36	1.113	1.222	1.421	0.957		
15	[6]	X52	51.0	379	0.83	0.00	17.30	0.121	-101.83	0.281	1.1	1.098	1.001	1.393	0.790		
16		X52	51.0	379	0.83	0.35	17.30	0.121	-58.99	0.205	1.62	1.161	1.395	1.513	1.071		
17	[69]	X56	64.3	393	0.90	0.00	7.70	0.442	-105.73	0.273	0.92	0.806	1.142	0.831	1.107		
18		X56	64.3	393	0.90	0.41	7.70	0.442	-57.35	0.195	1.16	0.926	1.252	1.062	1.092		
19		X56	64.3	393	0.90	0.81	7.70	0.442	-8.96	0.057	2.13	1.193	1.785	1.575	1.352		
20		X52	51.0	379	0.83	0.00	17.30	0.121	-101.83	0.281	0.68	1.098	0.619	1.393	0.488		
21		X52	51.0	379	0.83	0.35	17.30	0.121	-58.99	0.205	1.26	1.161	1.085	1.513	0.833		
22		X52	51.0	379	0.83	0.71	17.30	0.121	-19.66	0.107	1.93	1.353	1.426	1.882	1.025		
23	[21]	X80	48.9	676	0.86	0.45	3.90	2.949	0.00	0.000	2.15	1.081	1.989	1.359	1.582		
												Mean	Mean				
												TTP	0.992	TTP	1.017		
												(Orig)		(Corr)			
												S-dev	S-dev				
												TTP	0.402	TTP	0.327		
												(Orig)		(Corr)			

The Y/T ratio was reported by Ref. [54] as the input parameter for strain-hardening. However, since the PLUS ratio is required for CLS estimation using the developed models, a simple assumption was made to derive the ratio of the proportionality limit stress to the ultimate stress (P/T ratio) by applying a constant ‘knockdown’ value (P/Y ratio) to the Y/T ratio. An optimization procedure was, therefore, employed to produce a mean TTP (Orig) ratio close to a value of 1.0 thereby producing a P/Y ratio equal to 0.834. Assumptions were also made to produce the model curve shape constants (H_f and K/H) based on values obtained from previous research [49] on the typical values of the shape constants for pipeline steels. The compression factor (f_c) was calculated by first determining the limit stress using the limit stress equations presented above, and then calculating the ratio of the applied net-section axial stress to the limit stress.

The mean value (0.992) and the standard deviation (0.402) of the TTP ratios obtained using developed model indicates a fairly-good estimation of the experimental CLS values, notwithstanding the several material-related assumptions that were made. As shown in Figure 8-23 and Figure 8-24, using the values of the original gradient ($G_{orig} = 1.9196$) and the original intercept ($I_{orig} = -0.7157$), corrects the original bias of the model prediction and improves the standard deviation of the TTP ratios from 0.402 to 0.327.

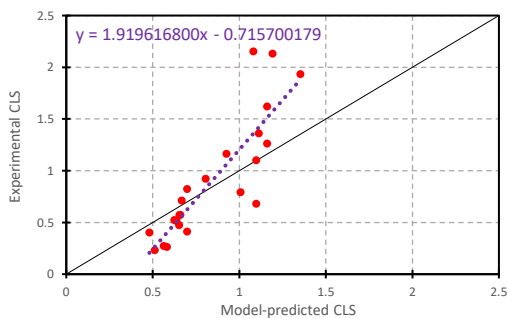


Figure 8-23: Model prediction vs. experimental CLS (original)

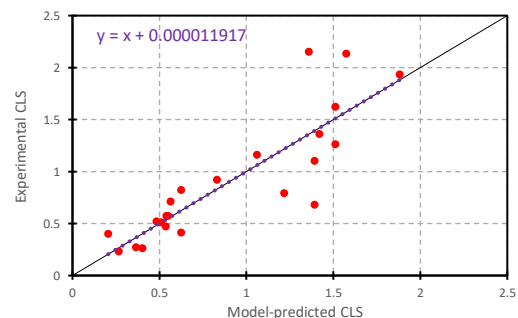


Figure 8-24: Model prediction vs. experimental CLS (corrected)

8.10 Conclusions

The numerical investigations performed in this study focused on estimating the critical strains associated with induced curvature, combined with uniform axial compression, in pressurized and unpressurized pipelines. A range of D/t ratios between 41.15 and 104.62, considered to be typical candidates for onshore pipeline applications [7], have been covered herein. Purely theoretical formulations for predicting the resultant stresses and bending moments in cylinders under induced curvature have been reviewed and deemed limited in applicability to analysis of buckling behavior in thin-walled cylinders, which typically undergo elastic buckling. Moreover, studies have shown that pipelines with D/t ratio less than 100 typically experience inelastic (or “plastic”) buckling [65,70] which is characterized by initiation of buckling in the pipe beyond the elastic limit of the material stress-strain response. The implication of nonlinearity in the material behavior is the associated complexity in estimating the moment-curvature response, thereby making the derivation of a solution to the buckling problem from first principles, based on fundamental mechanics theory, an arduous and often infeasible endeavor [27]. It, therefore, becomes imperative to resort to numerical computation techniques for estimating the resultant stress/moment and associated strain/curvature in pipes subjected to various loading phenomena. Computerized numerical analysis based on finite element discretization procedures has been employed for buckling analysis in this study as it offers an excellent and robust approach for simulating the buckling phenomena in pipe segments, and for tracking the development and up-to-collapse evolution of longitudinal wrinkles and cross-sectional flattening due to bifurcation or ovalization instabilities.

The test matrix for this study consists of four variations of the D/t ratio, five variations of the pressure factor (ratio of applied internal pressure to circumferential yield pressure), four variations of the material grade (YS), four variations (for RHT curves) or five variations (for YPT curves) of the material curve shape factor (comprising the two shape constants of the Ndubuaku material model), and four variations of the compression factor (ratio of the applied compressive stress to the limit stress of a similar pipe under uniform axial compression). A full-factorization testing approach was implemented to consider every possible combination of the investigated parameters, leading to extensive FE parametric analysis involving 1600 simulations for YPT pipes and 1280 simulations for RHT pipes. Visual observation of the graphical plots of

the critical limit strain (CLS) against the various parameters informed the development of appropriate mathematical expressions to characterize the influence of respective parameters on the pipe's deformational capacity, as well as to account for any observed significant interrelationships between the parameters.

In general, for both YPT pipes and RHT pipes, an inverse relationship is observed between the D/t ratio and the CLS while a direct relationship is observed between the pressure factor and the CLS. The yield stress directly correlates with the CLS of YPT pipes while the PLUS ratio exhibits a highly-nonlinear inverse correlation with the CLS of RHT pipes. At a low- D/t ratio, the relationship between the YPT shape factor (governed by the yield plateau length) and the CLS of YPT pipes varies from a negative relationship to a positive relationship, depending on the level of internal pressure. However, as the D/t ratio increases the effect of the shape factor on the CLS diminishes, as well as the indirect influence of the internal pressure on the CLS vs. YPT shape factor relationship. The CLS of RHT pipes is however observed to exhibit a generally-positive correlation with the RHT shape factor and, contrary to YPT pipes, more evidently at higher D/t ratios. The plot of the CLS features a negative shallow slope with respect to the compression factor; for both YPT pipes and RT pipes. The limit stress is negatively correlated with the D/t ratio and the internal pressure but positively correlated with the yield stress for both YPT pipes and RHT pipes. Typically, sudden transitions (as indicated in the YPT pipes) lead to instabilities and decrease in the CLS whereas more gradual transitions (as indicated in the RHT pipes), especially at lower PLUS ratios, leads to higher deformational capacities.

Four constitutive nonlinear regression equations (two equations for the CLS and two equations for the limit stress) were formulated, according to material curve shape classification, as an arithmetic product of the individual parameter functions. Advanced regression techniques were then employed, using Wolfram Mathematica, to derive the regression coefficients for the separate equations. An excellent goodness-of-fit between the model-predicted values and the FE-derived values, indicated by a high value (i.e., > 0.95) of the coefficient of multiple determination (R^2) was obtained for all four equations. Finally, a simple statistical bias-correction procedure was presented to apply a desired level of conservativeness to either of the two CLS models. The bias-correction procedure was applied for improving the CLS prediction of the developed models in comparison to a collection of experimental CLS values reported

independently by eight different researchers on the CLS of RHT pipes subjected to combined axial compression and bending.

The extensive and rigorous approach adopted for the parametric study in this paper fulfills the desire of the authors to develop a set of useful equations which, unlike any existing CLS prediction model, can be confidently and widely applied for strain-based design of pipelines subjected to combined axial compression and bending. The results obtained in this study indicate a significant variation in BTC ratios for different material classifications, pipe wall slenderness, and operating pressures; hence the prediction models presented herein are suitable for appropriate consideration of relevant input parameters to ensure better accuracy in the estimation of the CLS of pipe segments under combined axial compression and bending. Due to numerous uncertainties typically associated with the existence, form, and distribution of geometric imperfections in pipelines, explicit consideration of imperfection types has been omitted herein. However, the statistical procedure presented above provides a knockdown-factor avenue for including the effects of imperfections based on results of more elaborate statistical, and possibly probabilistic, assessment of real pipelines, or at the discretion of the designer.

8.11 References

- [1] Canadian Standards Association, Oil and gas pipeline systems. CSA-Z662-2007, (2007).
- [2] S. Kyriakides, C.D. Babcock, Experimental Determination of the Propagation Pressure of Circular Pipes, *J. Press. Vessel Technol.* 103 (1981) 328. doi:10.1115/1.3263410.
- [3] M.K. Yeh, S. Kyriakides, On the Collapse of Inelastic Thick-Walled Tubes Under External Pressure, *J. Energy Resour. Technol.* 108 (1986) 35. doi:10.1115/1.3231239.
- [4] E. Corona, S. Kyriakides, On the collapse of inelastic tubes under combined bending and pressure, *Int. J. Solids Struct.* 24 (1988) 505–535. doi:10.1016/0020-7683(88)90005-4.
- [5] A. Limam, L.-H. Lee, E. Corona, S. Kyriakides, Inelastic wrinkling and collapse of tubes under combined bending and internal pressure, *Int. J. Mech. Sci.* 52 (2010) 637–647. doi:10.1016/J.IJMECSCI.2009.06.008.
- [6] M.E. Mohareb, A.E. Elwi, G.L. Kulak, D.W. Murray, Deformation Behavior of Line Pipe, Structural Engineering Report No. 202, Edmonton, Alberta, 1994.

- [7] N. Yoosef-Ghodsi, I. Ozkan, Q. Chen, Comparison of Compressive Strain Limit Equations, in: Vol. 4 Prod. Pipelines Flowlines; Proj. Manag. Facil. Integr. Manag. Oper. Maintenance; Pipelining North. Offshore Environ. Strain-Based Des. Stand. Regul., ASME, 2014: p. V004T11A001. doi:10.1115/IPC2014-33182.
- [8] G.T. Ju, S. Kyriakides, Bifurcation and localization instabilities in cylindrical shells under bending—II. Predictions, *Int. J. Solids Struct.* 29 (1992) 1143–1171. doi:10.1016/0020-7683(92)90140-O.
- [9] C.S. Ades, Bending Strength of Tubing in the Plastic Range, *J. Aeronaut. Sci.* 24 (1957) 605–610. doi:10.2514/8.3916.
- [10] P. Tugcu, J. Schroeder, Plastic deformation and stability of pipes exposed to external couples, *Int. J. Solids Struct.* 15 (1979) 643–658. doi:10.1016/0020-7683(79)90077-5.
- [11] S. Gellin, The plastic buckling of long cylindrical shells under pure bending, *Int. J. Solids Struct.* 16 (1980) 397–407. doi:10.1016/0020-7683(80)90038-4.
- [12] J.L. Sanders, Nonlinear theories for thin shells, *Q. Appl. Math.* 21 (1963) 21–36. doi:10.1090/qam/147023.
- [13] S. Kyriakides, P.K. Shaw, Response and stability of elastoplastic circular pipes under combined bending and external pressure, *Int. J. Solids Struct.* 18 (1982) 957–973. doi:10.1016/0020-7683(82)90086-5.
- [14] E. Corona, L.-H. Lee, S. Kyriakides, Yield anisotropy effects on buckling of circular tubes under bending, *Int. J. Solids Struct.* 43 (2006) 7099–7118. doi:10.1016/J.IJSOLSTR.2006.03.005.
- [15] V.I. Weingarten, Effects of Internal Pressure on the Buckling of Circular-Cylindrical Shells Under Bending, *J. Aerosp. Sci.* 29 (1962) 804–807. doi:10.2514/8.9608.
- [16] H.S. Suer, L.A. Harris, W.T. Skene, R.J. Benjamin, The Bending Stability of Thin-Walled Unstiffened Circular Cylinders Including the Effects of Internal Pressure, *J. Aerosp. Sci.* 25 (1958) 281–287. doi:10.2514/8.7639.
- [17] R. Lorenz, Achsensymmetrische Verzerrungen in dünnwandigen Hohlzylindern, *Zeitschrift Des Vereines Dtsch. Ingenieure.* 52 (1908) 1706–1713.
- [18] S.P. Timoshenko, Einige stabilitäts probleme der elastizitäts theorie, *Zeitschrift Für Math. Und Phys.* 58 (1910) 337–385.

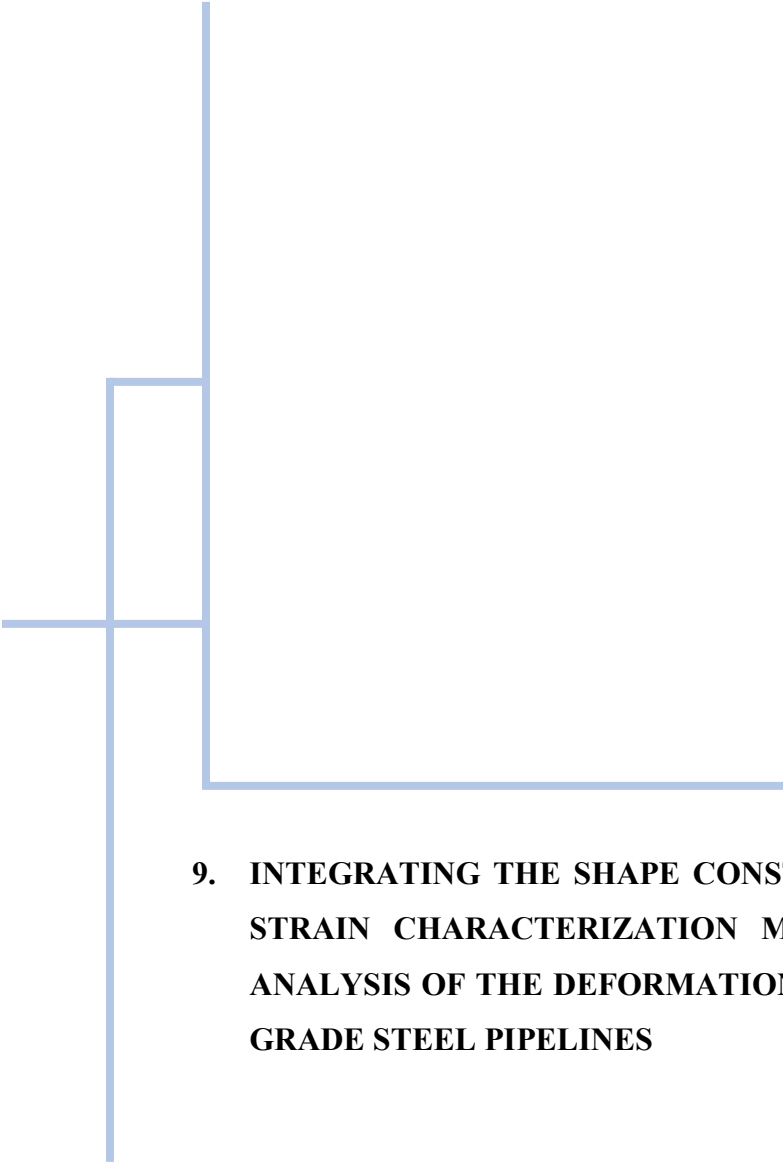
- [19] R. V. Southwell, On the General Theory of Elastic Stability, *Philos. Trans. R. Soc. A Math. Phys. Eng. Sci.* 213 (1914) 187–244. doi:10.1098/rsta.1914.0005.
- [20] A.M. Gresnigt, R.J. van Foeken, S.L. Chen, Effect of Local Buckling On Burst Pressure, in: *Sixth Int. Offshore Polar Eng. Conf.*, International Society of Offshore and Polar Engineers, Los Angeles, California, USA, 1996: pp. 80–88.
- [21] N. Suzuki, J. Kondo, N. Ishikawa, M. Okatsu, J. Shimamura, Strain Capacity of X80 High-Strain Line Pipes, in: *Vol. 3 Pipeline Riser Technol. CFD VIV*, ASME, 2007: pp. 475–483. doi:10.1115/OMAE2007-29505.
- [22] A. Limam, L.-H. Lee, E. Corona, S. Kyriakides, Plastic Buckling and Collapse of Tubes Under Bending and Internal Pressure, in: *Vol. 3 Pipeline Riser Technol. Ocean Sp. Util.*, ASME, 2008: pp. 675–683. doi:10.1115/OMAE2008-57986.
- [23] M.E. Mohareb, S.D.B. Alexander, G.L. Kulak, D.W. Murray, Laboratory testing of line pipe to determine deformational behavior, in: *Proc. 12th Int. Conf. Offshore Mech. Arct. Eng. Vol. 5*, ASME, Glasgow, UK, 1993: pp. 109–114.
- [24] N. Yoosef-Ghods, G.L. Kulak, D.W. Murray, Some test results for wrinkling of girth-welded line pipe, in: *Proc. 14th Int. Conf. Offshore Mech. Arct. Eng. Vol. 5*, ASME, Copenhagen, Denmark, 1995: pp. 379–387.
- [25] A.B. Dorey, D.W. Murray, J.J.R. Cheng, G.Y. Grondin, Z.J. Zhou, Testing and experimental results for NPS30 line pipe under combined loads, in: *Proc. 18th Int. Conf. Offshore Mech. Arct. Eng.*, ASME, St. Johns, Newfoundland, 1999: p. OMAE PL 99-5022.
- [26] A.B. Dorey, D.W. Murray, J.J.R. Cheng, An Experimental Evaluation of Critical Buckling Strain Criteria, in: *Vol. 1 Codes, Stand. Regul. Des. Constr. Environ. GIS/Database Dev. Innov. Proj. Emerg. Issues*, ASME, 2000: p. V001T01A011. doi:10.1115/IPC2000-110.
- [27] A.B. Dorey, D.W. Murray, J.J.R. Cheng, Critical Buckling Strain Equations for Energy Pipelines—A Parametric Study, *J. Offshore Mech. Arct. Eng.* 128 (2006) 248. doi:10.1115/1.2199561.
- [28] Zhou Z., Murray D. W., *Numeric Structural Analysis of Buried Pipelines*, Structural Engineering Report No. 181, Edmonton, Alberta, Canada, 1993.
- [29] L.T. Souza, D.W. Murray, *Prediction of Wrinkling Behaviour of Girth-Welded Line Pipe*, Structural Engineering Report No. 197, Edmonton, Alberta, Canada, 1994.

- [30] R. Bruschi, P. Monti, G. Bolzoni, R. Tagliaferri, Finite element method as numerical laboratory for analyzing pipeline response under internal pressure, axial load, bending moment, in: Proc. 14th Int. Conf. Offshore Mech. Arct. Eng. Vol. 5, ASME, Copenhagen, Denmark, 1995.
- [31] T.J.E. Zimmerman, M.J. Stephens, D.D. DeGeer, Q. Chen, Compressive strain limits for buried pipelines, in: Proc. 14th Int. Conf. Offshore Mech. Arct. Eng. Vol. 5, ASME, Copenhagen, Denmark, 1995.
- [32] S. Hauch, Y. Bai, Use of finite element analysis for local buckling design of pipelines, in: Proc. 14th Int. Conf. Offshore Mech. Arct. Eng., ASME, 1998.
- [33] L. Vitali, R. Bruschi, K.J. Mork, E. Levold, R. Verley, Hotpipe Project: Capacity of Pipes Subject to Internal Pressure, Axial Force And Bending Moment, in: Ninth Int. Offshore Polar Eng. Conf., International Society of Offshore and Polar Engineers, Brest, France , 1999: pp. 22–33.
- [34] S. Adeeb, J. Zhou, D. Horsley, Investigating the Effect of UOE Forming Process on the Buckling of Line Pipes Using Finite Element Modeling, in: Vol. 1 Proj. Manag. Des. Constr. Environ. Issues; GIS/Database Dev. Innov. Proj. Emerg. Issues; Oper. Maintenance; Pipelining North. Environ. Stand. Regul., ASME, 2006: pp. 169–174. doi:10.1115/IPC2006-10175.
- [35] A.B. Dorey, D.W. Murray, J.J.R. Cheng, Material Property Effects on Critical Buckling Strains in Energy Pipelines, in: 4th Int. Pipeline Conf. Parts A B, ASME, 2002: pp. 475–484. doi:10.1115/IPC2002-27225.
- [36] X. Liu, H. Zhang, O. Ndubuaku, M. Xia, J.J.R. Cheng, Y. Li, S. Adeeb, Effects of stress-strain characteristics on local buckling of X80 pipe subjected to strike-slip fault movement, J. Press. Vessel Technol. (2018).
- [37] W. Ramberg, W.R. Osgood, Description of stress-strain curves by three parameters, NACA Technical Note No. 902, Washinton, D.C., 1943.
- [38] M. Dundu, Evolution of stress-strain models of stainless steel in structural engineering applications, Constr. Build. Mater. 165 (2018) 413–423. doi:10.1016/J.CONBUILDMAT.2018.01.008.
- [39] M. Macdonald, J. Rhodes, G.T. Taylor, Mechanical properties of stainless metal lipped channels, in: 15th Int. Spec. Conf. Cold-Formed Met. Struct., University of Missouri-Rolla, Mo., 2000: pp. 673–686.

- [40] A. Olsson, Stainless steel plasticity – Material modelling and structural applications. Ph.D. thesis, Department of Civil and Mining Engineering, Lulea University of Technology, Sweden, 2001.
- [41] E. Mirambell, E. Real, On the calculation of deflections in structural stainless steel beams: an experimental and numerical investigation, *J. Constr. Steel Res.* 54 (2000) 109–133. doi:10.1016/S0143-974X(99)00051-6.
- [42] K.J.R. Rasmussen, Full-range stress-strain curves for stainless steel alloys, *J. Constr. Steel Res.* 59 (2003) 47–61. doi:10.1016/S0143-974X(02)00018-4.
- [43] L. Gardner, D.A. Nethercot, Experiments on stainless steel hollow sections—Part 1: Material and cross-sectional behaviour, *J. Constr. Steel Res.* 60 (2004) 1291–1318. doi:10.1016/J.JCSR.2003.11.006.
- [44] L. Gardner, M. Ashraf, Structural design for non-linear metallic materials, *Eng. Struct.* 28 (2006) 926–934. doi:10.1016/J.ENGSTRUCT.2005.11.001.
- [45] W.M. Quach, J.G. Teng, K.F. Chung, Three-Stage Full-Range Stress-Strain Model for Stainless Steels, *J. Struct. Eng.* 134 (2008) 1518–1527. doi:10.1061/(ASCE)0733-9445(2008)134:9(1518).
- [46] P. Hradil, A. Talja, E. Real, E. Mirambell, B. Rossi, Generalized multistage mechanical model for nonlinear metallic materials, *Thin-Walled Struct.* 63 (2013) 63–69. doi:10.1016/J.TWS.2012.10.006.
- [47] P. Zhang, M.S. Alam, Experimental investigation and numerical simulation of pallet-rack stub columns under compression load, *J. Constr. Steel Res.* 133 (2017) 282–299. doi:10.1016/J.JCSR.2017.02.023.
- [48] O. Ndubuaku, M. Martens, R. Cheng, A. Ahmed, S. Adeeb, A Novel Approach for True Stress-True Strain Material Characterization of Metallic Materials Using the Product-Log (Omega) Function, in: 6th Int. Conf. Eng. Mech. Mater., CSCE, May 31 - June 3, Vancouver, B.C., Canada, 2017.
- [49] O. Ndubuaku, M. Martens, J.J.R. Cheng, S. Adeeb, Expression of a Generic Full-Range True Stress-True Strain Model for Pipeline Steels Using the Product-Log (Omega) Function, in: Vol. 6B Mater. Fabr., ASME, 2017: p. V06BT06A050. doi:10.1115/PVP2017-65236.

- [50] O. Ndubuaku, X. Liu, M. Martens, J.J. Roger Cheng, S. Adeeb, The effect of material stress-strain characteristics on the ultimate stress and critical buckling strain of flat plates subjected to uniform axial compression, *Constr. Build. Mater.* 182 (2018) 346–359. doi:10.1016/j.conbuildmat.2018.06.100.
- [51] D. Hibbitt, B. Karlsson, P. Sorensen, *ABAQUS Standard User's and Reference Manuals, Version 6.14*, (2014).
- [52] American Petroleum Institute, *API 5L: Specification for Line Pipe*, 44th ed., American Petroleum Institute, USA, 2007.
- [53] EN 1993-1-4 2006, *Eurocode 3: Design of steel structures - Part 1-4: General rules - Supplementary rules for stainless steels*, CEN, Brussels, 2006.
- [54] M. Liu, Y.-Y. Wang, F. Zhang, K. Kotian, Realistic strain capacity models for pipeline construction and maintenance. Prepared for the US Department of Transportation. Pipeline and Hazardous Materials Safety Administration, Office of Pipeline Safety. Contract No. DTPH56-10-T-000016, Dublin, OH, USA, 2013.
- [55] M. Mohareb, G.L. Kulak, A. Elwi, D.W. Murray, Testing and Analysis of Steel Pipe Segments, *J. Transp. Eng.* 127 (2001) 408–417. doi:10.1061/(ASCE)0733-947X(2001)127:5(408).
- [56] X. Liu, H. Zhang, Y. Han, M. Xia, W. Zheng, A semi-empirical model for peak strain prediction of buried X80 steel pipelines under compression and bending at strike-slip fault crossings, *J. Nat. Gas Sci. Eng.* 32 (2016) 465–475. doi:10.1016/J.JNGSE.2016.04.054.
- [57] Wolfram Research Inc., *Mathematica, Version 11.3*, Champaign, IL, 2018.
- [58] S.C. Batterman, Plastic buckling of axially compressed cylindrical shells, *AIAA J.* 3 (1965) 316–325. doi:10.2514/3.2848.
- [59] E.T. Onat, Inelastic Instability and Incremental Theories of Plasticity, *J. Aeronaut. Sci.* 20 (1953) 181–186. doi:10.2514/8.2585.
- [60] L.H.N. Lee, Inelastic Buckling of Initially Imperfect Cylindrical Shells Subject to Axial Compression, *J. Aerosp. Sci.* 29 (1962) 87–95. doi:10.2514/8.9306.
- [61] M.J. Sewell, A general theory of elastic and inelastic plate failure—I, *J. Mech. Phys. Solids.* 11 (1963) 377–393. doi:10.1016/0022-5096(63)90016-4.

- [62] E. Ore, D. Durban, Elastoplastic buckling of axially compressed circular cylindrical shells, *Int. J. Mech. Sci.* 34 (1992) 727–742. doi:10.1016/0020-7403(92)90005-2.
- [63] J. Blachut, G.D. Galletly, S. James, On the Plastic Buckling Paradox for Cylindrical Shells, *Proc. Inst. Mech. Eng. Part C J. Mech. Eng. Sci.* 210 (1996) 477–488. doi:10.1243/PIME_PROC_1996_210_221_02.
- [64] D.R. Stephens, R.J. Olson, M.J. Rosenfeld, Pipeline Monitoring - Limit State Criteria, NG-18 Report No. 1888, Battelle, Columbus, Ohio., 1991.
- [65] J.G. Bouwkamp, R.M. Stephen, Full-scale studies on the structural behavior of large diameter pipes under combined loading. Report No. UCSESM 74-1, Berkeley, California, 1974.
- [66] P.R. DelCol, G.Y. Grondin, J.J.R. Cheng, D.W. Murray, Behavior of Large Diameter Line Pipe Under Combined Loads, Structural Engineering Report No. 224, Edmonton, AB, Canada, 1998.
- [67] C.Q. Chen, Local Buckling and Collapse of Corroded Pipes, PR-244-9827, 2008.
- [68] R.J. V. Foeken, A.M. Gresnigt, Buckling and Collapse of UOE Manufactured Steel Pipes, PR-238-9423, 1998.
- [69] N. Yoosef-Ghodsi, G.L. Kulak, D.W. Murray, Behavior of Girth-welded Line Pipe, Structural Engineering Report No. 203, Edmonton, Alberta, 1994.
- [70] D.R. Sherman, Test of Circular Steel Tubes in Bending, *J. Struct. Div.* 102 (1976) 2181–2195. <http://cedb.asce.org/CEDBsearch/record.jsp?dockey=0007059> (accessed October 29, 2018).



9. INTEGRATING THE SHAPE CONSTANTS OF A NOVEL MATERIAL STRESS-STRAIN CHARACTERIZATION MODEL FOR PARAMETRIC NUMERICAL ANALYSIS OF THE DEFORMATIONAL CAPACITY OF HIGH-STRENGTH X80-GRADE STEEL PIPELINES

This chapter is derived from a research article submitted for publication in the MDPI Applied Sciences journal.

9.1 Abstract

Pipelines typically exhibit significant inelastic deformation under various loading conditions, especially when subjected to displacement-controlled loading, as is the case when impacted by significant ground movement. It is therefore imperative for the limit state design of pipelines to include considerations for the deformational capacity of pipelines. The morphology of API-X80 grade line pipe steel is essentially characterized by an acicular ferrite microstructure consisting of grouped domains of bainite and dispersions of martensite/austenite (MA). The methods employed to achieve higher strength of API X80 line pipe steels during the plate manufacturing process tend to increase the hardness of the pipe material, howbeit at the cost of ductility and strain hardenability. This study features a simple and robust material model which is able to account for very slight variations in the stress-strain relationship of metallic materials and is able to mathematically characterize the shape of the stress-strain curve, even for materials with a distinct yield point and an extended yield plateau. Extensive parametric finite element analysis is performed to study the relationship between relevant parameters and the deformational capacity of API X80 pipelines subjected to uniform axial compression, uniform bending, and combined axial compression and bending, and the constitutive material model constants are included as dimensionless parameters. Nonlinear regression analysis is then employed to develop six nonlinear semi-empirical equations for the critical limit strain corresponding to the three loading conditions considered for each of two material classifications (i.e., yield-plateau type materials and round-house type materials). The goodness-of-fit of the developed equations was statistically evaluated, and excellent predictive accuracy was obtained for all six equations.

Nomenclature

ε	true strain
ε_{cr}	critical limit strain
ε_{pl}	corresponding strain at proportionality limit stress of Ndubuaku model
ε_R	Ndubuaku model strain ratio
ε_{up}	corresponding strain at ultimate proof stress of Ndubuaku stress-strain model

E	Young's modulus of elasticity
f_c	compression factor (ratio of applied compressive stress to pipe's limit stress)
f_p	pressure factor (ratio of applied pressure to pipe yield pressure)
h	Ndubuaku model heel constant
k	Ndubuaku model knee constant
μ	Poisson's ratio
n	Ramberg-Osgood strain-hardening exponent
OD	pipe's outer diameter
p	applied internal pressure
p_y	pipe's circumferential yield pressure
r	pipe's cross-sectional radius
$\sigma_{0.5}$	0.5% total strain proof stress
σ	true stress
σ_c	applied compressive stress
σ_c	pipe's maximum compressive stress capacity (limit stress)
σ_{pl}	proportionality limit stress of Ndubuaku stress-strain model
σ_R	Ndubuaku model stress ratio
σ_{up}	ultimate proof stress of Ndubuaku stress-strain model
σ_{us}	ultimate tensile stress of pipe material
σ_{ys}	yield stress of pipe material
sh_f	material curve shape factor
t	pipe's wall thickness
CLS	Critical limit strain
D/t ratio	Ratio of pipe's outer diameter to pipe's wall thickness
$PLUS$ ratio	Ratio of proportionality limit stress to ultimate tensile stress
RHT	Round-house type
SBD	Strain-based design
UTS	Ultimate tensile stress

<i>YPL</i>	Yield plateau length
<i>YPT</i>	Yield-plateau type
<i>YS</i>	Nominal yield stress
<i>Y/T ratio</i>	Ratio of yield stress to ultimate tensile stress

9.2 Introduction

Pipelines are commonly used as the primary means for transmission of hydrocarbon fluids in the energy industry, and for transportation of water resources in the public utility industry. Previous investigations into the main causes of damages and loss of mechanical and structural integrity in pipelines have highlighted the detrimental impacts of geological conditions or environmental actions associated with various time-dependent thermomechanical phenomena such as ground subsidence, soil liquefaction/land sliding, discontinuous frost heave/thaw settlement, fault movement due to seismic action, etc. [1–3]. Large displacements tend to induce significant strains in the wall of pipe segments which may ultimately result in the failure of a pipeline either due to tensile rupture, especially at welded regions, or due to bulging/wrinkling deformation of the pipe under the influence of compressive stresses [4–6]. As a result of the inevitable requirement for pipelines to traverse large geographical areas, a majority of pipelines in the onshore energy and public utility industry are installed below the soil surface. It is observed that, compared to above-ground pipelines, the mechanical behavior of buried pipelines is significantly influenced by the geophysical properties of the surrounding soil; hence, the intricacies of the mutual interaction between the pipe and the surrounding soil are regarded as an important consideration in the design of buried continuous pipelines [7–10].

The common consequence of ground movement and thermal buckling deformation on pipelines is the experience of high longitudinal stresses and strains. Conventional pipeline design procedures are generally based on an “*allowable stress*” concept which aims to limit the resultant longitudinal and circumferential stresses in pipelines, either due to load-controlled or displacement-controlled conditions, to a prescribed fraction of the yield stress of the pipe material. Unfortunately, the allowable stress design (ASD) approach tends to be severely limited by its inability to distinguish between stable and unstable failure modes, as well as between loss

of serviceability and loss of containment [11]. A strain-based design (SBD) approach has therefore been regarded as more appropriate, and has been recently more adopted, by various pipeline design standards (e.g., API RP 1111 [12], DNV-OS-F101 [13], ABS 2006 [14], CSA Z-662 [15]) for design of pipelines expected to experience high longitudinal strains caused by displacement-controlled environmental and operational conditions in service [16,17]. SBD circumvents the inherent conservativeness of the ASD approach by permitting a limited amount of plastic strain while maintaining relevant ultimate and serviceability limit state considerations. However, rather than consider the SBD and ASD approaches as independent techniques, best design practice recommends the application of SBD as a complementary tool to the more traditional ASD procedure [18]. SBD employs a limit state design approach whereby the in-service longitudinal tensile or compressive strain that a pipeline is expected to experience due to displacement-controlled loading conditions (i.e., strain demand) is evaluated and compared to the tolerable limit of strain which the pipeline has intrinsic ability to withstand (i.e., strain capacity). Estimation of strain demand in pipelines typically involves a rigorous and often complex process which requires all-inclusive consideration of numerous interrelating factors related to environmental, geological, and the pipe's mechanical properties. The strain demand is also highly dependent on a number of peculiar, and sometimes transient, environmental conditions making the development of deterministic prediction models difficult and often necessitating the use of probabilistic and reliability-based estimation techniques for the SBD [19,20]. Unlike strain demand, evaluation of the strain capacity is essentially based on the inherent mechanical resistance of the pipe segments and has relatively less dependency on external factors hence, analytical evaluation and deterministic prediction of strain capacity is thus relatively more straightforward as parameterization of influencing factors for incorporation in the SBD is relatively less complicated.

Extensive studies have been conducted by numerous researchers to investigate the limit load instability and deformational capacity of pipe segments, and cylindrical shells in general, subjected to various loading conditions. The earliest recorded investigations on the buckling behavior of pipe segments were analytical studies performed by Lorenz [21], Timoshenko [22] and Southwell [23] at the inception of the 20th century, which focused on deriving constitutive theoretical formulations for predicting the elastic critical buckling stress of perfect isotropic

cylindrical shells subjected to pure axial compression; known as the classical shell buckling theories. Subsequent experimental and analytical studies [24–28] pointed out some shortcomings of the classical shell buckling theories and prescribed the extension of the classical equations to include nonlinear large-deflection considerations, as well as adequate characterization of material, geometric, and boundary characteristics. An analytical study by Brazier [29] on the circumferential flattening mode of distortion (referred to as “*ovalization*” or “*Brazier instability*”) observed in an infinitely long, circular tube subjected to pure bending led to the derivation of an expression for the limit moment. Brazier’s theory is based on the relationship between the strain energy per unit tube length and the change in axial curvature such that the limit moment is directly related to the ovalization of the circular tube. Subsequent experimental studies [30–33] however indicate that bifurcation instability (buckling) in the form of longitudinal wrinkling or bulging may precede the limit moment in pipes subjected to bending due to increase in axial stress on the compression side of the pipe. Corona and Kyriakides [34] explained that bifurcation instability is more likely to precede *Brazier* instability in “thinner” tubes, and vice versa in “thicker” tubes. They further speculated that the transition between one preceding instability phenomenon and the other occurs in the range of D/t (diameter/thickness) ratios between 35 and 45. Mathon and Limam [35] performed statistical evaluation of results obtained from (1) experimental tests of circular tubes under pure bending [36], (2) empirically-derived analytical formulations for cylinders under combined axial compression and bending [37], and (3) semi-empirical derivation of the critical buckling stress for pressurized circular tubes subjected to uniform bending [38]. They observed that the critical buckling stress of cylinders under pure bending is generally between 20 to 60% higher, depending on the diameter-to-thickness ratio (D/t ratio), than that of cylinders under pure axial compression.

Using a special-purpose non-linear finite element technique, Houliara and Karamanos [39] studied the structural stability of long uniformly pressurized thin elastic tubular shells subjected to in-plane bending. They observed that external overpressure reduces the buckling moment and corresponding curvature but increases the buckling wavelength, whereas internal overpressure tends to increase the buckling moment but reduce the cross-sectional ovalization and the buckling wavelength. Following a systematic series of experiments and by Limam et al. [40] involving stainless steel tubes bent to failure at fixed values of internal pressure, it was shown

that cross-sectional ovalization and circumferential extension occur simultaneously due to bending and internal pressure respectively. Ref [40] also performed computational simulation of the evolution of wrinkling and its eventual localization using a finite element (FE) shell model and observed that internal pressure tends to stabilize the structure and increase the wavelength of the wrinkles while also shifting the initiation of buckling towards the plastic range of the material. Ref [40] indicate that accurate simulation of the structural stability of tubular shells requires accurate characterization of the nonlinear inelastic properties of the material stress-strain behavior, including yield anisotropies, as well as adequate representation of initial geometric imperfections. Highlighting the significant effect of the material properties on the moment-curvature relationship, Ref [34] established that for pipes with D/t ratios less than 200, the mechanical and structural instabilities of the structure are strongly influenced by the interaction of the induced ovalization and the plastic/nonlinear characteristics of the material.

This study focuses on the deformational capacity of high-strength API-X80 [41] grade pipelines subjected to various loading conditions. The continuous increase in world energy demand has compelled the hydrocarbon industry to venture into more remote and more environmentally hostile environments in search of fossil fuels. This predicament necessitates the construction and operation of pipelines with the best possible transport efficiency and at the lowest possible cost, therefore initiating a tendency towards using line pipes of larger diameter and/or maintaining higher operational pressures. High-strength steel grades provide the advantage of forming line pipes with high material yield strength thus reducing the wall thickness requirement for internal (or external in the case of deep to ultra-deep offshore environments) pressure containment [42]. Suzuki and Toyoda [43] explained that the peak moment strain, and invariably the deformational capacity of line pipes is strongly influenced by the strain-hardening characteristics of the pipe material. In a numerical study of API-X100 line pipes subjected to axial compression and/or bending moment, Suzuki et al. [44] pointed out that high-strength pipe steels tend to have inferior strain hardening properties, and consequently lower deformational capacity, compared to conventional pipeline steels of lower yield strength. However, results of a few experimental studies have shown that by carefully manipulating the thermomechanical control processes (TMCP) of slab reheating, rolling and cooling during the manufacture of parent steel plates, the

microstructural and mechanical properties of steel can be adjusted to produce line pipe steels with improved deformability, toughness, and resistance to strain-aging [45–47].

Kong et al. [48] explained that the basic morphology of most high-strength pipeline steels is a multiphase structure composed of ferrite, bainite, and martensite. While bainite and martensite ingredients naturally improve the strength and hardness of line pipe steel, ductile and plastic deformation capacities tend to be compromised. Also, variability in manufacturing processes of parent steel plates makes it inevitable for line pipes of the same grade classification to exhibit slight differences in material properties [49,50]. While manufacturing variability may be regarded as the primary cause of differences in the strain-hardening characteristics of materials with the same grade classification, other factors such as strain aging have also been observed to cause significant alteration of the material properties leading to higher yield strength but lower deformational capacity [51]. Moreover, it has been established that the buckling response of pipes is highly sensitive to the material behavior, especially in the nonlinear range of the stress-strain relationship; hence it is imperative that the mathematical model that serves for characterization of the material stress-strain relationship should simultaneously provide reasonable simplicity and representative accuracy. Recent studies by Ndubuaku et al. [52–54] have led to the development of a novel stress-strain expression, referred to as the ‘Ndubuaku model’, which has proven to be exceptionally convenient and effective for parameterizing the true stress-true strain relationship of any metallic material with a non-negative gradient throughout the stress-strain curve; including materials with a distinct yield point and an extended yield plateau. The ‘Ndubuaku model’ approximates the material stress-strain curve over the full range of strains using only two constitutive model constants (or ‘shape’ constants) referred to as the ‘knee’ constant and the ‘heel’ constant.

The bifurcation instability phenomenon in tubular shells typically presents as a multivariate problem involving a number of influencing parameters with complex inter-relationships, thus rendering the development of purely analytical formulations for the estimation of the limit stress/moment and deformational capacity of pipes a rigorous and highly-complicated process [55]. In view of this, the procedures implemented in this study for estimating the peak moment strain (i.e., the average strain corresponding to the peak value of the moment on the moment-curvature curve) and the compressive limit strain (i.e., the average strain corresponding to the

peak value of the compressive stress on the axial load-end shortening curve) take a cue from the semi-empirical modelling approach adopted by various prominent pipeline design standards [12–15]. A tubular FE shell model was created for this study using the general-purpose finite element package, ABAQUS CAE [56], and subjected to three different loading conditions: uniform axial compression, uniform bending, and combined axial compression and bending. To obtain the buckling response of the pipe models to combined axial compression and bending, a four-level variation of a constant uniform axial stress was initially applied to the ends of the pipe model followed by a monotonically-increasing rotation of the pipe ends to simulate the bending deformation. Four and five variations of the D/t ratio and applied internal pressure respectively were also applied to the pipe models. The ‘Ndubuaku model’ was used to create two sets of stress-strain curves according to the two main classifications of stress-strain curves for metallic materials, i.e., round-house type (RHT) curves and yield-plateau type (YPT) curves. Four and five variations of RHT and YPT curves respectively were created so that the numerical analyses performed in this study culminated in a total of 1080 separate FE runs; 180 runs for uniform axial compression, 180 runs for uniform bending, and 720 runs for combined axial compression and bending. Advanced nonlinear regression techniques were subsequently employed to develop mathematical expressions for predicting the critical limit strain (CLS) for each loading condition using a powerful computational package, Wolfram Mathematica [57]. The strain-hardening peculiarities of the stress-strain curves were parameterized by the model ‘shape’ constants of the ‘Ndubuaku model’ and incorporated in the derived semi-empirical models.

9.3 Characterization of Material Stress-Strain Behavior

The ‘Ndubuaku model’ was adopted in this study to adequately capture the slight variations that are generally observed to exist in the stress-strain response of metallic materials. The mathematical form of the material model derives the true stress (σ) as a function of the true strain (ϵ) using two ‘shape’ constants, the “knee” constant (k_{nm}) and the “heel” constant (h_{nm}):

$$\sigma = \begin{cases} E\varepsilon & \sigma \leq \sigma_{pl} \\ \sigma_{pl} + (\sigma_{up} - \sigma_{pl}) \left(\frac{\varepsilon - \varepsilon_{pl}}{\varepsilon_{up} - \varepsilon_{pl}} \right)^{k_{nm}} & \sigma > \sigma_{pl} \end{cases} \quad (9-1)$$

where E is Young's modulus of elasticity, σ_{pl} and ε_{pl} are the proportionality limit stress and the proportionality limit strain respectively, and the ultimate proof stress and corresponding ultimate proof strain are represented by σ_{up} and ε_{up} respectively. The first part of Eq. (9-1) represents the linear (elastic) portion of the stress-strain curve where the relationship between the stress and the strain is simply defined by the elastic modulus, E , while the second part characterizes the entire nonlinear portion of the stress strain curve, beginning at the proportionality limit stress (PLS) and terminating at the nominal ultimate proof stress (UPS).

The 'Ndubuaku model' is easily applicable for generating any desired number of idealized strain curves by simply specifying two stress control points (σ_{c1} and σ_{c2}) and corresponding strain control points (ε_{c1} and ε_{c2}) according to the following expressions [54]:

$$k_{nm} = \frac{\varepsilon_{R1}^{(h_{nm})} \ln(\sigma_{R1})}{\ln(\varepsilon_{R1})} \text{ or } \frac{\varepsilon_{R2}^{(h_{nm})} \ln(\sigma_{R2})}{\ln(\varepsilon_{R2})} \quad (9-2)$$

$$h_{nm} = \frac{\ln \left[\frac{\ln(\varepsilon_{R1}) \cdot \ln(\sigma_{R2})}{\ln(\sigma_{R1}) \cdot \ln(\varepsilon_{R2})} \right]}{[\ln(\varepsilon_{R1}) - \ln(\varepsilon_{R2})]} \quad (9-3)$$

where,

$$\sigma_{R1} = \frac{\sigma_{c1} - \sigma_{pl}}{\sigma_{up} - \sigma_{pl}}, \quad \sigma_{R2} = \frac{\sigma_{c2} - \sigma_{pl}}{\sigma_{up} - \sigma_{pl}}, \quad \varepsilon_{R1} = \frac{\varepsilon_{c1} - \varepsilon_{pl}}{\varepsilon_{up} - \varepsilon_{pl}}, \quad \text{and} \quad \varepsilon_{R2} = \frac{\varepsilon_{c2} - \varepsilon_{pl}}{\varepsilon_{up} - \varepsilon_{pl}}$$

To ensure conformity with API 5L [41] specifications for X80 grade line pipe steels, the material model was employed such that all the stress-strain curves for this study (shown in Figure 9-1) are characterized by the same nominal yield stress and nominal ultimate proof stress but different strain-hardening properties.

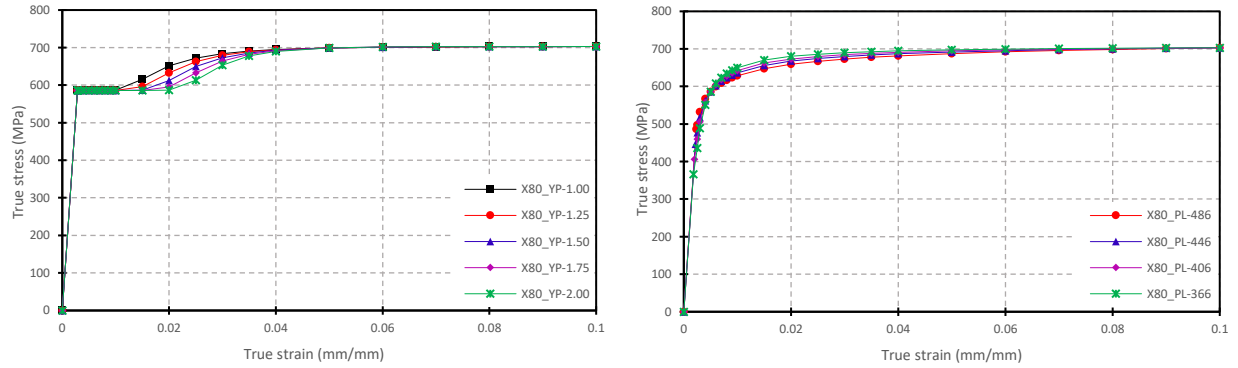


Figure 9-1: Idealized variations for stress-strain curves of (a) X80-YPT, and (b) X80-RHT materials

As indicated by the plots in Figure 9-1, the nominal yield stress (586 MPa) was maintained at the stress corresponding to a total strain of 0.5% (i.e., $\sigma_{0.5}$) while the nominal ultimate proof stress (703 MPa) was maintained at the stress corresponding to a total strain of 10% (i.e., σ_{10}). The value of the elastic modulus was selected as 205800 MPa. The strain-hardening for the YPT materials was varied by simply changing the yield plateau length (YPL) of the stress-strain curves while the various strain-hardening properties of the RHT curves were obtained by adjusting the proportionality limit stress (PLS) of the stress-strain curves. The numeric designations of the elements of the graph legends for the stress-strain curves in Figure 9-1(a) and Figure 9-1(b) represent the YPL and the PLS respectively. The YPLs are defined in terms of the total strain in percentage (%) units while the PLSs are defined in megapascal (MPa) units.

The constitutive model constants which define the shapes, and invariably the strain-hardening characteristics, of the generated stress-strain curves are presented in Table 9-1.

Table 9-1: Model shape constants for the derivation of stress-strain curves

<i>YPT</i>			<i>RHT</i>		
<i>Curve label</i>	$K_f = 1/K_{NM}$	$H_f = 1/H_{NM}$	<i>Curve label</i>	$K_f = 1/K_{NM}$	$H_f = 1/H_{NM}$
<i>YP-1.00</i>	83.7395	0.5187	<i>PL-486</i>	11.5448	3.9814
<i>YP-1.25</i>	115.2048	0.4221	<i>PL-446</i>	21.1099	2.7531
<i>YP-1.50</i>	162.9859	0.3510	<i>PL-406</i>	35.3391	2.1374
<i>YP-1.75</i>	240.2443	0.2953	<i>PL-366</i>	69.2445	1.5847
<i>YP-2.00</i>	374.3178	0.2501			

For better representation of the shape constants two new designations, the ‘knee’ factor (K_f) and the ‘heel’ factor (H_f), are defined in Table 9-1 as inverse functions of the ‘knee’ constant, K_{nm} , and the ‘heel’ constant, H_{nm} , respectively.

9.4 Methodology of Numerical Analysis

Pipelines made of API X80-grade line pipe steel were numerically simulated in this study using a tubular FE shell model developed with ABAQUS/Standard in order to study the stability of steel pipelines when subjected to uniform axial compression, uniform bending, or combined axial compression + bending. The parameters investigated in the FE study were selected according to three factors considered to be most influential to the buckling response and respective limit strains of tubular shell structures, i.e., the dimensional factor (related to the D/t ratio), the load factor (related to internal or external overpressure), and the strain-hardening factor (related to shape of stress-strain curve). Four variations of the D/t ratio were specified thus: DT1 = 41.152, DT2= 64.078, DT3 = 82.156 and DT4 = 104.622. The D/t ratio was varied by maintaining the pipe’s outer diameter (OD) at a constant nominal pipe size (NPS) of 36 inches (914.4 mm) and respectively changing the wall thickness of the pipe models thus: $t_1 = 22.22$ mm (for DT1), $t_2 = 14.27$ mm (for DT2), $t_3 = 11.13$ mm (for DT3), and $t_4 = 8.74$ mm (for DT4). In addition to non-

pressurized conditions, four levels of internal pressure corresponding to 20%, 40%, 60% and 80% of the yield pressure in the circumferential direction were applied to the pipe models. To properly account for the influence of the material's strain-hardening properties on the CLS, three material-related parameters each were derived for both YPT curves and RHT curves. The two parameters obtained for both RHT and YPT pipes comprised the two model 'shape' constants (K_{nm} and H_{nm}) while the yield plateau length (YPL) was applied as the third parameter for YPT pipes and the ratio of the PLS to the UPS (herein referred to as the "PLUS" ratio) were considered as the third parameter for RHT pipes.

The pipe geometry was modeled as a 3D deformable shell structure, and for computational efficiency, symmetric boundary conditions were applied in the longitudinal and transverse directions of the pipe so that only a quarter of the full pipe specimen (half of the specified length and half of the circumference) was modeled. The numerical analysis procedure conducted in this study is a geometric and material nonlinear type; hence, the boundary conditions applied to create the X- and Z-symmetries for the assumed quarter models are able to provide an accurate representation of the actual response of the full pipe models. With the application of the Z-symmetry boundary condition (symmetry across the X-Y plane), the quarter pipe models were therefore extruded to three times the pipe diameter ($3.0 \cdot D$). The assigned length of the pipe model was selected according to the recommendations of Liu et al. [58] to ensure that there are no interactions between the end boundary conditions and the strain and stress distribution at the pipe mid-length where initiation of local buckling deformation is expected to occur. At the loading end of the pipe model (i.e., the end where the rotation or axial displacement was applied), a reference point was created at the center of the pipe cross-section and restrained such that only translation along the Z-axis was allowed for uniform axial compression, and rotation about the X-axis plus translation along the Z-axis was allowed for uniform bending and combined axial compression + bending. A kinematic coupling constraint was then assigned for connecting the nodes at the loading end to the reference point to allow the end of the pressurized pipe to expand in the radial direction throughout the applied loading. The kinematic coupling constraint was defined in the cylindrical coordinate system to permit only one degree of freedom, i.e., circumferential extension, thereby inducing in a uniform stress field and consequently facilitating the initiation of buckling at the mid-length cross-section of the pipe segment.

The four-node reduced integration shell elements (S4R) with hourglass control in the ABAQUS element library were used for all the analyses; enabling up to five integration points through the thickness of the pipe models. The S4R elements are suitable for the analysis of thin to moderately thick shell structures with material and geometric nonlinearities. A mesh convergence study was conducted to establish the optimum number of elements required for the FE simulation, and a mesh size approximately equal to 3% of the pipe diameter ($0.03 \cdot D$) was applied respectively to all the FE pipe models. A large-strain von Mises plasticity model with isotropic hardening was applied to the line pipe steel material. Calibration of the material response is assumed to be related to the true stress vs. true strain relationship from a uniaxial tensile test performed on a coupon specimen of the pipe materials hence respective stress-strain curves were assigned to the pipe models using the standard multilinear material definition facility in ABAQUS.

For the three different loading conditions considered in this study, two loading steps (an initial load-controlled step followed by a displacement-controlled step) were defined in addition to the default “Initial” step in ABAQUS CAE for each simulation. To adequately track the nonlinear equilibrium path of deformation at the reference critical portions of the pipe segment, recording of the resultant moment and resultant compressive force, as well as the corresponding limit strains, was performed at the displacement-controlled stage of each simulation. The first loading step was defined as a “Static General” step which is performed based on the default “Newton’s method” iterative solution technique in ABAQUS. The second step for each run was defined as a “Static Riks” step which executes an equilibrium iterative procedure combined with a linearized arc-length control technique for sufficiently evaluating the buckling and post-buckling responses of the simulation process. In the initial load-controlled step of the simulation for uniform axial compression, specified levels of internal pressure were applied to the pipe models while a monotonically-increasing uniform axial displacement was applied to the loading-end reference point in the following displacement-controlled step. Internal pressure was applied in the load-controlled step for uniform bending while a monotonically-increasing rotation was subsequently applied to the loading-end reference point in the “Static Riks” step. For the load-controlled phase of the combined axial compression and bending, a finite compressive axial force was applied to the loading-end reference point while respective percentages of the circumferential yield

pressure were simultaneously applied to the internal surface of the pipe models. A monotonically-increasing rotation was then applied to the loading-end reference point in the second step. For combined axial compression + bending, the compressive axial force applied to the pipe prior to the monotonically-induced curvature was measured as respective percentages (20%, 40%, 60%, and 80%) of the peak force under uniform axial compression.

For uniformity of estimation, the same measurement scheme was employed to determine the average values of compressive strain in the pipe models. The measurement scheme was defined with reference to the pipe model under uniform bending by evaluating the average value of the compressive strain of all the meshed elements on the compressive side of the pipe model. The measurement area was selected immediately adjacent to both the Z -symmetry plane and the X -symmetry plane, and corresponded to a longitudinal distance of one times the pipe diameter ($1.0 \cdot D$) and a circumferential distance of approximately one-quarter of the pipe diameter ($0.25 \cdot D$) respectively (shown in Figure 9-2). The measurement scheme for the average compressive strain is adopted for this study in line with the recommendations of Liu et al. [58]. The critical limit strain was derived from the results of the individual FE runs in this study based on a “peak load criterion” [59] which regards the “critical” value as the resultant compressive longitudinal strain measured at the onset of local buckling, and is derived as the average strain that corresponds to the onset of “softening” in the load-deformation response (i.e., the X - Y plot of the average compressive strain on the X -axis versus the loading-end reaction moment or the loading-end reaction force on the Y -axis). A cylindrical coordinate system (with the origin at the center of the pipe cross-section) was assigned to the pipe model for obtaining the average longitudinal strains while the loading-end reaction moment and the loading-end reaction force were obtained in the default Cartesian coordinate system.

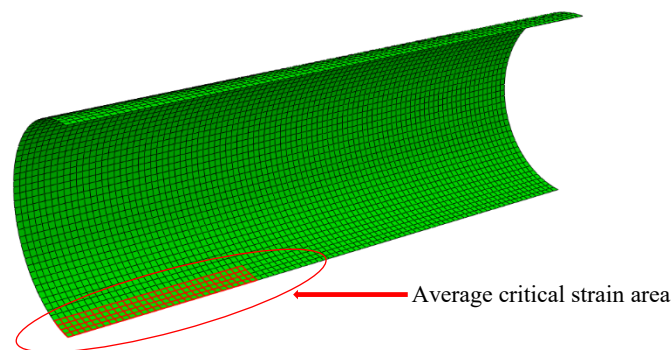


Figure 9-2: Meshed area for average strain measurement

9.5 Numerical Results

Based on the stipulated parameters, and using the above numerical simulation techniques, the post-processing module in ABAQUS CAE was used to extract field output data after each run such that the recorded incremental values for the reaction force (“RF3”) or reaction moment (“RM1”) and the corresponding average compressive strains over the gauge length area were exported to a Microsoft Excel spreadsheet to estimate the critical limit strain of API X-80 grade steel pipelines. The individual variable functions that form the semi-empirical models generated in this study emanate from the observed trends of the CLS with respect to the various parameters investigated.

9.5.1 Validation of numerical model

The pilot FE pipe model was validated by comparing the result obtained for pure bending of an unpressurized pipe model of D/t ratio = 64 to the result of an experimental study by Mohareb et al. [60] and satisfactory correspondence between the FE result and the experimental result was obtained for the end reaction bending moment vs. average induced curvature response, as well as the diamond-shaped wrinkling deformation at failure (Figure 9-3).

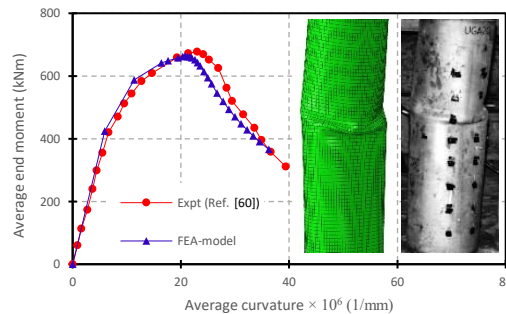
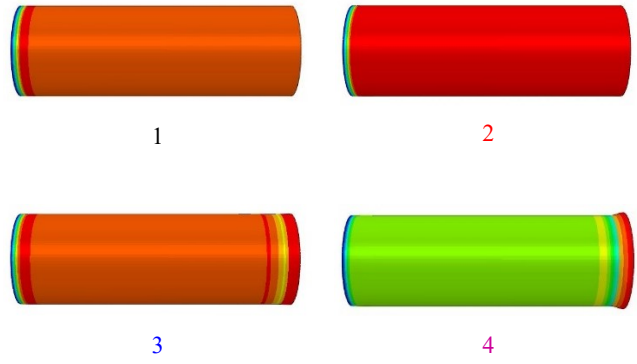
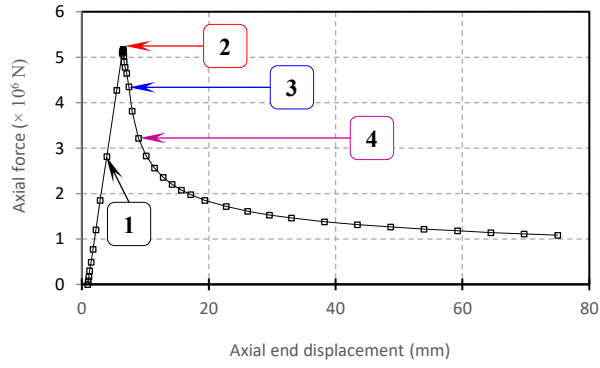


Figure 9-3: Comparison of FEA result with experimental result (UGA508) by Ref. [60]

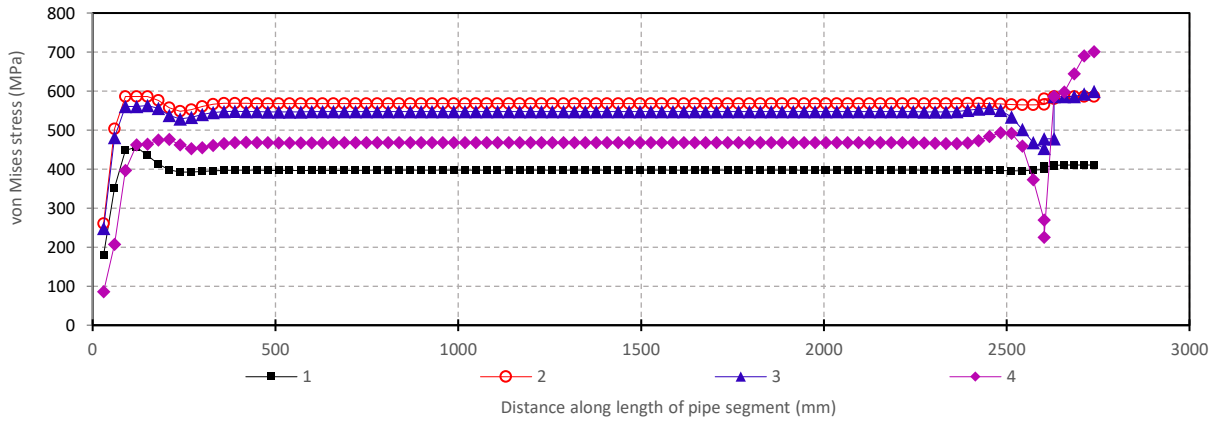
9.5.2 Evolution of stress in pipes

The evolution of the resultant stress along the length of pipe segments due to applied loads and induced deformation is portrayed in the following figures using contour plots of the von Mises stress. The contour plots are captured at various points along the path of the load-displacement (or moment-curvature) curve which coincide with three of the strategic stages of the load-deformation response, i.e., pre-buckling, limit load, and post-buckling. Figure 9-4(a) and Figure 9-5(a) represent the axial load-displacement plots of YPT pipes and RHT pipes, respectively, under uniform axial compression. Figure 9-6(a) and Figure 9-7(a) represent the moment-curvature plots of YPT pipes and RHT pipes, respectively, under uniform bending. The longitudinal distribution of the von Mises stress at the extreme of the compression side of the pipe's cross-section which is aligned with the bending plane is plotted in Figure 9-4(b) and Figure 9-5(b) for YPT pipes and RHT pipes, respectively, under uniform axial compression. The longitudinal stress distribution is plotted in Figure 9-6(b) and Figure 9-7(b) for YPT pipes and RHT pipes, respectively, under uniform bending. Contour plots of the von Mises stress at specified stages of the load-deformation response are respectively presented in Figure 9-4(c) and Figure 9-5(c) for YPT pipes and RHT pipes under uniform axial compression while the contour plots for YPT pipes and RHT pipes under uniform bending are presented in Figure 9-6(c) and Figure 9-7(c) respectively. The results presented in Figure 9-4 – Figure 9-7 are for DT4 pipes with $f_p = 0.4$; where the YPL = 1.0% for the YPT pipes and the PLUS ratio = 0.691 for the RHT pipes. The von Mises contour plots are longitudinally aligned with the longitudinal stress distribution plots such that the left end is the load end and the right end is the mid-length cross-section of the pipe.



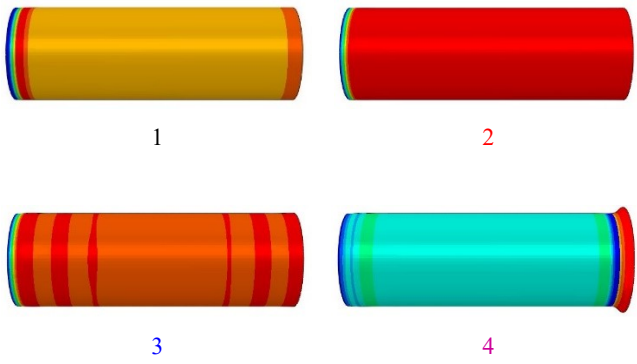
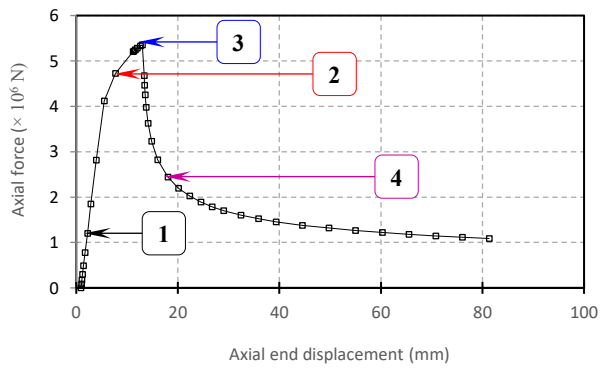
(a) Load-displacement curve

(b) von Mises stress contour plots



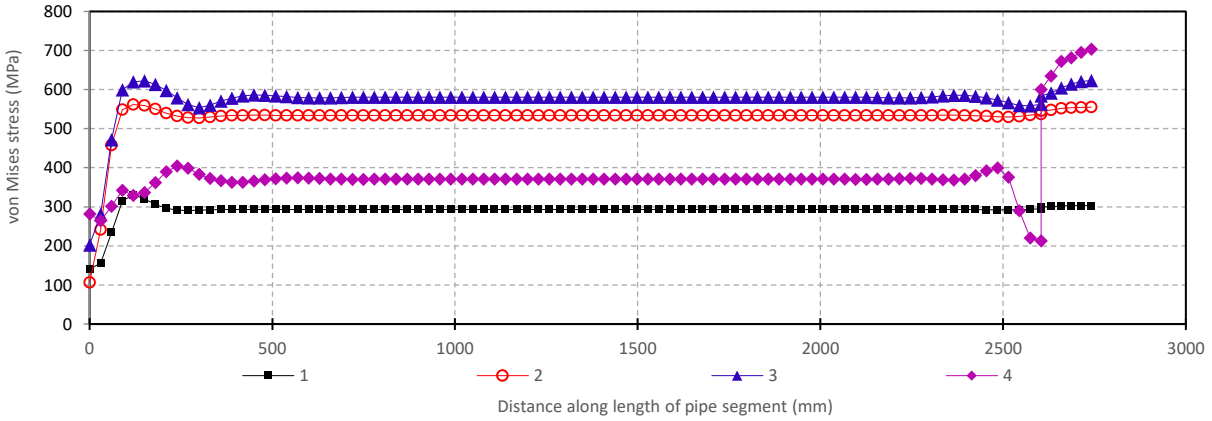
(c) Longitudinal stress distribution plots

Figure 9-4: Axial load-displacement response and stress evolution in YPT DT4 pipes under uniform axial compression ($YPL = 1.0\%$, $f_p = 0.4$)



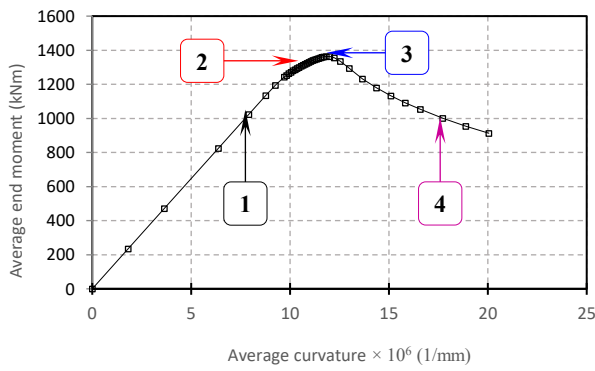
(a) Load-displacement curve

(b) von Mises stress contour plots

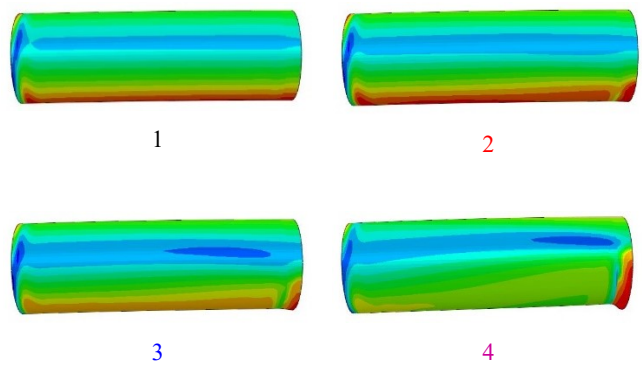


(c) Longitudinal stress distribution plots

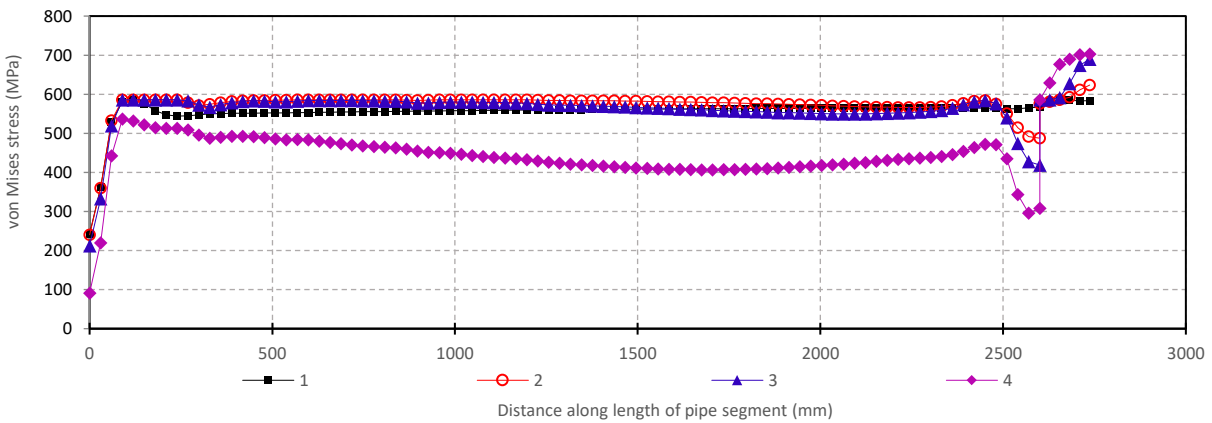
Figure 9-5: Axial load-displacement response and stress evolution in RHT DT4 pipes under uniform axial compression ($PL/US = 0.691, f_p = 0.4$)



(a) Moment-curvature curve

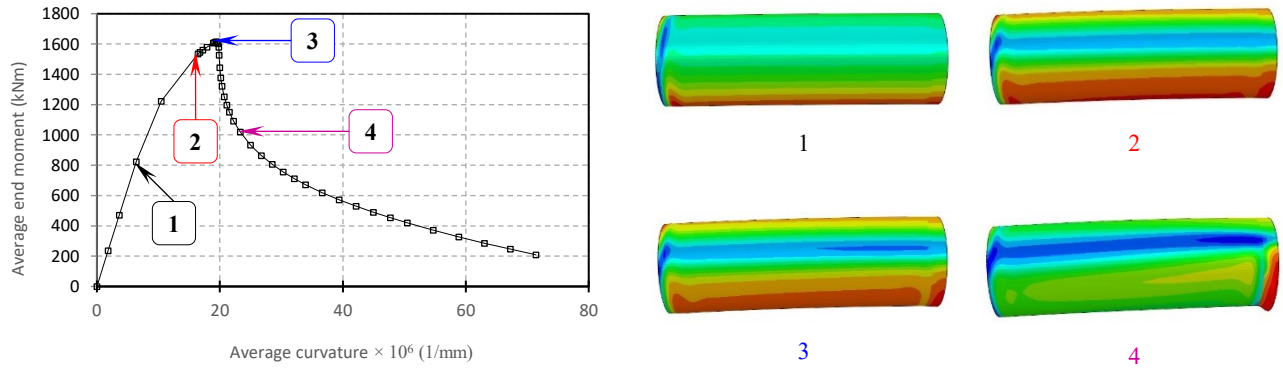


(b) von Mises stress contour plots



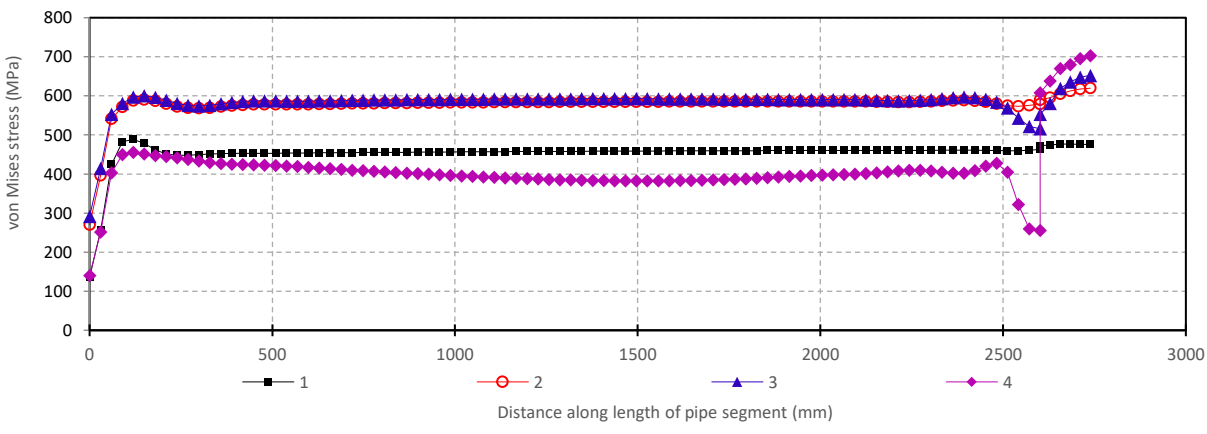
(c) Longitudinal stress distribution plots

Figure 9-6: Moment-curvature response and stress evolution in YPT DT4 pipes under uniform bending ($YPL = 1.0\%, f_p = 0.4$)



(a) Moment-curvature curve

(b) von Mises stress contour plots



(c) Longitudinal stress distribution plots

Figure 9-7: Moment-curvature response and stress evolution in RHT DT4 pipes under uniform bending ($PL/US = 0.691, f_p = 0.4$)

The plots presented in Figure 9-4 – Figure 9-7 indicate that the von Mises stress is constant over the entire length at the compression zone of the pipe from the beginning of load application until buckling occurs (i.e., in the pre-buckling stage). Buckling is associated with the formation of a longitudinal wrinkle and may either precede the limit load, as in Figure 9-5(a), Figure 9-6(a), and Figure 9-7(a), or coincide with the limit load, as in Figure 9-4(a). The limit load is typically reached when the von Mises stress in the extreme compression fibers of the pipe reaches the yield stress of the pipe material, after which localization of strains and resultant stresses commences at the mid-length region of the pipe and the remaining portions of the pipe experience stress relief. Attainment of the limit load is essentially followed by load collapse and softening of the load-deformation response. The above plots indicate that, beyond the limit load, the von Mises stresses in the compression zone evolve such that the stress at the mid-length

cross-section advances towards the UPS while the stress in the remaining portions of the pipe continues to decrease.

9.5.3 Results of parametric analysis

The influence of the D/t ratio, internal pressure, and material strain-hardening (represented by the YPL for YPT pipes, and PLUS ratio for RHT pipes) on the CLS of X80 pipes is outlined herein for the three different loading conditions considered. The PLUS ratios, defined as the ratios of respective values of the proportionality limit stress (as indicated by the stress-strain curve labels in Figure 9-1) to the specified value of the ultimate proof stress (703 MPa), are obtained as: PL486 = 0.691, PL446 = 0.634, PL406 = 0.577, PL366 = 0.520. The ratio of applied internal pressure to the circumferential yield pressure is herein referred to as the ‘pressure factor’, f_p , and various levels of internal pressurization are assigned numeric designations (0.0, 0.2, 0.4, 0.6, and 0.8) according to respective percentages (0%, 20%, 40%, 60%, and 80%) of the yield pressure. For combined axial compression + bending, the ratio of the applied stress to the limit stress of the pipe (obtained under uniform axial compression conditions) is herein referred to as the ‘compression factor’, f_c , and various levels of axial compression are assigned numeric designations (0.2, 0.4, 0.6, and 0.8) according to respective percentages (20%, 40%, 60%, and 80%) of the limit stress.

9.5.3.1 Influence of D/t ratio

The plots in Figure 9-8 and Figure 9-9 illustrate the relationship between the CLS and the D/t ratio of YPT and RHT pipes respectively. The plots in Figure 9-8 are obtained for YPT pipes with YPL = 1.50% while the plots in Figure 9-9 are obtained for RHT pipes with PLUS ratio = 0.634. The plots for combined axial compression + bending in Figure 9-8(c) and Figure 9-9(c) are both obtained for pipes subjected to compression factor, $f_c = 0.6$. The CLS trends are presented for all five levels of internal pressure considered.

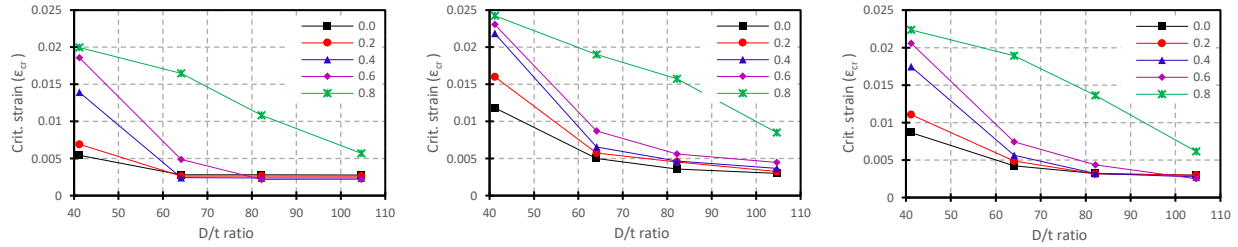


Figure 9-8: Plots of CLS vs. D/t ratio of YPT pipes with $YPL = 1.50\%$ for (a) uniform axial compression, (b) uniform bending, and (c) combined loading ($f_c = 0.6$)

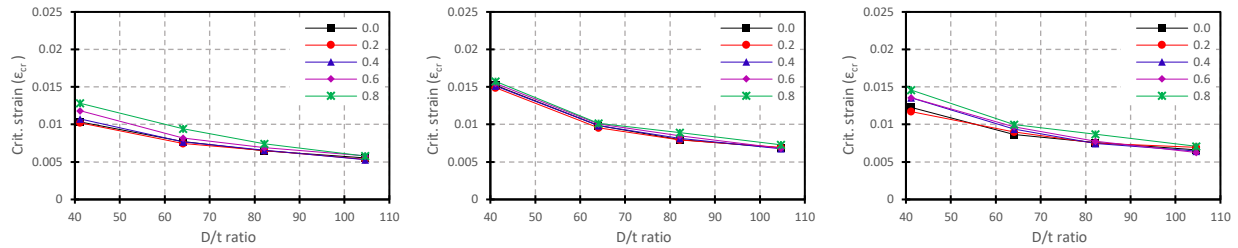


Figure 9-9: Plots of CLS vs. D/t ratio of RHT pipes with $PL/US = 0.634$ for (a) uniform axial compression, (b) uniform bending, and (c) combined loading ($f_c = 0.6$)

The most obvious aspect of the plots above is the nonlinear negative correlation between the CLS and the D/t ratio. The plots indicate the tendency for the CLS to reduce as the D/t ratio increases and even more evident is this phenomenon in YPT pipes, especially at high levels of internal pressure. It is also reasonable to deduce that the influence of internal pressure on the CLS vs. D/t ratio trends is minimal in RHT pipes compared to YPT pipes as the change in the slope of the CLS vs. D/t ratio trends for RHT pipes is observed to be generally much lower than for YPT pipes. The relationship between the CLS of YPT pipes and the D/t ratio becomes nearly linear at internal pressure = 80%. For intermediate D/t ratios (DT2 and DT3) and high D/t ratios (DT4), RHT pipes are observed to have a higher deformational capacity than YPT pipes at internal pressure $\leq 60\%$ YS. However, at high internal pressure ($f_p = 0.8$) and/or low D/t ratio (DT1), the deformational performance of YPT pipes tends to supersede that of RHT pipes. The CLS of pipes under uniform bending is generally observed to surpass the CLS under uniform axial compression while the CLS under combined axial compression and bending is somewhat bounded by the uniform axial and uniform bending CLS values.

9.5.3.2 Influence of internal pressure

The relationship between the CLS and internal pressure for YPT and RHT pipes is illustrated by the plots of CLS vs. f_p in Figure 9-10 and Figure 9-11 respectively. The plots in Figure 9-10 are obtained for YPT pipes with YPL = 1.25% while the plots in Figure 9-11 are obtained for RHT pipes with PLUS ratio = 0.691. Similar to the plots in Figure 9-8 and Figure 9-9, the plots for combined axial compression + bending in Figure 9-10(c) and Figure 9-11(c) are both obtained for pipes subjected to compression factor, $f_c = 0.6$. The CLS trends are presented for all four D/t ratios considered.

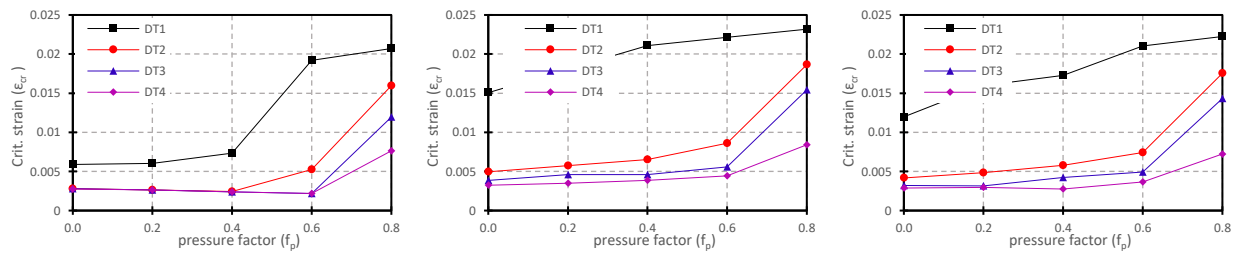


Figure 9-10: Plots of CLS vs. f_p of YPT pipes with YPL = 1.25% for (a) uniform axial compression, (b) uniform bending, and (c) combined loading ($f_c = 0.6$)

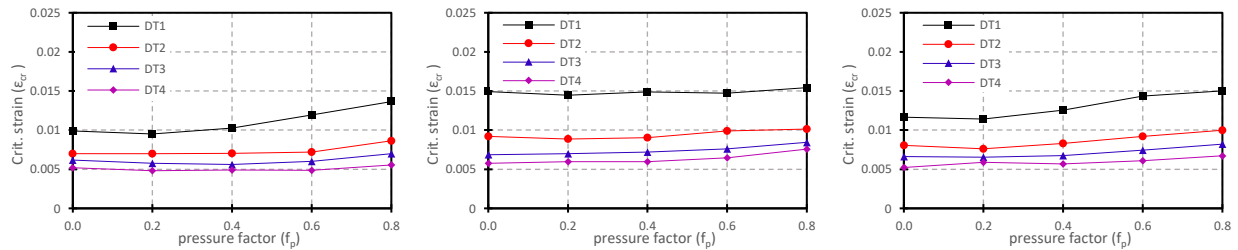


Figure 9-11: Plots of CLS vs. f_p of RHT pipes with PL/US = 0.691 for (a) uniform axial compression, (b) uniform bending, and (c) combined loading ($f_c = 0.6$)

Unlike the relationship between the CLS and the D/t ratio, the correlation between the CLS and internal pressure is characteristically positive and is more evident in YPT pipes. In conformance with the deductions from the CLS vs. D/t ratio plots in Figure 9-9, variation of the internal pressure is observed to have a negligible influence on the CLS of RHT pipes for all D/t ratios. On the other hand, the influence of internal pressure on the CLS of YPT pipes is only minimal at intermediate D/t ratios (DT2 and DT3) and high D/t ratios (DT4) for internal pressures $\leq 60\%$

YS. The most significant influence of internal pressure is observed in YPT pipes of low D/t ratios (DT1).

9.5.3.3 Influence of strain-hardening properties

The strain-hardening properties relate to the YPL of the stress-strain curve for YPT pipes, and the PLUS ratio for RHT pipes. The influence of variations in D/t ratio on the relationship between the CLS and the strain-hardening properties is considered to be significant and is therefore included in the CLS-trend illustrations in Figure 9-12 - Figure 9-15. The plots in Figure 9-12 and Figure 9-13 are both obtained for YPT pipes with D/t ratio = 41.15 and 82.16 respectively. The plots in Figure 9-14 and Figure 9-15 are both obtained for RHT pipes with D/t ratio = 41.15 and 82.16 respectively. The plots for combined axial compression + bending in Figure 9-12(c), Figure 9-13(c), Figure 9-14(c), and Figure 9-15(c) are all obtained for pipes subjected to compression factor, $f_c = 0.2$.

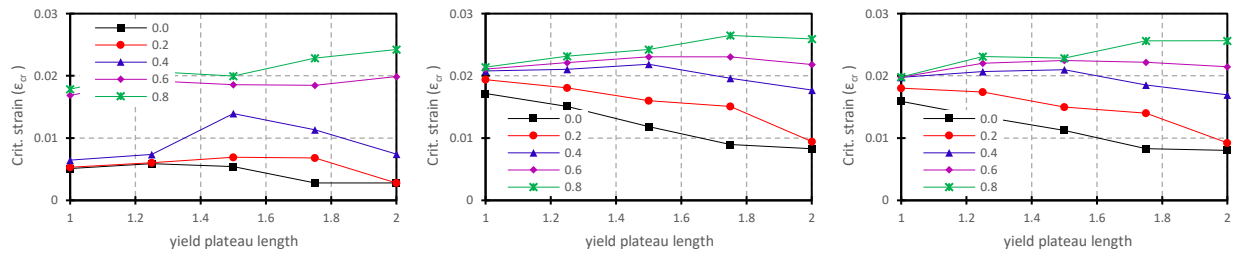


Figure 9-12: Plots of CLS vs. YPL of YPT DT1 pipes for (a) uniform axial compression, (b) uniform bending, and (c) combined loading ($f_c = 0.2$)

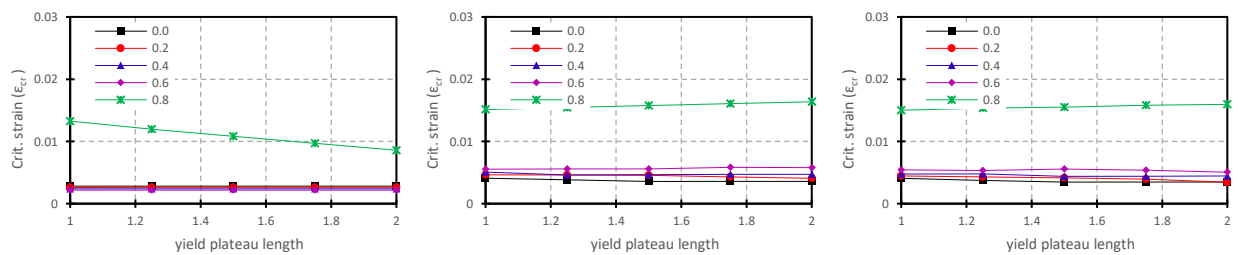


Figure 9-13: Plots of CLS vs. YPL of YPT DT3 pipes for (a) uniform axial compression, (b) uniform bending, and (c) combined loading ($f_c = 0.2$)

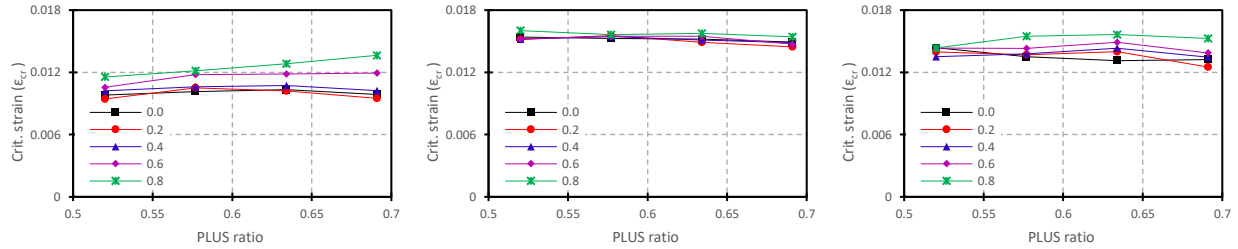


Figure 9-14: Plots of CLS vs. PLUS ratio of RHT DT1 pipes for (a) uniform axial compression, (b) uniform bending, and (c) combined loading ($f_c = 0.2$)

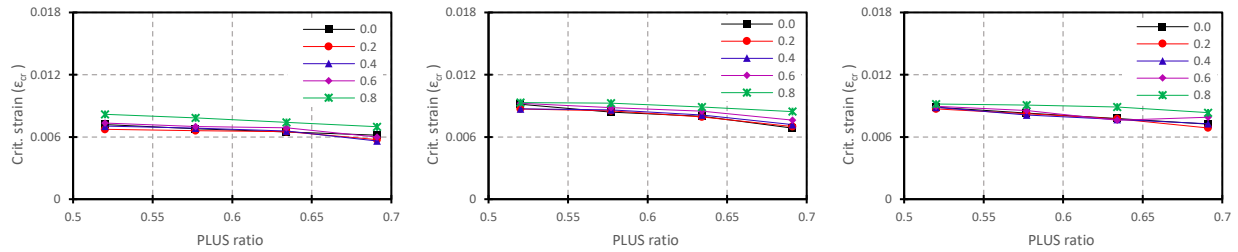


Figure 9-15: Plots of CLS vs. PLUS ratio of RHT DT3 pipes for (a) uniform axial compression, (b) uniform bending, and (c) combined loading ($f_c = 0.2$)

The plots above indicate that the influence of the strain-hardening properties of the pipe material is more prevalent in pipes with low D/t ratios (DT1) for YPT pipes; as the D/t ratio of the pipe increases, the influence of the YPL on the CLS diminishes. For YPT pipes of low D/t ratio (DT1), a positive relationship is observed between the YPL and the CLS at high internal pressure ($f_p = 0.8$). The YPL indicates a progressively negative correlation with the CLS as the internal pressure drops below 60% YS. On the other hand, a negative correlation between the PLUS ratio and the CLS is more apparent at higher D/t ratios and the influence tends to diminish as the D/t ratio decreases. As is the case for YPT pipes with low D/t ratio (DT1), a positive (but relatively less significant) relationship between the PLUS ratio and the CLS of RHT pipes with low D/t ratio (DT1) is also observed at high internal pressure ($f_p = 0.8$).

9.5.3.4 Influence of compressive net-section axial force for combined loading

The effect of a compressive net-section axial force on the CLS of pipes subjected to monotonically-increasing curvature is depicted in Figure 9-16 and Figure 9-17. The relationship between the CLS and the compression factor, f_c , is represented by the plots in

Figure 9-16 for YPT pipes with D/t ratio = 64.08 and YPL = 1.25%. Figure 9-17 comprises CLS vs. f_c plots for RHT pipes with D/t ratio = 41.15 and PLUS ratio = 0.577. Each plot corresponds to a respective level of internal pressure as indicated by the elements of the graph legends.

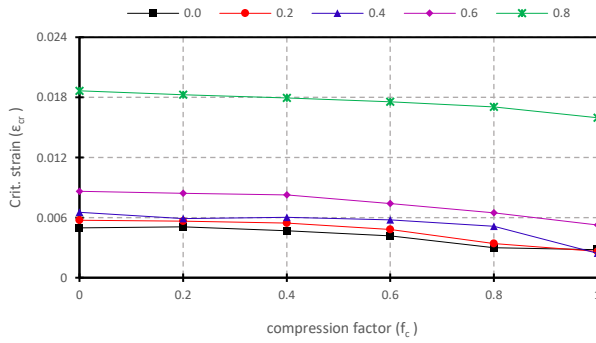


Figure 9-16: Plots of CLS vs. f_c for YPT pipes with YPL = 1.25%

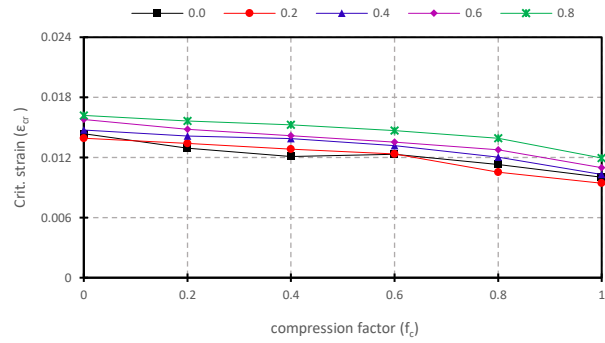


Figure 9-17: Plots of CLS vs. f_c for RHT pipes with PL/US = 0.577

An inverse relationship is observed between the compression factor and the CLS for both YPT and RHT pipes. Observation of various parametric combinations of the factors investigated in this study shows a strong and general indication that the upper and lower bounds of the CLS for pipes subjected to combined axial compression + bending is coincident with the CLS under uniform bending and the CLS under uniform axial compression respectively. The observed upper and lower bound phenomenon is portrayed accordingly on the horizontal axes of the plots in Figure 9-16 and Figure 9-17 such that a $f_c = 0$ represents uniform bending and $f_c = 1$ represents uniform axial compression. It can therefore be inferred that, for all combinations of investigated parameters, the CLS of both YPT and RHT pipes reduces progressively and somewhat nonlinearly from a state of uniform bending to a state of uniform axial compression as the compressive net-section axial force is increased from 0% to 100% of the limit axial stress.

9.6 Derivation of Semi-Empirical Models

9.6.1 CLS derivation

The CLS trends obtained with respect the various considered parameters were examined to derive appropriate individual variable functions for each parameter while taking any significant inter-relationships between the constitutive factors into consideration. Taking a cue for successful development of semi-empirical models for prediction of mechanical performance in pipelines from recent numerical studies (e.g., Ref. [58], Ref. [59], Ref. [61]), a multiplicative approach was employed for development of six nonlinear mathematical expressions, each formed as a product of the individual variable functions for the respective constitutive parameters. The basic form of the nonlinear expressions for the CLS of YPT and RHT pipes under the three loading conditions investigated is:

$$\varepsilon_{cr} = f_{cr}[\pi_1, \pi_2, \pi_3, \pi_4, \pi_5, \pi_6] = f_1 \cdot f_2 \cdot f_3 \cdot f_4 \cdot f_5 \cdot f_6 \quad (9-4)$$

where f_1, f_2, f_3, f_4, f_5 and f_6 represent the D/t ratio function (f_{dt}), the pressure factor function (f_{fp}), the strain-hardening function (f_{sh}), the heel factor function (f_{hf}), the knee-to-heel ratio function (f_{kh}), and the compression factor function (f_{fc}) respectively. π_1 represents the D/t ratio ($\frac{D}{t}$), π_2 represents the pressure factor ($\frac{p}{p_y}$), π_3 represents the yield plateau length (YPL) for YPT pipes or the PLUS ratio ($\frac{\sigma_{pl}}{\sigma_{us}}$) for RHT pipes, π_4 represents the heel factor (h_f), π_5 represents the “knee-to-heel” ratio ($\frac{k_f}{h_f}$), and π_6 represents the compression factor (f_c).

For simplicity of presentation, the three loading conditions investigated are hereafter assigned the following alphanumeric designations: LC1 for uniform axial compression, LC2 for uniform bending, and LC3 for combined axial compression + bending.

An iterative process was thoroughly implemented for deriving the final form of the individual variable functions by targeting the highest possible value of the coefficient of multiple determination (R^2). An R^2 value greater than 0.95 was considered to be a satisfactory goodness-

of-fit between the FEA-derived CLS values and the predictions of the derived nonlinear expressions.

The individual variable functions for YPT pipes are outlined thus:

$$\begin{aligned}
 f_1 = f_{dt} &= a_1 \cdot (\pi_1)^{b_1} \\
 f_2 = f_{fp} &= \left[a_2 + (b_2 + c_2 \pi_1) \cdot \text{Exp}(\pi_2)^{(d_2 + e_2 \pi_4)} \right] && (LC1 \& LC3) \\
 &= \left[a_2 \pi_4 + (b_2 + c_2 \pi_1) \cdot \text{Exp}(\pi_2)^{(d_2 + e_2 \pi_4)} \right] && (LC2 \text{ only}) \\
 f_3 = f_{sh} &= a_3 \pi_4 + (b_3 \pi_2 + c_3 \pi_1) \cdot (\pi_3)^{d_3} && (LC3 \text{ only}) \\
 f_4 = f_{hf} &= \left[a_4 + (b_4 \pi_1 + c_4 \pi_2) \cdot (\pi_4)^{d_4} \right] && (LC1 \& LC2) \\
 &= \left[a_4 + (b_4 \pi_1) \cdot (\pi_4)^{c_4} \right] && (LC3 \text{ only}) \\
 f_5 = f_{kh} &= a_5 + (b_5 \pi_3) \cdot (\pi_5)^{c_5} \\
 f_6 = f_{fc} &= a_6 + (b_6 \pi_2 + c_6 \pi_1) \cdot (\pi_6)^{d_6} && (LC3 \text{ only})
 \end{aligned} \tag{9-5}$$

The individual variable functions for RHT pipes are given by:

$$\begin{aligned}
 f_1 = f_{dt} &= a_1 \cdot (\pi_1)^{b_1} \\
 f_2 = f_{fp} &= (a_2 + b_2 \cdot \pi_2) \cdot [c_2 + (d_2 + e_2 \pi_1) \cdot \text{Exp}(\pi_2)^{(f_2)}] \\
 f_3 = f_{sh} &= a_3 + (b_3 \pi_2 + c_3) \cdot (\pi_3)^{d_3} \\
 f_4 = f_{hf} &= a_4 + b_4 \cdot (\pi_4)^{c_4} \\
 f_5 = f_{kh} &= a_5 + b_5 \cdot (\pi_5)^{c_5} \\
 f_6 = f_{fc} &= a_6 + (b_6 \pi_1) \cdot (\pi_6)^{c_6} && (LC3 \text{ only})
 \end{aligned} \tag{9-6}$$

The nonlinear regression coefficients and coefficients of multiple determination (R^2), obtained by advanced nonlinear regression analysis using the “NonlinearModelFit” command in the powerful computational package (Wolfram Mathematica [57]), are presented in Table 9-2.

Table 9-2: Nonlinear regression coefficients

Reg. Coeff.	YPT			RHT		
	<i>LC1</i>	<i>LC2</i>	<i>LC3</i>	<i>LC1</i>	<i>LC2</i>	<i>LC3</i>
<i>a</i>₁	0.07582	0.003171	0.7302	1.586	1.231	0.1829
<i>b</i>₁	-2.192	-2.386	-4.256	-0.5804	-1.112	-0.6736
<i>a</i>₂	0.06014	18.57	-386.2	2.919	0.4872	0.947
<i>b</i>₂	0.005009	-0.000358	-7.111	0.7857	-0.1282	-0.2245
<i>c</i>₂	-0.00003623	8.397×10^{-6}	0.02827	-218.1	-48.49	170.2
<i>d</i>₂	8.186	11.66	7.735	-34.63	-16.93	6.393
<i>e</i>₂	0.6897	3.537	-2.354	0.1272	-0.2596	-0.02223
<i>f</i>₂	-	-	-	3.565	1.335	2.82
<i>a</i>₃	-	-	72.59	-1.513	0.500779	7.783
<i>b</i>₃	-	-	182.2	-1.234	6.915×10^{-5}	14.71
<i>c</i>₃	-	-	1.116	3.225	-0.501086	1.263
<i>d</i>₃	-	-	3.632	0.2451	0.0002846	4.778
<i>a</i>₄	86.44	15.09	-30.34	-2.608	-1.272	3.37183
<i>b</i>₄	0.5966	0.004361	-1.788	1.392	2.396	-3.37182
<i>c</i>₄	-136.5	1.019	1.665	-0.1513	2.458	-1.127×10^{-6}
<i>d</i>₄	0.07415	-3.204	-	-	-	-
<i>a</i>₅	40.73	271.9	2.464×10^{-5}	-1.40902	-0.2618	-5.336
<i>b</i>₅	-0.0003071	-1.189	1.216	1.40905	0.4994	4.04
<i>c</i>₅	1.274	0.6593	-1.615	4.185×10^{-6}	0.9315	-0.1044
<i>a</i>₆	-	-	30.23	-	-	-18.19
<i>b</i>₆	-	-	-200.4	-	-	0.03894
<i>c</i>₆	-	-	3.893	-	-	2.456
<i>d</i>₆	-	-	-0.199	-	-	-
<i>R</i>²	0.962034	0.990746	0.983041	0.997271	0.998619	0.997224

The applicable ranges for the constitutive factors of the developed semi-empirical models are determined by the range of the parameters used in the FE analyses, given in Table 9-3 as follows:

Table 9-3: Applicable range for dimensionless parameters

<i>Par.</i>	YPT		RHT	
	\geq	\leq	\geq	\leq
π_1	41	105	41	105
π_2	0.0	0.8	0.0	0.8
π_3	1	2	0.520	0.691
π_4	0.250	0.519	1.58	3.98
π_5	161	1497	2.9	43.7
π_6	> 0.0	< 1.0	> 0.0	< 1.0

9.6.2 Limit stress derivation

The nonlinear regression procedures employed for deriving the above semi-empirical equations for the CLS were extended to obtain two nonlinear expressions for the limit stress; for YPT pipes and RHT pipes. The values of the limit stress were obtained based on the values of the peak load on the axial load vs. axial deformation plots for pipes subjected to uniform axial compression. The following regression equations are required for determining the appropriate fractions of the limit stress that feed into the semi-empirical equations for evaluating the CLS of pipes subjected to combined axial compression + bending:

For YPT pipes,

$$\begin{aligned} \sigma_{lim,YP} = & 6.163(\sigma_{ys}) * [(8.496 - 7.192.\pi_2) * (\pi_1^{-0.3075})] \\ & * [(-8.36548) + 8.36562 * (Exp(\pi_2)^{5.598*10^{-6}})] \\ & * [(1.523.\pi_1) + 350.3 * (\pi_3^{-0.03885})] \end{aligned} \quad \begin{matrix} (9- \\ 7) \end{matrix}$$

For RHT pipes,

$$\begin{aligned} \sigma_{lim,RH} = & 5.451(\sigma_{ys}) * [(7.321 - 6.485.\pi_2) * (\pi_1^{-0.107})] \\ & * [(8.416) + 6.906 * (Exp(\pi_2)^{0.8432})] \\ & * [(5.232) + 7.782 * (\pi_4^{-0.4513})] \\ & * [(-5.67028) + 5.67057 * (\pi_5^{-2.72*10^{-6}})] \end{aligned} \quad \begin{matrix} (9- \\ 8) \end{matrix}$$

9.7 Goodness-of-fit

In addition to highlighting the coefficients of multiple determination which indicate the level of correspondence between the predictions of the developed semi-empirical equations and the FEA results, the plots in Figure 9-18 and Figure 9-19 are presented to provide graphical illustrations of the accuracy of the developed models. The model-predicted CLS values were plotted against the FEA-derived CLS values in Figure 9-18 and Figure 9-19, respectively, for YPT pipes and RHT pipes subjected to (a) uniform axial compression, (b) uniform bending, and (c) combined axial compression + bending.

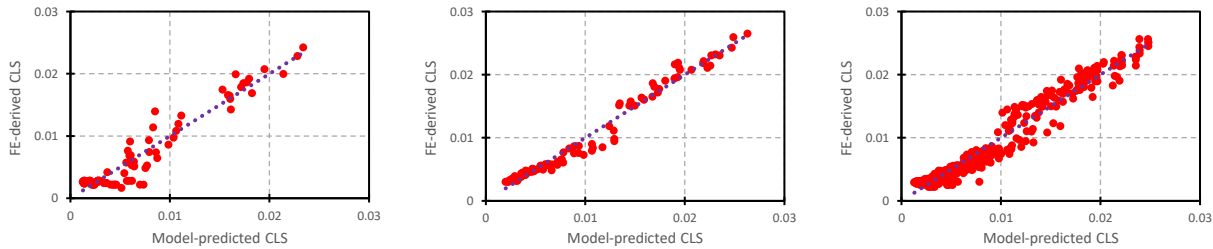


Figure 9-18: Model prediction vs. FEA results for YPT pipes for (a) LC1, (b) LC2, and (c) LC3

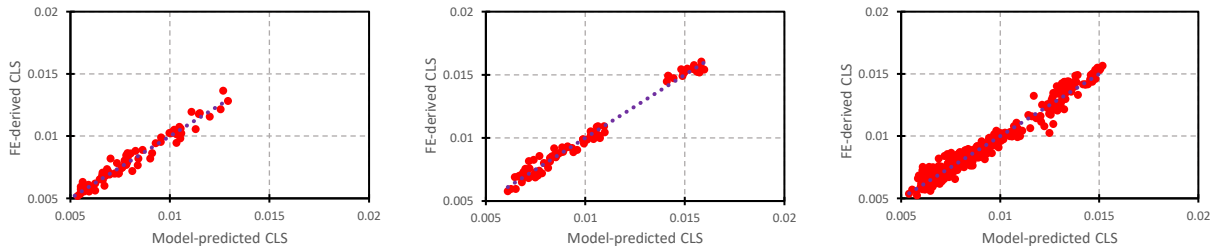


Figure 9-19: Model prediction vs. FEA results for RHT pipes for (a) LC1, (b) LC2, and (c) LC3

9.8 Discussion of Results

The results obtained for YPT and RHT pipes indicate that the CLS varies inversely with the D/t ratio for all combinations of parameters. For the CLS of RHT pipes, however, the effect of varying the D/t ratio is observed to be mild for all cases considered. The CLS trends for RHT pipes feature an average of a 30% drop in the CLS between DT1 and DT2 whereas the drop in CLS from DT2 to DT3 and from DT3 to DT4 is approximately 10%. The CLS trend observed

for RHT pipes also seems to apply to the three loading conditions considered. The CLS trend of YPT pipes, on the other hand, is observed to be less apparent as the influence of the D/t ratio is observed to vary with respect to the level of internal pressure as well as with respect to the loading condition. For YPT pipes under uniform axial compression, there is generally a sudden drop ranging from approximately 50% to approximately 90%, depending on the pressure level, between DT1 and DT2. However, there is virtually no effect of D/t ratio variation from DT2 to DT4 for pressure levels between 0% and 60% YS. Under bending and combined loading, the effect of D/t ratio variation becomes more apparent between DT2 and DT4 for pressure levels between 0% and 60% YS. The results, however, seem to generally portray an almost-linear drop of approximately 75% in the CLS of YPT pipes subjected to a high level of internal pressure ($f_p = 0.8$) for all three loading conditions. The observed deformation behavior, with respect to the D/t ratio, may be attributed to the somewhat dichotomous phenomenon associated with the buckling response of cylindrical shell structures as the initiation of buckling transitions from the elastic region of the material stress-strain curve (elastic buckling) to the nonlinear region of the material stress-strain curve (inelastic/plastic buckling). RHT pipes exhibit continuous strain-hardening, and invariably a gradual reduction in the tangential modulus of the stress-strain curve, beyond the proportionality limit point and therefore do not experience significant changes in deformational capacity due to the delay of buckling initiation. The effect of D/t variation on the CLS of RHT pipes can therefore be deduced to be predominantly influenced by the increase in axial or bending rigidity of the pipe due to decrease in slenderness of the pipe wall and vice versa. YPT pipes, on the other hand, feature a sudden zeroing of the slope of the stress-strain curve at the proportionality limit and subsequent strain-hardening that commences toward the end of a significantly-extended yield plateau. The existence of a distinct yield point in the stress-strain curve tends to cause an automatic trigger of buckling instability in YPT pipes once the initiation of buckling extends beyond the elastic region of the pipe material. However, there exists the possibility of recovery from initial softening of the load-deformation or moment-curvature response if intrinsic properties (e.g., D/t ratio) and/or loading conditions (e.g., internal pressure) provide additional stiffness that sufficiently counteracts the detrimental impact of the yield plateau on the deformational response of the pipe.

The deformational response of a pipe to uniform axial compression is characteristically different from the response to bending, even with the additional application of a compressive force. Under uniform axial compression, the entire cross-section of the pipe is susceptible to buckling, and the pipe relies on geometric, material, loading and boundary conditions for sustenance against induced deformation. Under bending, however, the pipe gains additional stiffness due to the counteractive interaction between tensile and compressive stresses in the pipe's cross-section. This can, therefore, be considered to be responsible for the more apparent effect of D/t variation on the CLS of YPT pipes subjected to uniform bending and combined bending and axial compression at pressure levels between 0% and 60% YS. The deformational response of a YPT pipe subjected to all three loading conditions at a high level of internal pressure ($f_p = 0.8$) is analogous to the deformational response of RHT pipes as an almost-linear relationship is observed between the CLS and the D/t ratio. This is attributable to the tendency that a pressure level of 80% YS significantly increases the stability of the pipe's response such that catastrophic collapse leading to failure of the pipe inevitably takes advantage of the strain-hardening portion of the stress-strain curve at the end of the yield plateau. This also implies that the influence of D/t ratio variation on the CLS will be predominantly impelled by the stiffness of the pipe response associated with pipe wall slenderness factors.

The results presented for the influence of internal pressure on the CLS further substantiate the assertion that increase of the internal pressure in a pipe results in a corresponding increase in the stability of the pipe's response to loading. Internal pressure hinders the localization of wrinkling and bulging deformation and also increases the tendency for buckling to be initiated further along the stress-strain curve. The results indicate a negligible influence of internal pressure variation on the CLS of RHT pipes at all levels of pressure. On the other hand, the CLS of YPT pipes tends to be unaffected by changes in internal pressure between 0% and 60% YS whereas at higher pressure ($f_p = 0.8$), there is a spike in the CLS depending on the D/t ratio.

For YPT pipes, varying the length of the yield plateau is observed to have a higher effect on the CLS as the D/t ratio of the pipe decreases. For YPT pipes with D/t ratio = 41.15, the CLS is likely to be negatively affected by an increase in YPL at levels of internal pressure between 0% and 60% YS whereas the YPL positively correlates with the CLS at a high level of internal pressure ($f_p = 0.8$). Unlike YPT pipes, varying the PLUS ratio tends to have a less significant

influence on the CLS of RHT pipes as the D/t ratio decreases. At DT1, however, the influence of the PLUS ratio on the CLS of RHT pipes is observed to be negligible except at a level of pressure equal to 80% YS. It can be inferred from the results for YPT pipes that improvement of the CLS for pipes with lower D/t ratio and/or high internal pressure is not necessarily automatic as the length of the yield plateau exhibits a secondary, but significant, influence on the deformational capacity. Figure 9-12(b) and Figure 9-12(c) further illustrate that subsection of a pipe to bending considerably enhances the stiffness response of the pipe, even at zero-to-low levels of internal pressure. Enhanced stiffness is, therefore, accompanied by an increased tendency for buckling to be initiated in the nonlinear region of the material stress-strain curve. The higher stiffness of a pipe under bending, compared to a pipe under uniform axial compression, leads to a relatively greater positive effect of a longer YPL on the CLS of a pipe under bending, especially at internal pressures as high as 80% YS. However, additional benefits of a longer yield plateau tend to diminish once the YPL exceeds 1.75%. For levels of internal pressure between 0% and 60% YS, increasing the length of the yield plateau results in a reduced ability of the pipe to recover from initial softening of the mechanical response before reaching the actual peak stress or moment. A decrease in the PLUS ratio for RHT pipes implies a lower proportionality limit point and, invariably, superior strain-hardening and vice versa. At higher D/t ratios, initiation of buckling tends to occur before the yield point of the material is reached implying that materials with a lower proportionality limit have a softer inelastic response which translates to higher deformability. As the D/t ratios become lower, initiation of buckling shift towards the yield point of the material where the stress-strain curves of materials with different PLUS ratios converge hence, the effect of PLUS ratio variation becomes negligible. However, beyond the yield point, the stress-strain curve of higher-PLUS ratio materials exhibits a softer response; hence, if the initiation of buckling is delayed beyond the yield point of the material (as is likely the case when internal pressure is as high as 80% YS) a higher PLUS ratio (i.e., inferior strain hardening) may have a positive effect on the deformational capacity of an RHT pipe, and vice versa.

9.9 Conclusions

A comparison is made herein between three different loading conditions, uniform axial compression, uniform bending, and combined axial compression and bending, for the relationships between the CLS and the relevant influencing parameters. The YPT steel material features a sudden drop in the slope of the stress-strain curve at the instance of the yield point whereas the transition of the stress-strain curve from the proportionality limit to the ultimate stress is gradual in RHT pipes. This distinction in the nonlinear strain-hardening of YPT and RHT pipes has been observed in previous studies [62-66] to significantly impact on the deformational capacity of pipes but marginally affect the limit stress and limit moment. An extensive parametric study was therefore conducted to derive the functional relationships between nondimensionalized parameters representing the relevant factors and the deformational performance of pipes made of API X80 grade line pipe steel while considering the material behavior under two classifications, according to the strain-hardening peculiarities that commonly exist.

Characterization of the material stress-strain relationship is imperative for proper evaluation of the CLS of pipes subjected to various loading conditions and particularly, the three loading conditions investigated in this study. A simple and robust mathematical expression for approximating the material stress-strain behavior over the full range of strains was employed. The material model features two constitutive model constants which fully describe the shape of the nonlinear portion of the stress-strain curve of the material - the shape constants were therefore included as dimensionless parameters in developing semi-empirical models for predicting the CLS.

Increase in the D/t ratio was generally observed to be detrimental to the CLS and vice versa whereas variation of the internal pressure had a generally positive correlation with the CLS. Variation of the material strain hardening properties was found to have a significant effect on the CLS, especially in low- D/t ratio YPT pipes subjected to high internal pressures. Less dispersion was obtained for the CLS of RHT pipes, even at high pressures and low D/t ratios and this was attributed to the characteristically gradual strain hardening of the material stress-strain curves.

Individual variable functions were developed to mathematically represent the trends of the CLS with respect to the parameters that constitute the semi-empirical models. A multiplicative

approach was then employed to combine the individual variable functions to form nonlinear mathematical expressions for respective loading conditions and material property classification. Advanced nonlinear multiple regression was performed using Wolfram Mathematica to obtain the nonlinear regression coefficients for each of the derived semi-empirical equations and effort was made to achieve the highest possible R^2 value for each nonlinear expression by accounting for the complex interrelationships between the different parameters. The nonlinear regression analysis yielded high R^2 values (> 0.95), indicating an excellent goodness-of-fit between the model prediction and the FEA-derived results of the CLS.

The semi-empirical models developed in this paper are considered as handy tools for evaluating the deformational capacity of both unpressurized and pressurized API X80 line pipes subjected to various loading conditions. The results clearly demonstrate that the CLS values for pipes subjected to combined axial compression and bending typically exist in a spectrum between the CLS obtained for uniform bending and that obtained for uniform axial compression. It is, however, the prerogative of the designer to determine the level of axial compression to consider, especially in the case of displacement-controlled loading conditions where the axial stress is not readily derivable. For cases such as this, it may be necessary to conservatively adopt the models for uniform axial compression as a lower bound measure of the CLS.

9.10 References

- [1] L.C. Taylor, Fault displacement and ground deformation associated with surface faulting, *Proc. ASCE Spec. Conf. Lifeline Earthq. Eng.* (1977) 338–353.
- [2] T. Ariman, G.E. Muleski, A review of the response of buried pipelines under seismic excitations, *Earthq. Eng. Struct. Dyn.* 9 (1981) 133–152. doi:10.1002/eqe.4290090204.
- [3] A.P.S. Selvadurai, Mechanics of buried pipelines induced by random ground movement, in: *Proc. CSCE Annu. Conf. (Engineering Mech. Symp., Vancouver, British Columbia Canada, 1991: pp. 142–151.*
- [4] H. Yun, S. Kyriakides, On the beam and shell modes of buckling of buried pipelines, *Soil Dyn. Earthq. Eng.* 9 (1990) 179–193. doi:10.1016/S0267-7261(05)80009-0.

- [5] E. Dama, S.A. Karamanos, A.M. Gresnigt, Failure of Locally Buckled Pipelines, *J. Press. Vessel Technol.* 129 (2007) 272. doi:10.1115/1.2716431.
- [6] O. V. Trifonov, V.P. Cherniy, Elastoplastic stress-strain analysis of buried steel pipelines subjected to fault displacements with account for service loads, *Soil Dyn. Earthq. Eng.* 33 (2012) 54–62. doi:10.1016/J.SOILDYN.2011.10.001.
- [7] American Lifelines Alliance, American Society of Civil Engineers, Guidelines for the Design of Buried Steel Pipe (with Addenda through February 2005), Reston, VA, USA, 2005.
- [8] P. Vazouras, S.A. Karamanos, P. Dakoulas, Finite element analysis of buried steel pipelines under strike-slip fault displacements, *Soil Dyn. Earthq. Eng.* 30 (2010) 1361–1376. doi:10.1016/J.SOILDYN.2010.06.011.
- [9] P. Vazouras, S.A. Karamanos, P. Dakoulas, Mechanical behavior of buried steel pipes crossing active strike-slip faults, *Soil Dyn. Earthq. Eng.* 41 (2012) 164–180. doi:10.1016/J.SOILDYN.2012.05.012.
- [10] P. Vazouras, P. Dakoulas, S.A. Karamanos, Pipe-soil interaction and pipeline performance under strike-slip fault movements, *Soil Dyn. Earthq. Eng.* 72 (2015) 48–65. doi:10.1016/J.SOILDYN.2015.01.014.
- [11] W.C. Kan, M. Weir, M.M. Zhang, D.B. Lillig, S.T. Barbas, M.L. Macia, N.E. Biery, Strain-Based Pipelines: Design Consideration Overview, in: Eighteenth Int. Offshore Polar Eng. Conf., International Society of Offshore and Polar Engineers, Vancouver, British Columbia, 2008.
- [12] API 1111, Design, construction, operation, and maintenance of offshore hydrocarbon pipelines, (1999).
- [13] Det Norske Veritas, Submarine pipeline systems - DNV-OS-F101, DNV, Oslo, Norway, 2010.
- [14] American Bureau of Shipping, ABS Guide for Building and Classing Subsea Pipeline Systems, (2006).
- [15] Canadian Standards Association, Oil and gas pipeline systems. CSA-Z662-2007, (2007).
- [16] M.L. Macia, S.A. Kibey, H. Arslan, F. Bardi, S.J. Ford, W.C. Kan, M.F. Cook, B. Newbury, Approaches to Qualify Strain-Based Design Pipelines, in: 2010 8th Int. Pipeline Conf. Vol. 4, ASME, 2010: pp. 365–374. doi:10.1115/IPC2010-31662.

- [17] B. Liu, X.J. Liu, H. Zhang, Strain-based design criteria of pipelines, *J. Loss Prev. Process Ind.* 22 (2009) 884–888. doi:10.1016/J.JLP.2009.07.010.
- [18] Y.-Y. Wang, M. Liu, D. Horsley, M. Salama, M. Sen, Overall Framework of Strain-Based Design and Assessment of Pipelines, in: Vol. 4 Prod. Pipelines Flowlines; Proj. Manag. Facil. Integr. Manag. Oper. Maintenance; Pipelining North. Offshore Environ. Strain-Based Des. Stand. Regul., ASME, 2014: p. V004T11A023. doi:10.1115/IPC2014-33745.
- [19] S. Kenny, J. Barrett, R. Phillips, R. Popescu, Integrating Geohazard Demand And Structural Capacity Modelling Within a Probabilistic Design Framework For Offshore Arctic Pipelines, in: Seventeenth Int. Offshore Polar Eng. Conf., International Society of Offshore and Polar Engineers, Lisbon, Portugal, 2007.
- [20] M. Nessim, W. Zhou, J. Zhou, B. Rothwell, Reliability-Based Design and Assessment for Location-Specific Failure Threats With Application to Natural Gas Pipelines, *J. Press. Vessel Technol.* 131 (2009) 041701. doi:10.1115/1.3110019.
- [21] R. Lorenz, Achsensymmetrische Verzerrungen in dünnwandigen Hohlzylindern, *Zeitschrift Des Vereines Dtsch. Ingenieure.* 52 (1908) 1706–1713.
- [22] S.P. Timoshenko, Einige stabilitäts probleme der elastizitäts theorie, *Zeitschrift Für Math. Und Phys.* 58 (1910) 337–385.
- [23] R. V. Southwell, On the General Theory of Elastic Stability, *Philos. Trans. R. Soc. A Math. Phys. Eng. Sci.* 213 (1914) 187–244. doi:10.1098/rsta.1914.0005.
- [24] A. Robertson, The Strength of Tubular Struts. Report and Memorandum No. 1185, 1929.
- [25] W.M. Wilson, N.M. Newmark, The strength of thin cylindrical shells as columns, in: *Sel. Pap. By Nathan M. Newmark Civ. Eng. Class.*, 1933: pp. 1–42.
- [26] E.E. Lundquist, Strength tests of thin-walled duralumin cylinders in compression. NACA Technical Note, No 473, Washington, D.C., 1934.
- [27] T. Von Kármán, H.S. Tsien, The Buckling of Thin Cylindrical Shells under Axial Compression, in: *Collect. Work. Hsue-Shen Tsien*, 2012: pp. 165–181. doi:10.1016/B978-0-12-398277-3.50009-9.
- [28] W.T. Koiter, The Stability of Elastic Equilibrium, *Dep. Mech. Shipbuilding, Airpl. Build. Ph.D.* (1945).

- [29] L.G. Brazier, On the Flexure of Thin Cylindrical Shells and Other "Thin" Sections, Proc. R. Soc. A Math. Phys. Eng. Sci. 116 (1927) 104–114. doi:10.1098/rspa.1927.0125.
- [30] J.O. Jirsa, F.H. Lee, J.C. Wilhoit, J.E. Merwin, Ovaling Of Pipelines Under Pure Bending, in: Offshore Technol. Conf., Offshore Technology Conference, 1972. doi:10.4043/1569-MS.
- [31] D.R. Sherman, Test of Circular Steel Tubes in Bending, J. Struct. Div. 102 (1976) 2181–2195.
- [32] P. Tugcu, J. Schroeder, Plastic deformation and stability of pipes exposed to external couples, Int. J. Solids Struct. 15 (1979) 643–658. doi:10.1016/0020-7683(79)90077-5.
- [33] B.D. Reddy, An experimental study of the plastic buckling of circular cylinders in pure bending, Int. J. Solids Struct. 15 (1979) 669–683. doi:10.1016/0020-7683(79)90066-0.
- [34] E. Corona, S. Kyriakides, On the collapse of inelastic tubes under combined bending and pressure, Int. J. Solids Struct. 24 (1988) 505–535. doi:10.1016/0020-7683(88)90005-4.
- [35] C. Mathon, A. Limam, Experimental collapse of thin cylindrical shells submitted to internal pressure and pure bending, Thin-Walled Struct. 44 (2006) 39–50. doi:10.1016/J.TWS.2005.09.006.
- [36] E.E. Lundquist, Strength Tests of Thin-walled Duralumin Cylinders in Pure Bending. NACA Technical Note, No 479, Langley Field, VA, United States, 1933.
- [37] L.H. Donnell, A new theory for the buckling of thin cylinders under axial compression and bending, Trans. A.S.M.E. 56 (1934) 795–806.
- [38] H.S. Suer, L.A. Harris, W.T. Skene, R.J. Benjamin, The Bending Stability of Thin-Walled Unstiffened Circular Cylinders Including the Effects of Internal Pressure, J. Aerosp. Sci. 25 (1958) 281–287. doi:10.2514/8.7639.
- [39] S. Houliara, S.A. Karamanos, Buckling and post-buckling of long pressurized elastic thin-walled tubes under in-plane bending, Int. J. Non. Linear. Mech. 41 (2006) 491–511. doi:10.1016/J.IJNONLINMEC.2005.11.002.
- [40] A. Limam, L.-H. Lee, E. Corona, S. Kyriakides, Inelastic wrinkling and collapse of tubes under combined bending and internal pressure, Int. J. Mech. Sci. 52 (2010) 637–647. doi:10.1016/J.IJMECSCI.2009.06.008.

- [41] American Petroleum Institute, API 5L: Specification for Line Pipe, 44th ed., American Petroleum Institute, USA, 2007.
- [42] Q. Bai, Y. Bai, Use of High-Strength Pipeline Steels, in: Subsea Pipeline Des. Anal. Install., Gulf Professional Publishing, Oxford, UK, 2014: pp. 675–694.
- [43] N. Suzuki, M. Toyoda, Critical Compressive Strain of Linepipes Related to Workhardening Parameters, in: 21st Int. Conf. Offshore Mech. Arct. Eng. Vol. 3, ASME, 2002: pp. 217–224. doi:10.1115/OMAE2002-28253.
- [44] N. Suzuki, R. Muraoka, A. Glover, J. Zhou, M. Toyoda, Local Buckling Behavior of X100 Linepipes, in: Vol. 3 Mater. Technol. Ocean Eng. Polar Arct. Sci. Technol. Work., ASME, 2003: pp. 67–76. doi:10.1115/OMAE2003-37145.
- [45] K.-B. Kang, J.-Y. Yoo, S.-S. Ahn, W.Y. Cho, T.-Y. Yoon, Buckling Behavior of API-X80 Linepipe, in: Seventeenth Int. Offshore Polar Eng. Conf., International Society of Offshore and Polar Engineers, Lisbon, Portugal , 2007: pp. 3254–3260.
- [46] N. Ishikawa, M. Okatsu, S. Endo, N. Shikanai, R. Muraoka, J. Kondo, Mechanical And Metallurgical Properties of Grade X80 High Strain Linepipe Produced By Heat Treatment On-line Process, in: Eighteenth Int. Offshore Polar Eng. Conf., International Society of Offshore and Polar Engineers, Vancouver, Canada, 2008: pp. 13–20.
- [47] J.-Y. Yoo, S.-S. Ahn, D.-H. Seo, W.-H. Song, K.-B. Kang, New Development of High-Grade X80 to X120 Pipeline Steels, Mater. Manuf. Process. 26 (2011) 154–160. doi:10.1080/10426910903202534.
- [48] L.Z. Kong, X.Y. Zhou, L.Q. Chen, J. Shuai, K. Huang, G.J. Yu, True Stress-Strain Curves Test and Material Property Analysis of API X65 and API X90 Gas Pipeline Steels, J. Pipeline Syst. Eng. Pract. 9 (2018) 04017030. doi:10.1061/(ASCE)PS.1949-1204.0000300.
- [49] D. Porter, A. Laukkanen, P. Nevasmaa, K. Rahka, K. Wallin, Performance of TMCP steel with respect to mechanical properties after cold forming and post-forming heat treatment, Int. J. Press. Vessel. Pip. 81 (2004) 867–877. doi:10.1016/J.IJPVP.2004.07.006.
- [50] N.S. Mouriño, R. Petrov, J. -h. Bae, K. Kim, L.A.I. Kestens, Texture Dependent Mechanical Anisotropy of X80 Pipeline Steel, Adv. Eng. Mater. 12 (2010) 973–980. doi:10.1002/adem.201000065.

- [51] J.R. Hines, C.M. Timms, D.D. DeGeer, Thermal Ageing Effects on Thickwalled Line Pipe, in: Vol. 3 Pipeline Riser Technol. CFD VIV, ASME, 2007: pp. 573–579. doi:10.1115/OMAE2007-29661.
- [52] O. Ndubuaku, M. Martens, R. Cheng, A. Ahmed, S. Adeeb, A Novel Approach for True Stress-True Strain Material Characterization of Metallic Materials Using the Product-Log (Omega) Function, in: 6th Int. Conf. Eng. Mech. Mater., CSCE, May 31 - June 3, Vancouver, B.C., Canada, 2017.
- [53] O. Ndubuaku, M. Martens, J.J.R. Cheng, S. Adeeb, Expression of a Generic Full-Range True Stress-True Strain Model for Pipeline Steels Using the Product-Log (Omega) Function, in: Vol. 6B Mater. Fabr., ASME, 2017: p. V06BT06A050. doi:10.1115/PVP2017-65236.
- [54] O. Ndubuaku, X. Liu, M. Martens, J.J. Roger Cheng, S. Adeeb, The effect of material stress-strain characteristics on the ultimate stress and critical buckling strain of flat plates subjected to uniform axial compression, *Constr. Build. Mater.* 182 (2018) 346–359. doi:10.1016/j.conbuildmat.2018.06.100.
- [55] Yong Bai, Wei-Liang Jin, Ultimate Strength of Cylindrical Shells, in: *Mar. Struct. Des.*, 2nd ed., Elsevier, Oxford, United Kingdom, 2016: pp. 353–365. doi:https://doi.org/10.1016/B978-0-08-099997-5.00018-6.
- [56] D. Hibbitt, B. Karlsson, P. Sorensen, ABAQUS Standard User's and Reference Manuals, Version 6.14, (2014).
- [57] Wolfram Research Inc., Mathematica, Version 11.3, Champaign, IL, 2018.
- [58] M. Liu, Y.-Y. Wang, F. Zhang, K. Kotian, Realistic strain capacity models for pipeline construction and maintenance. Prepared for the US Department of Transportation. Pipeline and Hazardous Materials Safety Administration, Office of Pipeline Safety. Contract No. DTPH56-10-T-000016, Dublin, OH, USA, 2013.
- [59] A.B. Dorey, D.W. Murray, J.J.R. Cheng, Critical Buckling Strain Equations for Energy Pipelines—A Parametric Study, *J. Offshore Mech. Arct. Eng.* 128 (2006) 248. doi:10.1115/1.2199561.
- [60] M.E. Mohareb, A.E. Elwi, G.L. Kulak, D.W. Murray, Deformation Behavior of Line Pipe, Structural Engineering Report No. 202, Edmonton, Alberta, 1994.

- [61] X. Liu, H. Zhang, Y. Han, M. Xia, W. Zheng, A semi-empirical model for peak strain prediction of buried X80 steel pipelines under compression and bending at strike-slip fault crossings, *J. Nat. Gas Sci. Eng.* 32 (2016) 465–475. doi:10.1016/J.JNGSE.2016.04.054.
- [62] A.B. Dorey, D.W. Murray, J.J.R. Cheng, Material Property Effects on Critical Buckling Strains in Energy Pipelines, in: 4th Int. Pipeline Conf. Parts A B, ASME, 2002: pp. 475–484. doi:10.1115/IPC2002-27225.
- [63] A.M. Gresnigt, S.A. Karamanos, Local Buckling Strength And Deformation Capacity of Pipes, in: Ninet. Int. Offshore Polar Eng. Conf., International Society of Offshore and Polar Engineers, Osaka, Japan, 2009: pp. 212–224.
- [64] S. Neupane, S. Adeeb, R. Cheng, J. Ferguson, M. Martens, Modeling the Deformation Response of High Strength Steel Pipelines—Part I: Material Characterization to Model the Plastic Anisotropy, *J. Appl. Mech.* 79 (2012) 051002. doi:10.1115/1.4006380.
- [65] S. Neupane, S. Adeeb, R. Cheng, J. Ferguson, M. Martens, Modeling the Deformation Response of High Strength Steel Pipelines—Part II: Effects of Material Characterization on the Deformation Response of Pipes, *J. Appl. Mech.* 79 (2012) 051003. doi:10.1115/1.4006381.
- [66] S. Adeeb, J. Zhou, D. Horsley, Investigating the Effect of UOE Forming Process on the Buckling of Line Pipes Using Finite Element Modeling, in: Vol. 1 Proj. Manag. Des. Constr. Environ. Issues; GIS/Database Dev. Innov. Proj. Emerg. Issues; Oper. Maintenance; Pipelining North. Environ. Stand. Regul., ASME, 2006: pp. 169–174. doi:10.1115/IPC2006-10175.



10. SUMMARY, CONCLUSIONS AND RECOMMENDATIONS

10.1 Summary

This research was conceptualized, designed and implemented to thoroughly and extensively investigate the effects of base metal stress-strain properties on the deformational response of onshore steel pipelines subjected to various loading combinations, with an overall objective to develop a set of constitutive design equations for predicting the deformational capacity. The equations presented in this study are intended to overcome the material-related limitations that exist in currently-available prediction models for the critical limit strain (CLS) of pipelines hence, a significant portion of the parametric composition of the constitutive equations is devoted to material characterization quantities.

The fundamental challenge in developing such constitutive CLS prediction models is the requirement of a suitable analytical model, devoid of prohibitive complexity, that is capable of effectively and accurately approximating the stress-strain behavior of the pipe material. A detailed review of literature reveals that while virtually all the existing CLS prediction models explicitly incorporate material-related parameters such as the elastic modulus and the yield stress in the constitutive equation, only a few models extend consideration of material influence to reflect the strain-hardening property, which naturally extends beyond the yield stress and/or the elastic limit of the stress-strain curve. It has, however, been established that the geometric attributes of onshore pipelines classify them into the group of cylindrical shell structures that are susceptible to inelastic buckling ramifications, the implication being that adequate consideration of the inelastic properties of the pipe material is imperative for appropriate estimation of the deformational capacity of pipe segments subjected to various loading conditions. The few attempts by researchers to incorporate the strain-hardening properties of the pipe material into the constitutive relationship for CLS estimation has either relied on a rather simplistic derivation of the ratio of the yield stress to the ultimate tensile stress (Y/T ratio) or a more representative measure of the nonlinearity of the stress-strain curve known as the Ramberg-Osgood strain-hardening exponent, “ n ”. Unfortunately, the above strain-hardening parameterization approaches are fraught with drawbacks that negatively impact on the validity and appropriateness of existing CLS prediction models: on one hand, the Y/T ratio is hardly representative of the strain-hardening behavior as it is simply based on the upper and lower bounds of the nonlinear portion of the stress-strain curve and does not account for the shape (or ‘flow’) of the deformational

response while on the other hand, the applicability of the Ramberg-Osgood stress-strain model has been observed by several researchers to be severely hampered by significant loss in accuracy of approximation beyond a limited strain range. A number of researchers have developed various modified versions of the Ramberg-Osgood stress-strain model but the accuracy of modified models tends to be achieved at a considerable cost to simplicity of expression and/or moderateness of constitutive parameters. Also, the only stress-strain models that are capable of approximating the stress-strain behavior of materials with a distinct yield point and an extended yield plateau rely on a cumbersome piecewise discretization procedure characterized by a large number of model constants.

In view of the above, the preliminary endeavor for developing a new set of highly-valid and strongly material-focused CLS prediction models was to create a versatile mathematical tool for accurately parameterizing the actual shape of the nonlinear portion of the material stress-strain curve. The developed stress-strain model is characteristically unlike existing stress-strain models as it mathematically relates the true stress to the true strain by a Product-Log (Omega) function, based on only two model constants (herein referred to as the '*heel*' constant and the '*knee*' constant) and four material parameters (the proportionality limit stress and corresponding strain, and the ultimate limit stress and uniform elongation strain). The concept behind the formulation of the stress-strain model is the normalization of the full stress range and the full strain range of the entire nonlinear portion of the stress-strain curve such that the exact magnitudes of the values of the stress and strain at any specified reference points are preserved. The developed model is also remarkably effective for capturing a reasonable approximation of the yield plateau in the stress-strain curve.

Least-squares curve-fitting techniques were employed to validate the applicability of the developed mathematical model for characterization of the stress-strain behavior of common pipeline steels, defined according to the API 5L pipeline steels standard. Experimental data points from uniaxial tensile tests, conducted at the University of Alberta on specimens of X52, X60, X65, X80 and X100 grade pipeline steel material steel pipes, were approximated using the developed stress-strain model. The model constants obtained from the curve-fitting procedure were observed to produce an excellent representation of the stress-strain behavior of the different pipeline steels. More generic application of the developed stress-strain model for stress-strain

characterization of various metallic materials was also explored based on experimental stress-strain data obtained from cryogenic tensile tests of three different metallic materials; 300 series austenitic stainless steel (AISI 304L), 5000 (Al-Mg) series aluminum alloy (AA5083), and nickel steel alloy (Invar steel-FeNi36). Using the developed stress-strain model, excellent approximations of the nonlinear load-deformation behavior of the tested specimens were also observed over the full range of the true stress-true strain relationship.

To improve the manipulability and accuracy of representation of the developed stress-strain model, a ‘*control point*’ approach was presented to allow the definition of specific values of the constitutive model constants that characterize a stress-strain curve that exactly passes through predefined points in the stress-strain curve. Four ‘*stress-control points*’ and four corresponding ‘*strain-control points*’ were defined and a simple procedure for deriving the two model constants was outlined. An extension of the ‘*control point*’ technique was also presented to control the yield plateau length of the stress-strain curve by iteratively manipulating the stress or strain values at the inflection point of the curve.

Adapting the developed stress-strain model for shell stability analysis was first performed by a parametric study on the effect of material stress-strain properties on the buckling and post-buckling behavior of uniformly-compressed metallic flat plates. The finite element (FE) simulation method was utilized to assign respective material, geometric, loading and boundary properties to computer-generated flat plated shell specimens. The plates were modeled as unstiffened plates with simply-supported boundary conditions on all the edges. An aspect ratio of three, and four variations of the plate thickness, was assigned to the plate models, which were assembled using S4R shell elements in ABAQUS. A total of 37 idealized stress-strain curves were developed for the parametric study using the developed stress-strain model and grouped according to three material curve shape classifications: bilinear (elastic-perfectly plastic) curves, yield-plateau type (YPT) curves, and round-house type (RHT) curves. XY plots of the average axial end-shortening vs. the applied axial stress were extracted from the ABAQUS software program and the maximum load-carrying capacity of the plate models (derived as the peak point on the axial load vs. axial deformation curves), as well as the corresponding end-shortening strain values (representative of the deformational capacity), was reported for each respective family of stress-strain curves.

A finite element (FE) numerical procedure was developed to evaluate the limit loads and corresponding limit strains of cylindrical shells under various loading combinations. Three different loading conditions were investigated including uniform axial compression (no bending), uniform bending (zero axial compression), and uniform axial compression with monotonically increasing curvature (combined axial compression and bending) of both unpressurized and pressurized pipe segments. FE pipe models were created using ABAQUS and were assembled, similar to the flat plate models, using S4R shell elements. To obtain the buckling response of the pipe models to uniform axial compression, internal pressure was initially applied to the inner surface of the pipe model followed by a displacement-controlled deformation, simulated by incrementally imposing an axial displacement onto the pipe-end cross-section. Simulating the buckling response of the pipe models to uniform bending was achieved by first applying internal pressure to the inner surface of the pipe, followed by a monotonically-increasing curvature, induced by specifying a finite rotational displacement rotation about the global x -axes at the pipe-end cross-section. The buckling response of the pipe models to combined axial compression and bending was simulated by simultaneously applying internal pressure onto the inner surface of the pipe models and applying a compressive axial force (derived as a percentage of the critical limit axial stress; herein referred to as the ‘compression factor’) onto the pipe-end cross-section, followed by inducing uniform curvature to the pipe segments by applying a displacement controlled rotation about the global x -axes at the pipe-end cross-section. The displacement-controlled loading schemes were implemented using the arc-length ‘Static Riks’ algorithm in ABAQUS, which executes an equilibrium iterative procedure combined with a linearized arc-length control technique for sufficiently evaluating the buckling and post-buckling responses of the simulation process

To adequately capture any nonlinearities in the relationship between the CLS and respective parameters, a minimum of four variations were applied to each investigated parameter as follows: four variations of the D/t ratio, five variations of the internal pressure, four variations of the material grade, four variations (for RHT curves) or five variations (for YPT curves) of the material curve shape factor, and four variations of the compression factor (applied for only combined axial compression and bending). For YPT materials, the material grade is represented by the ratio of the nominal yield stress (YS) to the elastic modulus of the material whereas for

RHT materials, the material grade is represented by the ratio of the proportionality limit stress to the ultimate proof stress (herein referred to as the ‘PLUS’ ratio). A full-factorial design-of-experiments (DOE) concept was applied to derive the parametric matrix for each loading condition. Hence, 320 simulations (for RHT pipes) plus 400 simulations (for YPT pipes) were performed for uniform axial compression, 320 simulations (for RHT pipes) plus 400 simulations (for YPT pipes) were performed for uniform bending, and 1280 simulations (for RHT pipes) plus 1600 simulations (for YPT pipes) were performed for combined axial compression and bending. Using nonlinear multiple regression techniques, two constitutive CLS prediction equations were developed for each loading condition according to the material curve type specifications. An excellent goodness-of-fit between the model-predicted values and the FE-derived values, indicated by a high value (i.e., > 0.95) of the coefficient of multiple determination (R^2) was obtained for all the developed constitutive equations. A simple statistical procedure was also presented to apply a desired level of conservativeness to the CLS prediction models.

10.2 Conclusions

The following are the main conclusions reached as a result of the extensive parametric numerical analyses conducted in this study on the effect of material stress-strain properties on the inelastic stability response of cylindrical shell structures.

1. The novel stress-strain model developed in this project has advanced capabilities to mathematically characterize any continuously-hardening (i.e., no strain-softening) stress-strain curve, such as is typical for metallic materials; including stress-strain curves of materials with a well-defined yield plateau.
2. The developed stress-strain model is able to mathematically represent the entire stress-strain curve using only two model constants namely: the ‘*heel*’ constant and the ‘*knee*’ constant. The ‘*heel*’ constant tends to control the concavity whereas the ‘*knee*’ constant tends to control the convexity of the stress-strain curve.
3. The mathematical form of the developed model engenders an inherent double curvature in the stress-strain approximation, even for RHT curves, as a fully convex curve can only be achieved if the *heel* constant has a value of zero. It is, therefore, necessary for control measures to be put in place to limit the inevitably-existent yield plateau in RHT curves to

infinitesimal proportions of the strain range. The double-curvature feature of the developed stress-strain model allows a desirable length of the yield plateau to be specified by performing an iterative procedure to determine the value of stress that corresponds to a specified value of strain at the inflection point of the curve.

4. In general, the ultimate strength and deformational capacity of simply-supported flat plates under uniform compression both have a negative nonlinear relationship with the slenderness ratio. However, under uniform compression, the existence of a yield plateau in the stress-strain relationship makes the load-deformation response of simply-supported plates unsusceptible to changes in the overall shape of the stress-strain curve. Contrastingly, the load-carrying capacity and deformational capacity of plates made of an RHT material are highly sensitive to slight variations in the overall shape of the material stress-strain curve.
5. Overlooking the effect of material property variation in the approximation of the ultimate strength of simply-supported flat plates subjected to uniform compression, and using a single curve such as the Winter curve, may lead to inaccurate results. Comparative evaluation of FE-derived results for the ultimate compressive strength with the Winter curve indicates a high likelihood of overestimating the ultimate strength of thick plates by the Winter curve and possible underestimation for thinner plates.
6. The effect of initial geometric imperfections on the CLS of pipe segments is not explicitly considered in this research. There is the tendency for geometric imperfections to have a more profound effect on the CLS of pipes under bending, compared to pipes under uniform axial compression. However, such presumption is strongly contingent on the coincidence of imperfections with the bending plane, as well as the compression side, of the pipe segment. On the other hand, circumferential variation in the nominal thickness of the pipe wall has a relatively more significant effect on the CLS compared to the commonly-existing corrugated modes of initial geometric imperfection. There is, however, very limited data on measured pipe wall thickness variation, which makes it difficult for adaptation to CLS prediction models.
7. At the later stages of collapse, the mode of deformation in a pipe segment is characterized by formation of a diamond-shaped wrinkle that that is longitudinally nonsymmetric at the

localized buckle location, especially under zero or low internal pressure conditions. The use of a half-length pipe model, however, imposes no errors to the evaluation of the CLS as the half-length pipe model and full-length pipe model follow the same trajectory of the moment-curvature response up to and slightly beyond the limit point. In the early stages of local buckling deformation, both models exhibit an outward-bulge mode of deformation which is longitudinally symmetric, and divergence in the moment-curvature response only commences beyond the limit point, when the wrinkle deformation of the full-length model transforms into a nonsymmetric mode.

8. The relationship between the pipe's D/t ratio and the CLS is generally negative and nonlinear for all loading conditions investigated. The nonlinearity of the CLS vs. D/t ratio relationship tends to increase due to a rise in the internal pressure. This trend is slightly different in YPT pipes subjected to a high level of internal pressure whereby the CLS vs. D/t ratio relationship features an almost-linear, but still negative, trend. The nonlinearity of the CLS vs. D/t ratio trends is more prominent in YPT pipes, compared to RHT pipes, especially at lower D/t ratios.
9. The relationship between the CLS and the internal pressure generally exhibits a positive nonlinear trend for all three investigated loading conditions. Similar to the CLS vs. D/t ratio relationship, nonlinearity of the CLS vs. internal pressure relationship is more prominent in YPT pipes, compared to RHT pipes.
10. A positive linear relationship tends to generally exist between the CLS of YPT pipes and the yield stress of the material. However, as the D/t ratio reduces, and the internal pressure increases, the slope of the linear trendline between the CLS and the yield stress reduces progressively and may become negative. On the other hand, the trend that characterizes the relationship between the PLUS ratio and the CLS of RHT pipes is generally negative and nonlinear. The CLS vs. PLUS ratio relationships for different material grades tend to be aligned along the path of a singular trendline indicating a negligible relevance of the material grade (i.e., the offset yield stress) to the CLS of RHT pipes.
11. At moderate-to-high D/t ratios, the length of the yield plateau (YPL) has no significant effect on the CLS of YPT pipes. However, at a low D/t ratio, the relationship between the

CLS of YPT pipes and the YPL ranges from a negative almost-linear trend (at zero internal pressure) to a positive almost-linear trend (at high internal pressure). Contrarily, superior strain hardening tends to generally improve the deformational capacity of RHT pipes and vice versa. However, the overall effect of strain-hardening on the CLS of RHT pipes tends to diminish as the pipe's D/t ratio decreases.

12. Derivation of constitutive semi-empirical models for prediction for the CLS of pipes under various loading combinations can be effectively achieved using the combinative multiplication approach adopted in this study, even for a large number of parameters. However, reasonable accuracy is only guaranteed if the mathematical form of the individual variable functions is systematically constructed to adequately reflect the interrelationships between the constituent parameters.

10.3 Recommendations

The equations developed in this study are not exhaustive of all possible combinations of the parameters considered to be most relevant to the deformational capacity of onshore pipelines under various loading conditions. However, the equations can be applied directly for preliminary design purposes but should be used with caution, especially for parameter values that fall outside the ranges considered herein.

This study stems from an attempt to fine-tune the material characterization process for application to mechanical response modeling purposes. However, the associated risk of the fine-tuning process is the greater possibility of misrepresentation with improper application. It is therefore recommended that the material model should be used with caution in order to avoid the potential consequences of wrong prediction of the CLS of pipes when using the developed equations.

The developed CLS prediction models are highly sensitive to the shape constants and the PLUS ratio (for RHT pipes) hence, the specific procedures that have been adopted for the material characterization procedure in this research should, as much as possible, be replicated in applying the developed stress-strain model to the CLS prediction models. Two very important aspects to carefully consider are: (1) determination of the proportionality limit stress, and (2) determination of the ultimate proof stress. In accordance with the procedures implemented in this research, the

ultimate proof stress at a uniform elongation equal to a total strain of 10% should be used to obtain the shape constants for the stress-strain curves. Deriving the proportionality limit point from available tensile coupon test data can be a tricky task. The rule of thumb adopted herein is to calculate the deviation of strain values from the linear elastic path of the stress-strain curve and pick the proportionality limit stress as the experimentally-obtained stress corresponding to the experimentally-obtained strain closest to a 20% deviation from the linear elastic path of the curve, i.e., a lower or higher value of strain than the nominal 20% deviation strain value can be selected, whichever is closest.

The precision of the developed stress-strain model makes it possible for an extremely large range of values to be obtained for either of the shape constants when a least-squares curve fitting method is utilized. A typical example is the *heel* constant obtained for the UGA508 material stress-strain curve used for experimental validation of the FE pipe models for this research (in [Section 6.6](#)). The initial value obtained from the least-squares curve fitting was 1.266×10^7 hence it became necessary to perform a simple sensitivity analysis to determine a reasonable value of the *heel* constant that does not significantly compromise the accuracy of the stress-strain curve approximation. The R-squared value is plotted against various values of the heel constant to illustrate the sensitivity analysis.

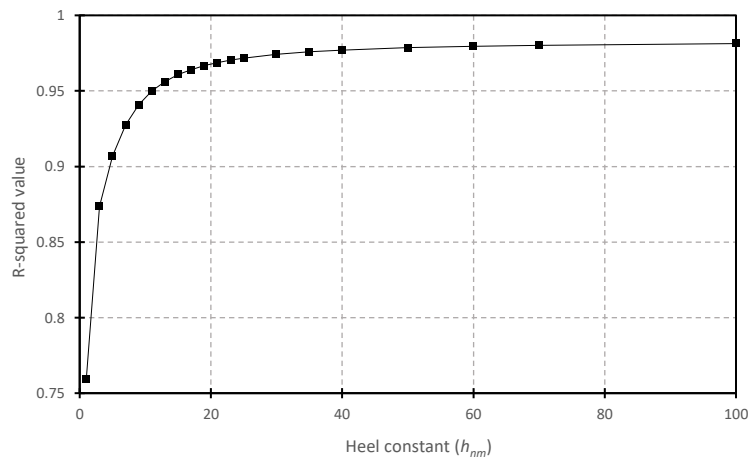


Figure 10-1: Plot of Curve-fitted R-squared value vs. heel constant

The plot in Figure 10-1 indicates that a value of the heel constant close to 30 gives a reasonable approximation of the stress-strain curve without significantly compromising the goodness-of-fit.

Values of the heel constant above 40 are, however, unnecessary as they do not produce any significant improvement in the goodness-of-fit and may lead to flawed predictions of the CLS when applied to the CLS prediction models. Nevertheless, it is recommended that future studies be conducted to further optimize the applicability of the developed stress-strain model for material stress-strain characterization

It may be necessary to extend the research conducted herein to investigate the effect of material properties of the parent metal to the buckling response of spiral-welded and longitudinally-seamed pipe segments, and ultimately derive similar constitutive equations, or simply produce knock-down factors to the current prediction models, if required.

Material anisotropy has been observed in past researches to be more prevalent in high strength steel materials and is not considered in this study. However, the effect of material anisotropy has been observed to be strongly dependent on the level of internal pressure as the buckling response of pipes under zero-to-low internal pressure tends to be governed by the longitudinal compressive stress-strain curve of the pipe material, whereas the buckling response of pipes under moderate-to-high internal pressure tends to be governed by the circumferential tensile stress-strain curve of the pipe material. Research has also shown that the effect of material anisotropy on the CLS tends to diminish at high internal pressures, therefore indicating that the longitudinal compressive stress-strain curve may be generally sufficient for predicting the deformational capacity of pipe segments under various loading combinations. It is therefore recommended that the developed material model should be used to characterize experimentally-obtained longitudinal compressive stress-strain curves and full-scale tests should be conducted to investigate and determine the appropriate stress-strain curve for better predicting the CLS.

Reports on axial tension coupon tests of various metallic materials indicate that the rate of application of displacement-controlled loading has a negligible effect on the stress-strain response. Review of past researches on the buckling behavior of buried pipelines subjected to seismic excitations also indicates that at the strain rate prevalent in earthquakes, a buried pipe buckles dynamically under an axial compressive stress or strain that is practically identical to the static buckling stress or strain. The effect of strain rate is therefore not accounted for in this research as the deformation induced by the ground displacements considered herein (e.g., slope failures) are assumed to be applied very slowly such that static application can be assumed. It is,

however, recommended for future research that the effect of dynamic application of loading on the CLS should be studied to properly ascertain its significance.

On a final note, it is recommended that the procedures implemented in this research should be extended to consider lower values of the D/t ratio (i.e., < 41), more material types (e.g. aluminum and other types of steel), more material grades for pipeline steels (i.e., lower grades than X52 and higher grades than X80), and a larger spread of variations of the material curve shapes for the different material grades. For higher grade steels, material anisotropy effects can be further explored, and the developed material model can be employed for incorporation into future CLS prediction models.



BIBLIOGRAPHY

- Abdoun, T. H. *et al.* (2009) ‘Factors influencing the behavior of buried pipelines subjected to earthquake faulting’, *Soil Dynamics and Earthquake Engineering*. Elsevier, 29(3), pp. 415–427. doi: 10.1016/J.SOILDYN.2008.04.006.
- Adeeb, S. M. (2011) *Introduction to solid mechanics and finite element analysis using Mathematica*. Dubuque, IA: Kendall Hunt Publishing Company.
- Adeeb, S., Zhou, J. and Horsley, D. (2006) ‘Investigating the Effect of UOE Forming Process on the Buckling of Line Pipes Using Finite Element Modeling’, in *Volume 1: Project Management; Design and Construction; Environmental Issues; GIS/Database Development; Innovative Projects and Emerging Issues; Operations and Maintenance; Pipelining in Northern Environments; Standards and Regulations*. ASME, pp. 169–174. doi: 10.1115/IPC2006-10175.
- Ades, C. S. (1957) ‘Bending Strength of Tubing in the Plastic Range’, *Journal of the Aeronautical Sciences*, 24(8), pp. 605–610. doi: 10.2514/8.3916.
- Afshan, S. and Gardner, L. (2013) ‘The continuous strength method for structural stainless steel design’, *Thin-Walled Structures*. Elsevier, 68, pp. 42–49. doi: 10.1016/J.TWS.2013.02.011.
- Ahmed, S., Ashraf, M. and Anwar-Us-Saadat, M. (2016) ‘The Continuous Strength Method for slender stainless steel cross-sections’, *Thin-Walled Structures*. Elsevier, 107, pp. 362–376. doi: 10.1016/J.TWS.2016.06.023.
- Akin, J. E. (2009) *FEA Buckling Analysis, MECH 403*. Available at: https://www.clear.rice.edu/mech403/HelpFiles/FEA_Buckling_analysis.pdf (Accessed: 28 August 2016).
- American Bureau of Shipping (2006) ‘ABS Guide for Building and Classing Subsea Pipeline Systems’. Houston, Texas: American Bureau of Shipping.
- American Lifelines Alliance (2005) *American Society of Civil Engineers, Guidelines for the Design of Buried Steel Pipe (with Addenda through February 2005)*. Reston, VA, USA.
- American Petroleum Institute (2007) *API 5L: Specification for Line Pipe*. 44th edn. USA: American Petroleum Institute.
- API 1111 (1999) ‘Design, construction, operation, and maintenance of offshore hydrocarbon pipelines’. Washington, DC, USA: American Petroleum Institute.
- API 579-1/ASME FFS-1 (2007) *Fitness-for-service*. Houston, Texas: The American Society of Mechanical Engineers.

- Arasaratnam, P., Sivakumaran, K. S. and Tait, M. J. (2011) 'True stress-true strain models for structural steel elements', *ISRN Civil Engineering*.
- Arbocz, J. (1982) 'The Imperfection Data Bank, a Mean to Obtain Realistic Buckling Loads', in *Buckling of Shells*. Berlin, Heidelberg: Springer Berlin Heidelberg, pp. 535–567. doi: 10.1007/978-3-642-49334-8_19.
- Arifin, R. B. *et al.* (2010) 'Seismic Analysis for the Subsea Pipeline System', in *29th International Conference on Ocean, Offshore and Arctic Engineering: Volume 5, Parts A and B*. ASME, pp. 659–667. doi: 10.1115/OMAE2010-20671.
- Ariman, T. and Muleski, G. E. (1981) 'A review of the response of buried pipelines under seismic excitations', *Earthquake Engineering & Structural Dynamics*, 9(2), pp. 133–152. doi: 10.1002/eqe.4290090204.
- Ashraf, M., Gardner, L. and Nethercot, D. A. (2008) 'Structural Stainless Steel Design: Resistance Based on Deformation Capacity', *Journal of Structural Engineering*, 134(3), pp. 402–411. doi: 10.1061/(ASCE)0733-9445(2008)134:3(402).
- Axelrad, E. L. (1965) 'Refinement of buckling-load analysis for tube flexure by way of considering precritical deformation', *Izvestiya Akademii Nauk SSSR, Otdelenie Tekhnicheskikh Nauk, Mekhanika i Mashinostroenie*, 4, pp. 133–139.
- Axelrad, E. L. (1987) *Theory of Flexible Shells*. 28th edn, *North-Holland Series in Applied Mathematics and Mechanics*. 28th edn. Edited by J. D. Achenbach *et al.* Amsterdam, The Netherlands: Elsevier Science Publishers B.V.
- Babcock, C. D. (1974) 'Experiments in shell buckling', in Fung, Y. C. and Sechler, E. E. (eds) *Thin-shell structures: Theory, experiment and design*. Englewood Cliffs, NJ: Prentice-Hall, pp. 345–369.
- Bai, Q. and Bai, Y. (2014) 'Use of High-Strength Pipeline Steels', in *Subsea Pipeline Design, Analysis, and Installation*. Oxford, UK: Gulf Professional Publishing, pp. 675–694.
- Bardi, F. C. and Kyriakides, S. (2006) 'Plastic buckling of circular tubes under axial compression—part I: Experiments', *International Journal of Mechanical Sciences*. Pergamon, 48(8), pp. 830–841. doi: 10.1016/J.IJMECSCI.2006.03.005.

- Bardi, F. C., Kyriakides, S. and Yun, H. D. (2006) 'Plastic buckling of circular tubes under axial compression—part II: Analysis', *International Journal of Mechanical Sciences*. Pergamon, 48(8), pp. 842–854. doi: 10.1016/J.IJMECSCI.2006.03.002.
- Bathe, K. J. and Saunders, H. (1984) 'Finite Element Procedures in Engineering Analysis', *Journal of Pressure Vessel Technology*. Englewood Cliffs, N.J.: Prentice-Hall, 106(4), p. 421. doi: 10.1115/1.3264375.
- Batterman, S. C. (1965) 'Plastic buckling of axially compressed cylindrical shells', *AIAA Journal*, 3(2), pp. 316–325. doi: 10.2514/3.2848.
- Batterman, S. C. and Lee, L. H. N. (1966) 'Effect of modes on plastic buckling of compressed cylindrical shells.', *AIAA Journal*, 4(12), pp. 2255–2257. doi: 10.2514/3.3900.
- Becque, J., Lecce, M. and Rasmussen, K. J. R. (2008) 'The direct strength method for stainless steel compression members', *Journal of Constructional Steel Research*. Elsevier, 64(11), pp. 1231–1238. doi: 10.1016/J.JCSR.2008.07.007.
- Betten, J. and Shin, C. H. (2000) 'Elastic-plastic buckling analysis of rectangular plates subjected to biaxial loads', *Forschung im Ingenieurwesen*, 65(9), pp. 273–278. doi: 10.1007/s100109900023.
- Bezkorovainy, P., Burns, T. and Rasmussen, K. J. R. (2003) 'Strength Curves for Metal Plates in Compression', *Journal of Structural Engineering*, 129(11), pp. 1433–1440. doi: 10.1061/(ASCE)0733-9445(2003)129:11(1433).
- Bijlaard, P. P. (1949) 'Theory and Tests on the Plastic Stability of Plates and Shells', *Journal of the Aeronautical Sciences*, 16(9), pp. 529–541. doi: 10.2514/8.11851.
- Blachut, J., Galletly, G. D. and James, S. (1996) 'On the Plastic Buckling Paradox for Cylindrical Shells', *Proceedings of the Institution of Mechanical Engineers, Part C: Journal of Mechanical Engineering Science*. SAGE PublicationsSage UK: London, England, 210(5), pp. 477–488. doi: 10.1243/PIME_PROC_1996_210_221_02.
- Bleich, F., Bleich, H. H. and Ramsey, L. B. (1952) *Buckling strength of metal structures*. 1st edn. New York: McGraw-Hill.
- Bodner, S. R. and Partom, Y. (1975) 'Constitutive Equations for Elastic-Viscoplastic Strain-Hardening Materials', *Journal of Applied Mechanics*. American Society of Mechanical Engineers, 42(2), p. 385. doi: 10.1115/1.3423586.

- Bouquerel, J., Verbeken, K. and De Cooman, B. C. (2006) ‘Microstructure-based model for the static mechanical behaviour of multiphase steels’, *Acta Materialia*. Pergamon, 54(6), pp. 1443–1456. doi: 10.1016/J.ACTAMAT.2005.10.059.
- Bouwkamp, J. G. and Stephen, R. M. (1973) ‘Large diameter pipe under combined loading’, *Transportation Engineering Journal of ASCE*, 99(3), pp. 521–536.
- Bouwkamp, J. G. and Stephen, R. M. (1974) *Full-scale studies on the structural behavior of large diameter pipes under combined loading. Report No. UCSESM 74-1*. Berkeley, California.
- Brazier, L. G. (1927) ‘On the Flexure of Thin Cylindrical Shells and Other “Thin” Sections’, *Proceedings of the Royal Society A: Mathematical, Physical and Engineering Sciences*. The Royal Society, 116(773), pp. 104–114. doi: 10.1098/rspa.1927.0125.
- Bruschi, R. *et al.* (1995) ‘Finite element method as numerical laboratory for analyzing pipeline response under internal pressure, axial load, bending moment’, in *Proceedings of the 14th International Conference on Offshore Mechanics and Arctic Engineering, Volume 5*. Copenhagen, Denmark: ASME.
- Brush, D. O. and Almroth, B. O. (1975) *Buckling of Bars, Plates, and Shells*. New York: McGraw-Hill.
- Bryan, G. H. (1890) ‘On the Stability of a Plane Plate under Thrusts in its own Plane, with Applications to the “Buckling” of the Sides of a Ship’, *Proceedings of the London Mathematical Society*, s1-22(1), pp. 54–67. doi: 10.1112/plms/s1-22.1.54.
- Buchanan, A. *et al.* (2004) ‘The effect of stress–strain relationships on the fire performance of steel beams’, *Engineering Structures*. Elsevier, 26(11), pp. 1505–1515. doi: 10.1016/J.ENGSTRUCT.2004.05.003.
- Bulson, P. S. (1970) *Theory of flat plates*. London: Chatto and Windus. Available at: https://scholar.google.ca/scholar?q=Bulson%2C+P.S.%2C+1970.+Theory+of+flat+plates&btnG=&hl=en&as_sdt=0%2C5 (Accessed: 14 August 2017).
- Bushnell, D. (1982) ‘Plastic Buckling of Various Shells’, *Journal of Pressure Vessel Technology, Transactions of the ASME*. American Society of Mechanical Engineers, 104(2), pp. 51–72. doi: 10.1115/1.3264190.

- Calladine, C. R. (1988) 'The theory of thin shell structures 1888–1988', *Proceedings of the Institution of Mechanical Engineers, Part A: Journal of Power and Energy*, pp. 141–149. doi: 10.1243/PIME_PROC_1988_202_020_02.
- Canadian Standards Association (2007) 'Oil and gas pipeline systems. CSA-Z662-2007'. Ontario, Canada: Canadian Standards Association.
- Castro, S. G. P. *et al.* (2014) 'Geometric imperfections and lower-bound methods used to calculate knock-down factors for axially compressed composite cylindrical shells', *Thin-Walled Structures*. Elsevier, 74, pp. 118–132. doi: 10.1016/j.tws.2013.08.011.
- Chen, C. C., Ariman, T. and Lee, L. H. N. (1980) 'Elastic buckling analysis of buried pipelines under seismic loads', in *ASME Century 2 Pressure Vessel and Piping Conference*. San Francisco, California.
- Chen, H. *et al.* (2011) 'Test Evaluation of High Strain Line Pipe Material', in *The Twenty-first International Offshore and Polar Engineering Conference*. Maui, Hawaii, USA: International Society of Offshore and Polar Engineers. Available at: <https://www.onepetro.org/conference-paper/ISOPE-I-11-122> (Accessed: 4 September 2018).
- Chen, J. and Young, B. (2006) 'Stress–strain curves for stainless steel at elevated temperatures', *Engineering Structures*. Elsevier, 28(2), pp. 229–239. doi: 10.1016/J.ENGSTRUCT.2005.07.005.
- Chen, Y. N. and Kempner, J. (1976) 'Buckling of oval cylindrical shells under compression and asymmetric bending', *AIAA Journal*, 14(9), pp. 1235–1240. doi: 10.2514/3.7215.
- Chryssanthopoulos, M. K. and Low, Y. M. (2001) 'A method for predicting the flexural response of tubular members with non-linear stress–strain characteristics', *Journal of Constructional Steel Research*. Elsevier, 57(11), pp. 1197–1216. doi: 10.1016/S0143-974X(01)00033-5.
- Corbett, K. T., Bowen, R. R. and Petersen, C. W. (2003) 'High Strength Steel Pipeline Economics', in *Proceedings of The Thirteenth International Offshore and Polar Engineering Conference*. Honolulu, Hawaii, USA: International Society of Offshore and Polar Engineers, pp. 105–112. Available at: <https://www.onepetro.org/conference-paper/ISOPE-I-03-345> (Accessed: 17 November 2018).

- Corona, E. and Kyriakides, S. (1988) ‘On the collapse of inelastic tubes under combined bending and pressure’, *International Journal of Solids and Structures*. Pergamon, 24(5), pp. 505–535. doi: 10.1016/0020-7683(88)90005-4.
- Corona, E., Lee, L.-H. and Kyriakides, S. (2006) ‘Yield anisotropy effects on buckling of circular tubes under bending’, *International Journal of Solids and Structures*. Pergamon, 43(22–23), pp. 7099–7118. doi: 10.1016/J.IJSOLSTR.2006.03.005.
- Curtze, S. *et al.* (2009) ‘Deformation behavior of TRIP and DP steels in tension at different temperatures over a wide range of strain rates’, *Materials Science and Engineering: A*. Elsevier, 507(1–2), pp. 124–131. doi: 10.1016/J.MSEA.2008.11.050.
- Dama, E., Karamanos, S. A. and Gresnigt, A. M. (2007) ‘Failure of Locally Buckled Pipelines’, *Journal of Pressure Vessel Technology*. American Society of Mechanical Engineers, 129(2), p. 272. doi: 10.1115/1.2716431.
- Das, S., Cheng, J. J. R. and Murray, D. W. (2002) *Fracture of Wrinkled Energy Pipelines. Structural Engineering Report No. 247*. Edmonton, AB, Canada.
- Davis, J. R. (1998) *Metals Handbook: Desk Edition*. 2nd edn. Materials Park, Ohio: American Society for Metals (ASM International).
- DeGeer, D. *et al.* (2007) ‘Local Buckling Assessments for the Medgaz Pipeline’, in *Volume 3: Pipeline and Riser Technology; CFD and VIV*. ASME, pp. 453–463. doi: 10.1115/OMAE2007-29493.
- DelCol, P. R. *et al.* (1998) *Behavior of Large Diameter Line Pipe Under Combined Loads, Structural Engineering Report No. 224*. Edmonton, AB, Canada.
- Deml, M. and Wunderlich, W. (1997) ‘Direct evaluation of the “worst” imperfection shape in shell buckling’, *Computer Methods in Applied Mechanics and Engineering*. North-Holland, 149(1–4), pp. 201–222. doi: 10.1016/S0045-7825(97)00055-8.
- Det Norske Veritas (2010) *Submarine pipeline systems - DNV-OS-F101*. Oslo, Norway: DNV.
- Donnell, L. H. (1933) *Stability of thin-walled tubes under torsion, NACA Report No. 479*. Washington D.C.
- Donnell, L. H. (1934) ‘A new theory for the buckling of thin cylinders under axial compression and bending’, *Transactions of the A.S.M.E*, 56(11), pp. 795–806. Available at: http://cybra.lodz.pl/Content/6356/AER_56_12.pdf (Accessed: 29 October 2018).

- Dorey, A. B. *et al.* (1999) ‘Testing and experimental results for NPS30 line pipe under combined loads’, in *Proceedings of the 18th International Conference on Offshore Mechanics and Arctic Engineering*. St. Johns, Newfoundland: ASME, p. OMAE PL 99-5022.
- Dorey, A. B., Cheng, J. J. R. and Murray, D. W. (2001) *Critical Buckling Strains for Energy Pipelines, Structural Engineering Report No. 237*. Edmonton, Alberta.
- Dorey, A. B., Murray, D. W. and Cheng, J. J. R. (2000) ‘An Experimental Evaluation of Critical Buckling Strain Criteria’, in *Volume 1: Codes, Standards and Regulations; Design and Constructions; Environmental; GIS/Database Development; Innovative Projects and Emerging Issues*. ASME, p. V001T01A011. doi: 10.1115/IPC2000-110.
- Dorey, A. B., Murray, D. W. and Cheng, J. J. R. (2002) ‘Material Property Effects on Critical Buckling Strains in Energy Pipelines’, in *4th International Pipeline Conference, Parts A and B*. ASME, pp. 475–484. doi: 10.1115/IPC2002-27225.
- Dorey, A. B., Murray, D. W. and Cheng, J. J. R. (2006) ‘Critical Buckling Strain Equations for Energy Pipelines—A Parametric Study’, *Journal of Offshore Mechanics and Arctic Engineering*. American Society of Mechanical Engineers, 128(3), p. 248. doi: 10.1115/1.2199561.
- Dundu, M. (2018) ‘Evolution of stress–strain models of stainless steel in structural engineering applications’, *Construction and Building Materials*. Elsevier, 165, pp. 413–423. doi: 10.1016/J.CONBUILDMAT.2018.01.008.
- El-Sawy, K. M., Nazmy, A. S. and Martini, M. I. (2004) ‘Elasto-plastic buckling of perforated plates under uniaxial compression’, *Thin-Walled Structures*. Elsevier, 42(8), pp. 1083–1101. doi: 10.1016/J.TWS.2004.03.002.
- Ellinas, C. P., Supple, W. J. and Walker, A. C. (1984) *Buckling of offshore structures: a state-of-the-art review*. Houston: Gulf Publishing Company.
- EN 1993-1-4 2006 (2006) *Eurocode 3: Design of steel structures - Part 1-4: General rules - Supplementary rules for stainless steels*. Brussels: CEN.
- Eskel, A. E. and Martin, D. C. (1977) ‘Seismic Risks of California’s Water Lifeline’, *Journal of the Technical Councils of ASCE*. ASCE, 103(1), pp. 25–37. Available at: <http://cedb.asce.org/CEDBsearch/record.jsp?dockey=0007746> (Accessed: 17 November 2018).

- Fabian, O. (1977) ‘Collapse of cylindrical, elastic tubes under combined bending, pressure and axial loads’, *International Journal of Solids and Structures*. Pergamon, 13(12), pp. 1257–1270. doi: 10.1016/0020-7683(77)90099-3.
- Fatemi, S. M., Showkati, H. and Maali, M. (2013) ‘Experiments on imperfect cylindrical shells under uniform external pressure’, *Thin-Walled Structures*. Elsevier, 65, pp. 14–25. doi: 10.1016/j.tws.2013.01.004.
- Faulkner, D. (1975) ‘A Review of Effective Plating to be Used in the Analysis of Stiffened Plating in Bending and Compression’, *Journal of Ship Research*, 19(1), pp. 1–17.
- Flügge, W. (1932) ‘Die Stabilität der Kreiszyinderschale’, *Ing Arch*, 3, pp. 463–506.
- Fyrileiv, O. and Collberg, L. (2005) ‘Influence of Pressure in Pipeline Design: Effective Axial Force’, in *24th International Conference on Offshore Mechanics and Arctic Engineering: Volume 3*. ASME, pp. 629–636. doi: 10.1115/OMAE2005-67502.
- Gardner, L. and Ashraf, M. (2006) ‘Structural design for non-linear metallic materials’, *Engineering Structures*. Elsevier, 28(6), pp. 926–934. doi: 10.1016/J.ENGSTRUCT.2005.11.001.
- Gardner, L. and Nethercot, D. A. (2004) ‘Experiments on stainless steel hollow sections—Part 1: Material and cross-sectional behaviour’, *Journal of Constructional Steel Research*. Elsevier, 60(9), pp. 1291–1318. doi: 10.1016/J.JCSR.2003.11.006.
- Gardner, L., Wang, F. and Liew, A. (2011) ‘Influence of strain-hardening on the behavior and design of steel structures’, *International Journal of Structural Stability and Dynamics*. World Scientific Publishing Company, 11(05), pp. 855–875. doi: 10.1142/S0219455411004373.
- Gellin, S. (1979) ‘Effect of an Axisymmetric Imperfection on the Plastic Buckling of an Axially Compressed Cylindrical Shell’, *Journal of Applied Mechanics*. American Society of Mechanical Engineers, 46(1), p. 125. doi: 10.1115/1.3424483.
- Gellin, S. (1980) ‘The plastic buckling of long cylindrical shells under pure bending’, *International Journal of Solids and Structures*. Pergamon, 16(5), pp. 397–407. doi: 10.1016/0020-7683(80)90038-4.
- Gerard, G. and Becker, H. (1957) *Handbook of structural stability part III: buckling of curved plates and shells*. NACA Technical Note 3783. Washington, DC, United States . Available at: <https://ntrs.nasa.gov/search.jsp?R=19930084510> (Accessed: 17 November 2018).

- Gresnigt, A. M. (1986) ‘Plastic Design of Buried Steel Pipelines in Settlement Areas’, *Heron*, 31(4).
- Gresnigt, A. M., van Foeken, R. J. and Chen, S. L. (1996) ‘Effect of Local Buckling On Burst Pressure’, in *The Sixth International Offshore and Polar Engineering Conference*. Los Angeles, California, USA: International Society of Offshore and Polar Engineers, pp. 80–88. Available at: <https://www.onepetro.org/conference-paper/ISOPE-I-96-096> (Accessed: 29 October 2018).
- Gresnigt, A. M. and Karamanos, S. A. (2009) ‘Local Buckling Strength And Deformation Capacity of Pipes’, in *The Nineteenth International Offshore and Polar Engineering Conference*. Osaka, Japan : International Society of Offshore and Polar Engineers, pp. 212–224. Available at: <https://www.onepetro.org/conference-paper/ISOPE-I-09-002> (Accessed: 29 October 2018).
- Guedes Soares, C. (1988) ‘Design equation for the compressive strength of unstiffened plate elements with initial imperfections’, *Journal of Constructional Steel Research*, 9(4), pp. 287–310. doi: 10.1016/0143-974X(88)90065-X.
- Guo, L. *et al.* (2016) ‘Behavior of thin-walled circular hollow section stub columns under axial compression’, *International Journal of Steel Structures*, 16(3), pp. 777–787. doi: 10.1007/s13296-015-0159-0.
- Ha, D. *et al.* (2008) ‘Buried high-density polyethylene pipelines subjected to normal and strike-slip faulting — a centrifuge investigation’, *Canadian Geotechnical Journal*, 45(12), pp. 1733–1742. doi: 10.1139/T08-089.
- Handelman, G. H. and Prager, W. (1948) *Plastic buckling of rectangular plates under edge thrusts*, *NACA Technical Note*, No. 1530. Washington, D.C. Available at: http://digital.library.unt.edu/ark:/67531/metadc60269/%5Cnhttp://digital.library.unt.edu/ark:/67531/metadc60269/m2/1/high_res_d/19930092011.pdf (Accessed: 14 August 2017).
- Harris, L. A. (1957) ‘The Stability of Thin-Walled Unstiffened Circular Cylinders Under Axial Compression Including the Effects of Internal Pressure’, *Journal of the Aeronautical Sciences*, 24(8), pp. 587–596. doi: 10.2514/8.3911.
- Hauch, S. and Bai, Y. (1998) ‘Use of finite element analysis for local buckling design of pipelines’, in *Proceedings of the 14th International Conference on Offshore Mechanics and Arctic Engineering*. ASME.

- Hibbit, Karlsson and Sorensen Inc. (2003) ‘ABAQUS/STANDARD - Theory Manual, Version 6.14’. Rhode Island, USA: Dassault Systèmes.
- Hibbitt, D., Karlsson, B. and Sorensen, P. (2014) ‘ABAQUS Standard User’s and Reference Manuals, Version 6.14’. Rhode Island, USA.
- Hilburger, M. W., Nemeth, M. P. and Starnes, J. H. (2006) ‘Shell Buckling Design Criteria Based on Manufacturing Imperfection Signatures’, *AIAA Journal*, 44(3), pp. 654–663. doi: 10.2514/1.5429.
- Hill, H. N. (1944) *Determination of stress–strain relations from the offset yield strength values. NACA Technical Note No. 927*. Washington, D.C.
- Hill, R. (1948) ‘A Theory of the Yielding and Plastic Flow of Anisotropic Metals’, *Proceedings of the Royal Society A: Mathematical, Physical and Engineering Sciences*. The Royal Society, 193(1033), pp. 281–297. doi: 10.1098/rspa.1948.0045.
- Hill, R. (1958) ‘A general theory of uniqueness and stability in elastic-plastic solids’, *Journal of the Mechanics and Physics of Solids*. Pergamon, 6(3), pp. 236–249. doi: 10.1016/0022-5096(58)90029-2.
- Hill, R. (1961) ‘Bifurcation and uniqueness in non-linear mechanics of continua’, in *Problems of continuum mechanics*. Philadelphia, PA: Society of Industrial and Applied Mathematics, pp. 155–164. Available at: https://scholar.google.ca/scholar?hl=en&as_sdt=0%2C5&q=Hill%2C+R.%2C+1961.+Bifurcation+and+uniqueness+in+non-linear+mechanics+of+continua.+In+Problems+of+continuum+mechanics%2C+pp.155-164.+Society+of+Industrial+and+Applied+Mathematics&btnG= (Accessed: 4 September 2018).
- Hines, J. R., Timms, C. M. and DeGeer, D. D. (2007) ‘Thermal Ageing Effects on Thickwalled Line Pipe’, in *Volume 3: Pipeline and Riser Technology; CFD and VIV*. ASME, pp. 573–579. doi: 10.1115/OMAE2007-29661.
- Hobbs, R. E. (1981) ‘Pipeline buckling caused by axial loads’, *Journal of Constructional Steel Research*. Elsevier, 1(2), pp. 2–10. doi: 10.1016/0143-974X(81)90027-4.
- Hobbs, R. E. (1984) ‘In-Service Buckling of Heated Pipelines’, *Journal of Transportation Engineering*, 110(2), pp. 175–189. doi: 10.1061/(ASCE)0733-947X(1984)110:2(175).

- Hollomon, J. H. (1945) ‘Tensile Deformation’, *Transactions of the Metallurgical Society of AIME*, 162, pp. 268–290.
- Holt, J. M. (2000) ‘Uniaxial tension testing’, in Kuhn, H. and Medlin, D. (eds) *ASM Handbook, Volume 8: Mechanical Testing and Evaluation*. Materials Park, Ohio: American Society for Metals (ASM International), pp. 124–142.
- Houliara, S. and Karamanos, S. A. (2006) ‘Buckling and post-buckling of long pressurized elastic thin-walled tubes under in-plane bending’, *International Journal of Non-Linear Mechanics*. Pergamon, 41(4), pp. 491–511. doi: 10.1016/J.IJNONLINMEC.2005.11.002.
- Hradil, P. *et al.* (2013) ‘Generalized multistage mechanical model for nonlinear metallic materials’, *Thin-Walled Structures*. Elsevier, 63, pp. 63–69. doi: 10.1016/J.TWS.2012.10.006.
- Hühne, C. *et al.* (2008) ‘Robust design of composite cylindrical shells under axial compression - Simulation and validation’, *Thin-Walled Structures*. Elsevier, 46(7–9), pp. 947–962. doi: 10.1016/j.tws.2008.01.043.
- Hühne, C., Rolfes, R. and Tessmer, J. (2005) ‘A new approach for robust design of composite cylindrical shells under axial compression’, in Karen Fletcher (ed.) *Proceedings of the European Conference on Spacecraft Structures, Materials and Mechanical Testing (ESA SP-581)*. Noordwijk, The Netherlands, p. 141.1-141.8. Available at: <http://adsabs.harvard.edu/full/2005ESASP.581E.141H>.
- Hutchinson, J. (1965) ‘Axial buckling of pressurized imperfect cylindrical shells’, *AIAA Journal*, 3(8), pp. 1461–1466. doi: 10.2514/3.3169.
- Ilyushin, A. A. (1947) *The Elasto-Plastic Stability of Plates*, *NACA Technical Memorandum, No. 1188*. Washington, D.C. Available at: <https://ntrs.nasa.gov/search.jsp?R=20030065223> (Accessed: 7 May 2018).
- Imperial F.F. (1932) *The criterion of elastic instability of thin duralumin tubes subjected to bending*. *MS Thesis*. Dept. of Mechanical Engineering. University of California.
- Isenberg, J. and Taylor, C. E. (1984) ‘Performance of Water and Sewer Lifelines in the May 2, 1983 Coalinga, California Earthquake’, in *Proceedings of the ASCE Lifeline Earthquake Engineering: Performance, Design and Construction*. San Francisco, California, USA, pp. 176–189.

- Ishikawa, N. *et al.* (2008) ‘Mechanical And Metallurgical Properties of Grade X80 High Strain Linepipe Produced By Heat Treatment On-line Process’, in *The Eighteenth International Offshore and Polar Engineering Conference*. Vancouver, Canada : International Society of Offshore and Polar Engineers, pp. 13–20. Available at: <https://www.onepetro.org/conference-paper/ISOPE-I-08-403> (Accessed: 29 October 2018).
- Iwasaki, T. (1986) ‘Soil liquefaction studies in Japan: state-of-the-art’, *Soil Dynamics and Earthquake Engineering*. Elsevier, 5(1), pp. 2–68. doi: 10.1016/0267-7261(86)90024-2.
- Jaberzadeh, E. and Azhari, M. (2009) ‘Elastic and inelastic local buckling of stiffened plates subjected to non-uniform compression using the Galerkin method’, *Applied Mathematical Modelling*. Elsevier, 33(4), pp. 1874–1885. doi: 10.1016/j.apm.2008.03.020.
- Jacques, P. J. (2004) ‘Transformation-induced plasticity for high strength formable steels’, *Current Opinion in Solid State and Materials Science*. Elsevier, 8(3–4), pp. 259–265. doi: 10.1016/J.COSSMS.2004.09.006.
- Jalali, H. H. *et al.* (2016) ‘Experimental and finite element study of the reverse faulting effects on buried continuous steel gas pipelines’, *Soil Dynamics and Earthquake Engineering*. Elsevier, 86, pp. 1–14. doi: 10.1016/J.SOILDYN.2016.04.006.
- Jayadevan, K. R., Ostby, E. and Thaulow, C. (2004) ‘Strain based fracture mechanics analysis of pipelines’, in *Proceedings of International Conference on Advances in Structural Integrity*, pp. 04–0198.
- Jee (2013) *Course Material for The Subsea Pipeline Design Course held for employees at IKM Ocean Design in Trondheim*. Tonbridge, Kent: Jee.
- Jennings, P. C. (1971) *Engineering features of the San Fernando earthquake of February 9, 1971*, EERL 71-02. Pasadena, California. Available at: <http://resolver.caltech.edu/CaltechEERL:1971.EERL-71-02> (Accessed: 13 November 2018).
- Jirsa, J. O. *et al.* (1972) ‘Ovaling Of Pipelines Under Pure Bending’, in *Offshore Technology Conference*. Offshore Technology Conference. doi: 10.4043/1569-MS.
- Ju, G. T. and Kyriakides, S. (1988) ‘Thermal Buckling of Offshore Pipelines’, *Journal of Offshore Mechanics and Arctic Engineering*. American Society of Mechanical Engineers, 110(4), p. 355. doi: 10.1115/1.3257073.

- Ju, G. T. and Kyriakides, S. (1992) 'Bifurcation and localization instabilities in cylindrical shells under bending—II. Predictions', *International Journal of Solids and Structures*. Pergamon, 29(9), pp. 1143–1171. doi: 10.1016/0020-7683(92)90140-O.
- Kadkhodayan, M. and Maarefdoust, M. (2014) 'Elastic/plastic buckling of isotropic thin plates subjected to uniform and linearly varying in-plane loading using incremental and deformation theories', *Aerospace Science and Technology*. Elsevier Masson, 32(1), pp. 66–83. doi: 10.1016/J.AST.2013.12.003.
- Kainat, M., Adeeb, S., Cheng, J. J. R., *et al.* (2012) 'Identifying Initial Imperfection Patterns of Energy Pipes Using a 3D Laser Scanner', in *2012 9th International Pipeline Conference*. ASME, pp. 57–63. doi: 10.1115/IPC2012-90201.
- Kainat, M., Adeeb, S., Cheng, J. J. R., *et al.* (2012) 'Measurement of Initial Imperfection of Energy Pipelines Using 3D Laser Scanner', in *3rd International Structural Specialty Conference*. Edmonton, AB, Canada.: CSCE.
- Kainat, M. *et al.* (2016) 'Effects of the Initial Geometric Imperfections on the Buckling Behavior of High-Strength UOE Manufactured Steel Pipes', *Journal of Pressure Vessel Technology, Transactions of the ASME*. American Society of Mechanical Engineers, 138(5), p. 051206. doi: 10.1115/1.4032990.
- Kan, W. C. *et al.* (2008) 'Strain-Based Pipelines: Design Consideration Overview', in *The Eighteenth International Offshore and Polar Engineering Conference*. Vancouver, British Columbia: International Society of Offshore and Polar Engineers. Available at: <https://www.onepetro.org/conference-paper/ISOPE-I-08-387> (Accessed: 29 October 2018).
- Kang, K.-B. *et al.* (2007) 'Buckling Behavior of API- X80 Linepipe', in *The Seventeenth International Offshore and Polar Engineering Conference*. Lisbon, Portugal : International Society of Offshore and Polar Engineers, pp. 3254–3260. Available at: <https://www.onepetro.org/conference-paper/ISOPE-I-07-513> (Accessed: 29 October 2018).
- Karamanos, S. A. (2002) 'Bending instabilities of elastic tubes', *International Journal of Solids and Structures*. Pergamon, 39(8), pp. 2059–2085. doi: 10.1016/S0020-7683(02)00085-9.
- Karamitros, D. K., Bouckovalas, G. D. and Kouretzis, G. P. (2007) 'Stress analysis of buried steel pipelines at strike-slip fault crossings', *Soil Dynamics and Earthquake Engineering*. Elsevier, 27(3), pp. 200–211. doi: 10.1016/J.SOILDYN.2006.08.001.

- Karbasian, H. *et al.* (2012) ‘Combined Loading Capacity of Pipelines: Approaches Towards the Compressive Strain Limit’, in *Volume 4: Pipelining in Northern and Offshore Environments; Strain-Based Design; Risk and Reliability; Standards and Regulations*. ASME, p. 375. doi: 10.1115/IPC2012-90615.
- Karman, T. H. (1911) ‘Über die Formänderung dünnwandiger Rohre’, *Z. VDI*, pp. 1889–1895.
- Von Kármán, T. (1910) ‘Festigkeitsprobleme im Maschinenbau’, in *Encyclopedie der mathematischen Wissenschaften IV*. Teubner, pp. 348–352.
- Von Kármán, T., Sechler, E. . and Donnell, L. . (1932) ‘The strength of Thin Plates in Compression’, *Transactions, Applied Mechanics Division, ASME*, 54(5), p. 53. doi: 1.
- Von Kármán, T. and Tsien, H. S. (2012) ‘The Buckling of Thin Cylindrical Shells under Axial Compression’, in *Collected Works of Hsue-Shen Tsien (1938-1956)*, pp. 165–181. doi: 10.1016/B978-0-12-398277-3.50009-9.
- Kempner, J. and Chen, Y.-N. (1974) ‘Buckling and initial postbuckling of oval cylindrical shells under combined axial compression and bending’, *Transactions of the New York Academy of Sciences*, 36(2 Series II), pp. 171–191. doi: 10.1111/j.2164-0947.1974.tb01564.x.
- Kennedy, R. P., Chow, A. M. and Williamson, R. A. (1977) ‘Fault movement effects on buried oil pipeline’, *Transportation Engineering Journal of the American Society of Civil Engineers*. American Society of Civil Engineers, 103(5), pp. 617–633. Available at: [https://www.safetylit.org/citations/index.php?fuseaction=citations.viewdetails&citationIds\[\]=citjournalarticle_78998_29](https://www.safetylit.org/citations/index.php?fuseaction=citations.viewdetails&citationIds[]=citjournalarticle_78998_29) (Accessed: 29 October 2018).
- Kenny, S. *et al.* (2007) ‘Integrating Geohazard Demand And Structural Capacity Modelling Within a Probabilistic Design Framework For Offshore Arctic Pipelines’, in *The Seventeenth International Offshore and Polar Engineering Conference*. Lisbon, Portugal: International Society of Offshore and Polar Engineers. Available at: <https://www.onepetro.org/conference-paper/ISOPE-I-07-492> (Accessed: 29 October 2018).
- Kim, H. O. and Velasco P. (1988) ‘Review of Pipe Buckling for Arctic Pipeline Design’, in *Proceedings of the 7th International Conference on Offshore Mechanics and Arctic Engineering*. Houston, Texas.

- Klever, F. J., Palmer, A. C. and Kyriakides, S. (1994) ‘Limit-state design of high-temperature pipelines’, in *13th International Conference on Offshore Mechanics and Arctic Engineering*. Houston, Texas, p. Vol. 5, pp. 77–92. Available at: <https://www.osti.gov/biblio/55743>.
- Koiter, W. T. (1945) ‘The Stability of Elastic Equilibrium’, *Department of Mechanics, Shipbuilding, and Airplane Building*, PhD. Available at: <http://www.dtic.mil/docs/citations/AD0704124> (Accessed: 4 September 2018).
- Kong, L. Z. *et al.* (2018) ‘True Stress–Strain Curves Test and Material Property Analysis of API X65 and API X90 Gas Pipeline Steels’, *Journal of Pipeline Systems Engineering and Practice*, 9(1), p. 04017030. doi: 10.1061/(ASCE)PS.1949-1204.0000300.
- Korol, R. . (1979) ‘Critical buckling strains of round tubes in flexure’, *International Journal of Mechanical Sciences*. Pergamon, 21(12), pp. 719–730. doi: 10.1016/0020-7403(79)90052-3.
- Kurzydłowski, K. J. (1999) ‘Structure and properties of metals’, *Acta Physica Polonica A*, 96(1), pp. 69–79. Available at: <http://przyrbwn.icm.edu.pl/APP/PDF/96/a096z1p05.pdf> (Accessed: 17 November 2018).
- Kyriakides, S. and Babcock, C. D. (1981) ‘Experimental Determination of the Propagation Pressure of Circular Pipes’, *Journal of Pressure Vessel Technology*. American Society of Mechanical Engineers, 103(4), p. 328. doi: 10.1115/1.3263410.
- Kyriakides, S., Bardi, F. C. and Paquette, J. A. (2005) ‘Wrinkling of Circular Tubes Under Axial Compression: Effect of Anisotropy’, *Journal of Applied Mechanics*, 72(2), pp. 301–305. doi: 10.1115/1.1839590.
- Kyriakides, S. and Ju, G. T. (1992) ‘Bifurcation and localization instabilities in cylindrical shells under bending—I. Experiments’, *International Journal of Solids and Structures*. Pergamon, 29(9), pp. 1117–1142. doi: 10.1016/0020-7683(92)90139-K.
- Kyriakides, S. and Shaw, P. K. (1982) ‘Response and stability of elastoplastic circular pipes under combined bending and external pressure’, *International Journal of Solids and Structures*. Pergamon, 18(11), pp. 957–973. doi: 10.1016/0020-7683(82)90086-5.
- Lara, P. F. (1987) ‘Revisiting the failure criteria of buried pipelines’, in *ASME Pipeline Engineering Symposium*. Dallas, Texas, pp. 143–145.
- Lee, G. M. (1987) ‘The 1985 Mexico Earthquakes: Effects on Water Supply Systems’, in *The Mexico Earthquakes—1985: Factors Involved and Lessons Learned*. ASCE, pp. 364–367.

Available at: <http://cedb.asce.org/CEDBsearch/record.jsp?dockey=0051060> (Accessed: 17 November 2018).

Lee, G. M. and Mejia, S. M. (1986) 'The Effects of the 1985 Mexico City Earthquake on Underground Water and Sewer Pipelines', in *Proceedings of the ASCE Lifeline Seismic Risk Analysis – Case Studies*. Seattle, Washington, USA, pp. 131–136.

Lee, J. P. and Bohinsky, J. A. (1996) 'Design of buried pipeline subjected to large fault movement', in *Proceedings of the 11th World Conference on Earthquake Engineering*. Acapulco, Mexico, pp. 23–28.

Lee, L. H. N. (1962) 'Inelastic Buckling of Initially Imperfect Cylindrical Shells Subject to Axial Compression', *Journal of the Aerospace Sciences*, 29(1), pp. 87–95. doi: 10.2514/8.9306.

Libai, A. and Bert, C. W. (1994) 'A mixed variational principle and its application to the nonlinear bending problem of orthotropic tubes—II. application to nonlinear bending of circular cylindrical tubes', *International Journal of Solids and Structures*. Pergamon, 31(7), pp. 1019–1033. doi: 10.1016/0020-7683(94)90009-4.

Liew, A. and Gardner, L. (2015) 'Ultimate capacity of structural steel cross-sections under compression, bending and combined loading', *Structures*. Elsevier, 1, pp. 2–11. doi: 10.1016/J.ISTRUC.2014.07.001.

Limam, A. *et al.* (1991) 'Buckling of Thin-Walled Cylinder Under Axial Compression and Internal Pressure', in Jullien, J. F. (ed.) *Buckling of Shell Structures, on Land, in the Sea and in the Air*. Essex, England: Elsevier, pp. 359–369.

Limam, A. *et al.* (2008) 'Plastic Buckling and Collapse of Tubes Under Bending and Internal Pressure', in *Volume 3: Pipeline and Riser Technology; Ocean Space Utilization*. ASME, pp. 675–683. doi: 10.1115/OMAE2008-57986.

Limam, A. *et al.* (2010) 'Inelastic wrinkling and collapse of tubes under combined bending and internal pressure', *International Journal of Mechanical Sciences*. Pergamon, 52(5), pp. 637–647. doi: 10.1016/J.IJMECSCI.2009.06.008.

Lin, M. (2015) *Characterization of Tensile and Fracture Properties of X52 Steel Pipes and Their Girth Welds (MSc. Thesis)*. Department of Civil and Environmental Engineering, University of Alberta, Canada.

- Liu, B., Liu, X. J. and Zhang, H. (2009) ‘Strain-based design criteria of pipelines’, *Journal of Loss Prevention in the Process Industries*. Elsevier, 22(6), pp. 884–888. doi: 10.1016/J.JLP.2009.07.010.
- Liu, M. *et al.* (2013) *Realistic strain capacity models for pipeline construction and maintenance. prepared for US department of transportation. Pipeline and Hazardous Materials Safety Administration, Office of Pipeline Safety. Contract No. DTPH56-10-T-000016*. Dublin, OH, USA. Available at: <https://trid.trb.org/view/1471401> (Accessed: 4 September 2018).
- Liu, M. *et al.* (2014) ‘Refined Modeling Processes and Compressive Strain Capacity Models’, in *Volume 4: Production Pipelines and Flowlines; Project Management; Facilities Integrity Management; Operations and Maintenance; Pipelining in Northern and Offshore Environments; Strain-Based Design; Standards and Regulations*. ASME, p. V004T11A002. doi: 10.1115/IPC2014-33202.
- Liu, R., Basu, P. and Xiong, H. (2015) ‘Laboratory tests and thermal buckling analysis for pipes buried in Bohai soft clay’, *Marine Structures*. Elsevier, 43, pp. 44–60. doi: 10.1016/J.MARSTRUC.2015.05.001.
- Liu, R. and Yan, S. (2013) ‘Brief History of Upheaval Buckling Studies for Subsea Buried Pipeline’, *Journal of Pipeline Systems Engineering and Practice*, 4(3), pp. 170–183. doi: 10.1061/(ASCE)PS.1949-1204.0000127.
- Liu, X., Zhang, H., Han, Y., *et al.* (2016) ‘A semi-empirical model for peak strain prediction of buried X80 steel pipelines under compression and bending at strike-slip fault crossings’, *Journal of Natural Gas Science and Engineering*. Elsevier, 32, pp. 465–475. doi: 10.1016/J.JNGSE.2016.04.054.
- Liu, X., Zhang, H., Li, M., *et al.* (2016) ‘Effects of steel properties on the local buckling response of high strength pipelines subjected to reverse faulting’, *Journal of Natural Gas Science and Engineering*. Elsevier, 33, pp. 378–387. doi: 10.1016/J.JNGSE.2016.05.036.
- Liu, X., Zhang, H., Wu, K., *et al.* (2017) ‘Buckling failure mode analysis of buried X80 steel gas pipeline under reverse fault displacement’, *Engineering Failure Analysis*. Pergamon, 77, pp. 50–64. doi: 10.1016/J.ENGFAILANAL.2017.02.019.

- Liu, X., Zhang, H., Wang, B., *et al.* (2017) ‘Local Buckling Behavior and Plastic Deformation Capacity of High-Strength Pipe at Strike-Slip Fault Crossing’, *Metals*. Multidisciplinary Digital Publishing Institute, 8(1), p. 22. doi: 10.3390/met8010022.
- Liu, X. *et al.* (2018) ‘Effects of stress-strain characteristics on local buckling of X80 pipe subjected to strike-slip fault movement’, *Journal of Pressure Vessel Technology*.
- Lockey, A. and Young, A. (2012) ‘Predicting Pipeline Performance in Geohazard Areas Using ILI Mapping Techniques’, in *Volume 2: Pipeline Integrity Management*. ASME, p. 491. doi: 10.1115/IPC2012-90496.
- Lorenz, R. (1908) ‘Achsensymmetrische Verzerrungen in dünnwandigen Hohlzylindern’, *Zeitschrift des Vereines Deutscher Ingenieure*, 52(43), pp. 1706–1713.
- Love, A. E. H. (1888) ‘The Small Free Vibrations and Deformation of a Thin Elastic Shell’, *Philosophical Transactions of the Royal Society of London, A: Mathematical, Physical and Engineering Sciences*, 179, pp. 491–546. doi: 10.1098/rsta.1888.0016.
- Ludwik, P. (1909) *Elemente der Technologischen Mechanik*. Berlin: Verl. v. Julius Springer.
- Lundquist, E. E. (1933) *Strength Tests of Thin-walled Duralumin Cylinders in Pure Bending*. NACA Technical Note, No 479. Langley Field, VA, United States. Available at: <https://ntrs.nasa.gov/search.jsp?R=19930081321> (Accessed: 29 October 2018).
- Lundquist, E. E. (1934) *Strength tests of thin-walled duralumin cylinders in compression*. NACA Technical Note, No 473. Washington, D.C. Available at: <https://ntrs.nasa.gov/search.jsp?R=19930081321>.
- Maarefdoust, M. and Kadkhodayan, M. (2015) ‘Elastoplastic buckling analysis of rectangular thick plates by incremental and deformation theories of plasticity’, *Proceedings of the Institution of Mechanical Engineers, Part G: Journal of Aerospace Engineering*. SAGE PublicationsSage UK: London, England, 229(7), pp. 1280–1299. doi: 10.1177/0954410014550047.
- Macdonald, M., Rhodes, J. and Taylor, G. T. (2000) ‘Mechanical properties of stainless metal lipped channels’, in *15th International Specialty Conference on Cold-Formed Metal Structures*. University of Missouri-Rolla, Mo., pp. 673–686.
- Macia, M. L. *et al.* (2010) ‘Approaches to Qualify Strain-Based Design Pipelines’, in *2010 8th International Pipeline Conference, Volume 4*. ASME, pp. 365–374. doi: 10.1115/IPC2010-31662.

- Mackenzie, A. C., Hancock, J. W. and Brown, D. K. (1977) 'On the influence of state of stress on ductile failure initiation in high strength steels', *Engineering Fracture Mechanics*. Pergamon, 9(1), pp. 167–188. doi: 10.1016/0013-7944(77)90062-5.
- Mateus, A. F. and Witz, J. A. (2001) 'Parametric study of the post-buckling behaviour of steel plates', *Engineering Structures*. Elsevier, 23(2), pp. 172–185. doi: 10.1016/S0141-0296(00)00005-5.
- Mathon, C. and Limam, A. (2006) 'Experimental collapse of thin cylindrical shells submitted to internal pressure and pure bending', *Thin-Walled Structures*. Elsevier, 44(1), pp. 39–50. doi: 10.1016/J.TWS.2005.09.006.
- Mirambell, E. and Real, E. (2000) 'On the calculation of deflections in structural stainless steel beams: an experimental and numerical investigation', *Journal of Constructional Steel Research*. Elsevier, 54(1), pp. 109–133. doi: 10.1016/S0143-974X(99)00051-6.
- Mohareb, M. *et al.* (2001) 'Testing and Analysis of Steel Pipe Segments', *Journal of Transportation Engineering*, 127(5), pp. 408–417. doi: 10.1061/(ASCE)0733-947X(2001)127:5(408).
- Mohareb, M. E. *et al.* (1993) 'Laboratory testing of line pipe to determine deformational behavior', in *Proceedings of the 12th International Conference on Offshore Mechanics and Arctic Engineering, Volume 5*. Glasgow, UK: ASME, pp. 109–114.
- Mohareb, M. E. *et al.* (1994) *Deformation Behavior of Line Pipe, Structural Engineering Report No. 202*. Edmonton, Alberta.
- Moosbrugger, C. (2002) 'Representation of stress-strain behavior', in Tamarin, Y. (ed.) *Atlas of stress-strain curves*. 2nd edn. Materials Park, Ohio: American Society for Metals (ASM International), pp. 1–19.
- Morgan, E. J., Seide, P. and Weingarten, V. I. (1965) 'Elastic stability of thin-walled cylindrical and conical shells under axial compression', *AIAA Journal*, 3(3), pp. 500–505. doi: 10.2514/3.2893.
- Morley, L. S. D. (1959) 'An improvement on donnell's approximation for thin-walled circular cylinders', *Quarterly Journal of Mechanics and Applied Mathematics*. Oxford University Press, 12(1), pp. 89–99. doi: 10.1093/qjmam/12.1.89.

- Mossman, R. W. and Robinson, R. G. (1930) *Bending tests of metal monocoque fuselage construction. NACA Technical Note 357*. Washington DC, United States.
- Mouriño, N. S. *et al.* (2010) ‘Texture Dependent Mechanical Anisotropy of X80 Pipeline Steel’, *Advanced Engineering Materials*. Wiley-Blackwell, 12(10), pp. 973–980. doi: 10.1002/adem.201000065.
- Muggeridge, D. B. and Tennyson, R. C. (1969) ‘Buckling of axisymmetric imperfect circular cylindrical shells under axial compression’, *AIAA Journal*, 7(11), pp. 2127–2131. doi: 10.2514/3.5568.
- Murphey, C. E. and Langner, C. G. (1985) ‘Ultimate pipe strength under bending, collapse and fatigue’, in *Proceedings of the 4th International Conference on Offshore Mechanics and Arctic Engineering*, pp. 467–477.
- Murphy, L. M. and Lee, L. H. N. (1971) ‘Inelastic buckling process of axially compressed cylindrical shells subject to edge constraints’, *International Journal of Solids and Structures*. Pergamon, 7(9), pp. 1153–1170. doi: 10.1016/0020-7683(71)90059-X.
- Murray, D. W. (1997) ‘Local buckling, strain localization, wrinkling and postbuckling response of line pipe’, *Engineering Structures*. Elsevier, 19(5), pp. 360–371. doi: 10.1016/S0141-0296(96)00096-X.
- Murray, N. W. and Bilston, P. (1992) ‘Local buckling of thin-walled pipes being bent in the plastic range’, *Thin-Walled Structures*. Elsevier, 14(5), pp. 411–434. doi: 10.1016/0263-8231(92)90011-K.
- Nazemi, N. (2009) *Behavior of X60 Line Pipe under Combined Axial and Transverse Loads with Internal Pressure, Electronic Theses and Dissertations, Paper 85*. University of Windsor.
- Nazemi, N. and Das, S. (2010) ‘Behavior of X60 Line Pipe Subjected to Axial and Lateral Deformations’, *Journal of Pressure Vessel Technology*. American Society of Mechanical Engineers, 132(3), p. 031701. doi: 10.1115/1.4001426.
- Ndubuaku, O., Martens, M., Cheng, R., *et al.* (2017) ‘A Novel Approach for True Stress-True Strain Material Characterization of Metallic Materials Using the Product-Log (Omega) Function’, in *6th International Conference on Engineering Mechanics and Materials*. May 31 - June 3, Vancouver, B.C., Canada: CSCE.

- Ndubuaku, O., Martens, M., Cheng, J. J. R., *et al.* (2017) ‘Expression of a Generic Full-Range True Stress-True Strain Model for Pipeline Steels Using the Product-Log (Omega) Function’, in *Volume 6B: Materials and Fabrication*. ASME, p. V06BT06A050. doi: 10.1115/PVP2017-65236.
- Ndubuaku, O. *et al.* (2018) ‘The effect of material stress-strain characteristics on the ultimate stress and critical buckling strain of flat plates subjected to uniform axial compression’, *Construction and Building Materials*, 182, pp. 346–359. doi: 10.1016/j.conbuildmat.2018.06.100.
- Nessim, M. *et al.* (2009) ‘Reliability Based Design and Assessment for Location-Specific Failure Threats With Application to Natural Gas Pipelines’, *Journal of Pressure Vessel Technology*. American Society of Mechanical Engineers, 131(4), p. 041701. doi: 10.1115/1.3110019.
- Neupane, S. *et al.* (2012a) ‘Modeling the Deformation Response of High Strength Steel Pipelines—Part I: Material Characterization to Model the Plastic Anisotropy’, *Journal of Applied Mechanics*. American Society of Mechanical Engineers, 79(5), p. 051002. doi: 10.1115/1.4006380.
- Neupane, S. *et al.* (2012b) ‘Modeling the Deformation Response of High Strength Steel Pipelines—Part II: Effects of Material Characterization on the Deformation Response of Pipes’, *Journal of Applied Mechanics*. American Society of Mechanical Engineers, 79(5), p. 051003. doi: 10.1115/1.4006381.
- Newmark, N. M. and Hall, W. J. (1975) ‘Pipeline design to resist large fault displacement’, in *Proceedings of US national conference on earthquake engineering*. June 18-20, 1975. Ann Arbor, Michigan: Earthquake Engineering Research Institute, pp. 416–425.
- Nielsen, N.-J. R., Lyngberg, B. and Pedersen, P. T. (1990) ‘Upheaval Buckling Failures of Insulated Buried Pipelines: A Case Story’, in *Offshore Technology Conference*. Offshore Technology Conference. doi: 10.4043/6488-MS.
- O’Rourke, M., Gadicherla, V. and Abdoun, T. (2003) ‘Centrifuge Modeling of Buried Pipelines’, in *Advancing Mitigation Technologies and Disaster Response for Lifeline Systems*. Reston, VA: American Society of Civil Engineers, pp. 757–768. doi: 10.1061/40687(2003)77.

- Odina, L. and Tan, R. (2009) ‘Seismic Fault Displacement of Buried Pipelines Using Continuum Finite Element Methods’, in *Volume 3: Pipeline and Riser Technology*. ASME, pp. 617–625. doi: 10.1115/OMAE2009-79739.
- Olsson, A. (2001) *Stainless steel plasticity – Material modelling and structural applications*. PhD thesis. Department of Civil and Mining Engineering, Lulea University of Technology, Sweden.
- Onat, E. T. (1953) ‘Inelastic Instability and Incremental Theories of Plasticity’, *Journal of the Aeronautical Sciences*, 20(3), pp. 181–186. doi: 10.2514/8.2585.
- Ore, E. and Durban, D. (1992) ‘Elastoplastic buckling of axially compressed circular cylindrical shells’, *International Journal of Mechanical Sciences*. Pergamon, 34(9), pp. 727–742. doi: 10.1016/0020-7403(92)90005-2.
- Paik, J. K., Lee, J. M. and Lee, D. H. (2003) ‘Ultimate strength of dented steel plates under axial compressive loads’, *International Journal of Mechanical Sciences*. Pergamon, 45(3), pp. 433–448. doi: 10.1016/S0020-7403(03)00062-6.
- Paik, J. K. and Thayamballi, A. K. (2003) *Ultimate limit state design of steel plated structures*. Chichester, England: John Wiley & Sons, Inc. Available at: https://books.google.ca/books/about/Ultimate_Limit_State_Design_of_Steel_Pla.html?id=e7NtH5xXnH0C&printsec=frontcover&source=kp_read_button&redir_esc=y#v=onepage&q&f=false (Accessed: 14 August 2017).
- Papadaki, C. I. *et al.* (2018) ‘Buckling of internally-pressurized spiral-welded steel pipes under bending’, *International Journal of Pressure Vessels and Piping*. Elsevier, 165, pp. 270–285. doi: 10.1016/J.IJPVP.2018.07.006.
- Paquette, J. A. and Kyriakides, S. (2006) ‘Plastic buckling of tubes under axial compression and internal pressure’, *International Journal of Mechanical Sciences*. Pergamon, 48(8), pp. 855–867. doi: 10.1016/J.IJMECSCI.2006.03.003.
- Paravicini Bagliani, E. *et al.* (2013) ‘Microstructure, tensile and toughness properties after quenching and partitioning treatments of a medium-carbon steel’, *Materials Science and Engineering: A*. Elsevier, 559, pp. 486–495. doi: 10.1016/J.MSEA.2012.08.130.

- Paredes, M. *et al.* (2018) ‘Modeling of plasticity and fracture behavior of X65 steels: seam weld and seamless pipes’, *International Journal of Fracture*. Springer Netherlands, 213(1), pp. 17–36. doi: 10.1007/s10704-018-0303-x.
- Park, W.-S. *et al.* (2011) ‘Comparative study on mechanical behavior of low temperature application materials for ships and offshore structures: Part II – Constitutive model’, *Materials Science and Engineering: A*. Elsevier, 528(25–26), pp. 7560–7569. doi: 10.1016/J.MSEA.2011.06.040.
- Park, W. S. *et al.* (2011) ‘Comparative study on mechanical behavior of low temperature application materials for ships and offshore structures: Part I—Experimental investigations’, *Materials Science and Engineering: A*. Elsevier, 528(18), pp. 5790–5803. doi: 10.1016/J.MSEA.2011.04.032.
- Parks, M. B., Santaputra, C. and Yu, W. W. (1986) ‘Local buckling of curved elements’, in *Proceedings of the Eighth International Specialty Conference on Cold-Formed Steel Structures*. University of Missouri-Rolla, p. 277. Available at: <http://scholarsmine.mst.edu/cgi/viewcontent.cgi?article=1209&context=iscscs> (Accessed: 17 November 2018).
- Peek, R. (2000) ‘Axisymmetric Wrinkling of Cylinders with Finite Strain’, *Journal of Engineering Mechanics*, 126(5), pp. 455–461. doi: 10.1061/(ASCE)0733-9399(2000)126:5(455).
- Peköz, T. (1987) *Development of a Unified Approach to the Design of Cold-Formed Steel Members (Report SG 86-4): AISI Specifications for the Design of Cold-Formed Steel Structural Members*. Washington, D.C.
- Porter, D. *et al.* (2004) ‘Performance of TMCP steel with respect to mechanical properties after cold forming and post-forming heat treatment’, *International Journal of Pressure Vessels and Piping*. Elsevier, 81(10–11), pp. 867–877. doi: 10.1016/J.IJPVP.2004.07.006.
- Pride, R. A. and Heimerl, G. J. (1949) *Plastic buckling of simply supported compressed plates*, *NACA Technical Note, No. 1817*. Washington, D.C. Available at: <https://ntrs.nasa.gov/archive/nasa/casi.ntrs.nasa.gov/19930082491.pdf> (Accessed: 14 August 2017).

- Prion, H. G. L. and Birkemoe, P. C. (1992) 'Beam-Column Behavior of Fabricated Steel Tubular Members', *Journal of Structural Engineering*, 118(5), pp. 1213–1232. doi: 10.1061/(ASCE)0733-9445(1992)118:5(1213).
- Quach, W. M. (2005) *Residual stresses in cold-formed steel sections and their effect on column behaviour*. The Hong Kong Polytechnic University, Hong Kong. Available at: <http://ira.lib.polyu.edu.hk/handle/10397/2147> (Accessed: 14 August 2017).
- Quach, W. M., Teng, J. G. and Chung, K. F. (2008) 'Three-Stage Full-Range Stress-Strain Model for Stainless Steels', *Journal of Structural Engineering*, 134(9), pp. 1518–1527. doi: 10.1061/(ASCE)0733-9445(2008)134:9(1518).
- Rahman, M. A. and Taniyama, H. (2015) 'Analysis of a buried pipeline subjected to fault displacement: A DEM and FEM study', *Soil Dynamics and Earthquake Engineering*. Elsevier, 71, pp. 49–62. doi: 10.1016/J.SOILDYN.2015.01.011.
- Ramberg, W. and Osgood, W. R. (1943) *Description of stress-strain curves by three parameters*, *NACA Technical Note No. 902*. Washinton, D.C. Available at: <https://ntrs.nasa.gov/search.jsp?R=19930081614> (Accessed: 7 May 2018).
- Rasmussen, K. J. R. (2003) 'Full-range stress–strain curves for stainless steel alloys', *Journal of Constructional Steel Research*. Elsevier, 59(1), pp. 47–61. doi: 10.1016/S0143-974X(02)00018-4.
- Rasmussen, K. J. R. *et al.* (2003) 'Numerical modelling of stainless steel plates in compression', *Journal of Constructional Steel Research*. Elsevier, 59(11), pp. 1345–1362. doi: 10.1016/S0143-974X(03)00086-5.
- Ravn-Jensen, K. and Tvergaard, V. (1990) 'Effect of residual stresses on plastic buckling of cylindrical shell structures', *International Journal of Solids and Structures*. Pergamon, 26(9–10), pp. 993–1004. doi: 10.1016/0020-7683(90)90013-L.
- Reddy, B. D. (1979) 'An experimental study of the plastic buckling of circular cylinders in pure bending', *International Journal of Solids and Structures*. Pergamon, 15(9), pp. 669–683. doi: 10.1016/0020-7683(79)90066-0.
- Reddy, B. D. and Calladine, C. R. (1978) 'Classical buckling of a thin-walled tube subjected to bending moment and internal pressure', *International Journal of Mechanical Sciences*. Pergamon, 20(9), pp. 641–650. doi: 10.1016/0020-7403(78)90022-X.

- Robertson, A. (1929) *The Strength of Tubular Struts. Report and Memorandum No. 1185.*
- Rojhani, M. *et al.* (2011) ‘Centrifuge modeling of buried pipelines response due to reverse faulting’, in *Proceedings of the 5th International Conference on Earthquake Geotechnical Engineering, January 10-13, 2011.* Santiago, Chile, p. CMBRO. Available at: <http://www.sochige.cl/download/10.2.CMBRO.pdf> (Accessed: 29 October 2018).
- Ross, C. T. F., Little, A. P. F. and Adeniyi, K. A. (2005) ‘Plastic buckling of ring-stiffened conical shells under external hydrostatic pressure’, *Ocean Engineering*. Pergamon, 32(1), pp. 21–36. doi: 10.1016/j.oceaneng.2004.05.007.
- Row, D., Powell, G. H. and Goodson, M. W. (1983) ‘Finite Element Techniques for Pipelines Subjected to Extreme Loads’, in *Pipelines in Adverse Environments II.* ASCE, pp. 474–485. Available at: <http://cedb.asce.org/CEDBsearch/record.jsp?dockkey=0039044> (Accessed: 17 November 2018).
- Sanders, J. L. (1963) ‘Nonlinear theories for thin shells’, *Quarterly of Applied Mathematics*, 21(1), pp. 21–36. doi: 10.1090/qam/147023.
- Schafer, B. W. (2008) ‘Review: The Direct Strength Method of cold-formed steel member design’, *Journal of Constructional Steel Research*. Elsevier, 64(7–8), pp. 766–778. doi: 10.1016/J.JCSR.2008.01.022.
- Schilling, C. G. (1965) ‘Buckling Strength of Circular Tubes’, *Journal of the Structural Division*. ASCE, 91(5), pp. 325–348. Available at: <http://cedb.asce.org/CEDBsearch/record.jsp?dockkey=0013985> (Accessed: 17 November 2018).
- Schneider, S. P. (1998) ‘Flexural Capacity of Pressurized Steel Pipe’, *Journal of Structural Engineering*, 124(3), pp. 330–340. doi: 10.1061/(ASCE)0733-9445(1998)124:3(330).
- Seide, P. and Weingarten, V. I. (1961) ‘On the Buckling of Circular Cylindrical Shells Under Pure Bending’, *Journal of Applied Mechanics*. American Society of Mechanical Engineers, 28(1), p. 112. doi: 10.1115/1.3640420.
- Selvadurai, A. P. S. (1991) ‘Mechanics of buried pipelines induced by random ground movement’, in *Proceedings of the CSCE Annual Conference (Engineering Mechanics Symposium).* Vancouver, British Columbia Canada, pp. 142–151.

- Sewell, M. J. (1963) 'A general theory of elastic and inelastic plate failure—I', *Journal of the Mechanics and Physics of Solids*. Pergamon, 11(6), pp. 377–393. doi: 10.1016/0022-5096(63)90016-4.
- Shamass, R., Alfano, G. and Guarracino, F. (2014) 'A numerical investigation into the plastic buckling paradox for circular cylindrical shells under axial compression', *Engineering Structures*. Elsevier, 75, pp. 429–447. doi: 10.1016/J.ENGSTRUCT.2014.05.050.
- Shanley, F. R. (1947) 'Inelastic Column Theory', *Journal of the Aeronautical Sciences*, 14(5), pp. 261–268. doi: 10.2514/8.1346.
- Shen, Y. F., Wang, C. M. and Sun, X. (2011) 'A micro-alloyed ferritic steel strengthened by nanoscale precipitates', *Materials Science and Engineering: A*. Elsevier, 528(28), pp. 8150–8156. doi: 10.1016/J.MSEA.2011.07.065.
- Sherman, D. R. (1976) 'Test of Circular Steel Tubes in Bending', *Journal of the Structural Division*. ASCE, 102(11), pp. 2181–2195. Available at: <http://cedb.asce.org/CEDBsearch/record.jsp?dockkey=0007059> (Accessed: 29 October 2018).
- Sherman, D. R. (1986) 'Inelastic flexural buckling of cylinders', in Pavlovic, M. N. (ed.) *Steel Structures: Recent Research Advances and Their Applications to Design*. Elsevier Applied Science Publishers, pp. 339–357.
- Shrivastava, S. C. (1979) 'Inelastic buckling of plates including shear effects', *International Journal of Solids and Structures*. Pergamon, 15(7), pp. 567–575. doi: 10.1016/0020-7683(79)90084-2.
- Singer, J. *et al.* (2002) *Buckling experiments : experimental methods in buckling of thin-walled structures. Shells, built-up structures, composites and additional topics, Volume 2*. John Wiley & Sons.
- Singer, J., Arbocz, J. and Weller, T. (1998) *Buckling Experiments, Volume 1: Basic Concepts, Columns, Beams and Plates*. New York: John Wiley & Sons.
- Skelton, R. P., Maier, H. J. and Christ, H.-J. (1997) 'The Bauschinger effect, Masing model and the Ramberg–Osgood relation for cyclic deformation in metals', *Materials Science and Engineering: A*. Elsevier, 238(2), pp. 377–390. doi: 10.1016/S0921-5093(97)00465-6.

- Slavik, D. and Sehitoglu, H. (1986) ‘Constitutive Models Suitable for Thermal Loading’, *Journal of Engineering Materials and Technology*. American Society of Mechanical Engineers, 108(4), p. 303. doi: 10.1115/1.3225887.
- Smith, C. S., Davidson, P. C. and Chapman, J. C. (1988) ‘Strength and stiffness of ships plating under in-plane compression and tension’, *Royal Institution of Naval Architects Transactions*, 130, pp. 227–96. Available at: <http://trid.trb.org/view.aspx?id=403900>.
- Southwell, R. V. (1914) ‘On the General Theory of Elastic Stability’, *Philosophical Transactions of the Royal Society A: Mathematical, Physical and Engineering Sciences*. The Royal Society, 213(497–508), pp. 187–244. doi: 10.1098/rsta.1914.0005.
- Souza, L. T. and Murray, D. W. (1994) *Prediction of Wrinkling Behaviour of Girth-Welded Line Pipe, Structural Engineering Report No. 197*. Edmonton, Alberta, Canada.
- Stephens, M. *et al.* (2010) ‘Large Scale Experimental Data for Improved Strain-Based Design Models’, in *2010 8th International Pipeline Conference, Volume 4*. ASME, pp. 195–203. doi: 10.1115/IPC2010-31396.
- Stephens, M. J. *et al.* (2009) ‘An Experimental Basis For Improved Strain-based Design Models’, in *The Nineteenth International Offshore and Polar Engineering Conference*. Osaka, Japan: International Society of Offshore and Polar Engineers (ISOPE), pp. 29–35. Available at: <https://www.onepetro.org/conference-paper/ISOPE-I-09-493> (Accessed: 13 November 2018).
- Stephens, W. B., Starnes, J. H. and Almroth, B. O. (1975) ‘Collapse of Long Cylindrical Shells under Combined Bending and Pressure Loads’, *AIAA Journal*, 13(1), pp. 20–25. doi: 10.2514/3.49624.
- Stowell, E. Z. (1948) *A Unified Theory of Plastic Buckling of Columns and Plates, NACA Technical Note, No. 1556*. Washington, D.C. doi: 10.1016/j.engstruct.2010.06.012.
- Suer, H. S. *et al.* (1958) ‘The Bending Stability of Thin-Walled Unstiffened Circular Cylinders Including the Effects of Internal Pressure’, *Journal of the Aerospace Sciences*, 25(5), pp. 281–287. doi: 10.2514/8.7639.
- Suzuki, N. *et al.* (2003) ‘Local Buckling Behavior of X100 Linepipes’, in *Volume 3: Materials Technology; Ocean Engineering; Polar and Arctic Sciences and Technology; Workshops*. ASME, pp. 67–76. doi: 10.1115/OMAE2003-37145.

- Suzuki, N. *et al.* (2007) ‘Strain Capacity of X80 High-Strain Line Pipes’, in *Volume 3: Pipeline and Riser Technology; CFD and VIV*. ASME, pp. 475–483. doi: 10.1115/OMAE2007-29505.
- Suzuki, N. and Toyoda, M. (2002) ‘Critical Compressive Strain of Linepipes Related to Workhardening Parameters’, in *21st International Conference on Offshore Mechanics and Arctic Engineering, Volume 3*. ASME, pp. 217–224. doi: 10.1115/OMAE2002-28253.
- Takada, S., Hassani, N. and Fukuda, K. (2001) ‘A new proposal for simplified design of buried steel pipes crossing active faults’, *Earthquake Engineering & Structural Dynamics*. Wiley-Blackwell, 30(8), pp. 1243–1257. doi: 10.1002/eqe.62.
- Tatting, B. F., Gürdal, Z. and Vasiliev, V. V. (1997) ‘The brazilier effect for finite length composite cylinders under bending’, *International Journal of Solids and Structures*. Pergamon, 34(12), pp. 1419–1440. doi: 10.1016/S0020-7683(96)00094-7.
- Taylor, L. C. (1977) ‘Fault displacement and ground deformation associated with surface faulting’, *Proc. ASCE Special Conf. on Lifeline Earthquake Engineering*, pp. 338–353. Available at: <https://ci.nii.ac.jp/naid/10003144236/> (Accessed: 29 October 2018).
- Teng, J. G. (1996) ‘Buckling of Thin Shells: Recent Advances and Trends’, *Applied Mechanics Reviews*. American Society of Mechanical Engineers, 49(4), p. 263. doi: 10.1115/1.3101927.
- Teng, J. G., Zhao, Y. and Lam, L. (2001) ‘Techniques for buckling experiments on steel silo transition junctions’, *Thin-Walled Structures*. Elsevier, 39(8), pp. 685–707. doi: 10.1016/S0263-8231(01)00030-1.
- Terada, D., Inoue, S. and Tsuji, N. (2007) ‘Microstructure and mechanical properties of commercial purity titanium severely deformed by ARB process’, *Journal of Materials Science*. Kluwer Academic Publishers-Plenum Publishers, 42(5), pp. 1673–1681. doi: 10.1007/s10853-006-0909-7.
- Timms, C. M. J. *et al.* (2009) ‘Compressive Strain Limits of Large Diameter X80 UOE Linepipe’, in *The Nineteenth International Offshore and Polar Engineering Conference*. Osaka, Japan: International Society of Offshore and Polar Engineers. Available at: <https://www.onepetro.org/conference-paper/ISOPE-I-09-332> (Accessed: 4 September 2018).
- Timoshenko, S. P. (1910) ‘Einige stabilitäts probleme der elastizitäts theorie’, *Zeitschrift für Mathematik und Physik*, 58(4), pp. 337–385.

- Timoshenko, S. P. and Gere, J. M. (1961) *Theory of Elastic Stability*. New York: McGraw-Hill Book Company.
- Trifonov, O. V. and Cherniy, V. P. (2012) ‘Elastoplastic stress–strain analysis of buried steel pipelines subjected to fault displacements with account for service loads’, *Soil Dynamics and Earthquake Engineering*. Elsevier, 33(1), pp. 54–62. doi: 10.1016/J.SOILDYN.2011.10.001.
- Tugcu, P. and Schroeder, J. (1979) ‘Plastic deformation and stability of pipes exposed to external couples’, *International Journal of Solids and Structures*. Pergamon, 15(8), pp. 643–658. doi: 10.1016/0020-7683(79)90077-5.
- Valiev, R. Z., Korznikov, A. V. and Mulyukov, R. R. (1993) ‘Structure and properties of ultrafine-grained materials produced by severe plastic deformation’, *Materials Science and Engineering: A*. Elsevier, 168(2), pp. 141–148. doi: 10.1016/0921-5093(93)90717-S.
- Vazouras, P., Dakoulas, P. and Karamanos, S. A. (2015) ‘Pipe–soil interaction and pipeline performance under strike–slip fault movements’, *Soil Dynamics and Earthquake Engineering*. Elsevier, 72, pp. 48–65. doi: 10.1016/J.SOILDYN.2015.01.014.
- Vazouras, P., Karamanos, S. A. and Dakoulas, P. (2010) ‘Finite element analysis of buried steel pipelines under strike-slip fault displacements’, *Soil Dynamics and Earthquake Engineering*. Elsevier, 30(11), pp. 1361–1376. doi: 10.1016/J.SOILDYN.2010.06.011.
- Vazouras, P., Karamanos, S. A. and Dakoulas, P. (2012) ‘Mechanical behavior of buried steel pipes crossing active strike-slip faults’, *Soil Dynamics and Earthquake Engineering*. Elsevier, 41, pp. 164–180. doi: 10.1016/J.SOILDYN.2012.05.012.
- Vinson, J. R. (1988) *The Behavior of Thin Walled Structures: Beams, Plates, and Shells, Mechanics of Surface Structures*. Dordrecht: Springer Netherlands. doi: 10.1007/978-94-009-2774-2.
- Vitali, L. *et al.* (1999) ‘Hotpipe Project: Capacity of Pipes Subject to Internal Pressure, Axial Force And Bending Moment’, in *The Ninth International Offshore and Polar Engineering Conference*. Brest, France : International Society of Offshore and Polar Engineers, pp. 22–33. Available at: <https://www.onepetro.org/conference-paper/ISOPE-I-99-123> (Accessed: 29 October 2018).
- Vougioukas, E. A., Theodosis, C. and Carydis, P. G. (1991) ‘Seismic Analysis of Buried Pipelines Subjected to Vertical Fault Movement’, *Lifeline Earthquake Engineering*. ASCE, pp.

432–441. Available at: <http://cedb.asce.org/CEDBsearch/record.jsp?dockey=0073914> (Accessed: 29 October 2018).

Voyiadjis, G. Z. and Woelke, P. (2008) *Elasto-Plastic and Damage Analysis of Plates and Shells*. Berlin, Heidelberg: Springer Science & Business Media. doi: 10.1007/978-3-540-79351-9.

Wagner, H. N. R., Hühne, C., Niemann, S., *et al.* (2017) ‘Robust design criterion for axially loaded cylindrical shells - Simulation and Validation’, *Thin-Walled Structures*. Elsevier, 115, pp. 154–162. doi: 10.1016/j.tws.2016.12.017.

Wagner, H. N. R., Hühne, C., Rohwer, K., *et al.* (2017) ‘Stimulating the realistic worst case buckling scenario of axially compressed unstiffened cylindrical composite shells’, *Composite Structures*. Elsevier, 160, pp. 1095–1104. doi: 10.1016/j.compstruct.2016.10.108.

Wagner, H. N. R., Hühne, C. and Niemann, S. (2016) ‘Constant single-buckle imperfection principle to determine a lower bound for the buckling load of unstiffened composite cylinders under axial compression’, *Composite Structures*. Elsevier, 139, pp. 120–129. doi: 10.1016/j.compstruct.2015.11.047.

Wang, C. M., Xiang, Y. and Chakrabarty, J. (2001) ‘Elastic/plastic buckling of thick plates’, *International Journal of Solids and Structures*. Pergamon, 38(48–49), pp. 8617–8640. doi: 10.1016/S0020-7683(01)00144-5.

Wang, L. R.-L. and Yeh, Y.-H. (1985) ‘A refined seismic analysis and design of buried pipeline for fault movement’, *Earthquake Engineering & Structural Dynamics*. Wiley-Blackwell, 13(1), pp. 75–96. doi: 10.1002/eqe.4290130109.

Wang, X.-Q. *et al.* (2014) ‘Stress–strain model of austenitic stainless steel after exposure to elevated temperatures’, *Journal of Constructional Steel Research*. Elsevier, 99, pp. 129–139. doi: 10.1016/J.JCSR.2014.04.020.

Wang, Y.-Y. *et al.* (2014) ‘Overall Framework of Strain-Based Design and Assessment of Pipelines’, in *Volume 4: Production Pipelines and Flowlines; Project Management; Facilities Integrity Management; Operations and Maintenance; Pipelining in Northern and Offshore Environments; Strain-Based Design; Standards and Regulations*. ASME, p. V004T11A023. doi: 10.1115/IPC2014-33745.

- Weingarten, V. I., Seide, P. and Peterson, J. P. (1968) 'Buckling of thin-walled circular cylinders', *NASA SP-8007*. Washington D.C., pp. 1–60. doi: 19690013955.
- Weingarten, V. I. (1962) 'Effects of Internal Pressure on the Buckling of Circular-Cylindrical Shells Under Bending', *Journal of the Aerospace Sciences*, 29(7), pp. 804–807. doi: 10.2514/8.9608.
- Wijewickreme, D., Karimian, H. and Honegger, D. (2009) 'Response of buried steel pipelines subjected to relative axial soil movement', *Canadian Geotechnical Journal*, 46(7), pp. 735–752. doi: 10.1139/T09-019.
- Wilhoit, J. C. and Merwin, J. E. (1973) 'Critical Plastic Bucking Parameter for Tubing in Bending Under Axial Tension', in *Offshore Technology Conference*. Offshore Technology Conference. doi: 10.4043/1874-MS.
- Wilson, W. M. and Newmark, N. M. (1933) 'The strength of thin cylindrical shells as columns', in *Selected Papers By Nathan M. Newmark: Civil Engineering Classics*, pp. 1–42.
- Winter, G. (1947) 'Strength of thin steel compression flanges', *Transactions of the American Society of Civil Engineers*, 112, p. 527. doi: 1.
- Winterstetter, T. A. and Schmidt, H. (2002) 'Stability of circular cylindrical steel shells under combined loading', *Thin-Walled Structures*. Elsevier, 40(10), pp. 893–909. doi: 10.1016/S0263-8231(02)00006-X.
- Wolfram Research Inc. (2018) *Mathematica, Version 11.3*. Champaign, IL.
- Workman, G. H. (1981) *Pipe wall stability analysis of 12.75 in OD* 0.25 in WT grade 52 pipe*.
- Workman, G. H. (1988) 'Manufacturing residual stress effects on buried pipeline structural response', in *Seventh International Conference on Offshore Mechanics and Arctic Engineering*. Houston, Texas, pp. 7–12.
- Wullschleger, L. and Meyer-Piening, H. R. (2002) 'Buckling of geometrically imperfect cylindrical shells - Definition of a buckling load', *International Journal of Non-Linear Mechanics*. Pergamon, 37(4–5), pp. 645–657. doi: 10.1016/S0020-7462(01)00089-0.
- Xie, X. (2008) *Numerical analysis and evaluation of buried pipeline response to earthquake-induced ground fault rupture*. Doctoral dissertation. Department of Civil and Environmental Engineering, Rensselaer Polytechnic Institute.

- Xue, J. (2012) ‘Local buckling in infinitely, long cylindrical shells subjected uniform external pressure’, *Thin-Walled Structures*. Elsevier, 53, pp. 211–216. doi: 10.1016/J.TWS.2012.01.008.
- Yeh, M. K. and Kyriakides, S. (1986) ‘On the Collapse of Inelastic Thick-Walled Tubes Under External Pressure’, *Journal of Energy Resources Technology*. American Society of Mechanical Engineers, 108(1), p. 35. doi: 10.1115/1.3231239.
- Yimsiri, S. *et al.* (2004) ‘Lateral and Upward Soil-Pipeline Interactions in Sand for Deep Embedment Conditions’, *Journal of Geotechnical and Geoenvironmental Engineering*, 130(8), pp. 830–842. doi: 10.1061/(ASCE)1090-0241(2004)130:8(830).
- Yong Bai and Wei-Liang Jin (2016) ‘Ultimate Strength of Cylindrical Shells’, in *Marine Structural Design*. 2nd edn. Oxford, United Kingdom: Elsevier, pp. 353–365. doi: <https://doi.org/10.1016/B978-0-08-099997-5.00018-6>.
- Yoo, J.-Y. *et al.* (2011) ‘New Development of High Grade X80 to X120 Pipeline Steels’, *Materials and Manufacturing Processes*. Taylor & Francis Group , 26(1), pp. 154–160. doi: 10.1080/10426910903202534.
- Yoo, S.-W. *et al.* (2011) ‘Temperature and strain rate dependent constitutive model of TRIP steels for low-temperature applications’, *Computational Materials Science*. Elsevier, 50(7), pp. 2014–2027. doi: 10.1016/J.COMMATSCI.2011.02.002.
- Yoosef-Ghodsi, N., Kulak, G. L. and Murray, D. W. (1994) *Behavior of Girth-welded Line Pipe, Structural Engineering Report No. 203*. Edmonton, Alberta.
- Yoosef-Ghodsi, N., Kulak, G. L. and Murray, D. W. (1995) ‘Some test results for wrinkling of girth-welded line pipe’, in *Proceedings of the 14th International Conference on Offshore Mechanics and Arctic Engineering, Volume 5*. Copenhagen, Denmark: ASME, pp. 379–387.
- Yoosef-Ghodsi, N., Ozkan, I. and Chen, Q. (2014) ‘Comparison of Compressive Strain Limit Equations’, in *Volume 4: Production Pipelines and Flowlines; Project Management; Facilities Integrity Management; Operations and Maintenance; Pipelining in Northern and Offshore Environments; Strain-Based Design; Standards and Regulations*. ASME, p. V004T11A001. doi: 10.1115/IPC2014-33182.
- Yun, H. D. and Kyriakides, S. (1986) ‘Buckling of pipelines in seismic environments’, in *Proceedings of 3rd U.S. National Conference on Earthquake Engineering*. Charleston, South Carolina, USA, pp. 2179–2189.

- Yun, H. and Kyriakides, S. (1990) 'On the beam and shell modes of buckling of buried pipelines', *Soil Dynamics and Earthquake Engineering*. Elsevier, 9(4), pp. 179–193. doi: 10.1016/S0267-7261(05)80009-0.
- Zhang, P. and Alam, M. S. (2017) 'Experimental investigation and numerical simulation of pallet-rack stub columns under compression load', *Journal of Constructional Steel Research*. Elsevier, 133, pp. 282–299. doi: 10.1016/J.JCSR.2017.02.023.
- Zhang, Y. and Das, S. (2008) 'Failure of X52 Wrinkled Pipelines Subjected to Monotonic Axial Deformation', *Journal of Pressure Vessel Technology*. American Society of Mechanical Engineers, 130(2), p. 021702. doi: 10.1115/1.2894294.
- Zhao, O., Afshan, S. and Gardner, L. (2017) 'Structural response and continuous strength method design of slender stainless steel cross-sections', *Engineering Structures*. Elsevier, 140, pp. 14–25. doi: 10.1016/J.ENGSTRUCT.2017.02.044.
- Zhao, X. *et al.* (2014) 'Effects of Intercritical Annealing Temperature on Mechanical Properties of Fe-7.9Mn-0.14Si-0.05Al-0.07C Steel', *Materials*. Multidisciplinary Digital Publishing Institute, 7(12), pp. 7891–7906. doi: 10.3390/ma7127891.
- Zhou Z. and Murray D. W. (1993) *Numeric Structural Analysis of Buried Pipelines, Structural Engineering Report No. 181*. Edmonton, Alberta, Canada.
- Zhou, Z. and Murray, D. W. (1993) 'Towards rational deformation limit states for buried pipelines', in *The Third International Offshore and Polar Engineering Conference*. Singapore, pp. 18–24.
- Zhou, Z. and Murray, D. W. (1995) 'Analysis of postbuckling behavior of line pipe subjected to combined loads', *International Journal of Solids and Structures*. Pergamon, 32(20), pp. 3015–3036. doi: 10.1016/0020-7683(94)00261-T.
- Ziemian, D. R. (2010) *Guide to Stability Design Criteria for Metal Structures*. Edited by R. D. Ziemian. Hoboken, NJ, USA: John Wiley & Sons, Inc. doi: 10.1002/9780470549087.
- Zimmerman, T. J. E. *et al.* (1995) 'Compressive strain limits for buried pipelines', in *Proceedings of the 14th International Conference on Offshore Mechanics and Arctic Engineering, Volume 5*. Copenhagen, Denmark: ASME.



**APPENDIX: MATHEMATICA CODES FOR IMPLEMENTING NEW MATERIAL
STRESS-STRAIN CHARACTERIZATION PROCEDURE**

YPT Model

(*Young's modulus is inputted here*)

Ee = 210 000;

(*The allowable deviation (in percentage) of the proportionality limit point from the linear elastic line is specified here*)

perc = 20;

(*The following implements the linearity deviation technique*)

LinDev[data_] :=

(For[i = 1, And[i ≤ Length[data],

((data[[i, 1]] - data[[i, 2]] / Ee) / (data[[i, 2]] / Ee) - (perc / 100) ≤ 0), i = i + 1];

If[i > Length[data], "N/A", {data[[i, 1]], data[[i, 2]], i}])

(*The experimentally-obtained true stress and true strain data are inputted here*)

NMdata = {{0.000001, 1}, {0.000683845735032329, 151.128007744468},
{0.0012786211651489, 277.991903097307}, {0.00139138350424701, 301.677780970505},
{0.0015963733678318, 350.004760147913}, {0.00171934711881737, 376.549566709815},
{0.00182181369384947, 397.413099536876}, {0.00214963619515995, 447.41340877525},
{0.002856137978247, 428.146545044879}, {0.00320408580040041, 430.823271220064},
{0.00370532714055431, 419.026545927621}, {0.0043698516609097, 434.489148208372},
{0.00496243940956016, 441.39365983589}, {0.00574860856306168, 422.417778047461},
{0.00652396212100882, 435.743111268571}, {0.00714585075753904, 437.60024859059},
{0.00797104002078921, 420.500334915249}, {0.00888711905166728, 440.90502547118},
{0.00959904522515132, 450.758819458258}, {0.0112244043203596, 450.855039560893},
{0.0118839525756212, 454.020982155237}, {0.0126038854651928, 439.038365991147},
{0.0135258591276335, 449.339903655948}, {0.0143154462691631, 449.694836772923},
{0.0150538544929348, 444.911300260419}, {0.0159331637173941, 447.54278220019},
{0.0164482616055076, 454.497118258187}, {0.0168520743737888, 453.399455817776},
{0.0174574879435691, 440.853961594804}, {0.0177600573365042, 460.223297281019},
{0.0178810594647707, 450.018586349246}, {0.0180322915383379, 435.335089680526},
{0.0183850774585687, 452.811854742244}, {0.0187075157082903, 450.711563424491},
{0.0239025513090791, 472.090991237808}, {0.0293199745266301, 474.006795286038},
{0.0346288870578243, 502.614169489397}, {0.0400083912828366, 506.308704695383},
{0.04552586102552, 514.383971550511}, {0.0509740376116739, 523.822593243647},
{0.0563538840989876, 529.98041016429}, {0.0619365301134391, 530.601822913627},
{0.0675745343557101, 546.069834301041}, {0.0731332269217274, 548.436016700846},
{0.0786611919563617, 552.839068557977}, {0.084234254972417, 562.096099892075},
{0.0898045819429076, 563.857701572909}, {0.0956146257194953, 549.468908905424},
{0.10140965910448, 575.667985547079}, {0.107125195636788, 579.318225966681},

```

    {0.112643181761291, 575.473570132642}, {0.118349771351957, 586.566509555767},
    {0.124241579417104, 580.760517042992}, {0.130279115488854, 598.269907110431},
    {0.136352074682096, 592.529127077113}, {0.142263734465732, 593.863697430129},
    {0.148379615827315, 593.488160604364}, {0.154599045198263, 599.39649561236},
    {0.160972303821279, 582.140919711331}, {0.167409400744139, 596.326161269091}};

(*The following outputs the PL stress and PL strain*)
prop = LinDev[NMdata];

(*The following value slightly scales up the PL stress and PL strain
to prevent indeterminacy issues*)
scale = 1.001;

(*The following truncates the linear elastic portion of the original
stress and strain data*)
n = Length[NMdata] - prop[[3]];
PLdata = Table[0, {i, 1, n}];
Do[PLdata[[i]] = NMdata[[i + prop[[3]]]], {i, 1, n}];
PLdata;
PLdata = Prepend[PLdata, scale * {prop[[1]], prop[[2]]}];

(*The following defines reference point inputs for the stress-
strain model equation*)
epsprop = prop[[1]] (*PL strain*)
sigprop = prop[[2]] (*PL stress*)
epsmax = NMdata[[Length[NMdata], 1]]; (*Ult. strain*)
sigmax = NMdata[[Length[NMdata], 2]]; (*Ult. stress*)
epsrang = epsmax - epsprop; (*strain range*)
sigrang = sigmax - sigprop; (*stress range*)

(*The following executes the curve-
fitting command and derives the model constants;  $k_f$  &  $h_f$ ,
as well as goodness-of-fit parameters*)
NMmod =
  sigprop + sigrang * ((eps - epsprop) / epsrang) ^ (kk * (((eps - epsprop) / epsrang) ^ hh));

```

```

NMfit = NonlinearModelFit[PLdata, NMmod, {kk, hh}, {eps},
  MaxIterations → 1 000 000 000];
du = Normal[NMfit];
NMfit["RSquared"]
NMfit["ParameterConfidenceIntervalTable"]
knm = kk /. NMfit["BestFitParameters"];
hnm = hh /. NMfit["BestFitParameters"];
Print["Knee factor,  $k_f =$ ", 1 / knm]
Print["Heel factor,  $h_f =$ ", 1 / hnm]

(*The following creates superimposed plots of the original stress-
strain data points and the model-approximated curve*)
NMplot =
  Piecewise[{{Ee * eps, eps < (sigprop / Ee)},
    {sigprop + sigrang * ((eps - epsprop) / epsrang) ^
      (knm * (((eps - epsprop) / epsrang) ^ hnm)), eps ≥ (sigprop / Ee)}}];

(*The following performs some of the above-
detailed procedures for approximating the shape of the stress-
strain curve using the Ramberg-Osgood model*)
sigY = 391;
ROdata = Reverse[NMdata, 2];
ROmod = (sig / Ee) + cc * ((sig / sigY) ^ nn);
ROfit = NonlinearModelFit[ROdata, ROmod, {cc, nn}, {sig},
  MaxIterations → 1 000 000 000];
dv = Normal[ROfit];
ROfit["RSquared"]
ROfit["ParameterConfidenceIntervalTable"]
cro = cc /. ROfit["BestFitParameters"];
nro = nn /. ROfit["BestFitParameters"];
Print["C-factor, c = ", cro]
Print["N-factor, n = ", nro]
ROplot = Table[{(sig / Ee) + cro * ((sig / sigY) ^ nro), sig}, {sig, 0, sigmax, 1}];
Plot[NMplot, {eps, 0, epsmax}, Epilog → {PointSize → Medium, Point[NMdata]},
  AxesLabel → {"True Strain", "True Stress"}, PlotRange → All]
ListLinePlot[ROplot, Epilog → {PointSize → Medium, Point[NMdata]},
  AxesLabel → {"True Strain", "True Stress"}, PlotRange → All]

```

Ndubuaku Model

R-squared = 0.999751

	Estimate	Standard Error	Confidence Interval
Out[16]= kk	0.273714	0.0237692	{0.225972, 0.321456}
hh	-0.432764	0.0441852	{-0.521513, -0.344016}

Knee factor, $k_f = 3.65345$

Heel factor, $h_f = -2.31073$

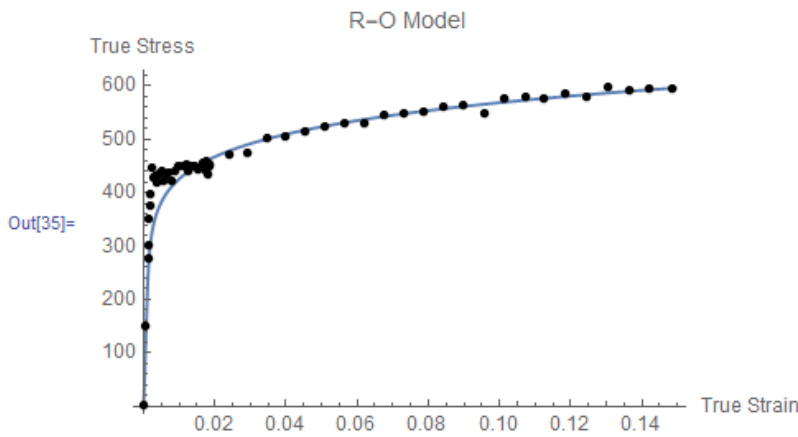
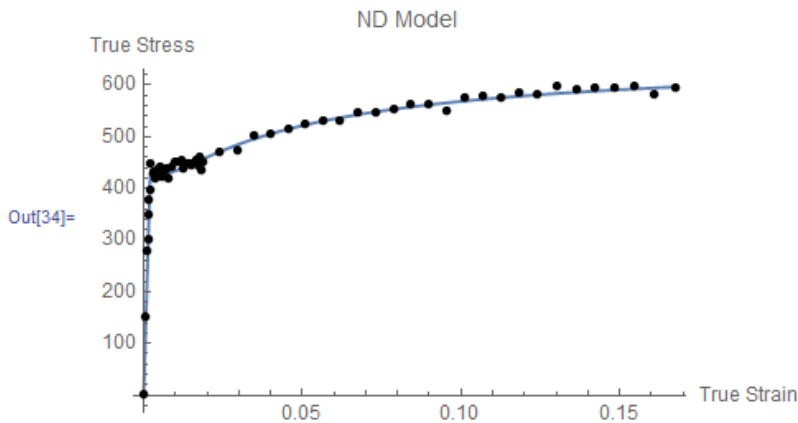
Ramberg-Osgood Model

R-squared = 0.985441

	Estimate	Standard Error	Confidence Interval
Out[28]= cc	0.00380454	0.000515541	{0.00277257, 0.00483651}
nn	8.66015	0.34277	{7.97402, 9.34628}

C-factor, $c = 0.00380454$

N-factor, $n = 8.66015$



RHT Model

(*Young's modulus is inputted here*)

Ee = 203704;

(*The allowable deviation (in percentage) of the proportionality limit point from the linear elastic line is specified here*)

perc = 20;

(*The following implements the linearity deviation technique. This procedure selects the proportionality limit point at the strain value closest to (i.e., greater or less than) the specified linearity deviator value (perc). Validity of the procedure relies on the premise that all successive strains are greater than the strains at each point on the stress-strain curve*)

LinDev[data_] :=

(For[i = 1, And[i ≤ Length[data] - 1,

Abs[(perc / 100) - Abs[(data[[i, 1]] - data[[i, 2]] / Ee) / (data[[i, 2]] / Ee)]] ≥
Abs[(perc / 100) - Abs[(data[[i + 1, 1]] - data[[i + 1, 2]] / Ee) /
(data[[i + 1, 2]] / Ee)]], i = i + 1];

If[i > Length[data] - 1, "N/A", {data[[i, 1]], data[[i, 2]], i}])

(*The experimentally-obtained true stress and true strain data are inputted here*)

**NMdata = {{0.000001, 0.204}, {0.001, 204}, {0.001998, 329}, {0.002996, 374},
{0.003992, 384}, {0.004988, 393}, {0.00995, 406}, {0.019803, 418},
{0.039221, 435}, {0.058269, 450}, {0.076961, 463}, {0.182322, 520}};**

(*The following outputs the PL stress and PL strain*)

prop = LinDev[NMdata];

(*The following value slightly scales up the PL stress and PL strain to prevent indeterminacy issues*)

scale = 1.001;

(*The following truncates the linear elastic portion of the original stress and strain data*)

n = Length[NMdata] - prop[[3]];

PLdata = Table[0, {i, 1, n}];

Do[PLdata[[i]] = NMdata[[i + prop[[3]]]], {i, 1, n}];

PLdata;

PLdata = Prepend[PLdata, scale * {prop[[1]], prop[[2]]}];

(*The following defines reference point inputs for the stress-strain model equation*)

epsprop = prop[[1]]; (*PL strain*)

sigprop = prop[[2]]; (*PL stress*)

epsmax = NMdata[[Length[NMdata], 1]]; (*Ult. strain*)

sigmax = NMdata[[Length[NMdata], 2]]; (*Ult. stress*)

epsrang = epsmax - epsprop; (*strain range*)

```

sigrang = sigmax - sigprop; (*stress range*)
(*The following executes the curve-
fitting command and derives the model constants; kf & hf,
as well as goodness-of-fit parameters*)
NMmod =
  sigprop + sigrang * ((eps - epsprop) / epsrang) ^ (kk * (((eps - epsprop) / epsrang) ^ hh));
NMfit = NonlinearModelFit[PLdata, NMmod, {kk, hh}, {eps},
  MaxIterations → 1 000 000 000];
du = Normal[NMfit];
NMfit["RSquared"]
NMfit["ParameterConfidenceIntervalTable"]
knm = kk /. NMfit["BestFitParameters"];
hnm = hh /. NMfit["BestFitParameters"];
Print["Knee factor, kf = ", 1 / knm]
Print["Heel factor, hf = ", 1 / hnm]
(*The following creates superimposed plots of the original stress-
strain data points and the model-approximated curve*)
NMplot =
  Piecewise[{{Ee * eps, eps < (sigprop / Ee)},
    (sigprop + sigrang * ((eps - epsprop) / epsrang) ^
      (knm * (((eps - epsprop) / epsrang) ^ hnm)), eps ≥ (sigprop / Ee)}}];
(*The following performs some of the above-
detailed procedures for approximating the shape of the stress-
strain curve using the Ramberg-Osgood model*)
sigY = 391;
ROdata = Reverse[NMdata, 2];
ROmod = (sig / Ee) + cc * ((sig / sigY) ^ nn);
ROfit = NonlinearModelFit[ROdata, ROmod, {cc, nn}, {sig},
  MaxIterations → 1 000 000 000];
dv = Normal[ROfit];
ROfit["RSquared"]
ROfit["ParameterConfidenceIntervalTable"]
cro = cc /. ROfit["BestFitParameters"];
nro = nn /. ROfit["BestFitParameters"];
Print["C-factor, c = ", cro]
Print["N-factor, n = ", nro]
ROplot = Table[{{(sig / Ee) + cro * ((sig / sigY) ^ nro), sig}, {sig, 0, sigmax, 1}}];
Plot[NMplot, {eps, 0, epsmax}, Epilog → {PointSize → Medium, Point[NMdata]},
  AxesLabel → {"True Strain", "True Stress"}, PlotRange → All]
ListLinePlot[ROplot, Epilog → {PointSize → Medium, Point[NMdata]},
  AxesLabel → {"True Strain", "True Stress"}, PlotRange → All]

```

Ndubuaku Model

R-squared = 0.999723

	Estimate	Standard Error	Confidence Interval
Out[191]= kk	0.353291	0.0297784	{0.284622, 0.42196}
hh	0.035917	0.0207502	{-0.011933, 0.083767}

Knee factor, $k_f = 2.83053$

Heel factor, $h_f = 27.842$

Ramberg-Osgood Model

R-squared = 0.985771

	Estimate	Standard Error	Confidence Interval
Out[203]= cc	0.0127469	0.00200115	{0.0082881, 0.0172058}
nn	9.35125	0.5982	{8.01837, 10.6841}

C-factor, $c = 0.0127469$

N-factor, $n = 9.35125$

